

nature



ONE YEAR. TEN STORIES.

Ten people who helped shape
science in 2020

366 days in science
The COVID pandemic,
environmental
extremes and more

Solid success
Crossed light beams
power rapid 3D printing
in high resolution

Events directory
The *Nature* guide to
global science events
and courses in 2021

Nature.2020.12.26

[Sat, 26 Dec 2020]

- [Donation](#)
- [2020: the year in review](#)
- [This Week](#)
- [News in Focus](#)
- [Books & Arts](#)
- [Opinion](#)
- [Work](#)
- [Research](#)
- [Amendments & Corrections](#)

Donation

- -> [**打賞 - Donation**](#)

打赏 - JUST FOR FUN

支持分享! 一杯咖啡钱, 打赏金额随意, 感谢大家~:)



本书来自: www.github.com/hehonghui

This article was downloaded by **calibre** from <http://economist.cool/donate.html>

2020: the year in review

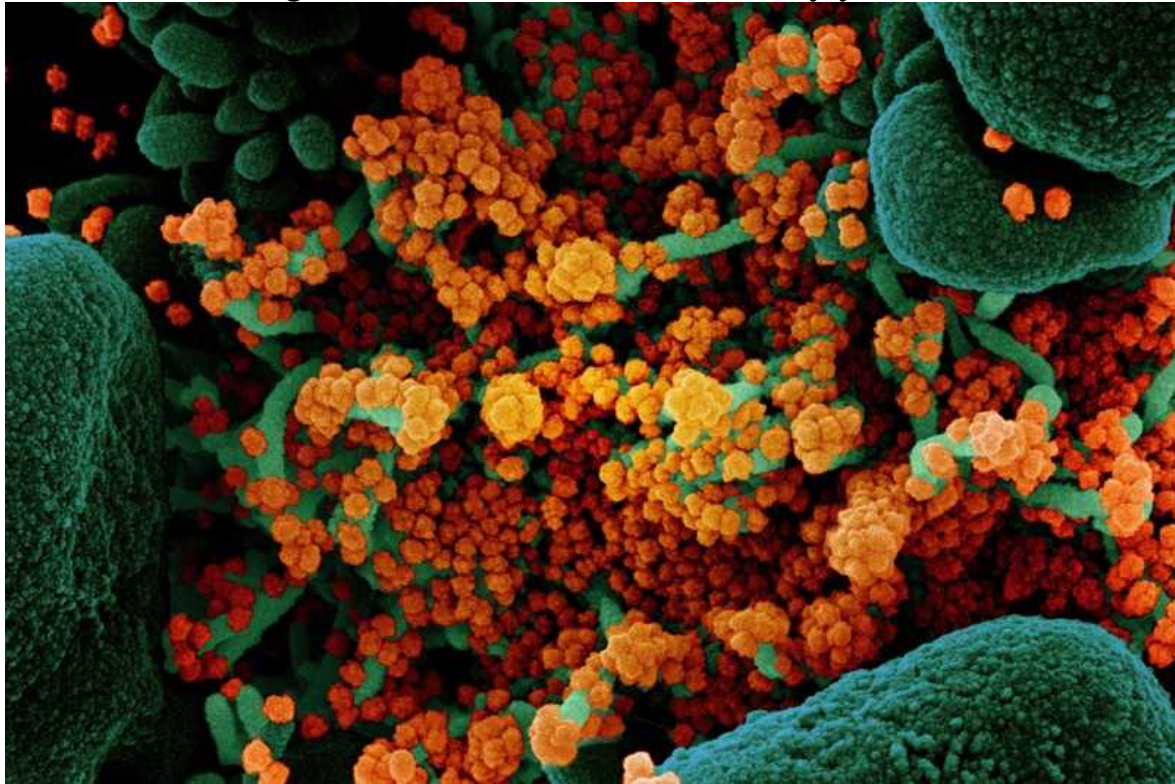
- [**A review of 2020 through Nature's editorials**](#) [22 December 2020]
Editorial • From the COVID pandemic to a momentous US election, Nature's editorials provide a lens through which to view an extraordinary year.
- [**Nature's 10: the human stories behind an extraordinary year in science**](#) [15 December 2020]
Editorial • Ten profiles illustrate an unforgettable year that propelled research teams to the front of the world's stage.
- [**COVID and 2020: An extraordinary year for science**](#) [14 December 2020]
News • The coronavirus pandemic shaped the year in research — from vaccines and treatments to campus shutdowns and virtual meetings.
- [**How a torrent of COVID science changed research publishing — in seven charts**](#) [16 December 2020]
News • A flood of coronavirus research swept websites and journals this year. It changed how and what scientists study, a Nature analysis shows.
- [**2020 beyond COVID: the other science events that shaped the year**](#) [14 December 2020]
News • Mars missions, record-breaking wildfires and a room-temperature superconductor are among this year's top non-COVID stories.
- [**The best science images of 2020**](#) [14 December 2020]
News • A new virus, wafer-thin solar cells, gene-edited squid and more.
- [**Nature's 10: ten people who helped shape science in 2020**](#) [15 December 2020]
News Feature • A COVID vaccine developer, an Arctic voyager and a prime minister are some of the people behind the year's big research stories.
- [**Viruses, microscopy and fast radio bursts: 10 remarkable discoveries from 2020**](#) [14 December 2020]
News & Views • Highlights from News & Views published this year.

EDITORIAL

22 December 2020

A review of 2020 through *Nature*'s editorials

From the COVID pandemic to a momentous US election, *Nature*'s editorials provide a lens through which to view an extraordinary year.



A virus is born: scanning electron micrograph of a dying cell (green) heavily infected with SARS-CoV-2 virus particles (orange), isolated from a patient sample. Credit: NIAID ([CC BY 4.0](#))

Editorials represent *Nature*'s collective voice on the week's news, providing a commentary on a range of topics, from research discoveries to major world events involving science. And although 2020 has been dominated by just one topic, we've aimed to stay on top of other important developments, too.

January: environmental ‘super-year’ ahead

Nature's first editorial of 2020 marked the beginning of what was expected to be a super-year for the environment and sustainable development, with world leaders poised to meet to update their commitments in these areas. Most of the Sustainable Development Goals (SDGs), which were established by the United Nations in 2015, were not on track even before the coronavirus pandemic, and global targets to tackle climate change and reduce biodiversity loss were also behind schedule. We urged nations to [consider mandatory reporting of their progress towards the SDGs](#), as most do for economic data. Research published in *Nature* from a joint US–China team provided [the outlines](#) for such a reporting framework¹.



[Nature's 10: ten people who helped shape science in 2020](#)

Throughout the year, *Nature* continued to publish research and commentary on the SDGs. This included a landmark study showing that, although almost 90% of children are expected to be completing primary school by 2030, only 61% of young adults will be finishing secondary education². We also called

for the [global development goals to be decoupled from economic growth targets](#). And we marked the launch of *Nature Food* with [a tribute to the late Donella Meadows](#), one of the early pioneers of the thinking that led to the SDGs .

February: stop the virus

Nature's [first editorial on the coronavirus](#) appeared on 21 January. By the first week of February, more than 400 people had died and worldwide case numbers had reached 20,000. In two papers in *Nature*, teams led by researchers in China — one group at the Wuhan Institute of Virology, the other at Fudan University in Shanghai — confirmed that the virus is similar to the one that caused severe acute respiratory syndrome (SARS), and reported evidence that it originated in bats. The Wuhan team analysed virus samples from a small number of people, most of whom had worked at the animal market where the first cases were reported to have come from³. The Fudan team sequenced a sample from one infected market worker⁴.

Nature and its publisher, Springer Nature, [signed a joint statement](#) with other publishers, funders and scientific societies to ensure the rapid sharing of research data and findings relevant to the coronavirus. And [we called for international donors to prioritize funding for the least developed countries](#) as nations prepared to tackle the virus.

March: locusts and lockdowns

While all eyes were on the coronavirus outbreak, an under-reported emergency was threatening food, health and jobs in a swathe of countries. Crops in East Africa, the Middle East and south Asia had been devoured by vast swarms of the desert locust *Schistocerca gregaria*. [A potential food crisis loomed](#) for some 20 million people, and we backed a UN appeal for US\$138 million in urgent funding — some of which was earmarked to lease aircraft that could drop chemicals to curb the insects' spread. Later in the year, research helped to illuminate [how locusts are able to congregate in swarms so quickly](#)⁵.



In Kenya, a farmer's daughter tries to chase swarms of desert locusts away from crops. This year's crisis has been the worse some regions have seen in 70 years. Credit: Ben Curtis/AP/Shutterstock

On 11 March, the World Health Organization (WHO) declared the coronavirus, SARS-CoV-2, to be a pandemic. By that point, the virus had reached more than 100 countries and infected some 120,000 people. More than 4,000 had died. Italy had declared a nationwide lockdown. But, worryingly, there were few signs that world leaders were willing to cooperate in efforts to bring the virus to heel. The United States and many European countries were not following the WHO's advice to aggressively test, track and isolate as many cases of COVID-19 as possible. Moreover, the administration of US President Donald Trump had chosen to [sideline the nation's public-health agency](#), the Centers for Disease Control and Prevention, seeking instead to centralize its pandemic response.

Nature urged government science advisers around the world to [publish the evidence on which policy decisions were being based](#), so that data could be scrutinized and policies improved — and so that all nations could defeat the virus on the basis of the best shared evidence.

April: not the time to turn against the WHO

As the virus continued on its destructive path, it became clear that the pandemic was also fuelling racism and discrimination against people of Asian descent around the world. [This, we said, had to stop.](#)



Stop the coronavirus stigma now

And, once again, *Nature* [urged world leaders to reach out and cooperate](#), as tens of thousands in the research community were doing, lending time, ideas, expertise, equipment and money to the emergency public-health effort. But such calls were dealt a hammer blow when Trump announced that the United States, the WHO's largest donor, would [freeze its funding for the agency](#).

In early March, WHO director-general Tedros Adhanom Ghebreyesus had appealed to the world to follow the agency's recommendations, saying, "You can't fight a virus if you don't know where it is. That means robust surveillance to find, isolate, test and treat every case, to break the chains of transmission." But the Trump administration took the view that the agency had acted too slowly and was being too deferential to China — which faced

questions about whether it could have acted more quickly to contain the virus, and been more transparent about the disease's early spread.



Withholding funding from the World Health Organization is wrong and dangerous, and must be reversed

Defunding the world's health agency amid the biggest global health crisis in a century was unthinkable, we said, and [not straightforward to implement](#). It would be especially dangerous for those low-income countries in which the agency's work is crucial to maintaining standards of public-health infrastructure and tackling killer diseases.

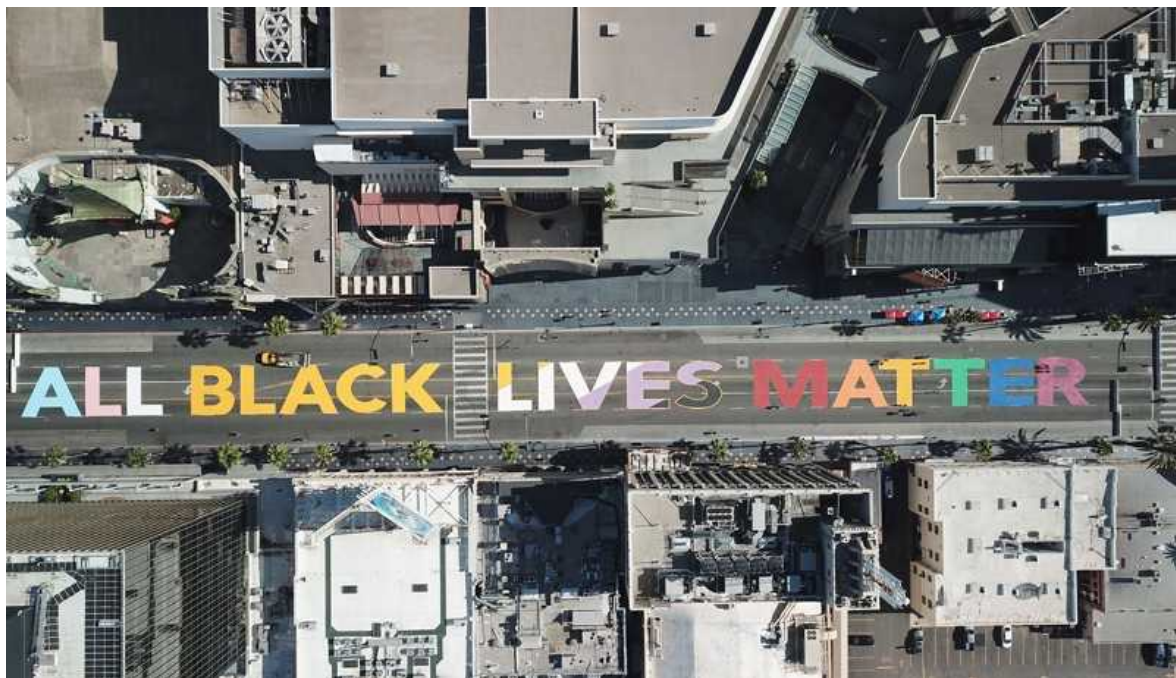
May: misinformation and vaccine hesitancy

The month coincided with an expansion of misleading claims about COVID-19. The [misinformation and disinformation](#), most of which was circulating online, concerned subjects ranging from unproven treatments to scepticism about the safety of the vaccines being developed against COVID-19 because

of the speed at which this research and development was moving. Among other things, [Nature urged transparency](#). We recommended that researchers and companies involved in vaccine development explain what is and isn't known about the virus, and how vaccines are made and work, and warned against over-promising or overselling their products.

June: Black Lives Matter

The killing of Black people in the United States, most notably that of George Floyd at the hands of the Minneapolis Police Department in Minnesota in late May, and Trump's crushing of subsequent protests, angered the world. On 10 June, [Nature joined #ShutDownSTEM](#) #ShutDownAcademia #Strike4BlackLives, an initiative of STEM (science, technology, engineering and mathematics) academics and organizations pausing their normal daily activities to focus on ways to eliminate anti-Black racism.



Hollywood Boulevard in Los Angeles, California, ahead of a march between the LGBTQ+ and Black Lives Matter communities in June. Credit: Robyn Beck/AFP/Getty

[We acknowledged that Nature is among the institutions responsible](#) for the racial bias that exists in research and scholarship, and that we must do more

to correct those injustices, amplify marginalized voices, and be held accountable for these actions. We also committed to producing a special issue of the journal, working with guest editors, to explore systemic racism in research, research policy and publishing, and the part *Nature* has played in that.



COVID and 2020: An extraordinary year for science

One example of such embedded inequities is the story of Henrietta Lacks, a Black woman who died of an aggressive cervical cancer in the United States in 1951. While diagnosing and treating Lacks, doctors took samples of her tumour without her knowledge or consent. When these cells, which were named HeLa, were cultured in the laboratory, they exhibited an extraordinary capacity to survive and reproduce, and they are now widely used in the biological sciences.

In an editorial [commemorating the centenary of Lacks's birth](#), we urged the relevant authorities to put stronger rules in place to govern the use of these precious specimens. And we called for consent to be obtained from anyone

who has had biological specimens taken before the samples are used in research.

The Lacks family was also keen for people to know about Lacks as a person. To Alfred Lacks Carter, one of her grandsons, the most important thing about HeLa cells is the contributions they have made to cancer research. “They were taken in a bad way but they are doing good for the world,” he told *Nature*.

July: mitochondria and missions to Mars

As funding agencies reassessed their priorities, a *Nature* paper gave a much-needed boost to the value of foundational research. Researchers at the University of Washington in Seattle and their colleagues [detailed their use of an exceptional enzyme](#) to edit the genomes of energy-generating cell structures called mitochondria⁶. That the team had embarked on the work with an entirely different goal in mind added to the significance of the achievement.

And, amid the coronavirus pandemic and raging geopolitical tensions, three long-planned [Mars missions finally got off the ground](#). The latest US rover, and orbiters designed by China and the United Arab Emirates — the first Arab nation to launch an interplanetary mission — offered a powerful symbol of how efforts to explore other worlds give nations the opportunity to transcend their Earthly woes, we wrote.

August: an anti-nuclear dawn

August marks an inauspicious anniversary for science, that of the first — and, so far, only — deployment of nuclear weapons in war. But 75 years on from the bombing of Japan on 6 and 9 August 1945, [a new international treaty](#) on the prohibition of nuclear weapons was on the table (this is set to become international law in January 2021). The treaty’s architects, the International Campaign to Abolish Nuclear Weapons, urged more scientists to play a part in helping it to succeed — a call that *Nature* supported.



Researchers: help free the world of nuclear weapons

A formal scientific advisory mechanism is yet to be established for the treaty, so setting up a global network of researchers with knowledge of various aspects of nuclear science and technology is an urgent outstanding task. The world's nuclear arsenal is alarmingly large, comprising an estimated 1,335 tonnes of highly enriched uranium and 13,410 warheads. Some 90% of these are in the United States and Russia.

September: postdocs in crisis

Nature's first-ever survey of postdoctoral researchers showed the extent to which the pandemic is hurting science's workforce. Half of the 7,670 respondents — a self-selecting sample, based mostly in Europe and North America, and covering 19 disciplines — revealed that they were [considering leaving academic research because of work-related mental-health concerns](#). Funders responded to coronavirus-related laboratory shutdowns by extending research-project deadlines, but there were few offers of extra funding.



Postdocs in crisis: science cannot risk losing the next generation

In two editorials, *Nature* called for postdocs to be funded through deadline extensions, because many have no other source of income. Some funders said that universities could step in to support postdocs — despite the fact that [institutions in many countries are not being given additional funds](#) to deal with the pandemic. It spells trouble for knowledge, discovery and invention if so many people are concluding that they have no future in academic research.

October: it has to be Biden

“We cannot stand by and let science be undermined. Joe Biden’s trust in truth, evidence, science and democracy make him the only choice in the US election.” So began *Nature*’s editorial less than three weeks before the presidential election of 3 November. *Nature*, along with colleagues across science and research publishing, [endorsed Biden](#). Since the election, [we have urged the incoming administration to follow through on Biden’s](#)

[promises](#) to restore science and evidence to policymaking, starting with [rebuilding the Environmental Protection Agency](#).



US presidential candidate Joe Biden talking to reporters in October, ahead of the November election.Credit: Brendan Smialowski/AFP/Getty

Following the Trump administration's relentless and high-profile attacks on science — and the politicization of the pandemic and threats to scholarly autonomy around the world — the journal [pledged to cover more politics news, commentary and primary research](#).

November: the ethics of facial recognition

Nature reported, in a series of Features, the increasing concerns of researchers in the field of facial-recognition technology about how the technology is being used, for example by governments and law-enforcement agencies. Some researchers, as our editorial highlighted, are rightly joining campaigners in [calling for greater regulation and transparency](#), as well as for communities that are being monitored by cameras to be consulted — and for

use of the technology to be suspended until lawmakers have reconsidered where and how it should be used. There might well be benefits to the technology, but these must be assessed against the risks, making proper regulation essential, we argued.

December: vaccines are coming

COVID-19 vaccine roll-outs began in the United Kingdom, Canada and the United States after the first emergency-use authorizations were granted in these countries. Vaccines are in use in Russia and China, too — and [China is also supplying other countries](#). But global coordination is still lacking, with countries conducting approvals according to different criteria, and with the wealthiest procuring the majority of early orders.



A health worker prepares to inoculate a trial volunteer with a COVID-19 vaccine produced by the Chinese company Sinopharm. Credit: Ernesto Benavides/AFP/Getty

We revived the long-standing question of [how the harmonization of vaccine regulation might be accelerated](#). A review of the regulatory landscape established that, across 24 countries, there are at least 51 pathways to various types of accelerated vaccine approval⁷.

Greater harmonization offers many benefits, we argued, but would also require companies to allow the creation of — or help to create — a secure means of sharing data for regulators, many of whom are not currently permitted to do this. If regulators all had access to the same data, it would be easier for them to compare their findings and analyses with those of others. Their decisions would be more robust and that, in turn, would shore up public confidence in immunization.

One year after the first known case of coronavirus infection, this pandemic, which has killed more than 1.7 million people, could, we hope, be coming to an end at last.

Nature **588**, 537-538 (2020)

doi: <https://doi.org/10.1038/d41586-020-03560-2>

References

1. 1.

Xu, Z. *et al.* Nature **577**, 74–78 (2020).

2. 2.

Friedman, J. *et al.* Nature **580**, 636–639 (2020).

3. 3.

Zhou, P. *et al.* Nature **579**, 270–273 (2020).

4. 4.

Wu, F. *et al.* Nature **579**, 265–269 (2020).

5. 5.

Guo, X. *et al. Nature* **584**, 584–588 (2020).

6. 6.

Mok, B. Y. *et al. Nature* **583**, 631–637 (2020).

7. 7.

Simpson, S., Chakrabarti, A., Robinson, D., Chirgwin, K. & Lumpkin, M. *npj Vaccines* **5**, 101 (2020).

Jobs from Nature Careers

- - - [All jobs](#)
 - - [Full Professorship for Translational Imaging in Oncology \(W3\)](#)

[German Cancer Research Center in the Helmholtz Association \(DKFZ\)](#)

[Dresden, Germany](#)

[JOB POST](#)
 - [MSc Position in Forest Research](#)

[The University of British Columbia \(UBC\)](#)

[Vancouver, Canada](#)

[JOB POST](#)

- **Research Associate - zero-emission hydrogen production project**

The University of British Columbia (UBC)

Vancouver, Canada

JOB POST

- **Laboratory Manager - Zamore Lab**

Howard Hughes Medical Institute (HHMI)

Worcester, United States

JOB POST

This article was downloaded by **calibre** from <https://www.nature.com/articles/d41586-020-03560-2>

| [Section menu](#) | [Main menu](#) |

EDITORIAL

15 December 2020

Nature's 10: the human stories behind an extraordinary year in science

Ten profiles illustrate an unforgettable year that propelled research teams to the front of the world's stage.



Nature's 10 is this journal's annual list of ten people who helped to shape science in a given year. They might have been involved in making noteworthy discoveries, brought attention to crucial issues or gained notoriety for controversial actions. It is explicitly not an award or a ranking. Instead, it's a way to highlight key events in the world of science through the compelling, human stories of those involved.

Most of the stories we feature in this extraordinary year have a connection to the pandemic that has already killed more than 1.5 million people and continues to grow.



Nature's 10: ten people who helped shape science in 2020

The [people in Nature's 10](#) raced to identify the rapidly spreading coronavirus; warned of its dangers; and developed the first vaccines in record time. Beyond the pandemic, researchers continued to make progress studying Earth's precarious climate. They also worked to combat racism and battled against other diseases that exact large tolls, especially in countries with limited resources.

Some might argue that picking one individual involved in a major advance fails to give due credit to the others who had valuable roles in that same work, especially today, when almost all research is done by collaborative teams. Picking a big name in a field can also risk seeming to elevate the influential over those with less power.

We are aware that this list risks being seen as exclusive or creating the wrong perception that these individuals are the most important people in science. So we have worked hard to address these potential concerns.

This year's *Nature*'s 10 includes a range of people from around the world. Some hail from countries that are too often overlooked by the global media. Some are at relatively early stages in their careers. And the stories highlight the contributions of many researchers, emphasizing that no advance is the work of one person.

That science is teamwork is especially clear this year. The pandemic has touched every person on the planet. And many researchers have joined the effort to combat the threat, sometimes forging new collaborations and exploring fields far from their normal work.

By telling the stories of individuals in *Nature*'s 10, we are simultaneously chronicling the collective efforts of scientists around the globe as they continue on their journey of discovery, invention and innovation.

Nature **588**, 538 (2020)

doi: <https://doi.org/10.1038/d41586-020-03551-3>

Jobs from Nature Careers

- - - [All jobs](#)
 -
 - [Full Professorship for Translational Imaging in Oncology \(W3\)](#)
 - [German Cancer Research Center in the Helmholtz Association \(DKFZ\)](#)
 - [Dresden, Germany](#)

JOB POST

- **MSc Position in Forest Research**

The University of British Columbia (UBC)

Vancouver, Canada

JOB POST

- **Research Associate - zero-emission hydrogen production project**

The University of British Columbia (UBC)

Vancouver, Canada

JOB POST

- **Laboratory Manager - Zamore Lab**

Howard Hughes Medical Institute (HHMI)

Worcester, United States

JOB POST

This article was downloaded by **calibre** from <https://www.nature.com/articles/d41586-020-03551-3>

| [Next](#) | [Section menu](#) | [Main menu](#) | [Previous](#) |

This article was downloaded by **calibre** from <https://www.nature.com/articles/d41586-020-03437-4>

| [Section menu](#) | [Main menu](#) |

NEWS

16 December 2020

- Clarification [17 December 2020](#)

How a torrent of COVID science changed research publishing — in seven charts

A flood of coronavirus research swept websites and journals this year. It changed how and what scientists study, a *Nature* analysis shows.

Holly Else

Search for this author in:

- [Pub Med](#)
- [Nature.com](#)
- [Google Scholar](#)

The COVID-19 pandemic [disrupted science in 2020](#) — and transformed research publishing, show data collated and analysed by *Nature*.

Around 4% of the world's research output was devoted to the coronavirus in 2020, according to one database. But 2020 also saw a sharp increase in articles on all subjects being submitted to scientific journals — perhaps because many researchers had to stay at home and focus on writing up papers rather than conducting science.

Submissions to publisher Elsevier's journals alone were up by around 270,000 — or 58% — between February and May when compared with the

same period in 2019, one analysis found¹. The increase was even higher for health and medicine titles, at a whopping 92%.

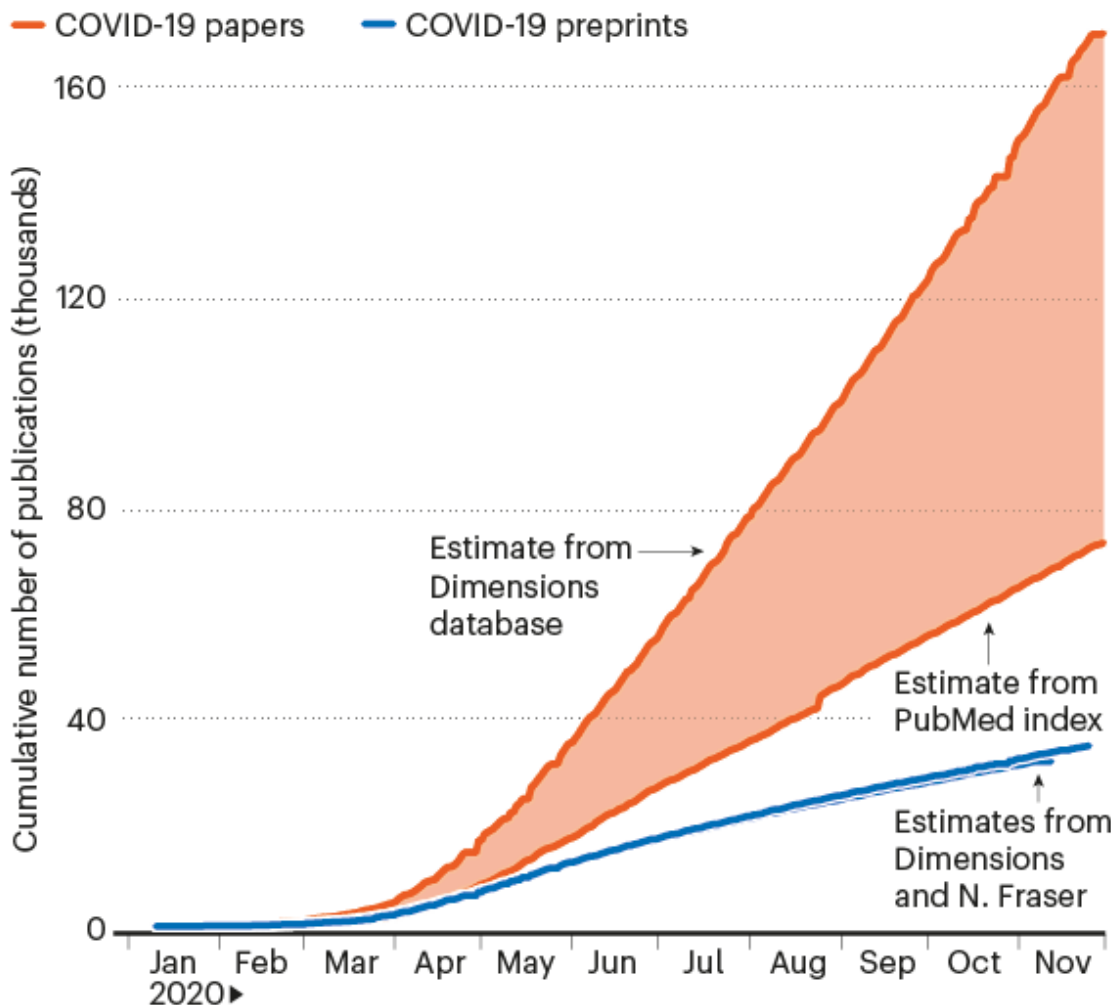
The pandemic also fuelled a sharp rise in sharing through preprints (articles posted online before peer review), advanced the output of male authors over female authors and affected review times — speeding them up in some topics but slowing them down in others.

COVID torrent

Scientists published well over 100,000 articles about the coronavirus pandemic in 2020. By one count, from the [Dimensions database](#), they might even have passed 200,000 by early December (see ‘Coronavirus cascade’). (Estimates differ depending on search terms, database coverage and definitions of a scientific article.) More than 4% of articles listed in the Dimensions database this year are COVID-related, and around 6% of those indexed in PubMed, which mostly covers life sciences, were dedicated to the topic.

CORONAVIRUS CASCADE

One estimate suggests that more than 200,000 coronavirus-related journal articles and preprints had been published by early December.



*Estimates differ depending on search terms, database coverage, and definitions of what counts as a scientific article; some preprints were posted on multiple sites online.

©nature

Sources: *Journal papers*: Dimensions & *Nature* tabulations; [Primer](#) (for PubMed estimate); *Preprints*: Dimensions; N. Fraser & B. Kramer
<https://doi.org/10.6084/m9.figshare.12033672> (2020)

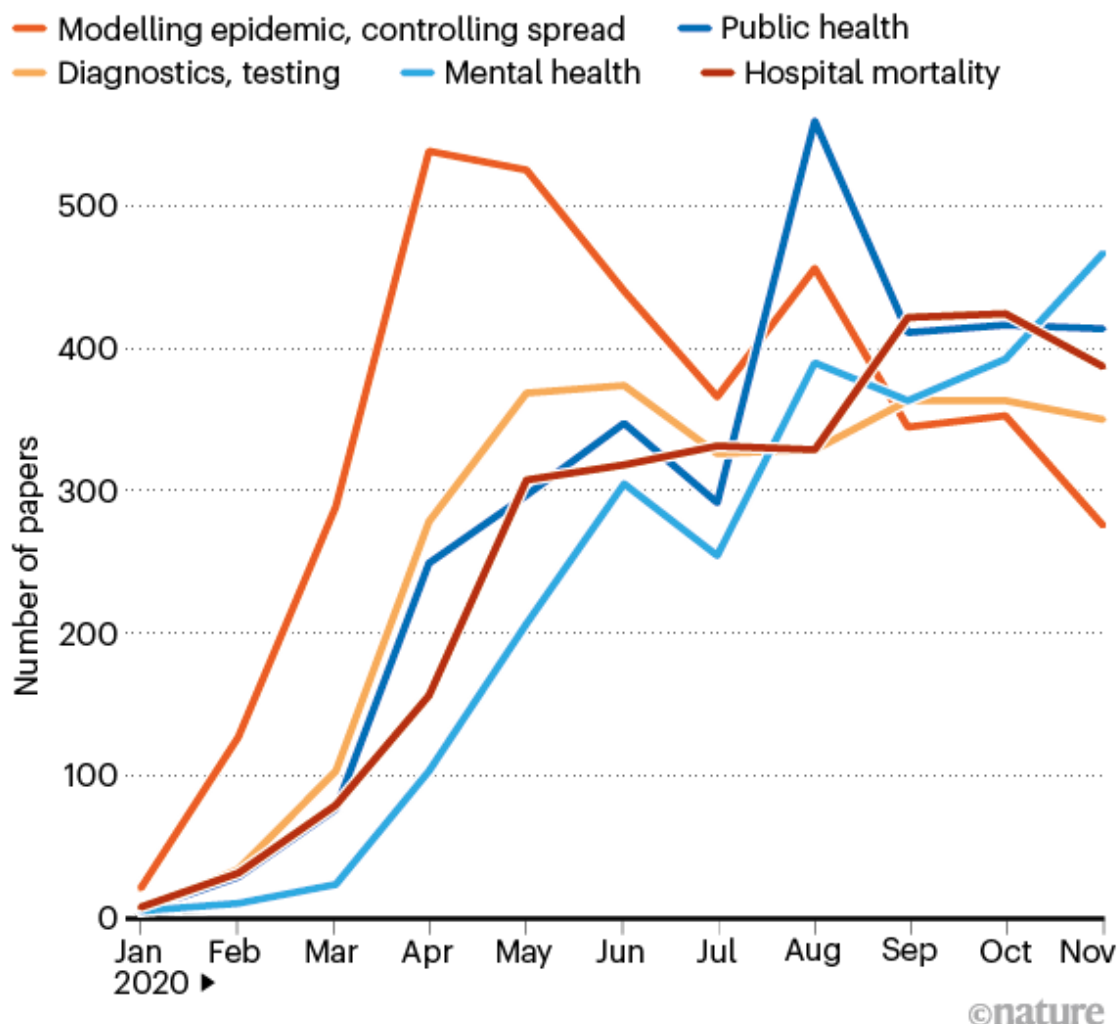
From disease spread to mental health

At first, COVID-19 papers (and preprints) focused on the spread of disease, the outcomes for people hospitalized, and diagnostics and testing, according

to an analysis of the topics of PubMed-indexed articles by [Primer](#), a company in San Francisco, California, that develops artificial-intelligence (AI) technologies. But these kinds of paper mostly plateaued after May (see ‘Coronavirus paper topics’), and there has been growing interest in mental-health research, notes Zein Tawil, a researcher at the company.

CORONAVIRUS PAPER TOPICS

After an early focus on modelling the spread of the pandemic, researchers are now turning to other topics, an analysis of PubMed papers and preprints suggests.



Source: Primer

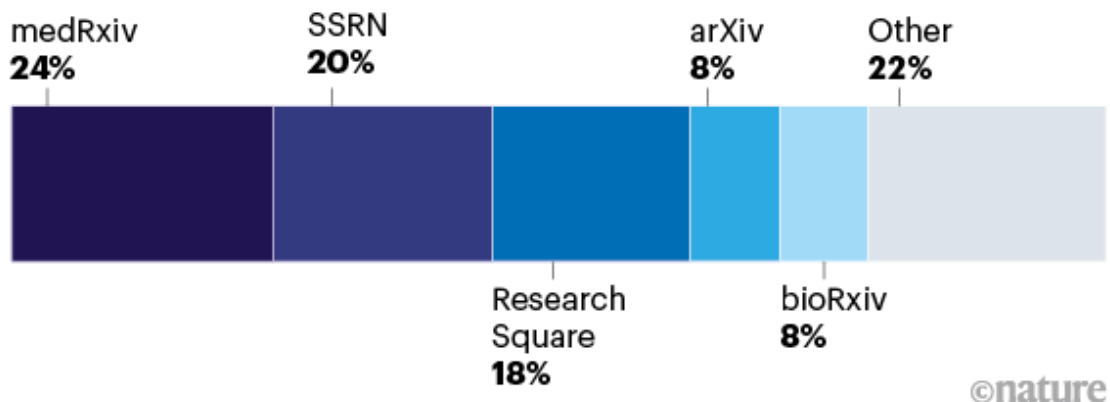
Preprint rush

More than 30,000 of the COVID-19 articles published in 2020 were preprints — between 17% and 30% of total COVID-19 research papers (depending on database searched). And, according to Dimensions, one-tenth of all preprints this year were about COVID-19.

More than half of the preprints appeared on one of three sites — medRxiv, SSRN and Research Square (see ‘Coronavirus preprints’).

CORONAVIRUS PREPRINTS

More than half of preprints appeared on medRxiv, SSRN or Research Square.



©nature

Source: Dimensions

And more than two-thirds of all the preprints posted on medRxiv, which only launched in June last year, were about COVID-19 (see ‘MedRxiv growth’). By early December, almost one-quarter of medRxiv’s COVID-related preprints had gone on to be published in journals, says John Inglis, co-founder of medRxiv and bioRxiv and executive director of Cold Spring Harbor Laboratory Press in New York.

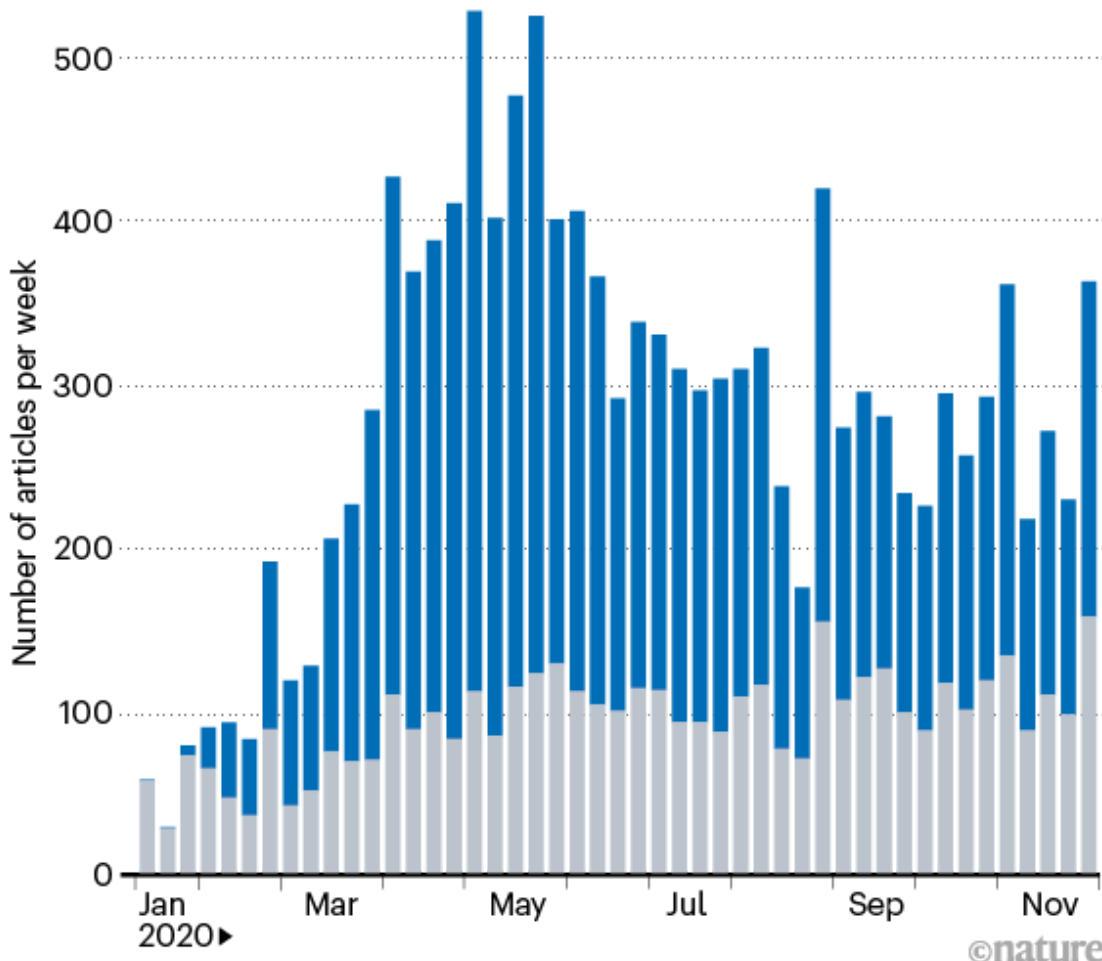
“This has been a pivotal year for preprints,” Inglis says, especially as clinicians have become aware of medRxiv. “We anticipate more momentum for preprints across the board in 2021 as enthusiasm for early sharing gathers pace,” he says.

MEDRXIV GROWTH

More than two-thirds of the preprints at medRxiv were related to COVID-19.

medRxiv submissions

COVID-19 papers Other papers



Source: J. Inglis, medRxiv.

Speedy review

Journals rushed to get COVID-19 articles through peer review. MedRxiv COVID-19 preprints appeared in peer-reviewed journals after a median review time of 72 days, twice as fast as preprints from the server on other topics, says Inglis. He gives credit to journal editors and publishers for pushing their peer-review systems to work faster, and scientists for agreeing to review many more papers than usual.

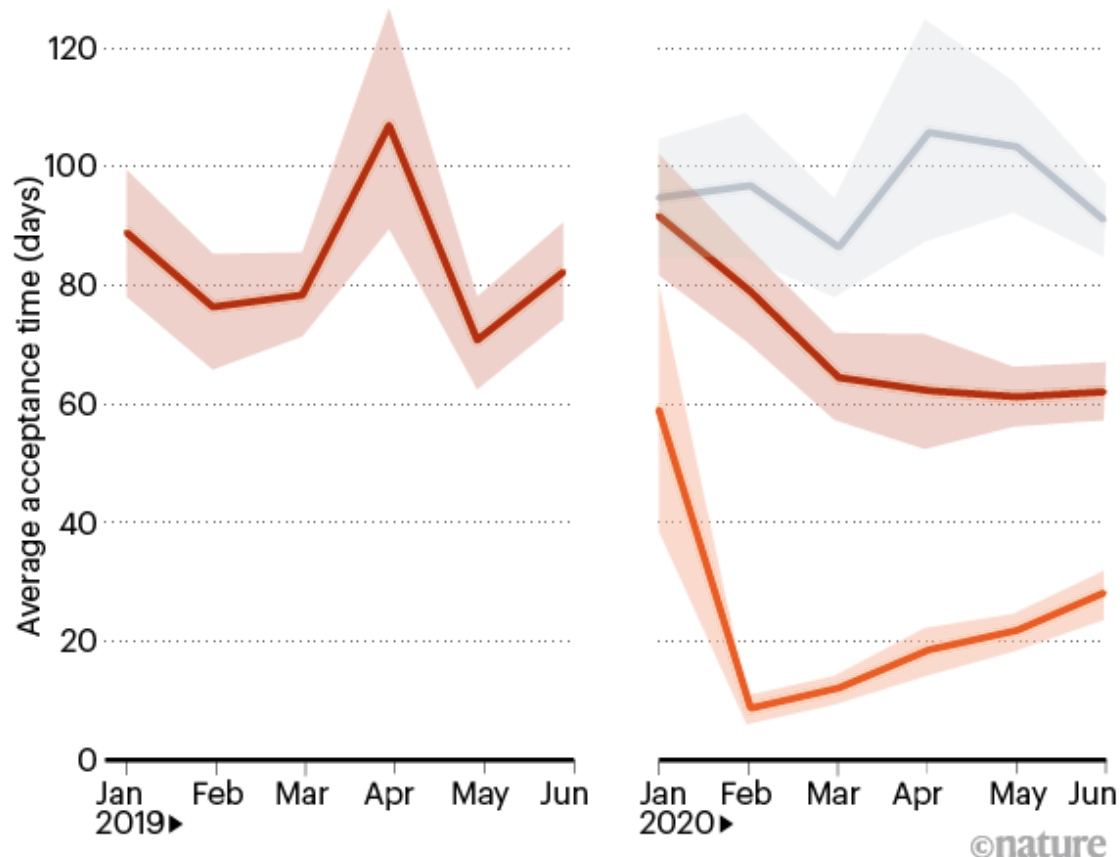
A study of 11 medical journals in the first half of the year found that they published coronavirus papers much faster than normal, but at the expense of publishing other research more slowly² (see ‘Faster review at medical journals’).

FASTER REVIEW AT MEDICAL JOURNALS

COVID-related publications were peer reviewed quickly at 11 medical journals — but other research took longer than usual to be published.

Publications:

— Total — COVID-19 — Non-COVID-19



Source: ref. 2

“The need for speed has put considerable pressure on typical peer-review systems that will be hard to sustain,” Inglis says. He adds that pandemic-related preprints published in the first quarter of 2020 appeared in journals more rapidly than those published later, which might be evidence of strain in the system. It’s possible, he says, that the events of this year will add

momentum to new ways of conducting peer review after results have been disseminated as preprints.

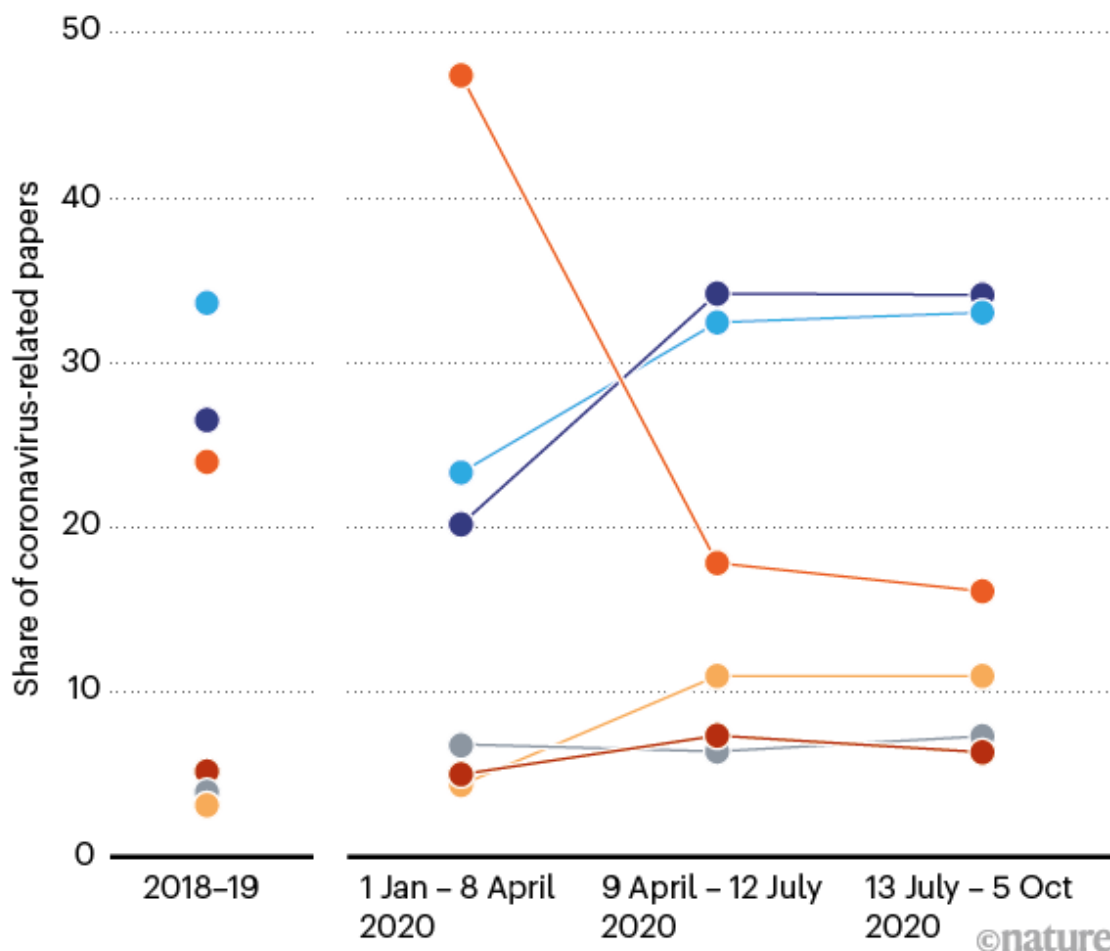
China surge

The contributions that scientists made to the research effort seemed to trace the virus's path around the world, according to one analysis of published papers³. Articles about COVID-19 with authors in China peaked early in the year (see 'Coronavirus papers by country'). And as the virus moved to ravage Italy, the number of papers from scientists there swelled.

CORONAVIRUS PAPERS BY COUNTRY

China had authors on almost half of COVID-19 papers in the year's first quarter.

● China ● United States ● Europe ● United Kingdom ● Italy ● India



Source: ref. 3

Most-cited research

One of the first papers about COVID-19 to appear in the literature — a 24 January publication in *The Lancet* about 41 people hospitalized in Wuhan, China⁴ — is the most cited. And the most-cited preprint⁵ — a 16 March report from pandemic modellers at Imperial College London that estimated how lockdown and other distancing measures could avert millions of deaths — had [a significant effect on UK policy and made worldwide headlines.](#)

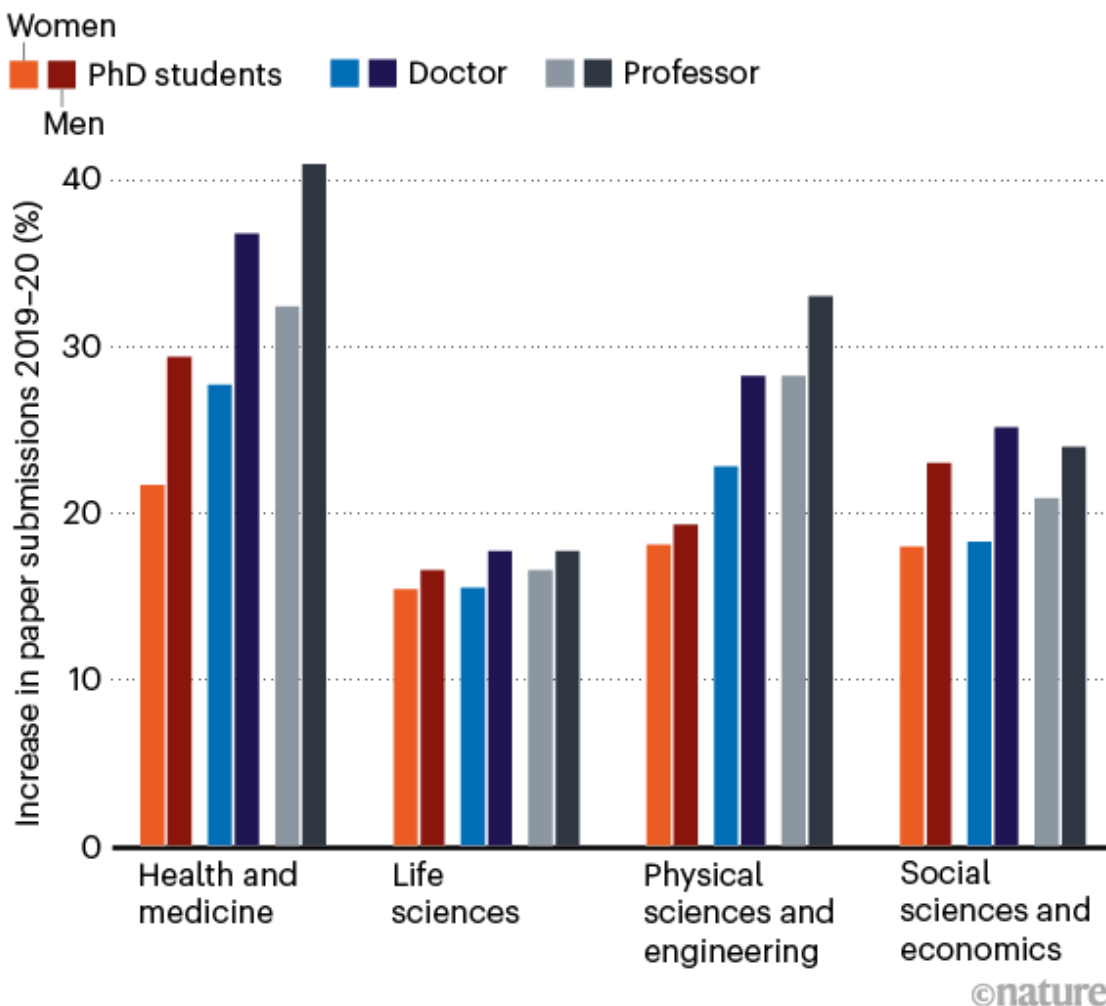
That preprint is also the article that attracted the most buzz on social media, according to Altmetric, a London-based firm that monitors metrics other than citations. (Second was a 2005 paper that suggested that the anti-malaria drug chloroquine inhibited the coronavirus that caused severe acute respiratory syndrome (SARS) in laboratory samples⁶, and a paper that argued that the coronavirus SARS-CoV-2 didn't emerge from a laboratory was third⁷.)

Unequal burden

The pandemic publishing frenzy had winners and losers. Although researchers submitted more papers to journals than last year, on average, growth in submissions from female authors trailed behind growth from male authors across all subject areas, and senior women saw the largest paper penalty (see ‘Lower rates’), according to the analysis of hundreds of thousands of articles sent to Elsevier journals between February and May¹.

LOWER RATES

An analysis of papers submitted to Elsevier journals between February and May found that all scientists sent in more papers, on average, but the growth in submissions from male authors was highest.



Source: ref. 1

This is probably because women shouldered the burden of childcare and home-schooling during lockdowns, says Flaminio Squazzoni, a social scientist at the University of Milan, Italy, who co-authored the preprint analysis. The same effect was not seen in peer review, where men and women received and accepted invitations to evaluate papers at around the same rate.

“The pandemic has given incredible opportunities for researchers but it has also been a shock to the academic system, with an explosion of publications and citations for COVID-19 papers. This is distorting the rewards of science. We need to make sure these things are taken into account when promoting and hiring in the years ahead,” says Squazzoni.

COVID retractions

There were also research-publishing scandals. Some high-profile articles on COVID-19 were retracted, including [studies that relied on electronic health records from Surgisphere in Chicago, Illinois](#) — which were thrown into doubt after the company said it wouldn’t let anyone else see the health data for auditing. In total, 15 preprints and 24 journal papers on COVID-19 had been withdrawn or retracted by December, [according to the site Retraction Watch](#). (Five other papers have been ‘temporarily retracted’; five more have expressions of concern.) Given the volume of coronavirus research, that proportion is about the same as for research in general.

It is too soon to tell whether COVID-19 papers are any more likely than others to be retracted, says Ivan Oransky, a journalist in New York City who co-founded Retraction Watch. Typically, it takes three years for editors to retract a paper, but during the pandemic it has taken just months — in part because these papers are facing so much scrutiny. “Retractions are a proxy for attention perhaps more than anything else,” says Oransky.

Nature **588**, 553 (2020)

doi: <https://doi.org/10.1038/d41586-020-03564-y>

Updates & Corrections

- **Clarification 17 December 2020:** This story now notes that preprints were posted on multiple sites, so estimates may represent slight overcounts.

References

1. 1.

Squazzoni, F. *et al.* Preprint at SSRN
<http://doi.org/10.2139/ssrn.3712813> (2020).

2. 2.

Aviv-Reuven, S. & Rosenfeld, A. Preprint at
<https://arxiv.org/abs/2010.02594> (2020).

3. 3.

Cai, X., Fry, C. V. & Wagner, C. Preprint at SSRN
<https://doi.org/10.2139/ssrn.3729672> (2020).

4. 4.

Huang, C. *et al.* *Lancet* **395**, 497–506 (2020).

5. 5.

Ferguson, N. M. *et al.* Preprint at Spiral <https://doi.org/10.25561/77482> (2020).

6. 6.

Vincent, M. J. *et al.* *Virology J.* **2**, 69 (2005).

7. 7.

Andersen, K. G., Rambaut, A., Lipkin, W. I., Holmes, E. C. & Garry, R. F. *Nature Med.* **26**, 450–452 (2020).

Jobs from Nature Careers

- - - [All jobs](#)
 -

- **Full Professorship for Translational Imaging in Oncology (W3)**

German Cancer Research Center in the Helmholtz Association (DKFZ)

Dresden, Germany

JOB POST

- **MSc Position in Forest Research**

The University of British Columbia (UBC)

Vancouver, Canada

JOB POST

- **Research Associate - zero-emission hydrogen production project**

The University of British Columbia (UBC)

Vancouver, Canada

JOB POST

- **Laboratory Manager - Zamore Lab**

Howard Hughes Medical Institute (HHMI)

Worcester, United States

JOB POST

| [Section menu](#) | [Main menu](#) |

| [Next](#) | [Section menu](#) | [Main menu](#) | [Previous](#) |

This article was downloaded by **calibre** from <https://www.nature.com/articles/d41586-020-03438-3>

| [Section menu](#) | [Main menu](#) |

| [Next](#) | [Section menu](#) | [Main menu](#) | [Previous](#) |

This article was downloaded by **calibre** from <https://www.nature.com/articles/d41586-020-03436-5>

| [Section menu](#) | [Main menu](#) |

| [Next](#) | [Section menu](#) | [Main menu](#) | [Previous](#) |

This article was downloaded by **calibre** from <https://www.nature.com/articles/d41586-020-03435-6>

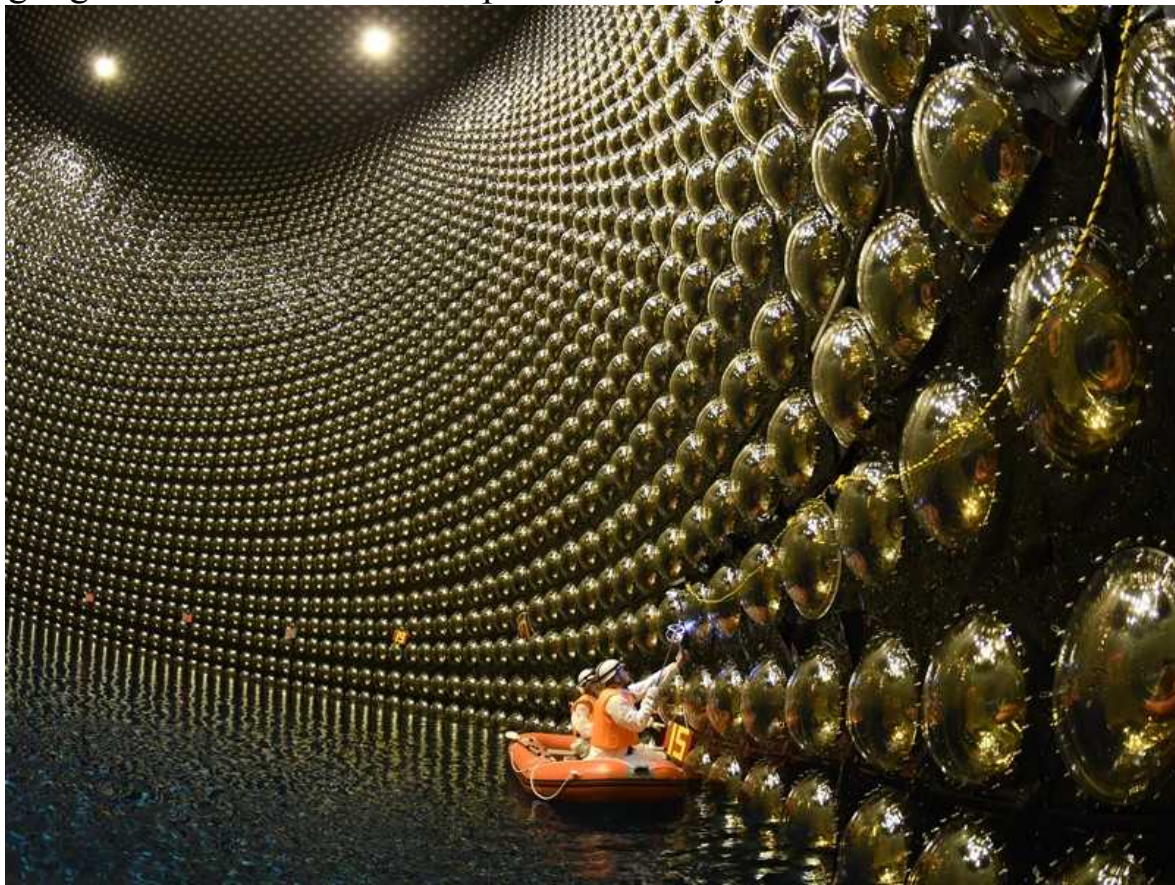
| [Section menu](#) | [Main menu](#) |

NEWS AND VIEWS

14 December 2020

Viruses, microscopy and fast radio bursts: 10 remarkable discoveries from 2020

Highlights from News & Views published this year.



Credit: Kamioka Observatory/Institute for Cosmic Ray Research/The University of Tokyo

Matter–antimatter symmetry violated — Silvia Pascoli and Jessica Turner

The T2K Collaboration reports possible findings of the violation of particle–antiparticle mirror symmetry (also known as CP symmetry) by particles from the lepton group. Leptonic CP violation can be searched for using neutrinos. Neutrinos come in three ‘flavours’ determined by their associated charged lepton (an electron, a muon or a tau particle), and can change from one flavour to another as they travel. If CP symmetry is conserved, the oscillation probability for muon-to-electron neutrino conversion would be the same as that for muon-to-electron antineutrino conversion. In the T2K experiment, neutrinos (or antineutrinos) that have travelled 295 kilometres through Earth are detected by the underground detector at the Kamioka Observatory in Japan (pictured). The experiment measures the oscillation probability of muon-to-electron neutrino conversion. The results exclude CP conservation at a 95% confidence level, and could be the first indications of the origin of the matter–antimatter asymmetry in our Universe. *Original research: [Nature 580](#), 339–344 (2020).*

Jet stream stops shifting as ozone layer recovers — Alexey Yu. Karpechko

The discovery of a hole in the springtime atmospheric ozone layer over the Antarctic in the mid-1980s revealed the threat posed by human-made ozone-depleting substances (ODSs). The Antarctic ozone hole, which resides at altitudes of around 10–20 kilometres, has also affected atmospheric circulation all the way down to the surface in the Southern Hemisphere — most notably, by shifting the summertime jet stream polewards. The production and use of ODSs was banned by the Montreal Protocol of 1987 and its subsequent amendments. Atmospheric ODS concentrations are therefore decreasing, and the first signs of ozone-layer recovery have emerged. Banerjee *et al.* report that the hole-associated circulation effects have paused since ozone recovery started. A cessation of the circulation trends has been noted previously, but Banerjee and colleagues are the first to formally attribute it to the effects of the Montreal Protocol. *Original research: [Nature 579](#), 544–548 (2020).*



Credit: Ken Williams

Incest uncovered at elite prehistoric Irish burial site — Alison Sheridan

Cassidy *et al.* examined the social structures of farming communities, focusing on the people buried in passage tombs. The most famous Irish passage tomb is the enormous monument at Newgrange (pictured). It was built using sophisticated engineering to ensure that, at the end of a long, stone-lined passage, a burial chamber is lit up by the rays of the rising Sun on the shortest day of the year. Ancient DNA from human remains found there reveals a rare and unexpected incidence of incest. A man buried in the chamber of Newgrange around 5,000 years ago was the offspring of a first-degree incestuous union: his parents were either siblings or parent and child. This finding led the team to speculate that the elite associated with this

magnificent monument practised incest as a way of maintaining a dynastic bloodline. *Original research: [Nature 582](#), 384–388 (2020)*.

Satellites could soon map every tree on Earth — Niall P. Hanan and Julius Y. Anchang

Brandt *et al.* report their analysis of high-resolution satellite images covering more than 1.3 million square kilometres of the western Sahara and Sahel regions of West Africa. The authors mapped the location and size of around 1.8 billion individual tree canopies; never before have trees been mapped at this level of detail across such a large area. Commercial satellites have begun to collect data capable of capturing ground objects measuring one square metre or less. This places the field of terrestrial remote sensing on the threshold of a fundamental leap forward: from focusing on aggregate landscape-scale measurements to having the potential to map the location and canopy size of every tree over large regional or global scales. This advance will undoubtedly drive fundamental changes in how we think about, monitor, model and manage global terrestrial ecosystems. *Original research: [Nature 587](#), 78–82 (2020)*.

Latent HIV gets a shock — Mathias Lichterfeld

HIV can hide out in a ‘latent’ form in viral-reservoir cells, undergoing little or no transcription and thus remaining undetected by the immune system. ‘Shock and kill’ treatments aim to reverse this latency and increase viral gene expression (shock), rendering the viral-reservoir cells vulnerable to elimination (kill) by the immune system. Two groups describe interventions in animal models that cause perhaps the most robust and reproducible shock reported so far. Nixon and colleagues used a drug called AZD5582, which can activate the transcription factor NF- κ B — a major instigator of HIV-1 gene expression. McBrien *et al.* combined two immunological interventions — antibody-mediated depletion of CD8 $^{+}$ T cells (immune cells that reduce levels of viral transcription) and treatment with a drug called N-803 that activates HIV-1 transcription. In addition to the advances they make, the studies showcase the conceptual and technical challenges associated with

pharmacological latency reversal. *Original research: [Nature 578](#), 154–159 (2020); [Nature 578](#), 160–165 (2020).*



Credit: Benjamin Fabian

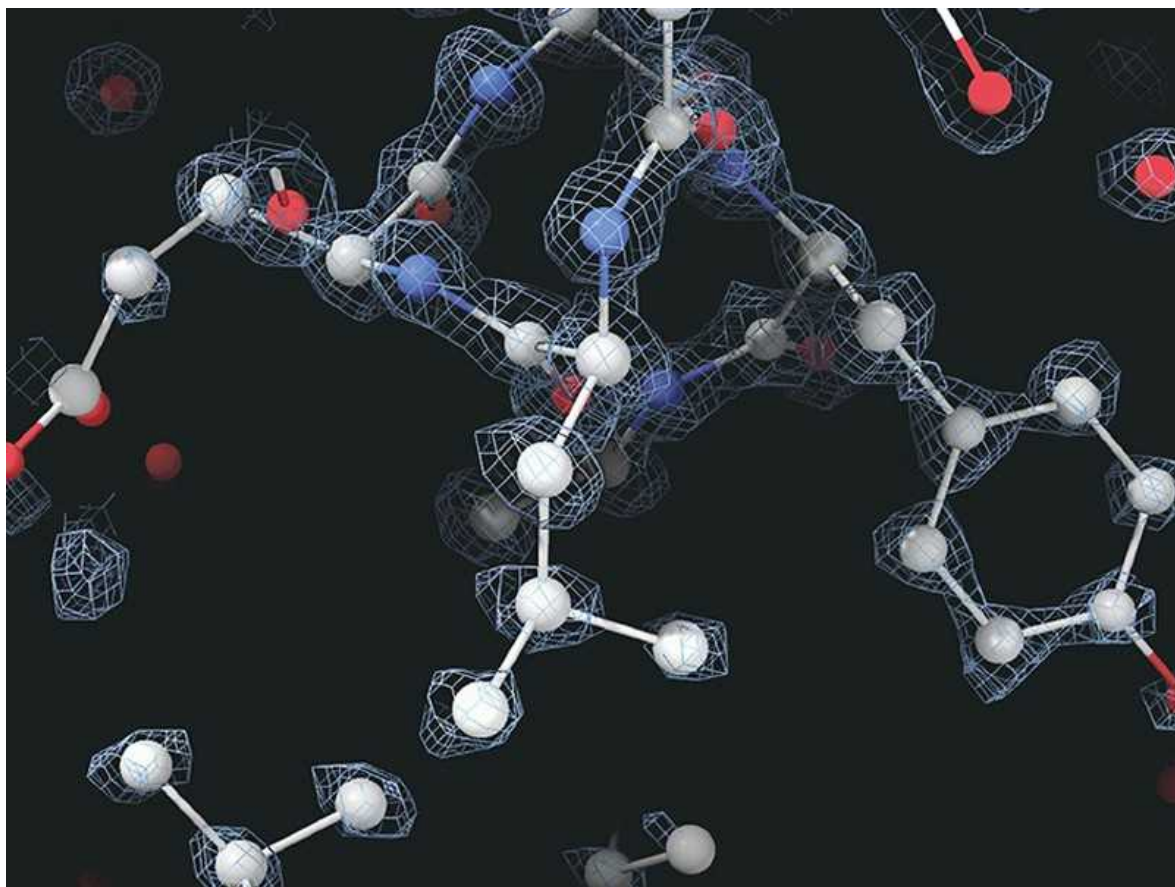
[Engineering a picky eater](#) — Jessica L. Zung and Carolyn S. McBride

The fly *Drosophila sechellia* feeds exclusively on the toxic noni fruit (*Morinda citrifolia*). What makes this species such a picky eater compared with its generalist relatives? Auer *et al.* cracked the case using the genome-editing tool CRISPR–Cas9. One class of sensory neuron that expresses the odorant receptor 22a (Or22a) protein is more abundant in *D. sechellia* than in other fly species — the group showed that small changes in Or22a's amino-acid sequence have contributed to *D. sechellia*'s partiality for noni. They also identified several other evolutionary changes that might contribute

to this apparently simple behavioural shift. Even tiny flies that love stinky fruit can provide powerful insight into how brains evolve to shape complex behaviours. *Original research: [Nature 579, 402–408 \(2020\)](#).*

A fast radio burst in our own Galaxy — Amanda Weltman and Anthony Walters

Three papers published in *Nature* report the detection of a phenomenon called a fast radio burst (FRB) coming from a source in our Galaxy. Intriguingly, the FRB was accompanied by a burst of X-rays. The discovery was made and understood by piecing together observations from multiple space- and ground-based telescopes. The name ‘fast radio bursts’ is a good description of what they are: bright bursts of radio waves with durations roughly at the millisecond scale. First discovered in 2007, their short-lived nature makes it particularly challenging to detect them and to determine their position on the sky. This FRB is the first for which emissions other than radio waves have been detected, the first to be found in the Milky Way, and the first to be associated with a stellar remnant called a magnetar — proving that magnetars can drive FRBs. *Original research: [Nature 587, 54–58 \(2020\)](#); [Nature 587, 59–62 \(2020\)](#); [Nature 587, 63–65 \(2020\)](#).*



Credit: Mark Herzik

[Cryo-electron microscopy reaches atomic resolution](#) — Mark A. Herzik Jr

A founding principle of structural biology is that, once researchers can directly observe macromolecules in enough detail, it should be possible to understand how their 3D structures confer their biological functions. Writing in *Nature*, Yip *et al.* and Nakane *et al.* report the sharpest images yet obtained using a method termed single-particle cryo-electron microscopy (cryo-EM), enabling the location of individual atoms in a protein to be determined for the first time. Each team used hardware that tackled distinct aspects of cryo-EM imaging that had previously limited the resolution attainable. With these technologies, the increased signal-to-noise ratio of cryo-EM images will expand the technique's applicability. Perhaps the melding of these technologies will enable the determination of cryo-EM

structures at a resolution beyond even one ångström — an achievement that might once have seemed impossible. *Original research: [Nature 587, 157–161 \(2020\)](#); [Nature 587, 152–156 \(2020\)](#).*

Interferon deficiency can lead to severe COVID — Eric Meffre and Akiko Iwasaki

Zhang *et al.* and Bastard *et al.* shed light on a key factor that affects whether life-threatening COVID-19 develops. The studies implicate deficiencies in interferon proteins, specifically, type I interferons (IFN-I). Such deficiencies might arise through inherited mutations in genes encoding key antiviral signalling molecules, or by the development of antibodies that bind to and ‘neutralize’ IFN-I. How does a defective IFN-I response lead to life-threatening COVID-19? The most direct explanation is that IFN-I deficiencies lead to uncontrolled viral replication and spread. However, IFN-I deficiencies might also have other consequences for immune-system function. Individuals with genetic mutations in the IFN-I-induction pathway would benefit from therapy that provides interferon. Furthermore, people who have neutralizing antibodies to IFN- α and IFN- ω might benefit from therapy that provides other types of interferon, such as IFN- β and IFN- λ . *Original research: [Science 370, eabd4570 \(2020\)](#); [Science 370, eabd4585 \(2020\)](#).*

Most viewed

The News & Views story that was most popular online in 2020.

Fight or flight turns hair white — Shayla A. Clark and Christopher D. Deppmann

The relative contribution of stress to greying of the hair is not known. Hair colour is determined by cells called melanocytes, which are derived from melanocyte stem cells (MeSCs) located in a part of the hair follicle called the bulge. Zhang *et al.* report that noradrenaline — a neurotransmitter molecule involved in the ‘fight or flight’ response to stress — is released

from neurons of the sympathetic nervous system that innervate the bulge. MeSC proliferation and differentiation increase markedly under extreme stress or on exposure to a high level of noradrenaline, resulting in mass migration of melanocytes away from the bulge and leaving no remaining stem cells to replace them, thus causing greying. Beyond the development of anti-greying therapies, Zhang and colleagues' work promises to usher in a better understanding of how stress influences other stem-cell pools and their niches. *Original research: [Nature 577, 676–681 \(2020\)](#).*

Nature **588**, 596-598 (2020)

doi: <https://doi.org/10.1038/d41586-020-03514-8>

Jobs from Nature Careers

- - - [All jobs](#)
 - - [**Full Professorship for Translational Imaging in Oncology \(W3\)**](#)
[German Cancer Research Center in the Helmholtz Association \(DKFZ\)](#)
[Dresden, Germany](#)
[JOB POST](#)
 - [**MSc Position in Forest Research**](#)
[The University of British Columbia \(UBC\)](#)
[Vancouver, Canada](#)
[JOB POST](#)

- **Research Associate - zero-emission hydrogen production project**

The University of British Columbia (UBC)

Vancouver, Canada

JOB POST

- **Laboratory Manager - Zamore Lab**

Howard Hughes Medical Institute (HHMI)

Worcester, United States

JOB POST

This article was downloaded by **calibre** from <https://www.nature.com/articles/d41586-020-03514-8>

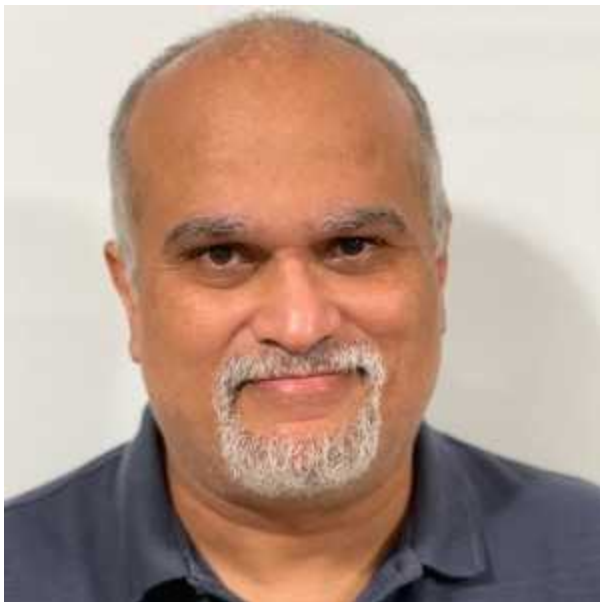
| [Section menu](#) | [Main menu](#) |

This Week

- **[Arecibo Observatory: another great lost in 2020](#)** [18 December 2020]
World View • Amid all the year's losses, I grieve what was once the world's biggest radio telescope, where I got my scientific start.
- **[The ferocious sex lives of giant shipworms: rivalry and wrestling matches](#)** [18 December 2020]
Research Highlight • First footage of 'pseudocopulation' shows the lengths certain molluscs go to to mate.
- **[Chemists tie an 'endless' knot — one of the most complex ever made](#)** [16 December 2020]
Research Highlight • Long atomic strings that are woven together create a structure with symbolic power for adherents of Buddhism.
- **[Why obesity can weaken the body's tumour-fighting defences](#)** [16 December 2020]
Research Highlight • Changes triggered by obesity help to give tumour cells the upper hand in the struggle for nutrients.
- **[Colour me beautiful: US rivers try a new hue](#)** [18 December 2020]
Research Highlight • In the past 35 years, some US waterways have become greener and others yellower, providing clues to ecosystem health.

WORLD VIEW
18 December 2020

Arecibo Observatory: another great lost in 2020



Amid all the year's losses, I grieve what was once the world's biggest radio telescope, where I got my scientific start.

Abel Méndez

Abel Méndez is a planetary astrobiologist and director of the Planetary Habitability Laboratory at the University of Puerto Rico at Arecibo. He used the Arecibo Observatory to study stars with known potentially habitable exoplanets.

[Contact](#)

Search for this author in:

- [Pub Med](#)

- [Nature.com](#)
- [Google Scholar](#)

The 305-metre radio telescope at the Arecibo Observatory in Puerto Rico survived decades of hurricanes, including Hurricane Maria in 2017, and earthquakes, including unusually strong ones in early January 2020. It also survived attempts by its owner, the US National Science Foundation, to reduce its funding. But in the early morning of 1 December 2020, its 900-tonne suspended instrument platform collapsed, destroying the 57-year-old telescope.

Arecibo contributed to many significant discoveries, including observations of pulsars that captured a Nobel prize, and the first confirmed exoplanets. Closer to home, the observatory's radar equipment emitted radio signals to identify the shape, spin and speed of potentially hazardous asteroids for NASA. The telescope also monitored dwarf stars, planets in our Solar System and disturbances in Earth's atmosphere.

Arecibo's collapse was a hard blow in what was already a year of loss. The pandemic has forced my interactions with students and colleagues online, and I worry about the health of my family: my octogenarian parents as well as my wife, a health-care worker who has lost a friend and colleague to COVID-19. In such times, it can be a comfort to remember beginnings.



Gut-wrenching footage documents

Arecibo telescope's collapse

I was 12 years old when I visited the Arecibo Observatory for the first time. Back in 1981, visits were by appointment, and I called from a payphone to try to make a reservation. Garred ‘Gerry’ Giles, the observatory’s head of scientific services, answered the phone in broken Spanish and assigned me a day and time. My parents agreed to make the two-hour drive. We all knew my enthusiasm for astronomy, but I don’t think anyone predicted that I’d grow up to be a physicist and astrobiologist at the University of Puerto Rico at Arecibo.

Gerry showed us the observatory control room, where a big window looked out at the massive suspended platform, a rotating structure that held the receivers in which radio signals reflected from the dish below came into focus. That year, the observatory’s measurements had been used to create the first radar maps of the surface of Venus: the planet’s thick clouds had hindered optical observations, but Arecibo’s strong radio signals could pass through and bounce back. I still have the printed pictures of Venus that Gerry gave me that day.

My parents and I went below the dish, riding in a Jeep down a dirt road. From afar, the dish looked like a solid shell, but it was made of many mesh-like plates through which light reached the ground below. The area was humid, calm and lush with vegetation. The dish was far above us, and the suspended platform visible even further up, through the mesh.

Decades later, I presented my first scientific lecture at the observatory as a visiting scientist. My research is about habitability of planets, understanding the conditions necessary for any life, from microbial to intelligent. A week before my arrival, I looked Gerry up in an old phone directory, unsure whether he was still in Puerto Rico. I told him that more than 25 years ago, he had given a kid a wonderful experience, and told him the date and time of my presentation. He’d retired by then, but he came — and I was delighted.

More telescopes mean more observations, confirmations and discoveries. Most radio telescopes, such as the world's current largest, the Five-hundred-meter Aperture Spherical Telescope (FAST) in China, were designed only to receive signals, but Arecibo's 305-metre dish was capable of both receiving and transmitting. Our best tool for listening and talking to the Universe is now silent.



Legendary Arecibo telescope will close forever — scientists are reeling

The last time that Arecibo was used for a targeted search for signs of extraterrestrial technology, called technosignatures, was from 1998 to 2004, as part of the privately funded Project Phoenix, run by the SETI Institute in Mountain View, California. The project observed 800 nearby stars, but picked up no transmissions. In 2019, NASA restored funding for exoplanet and exobiology research to look for technosignatures.

No such project was running at the observatory when it collapsed, but I was aiming to change that. My research students had planned to observe stellar systems with potentially habitable planets for longer than anybody else has done, and so increase sensitivity to weak signals. We did our last observations of one red-dwarf star in early August 2020, just four days

before the first of two cable failures closed the observatory. Soon afterwards, I became one of the dozens of scientists — cosmologists, stellar physicists, atmospheric scientists — who met weekly to brainstorm ideas about how to save and improve the telescope. We did not give up after the December collapse; we plan to find support to rebuild Arecibo with a new, better telescope.

As a child, I learnt from Gerry how one telescope, one moment, one person, can impact your life. It took me years of hard work to learn to use the Arecibo Observatory, and it was tough for me to see it go in less than one minute. Generations of scientists across Puerto Rico are also grieving.

Although I log most of my observations electronically, I like to keep a written notebook when I'm physically with the instruments. January 2020 was the time to start a new one, but with the earthquakes, pandemic and remote work, I didn't make a single entry. I plan to start writing again in 2021 — although I'll never regain that missing year, one in which we all lost so much.

Nature **588**, 539 (2020)

doi: <https://doi.org/10.1038/d41586-020-03552-2>

Jobs from Nature Careers

- - - [All jobs](#)
 - - [Full Professorship for Translational Imaging in Oncology \(W3\)](#)

[German Cancer Research Center in the Helmholtz Association \(DKFZ\)](#)

[Dresden, Germany](#)

JOB POST

- **MSc Position in Forest Research**

The University of British Columbia (UBC)

Vancouver, Canada

JOB POST

- **Research Associate - zero-emission hydrogen production project**

The University of British Columbia (UBC)

Vancouver, Canada

JOB POST

- **Laboratory Manager - Zamore Lab**

Howard Hughes Medical Institute (HHMI)

Worcester, United States

JOB POST

This article was downloaded by **calibre** from <https://www.nature.com/articles/d41586-020-03552-2>



The molluscs called giant feathery shipworms use their long siphons (pictured) to wrestle for the chance to mate. Credit: Dr Reuben Shipway/University of Portsmouth

Animal behaviour

18 December 2020

The ferocious sex lives of giant shipworms: rivalry and wrestling matches

First footage of ‘pseudocopulation’ shows the lengths certain molluscs go to mate.

Researchers have captured videos of acrobatic styles of sex in shipworms, molluscs that colonize ships, piers and driftwood as larvae and then spend their lives burrowing into and eating the wood around them.

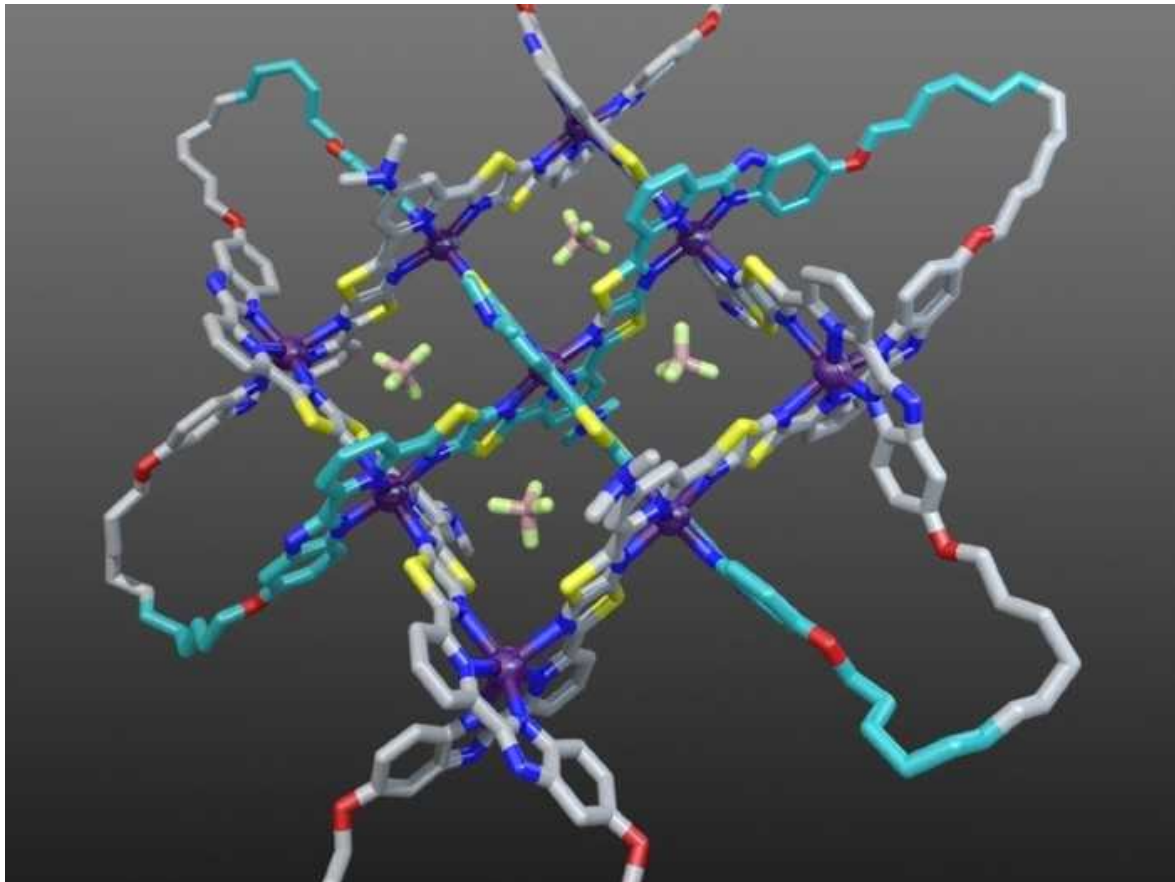
The only part of a shipworm’s long, soft body that is visible outside its wooden hideout is a retractable ‘siphon’ — a tube used to bring in food and oxygen and expel waste. Faced with the constant danger of literally eating themselves out of house and home, the various species of shipworm have developed a smorgasbord of sexual strategies, from males releasing a huge amount of sperm into the sea to females keeping miniature males in a side pocket.

Reuben Shipway at the University of Portsmouth, UK, and his colleagues recorded giant feathery shipworms (*Bankia setacea*) using their siphons to deposit sperm directly into their neighbours — in probably the first ever films of what is known as pseudocopulation. The astonished team also saw competing shipworms wrestling with their siphons over the opportunity to deposit sperm, and pulling the siphons of potential mates out of rivals’ reach.

[Biol. Lett. \(2020\)](#)

- [Animal behaviour](#)

This article was downloaded by **calibre** from <https://www.nature.com/articles/d41586-020-03604-7>



A molecule in the form of an endless knot includes atoms of carbon (light grey or turquoise), nitrogen (dark blue) and sulfur (yellow). Credit: David A. Leigh

Chemistry

16 December 2020

Chemists tie an ‘endless’ knot — one of the most complex ever made

Long atomic strings that are woven together create a structure with symbolic power for adherents of Buddhism.

Chemists have created the first molecule to form a structure called an endless knot, one of the eight auspicious symbols shared by Eastern traditions, including Buddhism and Hinduism. It is one of the most complex molecular knots to have been synthesized so far.

Knots often form spontaneously in DNA and other polymers, molecules made of repeated subunits connected in a long chain. But chemists can synthesize a specific molecular knot by guiding the molecule to twist and turn in the desired way.

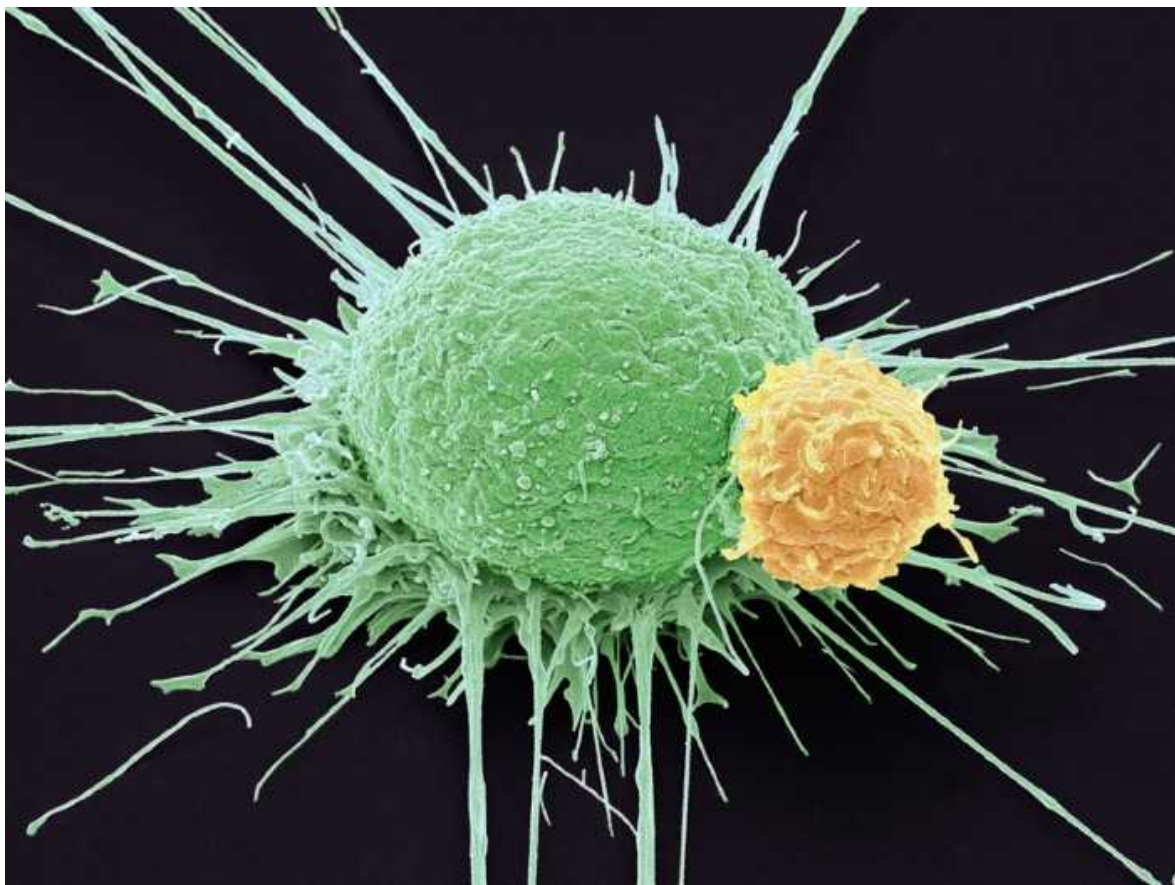
David Leigh at the University of Manchester, UK, and his collaborators instead started by arranging suitably flexible organic polymers into a woven pattern. They then joined the polymers' free ends to form one endless loop.

The process created several types of knots, including a 258-atom-long molecule in the form of an endless knot, which contains 7 crossings. The team used two techniques — nuclear magnetic resonance and X-ray crystallography — to confirm that they had created endless knots. The researchers say the technique could be further developed to produce larger woven molecules and materials.

[Nature Chem. \(2020\)](#)

- [Chemistry](#)

This article was downloaded by **calibre** from <https://www.nature.com/articles/d41586-020-03579-5>



A cancer cell (green; artificially coloured) and an immune cell called a T cell. Obesity puts a strain on the body's antitumour immune brigade. Credit: Steve Gschmeissner/SPL

Cancer

16 December 2020

Why obesity can weaken the body's tumour-fighting defences

Changes triggered by obesity help to give tumour cells the upper hand in the struggle for nutrients.

Excess weight can increase the risk of several diseases, including some cancers. Now, a study in overweight mice suggests that obesity's effects help cancer cells to gobble fuel — depriving tumour-killing immune cells of energy.

Tumours consume fats, which serve as fuel for some immune cells that can recognize and destroy cancer cells. Arlene Sharpe and Marcia Haigis at Harvard Medical School in Boston, Massachusetts, and their colleagues fed mice a high-fat diet, which caused changes such as weight gain and increased blood levels of fatty molecules. Then, the researchers injected the rodents with cancer cells, which grew into tumours.

The high-fat diet reduced the number and activity of cancer-killing immune cells inside the tumours, accelerating cancer growth. Additional experiments provided an explanation: when fat molecules are plentiful, cancer cells use them up, starving immune cells and reducing their activity.

The authors also genetically engineered cancer cells to prevent them from making use of fats. In mice eating high-fat diets, treatment with these altered cells led to reduced tumour growth compared with an infusion of standard cancer cells.

[Cell \(2020\)](#)

- [Cancer](#)

This article was downloaded by **calibre** from <https://www.nature.com/articles/d41586-020-03591-9>



Rivers in the United States tend to be either yellow or, like the Tennessee River (pictured), green. Credit: J. R. Gardner *et al./Geophys. Res. Lett.*

Hydrology

18 December 2020

Colour me beautiful: US rivers try a new hue

In the past 35 years, some US waterways have become greener and others yellower, providing clues to ecosystem health.

One-third of large rivers in the United States have changed colour over the past 35 years.

Algae, suspended sediment and organic matter can affect a river's colour and health. As a result, researchers have used colour to monitor the health of river ecosystems for more than a century.

Using satellite images dating back to 1984, John Gardner at the University of North Carolina at Chapel Hill and his colleagues built a database of US rivers' colour and how much light they reflect. The team classified rivers across the United States as yellow, green or blue and catalogued colour changes over three and a half decades.

Rivers near dams and urban areas were the most likely to have changed rapidly over the years. The northwestern United States was a hotspot for rivers that became greener over time, whereas in the northeast, rivers were more likely to turn yellower. It is straightforward to classify colour on the basis of satellite imagery, so this database could be used to monitor large-scale changes in river ecosystems, the authors say.

[*Geophys. Res. Lett. \(2020\)*](#)

- [Hydrology](#)

This article was downloaded by **calibre** from <https://www.nature.com/articles/d41586-020-03592-8>

News in Focus

- **[Asteroid treasure, COVID vaccine and public peer review](#)**

[23 December 2020]

News Round-Up • The latest science news, in brief.

- **[Can Joe Biden rebuild the ravaged US Environmental Protection Agency?](#)**

[16 December 2020]

News • Scientists reveal further details about the damage sustained under Trump — and the challenges for Biden in restoring science's standing at the agency.

- **[Is a racially-biased algorithm delaying health care for one million Black people?](#)**

[16 December 2020]

News • Sweeping calculation suggests it could be — but how to fix the problem is unclear.

- **[Arab nations first to approve Chinese COVID vaccine — despite lack of public data](#)**

[14 December 2020]

News • The United Arab Emirates and Bahrain say the vaccine is 86% effective, but scientists would like to see data to support the claim.

- **[Coronavirus and public holidays: what the data say](#)**

[16 December 2020]

News Explainer • With the festive season ahead, Nature examines what is known about the risks of COVID spread, and how researchers will spend their time off.

NEWS ROUND-UP

23 December 2020

Asteroid treasure, COVID vaccine and public peer review

The latest science news, in brief.



The Hayabusa2 capsule that landed in the desert in South Australia.Credit: AP/Shutterstock

Asteroid dust recovered from Hayabusa2

Japan's mission to bring asteroid dust back to Earth has succeeded. The Japan Aerospace Exploration Agency (JAXA) confirmed on 14 December that a capsule from the spacecraft Hayabusa2, which landed in an Australian desert last week, [contained black grains from asteroid Ryugu](#). It is only the second time that scientists have returned material from an asteroid.

Hayabusa2 collected the samples during a year and a half of poking and prodding Ryugu — a small asteroid shaped like a squashed sphere, peppered with giant boulders. Ryugu is a C-type, or carbon-rich, asteroid, which scientists think contains organic and hydrated minerals preserved from as far back as 4.6 billion years ago. The samples could help to explain how Earth became covered with water. Scientists think water came on asteroids or similar planetary bodies from the outer regions of the Solar System.

“The samples containing precious asteroid material will provide scientists with key information about the formation of the Solar System,” says Ed Kruzins, director of the Canberra Deep Space Communication Complex at the Commonwealth Scientific and Industrial Research Organisation, which helped to track the spacecraft and its encounter with the asteroid.

Moderna's COVID vaccine wins US approval

A week after granting an emergency-use authorization for the country's first COVID-19 vaccine, [US regulators have followed with a second](#): another RNA vaccine, made by Moderna of Cambridge, Massachusetts.

The authorization came after a panel of external advisers to the US Food and Drug Administration (FDA) voted to recommend use of the vaccine on 17 December. A similar vaccine made by Pfizer of New York City and BioNTech of Mainz, Germany, had [already received emergency authorization from US and UK regulators](#). The green light is a first for Moderna, a ten-year-old biotechnology company that pledged to revolutionize medicine by harnessing RNA in therapies, but had yet to get a drug or vaccine into the clinic.

FDA advisers spent much of the 17 December meeting discussing when and how to offer a vaccine to participants in the placebo arm of Moderna's trial

after authorization. Once a coronavirus vaccine becomes available, participants might choose to leave the trial to guarantee that they can get a jab. Maintaining the integrity of clinical trials — to collect data on long-term safety and the duration of protection — is a looming challenge for developers.

Journal announces ‘preprint first’ publishing model

The open-access journal *eLife* has [unveiled plans to introduce a new publishing model](#). Starting next July, the journal will adopt a “publish, then review” policy, and will make all of its peer-review reports publicly available.

Under the policy, which the journal announced on 1 December ([M. B. Eisen et al. *eLife* 9, e64910; 2020](#)), *eLife* will only review and publish papers that have already been posted on a preprint server, such as bioRxiv, medRxiv or arXiv. Submitted papers that aren’t already on preprint servers will be posted on bioRxiv or medRxiv.

One of the driving forces behind the policy change was an internal analysis, which revealed that around 70% of the papers reviewed by *eLife* during May, June and July 2020 had already been posted as preprints.

The new policy won’t come into effect right away. Over the next six months, authors will be able to opt out of posting their submitted manuscripts as preprints, but will be asked to explain the reason.

eLife also plans to start posting all of its peer-review reports on preprint servers, whether or not a paper is accepted for publication. The authors of rejected papers will be allowed to delay the posting of their reviews until their articles are accepted elsewhere. The journal is developing a platform, Scity, for sharing public peer reviews.

Nature **588**, 543 (2020)

doi: <https://doi.org/10.1038/d41586-020-03553-1>

Jobs from Nature Careers

- - - [All jobs](#)
 - - [Full Professorship for Translational Imaging in Oncology \(W3\)](#)

[German Cancer Research Center in the Helmholtz Association \(DKFZ\)](#)

[Dresden, Germany](#)

[JOB POST](#)
 - [MSc Position in Forest Research](#)

[The University of British Columbia \(UBC\)](#)

[Vancouver, Canada](#)

[JOB POST](#)
 - [Research Associate - zero-emission hydrogen production project](#)

[The University of British Columbia \(UBC\)](#)

[Vancouver, Canada](#)

[JOB POST](#)
 - [Laboratory Manager - Zamore Lab](#)

[Howard Hughes Medical Institute \(HHMI\)](#)

Worcester, United States

JOB POST

This article was downloaded by **calibre** from <https://www.nature.com/articles/d41586-020-03553-1>

| [Section menu](#) | [Main menu](#) |

NEWS

16 December 2020

- Correction [17 December 2020](#)

Can Joe Biden rebuild the ravaged US Environmental Protection Agency?

Scientists reveal further details about the damage sustained under Trump — and the challenges for Biden in restoring science's standing at the agency.

Jeff Tollefson

Search for this author in:

- [Pub Med](#)
- [Nature.com](#)
- [Google Scholar](#)



Scientists at the US Environmental Protection Agency are hopeful their roles in regulatory decision-making will be restored under president-elect Joe Biden. Credit: Bill Clark/CQ Roll Call/Getty

For many scientists at the US Environmental Protection Agency (EPA), the past four years working in President Donald Trump's government have [felt like an eternity](#). Largely sidelined, they could only watch as his administration dismantled science advisory panels, disregarded scientific evidence and weakened pollution regulations.

Expectations are high that the next four years will see improvements under incoming president Joe Biden — and there are clear and positive steps he can take, according to more than a dozen current and former EPA scientists interviewed by *Nature*. But these insiders also say that Biden will have his work cut out in repairing the damage, including restoring the role of science — and scientists — in crafting environmental rules to protect public health.



Can Joe Biden make good on his revolutionary climate agenda?

They point to changes the Trump administration made that have undermined expert advice and scientific data, and that will take time to undo. “We are not naive,” says one mid-career scientist currently at the EPA who, like other insiders in this story, declined to be named because they were not authorized to speak to the press. “It’s going to take time.”

Multiple sources told *Nature* that EPA leadership ignored complaints filed by staff that claimed that senior political appointees had violated the agency’s scientific-integrity policy. The EPA declined to comment on the allegations.

EPA scientists have been in Trump’s cross hairs ever since his run for president in 2016, when he promised to slash budgets and jobs at the agency, arguing that environmental regulations were costing jobs and “making it impossible for our country to compete”. Just weeks after entering the White House, his administration proposed cutting the EPA’s budget by nearly one-third and laying off more than 20% of its 15,000 staff members. Trump targeted no other major US agency to the same extent.

A seat at the table

Ultimately, the US Congress rejected those cuts, but the administration continued its overhaul of the EPA over the next four years. Many senior EPA staff left, and the atmosphere dampened considerably, insiders say.

“There's been an enormous loss of trust; people are exceptionally edgy, and they're not going to bounce back quickly,” says one senior EPA scientist. “Biden has a lot of terrific policies he wants to carry out, but the first job will be to bring the agency back to health.”



Biden will soon choose a new agency head for the EPA who can push his environmental agenda forward. Credit: Drew Angerer/Getty

The first step Biden can take is to appoint a new agency head, and EPA observers expect a science-minded individual to be put in place. “I’m sure whoever the Biden administration appoints will be someone who embraces science and recognizes that EPA is a science-based regulatory agency,” says Chris Frey, an environmental engineer at North Carolina State University in Raleigh who served on an EPA advisory panel that was disbanded by the

Trump administration in 2018. By contrast, Trump's appointees, starting with Scott Pruitt and continuing under Andrew Wheeler, sidelined career scientists at the agency while implementing an industry-friendly agenda.



Science under siege: behind the scenes at Trump's troubled environment agency

But one of the most important things Biden can do to boost morale among scientists, insiders say, is to quickly nominate a leader for the agency's main science arm, the Office of Research and Development (ORD). The division houses more than 1,000 scientists and engineers who assess scientific data and conduct research that feeds into regulatory decisions, but it has been without a Senate-confirmed leader since 2012. Although former president Barack Obama nominated a leader for ORD in 2013, Senate Republicans blocked the nominee's confirmation, leaving the division in the hands of acting or deputy assistant administrators; Trump never nominated anyone for the post.

This vacancy has diminished the influence of the scientists in ORD, says Bob Kavlock, who served as acting head of ORD before retiring in 2017. "It sends a signal when you have somebody who is confirmed by the Senate —

they have much more influence,” he says. “It puts them at the table with all of the regulatory folks.”

Science watchdogs

Another way to restore EPA scientists’ confidence is to strengthen the agency’s scientific-integrity policy. Scientists both inside and outside the agency say the policy is strong, but it has shown its limitations under the Trump administration.



Current EPA administrator Andrew Wheeler is a former coal industry lobbyist. Credit: Shutterstock

In the past few years, according to current and former EPA officials with knowledge of the matter, staff have filed “more than a dozen” complaints against senior political appointees with the EPA’s scientific-integrity office, which is responsible for upholding the policy. The complaints alleged actions such as intimidating scientists and suppressing science, the officials say. But the EPA’s leadership has been “less than cooperative” with the

office's investigations, they add — and threatened to withdraw the policy altogether.

EPA officials declined to comment on these allegations.



Five ways that Trump is undermining environmental protections under the cover of coronavirus

Gretchen Goldman, research director for the Union of Concerned Scientists' Center for Science and Democracy, in Washington DC, says she does not know anything about these allegations. But she says that the current EPA leadership has created a "culture of fear", and so if staff still did file formal complaints, it is noteworthy. Goldman notes that her own organization has filed two complaints with the EPA's scientific-integrity office, alleging that agency officials suppressed scientific information while conducting and making decisions on chemical assessments.

To ensure the agency's leadership abides by the integrity policy in the future, the Biden administration could elevate the integrity office so that it reports directly to the EPA administrator, while having its officials work alongside the EPA inspector general's office, a move that would give it more authority and independence, says Goldman.

Unstacking the deck

Many EPA observers also expect Biden's administration to overhaul the network of independent advisory panels — comprised of scientists from academia, industry and state or local government — that advise the agency on public health and environmental issues.



How Trump damaged science — and why it could take decades to recover

Trump's appointees at the EPA instituted a series of changes that pushed academic scientists off the rosters, often in favour of scientists more

sympathetic to industry, says Chris Zarba, who managed activities for the main Science Advisory Board (SAB) before retiring in 2018 and now works with the Environmental Protection Network, an advocacy group of former EPA employees.

Most controversially, in 2017, [the administration barred](#) academic scientists with EPA grants from serving on advisory panels, claiming the grants compromised the scientists' independence. Officials did not apply the same logic to the scientists with ties to industry who took the academics' place, says Zarba.

"It was a thinly veiled attempt to remove particular perspectives so that they could do what they want to do," says Robyn Wilson, a researcher who investigates risk assessment and behavioural science at the Ohio State University in Columbus, who was pushed off the SAB by the rule — and successfully sued over her dismissal.



Air pollution science under siege at US environment agency

As part of that lawsuit, an appeals court rejected the grants rule altogether. Acknowledging the court decision, an EPA spokesperson said that scientists with grants weren't kicked off the panels, but rather given a choice about

whether to keep their grant or resign — and noted that industry advisers account for only 9% of the SAB’s current membership.

That figure doesn’t include consultants with ties to industry or scientists who are known to sympathize with the positions of regulated industries, Frey and others contend. According to an analysis by Goldman’s group, academic scientists occupied 75% of the SAB’s seats at the end of Obama’s presidency, and that number is now less than 50%.

Advocacy groups say the Trump administration stacked the decks on the EPA’s boards to such an extent that Biden has little choice but to start over with new appointees. “These were committees that were constituted with an illegitimate process,” says Goldman. “They need to start from scratch and reconstitute them with legitimate scientists.”

On the way out

Even in Trump’s final weeks as US president, his administration is still pushing through controversial rules at the EPA. On 9 December, [officials finalized a rule](#) that lays out new requirements for calculating the costs and benefits of future air-quality regulations. They say the rule promotes transparency, but critics say it will make it harder to justify new regulations and easier to write off the health benefits of restricting air pollution.

Analysts also expect another, potentially ground-shaking measure — known as [the ‘transparency’ rule](#) — to be finalized before Trump’s exit from the White House. Many scientists fear it could prevent the EPA from considering non-public data — including private health data that are often the cornerstone of pollution regulations — when crafting rules.

Reversing course on these and other rules could occupy much of Biden’s first term, but EPA observers are hopeful that the new leadership will be able to turn things around.

“We have a chance to move forward and restore the role of science in sound public policymaking,” says Carol Browner, who headed the agency under former President Bill Clinton. “But this will take time, to rebuild capacity and rebuild the expertise.”

Nature **588**, 545-546 (2020)

doi: <https://doi.org/10.1038/d41586-020-03585-7>

Updates & Corrections

- **Correction 17 December 2020:** This story was updated to reflect that Carol Browner headed the EPA under former President Bill Clinton, not under former President Barack Obama.

Jobs from Nature Careers

- - - [All jobs](#)
 - - [Full Professorship for Translational Imaging in Oncology \(W3\)](#)
[German Cancer Research Center in the Helmholtz Association \(DKFZ\)](#)
[Dresden, Germany](#)
[JOB POST](#)
 - [MSc Position in Forest Research](#)
[The University of British Columbia \(UBC\)](#)
[Vancouver, Canada](#)
[JOB POST](#)
 - [Research Associate - zero-emission hydrogen production project](#)

The University of British Columbia (UBC)

Vancouver, Canada

JOB POST

▪ **Laboratory Manager - Zamore Lab**

Howard Hughes Medical Institute (HHMI)

Worcester, United States

JOB POST

This article was downloaded by **calibre** from <https://www.nature.com/articles/d41586-020-03585-7>

| [Section menu](#) | [Main menu](#) |

NEWS

16 December 2020

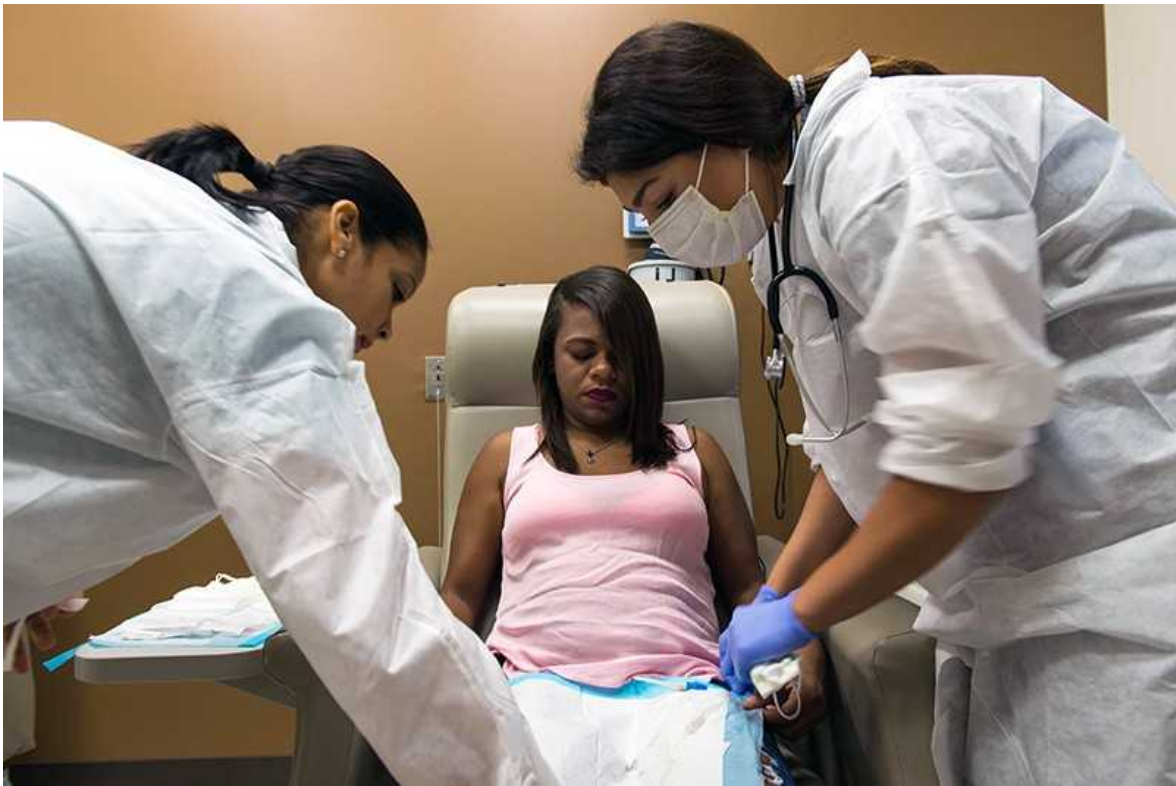
Is a racially-biased algorithm delaying health care for one million Black people?

Sweeping calculation suggests it could be — but how to fix the problem is unclear.

Jyoti Madhusoodanan

Search for this author in:

- [Pub Med](#)
- [Nature.com](#)
- [Google Scholar](#)



A woman receives dialysis, a common treatment for people with kidney disease. Black people in the United States are almost four times as likely to experience kidney failure as are white people. Credit: AB Forces News Collection/Alamy

One million Black adults in the United States might be treated earlier for kidney disease if doctors were to remove a controversial ‘race-based correction factor’ from an algorithm they use to diagnose people and decide whether to administer medication, a comprehensive analysis finds.

Critics of the factor question its medical validity and say it potentially perpetuates racial bias — and that the latest study, published on 2 December in *JAMA*¹, strengthens growing calls to discontinue its use.

“A population that is marginalized and much less likely to have necessary resources and support is the last group we want to put in a situation where they’re going to have delays in diagnosis and treatment,” says nephrologist Keith Norris at the University of California, Los Angeles, who argues for retiring the correction until there’s clear evidence that it’s necessary.

On the flip side, others say that the correction is based on scientific data that can't be ignored, although they, too, agree that its basis on race is a problem.

A correction arises

Researchers introduced the correction factor² in the late 1990s to take into account results showing that, on average, Black people in the United States tend to have higher blood levels of a molecule called creatinine than do white people — despite having similar kidney function. Creatinine levels are a marker of how well a person's kidneys filter waste from the body. Doctors feed the measurement, along with other information, into algorithms that calculate a person's estimated glomerular filtration rate (eGFR) to evaluate kidney function. High creatinine levels lead to a low eGFR, which is a sign of kidney disease; the correction inserts a multiplier of about 1.2 when calculating the eGFR of Black people, potentially making their kidneys seem healthier than they actually are.



Millions of black people affected by racial bias in health-care algorithms

Variations of race-corrected eGFR algorithms are now used in more than 90% of pathology labs across the United States, according to the College of American Pathologists in Northfield, Illinois.

In the past few years, institutions including Beth Israel Deaconess Medical Center in Boston, Massachusetts, have dropped the correction factor. None of them has yet released data on the action's impact. In August, the American Society of Nephrology in Washington DC and the National Kidney Foundation in New York City convened a task force to evaluate whether the entire medical community should stop using it. The group's initial recommendations are expected by the end of the month, with a final decision on whether to continue using the correction due in the first half of next year.

Those who want to abolish the correction say it perpetuates the problematic idea that people of different ethnicities have different biology. Also, the eGFR algorithms are just an estimate of kidney function that describe a collection of "noisy data", says nephrologist Rajnish Mehrotra of the University of Washington in Seattle, one of the institutions that has dropped the correction. The question, he says, is whether you're willing to perpetuate the false idea that race reflects biological differences for a "small gain in precision" that you might get from using it to evaluate kidney function.

Others worry that simply removing the correction could cause harm. Mathematical analyses such as the one in *JAMA*, they say, do not represent real-world health outcomes: it's unclear whether removing the race multiplier would actually help or hurt the health of those one million Black adults. Neil Powe, an internal-medicine specialist at the University of California, San Francisco, and a co-author of the study, points out that removing the factor could lead to over-diagnosis of kidney disease in Black people, causing burdens such as extra medical bills and denying them access to medicines, such as diabetes drugs considered too risky for those with unhealthy kidneys. The correction arose because of creatinine data, he says — and as long as creatinine alone is used as a biomarker to gauge kidney function, researchers can't just ignore those data, which have been replicated³ for US study participants multiple times.

Assessing a correction

In the United States, kidney disease disproportionately affects Black people. They are currently [almost four times as likely](#) as white people to experience kidney failure.



Bias detectives: the researchers striving to make algorithms fair

It's tough to tell whether — or how much — the race-corrected algorithm has worsened this crisis, because the rate of disease is affected by other factors influenced by systemic racism, including socio-economic inequalities and a lack of health insurance, scientists say. "Race corrections to eGFRs are most likely contributing, but it's not reasonable to expect that removing the race correction will automatically solve all inequities for Black Americans with chronic kidney disease," says Nwamaka Eneanya, a nephrologist at the University of Pennsylvania in Philadelphia who advocates dropping the correction.

In the latest analysis, researchers including Powe aimed to assess what would happen if they removed the race-based correction factor for a

representative group of people. The team examined the medical records of 9,522 Black people included in the National Health and Nutrition Examination Survey, a programme run by the US Centers for Disease Control and Prevention that maintains a national database of health statistics.



What the data say about police brutality and racial bias — and which reforms might work

Although it was unsurprising that dropping the correction would increase the number of Black people diagnosed with kidney disease, “the size of the effect surprised us”, says Arjun Manrai, a computational health researcher at Harvard Medical School in Boston, who led the study. Removing it would lead to a change in diagnosis for 3.5% of Black adults from ‘disease free’ to having early-stage kidney disease (extended to the US population, this would be one million Black adults). Removing it would also shift the status of 29% of Black patients from having early-stage to advanced disease. Getting rid of the correction, says Manrai, could drastically alter these people’s access to medications for common conditions such as hypertension or diabetes, because the drugs can have side effects on the kidneys. Overall,

it would also increase the number of Black people with kidney disease who are eligible to receive a transplant.

Correcting a correction

Andrew Levey, a nephrologist at Tufts University in Boston, is one of the researchers who originally established the correction factor. Although he has come to question whether the multiplier should be used, he isn't certain that dropping it is a perfect solution. The latest study does show that more Black people could be diagnosed earlier if the correction were removed, he says, but that doesn't mean they will all benefit. "Some of them will probably be helped by getting into treatment earlier because they're on their way to getting kidney disease, and some of them won't be helped," he adds. "It's a typical tension we face between diagnosing too early versus too late."



The researcher fighting to embed analysis of sex and gender into science

A better solution, says Levey, might be to develop an algorithm that relies on biomarkers beyond creatinine. On 7 December, he and his colleagues

published an eGFR algorithm that has no race-based correction factor and instead uses multiple biomarkers, in addition to creatinine⁴.

Until such algorithms are vetted for wider clinical use, Levey and others suggest talking to patients about how their race might be used in clinical decisions. He adds: “I don’t think that we have been transparent in speaking with our patients about how we do this.”

Nature **588**, 546-547 (2020)

doi: <https://doi.org/10.1038/d41586-020-03419-6>

References

1. 1.

Diao, J. A. *et al. J. Am. Med. Assoc.*
<https://doi.org/10.1001/jama.2020.22124> (2020).

2. 2.

Levey, A. S. *et al. Ann. Int. Med.* **130**, 461–470 (1999).

3. 3.

Peralta, C. A. *et al. Am. J. Nephrol.* **31**, 202–208 (2010).

4. 4.

Inker, L. A. *et al. Am. J. Kidney Dis.*
<https://doi.org/10.1053/j.ajkd.2020.11.005> (2020).

Jobs from Nature Careers

- - - [All jobs](#)
 -

- **Full Professorship for Translational Imaging in Oncology (W3)**

German Cancer Research Center in the Helmholtz Association (DKFZ)

Dresden, Germany

JOB POST

- **MSc Position in Forest Research**

The University of British Columbia (UBC)

Vancouver, Canada

JOB POST

- **Research Associate - zero-emission hydrogen production project**

The University of British Columbia (UBC)

Vancouver, Canada

JOB POST

- **Laboratory Manager - Zamore Lab**

Howard Hughes Medical Institute (HHMI)

Worcester, United States

JOB POST

| [Section menu](#) | [Main menu](#) |

NEWS

14 December 2020

Arab nations first to approve Chinese COVID vaccine — despite lack of public data

The United Arab Emirates and Bahrain say the vaccine is 86% effective, but scientists would like to see data to support the claim.

David Cyranoski

David Cyranoski reports for *Nature* from Shanghai, China.

Search for this author in:

- [Pub Med](#)
- [Nature.com](#)
- [Google Scholar](#)



Sinopharm's COVID vaccine is being trialled in Egypt, Jordan, Argentina and elsewhere.Credit: Mazen Mahdi/AFP/Getty

Two Arab nations have become the first countries to approve a Chinese COVID-19 vaccine, a significant boost for China's plans to roll out its vaccines worldwide. The United Arab Emirates (UAE) approved a vaccine developed by Chinese state-owned Sinopharm on 9 December, and Bahrain followed days later. But researchers say a lack of public data on the safety and efficacy of the vaccine could hinder the company's plans to distribute the vaccine in a range of other countries.

The Sinopharm vaccine is probably safe and effective and could be a great help in fighting the pandemic, says Jin Dong-Yan, a virologist at the University of Hong Kong. But he notes a lack of available clinical-trial data, and adds that confidence in the vaccine's safety and efficacy will be key to its successful international distribution.

“Chinese state-run companies, like Sinopharm, can produce billions of doses. They have the capacity and expertise,” he says. “They need to have an open and transparent system, but they are not good at doing that,” he adds.

The UAE and Bahrain are also the first countries to grant full approval to sell a COVID-19 vaccine. Russian officials have licensed two vaccines, but the approvals are conditional and subject to the results of ongoing phase III trials. In China, Sinopharm’s vaccine has been widely deployed under emergency-use authorization, but full approval is expected very soon. The [United States](#) and the United Kingdom have issued emergency authorizations for a COVID-19 vaccine made by Pfizer of New York City and BioNTech of Mainz, Germany.

UAE regulators said in a press release that they had approved an inactivated vaccine developed by Sinopharm’s Beijing Institute of Biological Products. The approval was based on company data stating that the efficacy of the two-dose vaccine was 86% in final-stage testing, including a trial in 31,000 people in the UAE, according to the press release. The vaccine had been granted emergency-use authorization in September. Bahrain officials did not state whether they approved the same Sinopharm vaccine, but it is thought to be the same jab, because they, too, reported 86% efficacy. Some 7,700 people participated in Sinopharm trials there.

The UAE press release also states that 99% of those vaccinated developed neutralizing antibodies to SARS-CoV-2 and that the vaccine prevented moderate and severe disease in everyone vaccinated.

Data gap

But scientists not involved in developing and approving the Chinese vaccines are finding it hard to make sense of the data behind the latest announcements. The UAE reported the phase III efficacy data before Sinopharm did, and the company has yet to confirm that they are correct. Neither the UAE, Bahrain nor Sinopharm have released the data used to make the 86% efficacy claims. “They give no real data. That’s a bit weird,”

says Zhengming Chen, an epidemiologist at the University of Oxford, UK. “It’s difficult to tell how well the vaccine works. I hope it is real.”

Sinopharm did not respond to *Nature*’s request for more detail on its trial results.

Scientists would like to see data on the number of infections in the groups that received the vaccine and in those that were given a placebo. Such data are used to calculate a vaccine’s effectiveness — and have been released by the makers of several other leading coronavirus vaccines, including that developed by Pfizer and BioNTech. They released some detailed data in a [press release](#) in November, before the UK authorization, and published the phase III trial results on 10 December in the *New England Journal of Medicine*¹.

International orders

Chinese state media have reported that Sinopharm has vaccine orders from more than 100 countries, including many in Africa, but few details of such deals have been reported. Sinopharm’s vaccine is also undergoing phase III testing in Egypt, Jordan, Argentina and other countries, so they are likely to be among the next to consider approving it.

Other countries are probably also planning to rely on China for vaccines, because the United States and European nations have pre-purchased billions of doses of the vaccines being developed there, says Jin. Sinopharm’s jab is also appealing because it uses inactivated virus and — unlike the Pfizer–BioNTech vaccine — does not need to be stored at extremely cold temperatures, making it easier to transport and distribute.

Chen thinks that there will be some resistance to Chinese vaccines if the companies do not allow independent analysis of the safety and efficacy data. “I don’t think other countries will follow suit unless there is really convincing, robust data. You need really strong scientific evidence that can be scrutinized to convince people,” says Chen. In the United States, the Food and Drug Administration has an independent committee that evaluates

vaccine trial data and makes its findings public, which then makes a recommendation to the regulator.

Jin worries that countries might have to choose between accepting the vaccine without independent analysis or not using the vaccine.

Looking ahead

Whether vaccine approvals will allow life in the UAE and Bahrain to return to normal is unclear. The UAE will need approximately 20 million doses — two per person — to vaccinate the entire country, but securing and administering that many doses will take time, says Ben Cowling an epidemiologist at the University of Hong Kong.

Scientists think that around 70% of the population will need to get the vaccine to achieve herd immunity — when enough people are immune to a virus that spread becomes unlikely, says Cowling.

When Sinopharm will have capacity to meet the UAE's and Bahrain's requirements is unclear. The company says it has 500 million doses, but scientists have previously told *Nature* that most of those will probably be distributed in China.

Nature **588**, 548 (2020)

doi: <https://doi.org/10.1038/d41586-020-03563-z>

References

1. 1.

Polack, F. P. *et al.* *N. Engl. J. Med.*

<https://www.nejm.org/doi/10.1056/NEJMoa2034577> (2020).

Jobs from Nature Careers

•

- - [All jobs](#)
- - **[Full Professorship for Translational Imaging in Oncology \(W3\)](#)**
[German Cancer Research Center in the Helmholtz Association \(DKFZ\)](#)
[Dresden, Germany](#)
[JOB POST](#)
 - **[MSc Position in Forest Research](#)**
[The University of British Columbia \(UBC\)](#)
[Vancouver, Canada](#)
[JOB POST](#)
 - **[Research Associate - zero-emission hydrogen production project](#)**
[The University of British Columbia \(UBC\)](#)
[Vancouver, Canada](#)
[JOB POST](#)
 - **[Laboratory Manager - Zamore Lab](#)**
[Howard Hughes Medical Institute \(HHMI\)](#)
[Worcester, United States](#)
[JOB POST](#)

This article was downloaded by **calibre** from <https://www.nature.com/articles/d41586-020-03563-z>

| [Section menu](#) | [Main menu](#) |

NEWS EXPLAINER

16 December 2020

Coronavirus and public holidays: what the data say

With the festive season ahead, *Nature* examines what is known about the risks of COVID spread, and how researchers will spend their time off.

Giorgia Guglielmi

Search for this author in:

- [Pub Med](#)
- [Nature.com](#)
- [Google Scholar](#)



Crowds gathered at Hongqiao railway station in Shanghai, China, ahead of celebrations for the Lunar New Year in January 2020.Credit: Qilai Shen/Bloomberg/Getty

As worldwide coronavirus cases continue to surge, countries are grappling with how to manage big public holidays such as Christmas and Lunar New Year, which researchers are warning could become superspreader events.

“We’re already at a high level of community spread, and we’re about to see a lot of people travelling and gathering indoors,” says Julia Marcus, an infectious-disease epidemiologist at Harvard Medical School in Boston, Massachusetts. “It’s hard to see any way that this is going to go well.”

Nature examines what scientists have already learnt about the spread of COVID-19 during holidays.

How has SARS-CoV-2 spread during past holidays?

Five million people left the city of Wuhan in China in preparation for the 2020 Lunar New Year holiday, an event that coincided with the start of the pandemic¹. The holiday is one of the world's largest mass migrations, when hundreds of millions of people travel to visit relatives.



COVID and 2020: An extraordinary year for science

Elsewhere, such as in the United Kingdom, the epidemic followed a one-week school holiday break from 17 to 21 February, when thousands of people came back infected with the virus from ski resorts in northern Italy and tourist locations in Spain², says Zhengming Chen, an epidemiologist at the University of Oxford, UK.

More recently, Canada saw its [highest numbers of COVID-19 infections](#) in the two weeks following Thanksgiving on 12 October.

Are any countries applying lessons from last winter, now?

Although China has largely brought its epidemic under control, reporting close to zero local transmission in recent months, the country's health minister Ma Xiaowei said last month that travel and gatherings should be

restricted during the 2021 Lunar New Year, a 7-day-long holiday that will start on 11 February. Coronavirus-prevention measures were eased ahead of a major Chinese national holiday in October.

At the end of November, Japan's officials asked residents not to travel between hard-hit areas of the country for three weeks.

Does the size of a gathering matter?

Mass gatherings contribute to the spread of coronavirus. For example, a football match in northern Italy in February attended by more than 45,000 people might have led to the region becoming an early epicentre of the coronavirus pandemic, says Stefania Boccia, a public-health expert at the Catholic University of the Sacred Heart in Rome and at Gemelli University Hospital in Rome.



'We didn't model that people would go to a party if they tested positive'

But small gatherings pose risks, too. According to a [report released by the World Health Organization \(WHO\) in February](#), the virus was largely

transmitted within households in China, with up to 85% of the infection clusters in two provinces occurring in families.

A different study³ in Wuhan, carried out in February, suggested that if a person is infected, 30% of their household — about one in three people — will get infected. A third study⁴, which is not yet peer reviewed, suggests that limiting gatherings to ten people or fewer can reduce the virus's transmission rate.



Christmas preparations in Warsaw.Credit: Czarek Sokolowski/AP/Shutterstock

Does COVID-19 spread faster indoors, in cold climates?

Warm and wet climates seem, in part, to reduce the spread of the disease⁵. That's probably because when it's hot and humid, viral particles tend to fall to the ground rapidly, Chen says.

But human behaviour also plays an important part: when it's cold, people tend to gather indoors. Such [gatherings pose a higher risk](#) because the virus travels through the air in tiny droplets when an infected person talks, coughs, laughs, sings or even breathes. That's why it's important for people gathering indoors to maintain physical distancing of at least two metres, wear a mask and keep a door or window open to allow proper ventilation, says Boccia. She adds that, in winter, when people shut their doors and windows to keep out the cold, the air in the room stagnates, giving the virus a better opportunity to linger.

What do scientists say about encouraging safe behaviour?

The WHO is concerned that upcoming festivities in Europe could coincide with [a rise in “pandemic fatigue”](#) — people's sense of being exhausted with changing their behaviour to help curb viral spread.



Face masks: what the data say

For instance, [millions of Americans travelled for the Thanksgiving holiday](#) in November, ignoring warnings from health authorities. “The challenge for

public-health experts is to ensure that we are communicating the very high risk right now, and that the safest option is for people to stay home during the holidays,” Marcus says.

Communicating risk is helpful, but “shaming and blaming doesn’t help”, says Aderonke Bamgbose Pederson, a psychiatrist and behavioural scientist at Northwestern University Feinberg School of Medicine in Chicago, Illinois. “Saying ‘people are dying’ doesn’t necessarily produce positive outcomes in behaviour modification,” Pederson says. She adds that it could be helpful to encourage people to think beyond their short-term desires, which probably include seeing their family and friends, and focus on long-term goals such as protecting their loved ones.

How do researchers plan to spend the holidays?

Aware of the risks of gatherings in the middle of a pandemic, the researchers interviewed for this article say they plan to spend the holidays only with immediate family or very close relatives.

Barbara Alexander, a physician and president of the Infectious Diseases Society of America in Arlington, Virginia, says she won’t attend her family’s traditional Christmas gathering, during which more than 30 family members usually get together. Instead, she’ll stay at home with her husband, 96-year-old mother, teenage son and 25-year-old au pair. “My mother has diabetes and hypertension — if she gets COVID, she’s not liable to do well,” Alexander says.

Chen had planned to travel to China for the 2021 Lunar New Year to visit relatives, but probably won’t now do so owing to travel restrictions. He says he will celebrate the festival in the United Kingdom with his wife and children, connecting virtually with friends and family in China.

Alessandro Vespignani, a computational epidemiologist at Northeastern University in Boston, who analysed the effects of travel restrictions on the spread of the virus, will also be spending Christmas at home with his immediate family. He says that not spending the holidays with one’s extended family and friends can be tough. But, he adds, “We have some

effective vaccines that will be distributed in a few weeks — we need to hold on tight, make one extra sacrifice and then, next Christmas, we can go back to normal.”

Nature **588**, 549 (2020)

doi: <https://doi.org/10.1038/d41586-020-03545-1>

References

1. 1.

Chen, S., Yang, J., Yang, W., Wang, C. & Bärnighausen, T. *Lancet* **395**, 764–766 (2020).

2. 2.

Du Plessis, L. *et al.* Preprint at medRxiv
<https://doi.org/10.1101/2020.10.23.20218446> (2020).

3. 3.

Wang, Z., Ma, W., Zheng, X., Wu, G. & Zhang, R. *J. Infect.* **81**, 179–182 (2020).

4. 4.

Brauner, J. M. *et al.* Preprint at medRxiv
<https://doi.org/10.1101/2020.05.28.20116129> (2020).

5. 5.

Mecenas, P., Bastos, R. T. d. R. M., Vallinoto, A. C. R. & Normando, D. *PLoS ONE* **15**, e0238339 (2020).

Jobs from Nature Careers

•

- - [All jobs](#)
- - **[Full Professorship for Translational Imaging in Oncology \(W3\)](#)**
[German Cancer Research Center in the Helmholtz Association \(DKFZ\)](#)
[Dresden, Germany](#)
[JOB POST](#)
 - **[MSc Position in Forest Research](#)**
[The University of British Columbia \(UBC\)](#)
[Vancouver, Canada](#)
[JOB POST](#)
 - **[Research Associate - zero-emission hydrogen production project](#)**
[The University of British Columbia \(UBC\)](#)
[Vancouver, Canada](#)
[JOB POST](#)
 - **[Laboratory Manager - Zamore Lab](#)**
[Howard Hughes Medical Institute \(HHMI\)](#)
[Worcester, United States](#)
[JOB POST](#)

This article was downloaded by **calibre** from <https://www.nature.com/articles/d41586-020-03545-1>

| [Section menu](#) | [Main menu](#) |

Books & Arts

- **The pandemic bookshelf grows** [18 December 2020]

Book Review • Outbreaks have long wrought fear, lies, intolerance, inequality and ruin — will we ever learn?

- **What are COVID archivists keeping for tomorrow's historians?** [17 December 2020]

Essay • Records of past pandemics are patchy. This one has seen a global frenzy of collecting.

BOOK REVIEW
18 December 2020

The pandemic bookshelf grows

Outbreaks have long wrought fear, lies, intolerance, inequality and ruin — will we ever learn?

Tilli Tansey

Tilli Tansey is emeritus professor of medical history and pharmacology at Queen Mary, University of London.

[Contact](#)

Search for this author in:

- [Pub Med](#)
- [Nature.com](#)
- [Google Scholar](#)



Cemetery workers wear personal protective equipment to prepare graves for those who have died from COVID-19 in Juárez, Mexico. Credit: Mario Tama/Getty

The Rules of Contagion: Why Things Spread — and Why They Stop
Adam Kucharski Wellcome Collection (2020)

COVID-19: The Pandemic that Never Should Have Happened and How to Stop the Next One *Debora Mackenzie* Hachette (2020)

Apollo's Arrow: The Profound and Enduring Impact of Coronavirus on the Way We Live *Nicholas A. Christakis* Little, Brown Spark (2020)

Understanding Coronavirus *Raul Rabadan* Cambridge University Press (2020)

The Pandemic Century: A History of Global Contagion from the Spanish Flu to Covid-19 *Mark Honigsbaum* WH Allen (2020)

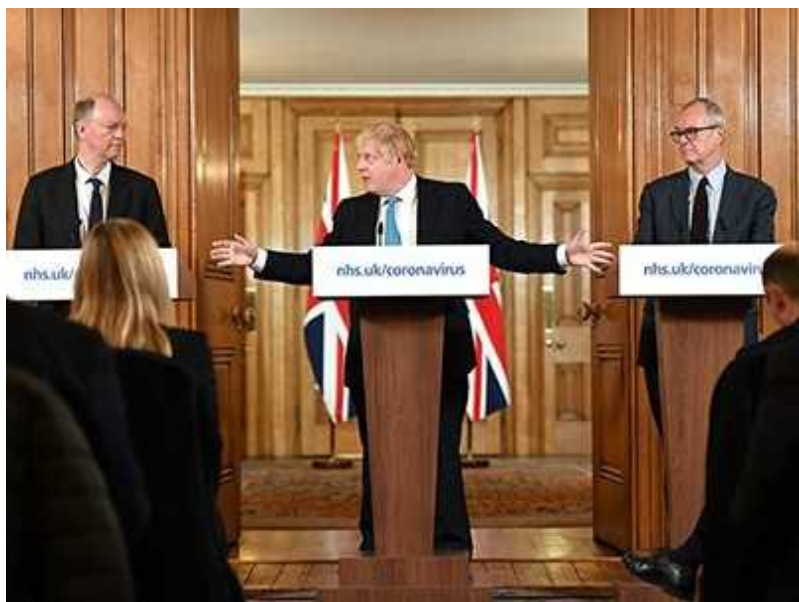
The Plague Cycle: The Unending War Between Humanity and Infectious Disease Charles Kenny Scribner (2021)

To make sense of a year in which decades' worth of events have happened in weeks, books help — from those that are centuries old, to those that are out of date as they hit the shelves. Just as diarist Samuel Pepys showed us the Great Plague of 1665 through the eyes of a government administrator, pandemic-era scientists, doctors, historians and journalists are already refracting history-in-the-making through the prism of their own experiences.

Adam Kucharski's *The Rules of Contagion* makes eerie reading now. Written pre-pandemic, it was published in February when, according to the World Health Organization (WHO), SARS-CoV2 was a public-health emergency of international concern but not yet a pandemic. The words 'coronavirus' and 'COVID-19' don't even appear in the index; Chris Whitty, the chief medical officer for England and an almost-daily fixture in the UK media for much of 2020, makes only a fleeting appearance as an advocate of mathematical models, saying: "[T]he key is usually not that they are "right", but that they provide an unpredicted insight."

Unpredicted insights are what the author, a mathematician at the London School of Hygiene & Tropical Medicine, reveals by considering the concept of contagion in biology and society, from financial markets to social media and fake news.

As a toddler, Kucharski had the rare immune condition Guillain–Barré syndrome (GBS). Discharged from hospital with a toy horn to test his respiratory muscles, his long recovery faded from memory until many years later, when he came across the disease again as an epidemiologist working in Fiji. A WHO report of unusual clusters of GBS across several Pacific islands ultimately pointed to Zika virus infections as the cause, which Kucharski and his team then modelled mathematically.



Scathing COVID-19 book from Lancet editor — rushed but useful

Kucharski's examples range widely: British physician Ronald Ross's early investigations into the role of mosquitoes in malaria transmission; physician John Snow's experiments in cholera-ravaged Soho; the flu of a century ago; and more recent investigations into the spread of HIV/AIDS. He notes that Gaëtan Dugas was misidentified as Patient Zero in the US HIV epidemic as a result of the misreading of his clinical record card that was marked 'O', not zero, for 'Outside California'. How often do such errors occur? And his accounts of tracking Dengue, Ebola, Zika and severe acute respiratory syndrome (SARS) trace the conflicts and convergences between biological evidence, political necessities, social control and the awful rise of fear, racism, inequality and economic strife. With every disease comes missed opportunities, obfuscation and marginalization — see, for instance, Laura Spinney's outstanding account of the 1918–19 pandemic, *Pale Rider* (see [T. Tansey Nature 546, 207–208; 2017](#)) and journalist David Randall's tale of the 1900 plague outbreak in San Francisco (see [T. Tansey Nature 568, 454–455; 2019](#)).

Kucharski considers other clusters. Suicide rates can increase in the wake of a celebrity taking their own life; a study from Columbia University in New York City identified a 10% increase following the suicide of comedian Robin Williams, for instance. One-quarter of gun murders in the United States in 2015 occurred in areas containing less than 2% of the country's total population. And he explores economic panics, from seventeenth-century tulip mania in the Netherlands to the Bitcoin craze of the past decade, and the way that markets spread economic problems from country to country. Clearly, his role as an intern at a London investment bank during the 2007–08 financial crash made a lasting impression.

The most pressing question he tackles is why do contagions stop? There is no neat answer on the final pages. But it is clear throughout that the prompt interaction between understanding and control is key. This rule applies for

biological pandemics, financial disruptions, crime, violence and every form of social-media contagion Kucharski identifies.

Righteous fury

Of several authors that explicitly address the present pandemic, two take similar approaches: Debora Mackenzie (*COVID-19*) and Nicholas Christakis (*Apollo's Arrow*). Mackenzie, who writes on health for *New Scientist*, and physician and sociologist Christakis are players in the stories they tell, and both have produced crucial works at phenomenal speed (Mackenzie's was published in July, Christakis's in October). And, like *The Lancet* editor-in-chief Richard Horton in *The COVID-19 Catastrophe* (see [S. Buranyi *Nature* 582, 478–479; 2020](#)), they are angry. Angry at the mistakes that allowed the virus to flourish, and at the inequalities that the epidemic has exposed and amplified. Still, neither matches Horton's fury that so many have died owing to the complacency of governments.

Christakis directs Yale University's Human Nature Lab in New Haven, Connecticut. He focuses particularly on the US experience of COVID-19 from epidemiological, social and medical perspectives. As befits an erstwhile hospice physician and friend of the late medical ethicist Renée Fox, to whom the book is dedicated, he gives moving accounts of patients, their experiences of the disease and their sad, lonely deaths. He bears witness to the doctors and nurses forced to use refuse sacks because of a lack of personal protective equipment, and turned out of their accommodation by landlords and neighbours fearing contagion. And he recognizes the personal and community grief that has resulted — for the lives and ways of living lost across the globe.

His rage at health inequalities and lack of access to universal health care for homeless people, prisoners and low-income workers is palpable, as is his wrath, for example, at the threat of enforced water shut-offs in the middle of the pandemic, with an estimated 15 million Americans unable to pay their utility bills. Not surprisingly, much of his anger is directed at US President Donald Trump and his administration, and in particular the snake-oil salesmen peddling unsubstantiated 'cures', such as bleach, silver solutions

and the antimalarial drug hydroxychloroquine, encouraged by the confusion emanating from the White House.



A physician takes a coronavirus swab from a visitor outside a clinic in Shah Alam, Malaysia. Credit: Lim Huey Teng/Reuters

Yet Christakis is an optimist. History suggests, he argues, that humanity will emerge from COVID-19 with renewed senses of purpose and possibilities, “albeit after tremendous sorrow”. He foresees a licentious era beginning around 2024, akin to the Roaring Twenties that followed the First World War and the 1918 flu pandemic. We can look forward to increased religiosity, risk-taking and intemperance.

Mackenzie relates the United Kingdom’s catastrophically slow response compared with other research-rich economies, such as New Zealand, Singapore and Taiwan, where COVID-19 was swiftly contained. She quotes some of her own prescient reporting from years past. In 2013, after watching a less-than-satisfactory simulation of a bird-flu pandemic at the WHO’s headquarters in Geneva, Switzerland, she wrote in *New Scientist*: “Information will flood in; body counts will mount. Governments will be

told that their demands for vaccines and drugs cannot be met. [The WHO] will issue declarations, hold briefings, organise research, tell people to wash their hands and stay home. Mostly, though, it will just watch helplessly.”



What are COVID archivists keeping for tomorrow's historians?

She reflects on how COVID-19 has brought home the terrible power of pestilence to wealthy countries, which for too long have been oblivious to the toll of malaria, tuberculosis, HIV and more in the global south. How could this have happened, she asks, despite all the wonder drugs and high technology? Mackenzie’s diagnosis points to global ecological problems: too many people, increasing pressure of space for food and habitation, and the encroaching dangers of forests as intensive farming pushes people and livestock into wildernesses that harbour new animal-borne diseases.

Paul Rabadan’s *Understanding Coronavirus* is a very different offering. This pocket volume offers a series of questions and answers, ranging from basic virology, such as ‘What is a coronavirus?’, to more complex issues such as ‘How does the COVID-19 outbreak compare to the SARS outbreak in 2003?’ There is a ‘Summary of common misunderstandings’ and a couple of

pages of notes added as the book went to press. Although the text is clear and cogent, the problems of balancing content with presentation are clear in the illustrations — many are too small, and several are too complex for the non-specialist. Some sections have inevitably dated quickly, such as ‘Are there vaccines for coronaviruses?’. That said, this small book could be required reading for many politicians and journalists — along with Carl Bergstrom and Jevin West’s book, *Calling Bullshit*, on data presentation and interpretation, and their significance in the contagion of ideas (see [E.-J. Wagenmakers *Nature* 584, 36; 2020](#)).

Until next time

Two more volumes take broader historical sweeps. Mark Honigsbaum, a medical historian and investigative journalist, has reissued his well-received 2019 volume *The Pandemic Century* with new material addressing the current pandemic. A gripping read, it covers the usual wide range of infectious diseases — plague, flu, Ebola, AIDS, SARS, Legionnaires’ and Zika (see [B. Kiser *Nature* 567, 459; 2019](#)). There is also a chapter on the outbreak of psittacosis, or parrot fever, that started in 1929 in the United States: a respiratory disease caused by the bacterium *Chlamydia psittaci*. In a similar way to COVID, psittacosis can be mild or appalling. It is now very rare, thanks to widespread antibiotic treatment of infected people and commercial flocks of birds, especially domestic poultry.



We were warned what to expect in the pandemic, shows health-care league table

In the new final chapter on ‘Disease X’, now known as COVID-19, Honigsbaum also blames complacent politicians but bemoans the lack of medical research into coronaviruses, too. He calls them the “Cinderellas” of the virus world: ambitious young microbiologists were warned that the waxing and waning of interest and funding for such research was no way to ensure a successful scientific career.

An economist at the Center for Global Development in Washington DC, Charles Kenny (*The Plague Cycle*) takes an even longer view. His starting point is a discussion of prehistoric humans’ susceptibility to disease, focusing on 2,500 years of civilization’s interaction with infections, especially in today’s urban societies. This is big-picture medical history. It takes in pestilence including plagues, malaria, smallpox and polio. It snapshots antibiotics and vaccines, and the problems of drug development, anti-vaccine campaigners and drug resistance. And he looks at social and medical reform, including sanitation, nutrition and the development of professional medical science and public-health systems. This all-encompassing view of humanity’s battles against disease provides a useful background to the more-specialized COVID-19 volumes.

The conclusion of *The Rules of Contagion* makes poignant reading. Kucharski writes that close analysis of previous outbreaks — learning what was predicted and what was ignored — offers the opportunity to prevent or control future outbreaks. Unfortunately, as the rest of these books relate, memories are short, political wills are weak and effective contingency plans are tweaked, ignored or forgotten. Reading Pepys’ diary entry for 31 December 1665 — “Now the plague is abated almost to nothing ... to our great joy, the town fills apace, and shops begin to be open again” — we know there’s always a next time.

Nature **588**, 580-582 (2020)

doi: <https://doi.org/10.1038/d41586-020-03555-z>

Jobs from Nature Careers

- - - [All jobs](#)
 -
 - **Full Professorship for Translational Imaging in Oncology (W3)**
 - [German Cancer Research Center in the Helmholtz Association \(DKFZ\)](#)
 - [Dresden, Germany](#)
 - [JOB POST](#)
 - **MSc Position in Forest Research**
 - [The University of British Columbia \(UBC\)](#)
 - [Vancouver, Canada](#)
 - [JOB POST](#)
 - **Research Associate - zero-emission hydrogen production project**
 - [The University of British Columbia \(UBC\)](#)
 - [Vancouver, Canada](#)
 - [JOB POST](#)

▪ **Laboratory Manager - Zamore Lab**

Howard Hughes Medical Institute (HHMI)

Worcester, United States

JOB POST

This article was downloaded by **calibre** from <https://www.nature.com/articles/d41586-020-03555-z>

| [Section menu](#) | [Main menu](#) |

ESSAY

17 December 2020

- Correction [18 December 2020](#)
- Clarification [23 December 2020](#)

What are COVID archivists keeping for tomorrow's historians?

Records of past pandemics are patchy. This one has seen a global frenzy of collecting.

Laura Spinney

Laura Spinney is a science writer based in Paris. She is the author of *Pale Rider: The Spanish Flu of 1918 and How it Changed the World* (2017).

[Contact](#)

Search for this author in:

- [Pub Med](#)
- [Nature.com](#)
- [Google Scholar](#)



A composite photograph of surgical gloves and masks discarded in Cardiff, UK, in December 2020. Credit: Matthew Horwood/Getty

If only somebody had counted the orphans.

That was one wish I had while trawling archives on the 1918 influenza pandemic to research my book *Pale Rider*. Another yearning? If only someone had saved biological samples of the unidentified respiratory disease that ravaged China in late 1917.

Historians a century hence will, I think, have a lot more to go on.

On 30 January this year, the World Health Organization (WHO) sounded a global alarm when it designated an outbreak of respiratory illness a ‘public health emergency of international concern’. On the same day, the US National Library of Medicine (NLM) launched a [web archive for the incipient pandemic](#). “The disease didn’t even have a name yet,” says Susan Speaker, a historian at the NLM in Bethesda, Maryland. “We collected the tweet in which the WHO named it.”

Since then, the NLM has archived thousands of websites and social-media posts from governments and non-governmental organizations, journalists, health-care workers and scientists around the world. That's in addition to all the COVID-related publications in its literature database, PubMed.

Efforts to document the pandemic for posterity have been under way everywhere since early in the year. Government agencies such as the US Centers for Disease Control and Prevention (CDC) in Atlanta, Georgia, and scientific institutions including the Pasteur Institute in Paris weren't far behind the NLM. Their archives are being complemented by those of museums, libraries, historical societies and community groups. The global frenzy of collecting has even prompted talk of curatorial burnout.

Museum curators are on the lookout for discarded ventilators and failed prototype COVID-19 tests — but they must choose the moment they ask with care. “We can’t just say to busy people, ‘Would you stop developing the vaccine and talk to me about collecting stuff?’” says Natasha McEnroe, keeper of medicine at the Science Museum in London. “We have to tread very, very carefully.”



Plague in San Francisco: rats, racism and reform

Others are storing souvenirs of people's lived experience — video diaries, mask fashion, recordings of the quiet of locked-down streets. Or they're salting away objects that the pandemic has rendered iconic: the signage around the lectern from which UK Prime Minister Boris Johnson spoke to the press; a wooden spoon that a little girl broke while banging her family's cooking pots in support of medical personnel. For the first time, a pandemic has triggered institutional plans for rapid-response collecting — an initiative pioneered by London's Victoria and Albert Museum (its virtual COVID-19 collection even includes a toilet roll).

Collectors are motivated by an awareness that something historic is unfolding, and that past pandemics were relatively poorly documented. Some archivists warn that future historians will have more data than they can make sense of. Others worry about blind spots. Either way, COVID-19 could buck a trend, says Astrid Erll, a memory scholar at the Goethe University Frankfurt in Germany. "It is the first worldwide digitally witnessed pandemic," she wrote in September in the journal *Memory Studies*¹: "a test case for the making of global memory in the new media ecology."

What to save?

In the decades after the 1918 influenza pandemic, the only people who really paid attention to it were virologists, medical historians and actuaries employed by insurance companies. Later in the twentieth century, its study became multidisciplinary, with economists, sociologists and psychologists showing an interest — along with 'mainstream' historians. But by then, much was lost, if it had ever been preserved.

The absences are eloquent in themselves: the lack of a reliable lab test for flu led to massive diagnostic confusion, for example, and women's accounts are relatively rare.

So twenty-first-century archivists are trying to think ahead, to save material that might otherwise pass into oblivion (while trying to distinguish the real from the fake news). At the Pasteur Institute, for example, all internal documentation is being collected, including meeting reports; the same is true at the beleaguered CDC. “We are also beginning to ramp up efforts to collect more personal materials from CDC staff, including video diaries, journals and photographs,” says Judy Gantt, director of the David J. Sencer CDC Museum in Atlanta.

The 1918 flu outbreak, like all epidemics that have been measured, highlighted inequality. Today’s public-health organizations are — to a greater or lesser extent — documenting that dimension of the current pandemic. For example, Gantt’s team is collecting data on how CDC guidelines are being implemented in communities, as well as on health disparities, social justice and activism.



An iron lung, a breathing aid for people paralysed by polio, in the Science Museum, London.Credit: SSPL/Getty

International archiving projects are trying to capture the interconnected and globally variable nature of what we're living through. The NLM, for example, contributes to [an effort launched by the International Internet Preservation Consortium](#) (IIPC) in February. With members in more than 45 countries, including national, regional and university libraries and archives, the IIPC aims as far as possible to sample the multiplicity of the pandemic across the world. "We want to get a lot of nitty-gritty detail about individual countries, selected by experts in those countries," says Alex Thurman, a librarian at Columbia University in New York City and one of the collection's lead curators.

At the other end of the scale, there are local and specialized initiatives. The National Library of Israel in Jerusalem is documenting the impact of COVID-19 on Jewish communities globally through what it calls "ephemera" — e-mails about synagogue services that have moved online, for example, or announcements of innovative Jewish law rulings. The American Institute of the History of Pharmacy in Madison, Wisconsin, is gathering pharmacists' testimonies in any and all media. The Museum of the Home in London is asking Britons to submit photos of their domestic lives, in a project called Stay Home.

Data deluge

Archivists are aware that it's not for them to decide what future historians will consider relevant. In 1918, many people doubted that the first wave of the pandemic, which resembled seasonal flu, was caused by the same pathogen as the much more lethal second wave (it was). As evidence comes in, new connections are made while others fade. The tendency today has therefore been to collect everything, within each organization's broad remit. Hence the ocean of data — and the pandemic rages still.



Chasing epidemics

“We had to slow our colleagues down early on because we were using our data budget so quickly,” says Thurman. The IIPC’s 2020 allocation, fixed before the outbreak at 3 terabytes, was full by June. The Internet Archive, a non-profit organization that is sponsoring the IIPC’s COVID-19 collection, gifted it another two, and it has used nearly four so far — storing archived copies of close to 11,000 selected web resources in 66 languages.

Data mining and machine learning tools are going to be needed to explore such large data sets, and Speaker worries that those tools are not yet as well developed as the ones for collecting. It’s a concern others share. “The interesting thing about this pandemic is that we may end up with too much information and very little sense of how to sort through it,” says historian Erica Charters at the University of Oxford, UK.

Holes in history

Pandemics pose logistical problems — one reason they have tended to leave such light archival footprints. “Collecting infectious disease is a real challenge,” says McEnroe, speaking from her son’s bedroom. Many museums have closed, and archivists have been working from home.

Physical collecting has health and safety risks, and raises ethical concerns. Samples of infected lung tissue taken from patients in 1918 were used in 2005, controversially, to bring the virus back to life² — something that nobody in 1918 would have dreamed possible.

So there are holes in the wealth of collected material. Senior scientists and politicians might have their deliberations captured by normal reporting mechanisms such as *Hansard*, the official transcriptions of UK Parliamentary debates, but they tend not to have time to keep video diaries or screenshot their Slack channels. Nor do patients or front-line workers — especially those from vulnerable groups. “Those who will be suffering the most … will have the least time, energy, and ability to create a full documentary record of what’s going on as it unfolds,” wrote Eira Tansey, a digital archivist at the University of Cincinnati in Ohio, in a blogpost in June (see go.nature.com/2kci5vp).



Lessons from the Ebola front lines

Geographical coverage is patchy, too. The Russian Museum of Medicine in Moscow plans to collect information about the medical response across Russia’s ‘red zones’ — where infection rates are high — but the project has been delayed by the pandemic. At Krea University in Sri City, India,

historian John Mathew didn't have his proposal to collect the oral histories of migrant workers approved until October. The IIPC has only one member in Africa and few in Asia. Thurman and his co-lead curator, Nicola Bingham at the British Library in Boston Spa, are conscious of the organization's membership bias towards wealthier nations.

During the 1918 pandemic, the continents that experienced the highest mortality rates — Asia and Africa — were the least well documented. Something similar could happen again. “There is a privilege in being able to collect, in having the resources to do so,” says Charters.

Whose record?

Debates around the recording of epidemics — or any historical event — are not new. The choice of recording tools changes according to culture and period, too. In some places, the personal COVID-19 diary has flourished, be it on paper, Instagram or TikTok. But the diary as an everyday tool for introspection was developed in Christian cultures, Charters says, and might not be privileged in the same way in non-Christian ones.

And when should you have started your diary — or your archive? People living in countries where epidemics are rare perceive a clear before and after for COVID-19. That is not true everywhere. For instance, many Kenyans see the pandemic as a continuation of an old and unremitting drama. As anthropologists Wenzel Geissler and Ruth Prince at the University of Oslo observed in July³: “People in this region have experienced a long century of epidemics and anti-epidemic measures of varying duration and intensity”.

We're no more likely to agree on the end of the pandemic. If COVID-19 becomes a regularly circulating disease, as many predict, and if its social and economic consequences linger for years or decades, when do we say it's over? Archivists need to fix an end date, if only to manage their dwindling resources. They know that date will be arbitrary, yet it will shape the histories that will be written. Convention in the global north is that the 1918 pandemic lasted for 18–24 months. It raged in the Pacific islands well into 1921.

The only comfort, says Charters, is that histories can be rewritten in light of accumulated knowledge, and in ways that it's difficult to predict. Think of the less well known influenza pandemic of the 1890s. There is now debate about whether it was actually caused by a coronavirus, thanks to some results⁴ that have resurfaced this year. “A hundred years from now, they really will write a completely new version of COVID-19 that it’s very unlikely we would recognize,” says Charters.

Nature **588**, 578–580 (2020)

doi: <https://doi.org/10.1038/d41586-020-03554-0>

Updates & Corrections

- **Correction 18 December 2020:** An earlier version of this article misstated the nature of the resources archived by the IIPC, which covers 66 languages, rather than 15. The article also gave an incorrect affiliation for Ruth Prince. The text has now been corrected.
- **Clarification 23 December 2020:** A picture caption in this article originally implied that the iron lung display is contemporary, when in fact it is from the 1950s. The text has been updated.

References

1. 1.

Erll, A. *Mem. Stud.* **13**, 861–874 (2020).

2. 2.

Tumpey, T. M. *et al.* *Science* **310**, 77–80 (2005).

3. 3.

Geissler, P. W. & Prince, R. J. *Centauros* **62**, 248–256 (2020).

4. 4.

Vijgen, L. *et al.* *J. Virol.* **79**, 1595–1604 (2005).

Jobs from Nature Careers

- - - [All jobs](#)
 - - [**Full Professorship for Translational Imaging in Oncology \(W3\)**](#)
[German Cancer Research Center in the Helmholtz Association \(DKFZ\)](#)
[Dresden, Germany](#)
[JOB POST](#)
 - [**MSc Position in Forest Research**](#)
[The University of British Columbia \(UBC\)](#)
[Vancouver, Canada](#)
[JOB POST](#)
 - [**Research Associate - zero-emission hydrogen production project**](#)
[The University of British Columbia \(UBC\)](#)
[Vancouver, Canada](#)
[JOB POST](#)
 - [**Laboratory Manager - Zamore Lab**](#)

Howard Hughes Medical Institute (HHMI)

Worcester, United States

JOB POST

This article was downloaded by **calibre** from <https://www.nature.com/articles/d41586-020-03554-0>

| [Section menu](#) | [Main menu](#) |

Opinion

- **The WHO's chief scientist on a year of loss and learning**

[17 December 2020]

Comment • The head of scientific work at the World Health Organization reflects on the agency's challenges and achievements as it navigates the COVID pandemic.

- **Science advisers around the world on 2020**

[18 December 2020]

Correspondence • Seven government researchers who helped to guide their governments' responses to the COVID-19 pandemic speak out.

COMMENT

17 December 2020

The WHO's chief scientist on a year of loss and learning

The head of scientific work at the World Health Organization reflects on the agency's challenges and achievements as it navigates the COVID pandemic.

Soumya Swaminathan

Soumya Swaminathan is chief scientist at the World Health Organization, Geneva, Switzerland.

[Contact](#)

Search for this author in:

- [Pub Med](#)
- [Nature.com](#)
- [Google Scholar](#)



Clinician-researcher Soumya Swaminathan oversees the gathering of scientific evidence at the World Health Organization in Geneva. Credit: Fabrice Coffrini/AFP/Getty

I was appointed to the new post of chief scientist to the World Health Organization (WHO) by the director-general in March 2019. I was charged with overseeing how the 72-year-old United Nations agency gathers scientific evidence and creates guidelines. My original plan for 2020 included rolling out new processes to ensure the quality of technical documents, such as guidelines on water quality, tobacco advertising and immunization programmes. I'd resolved to find ways to focus research on

the right questions and to speed up the development of vaccines, medicines and diagnostics to address unmet public-health needs. With my colleagues in the digital-health department, I intended to finalize a global strategy for that field, incorporating telemedicine, interoperability standards and mobile health, and take it to the World Health Assembly for approval. After that, I would work with member states to make sure pathogen samples were shared rapidly with equitable access to benefits, a subject area that has been the focus of protracted negotiations (see go.nature.com/3ab4q9g).

All those plans changed on 31 December 2019. The WHO was informed about a cluster of viral-pneumonia cases of unknown origin in Wuhan, China: the disease later named COVID-19.

This year has been a roller coaster — a challenging, humbling and painful time because of the suffering and deaths worldwide. I am proud of many things my team has achieved in the past 12 months, even as the shortcomings of both the WHO and the global community have been laid bare.

What does someone charged with synthesizing evidence into guidelines do when confronted with a virus for which no evidence exists? I remember thinking that the WHO's Science Division, which I direct, was created for exactly this situation: to collect, vet, analyse and apply information quickly.

We drew on experience from the West African Ebola outbreak in 2014–16 and the 2009–10 H1N1 influenza pandemic, but mostly we have been building the ship while sailing it. We've had to balance speed and rigour. We've had to raise alarm without causing panic. We've had to convince countries to heed advice without openly criticizing them (which would risk losing their cooperation). And we've had to fight the 'infodemic', sticking to science amid attacks and false information from all sides.

Accurate and fast

Countries, especially low- and middle-income ones, depend on the WHO to decide how to combat disease and preserve public health. Under international health regulations, the agency has coordinated binding

agreements for nations to report single cases of diseases, such as smallpox or polio, within 24 hours of assessing public-health information related to the case. Global health funders, such as the UN children's charity UNICEF and Gavi, the Vaccine Alliance, look to WHO assessments to decide which childhood vaccines to pay for.

In 2007, following much (largely deserved) criticism of some of its procedures, such as not always basing decisions on evidence, the WHO set out rigorous, standardized procedures for the documents that guide these decisions, making sure that their compilation was transparent and based on evidence, and that any potential conflicts of interest were made explicit. Part of the reason the Science Division was created was to boost the compilation speed, rigour and impact of these technical documents.

The COVID-19 outbreak brought a new urgency to these goals. In the second week of February, the WHO held a conference on the new disease, to identify knowledge gaps and prioritize research questions. A typical WHO conference requires months to plan — it takes that long for visas to come through. We pulled it off with three weeks' notice, finding ways to involve those who couldn't travel. Even before the disease or virus had an official name, some 400 scientists from more than 60 countries on all continents came together. That meeting set out many crucial goals: the target product profiles for drugs, vaccines and diagnostics; criteria for vaccine prioritization; evidence-based public-health measures and treatment guidelines.

This groundwork got scientists to focus on important questions — such as what research was needed to identify the virus's incubation period and what mechanisms were responsible for the lung injury being observed — and established a network of expertise. The conference participants and additional scientists met again (virtually) in July, and it quickly became apparent that we needed global coordination for clinical trials — some 2,000 were already under way, most of which were too small to be definitive. We launched prospective meta-analyses encouraging principal investigators running trials of corticosteroids for treatment of COVID-19 to collaborate and share data, so that it could be pooled for more definitive evidence. When we convene again early next year, I expect vaccine logistics and diagnostic use to be much discussed.

In February, the Science Division developed a protocol to expedite reviews of evidence when a public-health emergency of international concern (PHEIC) is declared. During past outbreaks of Ebola, Zika and so on, different WHO programmes produced dozens of technical papers without any central coordination or quality checks, sometimes leading to confusion and mixed messages. Now, a publication-review committee draws in members from WHO headquarters and our six regional offices.

This committee, comprising 10–15 people in rotation, vets documents quickly — some 800 have been submitted so far — and eliminates duplicate work. It also connects the dots. When the committee spotted separate reports on how COVID-19 was affecting treatment for many common conditions, such as malaria, tuberculosis and diarrhoea, it pooled them into a single, streamlined document on how health systems in low-income countries could adapt to cope with the pandemic (see go.nature.com/3qzopjw).



Volunteers in Hanoi gave tourists face masks in February to help to prevent the spread of COVID-19 in Vietnam. Credit: Lillian Suwanrumpha/AFP/Getty

In another case, the committee set out guidelines for drugs being tested in clinical trials, such that it could quickly detect and announce evidence for efficacy. It contacted about a dozen researchers running clinical trials of the steroid dexamethasone, and convinced them to share data even while the trials were ongoing. It published the guidelines in September (see go.nature.com/3qfxb3h). Normally, such guidelines take 6–12 months to produce; the committee has cut the time to 6 weeks.

There was initially too little evidence to enable comprehensive, systematic reviews of primary research on COVID-19. These summarize the state of the art in a particular area, and provide the necessary evidence on which to base recommendations for interventions. This led to the WHO engaging more than 90 institutions in a new partnership called the Evidence Collaborative for COVID-19. We set up advisory groups of global experts focusing on more than 20 topics — from mask use and virus-transmission modes to health workers' protective equipment. The groups coordinate with national health systems and meet regularly to review data, debate ideas and discuss public-health recommendations. The Cochrane Collaboration has a similar initiative (see go.nature.com/3gyhdap) — there is more than enough of this work to do.

The sheer volume of new information on COVID-19 means that it is impossible for anyone to keep up. So we assembled a few dozen volunteers — scientists, doctors and technical experts working at the WHO — to screen preprints and journal articles mentioning the virus or disease for quality and novelty. Every day, they assess content published the day before (about 200 items, most of which they dismiss as poor quality or repetitive) and produce a digest. They deposit citations in the WHO Library COVID-19 database, which now contains more than 120,000 vetted papers and preprints in the 6 official WHO languages, plus Portuguese (see go.nature.com/38htjwz). The database has more than 2,500 unique visitors daily.



How to shape research to advance global health

The one thing I'm proudest of is the setting up by the R&D blueprint team of a multi-country, adaptive clinical trial to test multiple treatments at once. This format adds or removes trialled therapeutic agents as new data emerge, while continuing to recruit participants. The original thought was that some drugs already approved for other diseases might be repurposed as treatments for COVID-19. Interim results from 12,000 participants from 30 countries have been disappointing, with none of the tested drugs showing reductions in mortality or disease progression ([WHO Solidarity Trial Consortium N. Engl. J. Med. https://doi.org/10.1053/j.ajtmh.2020.20000](https://doi.org/10.1053/j.ajtmh.2020.20000)). But the approach has shown how to perform high-quality randomized clinical trials to assess potential drugs and answer public-health questions even during a pandemic. I hope we can learn from this and try a similar approach soon for diseases such as tuberculosis and cancer.

Tackling the infodemic

Meanwhile, the WHO has been communicating evidence and debunking misinformation as never before. Launched in March, the WHO Health Alert chatbot counters false information and offers features such as interactive quizzes to let people build and test their knowledge of COVID-19. It is now accessible in 30 languages across platforms including WhatsApp, Facebook Messenger and Rakuten Viber. With about 20 million users, it can reach people even in countries and regions where fragile health systems cannot keep communities informed.

The WHO has also opened lines of communication with other social-media companies. For example, WHO vaccine experts spoke to YouTube's policy team to debunk a number of vaccine myths on the platform. And the agency has worked with Google to ensure that searches produce reliable information on COVID-19 from the WHO or other credible sources. These companies, in turn, have provided insights — about which topics are trending and how to make sure that WHO information gets noticed in search results.

To-do list

So, what's next for the WHO Science Division? One priority is to collect and share more and better data in full. This applies to both routine health data and research data. Some countries lag or lapse in providing information on COVID-19 infections to the WHO. Less than half of the countries that do report to us disaggregate data by sex and other demographics.

We need a stronger infrastructure and culture of sharing. There was a meagre response when the WHO launched a COVID-19 technology-access pool to allow sharing of everything from data sets to methods for 3D-printing personal protective equipment, and to lower barriers to accessing drugs and vaccines. We are working with Gavi and the Coalition for Epidemic Preparedness Innovations (CEPI) on the COVAX initiative to ensure equitable access to COVID-19 vaccines globally — both the world's health and economy depend on protecting vulnerable people everywhere.

The data-science initiative GISAID has been a game changer. It was launched in 2008 to overcome access restrictions to avian-influenza data by creating a transparent sharing mechanism that permits providers to retain

their rights to virus data. Since January, GISAID's data-sharing platform has been the primary source of genomic and associated data from SARS-CoV-2 cases. The platform fosters collaboration among researchers and ensures that data providers are acknowledged in publications. GISAID has enabled dozens of web efforts to aid with analyses during the outbreak. Its EpiCoV database already offers more than 260,000 viral whole-genome sequences from 142 countries.

Looking ahead, funders, institutions and other players need to create better mechanisms to reward researchers who share pathogen genomic-sequence data completely openly, especially scientists in the global south.

As I have sought ways to make good decisions quickly, the lesson that repeats itself is how important it is to have thoughtful plans prepared and in place. The countries that have best protected the lives and livelihoods of their citizens have also demonstrated strong, compassionate leadership, at political and technical levels, and generally have health-care systems that engage local and global communities. These qualities require long-standing investments in people and relationships, as well as in research and development.

Not coincidentally, I have also seen the value of listening and two-way communication. Scientists talk to each other, but too often leave others behind. Citizens want to know what the evidence is, and that includes explaining gaps or mistakes. The vetting networks and committees that the WHO has established have the added benefit of letting us know what people are thinking and talking about on the ground, and what messages are or are not getting through.

In many ways, the pandemic has driven the WHO's Science Division to work out how to do what it was meant to do — only much faster.

Nature **588**, 583-585 (2020)

doi: <https://doi.org/10.1038/d41586-020-03556-y>

Jobs from Nature Careers

- - - [All jobs](#)
 - - **[Full Professorship for Translational Imaging in Oncology \(W3\)](#)**

[German Cancer Research Center in the Helmholtz Association \(DKFZ\)](#)

[Dresden, Germany](#)

[JOB POST](#)

■ **[MSc Position in Forest Research](#)**

[The University of British Columbia \(UBC\)](#)

[Vancouver, Canada](#)

[JOB POST](#)

■ **[Research Associate - zero-emission hydrogen production project](#)**

[The University of British Columbia \(UBC\)](#)

[Vancouver, Canada](#)

[JOB POST](#)

■ **[Laboratory Manager - Zamore Lab](#)**

[Howard Hughes Medical Institute \(HHMI\)](#)

[Worcester, United States](#)

JOB POST

This article was downloaded by **calibre** from <https://www.nature.com/articles/d41586-020-03556-y>.

| [Section menu](#) | [Main menu](#) |

CORRESPONDENCE

18 December 2020

Science advisers around the world on 2020

Seven government researchers who helped to guide their governments' responses to the COVID-19 pandemic speak out.

Gordon Awandare,

Director, West African Centre for Cell Biology of Infectious Pathogens,
University of Ghana.

[Contact](#)

Search for this author in:

- [Pub Med](#)
- [Nature.com](#)
- [Google Scholar](#)

Emmanuel André,

Microbiologist, National Reference Laboratory for COVID-19 and KU Leuven.

[Contact](#)

Search for this author in:

- [Pub Med](#)
- [Nature.com](#)
- [Google Scholar](#)

Eugenia Corrales-Aguilar,

Virologist, University of Costa Rica.

[Contact](#)

Search for this author in:

- [Pub Med](#)
- [Nature.com](#)
- [Google Scholar](#)

Chien-jen Chen,

Epidemiologist, Academia Sinica; former vice-president of Taiwan; and senior adviser of epidemic prevention and economic revitalization.

[Contact](#)

Search for this author in:

- [Pub Med](#)
- [Nature.com](#)
- [Google Scholar](#)

Mohammed A. Mostajo-Radji,

Former Bolivian extraordinary and plenipotentiary ambassador for science, technology, and innovation. Currently at the University of California, San Francisco, USA.

[Contact](#)

Search for this author in:

- [Pub Med](#)
- [Nature.com](#)
- [Google Scholar](#)

Ligita Jancoriene &

Head, Centre of Infectious Diseases, Vilnius University Hospital, Lithuania.
[Contact](#)

Search for this author in:

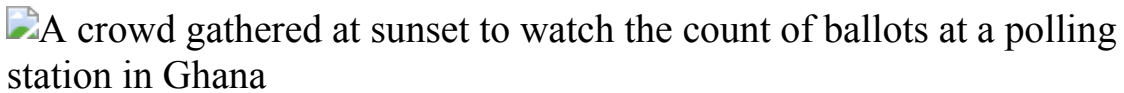
- [Pub Med](#)
- [Nature.com](#)
- [Google Scholar](#)

Mona Nemer

Chief science adviser of Canada.

Search for this author in:

- [Pub Med](#)
- [Nature.com](#)
- [Google Scholar](#)



Crowds during Ghana's election in December have fuelled fears of a surge in COVID cases. Credit: Cristina Aldehuela/AFP/Getty

GHANA: We are building capacity

Gordon Awandare

In Ghana, the pandemic has not been severe, and deaths have been very low compared with those in other parts of the world. Our group was among the first to sequence SARS-CoV-2 in Africa. We achieved this because we are building capacity for next-generation sequencing for other research purposes, including malaria-parasite genomics.

When the pandemic hit, we quickly redirected those resources and personnel to work on sequencing the virus because we felt it was important to be able to track the transmission and evolution of the virus locally. This was challenging because we did not have all the necessary reagents and had to improvise. We also had to obtain some reagent components from various collaborators in the United Kingdom. Many exciting projects have had to be put on hold. Students' research has been delayed, and they've been unable to complete their PhD or master's programmes on schedule.

In responding to pandemics, leadership has to be decisive. For example, masks should have been mandated early on. And lockdowns would have worked better had they been targeted, imposed quickly and enforced strictly.

In the big picture, African governments need to build scientific capacity sustainably rather than resorting to firefighting only when a pandemic hits. We should be preparing for the next pandemic as soon as this one ends.

BELGIUM: We were stymied by politics

Emmanuel André

In recent decades, Belgium has disrupted the continuity between prevention and curative care, thereby dismantling a health system that was built over centuries. As a consequence, we entered this pandemic unprepared, with no protective equipment in stock and a scarcity of doctors, nurses and laboratory technicians. This compounded other, less easily preventable vulnerabilities: a dense, ageing population, and one that is highly mobile both inside and beyond the borders.

Crisis management was further hampered by Belgium's complex institutional system. This meant that nine health ministers had to respond to six separate governments, each having a different balance of political parties. Despite national elections taking place in May 2019, a federal government was not set up until October 2020. This situation seeded an uncoordinated constellation of 'advisory committees' with overlapping prerogatives and variable lifetimes. The composition of these committees was subject to politicians' whims. In early September, when signs of the

second wave became obvious, virologists were partly replaced in the most influential advisory organ by a lobbyist and a former chief executive of the postal services.



COVID and 2020: An extraordinary year for science

For months, no political leader took responsibility for putting in place a long-term plan that would include clear thresholds for implementing disease control measures or for ensuring that compensation would be fairly and promptly distributed to vulnerable people and to the economic sector affected most.

The media placed scientists at the forefront of the crisis; public opinion praised iconic scientists to the skies. Meanwhile, some politicians pushed for an early easing of unpopular disease-control measures to gain public approval and in the hope of minimizing their economic impact. But epidemiological risk-taking ultimately led to prolonged lockdown and extra damage to an economy that requires stability and consumer confidence.

Next year must be different. We need to be consistent and make sure that hopes do not become deceptions. There will be vaccine hesitancy, unforeseen difficulties and unequal access. Increased testing capacity will not stop people becoming infected unless it is coordinated with a fully functional infection control and tracing system. All interventions should recognize that the most fragile people are also the ones most affected by this pandemic.

The scientific community should continue transgressing the boundaries between disciplines and countries to offer society more knowledge, more evidence and better policies, so as to finally alleviate the ravages of this pandemic. We should make sure that exiting this complex crisis leaves no one behind — and that our shaken world becomes more equal, collaborative and efficient in tackling worldwide challenges.

COSTA RICA: We fought misinformation

Eugenia Corrales-Aguilar

When the pandemic began, politicians and journalists in Costa Rica started talking to me because I am a virologist and had worked with bats and coronavirus. I thought that maybe we would be able to control this virus with the same public-health measures that we used for severe acute respiratory syndrome (SARS) in 2003. We were naive.

One of the things that's been really different this time has been the response of the Centers for Disease Control and Prevention (CDC) in the United States. We'd always looked to it for guidance on everything to do with infectious disease — until now. The lack of un politicized, evidence-based information from the CDC has been a challenge throughout this outbreak.

Another challenge has been the tsunami of information. I've never studied so much in my life, not even for my PhD. And this real-time scientific information has to be translated and applied almost immediately.



2020 beyond COVID: the other science events that shaped the year

What is really difficult is knowing how to communicate all this to non-scientists. There's so much nonsense and disinformation. I think vaccine communication — reaching people who do not want to understand that vaccines are game-changers — will take up much of my time for next year.

I've also been attacked: "What do you know? You're just a young lady that doesn't care about my restaurant that's closing," or "Viruses do not exist." But for every 50 people who think like that, there are hundreds or thousands who are thankful, who are really eager to understand.

My biggest success? Women are still under-represented in decision-making committees in Costa Rica, and I'm there giving evidence-based information to the national ministry of health and being heard. That is an example for younger generations.

TAIWAN: We learnt from SARS

Chien-jen Chen

I wish I'd been able to urge the World Health Organization (WHO), China and other authorities to take prompt actions to stop COVID-19 progressing from a local outbreak into a catastrophic pandemic. Taiwan tried, but failed, to join the 23 January emergency meeting held by the WHO, which did not announce COVID-19 as a public-health emergency of international concern for a further 10 days.

It has been my privilege to work alongside my fellow citizens in Taiwan to combat COVID-19. Almost everyone in Taiwan complied with guidelines and regulations for epidemic control. Only around 1,000 of around 400,000 people isolated or quarantined at home violated the restriction. The rest sacrificed 14 days of freedom to let 23 million people live, work and go to school normally. We have been COVID-free now since 13 April.

Key elements of Taiwan's success include prudent action, rapid response (we took action on 31 December) and early deployment of control measures, together with transparency and public trust with solidarity. We did not need to implement city lockdowns or mass screening. Instead, we applied information technology and artificial intelligence to carry out precision disaster prevention and mitigation. These efforts included border control and quarantine, social distancing, contact tracing, precision testing, hospital infection control, and rationing and mass production of face masks and other personal protective equipment. The government also provided financial support to low-income families and affected industries, and economic stimulus vouchers to every citizen.

The 2003 SARS pandemic taught us the effectiveness and efficiency of measures such as border control, mandatory case reporting and isolation treatment, as well as contact tracing, testing and isolation. I'd also like to stress the importance of professionalism and political neutrality, which earn public trust and compliance with epidemic control measures.



Disinfecting Bolivia's streets during lockdown in April.Credit: Aizar Raldes/AFP/Getty

BOLIVIA: Against all odds we did not fail

Mohammed A. Mostajo-Radji

Every international agency we spoke to predicted that Bolivia would be hit harder by COVID than most nations. It has one of the worst health-care systems in the world, with several regions refusing to share information with the central government. Our neighbours, including Brazil, Peru, Argentina and Chile, have all been badly affected by the pandemic.

The first meeting between the country's strategic response team and the WHO, in early March, showed us that Bolivia had not yet recovered from a catastrophic dengue epidemic — and, for the first time in more than 20 years, measles had reappeared. The country's three public molecular-testing laboratories were already saturated.

So on 17 March, we implemented one of the strictest lockdowns in the world. This gave us time to take stock of the health-care system. Supplies

were scarce. And because much of the population lives at high altitude, where atmospheric pressure is low, most of the available equipment was of no use. It was therefore essential to have our own scientific advisory committee and to connect with specialists from across the world to receive real-time feedback and updates. Science diplomacy has never been so important: it allowed us to access donations of equipment and vaccines, coordinate the rapid transport of medications and design a shared response strategy with other countries.

In the months leading up to the general elections in October, COVID-19 became highly politicized. From protesters impeding the movement of ambulances and oxygen tanks, to technicians stealing testing reagents to sell on the black market, the battle became more difficult every day. Internally, I fought ageism from members of the cabinet and the armed forces who refused to take advice from someone less than half their age.

Still, Bolivia has one of the lowest infection rates in the Americas. I look back on all the discussions, and all the people whose hard work became vital during these months, and think “against all odds, we did not fail”.

LITHUANIA: We feel we’re still fighting a war

Ligita Jancoriene

Working in this pandemic feels like war — or exile. As we strive to make sense of the battle against COVID-19, my colleagues and I in Lithuania, at Vilnius University Hospital, have started comparing cataclysms that our families have experienced — from military conflicts to the mass deportations carried out by the Soviet Union. We physicians face a constant struggle with an invisible enemy, anxiety about the future, daily encounters with dying patients, and unbearable strain, fatigue and overwork.

In the hospital, the first challenge was redeploying medical staff to work with people with COVID-19, and setting up new units to treat them. Everyone had to leave their comfort zone, and it was not easy. Some staff refused; others volunteered. Later, during the second wave in early October, treatment units were opened in regional, non-university hospitals. There,

staff resistance was particularly high — possibly out of fear or lack of knowledge.

So we invited regional doctors to our virtual meetings, case discussions and internal seminars. They became members of our COVID team. A sense of collegiality and teamwork — that no one was alone on the battlefield — helped medical staff on the pandemic front to keep going.

There was chaos at the beginning. Decisions were made on the fly, and orders changed frequently. I have been involved in two expert groups advising the government, but there was no dedicated team for managing the pandemic. Medical institutions often had to make immediate decisions on their own. Medical staff working with people with COVID-19 were promised extra pay, which was repeatedly delayed by the ministry of health. Greater trust in professionals, and decision-making on a horizontal basis rather than a hierarchical one, would have speeded the response — and boosted trust in government.

In treatment and care facilities, sometimes all the staff, and nearly all the patients, became infected within a few days of the first case. In such instances, emergency assistance was paralysed, and whole departments had to close temporarily. This caused complete despair.

As we face future waves, we need to strengthen resources for health-care workers on the front lines. Clear guidelines must be prepared on how to manage COVID-19 infection in a regional hospital or nursing home, rather than every patient being referred as quickly as possible to a larger centre. Early on, health authorities focused on university hospitals equipped with personal protective gear and other specialized equipment. Now, there are simply too many patients, and each facility must be prepared to diagnose and treat those who are infected. Otherwise, we risk continuing to lose this war.

CANADA: Science guided our decisions

Mona Nemer

In 2017, a few weeks after my appointment to the newly created position of Canada's chief science adviser, the question about my role in national emergencies arose. I looked internationally for advice. Starting with consultations with my UK counterpart and culminating last year with joint tabletop simulations with the United Kingdom and the United States — including one of a pandemic — these exercises provided guidance on how science can assist government in times of crisis. The connections developed then have proved invaluable this year, because my international counterparts and I met regularly throughout 2020 to share data and best practices on virus spread, public-health measures, diagnostics development and roll out, and therapeutics and vaccine trials.

Soon after the pandemic arrived in Canada in late January, my staff and I assembled several multidisciplinary scientific advisory groups to help me provide up-to-date COVID-19 advice to the prime minister and cabinet. As we focused on areas ranging from vaccines and aerosol transmission to children and long-term care, researchers mobilized to share their findings and advice quickly and openly. As a result, science guided decision-making in real time like I have never seen before. The contrast with some other parts of the Americas has been striking.

It has been gratifying to witness public appreciation of, and government interest in, science. This has provided welcome encouragement in such stressful and uncertain times. The sheer objectivity of science can go a long way in a crisis, especially when response is hampered by inaccessibility to data, reagents and personal protective equipment.

To take on future existential threats, nations need to strengthen their science advisory systems locally and globally, and build public trust in research. Understanding the scientific method empowers people to question information sources and to deal with uncertainty, which ultimately helps to minimize the spread of misinformation. Researchers can help — by openly sharing their knowledge and inspiration, and by helping to rebuild societies in a way that puts evidence at the centre of all decisions.

Nature **588**, 586-588 (2020)

doi: <https://doi.org/10.1038/d41586-020-03557-x>

Jobs from Nature Careers

- - - [All jobs](#)
 - - [Full Professorship for Translational Imaging in Oncology \(W3\)](#)

[German Cancer Research Center in the Helmholtz Association \(DKFZ\)](#)

[Dresden, Germany](#)

[JOB POST](#)
 - [MSc Position in Forest Research](#)

[The University of British Columbia \(UBC\)](#)

[Vancouver, Canada](#)

[JOB POST](#)
 - [Research Associate - zero-emission hydrogen production project](#)

[The University of British Columbia \(UBC\)](#)

[Vancouver, Canada](#)

[JOB POST](#)
 - [Laboratory Manager - Zamore Lab](#)

[Howard Hughes Medical Institute \(HHMI\)](#)

Worcester, United States

JOB POST

This article was downloaded by **calibre** from <https://www.nature.com/articles/d41586-020-03557-x>

| [Section menu](#) | [Main menu](#) |

Work

- **Ways to look after yourself and others in 2021** [18 December 2020]
Career Feature • Scientists offer their views on what's important for the coming year.
- **'I want to generate opportunities for Black scientists'** [17 December 2020]
Where I Work • UK geoscientist Christopher Jackson will be the first Black researcher to deliver a Christmas lecture at the Royal Institution of Great Britain.

CAREER FEATURE

18 December 2020

Ways to look after yourself and others in 2021

Scientists offer their views on what's important for the coming year.

Virginia Gewin

Virginia Gewin is a freelance writer in Portland, Oregon.

Search for this author in:

- [Pub Med](#)
- [Nature.com](#)
- [Google Scholar](#)

[Find a new job](#)



Climate scientist Kim Cobb speaks at a women's empowerment event in Atlanta, Georgia. Credit: Lorikay Stone

As the world hopes for swift roll-outs of COVID-19 vaccines in 2021, researchers' ambitions are likely to still be constrained by the continuing pandemic and its effects. Amid shifting career priorities, *Nature* asked scientists for their advice to colleagues and what they plan to start, limit or keep doing.

Create boundaries. Researchers at all career stages whose workspace is mainly or exclusively at home should set firm limits on working hours, says Stéphanie Lizy-Destrez, who studies the design and function of future space systems at the Higher Institute of Aeronautics and Space in Toulouse, France. “The biggest challenge is to separate professional and private lives,” she says.

When France first imposed a lockdown in March, she examined the impacts of isolation on 80 graduate and undergraduate students who were confined to their small dormitory rooms on campus. She says that it’s hard for people working remotely to separate personal and professional time. “There are no

borders,” she says. “Sometimes you don’t take time for rest or leisure.” In addition to establishing regular waking and meal times during the week, she advises setting non-negotiable periods for time off and exercise, especially at the weekend.



New Year's resolution: One meeting-free week a quarter

For scientists who share living space, it’s important to establish a private zone, or, at least, stretches of undisturbed time, she adds.

When Heidi Rehm resolved this year to create a meeting-free week once a quarter, she couldn’t have anticipated the pandemic. Even so, says Rehm, medical director of the Broad Institute Clinical Research Sequencing Platform in Cambridge, Massachusetts, she hasn’t slipped once. If anything, she says, the strategy has flourished: the Broad Institute is planning to expand it institution-wide next month.

Enhance virtual interactions. Online conferences level the playing field and allow for higher attendance, says Emmanuel Adukuwu, acting deputy head of the department of applied sciences at the University of the West of

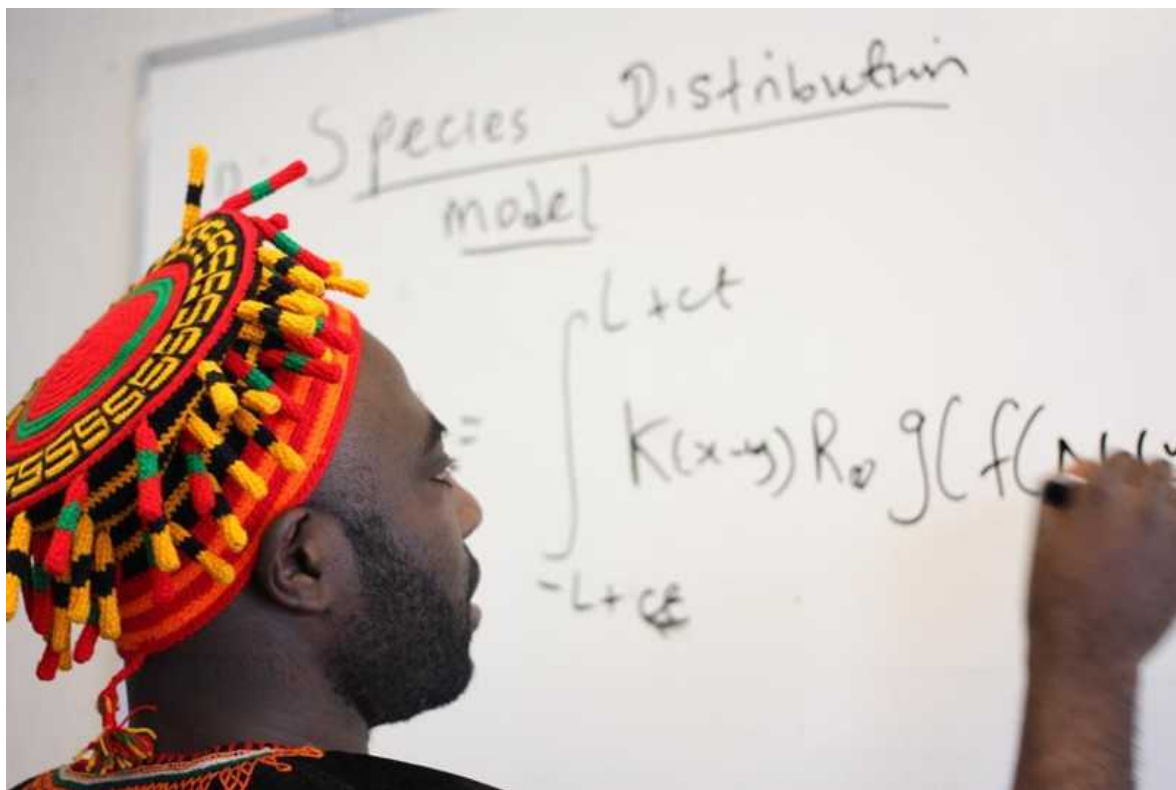
England in Bristol, UK, who says he will call for more of them in 2021. He cites the success of the 2020 Royal Society of Biology's annual Careers Day, which he says drew 5 times the usual number of student attendees, including 100 from his department. "They open opportunities to anyone with access to the Internet," he says of virtual meetings, adding that they benefit junior scientists who can't afford the cost of far-flung conference travel.



Lauren May is a molecular pharmacologist at Monash University in Melbourne, Australia. Credit: Monash University

Molecular pharmacologist Lauren May at Monash University in Melbourne, Australia, says that certain voices can dominate in-person conference sessions or classroom discussions. Conversely, she says, students are often more likely to pose questions or add comments to an online meeting's chat function than to speak up in a classroom or conference setting. May recommends conference apps that can help virtual attendees to connect with one another during or after sessions. She particularly likes one called Pollev that allows users to ask and answer questions among themselves during a presentation. Such tools, she says, can spur conversation more swiftly and easily than in person.

Mathematician Jude Kong at York University in Toronto, Canada, plans to keep using the video-conferencing software Zoom specifically to mentor disadvantaged students, often from minority ethnic groups. Kong, a member of the newly established Canadian Black Scientist Network, has been reaching out to high-school and undergraduate students through free public webinars such as Café Mathematique. Many, he says, aren't aware of funding opportunities for graduate programmes. "I will keep using Zoom to reach out to people in underserved communities," he says. "I want to uplift them and encourage them to explore research." He's found that sometimes-shy students feel more confident contacting him virtually from home than they might have been in person.



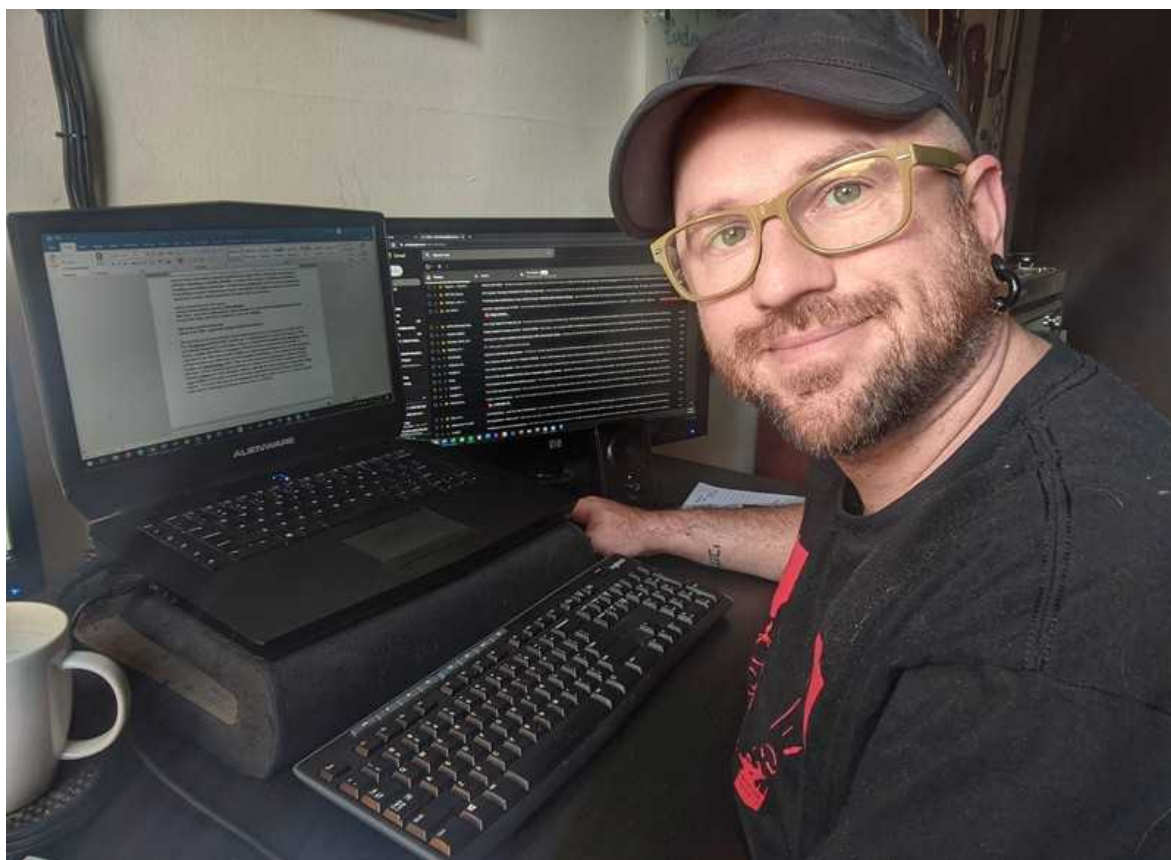
Mathematician Jude Kong now uses video-conferencing to interact with students. Credit: Edward Tekwa

Adjust expectations. Climate scientist Kim Cobb advises scientists to schedule more time than they expect to need to meet work expectations and family obligations. She struggled to stay optimistic this year as she juggled teaching three online classes, home-schooling four children and finishing a 770-page, US\$18 million National Science Foundation grant proposal, all in

six months. “I call it my pandemic proposal,” says Cobb, at the Georgia Institute of Technology in Atlanta. “It’s been a learning curve.”

Advocate for remote work. Virtual working can still be effective for PhD students and postdocs even after restrictions lift, says Kevin Burgio, who was lead author on a paper this year that highlighted ten rules for doing a remote postdoctoral position ([K. R. Burgio et al. PLoS Comput. Biol. 16, e1007809; 2020](#)). Burgio, who is finishing his own virtual postdoc job in Connecticut with Environment and Climate Change Canada, a department of the Canadian government, says that clear communication between the laboratory member and principal investigator is key to success.

Particularly important, he says, is covering granular details such as how many hours to spend weekly on manuscripts or dissertations. “Having a direct conversation with your supervisor about expectations and how they may change is the most important thing,” says Burgio.



Kevin Burgio is a postdoctoral research associate at the Wildlife Research Division of Environment and Climate Change Canada. Credit: Kevin R. Burgio

Support team well-being. Cobb urges principal investigators to be mindful of the power dynamics that could prompt students to work in the lab to please supervisors, especially if there is no clear direction for prioritizing their well-being. Her team works from home on computational and data analyses, manuscripts and grants. For her, she adds, any potential decrease in productivity is less important than her lab members' health.

Lee Cronin, a chemist at the University of Glasgow, UK, says that the pandemic is a good reason to take the time to do research with greater impact. "Let's write less and say more," says Cronin. "Everyone's in the same boat."

Track pandemic career effects. Cobb calls for continuing data collection on the consequences of the pandemic on female academic scientists and those from minority ethnic groups. She has watched colleagues, particularly those who have care-giving roles, withdraw their abstracts from conferences, walk away from proposals, forego writing papers, or abandon prestigious opportunities. She is concerned that career setbacks now will have lasting detrimental impact on young researchers' career progression.



Collection: Coronavirus and scientific careers

Information from data collection should inform strategies to address structural biases in the academic system, Cobb says, such as extending start-up packages or augmenting the tenure and review process. “We have to firmly recognize the inequities that impact people every day and make sure we are not pushing people permanently out of science because they fall short of their own expectations,” she says. “Our response can’t be, ‘Try harder and hang on’.” Rather, she says, the scientific community needs to encourage researchers to be present for work however they can in these times, and to value their contributions.

May urges scientist-parents, particularly mums, to take careful notes on how the pandemic has directly affected their research output. In 2019, May co-founded Her Research Matters, a university-based group that supports equitable leadership. She says that documentation detailing achievements in the face of lost or restricted opportunities can support applications for grant and fellowship extensions or annotate academic promotion packages.



Molecular biologist Michelle Halls is group secretary of Her Research Matters — a collective that promotes equitable leadership. Credit: Monash University

Michelle Halls, group secretary of Her Research Matters and a molecular biologist at Monash university, says that it is crucial for scientist-parents to quantify hours spent helping children with school work, and to list missed conference-speaking opportunities. “Put it in real terms with real-time losses to make clear how work time has been limited by the pandemic,” she says. Parents should record specific dates of university shutdowns, travel bans and primary-school closures, she adds.

Spread knowledge. PhD student Roger Gonzales, who studies public health at the University of Nebraska Medical Center in Omaha, will carry on working in underserved communities to boost trust in science and awareness of COVID-19’s health effects.

Gonzales, who is fluent in Spanish, realized that non-English-speaking neighbourhoods around Omaha had little access to coronavirus-related information in their own language. So he created infographics in Spanish about avoiding infection, which have appeared in hospitals and clinics and on social media. He’ll continue his efforts to distinguish science from disinformation, particularly as vaccines become available so that he can reassure community members about vaccine safety. Often, he says, “science stays in academia — and that leaves a lot of people out”.

Nature **588**, 717-718 (2020)

doi: <https://doi.org/10.1038/d41586-020-03558-w>

Jobs from Nature Careers

- - - [All jobs](#)
 -
 -

Full Professorship for Translational Imaging in Oncology (W3)

German Cancer Research Center in the Helmholtz Association (DKFZ)

Dresden, Germany

JOB POST

MSc Position in Forest Research

The University of British Columbia (UBC)

Vancouver, Canada

JOB POST

Research Associate - zero-emission hydrogen production project

The University of British Columbia (UBC)

Vancouver, Canada

JOB POST

Laboratory Manager - Zamore Lab

Howard Hughes Medical Institute (HHMI)

Worcester, United States

JOB POST

| [Section menu](#) | [Main menu](#) |

WHERE I WORK

17 December 2020

- Correction [23 December 2020](#)

‘I want to generate opportunities for Black scientists’

UK geoscientist Christopher Jackson will be the first Black researcher to deliver a Christmas lecture at the Royal Institution of Great Britain.

Virginia Gewin

Virginia Gewin is a freelance writer in Portland, Oregon.

Search for this author in:

- [Pub Med](#)
- [Nature.com](#)
- [Google Scholar](#)



Christopher Jackson is a geoscientist at Imperial College London. Credit: Paul Wilkinson Photography

I study the structure and evolution of Earth. To imagine what Earth looked like millions of years ago, I probe the preserved recordings deep beneath our feet. For example, I look at 3D seismic reflections, essentially computed tomography scans of Earth, for clues to ancient volcanoes or mountain valleys, and I analyse rocks from 7 kilometres below the ocean’s surface.

The Royal Institution of Great Britain in London (which supports scientific research and education through a lecture series and other programmes) asked me in March to give one of its three Christmas lectures this year on Earth science and climate change. It makes sense for a geoscientist to contextualize the rate of change we are seeing, which is quite extreme compared with thousands of years ago. After 195 years in which the Royal Institution has had no Black lecturers, this is an opportunity for me to positively represent Black people on that stage.

While responses from my peers were overwhelmingly positive, aggressively race-related criticisms came from the public. Some people suggested that I was asked as a pointed response to the George Floyd killing and subsequent global racial unrest. I was invited before any of those events. There was also a very vocal minority that was cross about the fact that I'm Black. I received direct messages on Twitter and had to report an e-mail to the police. I'm thankful that the Royal Institution issued tweets calling out the racism, and offered me its counselling services in the run-up to the lectures.

I'm the first Black geoscientist to be a professor at Imperial College London. That rarity has helped me to deal with some of the 'firstness' about this remote presentation, which will be broadcast on 28 December on BBC Four and will be available on the Royal Institution's website. I'm a bit nervous, but I hope to expand the public's view of scientists and to generate more opportunities for other Black scientists.

Nature **588**, 720 (2020)

doi: <https://doi.org/10.1038/d41586-020-03559-9>

Updates & Corrections

- **Correction 23 December 2020:** An earlier version of this article gave the wrong date for the broadcast of Christopher Jackson's Christmas lecture.

[Jobs from Nature Careers](#)

- - - [All jobs](#)
 - - [**Full Professorship for Translational Imaging in Oncology \(W3\)**](#)

[German Cancer Research Center in the Helmholtz Association \(DKFZ\)](#)

[Dresden, Germany](#)

[JOB POST](#)

■ [**MSc Position in Forest Research**](#)

[The University of British Columbia \(UBC\)](#)

[Vancouver, Canada](#)

[JOB POST](#)

■ [**Research Associate - zero-emission hydrogen production project**](#)

[The University of British Columbia \(UBC\)](#)

[Vancouver, Canada](#)

[JOB POST](#)

■ [**Laboratory Manager - Zamore Lab**](#)

[Howard Hughes Medical Institute \(HHMI\)](#)

[Worcester, United States](#)

JOB POST

This article was downloaded by **calibre** from <https://www.nature.com/articles/d41586-020-03559-9>

| [Section menu](#) | [Main menu](#) |

Research

- **[River conservation by an Indigenous community](#)** [11 December 2020]
News & Views • Populations of river fish are threatened by pressures on land and water resources. Networks of reserves managed by Indigenous people at community level offer a way to conserve fish diversity and enhance yields of nearby fisheries.
- **[Bacterial species singled out from a diverse crowd](#)** [02 December 2020]
News & Views • Microscopy methods that reveal the spatial patterns of individual types of microbe are limited by the number of different species that can be monitored together. A new technique now provides progress on this front.
- **[Targeted wetland restoration could greatly reduce nitrogen pollution](#)** [17 December 2020]
News & Views • Wetlands remove nitrate pollution from water effectively. An analysis shows that this effect is constrained in the United States by the distribution of wetlands, and could be increased by targeting wetland restoration to nitrate sources.
- **[High-resolution 3D printing in seconds](#)** [23 December 2020]
News & Views • A 3D-printing technique has been developed that can produce millimetre- to centimetre-scale objects with micrometre-scale features. It relies on chemical reactions triggered by the intersection of two light beams.
- **[Superconducting qubit to optical photon transduction](#)** [23 December 2020]
Article • A chip-scale platform is developed for the conversion of a single microwave excitation of a superconducting qubit into optical photons, with potential uses in quantum computer networks.
- **[Mastering Atari, Go, chess and shogi by planning with a learned model](#)** [23 December 2020]
Article • A reinforcement-learning algorithm that combines a tree-based search with a learned model achieves superhuman performance in high-performance planning and visually complex domains, without any knowledge of their underlying dynamics.
- **[Strongly correlated Chern insulators in magic-angle twisted bilayer graphene](#)** [14 December 2020]
Article • Strong electron–electron interactions in magic-angle twisted bilayer graphene can fundamentally change the topology of the system’s flat bands, producing a hierarchy of strongly correlated topological insulators in modest magnetic fields.

- [Plasmonic topological quasiparticle on the nanometre and femtosecond scales](#) [23 December 2020]

Article • Topological plasmonic spin textures are excited by shining light on a structured silver film, and imaging defines how these quasiparticle field and spin textures evolve on the nanometre and femtosecond scales.
- [Xolography for linear volumetric 3D printing](#) [23 December 2020]

Article • By combining the use of photoswitchable photoinitiators and intersecting light beams, objects and complex systems can be produced rapidly with higher definition than is possible using state-of-the art macroscopic volumetric methods.
- [Maximizing US nitrate removal through wetland protection and restoration](#) [16 December 2020]

Article • Analysis of US continental wetland inventory data combined with model simulations indicate that a spatially targeted 10% increase in wetland area could double wetland nitrogen removal.
- [A network of grassroots reserves protects tropical river fish diversity](#) [25 November 2020]

Article • A network of small, community-run river reserves in Thailand increases local fish biomass, diversity and richness.
- [Impacts of speciation and extinction measured by an evolutionary decay clock](#) [09 December 2020]

Article • Analysis of data on species co-occurrence in the Paleobiology Database using a new machine learning algorithm reveals that mass extinctions and mass radiations are not coupled in evolutionary history.
- [Transcriptome and translatome co-evolution in mammals](#) [11 November 2020]

Article • An analysis using ribosome-profiling and matched RNA-sequencing data for three organs across five mammalian species and a bird enables the comparison of translatomes and transcriptomes, revealing patterns of co-evolution of these two expression layers.
- [Spatial connectivity matches direction selectivity in visual cortex](#) [11 November 2020]

Article • In the mouse visual cortex, the excitatory and inhibitory presynaptic neurons of individual layer 2/3 pyramidal neurons are spatially offset to generate direction-selective responses.
- [The neuropeptide Pth2 dynamically senses others via mechanosensation](#) [02 December 2020]

Article • In zebrafish, the expression levels of the neuropeptide Pth2 change as exposure to conspecifics is limited or increased, and these changes track the presence of individuals and

group density through mechanical stimulations induced by the movements of other fish.

- **The NAD⁺-mediated self-inhibition mechanism of pro-neurodegenerative SARM1** [14 October 2020]

Article • NAD⁺ is shown to be a ligand of the armadillo/heat repeat motifs (ARM) domain of SARM1, and it is suggested that this binding of NAD⁺ mediates self-inhibition of SARM1.

- **Creation of bladder assembloids mimicking tissue regeneration and cancer** [16 December 2020]

Article • Multilayer 3D reconstitution of bladder stem cells with stromal cells enables recapitulation of the architecture and molecular functions of bladder tissue.

- **Progenitor identification and SARS-CoV-2 infection in human distal lung organoids** [25 November 2020]

Article • A long-term culture method for organoids derived from single adult human lung cells is used to identify progenitor cells and study SARS-CoV-2 infection.

- **Highly multiplexed spatial mapping of microbial communities** [02 December 2020]

Article • High-phylogenetic-resolution microbiome mapping by fluorescence in situ hybridization (HiPR-FISH) enables the spatial mapping of hundreds of species of microorganisms and shows how microbial networks in the mouse gut are affected by antibiotic treatment.

- **SARS-CoV-2 neutralizing antibody structures inform therapeutic strategies** [12 October 2020]

Article • Eight structures of human neutralizing antibodies that target the SARS-CoV-2 spike receptor-binding domain are reported and classified into four categories, suggesting combinations for clinical use.

- **Galactosaminogalactan activates the inflammasome to provide host protection** [02 December 2020]

Article • Galactosaminogalactan of Aspergillus fumigatus acts as a pathogen-associated molecular pattern that activates the NLRP3 inflammasome, which is crucial for anti-fungal host defence.

- **Inhibition of PCSK9 potentiates immune checkpoint therapy for cancer** [11 November 2020]

Article • Inhibiting the PCSK9 protein, a regulator of cholesterol metabolism, enhances immune checkpoint therapy in mouse models of cancer, in a manner that depends on the regulation of antigen-presenting MHC I molecules.

- **MFSD12 mediates the import of cysteine into melanosomes and lysosomes** [18 November 2020]

Article • A rapid labelling and immunopurification-based method is used to isolate melanosomes and profile their labile metabolites, revealing that MFSD12 has a key role in cysteine import into melanosomes and lysosomes.

- **Lymphoangiocrine signals promote cardiac growth and repair** [09 December 2020]

Article • Lymphatic endothelium secretes factors needed for heart growth and repair such as RELN, which helps with heart regeneration and cardioprotection after myocardial infarction.

- **Small-molecule inhibitors of human mitochondrial DNA transcription** [16 December 2020]

Article • Inhibitors of mitochondrial transcription that target human mitochondrial RNA polymerase provide a chemical biology tool for studying the role of mitochondrial DNA expression in a wide range of pathologies.

- **The effect of interventions on COVID-19** [23 December 2020]

Matters Arising •

- **Reply to: The effect of interventions on COVID-19** [23 December 2020]

Matters Arising •

NEWS AND VIEWS

11 December 2020

River conservation by an Indigenous community

Populations of river fish are threatened by pressures on land and water resources. Networks of reserves managed by Indigenous people at community level offer a way to conserve fish diversity and enhance yields of nearby fisheries.

Edward H. Allison &

Edward H. Allison is at WorldFish, Penang 11960, Malaysia.

[Contact](#)

Search for this author in:

- [Pub Med](#)
- [Nature.com](#)
- [Google Scholar](#)

Violet Cho

Violet Cho is in the School of Culture, History and Languages, College of Asia and the Pacific, the Australian National University, Canberra 2600, ACT, Australia.

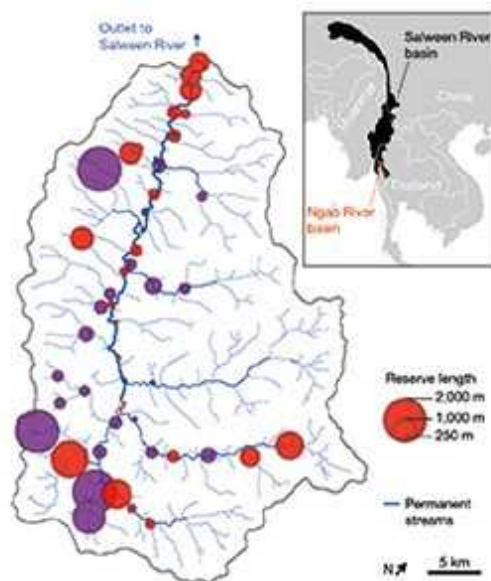
[Contact](#)

Search for this author in:

- [Pub Med](#)
- [Nature.com](#)

- [Google Scholar](#)

Rivers are a major source of renewable water, and provide food, jobs and a sense of place and cultural identity for people living in the vicinity. For many Indigenous peoples, rivers are central to how they understand themselves, their origins and their relationships to the rest of nature. As a citizen of the Penobscot Nation in Maine put it¹, “The river is us: the river is in our veins.” [Writing in Nature](#), Koning *et al.*² report ecological surveys that demonstrate how local Indigenous people in the Salween River basin on the border between Thailand and Myanmar have successfully managed the river for conservation purposes and to protect livelihoods.



Read the paper: A network of grassroots reserves protects tropical river fish diversity

Both biodiversity and the people in river-associated communities are under severe stress the world over. Across the globe, 30% of freshwater fish (see go.nature.com/3ixfd9l) are classified as being at risk (in either the critically endangered, endangered or vulnerable categories) in the 2020 Red List of

threatened species compiled by the International Union for the Conservation of Nature. Furthermore, it is projected³ that half the human population will live in water-insecure areas by 2050. Principal among the threats to rivers are pollution, climate change, invasive species, changes in surrounding land use, and the construction of dams and infrastructure that affect river flow. These issues need to be addressed on scales ranging from local to global, and solutions should draw on the knowledge, practices and aspirations of those whose lives are most closely entwined with river health.

Koning *et al.* assessed the outcome of a network of small fishery no-take reserves (areas where fishing is not allowed), and found that there was an average 27% rise in species richness, 124% higher fish density and 2,247% higher fish biomass in the reserve-associated waters compared with the corresponding values for nearby areas open to fishing. The presence of larger species and more individuals in the reserves is what drives the much higher biomass there. The authors suggest that such networks of locally managed, small, protected river areas could be used in other river systems to enhance fisheries and to conserve biodiversity.

The authors' work highlights the importance of inland waters to food and livelihood systems, demonstrates the value of community-led conservation, and points out commonalities between protected-area conservation strategies in marine and freshwater ecosystems. Marine-protected areas, which are usually created by governments, are used widely in ocean conservation and fisheries, but much less commonly in fresh waters⁴. The authors characterize the reserves studied as being created by the S'gaw Karen (also known as Pwak'nyaw) Indigenous people who live in the river catchment areas. The paper thus also supports the growing recognition⁵ among scientists and conservationists of the effectiveness of Indigenous resource-management practices.



The race to fish slows down

Koning and colleagues' study draws on natural sciences — limnology (the freshwater equivalent of oceanography) and fish ecology — but also discusses how river management operates at a community level. Their natural-sciences disciplinary lens allows them to rigorously evaluate the benefits that protected areas confer on fish conservation and on the sustainability of local fish catches. In the area studied, Indigenous communities had planned and implemented local no-take reserves that complement other community-based conservation initiatives, including the management of adjacent land.

However, the context in which this management system evolved, the knowledge and politics involved in its creation, and how local forms of knowledge and practice can be supported and valued are less in focus in Koning and colleagues' study. Pwak'nyaw communities have been profoundly transformed as a result of colonization in Myanmar, the arrival of foreign missionaries in Myanmar and Thailand, and state modernization projects in both countries. Supporting river conservation here and elsewhere at locations where other Indigenous peoples live will require a reckoning with such legacies and a willingness to make space for local and Indigenous voices to be heard, alongside those of scientists, in river-basin planning.

One of us (V.C.) is a Pwak'nyaw person, born in Hpa'an, Myanmar, on the banks of the Salween River, and believes that it is crucial that science conducted in Indigenous territory incorporates Indigenous systems of knowledge and beliefs, and for Indigenous people to have ownership over data that involve them. Although, during a period of 8 years of research, Koning *et al.* worked with local people for more than 18 months when living in the study area, there is scope for furthering these relationships so that Indigenous perspectives have increased visibility. An absence of Indigenous agency and control in the production of knowledge is a key issue, leading to calls for Indigenous data sovereignty and the decolonization of science⁶.



How the global fish market contributes to human micronutrient deficiencies

Koning and colleagues' study positively recognizes Pwak'nyaw involvement in conservation, and includes some cultural context, although Pwak'nyaw perspectives are lacking. One consequence of this might be the study's focus on what the Pwak'nyaw would regard as only part of their integrated system of land and water management. For example, Pwak'nyaw

don't commonly identify themselves by categories that are familiar to those in Western culture, such as being a farmer or a fisher. Rather, rotational farming, growing rice, gardening, hunting, gathering and fishing are integrated parts of a Pwak'nyaw livelihood.

Community-based research on Pwak'nyaw livelihoods in northern Thailand has found that fish conservation is also integrated into rotational farming practices. For instance, the concept *nya pla htau*, meaning fish surface, prohibits the clearing of a field on adjacent sides of a river bank in successive years to conserve fish-breeding grounds, and knowledge about fish is a factor in the selection of farmland⁷. In this sense, farming cannot be separated from fishing, which cannot be separated from conservation, because they are all part of a whole — and it is beneficial for them to be studied as such.

Future studies, which should involve collaboration with Indigenous researchers, could adopt approaches to integrate Indigenous and scientific knowledge and Indigenous and Western legal and management approaches in ways that recognize and draw on both⁸. This would help to address some of the unanswered questions in Koning and colleagues' valuable study on the origins, sustainability and future of this successful network of reserves.

Conflict can arise in Thailand and elsewhere when there is confrontation between Indigenous people and the state, or other groups, regarding competing conservation models. Indigenous lives are in danger — around the world in 2019, more than 200 environmental activists died, 40% of whom were Indigenous people (see go.nature.com/36w68di). In the past decade, the deaths of prominent Pwak'nyaw environmental activists in Myanmar (see go.nature.com/2vspujn) and in Thailand (see go.nature.com/3mwjqm1) have hit the headlines.



Figure 1 | The Salween Peace Park. Pwak'nyaw (also known as S'gaw Karen) people living at this site in Myanmar, located on a tributary of the Salween River, use their Indigenous knowledge to obtain food. For example, the basket-style nets in this image are a traditional way to catch fish and shellfish in shallow waters. Koning *et al.*² report that conservation efforts by the Pwak'nyaw community in the Salween River basin area have substantially boosted fish diversity and might increase the yields of fishing catches. Credit: Paul Sein Twa/KESAN

Indigenous resource-management systems can persist despite difficult circumstances. On the Myanmar side of the Salween River, Pwak'nyaw communities, whose livelihoods are affected by ongoing civil war, displacement and militarized development, have created a large-scale conservation project named the Salween Peace Park (Fig. 1), based on *kaw* (country), a holistic concept that encompasses the localized practice of social and environmental governance, based on Indigenous sovereignty. Pwak'nyaw living there conserve the environment using Indigenous

knowledge (see go.nature.com/36tigxg), and are working to revive Indigenous practices lost through decades of conflict.

Without such contextual cultural and political knowledge, it is difficult to say how easily the successes in the Salween River basin, convincingly enumerated by Koning and colleagues' study, can be achieved elsewhere by trying to transfer this approach. The key insight here may be that the small reserves are potentially useful conservation measures that need to be understood from the perspectives of those who created them. Such reserves should be supported and legitimized where they exist, revived where they existed previously, and perhaps tried out where they haven't been used before, as part of efforts to meet global river-conservation challenges. This would support a growing movement led by Indigenous peoples to focus on putting rivers at the centre of conservation efforts — including by assigning legal personhood to rivers, as part of a 'rights of nature' approach to environmental governance⁹.

Nature **588**, 589–590 (2020)

doi: <https://doi.org/10.1038/d41586-020-03316-y>

References

1. 1.

Fox, C. A. *et al. Sustain. Sci.* **12**, 521–533 (2017).

2. 2.

Koning, A. A., Perales, K. M., Fluet-Chouinard, E. & McIntyre, P. B. *Nature* **588**, 631–635 (2020).

3. 3.

Dudgeon, D. *Freshwater Biodiversity* (Cambridge Univ. Press, 2020).

4. 4.

Abell, R., Allan, J. D. & Lehner, B. *Biol. Conserv.* **134**, 48–63 (2007).

5. 5.

Reyes-García, V. & Benyei, P. *Nature Sustain.* **2**, 657–658 (2019).

6. 6.

Kukutu, T. & Taylor, J. (eds) *Indigenous Data Sovereignty: Toward an Agenda* (Australian Natl Univ. Press, 2016).

7. 7.

Trakansuphakon, P. *Pga k' nyau Knowledge on Rotational Farming in Northern Thailand* (IKAP-Network, 2006).

8. 8.

Reid, A. J. *et al. Fish Fish.* <https://doi.org/10.1111/faf.12516> (2020).

9. 9.

O'Donnell, E. L. & Talbot-Jones, J. *Ecol. Society* **23**, 7 (2018).

Jobs from Nature Careers

- - - [All jobs](#)
 - - [Full Professorship for Translational Imaging in Oncology \(W3\)](#)

[German Cancer Research Center in the Helmholtz Association \(DKFZ\)](#)

[Dresden, Germany](#)

JOB POST

- **MSc Position in Forest Research**

The University of British Columbia (UBC)

Vancouver, Canada

JOB POST

- **Research Associate - zero-emission hydrogen production project**

The University of British Columbia (UBC)

Vancouver, Canada

JOB POST

- **Laboratory Manager - Zamore Lab**

Howard Hughes Medical Institute (HHMI)

Worcester, United States

JOB POST

This article was downloaded by **calibre** from <https://www.nature.com/articles/d41586-020-03316-y>.

NEWS AND VIEWS

02 December 2020

Bacterial species singled out from a diverse crowd

Microscopy methods that reveal the spatial patterns of individual types of microbe are limited by the number of different species that can be monitored together. A new technique now provides progress on this front.

Jen Nguyen &

Jen Nguyen is at the School of Biomedical Engineering and the Department of Microbiology and Immunology, University of British Columbia, Vancouver V6T-1Z3, Canada.

Search for this author in:

- [Pub Med](#)
- [Nature.com](#)
- [Google Scholar](#)

Carolina Tropini

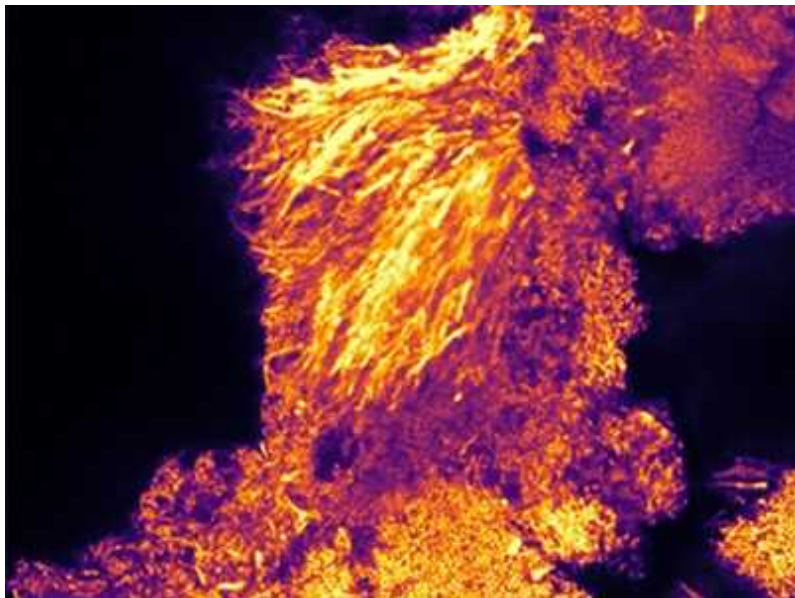
Carolina Tropini is at the School of Biomedical Engineering and the Department of Microbiology and Immunology, University of British Columbia, Vancouver V6T-1Z3, Canada, and at the Humans and the Microbiome Program, Canadian Institute for Advanced Research, Toronto, Canada.

[Contact](#)

Search for this author in:

- [Pub Med](#)
- [Nature.com](#)
- [Google Scholar](#)

Understanding an ecosystem requires maps of where the organisms present live and act. For example, sea otters reside on the surface of kelp beds and feed on sea urchins that consume kelp from the ocean floor. An organism's location in an ecosystem reflects its physiology and function. This is particularly true for microbes, which live in and respond to highly dynamic and diverse habitats. Micrometre-scale gradients of nutrients or pH, for instance, are a typical feature of microbial habitats that drive bacterial spatial organization and behaviour^{1,2}. Yet, despite the incredible range of functions that different bacteria perform independently and in association with other living systems^{3,4}, most microbes are similar in shape and indistinguishable under the microscope. [Writing in Nature](#), Shi *et al.*⁵ present a method to tackle the major challenge of differentiating between the hundreds to thousands of bacterial species found in microbes' natural habitats.



[Read the paper: Highly multiplexed spatial mapping of microbial](#)

communities

A key tool used in biogeographical studies to assess the spatial location of components of interest is called fluorescence *in situ* hybridization (FISH). This technique relies on the use of fluorescently labelled nucleic-acid sequences called probes to locate matching specific sequences of DNA or RNA in a sample that has been immobilized by a process termed fixation. When applied to samples containing bacteria, a DNA probe can be used to identify a target species in the context of its native environment, and a fluorescent molecule (a fluorophore) attached to the probe enables the location of the species to be observed under the microscope⁶.

Designing the DNA component of FISH probes is now relatively easy⁷. However, the maximum number of bacterial species identifiable by FISH within a single sample has been constrained by the limited number of fluorophores available for simultaneous visualization. Methods that exceed the limits of traditional fluorescence microscopy, using spectral imaging and combinations of fluorophores, can distinguish between 15 and 120 different types of microbe captured in the same image^{8,9}. But a drawback of these techniques is the cost of the large number of fluorescently tagged probes needed.

Shi and colleagues introduce a method that exceeds previous FISH benchmarks by combining a new type of probe design with custom image analysis. Their technique (Fig. 1), named high phylogenetic resolution microbiome mapping by fluorescence *in situ* hybridization (HiPR-FISH), builds on a combinatorial strategy in which bacteria are targeted and labelled in two steps¹⁰.

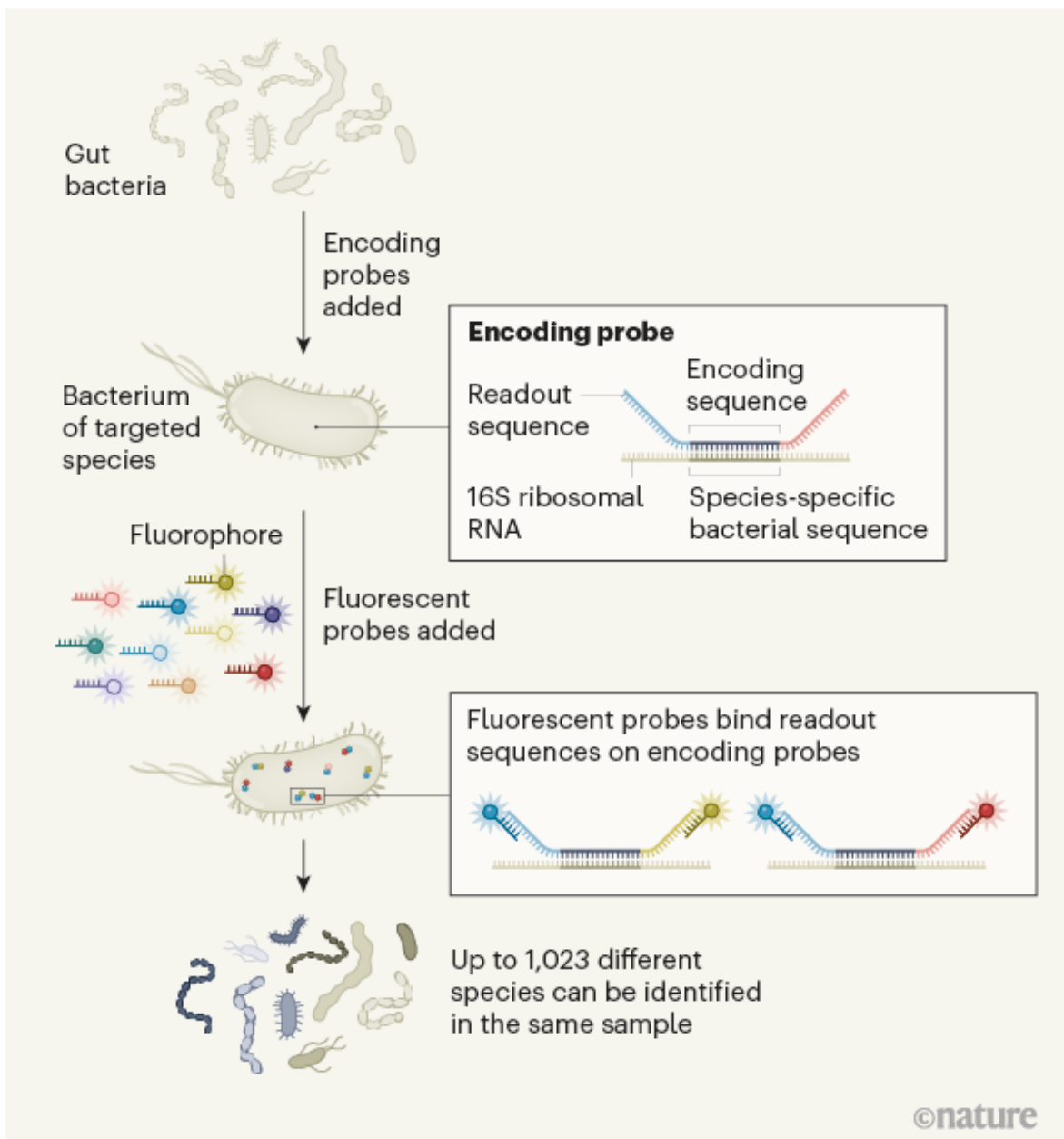


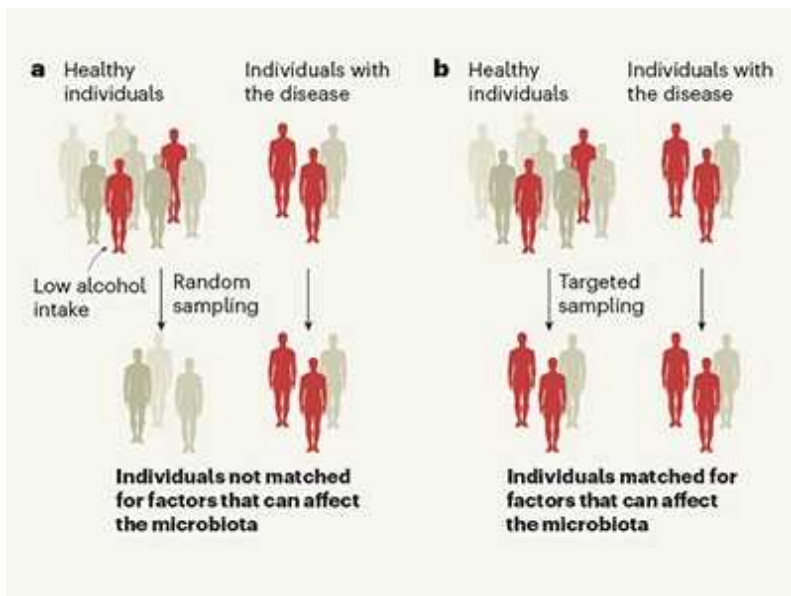
Figure 1 | A method to identify more than 1,000 bacterial species at high spatial resolution. Shi *et al.*⁵ present their technique called high phylogenetic resolution microbiome mapping by fluorescence *in situ* hybridization (HiPR-FISH). In this approach, DNA sequences called encoding probes are designed to match a species-specific sequence of RNA (16S ribosomal RNA is the sequence targeted for every species). Each encoding probe is flanked by two sequences called readout sequences, which are each chosen from ten possible readout sequences. A variety of encoding probes that target the same species-specific sequence are designed to

generate a unique combination of readout sequences that corresponds to a particular species. Ten types of probe attached to a fluorescent molecule called a fluorophore are added, and each different probe binds the one readout sequence that it matches. The sample is imaged to record which of the fluorophores (up to ten in total) are bound to RNA in each cell. This information enables the genetic identification of individual bacteria.

First, a DNA probe, described as an encoding probe, is designed to match a species-specific sequence (16S ribosomal RNA) for the targeted bacteria. This encoding probe is flanked on either side by integral parts of the probe described as readout sequences. Each of these two readout sequences in an encoding probe can be one of ten possible readout sequences. Then, each readout sequence is targeted by another DNA probe fused to a fluorophore that is specific for the particular readout sequence.

Bacterial cells contain hundreds of copies of 16S rRNA, and so each bacterial species can be targeted by an array of encoding probes: each targeting the same RNA sequence, yet flanked by different pairs of readout sequences, enabling a variety of readout sequences to be associated with a particular species. Choosing the readout sequences for each targeted bacterial species allows the assignment of a unique combination of readout sequences (and therefore fluorophores) to correspond to each species. Depending on the encoding probes used, each bacterial species can bind up to ten of the possible fluorophores. Thus, this system can generate 1,023 unique visual ‘barcodes’ for the identification of individual bacterial species. Bacterial identities are simultaneously assigned through monitoring by spectral imaging and classification of microbes in the images using a machine-learning algorithm. HiPR-FISH bypasses the previous financial constraints by simplifying the encoding sequence to cheaply synthesized DNA sequences and requiring only ten different types of fluorophore.

Using an automated program to delineate a multitude of single cells in a dense crowd, Shi and colleagues used HiPR-FISH to locate and determine the species identity of individual bacteria in samples from the mouse gut and in samples of oral microbes in human plaque. These different microbial ecosystems are both examples of bacterial communities that can contain hundreds of distinct species.



Identifying gut microbes that affect human health

This demonstration of a previously impossible level of analysis of complex communities using single-cell level mapping, enables the quantitative study of bacterial spatial organization, such as the determination of the distance between specific microbial species residing in a host. Such high-resolution data are important to answer key questions concerning the behaviour of microbial communities, such as who interacts with whom, and where those interactions take place. Interactions are theoretically possible between microbes in close spatial proximity, so HiPR-FISH opens a new era in the study of microbial ecology by enabling micrometre-scale mapping of the spatial distance between hundreds of microbial species in complex communities.

Shi *et al.* assessed the distance between different bacterial species normally resident in the mouse gut and measured how these distances changed after antibiotic treatment. Such therapy is known to alter the assortment and abundance of bacterial species in the gut¹¹. The largest distance changes due to antibiotic treatment observed by Shi and colleagues were between *Oscillibacter* and *Veillonella*, which are microbes that are both individually

associated with health benefits in the human gut^{12,13}. Whether and how these bacteria interact functionally remains to be uncovered. However, the fourfold increase in spatial distance between these bacteria after antibiotic use raises the possibility that the antibiotic treatment might disrupt an interaction that aids the host. Identifying such interactions and deciphering the underlying mechanisms will boost our understanding of how microbial communities respond to, and recover from, environmental perturbation.

By shedding light on microbial biogeography, this work charts new paths for exploring microbial interactions in complex ecosystems. Exciting next steps to anticipate include the elucidation of mechanisms by which environmental disturbances alter bacterial spatial organization, and how altered organization affects community function. For example, how does antibiotic exposure result in an increase in distance between *Oscillibacter* and *Veillonella*? Is the spatial proximity between specific bacteria important for community recovery after disturbances such as antibiotic exposure?

Finally, expanding on this technology to access the spatial organization of transcriptional responses would enable maps to be generated that reveal the spatial gradients of bacterial species and their functions. These future applications will truly revolutionize our understanding of complex microbial communities and the spatial diversity that is so fundamental for life.

Nature **588**, 591–592 (2020)

doi: <https://doi.org/10.1038/d41586-020-03315-z>

References

1. 1.

Stacy, A., McNally, L., Darch, S. E., Brown, S. P. & Whiteley, M. *Nature Rev. Microbiol.* **14**, 93–105 (2016).

2. 2.

Tropini, C., Earle, K. A., Huang, K. C. & Sonnenburg, J. L. *Cell Host Microbe* **21**, 433–442 (2017).

3. 3.

Falkowski, P. G., Fenchel, T. & Delong, E. F. *Science* **320**, 1034–1039 (2008).

4. 4.

Donia, M. S. & Fischbach, M. A. *Science* **349**, 1254766 (2015).

5. 5.

Shi, H. *et al. Nature* **588**, 676–681 (2020).

6. 6.

Moter, A. & Göbel, U. B. *J. Microbiol. Methods* **41**, 85–112 (2000).

7. 7.

Beliveau, B. J. *et al. Proc. Natl Acad. Sci. USA* **115**, E2183–E2192 (2018).

8. 8.

Valm, A. M. *et al. Proc. Natl Acad. Sci. USA* **108**, 4152–4157 (2011).

9. 9.

Valm, A. M., Oldenbourg, R. & Borisy, G. G. *PLoS ONE* **11**, e0158495 (2016).

10. 10.

Moffitt, J. R. *et al. Proc. Natl Acad. Sci. USA* **113**, 14456–14461 (2016).

11. 11.

Ng, K. M. *et al. Cell Host Microbe* **26**, 650–665 (2019).

12. 12.

Li, J. et al. *Proc. Natl Acad. Sci. USA* **113**, E1306–E1315 (2016).

13. 13.

Scheiman, J. et al. *Nature Med.* **25**, 1104–1109 (2019).

Jobs from Nature Careers

- - - [All jobs](#)
 - - **[Full Professorship for Translational Imaging in Oncology \(W3\)](#)**
[German Cancer Research Center in the Helmholtz Association \(DKFZ\)](#)
[Dresden, Germany](#)
[JOB POST](#)
 - **[MSc Position in Forest Research](#)**
[The University of British Columbia \(UBC\)](#)
[Vancouver, Canada](#)
[JOB POST](#)
 - **[Research Associate - zero-emission hydrogen production project](#)**
[The University of British Columbia \(UBC\)](#)

Vancouver, Canada

JOB POST

▪ **Laboratory Manager - Zamore Lab**

Howard Hughes Medical Institute (HHMI)

Worcester, United States

JOB POST

This article was downloaded by **calibre** from <https://www.nature.com/articles/d41586-020-03315-z>

| [Section menu](#) | [Main menu](#) |

NEWS AND VIEWS

17 December 2020

Targeted wetland restoration could greatly reduce nitrogen pollution

Wetlands remove nitrate pollution from water effectively. An analysis shows that this effect is constrained in the United States by the distribution of wetlands, and could be increased by targeting wetland restoration to nitrate sources.

Jacques C. Finlay

Jacques C. Finlay is in the Department of Ecology, Evolution and Behavior, University of Minnesota, Saint Paul 55108, Minnesota, USA.

[Contact](#)

Search for this author in:

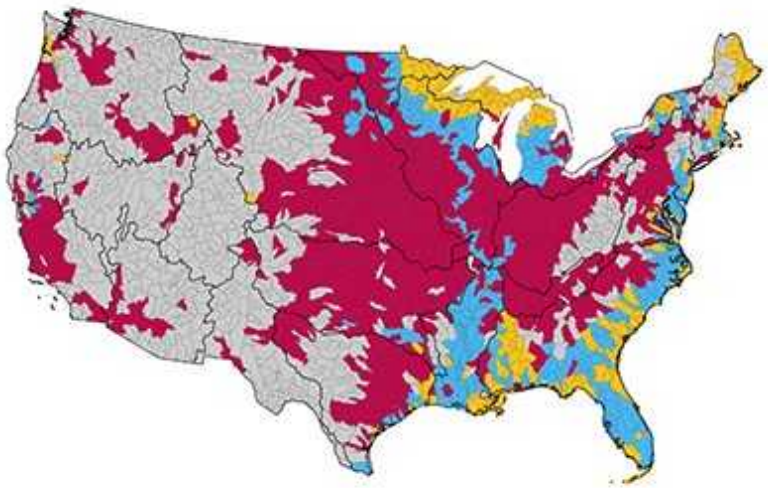
- [Pub Med](#)
- [Nature.com](#)
- [Google Scholar](#)



Figure 1 | Restored wetlands in the South San Francisco Bay Area.

Cheng *et al.*³ report that wetland restoration targeted to the regions of the United States that contribute most to nitrate pollution could have a big effect on environmental water quality. Credit: Getty

Human activities have increased the amounts of reactive nitrogen compounds — forms of nitrogen that can be used by organisms for growth — in the environment. The resulting overabundance of reactive nitrogen has far-reaching consequences for ecosystems, climate, and human health and well-being¹. Fertilizers are the largest global source of anthropogenic nitrogen inputs², and so intensive efforts have been made to reduce nitrogen transport from agricultural land to ground and surface waters, but with mixed results. [Writing in Nature](#), Cheng *et al.*³ report that sources of river nitrogen pollution in the United States are often spatially separated from existing wetlands (Fig. 1), which can remove nitrate from water, and show that wetland restoration targeted to nitrate sources would yield substantial benefits for downstream water quality.



Read the paper: Maximizing US nitrate removal through wetland protection and restoration

The beneficial effects of wetlands on water quality are well documented, and wetlands are widely used both in urban and rural settings to remove pollution arising from human activities⁴. The biogeochemical conditions in wetlands particularly favour the removal of nitrate, which is often the dominant form of nitrogen pollution in water. However, the global area of wetlands has reduced drastically over the past two centuries^{5,6}, and losses continue despite greater protections being established. The need for wetland restoration is clear, but it is difficult to calculate the potential contributions that restorations could make to nitrate removal for large water catchment areas by scaling up the effects of individual wetlands. This is because water-quality outcomes are highly sensitive to the geographical distribution of wetlands relative to that of nitrogen sources^{7–9}.

Cheng *et al.* tackle this problem by combining an inventory of US wetland distribution with models of nitrogen transport. Their analysis affirms — with much greater precision than was possible in past studies — that remnant and

restored wetlands in agricultural areas have a disproportionately large role in mitigating river nitrogen pollution. Without these wetlands, the negative impacts of nitrogen pollution on coastal zones and on many inland waters would be much worse.

The authors then develop scenarios for expanding wetland coverage in the United States, taking into account the large misalignment between current wetland distributions and regions that have high nitrogen levels in water runoff. They estimate that an aggressive strategy that increases wetland area by 10% in agricultural areas that have the highest nitrogen run-off would almost double nitrogen removal by wetlands, compared with current levels. Such a restoration effort would be costly, requiring investments of several billions of US dollars annually to convert a modest amount of productive farmland to wetlands. However, as Cheng *et al.* discuss, current conservation spending is probably similar in magnitude, and so reprioritizing funds to target nitrogen sources more effectively could help to pay some of the costs. The study makes a compelling case for better use of conservation investments to deal with the stubborn problem of nitrogen pollution.



Future of tidal wetlands depends on coastal management

Many other challenges remain to be addressed before large-scale expansion of wetland restoration could begin. A more comprehensive accounting of the benefits, and of other costs, is needed to fully understand the economic implications of restorations along the lines described by the authors. For example, wetlands provide other important ecosystem services such as sequestering atmospheric carbon, supporting biodiversity, and reducing flooding and stream-bank erosion⁶. Thus, the benefits of wetland restoration would extend to other ecosystem services.

However, wetland disservices, such as the release of greenhouse gases¹⁰, could offset some of these benefits. Continued efforts to reduce the transport of agricultural pollutants that cannot be effectively removed by wetlands, such as phosphorus, will also be necessary. Finally, substantial policy and legal uncertainties regarding US federal rules governing water management on private land¹¹ must be resolved to overcome barriers to conservation efforts. Despite these challenges, Cheng and colleagues' work describes a way forward to achieve long-standing, but elusive, US policy goals.

The authors point out that the increasing availability of data and modelling tools will create further opportunities to use wetland restorations effectively within individual river catchment areas. For example, the benefits of a downstream wetland might be less if an upstream wetland has already reduced the amount of incoming nitrate; Cheng *et al.* could not address this effect in depth in their nationwide study, but detailed studies at smaller scales (see refs 9 and 12, for example) could help to further optimize the placement of restored wetlands to maximize the benefits for nitrate removal and other services¹³.

The costs of large-scale wetland restoration are sure to be a challenge given increased economic pressure on US farming from global competition, trade policies and climate shifts. However, the lack of progress in meeting goals for reducing nitrogen pollution, and the likelihood that such pollution will worsen in a warming world, mean that new approaches are needed. Cheng and colleagues' findings make a compelling case for a renewed emphasis on wetland restorations in the catchment-scale management of agricultural land. By identifying current mismatches between sources and sinks of nitrogen pollution in the United States, the authors provide a road map for more

effectively unleashing the potential of wetland restoration to help solve water-quality problems.

Nature **588**, 592–593 (2020)

doi: <https://doi.org/10.1038/d41586-020-03515-7>

References

1. 1.

Organisation of Economic Co-operation and Development. *Human Acceleration of the Nitrogen Cycle* (OECD, 2018).

2. 2.

Galloway, J. N. *et al.* *Bioscience* **53**, 341–356 (2003).

3. 3.

Cheng, F. Y. *et al.* *Nature* **588**, 625–630 (2020).

4. 4.

Mitsch, W. & Gosselink, J. *Wetlands* 5th edn, Ch. 19 (Wiley, 2015).

5. 5.

Gardner, R. C. & Finlayson, M. *Global Wetland Outlook: State of the World's Wetlands and their Services to People 2018* (Ramsar Convention Secretariat, 2018).

6. 6.

Zedler, J. B. & Kercher, S. *Annu. Rev. Environ. Resour.* **30**, 39–74, (2005).

7. 7.

Mitsch, W. J. & Gosselink, J. G. *Ecol. Econ.* **35**, 25–33 (2000).

8. 8.

Crumpton, W. G. *Water Sci. Technol.* **44**, 559–564 (2001).

9. 9.

Hansen, A. T., Dolph, C. L., Foufoula-Georgiou, E. & Finlay, J. C. *Nature Geosci.* **11**, 127 (2018).

10. 10.

Burgin, A. J., Lazar, J. G., Groffman, P. M., Gold, A. J. & Kellogg, D. Q. *Ecol. Eng.* **56**, 26–35 (2013).

11. 11.

Creed, I. F. *et al.* *Nature Geosci.* **10**, 809–815 (2017).

12. 12.

Czuba, J. A., Hansen, A. T., Foufoula-Giorgiu, E. & Finlay, J. C. *Water Resour. Res.* **54**, 1312–1337 (2018).

13. 13.

Zedler, J. B. *Front. Ecol. Environ.* **1**, 65–72 (2003).

Jobs from Nature Careers

- - - [All jobs](#)
 - - [**Full Professorship for Translational Imaging in Oncology \(W3\)**](#)

German Cancer Research Center in the Helmholtz Association (DKFZ)

Dresden, Germany

JOB POST

▪ **MSc Position in Forest Research**

The University of British Columbia (UBC)

Vancouver, Canada

JOB POST

▪ **Research Associate - zero-emission hydrogen production project**

The University of British Columbia (UBC)

Vancouver, Canada

JOB POST

▪ **Laboratory Manager - Zamore Lab**

Howard Hughes Medical Institute (HHMI)

Worcester, United States

JOB POST

This article was downloaded by **calibre** from <https://www.nature.com/articles/d41586-020-03515-7>

NEWS AND VIEWS

23 December 2020

High-resolution 3D printing in seconds

A 3D-printing technique has been developed that can produce millimetre- to centimetre-scale objects with micrometre-scale features. It relies on chemical reactions triggered by the intersection of two light beams.

Cameron Darkes-Burkey &

Cameron Darkes-Burkey is in the Organic Robotics Laboratory, Department of Mechanical and Aerospace Engineering, Cornell University, Ithaca, New York 14853, USA.

Search for this author in:

- [Pub Med](#)
- [Nature.com](#)
- [Google Scholar](#)

Robert F. Shepherd

Robert F. Shepherd is in the Organic Robotics Laboratory, Department of Mechanical and Aerospace Engineering, Cornell University, Ithaca, New York 14853, USA.

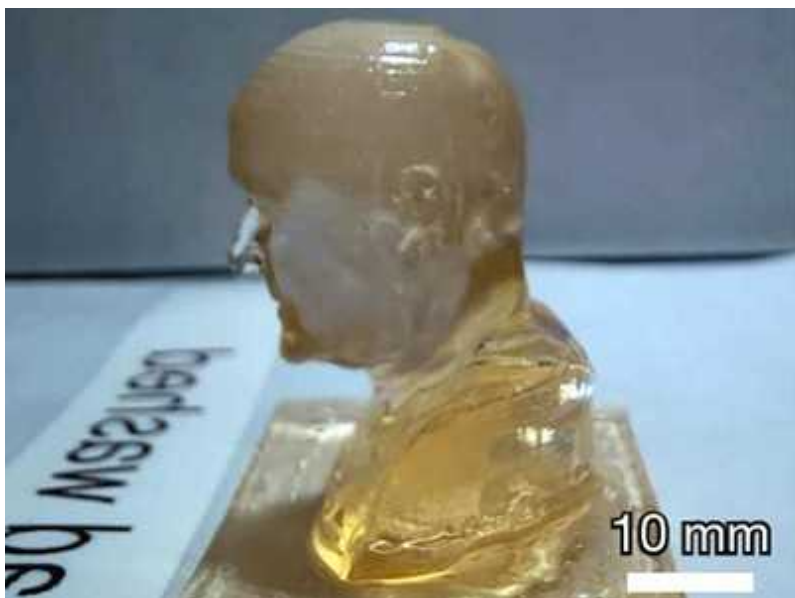
[Contact](#)

Search for this author in:

- [Pub Med](#)
- [Nature.com](#)

- [Google Scholar](#)

In the *Star Trek* universe, devices called replicators can manifest solid matter in seconds. Thanks to advances in materials science, these science-fiction devices might be closer to reality than we think. A type of 3D printing called volumetric additive manufacturing (VAM) uses light to rapidly solidify an object in a volume of a liquid precursor. [Writing in Nature](#), Regehly *et al.*¹ report an advance in VAM that allows solid objects to be printed with a feature resolution of up to 25 micrometres and a solidification rate of up to 55 cubic millimetres per second. The authors call this process xolography because it uses two crossing (x) light beams of different wavelengths to solidify a whole object (*holos* is the Greek word for whole).



[Read the paper: Xolography for linear volumetric 3D printing](#)

Conventional 3D printers have gantries that manoeuvre either the printheads or the printed object in three orthogonal directions to orient the printer's nozzle to the next position to deposit material. However, the fastest 3D printers use light to induce the polymerization of an entire layer of a liquid starting material at a time, thereby allowing solid objects to be drawn out

from the liquid with rates of 500 millimetres per hour². If the light flux and polymerization kinetics are tuned properly, the printed object is monolithic — it has none of the artefacts that could be produced by the layer-by-layer printing process. VAM removes the need to draw an object out from the starting material, simplifying the mechanics of the process and allowing even faster fabrication. It also enables the production of higher-quality parts than is possible with other methods, and it removes the need to print support structures for the object that must then be removed after printing.

Previous variants of VAM included two-photon photopolymerization (TPP)^{3,4} and computed axial lithography (CAL)^{5,6}. In TPP, femtosecond laser pulses (1 femtosecond is 10^{-15} seconds) are used to polymerize nanoscale building blocks, which can be layered to fabricate microstructures. TPP is slow, with a printing rate of just 1–20 cubic millimetres per hour, and is typically used to make millimetre-scale objects, but it can print features at a resolution of 100 nanometres.

By contrast, CAL moved the abilities of VAM in the other direction by allowing high-speed solidification of centimetre-scale objects. In CAL, images are projected at different angles around a rotating volume of a liquid precursor, using algorithms to control the cumulative light exposure at different voxels (3D pixels). This is done in concert with a system that uses dissolved oxygen to prevent free-radical species from initiating unwanted polymerization, so only the volumes of interest are solidified. CAL can achieve feature sizes of 100 micrometres and fabricate centimetre-scale parts in just seconds, but it requires computer optimization using a feedback system, which adds to the cost of the equipment and the total printing time.

Regehly and colleagues report new chemistry for initiating polymerization in VAM that better controls the volume of liquid in which initiation and polymerization occur. Their technique increases the resolution to up to ten times that of previously reported macroscopic VAM techniques, without sacrificing the printing rate.

The xolography process works as follows. A rectangular sheet of light with a set thickness is shone through a volume of a viscous resin (Fig. 1). The wavelength of the light is chosen to excite molecules known as dual-colour photoinitiators (DCPIs) dissolved in the resin by cleaving a molecular ring

in the backbone of the molecule; this reaction occurs only within the sheet of light.

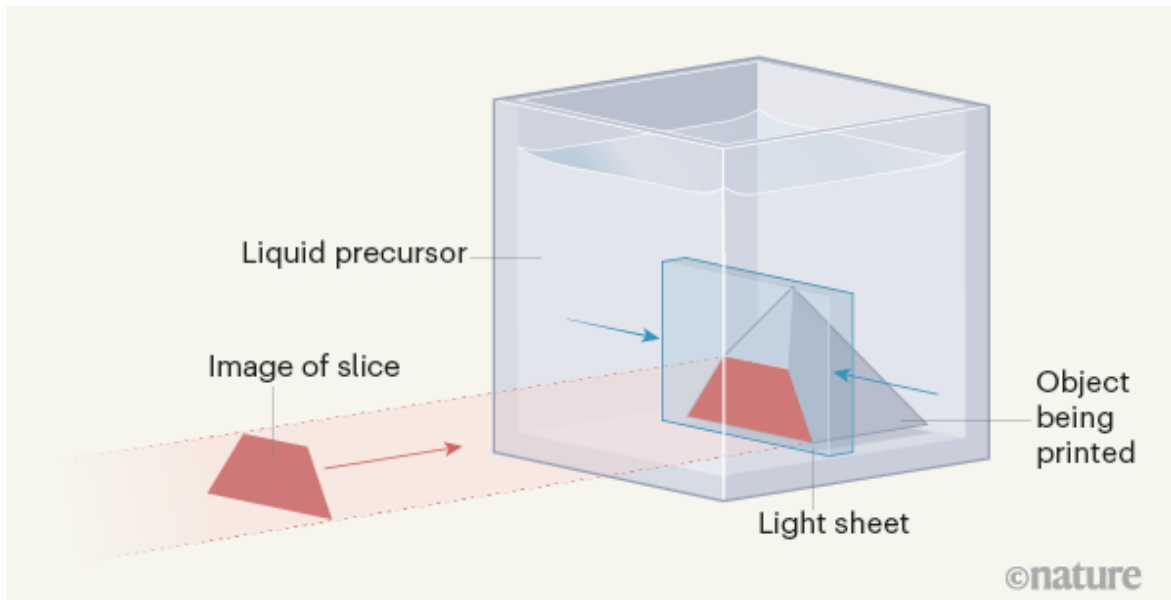


Figure 1 | A method for high-resolution 3D printing. Regehly *et al.*¹ report a technique called xoholography, which uses light to solidify objects from a liquid precursor. A rectangular sheet of light (blue) is shone through a volume of a viscous resin, and activates molecules known as dual-colour photoinitiators (DCPIs, not shown) dissolved in the resin. A second beam of light (red) then projects an image of a slice of the object to be printed into the plane of the light sheet. The wavelength of the second beam is different from that of the first, and causes any activated DCPIs to initiate polymerization of the resin, solidifying the resin where the two wavelengths of light cross. The light sheet is then moved to a new position by shifting the resin volume on a linear stage, and the process begins again, building up the object slice by slice.

A second beam of light projects an image of a slice of the 3D object to be printed into the plane of the light sheet. The wavelength of the second beam is different from that of the first and causes any excited DCPI molecules to initiate polymerization of the resin, solidifying the slice. The resin volume is then moved relative to the position of the light sheet, which is fixed. This changes the position of the light sheet in the resin, so the activation and initiation processes can begin again at a new position, thereby building up the object slice by slice.

The authors demonstrated the effectiveness of their technique by printing a ball trapped as a loose object in a spherical cage, which was 8 millimetres in diameter (Fig. 2). Using conventional layer-by-layer 3D printing, the ball would have needed to have been printed with supports connecting it to the cage, and they would have been difficult to remove afterwards. The high resolution afforded by xolography also allows it to print mechanical systems directly, such as blades that can spin on an axle in a flow of liquid or air (see Fig. 2d–f of the paper¹).

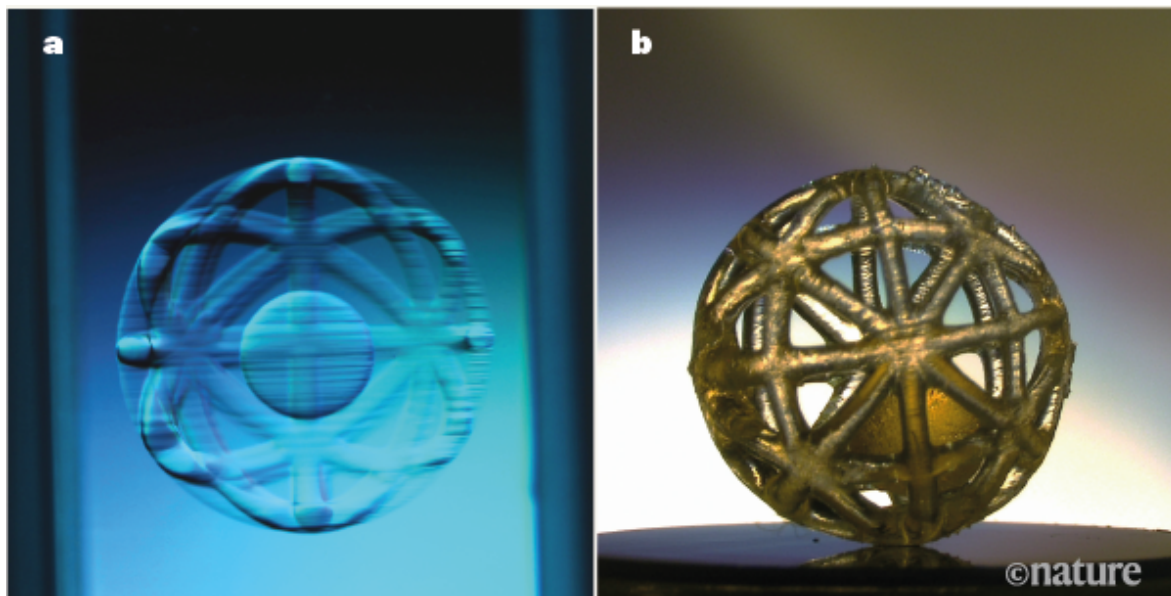
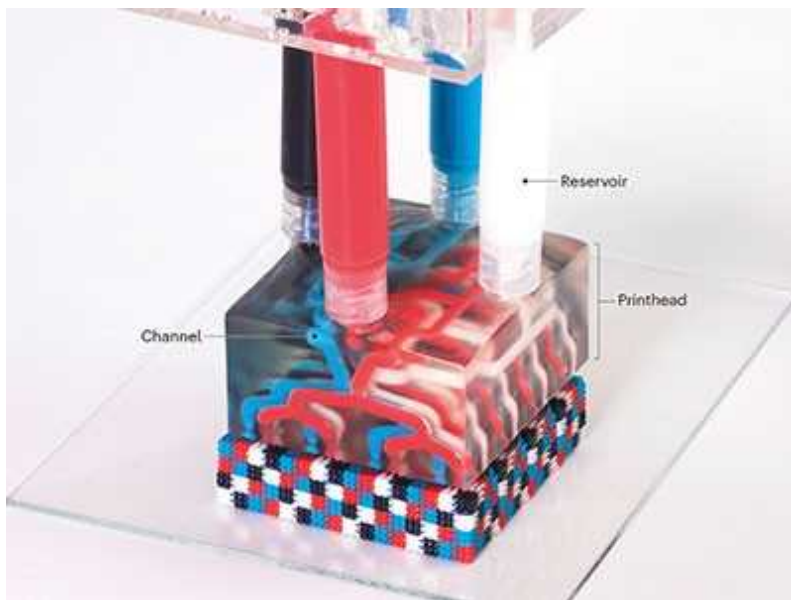


Figure 2 | A complex object produced by xolography. Regehly and colleagues have used xolography to print several complex objects with high feature resolution, including a ball trapped as a loose object in a spherical cage. Such objects are often difficult to print directly using conventional 3D-printing processes. These images show the object as it is being printed (**a**) and after processing (**b**). Cage diameter, 8 millimetres.

In an even more ambitious demonstration, Regehly *et al.* used xolography to print an aspherical Powell lens (see Fig. 2g–i of the paper) — a type of lens used to convert laser beams into straight, uniform lines of light. In air, the lens stretched a narrow green laser beam into a projected straight line. The optical properties of the lens demonstrate that the structure of the printed material is remarkably uniform and free from defects. Finally, the authors printed a highly detailed 3-cm-diameter bust of a person, with precisely

defined internal anatomical features, such as a hollowed-out nasal passage and oesophagus (see Fig. 2j–l of the paper).

Currently, the major limitation of xolography is the volume that can be printed, because this is restricted by the distance the light beams can penetrate into the resin. Moreover, because the method requires the resin volume to be moved, objects with large dimensions in the direction of movement will take proportionally more time to make than shorter ones. And although the reported chemistry enables high-resolution printing, it also limits the materials that can be used for xolography.



How to print multi-material devices in one go

Despite these limitations, the future holds many possibilities for xolography, and for other VAM methods in general. Techniques similar to those pioneered for digital light processing (DLP, a conventional layer-by-layer 3D-printing method in which solidification is initiated by light) could now be applied to VAM. For example, greyscale illumination could be used to fabricate objects with gradients of stiffness. This would find many applications, such as toughening the interfaces between different 3D-printed

components, and in unusual engineering mechanisms such as living hinges (flexible joints formed from the same material as the rigid pieces they connect).

Regehly *et al.* predict that the feature resolution and volume-generation rate of xolography could be enhanced further by using better optical systems, such as more powerful lasers. But some challenges remain for all VAM systems, such as scaling up printing volumes from cubic centimetres to cubic metres, and finding ways to use multiple materials in the same print.

The advent of improved printing speeds and new materials has allowed a DLP method to be used for the mass customization of midsoles for running shoes, as part of a product-development process (see go.nature.com/3gy86wp). If similar advances can be made using VAM and xolography, this might enable the mass production of commercial products. Other opportunities, including applications that are not yet possible using 3D printing, are sure to be in the offing. As Regehly and colleagues' work shows, it is truly an exciting time for this field.

Nature **588**, 594–595 (2020)

doi: <https://doi.org/10.1038/d41586-020-03543-3>

References

1. 1.

Regehly, M. *et al.* Nature **588**, 620–624 (2020).

2. 2.

Tumbleston, J. R. *et al.* Science **347**, 1349–1352 (2015).

3. 3.

Baldacchini, T. (ed.) *Three-Dimensional Microfabrication Using Two-Photon Polymerisation: Fundamentals, Technology and Applications* (Elsevier, 2019).

4. 4.

Geng, Q., Wang, D., Chen, P. & Chen, S.-C. *Nature Commun.* **10**, 2179 (2019).

5. 5.

Loterie, D., Delrot, P. & Moser, C. *Nature Commun.* **11**, 852 (2020).

6. 6.

Kelly, B. E. *et al.* *Science* **363**, 1075–1079 (2019).

Jobs from Nature Careers

- - - [All jobs](#)
 - - [**Full Professorship for Translational Imaging in Oncology \(W3\)**](#)
[German Cancer Research Center in the Helmholtz Association \(DKFZ\)](#)
[Dresden, Germany](#)
[JOB POST](#)
 - [**MSc Position in Forest Research**](#)
[The University of British Columbia \(UBC\)](#)
[Vancouver, Canada](#)
[JOB POST](#)

- **Research Associate - zero-emission hydrogen production project**

The University of British Columbia (UBC)

Vancouver, Canada

JOB POST

- **Laboratory Manager - Zamore Lab**

Howard Hughes Medical Institute (HHMI)

Worcester, United States

JOB POST

This article was downloaded by **calibre** from <https://www.nature.com/articles/d41586-020-03543-3>

| [Section menu](#) | [Main menu](#) |

- Article
- [Published: 23 December 2020](#)

Superconducting qubit to optical photon transduction

- [Mohammad Mirhosseini](#)^{1,2,3 na1},
- [Alp Sipahigil](#) ORCID: orcid.org/0000-0003-1469-5272^{1,2,3 na1},
- [Mahmoud Kalaei](#)^{1,2,3,4 na1} &
- [Oskar Painter](#) ORCID: orcid.org/0000-0002-1581-9209^{1,2,3,4}

[Nature](#) volume **588**, pages 599–603(2020) [Cite this article](#)

- 1512 Accesses
- 35 Altmetric
- [Metrics details](#)

Subjects

- [Qubits](#)
- [Single photons and quantum effects](#)
- [Superconducting devices](#)

Abstract

Conversion of electrical and optical signals lies at the foundation of the global internet. Such converters are used to extend the reach of long-haul fibre-optic communication systems and within data centres for high-speed optical networking of computers. Likewise, coherent microwave-to-optical conversion of single photons would enable the exchange of quantum states

between remotely connected superconducting quantum processors¹. Despite the prospects of quantum networking², maintaining the fragile quantum state in such a conversion process with superconducting qubits has not yet been achieved. Here we demonstrate the conversion of a microwave-frequency excitation of a transmon—a type of superconducting qubit—into an optical photon. We achieve this by using an intermediary nanomechanical resonator that converts the electrical excitation of the qubit into a single phonon by means of a piezoelectric interaction³ and subsequently converts the phonon to an optical photon by means of radiation pressure⁴. We demonstrate optical photon generation from the qubit by recording quantum Rabi oscillations of the qubit through single-photon detection of the emitted light over an optical fibre. With proposed improvements in the device and external measurement set-up, such quantum transducers might be used to realize new hybrid quantum networks^{2,5} and, ultimately, distributed quantum computers^{6,7}.

[Access through your institution](#)

[Change institution](#)

[Buy or subscribe](#)

Access options

Subscribe to Journal

Get full journal access for 1 year

\$199.00

only \$3.83 per issue

[Subscribe](#)

All prices are NET prices.

VAT will be added later in the checkout.

Rent or Buy article

Get time limited or full article access on ReadCube.

from \$8.99

[Rent or Buy](#)

All prices are NET prices.

Additional access options:

- [Log in](#)
- [Access through your institution](#)
- [Learn about institutional subscriptions](#)

Fig. 1: Quantum transducer set-up.

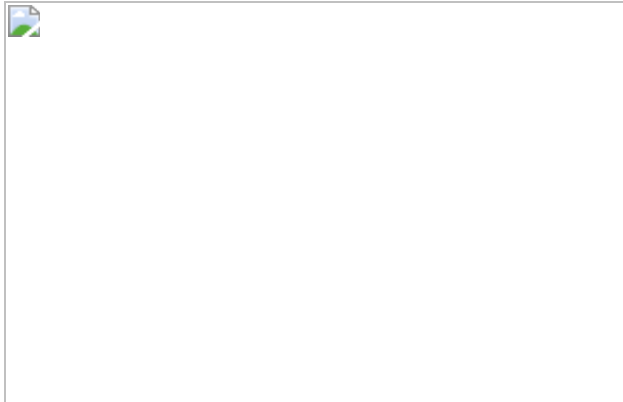


Fig. 2: Microwave and optical spectroscopy of mechanics.

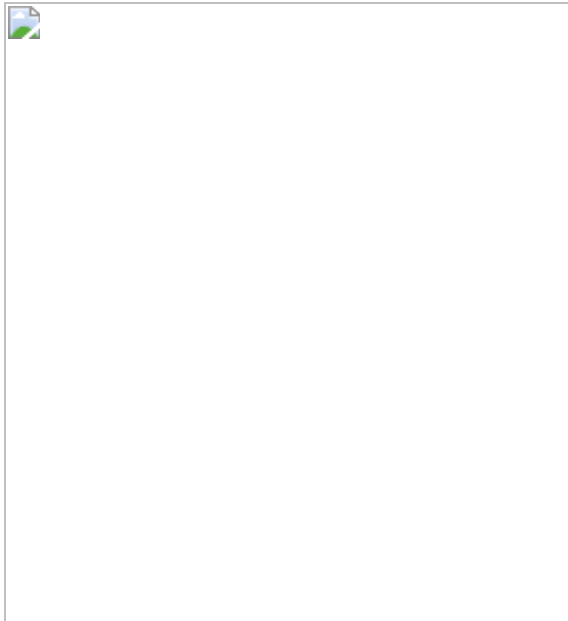


Fig. 3: Qubit-mechanics swap.

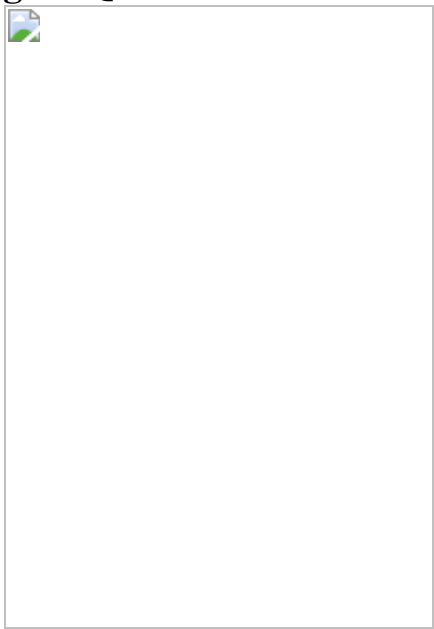


Fig. 4: Detecting optical photons from a superconducting qubit.

Data availability

The data that support the findings of this study are available from the corresponding author (O.P.) upon reasonable request.

References

1. 1.

Arute, F. et al. Quantum supremacy using a programmable superconducting processor. *Nature* **574**, 505–510 (2019).

[ADS](#) [CAS](#) [Article](#) [Google Scholar](#)

2. 2.

Briegel, H., Dür, W., Cirac, J. I. & Zoller, P. Quantum repeaters: the role of imperfect local operations in quantum communication. *Phys. Rev. Lett.* **81**, 5932–5935 (1998).

[ADS](#) [CAS](#) [Article](#) [Google Scholar](#)

3. 3.

O’Connell, A. D. et al. Quantum ground state and single-phonon control of a mechanical resonator. *Nature* **464**, 697–703 (2010).

[ADS](#) [Article](#) [Google Scholar](#)

4. 4.

Meenehan, S. M. et al. Pulsed excitation dynamics of an optomechanical crystal resonator near its quantum ground state of motion. *Phys. Rev. X* **5**, 041002 (2015).

[Google Scholar](#)

5. 5.

Muralidharan, S. et al. Optimal architectures for long distance quantum communication. *Sci. Rep.* **6**, 20463 (2016).

[ADS](#) [CAS](#) [Article](#) [Google Scholar](#)

6. 6.

Monroe, C. et al. Large-scale modular quantum-computer architecture with atomic memory and photonic interconnects. *Phys. Rev. A* **89**, 022317 (2014).

[ADS](#) [Article](#) [Google Scholar](#)

7. 7.

Fitzsimons, J. F. Private quantum computation: an introduction to blind quantum computing and related protocols. *npjQuantum Inf.* **3**, 23 (2017).

[ADS](#) [Article](#) [Google Scholar](#)

8. 8.

Devoret, M. H. & Schoelkopf, R. J. Superconducting circuits for quantum information: an outlook. *Science* **339**, 1169–1174 (2013).

[ADS](#) [CAS](#) [Article](#) [Google Scholar](#)

9. 9.

Kimble, H. J. The quantum internet. *Nature* **453**, 1023–1030 (2008).

[ADS](#) [CAS](#) [Article](#) [Google Scholar](#)

10. 10.

O'Brien, J. L., Furusawa, A. & Vuckovic, J. Photonic quantum technologies. *Nat. Photon.* **3**, 687–695 (2009).

[ADS](#) [Article](#) [Google Scholar](#)

11. 11.

Reagor, M. et al. Reaching 10 ms single photon lifetimes for superconducting aluminum cavities. *Appl. Phys. Lett.* **102**, 192604 (2013).

[ADS](#) [Article](#) [Google Scholar](#)

12. 12.

Fan, L. et al. Superconducting cavity electro-optics: a platform for coherent photon conversion between superconducting and photonic circuits. *Sci. Adv.* **4**, eaar4994 (2018).

[ADS](#) [CAS Article](#) [Google Scholar](#)

13. 13.

Hisatomi, R. et al. Bidirectional conversion between microwave and light via ferromagnetic magnons. *Phys. Rev. B* **93**, 174427 (2016).

[ADS](#) [Article](#) [Google Scholar](#)

14. 14.

O'Brien, C., Lauk, N., Blum, S., Morigi, G. & Fleischhauer, M. Interfacing superconducting qubits and telecom photons via a rare-earth-doped crystal. *Phys. Rev. Lett.* **113**, 063603 (2014).

[ADS](#) [Article](#) [Google Scholar](#)

15. 15.

Lambert, N. J., Rueda, A., Sedlmeir, F. & Schwefel, H. G. L. Coherent conversion between microwave and optical photons—an overview of physical implementations. *Adv. Quantum Technol.* **3**, 1900077 (2020).

[CAS](#) [Article](#) [Google Scholar](#)

16. 16.

Teufel, J. D. et al. Sideband cooling of micromechanical motion to the quantum ground state. *Nature* **475**, 359–363 (2011).

[ADS](#) [CAS](#) [Article](#) [Google Scholar](#)

17. 17.

Chan, J. et al. Laser cooling of a nanomechanical oscillator into its quantum ground state. *Nature* **478**, 89–92 (2011).

[ADS](#) [CAS](#) [Article](#) [Google Scholar](#)

18. 18.

Bochmann, J., Vainsencher, A., Awschalom, D. D. & Cleland, A. N. Nanomechanical coupling between microwave and optical photons. *Nat. Phys.* **9**, 712–716 (2013).

[CAS](#) [Article](#) [Google Scholar](#)

19. 19.

Andrews, R. W. et al. Bidirectional and efficient conversion between microwave and optical light. *Nat. Phys.* **10**, 321–326 (2014).

[CAS](#) [Article](#) [Google Scholar](#)

20. 20.

Bagci, T. et al. Optical detection of radio waves through a nanomechanical transducer. *Nature* **507**, 81–85 (2014).

[ADS](#) [CAS](#) [Article](#) [Google Scholar](#)

21. 21.

Balram, K. C., Davanço, M. I., Song, J. D. & Srinivasan, K. Coherent coupling between radiofrequency, optical and acoustic waves in piezo-optomechanical circuits. *Nat. Photon.* **10**, 346–352 (2016).

[ADS](#) [CAS](#) [Article](#) [Google Scholar](#)

22. 22.

Forsch, M. et al. Microwave-to-optics conversion using a mechanical oscillator in its quantum groundstate. *Nat. Phys.* **16**, 69–74 (2020).

[CAS](#) [Article](#) [Google Scholar](#)

23. 23.

Higginbotham, A. P. et al. Harnessing electro-optic correlations in an efficient mechanical converter. *Nat. Phys.* **14**, 1038–1042 (2018).

[CAS](#) [Article](#) [Google Scholar](#)

24. 24.

Zeuthen, E., Schliesser, A., Sørensen, A. S. & Taylor, J. M. Figures of merit for quantum transducers. Preprint at <https://arXiv.org/1610.01099v2> (2017).

25. 25.

Aspelmeyer, M., Kippenberg, T. J. & Marquardt, F. Cavity optomechanics. *Rev. Mod. Phys.* **86**, 1391–1452 (2014).

[ADS](#) [Article](#) [Google Scholar](#)

26. 26.

Chu, Y. et al. Quantum acoustics with superconducting qubits. *Science* **358**, 199–202 (2017).

[ADS](#) [MathSciNet](#) [CAS](#) [Article](#) [Google Scholar](#)

27. 27.

Arrangoiz-Arriola, P. et al. Resolving the energy levels of a nanomechanical oscillator. *Nature* **571**, 537–540 (2019).

[ADS](#) [CAS](#) [Article](#) [Google Scholar](#)

28. 28.

Hong, S. et al. Hanbury Brown and Twiss interferometry of single phonons from an optomechanical resonator. *Science* **358**, 203–206 (2017).

[ADS](#) [MathSciNet](#) [CAS](#) [Article](#) [Google Scholar](#)

29. 29.

Keller, A. J. et al. Al transmon qubits on silicon-on-insulator for quantum device integration. *Appl. Phys. Lett.* **111**, 042603 (2017).

[ADS](#) [Article](#) [Google Scholar](#)

30. 30.

Chan, J., Safavi-Naeini, A. H., Hill, J. T., Meenehan, S. & Painter, O. Optimized optomechanical crystal cavity with acoustic radiation shield. *Appl. Phys. Lett.* **101**, 081115 (2012).

[ADS](#) [Article](#) [Google Scholar](#)

31. 31.

Fang, K., Matheny, M. H., Luan, X. & Painter, O. Optical transduction and routing of microwave phonons in cavity-optomechanical circuits. *Nat. Photonics* **10**, 489–496 (2016).

[ADS](#) [CAS](#) [Article](#) [Google Scholar](#)

32. 32.

Cohen, J. D. et al. Phonon counting and intensity interferometry of a nanomechanical resonator. *Nature* **520**, 522–525 (2015).

[ADS](#) [CAS](#) [Article](#) [Google Scholar](#)

33. 33.

Johnson, M. Direct real time measurement of quasiparticle lifetimes in a superconductor. *Phys. Rev. Lett.* **67**, 374–377 (1991).

[ADS](#) [CAS](#) [Article](#) [Google Scholar](#)

34. 34.

Borselli, M., Johnson, T. J. & Painter, O. Measuring the role of surface chemistry in silicon microphotonics. *Appl. Phys. Lett.* **88**, 131114 (2006).

[ADS](#) [Article](#) [Google Scholar](#)

35. 35.

Ren, H. et al. Two-dimensional optomechanical crystal cavity with high quantum cooperativity. *Nat. Commun.* **11**, 3373 (2020).

[ADS](#) [Article](#) [Google Scholar](#)

36. 36.

Qiu, L., Shomroni, I., Seidler, P. & Kippenberg, T. J. Laser cooling of a nanomechanical oscillator to its zero-point energy. *Phys. Rev. Lett.* **124**, 173601 (2020).

[ADS](#) [CAS](#) [Article](#) [Google Scholar](#)

37. 37.

MacCabe, G. S. et al. Nano-acoustic resonator with ultralong phonon lifetime. *Science* **370**, 840–843 (2020).

38. 38.

Wang, C. et al. Measurement and control of quasiparticle dynamics in a superconducting qubit. *Nat. Commun.* **5**, 5836 (2014).

[ADS](#) [CAS](#) [Article](#) [Google Scholar](#)

[Download references](#)

Acknowledgements

We thank M. Shaw, J. Bunker, H. Ren, E. Kim and X. Zhang for their various contributions to this work. This work was supported by the ARO/LPS Cross Quantum Technology Systems programme (grant W911NF-18-1-0103), the Institute for Quantum Information and Matter, an NSF Physics Frontiers Center (grant PHY-1125565) with support of the Gordon and Betty Moore Foundation, and the Kavli Nanoscience Institute at Caltech. M.M (A.S.) acknowledges support from a KNI (IQIM) Postdoctoral Fellowship.

Author information

Author notes

1. These authors contributed equally: Mohammad Mirhosseini, Alp Sipahigil, Mahmoud Kalaei

Affiliations

1. Kavli Nanoscience Institute, Laboratory of Applied Physics, California Institute of Technology, Pasadena, CA, USA

Mohammad Mirhosseini, Alp Sipahigil, Mahmoud Kalaei & Oskar Painter

2. Thomas J. Watson, Sr., Laboratory of Applied Physics, California Institute of Technology, Pasadena, CA, USA

Mohammad Mirhosseini, Alp Sipahigil, Mahmoud Kalaee & Oskar Painter

3. Institute for Quantum Information and Matter, California Institute of Technology, Pasadena, CA, USA

Mohammad Mirhosseini, Alp Sipahigil, Mahmoud Kalaee & Oskar Painter

4. AWS Center for Quantum Computing, Pasadena, CA, USA

Mahmoud Kalaee & Oskar Painter

Authors

1. Mohammad Mirhosseini
[View author publications](#)

You can also search for this author in [PubMed](#) [Google Scholar](#)

2. Alp Sipahigil
[View author publications](#)

You can also search for this author in [PubMed](#) [Google Scholar](#)

3. Mahmoud Kalaee
[View author publications](#)

You can also search for this author in [PubMed](#) [Google Scholar](#)

4. Oskar Painter
[View author publications](#)

You can also search for this author in [PubMed](#) [Google Scholar](#)

Contributions

All authors contributed to the concept and planning of the experiment, the device design and fabrication, the measurements and analysis of data, and

the writing of the manuscript.

Corresponding author

Correspondence to [Oskar Painter](#).

Ethics declarations

Competing interests

The authors declare no competing interests.

Additional information

Peer review information *Nature* thanks Konrad Lehnert and the other, anonymous, reviewer(s) for their contribution to the peer review of this work. Peer review reports are available.

Publisher's note Springer Nature remains neutral with regard to jurisdictional claims in published maps and institutional affiliations.

Extended data figures and tables

[Extended Data Fig. 1 Device fabrication process.](#)

(i) Starting substrate: AlN-on-SOI. (ii) Defining the boundaries of the piezoelectric resonator with plasma etching. (iii) Deposition of silicon oxide protective mask. (iv) Patterning of the silicon oxide mask with plasma etching. (v) Removing the AlN layer outside the device boundaries with phosphoric acid wet etch. (vi) Removing the silicon oxide mask with a BHF acid wet etch. (vii) Patterning of the silicon device layer with plasma etching. (viii) Evaporation of aluminium for IDT, qubit capacitor, resonator, CPW and device ground layer. (ix) Angled evaporation of Josephson junction leads. (x) Vapour-HF etch of buried oxide layer for releasing the

device membrane. Images are not to scale. All patterning is performed with electron beam lithography using a ZEP-520A electron beam resist mask.

Extended Data Fig. 2 Optomechanical and piezoelectric design.

a, Simulated mechanical mode shape (deformation) and electric voltage (colour) of the piezoacoustic cavity mode of interest with an IDT period of 930 nm and a beam width of 600 nm. **b**, Simulated optical (top) and mechanical (bottom) mode profile of an OMC designed with the mechanical mode near 5 GHz. **c**, Simulated optical (top) and mechanical (bottom) mode profile of the full piezo-optomechanical transducer device formed by attaching the piezoacoustic cavity of **(a)** and the OMC cavity of **(b)** through a phonon waveguide section in which the mirror holes in the OMC cavity are modified nearest the piezoacoustic cavity. The optomechanical and piezoelectric coupling rates listed are calculated for the hybridized mode with the largest optomechanical coupling. **d**, Radii of the patterned holes along the nanobeam OMC cavity and phonon waveguide section. d_1 (d_2) designates the hole diameter normal (parallel) to the nanobeam's long axis. The optical cavity region (shaded 13 central holes) is located between a phonon/photon mirror (left seven holes) and a photon mirror/phonon waveguide section (right seven holes).

Extended Data Fig. 3 Design of the phonon waveguide unit cell.

a, Schematics of the original (top) and modified (bottom) unit cell of the OMC cavity mirror section adjacent to the phonon waveguide. The dimensional parameters are equal to $d_1 = 366$ nm ($d_1 = 295$ nm) and $d_2 = 205$ nm ($d_2 = 320$ nm) for the original (modified) holes. The nanobeam parameters ($h = 220$ nm, $a = 436$ nm, $b = 529$ nm) are identical for both cases. **b**, Simulated mechanical band structures. The dashed line marks a nominal mechanical resonance frequency of $f_m = 5.3$ GHz for the decoupled OMC and piezoacoustic cavity modes. The intersection of the dashed line and the energy band in the bottom acoustic band-structure plot for the modified hole structure allows for guiding of acoustic waves between the piezoacoustic and OMC cavity. **c**, Optical band structure for TE-like modes of the OMC cavity, again with the top plot being for the original OMC

cavity and the bottom plot for the OMC cavity with modified holes. The solid black line marks the light line, and the dashed line refers to a nominal optical resonance frequency of the fundamental mode of the OMC cavity at a frequency $f_0 = 193$ THz. Unlike the acoustic mode case, the hole modifications in the OMC cavity actually increase the optical bandgap, further suppressing optical radiation into the phonon waveguide.

Extended Data Fig. 4 Mechanical mode hybridization.

Optomechanical and piezoelectric coupling rates from COMSOL Multiphysics simulations of the integrated piezo-optomechanical transducer consisting of a piezoacoustic cavity connected by a phonon waveguide to the OMC cavity (see Fig. 1b). Each resonant acoustic mode of the simulated structure is plotted as a ‘pin’ in each plot, with the horizontal axis corresponding to the resonant mode frequency, $\omega_m/2\pi$. The period of the IDT has been varied along with the total length of the piezoacoustic cavity (that is, fixed total number of periods and exterior boundary region to AlN box), leading to an approximate linear change in the frequency of the mechanical modes with IDT period. The OMC cavity and phonon waveguide parameters are identical for all of the plots.

Extended Data Fig. 5 Transduction measurement set-up.

Simplified diagram of the experimental set-up used for low-temperature piezoelectric and optomechanical device characterization. The laser emission is passed through a 50-MHz bandwidth filter to suppress broadband spontaneous emission noise. The optical readout pulses are generated using high-extinction modulation components (AOM, Ag.). Microwave pulses are synthesized using arbitrary waveform generators at intermediate frequency band (IF, <500 MHz) and up-converted using mixers and microwave sources to the gigahertz frequency band. Readout of microwave signals is performed using an analogue-to-digital converter after down-conversion to IF band. The optical modulation and microwave synthesis/readout components are triggered by a digital delay generator. Upon reflection from the device under test (DUT), a fibre optical circulator routes the outgoing light to either an EDFA and spectrum analyser, or a

sideband-filtering bank consisting of three cascaded fibre Fabry–Perot filters (Micron Optics FFP-TF2) and the SPD operated at ~ 760 mK. Electrical (optical) signal/control line shown in black (blue). λ -meter: wavemeter; ϕ -m: electro-optic phase modulator; Ag., Agiltron 1 \times 1 MEMS switch; AOM, acousto-optic modulator; EDFA, erbium-doped fibre amplifier; SPD, single photon detector; SW, optical 2 \times 2 switch; TCSPC, time-correlated single photon counting module (PicoQuant PicoHarp 300); VOA, variable optical attenuator; VNA, vector network analyser.

Extended Data Fig. 6 Laser-induced heating.

Plot of the measured thermal noise in the mechanical mode (red) and optomechanical readout efficiency (blue) as a function of integration time (τ_{ro}). Here the noise and efficiency are calibrated from measurements of the optomechanical sideband asymmetry. As for the transduction measurements, the optical pump power is set to $P_{\text{in}} = 2 \mu\text{W}$ at the optical input fibre to the dilution refrigerator, which corresponds to an estimated intra-cavity photon number of $n_c = 44$ and an optomechanical readout rate of $\gamma_{\text{rm}} = g_{\text{rm}}^2 / \kappa = 2 \pi \times 19 \text{ kHz}$. The measurement sequence contains no microwave drive, with the qubit detuned from the mechanical mode, and contains a 250- μs delay between consecutive optical readout pulses to ensure relaxation of the mechanical mode occupancy to its base-temperature value ($\ll 1$) with the laser off. The error bars mark the standard deviation at each point, which is calculated by using the raw counts, assuming Poissonian shot noise. For comparison to the transduction measurements presented in Fig. 4, the operational readout window of $\tau_{\text{ro}} = 38 \text{ ns}$ (marked with the vertical dashed line) yields a photon detection efficiency of $p_d = 8.8 \pm 1.3 \times 10^{-6}$ (horizontal blue dashed line) and a thermal noise of $n_m = 0.64 \pm 0.15$ phonons (horizontal red dashed line).

Extended Data Fig. 7 Light-induced QP generation.

Plot of the qubit Rabi contrast measured when the transmon qubit is driven with a variable-length microwave drive after illumination by an optical

pulse (Rabi oscillation period 150 ns). The horizontal axis marks the separation between incident optical pulse and the beginning of the Rabi measurement. The optical pulse duration is $\tau_{\text{pulse}} = 100$ ns and the pulse repetition rate is $R = 10$ Hz. The peak optical power of the pulses corresponds to $P_{\text{in}} = 40 \mu\text{W}$ at the input fibre to the dilution refrigerator. Vortex trapping is done with a cooling magnetic field estimated to be 15 G at the chip.

Rights and permissions

[Reprints and Permissions](#)

About this article



Check for
updates

Cite this article

Mirhosseini, M., Sipahigil, A., Kalaei, M. *et al.* Superconducting qubit to optical photon transduction. *Nature* **588**, 599–603 (2020).
<https://doi.org/10.1038/s41586-020-3038-6>

[Download citation](#)

- Received: 10 April 2020
- Accepted: 02 October 2020
- Published: 23 December 2020
- Issue Date: 24 December 2020
- DOI: <https://doi.org/10.1038/s41586-020-3038-6>

Comments

By submitting a comment you agree to abide by our [Terms](#) and [Community Guidelines](#). If you find something abusive or that does not comply with our terms or guidelines please flag it as inappropriate.

[Access through your institution](#)

[Change institution](#)

[Buy or subscribe](#)

This article was downloaded by **calibre** from <https://www.nature.com/articles/s41586-020-3038-6>

| [Section menu](#) | [Main menu](#) |

- Article
- [Published: 23 December 2020](#)

Mastering Atari, Go, chess and shogi by planning with a learned model

- [Julian Schrittwieser¹](#), [nal](#),
- [Ioannis Antonoglou^{1,2}](#), [nal](#),
- [Thomas Hubert¹](#), [nal](#),
- [Karen Simonyan¹](#),
- [Laurent Sifre¹](#),
- [Simon Schmitt¹](#),
- [Arthur Guez¹](#),
- [Edward Lockhart¹](#),
- [Demis Hassabis¹](#),
- [Thore Graepel^{1,2}](#),
- [Timothy Lillicrap¹](#) &
- [David Silver](#) [ORCID: orcid.org/0000-0002-5197-2892^{1,2}](#), [nal](#)

[Nature](#) volume **588**, pages604–609(2020) [Cite this article](#)

- 5806 Accesses
- 778 Altmetric
- [Metrics details](#)

Subjects

- [Computational science](#)

- [Computer science](#)

Abstract

Constructing agents with planning capabilities has long been one of the main challenges in the pursuit of artificial intelligence. Tree-based planning methods have enjoyed huge success in challenging domains, such as chess¹ and Go², where a perfect simulator is available. However, in real-world problems, the dynamics governing the environment are often complex and unknown. Here we present the MuZero algorithm, which, by combining a tree-based search with a learned model, achieves superhuman performance in a range of challenging and visually complex domains, without any knowledge of their underlying dynamics. The MuZero algorithm learns an iterable model that produces predictions relevant to planning: the action-selection policy, the value function and the reward. When evaluated on 57 different Atari games³—the canonical video game environment for testing artificial intelligence techniques, in which model-based planning approaches have historically struggled⁴—the MuZero algorithm achieved state-of-the-art performance. When evaluated on Go, chess and shogi—canonical environments for high-performance planning—the MuZero algorithm matched, without any knowledge of the game dynamics, the superhuman performance of the AlphaZero algorithm⁵ that was supplied with the rules of the game.

[Access through your institution](#)

[Change institution](#)

[Buy or subscribe](#)

Access options

Subscribe to Journal

Get full journal access for 1 year

\$199.00

only \$3.83 per issue

[Subscribe](#)

All prices are NET prices.
VAT will be added later in the checkout.

Rent or Buy article

Get time limited or full article access on ReadCube.
from \$8.99

[Rent or Buy](#)

All prices are NET prices.

Additional access options:

- [Log in](#)
- [Access through your institution](#)
- [Learn about institutional subscriptions](#)

Fig. 1: Planning, acting and training with a learned model.

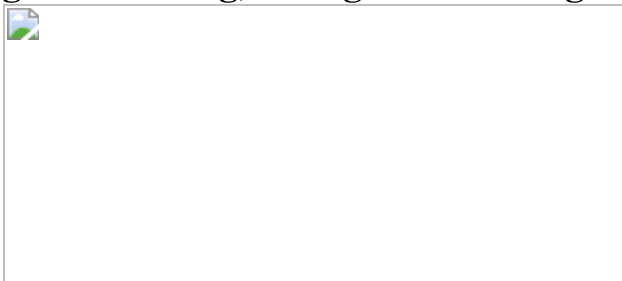
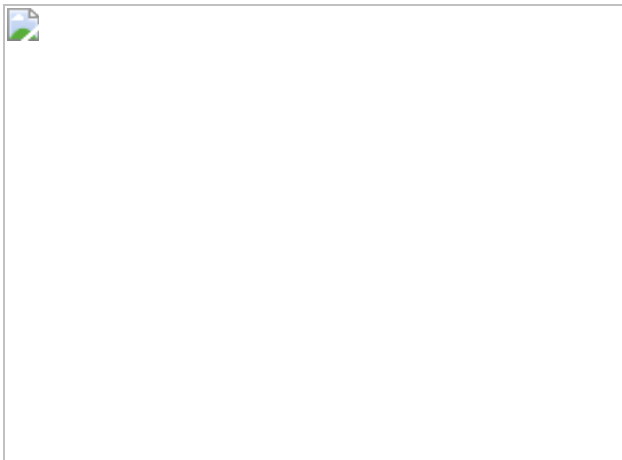


Fig. 2: Evaluation of MuZero throughout training in chess, shogi, Go and Atari.



Fig. 3: Evaluations of MuZero on Go, all 57 Atari games and Ms. Pac-Man.



Data availability

MuZero is trained only on data generated by MuZero itself; no external data were used to produce the results presented in the article. Data for all figures and tables presented are available in JSON format in the [Supplementary Information](#).

Code availability

The Arcade Learning Environment³ is available open source at <https://github.com/mgbellemare/Arcade-Learning-Environment>. The Go and chess environments are available open source in OpenSpiel⁵² at https://github.com/deepmind/open_spiel. The pseudocode for the MuZero algorithm can be found in the file pseudocode.py in the [Supplementary Information](#). All the neural architecture details and hyperparameters are described in Methods.

References

1. 1.

Campbell, M., Hoane, A. J. Jr & Hsu, F.-h. Deep Blue. *Artif. Intell.* **134**, 57–83 (2002).

[Article](#) [Google Scholar](#)

2. 2.

Silver, D. et al. Mastering the game of Go with deep neural networks and tree search. *Nature* **529**, 484–489 (2016).

[ADS](#) [CAS](#) [Article](#) [Google Scholar](#)

3. 3.

Bellemare, M. G., Naddaf, Y., Veness, J. & Bowling, M. The arcade learning environment: an evaluation platform for general agents. *J. Artif. Intell. Res.* **47**, 253–279 (2013).

[Article](#) [Google Scholar](#)

4. 4.

Machado, M. et al. Revisiting the arcade learning environment: evaluation protocols and open problems for general agents. *J. Artif. Intell. Res.* **61**, 523–562 (2018).

[MathSciNet](#) [Article](#) [Google Scholar](#)

5. 5.

Silver, D. et al. A general reinforcement learning algorithm that masters chess, shogi, and Go through self-play. *Science* **362**, 1140–1144 (2018).

[ADS](#) [MathSciNet](#) [CAS](#) [Article](#) [Google Scholar](#)

6. 6.

Schaeffer, J. et al. A world championship caliber checkers program. *Artif. Intell.* **53**, 273–289 (1992).

[Article](#) [Google Scholar](#)

7. 7.

Brown, N. & Sandholm, T. Superhuman AI for heads-up no-limit poker: Libratus beats top professionals. *Science* **359**, 418–424 (2018).

[ADS](#) [MathSciNet](#) [CAS](#) [Article](#) [Google Scholar](#)

8. 8.

Moravčík, M. et al. Deepstack: expert-level artificial intelligence in heads-up no-limit poker. *Science* **356**, 508–513 (2017).

[ADS](#) [MathSciNet](#) [Article](#) [Google Scholar](#)

9. 9.

Vlahavas, I. & Refanidis, I. *Planning and Scheduling* Technical Report (EETN, 2013).

10. 10.

Segler, M. H., Preuss, M. & Waller, M. P. Planning chemical syntheses with deep neural networks and symbolic AI. *Nature* **555**, 604–610 (2018).

[ADS](#) [CAS](#) [Article](#) [Google Scholar](#)

11. 11.

Sutton, R. S. & Barto, A. G. *Reinforcement Learning: An Introduction* 2nd edn (MIT Press, 2018).

12. 12.

Deisenroth, M. & Rasmussen, C. PILCO: a model-based and data-efficient approach to policy search. In *Proc. 28th International Conference on Machine Learning, ICML 2011* 465–472 (Omnipress, 2011).

13. 13.

Heess, N. et al. Learning continuous control policies by stochastic value gradients. In *NIPS'15: Proc. 28th International Conference on Neural Information Processing Systems* Vol. 2 (eds Cortes, C. et al.) 2944–2952 (MIT Press, 2015).

14. 14.

Levine, S. & Abbeel, P. Learning neural network policies with guided policy search under unknown dynamics. *Adv. Neural Inf. Process. Syst.* **27**, 1071–1079 (2014).

[Google Scholar](#)

15. 15.

Hafner, D. et al. Learning latent dynamics for planning from pixels. Preprint at <https://arxiv.org/abs/1811.04551> (2018).

16. 16.

Kaiser, L. et al. Model-based reinforcement learning for atari. Preprint at <https://arxiv.org/abs/1903.00374> (2019).

17. 17.

Buesing, L. et al. Learning and querying fast generative models for reinforcement learning. Preprint at <https://arxiv.org/abs/1802.03006>

(2018).

18. 18.

Espeholt, L. et al. IMPALA: scalable distributed deep-RL with importance weighted actor-learner architectures. In *Proc. International Conference on Machine Learning, ICML* Vol. 80 (eds Dy, J. & Krause, A.) 1407–1416 (2018).

19. 19.

Kapturowski, S., Ostrovski, G., Dabney, W., Quan, J. & Munos, R. Recurrent experience replay in distributed reinforcement learning. In *International Conference on Learning Representations* (2019).

20. 20.

Horgan, D. et al. Distributed prioritized experience replay. In *International Conference on Learning Representations* (2018).

21. 21.

Puterman, M. L. *Markov Decision Processes: Discrete Stochastic Dynamic Programming* 1st edn (John Wiley & Sons, 1994).

22. 22.

Coulom, R. Efficient selectivity and backup operators in Monte-Carlo tree search. In *International Conference on Computers and Games* 72–83 (Springer, 2006).

23. 23.

Wahlström, N., Schön, T. B. & Deisenroth, M. P. From pixels to torques: policy learning with deep dynamical models. Preprint at <http://arxiv.org/abs/1502.02251> (2015).

24. 24.

Watter, M., Springenberg, J. T., Boedecker, J. & Riedmiller, M. Embed to control: a locally linear latent dynamics model for control from raw images. In *NIPS' 15: Proc. 28th International Conference on Neural Information Processing Systems* Vol. 2 (eds Cortes, C. et al.) 2746–2754 (MIT Press, 2015).

25. 25.

Ha, D. & Schmidhuber, J. Recurrent world models facilitate policy evolution. In *NIPS' 18: Proc. 32nd International Conference on Neural Information Processing Systems* (eds Bengio, S. et al.) 2455–2467 (Curran Associates, 2018).

26. 26.

Gelada, C., Kumar, S., Buckman, J., Nachum, O. & Bellemare, M. G. DeepMDP: learning continuous latent space models for representation learning. *Proc. 36th International Conference on Machine Learning: Volume 97 of Proc. Machine Learning Research* (eds Chaudhuri, K. & Salakhutdinov, R.) 2170–2179 (PMLR, 2019).

27. 27.

van Hasselt, H., Hessel, M. & Aslanides, J. When to use parametric models in reinforcement learning? Preprint at <https://arxiv.org/abs/1906.05243> (2019).

28. 28.

Tamar, A., Wu, Y., Thomas, G., Levine, S. & Abbeel, P. Value iteration networks. *Adv. Neural Inf. Process. Syst.* **29**, 2154–2162 (2016).

[Google Scholar](#)

29. 29.

Silver, D. et al. The predictron: end-to-end learning and planning. In *Proc. 34th International Conference on Machine Learning* Vol. 70 (eds Precup, D. & Teh, Y. W.) 3191–3199 (JMLR, 2017).

30. 30.

Farahmand, A. M., Barreto, A. & Nikovski, D. Value-aware loss function for model-based reinforcement learning. In *Proc. 20th International Conference on Artificial Intelligence and Statistics: Volume 54 of Proc. Machine Learning Research* (eds Singh, A. & Zhu, J) 1486–1494 (PMLR, 2017).

31. 31.

Farahmand, A. Iterative value-aware model learning. *Adv. Neural Inf. Process. Syst.* **31**, 9090–9101 (2018).

[Google Scholar](#)

32. 32.

Farquhar, G., Rocktaeschel, T., Igl, M. & Whiteson, S. TreeQN and ATreeC: differentiable tree planning for deep reinforcement learning. In *International Conference on Learning Representations* (2018).

33. 33.

Oh, J., Singh, S. & Lee, H. Value prediction network. *Adv. Neural Inf. Process. Syst.* **30**, 6118–6128 (2017).

[Google Scholar](#)

34. 34.

Krizhevsky, A., Sutskever, I. & Hinton, G. E. Imagenet classification with deep convolutional neural networks. *Adv. Neural Inf. Process. Syst.* **25**, 1097–1105 (2012).

[Google Scholar](#)

35. 35.

He, K., Zhang, X., Ren, S. & Sun, J. Identity mappings in deep residual networks. In *14th European Conference on Computer Vision* 630–645 (2016).

36. 36.

Hessel, M. et al. Rainbow: combining improvements in deep reinforcement learning. In *Thirty-Second AAAI Conference on Artificial Intelligence* (2018).

37. 37.

Schmitt, S., Hessel, M. & Simonyan, K. Off-policy actor-critic with shared experience replay. Preprint at <https://arxiv.org/abs/1909.11583> (2019).

38. 38.

Azizzadenesheli, K. et al. Surprising negative results for generative adversarial tree search. Preprint at <http://arxiv.org/abs/1806.05780> (2018).

39. 39.

Mnih, V. et al. Human-level control through deep reinforcement learning. *Nature* **518**, 529–533 (2015).

[ADS](#) [CAS](#) [Article](#) [Google Scholar](#)

40. 40.

Open, A. I. OpenAI five. *OpenAI* <https://blog.openai.com/openai-five/> (2018).

41. 41.

Vinyals, O. et al. Grandmaster level in StarCraft II using multi-agent reinforcement learning. *Nature* **575**, 350–354 (2019).

[ADS](#) [CAS](#) [Article](#) [Google Scholar](#)

42. 42.

Jaderberg, M. et al. Reinforcement learning with unsupervised auxiliary tasks. Preprint at <https://arxiv.org/abs/1611.05397> (2016).

43. 43.

Silver, D. et al. Mastering the game of Go without human knowledge. *Nature* **550**, 354–359 (2017).

[ADS](#) [CAS](#) [Article](#) [Google Scholar](#)

44. 44.

Kocsis, L. & Szepesvári, C. Bandit based Monte-Carlo planning. In *European Conference on Machine Learning* 282–293 (Springer, 2006).

45. 45.

Rosin, C. D. Multi-armed bandits with episode context. *Ann. Math. Artif. Intell.* **61**, 203–230 (2011).

[MathSciNet](#) [Article](#) [Google Scholar](#)

46. 46.

Schadd, M. P., Winands, M. H., Van Den Herik, H. J., Chaslot, G. M.-B. & Uiterwijk, J. W. Single-player Monte-Carlo tree search. In *International Conference on Computers and Games* 1–12 (Springer, 2008).

47. 47.

Pohlen, T. et al. Observe and look further: achieving consistent performance on Atari. Preprint at <https://arxiv.org/abs/1805.11593> (2018).

48. 48.

Schaul, T., Quan, J., Antonoglou, I. & Silver, D. Prioritized experience replay. In *International Conference on Learning Representations* (2016).

49. 49.

Cloud TPU. *Google Cloud* <https://cloud.google.com/tpu/> (2019).

50. 50.

Coulom, R. Whole-history rating: a Bayesian rating system for players of time-varying strength. In *International Conference on Computers and Games* 113–124 (2008).

51. 51.

Nair, A. et al. Massively parallel methods for deep reinforcement learning. Preprint at <https://arxiv.org/abs/1507.04296> (2015).

52. 52.

Lanctot, M. et al. OpenSpiel: a framework for reinforcement learning in games. Preprint at <http://arxiv.org/abs/1908.09453> (2019).

[Download references](#)

Acknowledgements

We thank L. Bennett, O. Smith and C. Apps for organizational assistance; K. Kavukcuoglu for reviewing the paper; T. Anthony, M. Lai, N. Tomasev, U. Paquet, S. Ghaisas for many discussions; and the rest of the DeepMind team for their support.

Author information

Author notes

1. These authors contributed equally: Julian Schrittwieser, Ioannis Antonoglou, Thomas Hubert, David Silver

Affiliations

1. DeepMind, London, UK

Julian Schrittwieser, Ioannis Antonoglou, Thomas Hubert, Karen Simonyan, Laurent Sifre, Simon Schmitt, Arthur Guez, Edward Lockhart, Demis Hassabis, Thore Graepel, Timothy Lillicrap & David Silver

2. University College London, London, UK

Ioannis Antonoglou, Thore Graepel & David Silver

Authors

1. Julian Schrittwieser

[View author publications](#)

You can also search for this author in [PubMed](#) [Google Scholar](#)

2. Ioannis Antonoglou

[View author publications](#)

You can also search for this author in [PubMed](#) [Google Scholar](#)

3. Thomas Hubert

[View author publications](#)

You can also search for this author in [PubMed](#) [Google Scholar](#)

4. Karen Simonyan

[View author publications](#)

You can also search for this author in [PubMed](#) [Google Scholar](#)

5. Laurent Sifre

[View author publications](#)

You can also search for this author in [PubMed](#) [Google Scholar](#)

6. Simon Schmitt

[View author publications](#)

You can also search for this author in [PubMed](#) [Google Scholar](#)

7. Arthur Guez

[View author publications](#)

You can also search for this author in [PubMed](#) [Google Scholar](#)

8. Edward Lockhart

[View author publications](#)

You can also search for this author in [PubMed](#) [Google Scholar](#)

9. Demis Hassabis

[View author publications](#)

You can also search for this author in [PubMed](#) [Google Scholar](#)

10. Thore Graepel

[View author publications](#)

You can also search for this author in [PubMed](#) [Google Scholar](#)

11. Timothy Lillicrap

[View author publications](#)

You can also search for this author in [PubMed](#) [Google Scholar](#)

12. David Silver

[View author publications](#)

You can also search for this author in [PubMed](#) [Google Scholar](#)

Contributions

J.S., I.A., T.H. and D.S. designed the MuZero algorithm with advice from A.G., K.S., L.S., E.L., T.L. and T.G.; J.S., I.A., T.H. and S.S. implemented the MuZero program, ran experiments and analysed data. D.S., J.S., I.A. and T.H. wrote the paper with contributions from A.G., K.S., L.S., E.L., T.L., T.G. and D.H.

Corresponding author

Correspondence to [David Silver](#).

Ethics declarations

Competing interests

DeepMind filed Greek patent GR20200100037 on 28 January 2020, covering the MuZero algorithm described in this paper, listing the authors J.S., I.A. and T.H. as inventors. The other authors declare no competing interests.

Additional information

Peer review information *Nature* thanks Jaap van den Herik and the other, anonymous, reviewer(s) for their contribution to the peer review of this work.

Publisher's note Springer Nature remains neutral with regard to jurisdictional claims in published maps and institutional affiliations.

Supplementary information

[Supplementary Information](#)

This file contains Supplementary Figures S1-S5 and Supplementary Tables S1-S2.

Supplementary Data

The ZIP file contains Supplementary Data.

Rights and permissions

Reprints and Permissions

About this article



Check for
updates

Cite this article

Schrittwieser, J., Antonoglou, I., Hubert, T. *et al.* Mastering Atari, Go, chess and shogi by planning with a learned model. *Nature* **588**, 604–609 (2020). <https://doi.org/10.1038/s41586-020-03051-4>

Download citation

- Received: 03 April 2020
- Accepted: 07 October 2020
- Published: 23 December 2020
- Issue Date: 24 December 2020
- DOI: <https://doi.org/10.1038/s41586-020-03051-4>

Comments

By submitting a comment you agree to abide by our [Terms](#) and [Community Guidelines](#). If you find something abusive or that does not comply with our terms or guidelines please flag it as inappropriate.

[Access through your institution](#)

[Change institution](#)

[Buy or subscribe](#)

This article was downloaded by **calibre** from <https://www.nature.com/articles/s41586-020-03051-4>

| [Section menu](#) | [Main menu](#) |

- Article
- [Published: 14 December 2020](#)

Strongly correlated Chern insulators in magic-angle twisted bilayer graphene

- [Kevin P. Nuckolls](#) ORCID: [orcid.org/0000-0002-1078-7113¹](https://orcid.org/0000-0002-1078-7113) na1,
- [Myungchul Oh](#) ORCID: [orcid.org/0000-0003-0477-1390¹](https://orcid.org/0000-0003-0477-1390) na1,
- [Dillon Wong](#) ¹ na1,
- [Biao Lian](#) ORCID: [orcid.org/0000-0002-8956-5619²](https://orcid.org/0000-0002-8956-5619),
- [Kenji Watanabe](#) ORCID: [orcid.org/0000-0003-3701-8119³](https://orcid.org/0000-0003-3701-8119),
- [Takashi Taniguchi](#) ORCID: [orcid.org/0000-0002-1467-3105⁴](https://orcid.org/0000-0002-1467-3105),
- [B. Andrei Bernevig](#) ORCID: [orcid.org/0000-0001-6337-4024¹](https://orcid.org/0000-0001-6337-4024) &
- [Ali Yazdani](#) ORCID: [orcid.org/0000-0003-4996-8904¹](https://orcid.org/0000-0003-4996-8904)

[Nature](#) volume **588**, pages 610–615(2020) [Cite this article](#)

- 4082 Accesses
- 127 Altmetric
- [Metrics details](#)

Subjects

- [Electronic properties and materials](#)
- [Ferromagnetism](#)
- [Topological insulators](#)

Abstract

Interactions between electrons and the topology of their energy bands can create unusual quantum phases of matter. Most topological electronic phases appear in systems with weak electron–electron interactions. The instances in which topological phases emerge only as a result of strong interactions are rare and mostly limited to those realized in intense magnetic fields¹. The discovery of flat electronic bands with topological character in magic-angle twisted bilayer graphene (MATBG) has created a unique opportunity to search for strongly correlated topological phases^{2,3,4,5,6,7,8,9}. Here we introduce a local spectroscopic technique using a scanning tunnelling microscope to detect a sequence of topological insulators in MATBG with Chern numbers $C = \pm 1, \pm 2$ and ± 3 , which form near filling factors of $\pm 3, \pm 2$ and ± 1 electrons per moiré unit cell, respectively, and are stabilized by modest magnetic fields. One of the phases detected here ($C = +1$) was previously observed when the sublattice symmetry of MATBG was intentionally broken by a hexagonal boron nitride substrate, with interactions having a secondary role⁹. We demonstrate that strong electron–electron interactions alone can produce not only the previously observed phase, but also other unexpected Chern insulating phases in MATBG. The full sequence of phases that we observe can be understood by postulating that strong correlations favour breaking time-reversal symmetry to form Chern insulators that are stabilized by weak magnetic fields. Our findings illustrate that many-body correlations can create topological phases in moiré systems beyond those anticipated from weakly interacting models.

[Access through your institution](#)

[Change institution](#)

[Buy or subscribe](#)

Access options

Subscribe to Journal

Get full journal access for 1 year

\$199.00

only \$3.83 per issue

Subscribe

All prices are NET prices.
VAT will be added later in the checkout.

Rent or Buy article

Get time limited or full article access on ReadCube.

from \$8.99

Rent or Buy

All prices are NET prices.

Additional access options:

- [Log in](#)
- [Access through your institution](#)
- [Learn about institutional subscriptions](#)

Fig. 1: Magnetic-field-dependent spectroscopic gaps in MATBG at 200 mK.

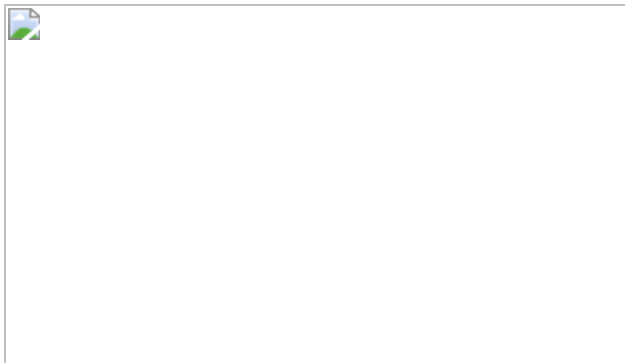


Fig. 2: Spectroscopic gap morphology of strongly correlated Chern insulating gaps and ZLLs.

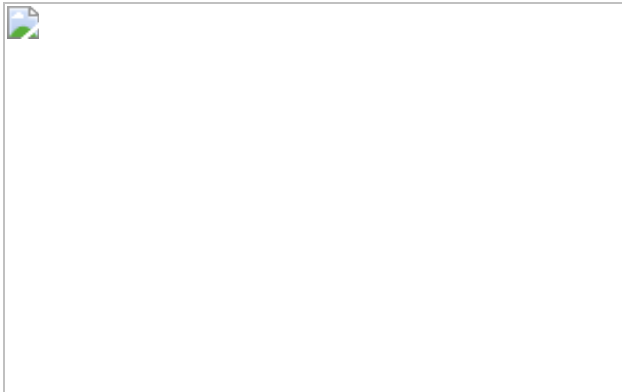


Fig. 3: Quantized magnetic-field response of strongly correlated Chern insulating phases.

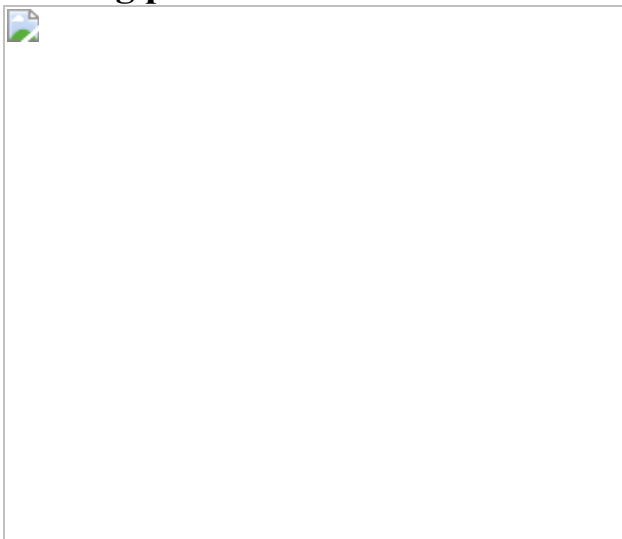
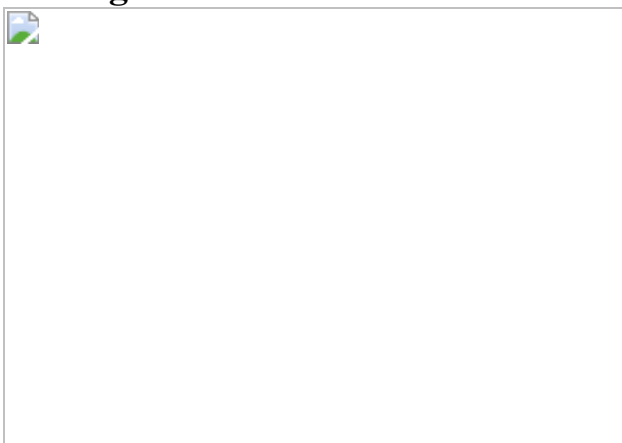


Fig. 4: Theoretical interpretation using an interaction-induced, sign-switching Haldane mass.



Data availability

The data that support the findings of this study are available from the corresponding author upon reasonable request.

References

1. 1.

Rachel, S. Interacting topological insulators: a review. *Rep. Prog. Phys.* **81**, 116501 (2018).

[ADS](#) [Article](#) [Google Scholar](#)

2. 2.

Bistritzer, R. & MacDonald, A. H. Moire bands in twisted double-layer graphene. *Proc. Natl Acad. Sci. USA* **108**, 12233–12237 (2011).

[ADS](#) [CAS](#) [Article](#) [Google Scholar](#)

3. 3.

Suárez Morell, E., Correa, J. D., Vargas, P., Pacheco, M. & Barticevic, Z. Flat bands in slightly twisted bilayer graphene: tight-binding calculations. *Phys. Rev. B* **82**, 121407 (2010).

[ADS](#) [Article](#) [Google Scholar](#)

4. 4.

Cao, Y. et al. Correlated insulator behaviour at half-filling in magic-angle graphene superlattices. *Nature* **556**, 80–84 (2018).

[ADS](#) [CAS](#) [Article](#) [Google Scholar](#)

5. 5.

Cao, Y. et al. Unconventional superconductivity in magic-angle graphene superlattices. *Nature* **556**, 43–50 (2018).

[ADS](#) [CAS](#) [Article](#) [Google Scholar](#)

6. 6.

Yankowitz, M. et al. Tuning superconductivity in twisted bilayer graphene. *Science* **363**, 1059–1064 (2019).

[ADS](#) [CAS](#) [Article](#) [Google Scholar](#)

7. 7.

Lu, X. et al. Superconductors, orbital magnets and correlated states in magic-angle bilayer graphene. *Nature* **574**, 653–657 (2019).

[ADS](#) [CAS](#) [Article](#) [Google Scholar](#)

8. 8.

Sharpe, A. L. et al. Emergent ferromagnetism near three-quarters filling in twisted bilayer graphene. *Science* **365**, 605–608 (2019).

[ADS](#) [CAS](#) [Article](#) [Google Scholar](#)

9. 9.

Serlin, M. et al. Intrinsic quantized anomalous Hall effect in a moiré heterostructure. *Science* **367**, 900–903 (2020).

[ADS](#) [CAS](#) [Article](#) [Google Scholar](#)

10. 10.

Chen, G. et al. Tunable correlated Chern insulator and ferromagnetism in a moiré superlattice. *Nature* **579**, 56–61 (2020); correction **581**, E3 (2020).

[ADS](#) [CAS](#) [Article](#) [Google Scholar](#)

11. 11.

Polshyn, H. et al. Electrical switching of magnetic order in an orbital Chern insulator. *Nature* **588**, 66–70 (2020).

12. 12.

Chen, S. et al. Electrically tunable correlated and topological states in twisted monolayer-bilayer graphene. *Nat. Phys.*
<https://doi.org/10.1038/s41567-020-01062-6> (2020).

13. 13.

Liu, J. & Dai, X. Theories for the correlated insulating states and quantum anomalous Hall phenomena in twisted bilayer graphene. Preprint at <https://arxiv.org/abs/1911.03760> (2019).

14. 14.

Stepanov, P. et al. Untying the insulating and superconducting orders in magic-angle graphene. *Nature* **583**, 375–378 (2020).

[ADS](#) [CAS](#) [Article](#) [Google Scholar](#)

15. 15.

Haldane, F. D. M. Model for a quantum Hall effect without Landau levels: condensed-matter realization of the “parity anomaly”. *Phys. Rev. Lett.* **61**, 2015–2018 (1988).

[ADS](#) [CAS](#) [Article](#) [Google Scholar](#)

16. 16.

Wong, D. et al. A modular ultra-high vacuum millikelvin scanning tunneling microscope. *Rev. Sci. Instrum.* **91**, 023703 (2020).

[ADS](#) [CAS](#) [Article](#) [Google Scholar](#)

17. 17.

Li, G. et al. Observation of Van Hove singularities in twisted graphene layers. *Nat. Phys.* **6**, 109–113 (2010).

[Article](#) [Google Scholar](#)

18. 18.

Brihuega, I. et al. Unraveling the intrinsic and robust nature of Van Hove singularities in twisted bilayer graphene by scanning tunneling microscopy and theoretical analysis. *Phys. Rev. Lett.* **109**, 196802 (2012).

[ADS](#) [CAS](#) [Article](#) [Google Scholar](#)

19. 19.

Wong, D. et al. Local spectroscopy of moiré-induced electronic structure in gate-tunable twisted bilayer graphene. *Phys. Rev. B* **92**, 155409 (2015).

[ADS](#) [Article](#) [Google Scholar](#)

20. 20.

Xie, Y. et al. Spectroscopic signatures of many-body correlations in magic-angle twisted bilayer graphene. *Nature* **572**, 101–105 (2019).

[ADS](#) [CAS](#) [Article](#) [Google Scholar](#)

21. 21.

Wong, D. et al. Cascade of electronic transitions in magic-angle twisted bilayer graphene. *Nature* **582**, 198–202 (2020).

[ADS](#) [CAS](#) [Article](#) [Google Scholar](#)

22. 22.

Zondiner, U. et al. Cascade of phase transitions and Dirac revivals in magic-angle graphene. *Nature* **582**, 203–208 (2020).

[ADS](#) [CAS](#) [Article](#) [Google Scholar](#)

23. 23.

Choi, Y. et al. Electronic correlations in twisted bilayer graphene near the magic angle. *Nat. Phys.* **15**, 1174–1180 (2019); correction **15**, 1205 (2019).

[CAS](#) [Article](#) [Google Scholar](#)

24. 24.

Kerelsky, A. et al. Maximized electron interactions at the magic angle in twisted bilayer graphene. *Nature* **572**, 95–100 (2019).

[ADS](#) [CAS](#) [Article](#) [Google Scholar](#)

25. 25.

Jiang, Y. et al. Charge order and broken rotational symmetry in magic-angle twisted bilayer graphene. *Nature* **573**, 91–95 (2019).

[ADS](#) [CAS](#) [Article](#) [Google Scholar](#)

26. 26.

Lian, B., Xie, F. & Bernevig, B. A. Landau level of fragile topology. *Phys. Rev. B* **102**, 041402 (2020).

[ADS](#) [CAS](#) [Article](#) [Google Scholar](#)

27. 27.

Bi, Z., Yuan, N. F. Q. & Fu, L. Designing flat bands by strain. *Phys. Rev. B* **100**, 035448 (2019).

[ADS](#) [CAS](#) [Article](#) [Google Scholar](#)

28. 28.

Moon, P., Son, Y. W. & Koshino, M. Optical absorption of twisted bilayer graphene with interlayer potential asymmetry. *Phys. Rev. B* **90**, 155427 (2014).

[ADS](#) [Article](#) [Google Scholar](#)

29. 29.

Bultinck, N., Chatterjee, S. & Zaletel, M. P. Mechanism for anomalous Hall ferromagnetism in twisted bilayer graphene. *Phys. Rev. Lett.* **124**, 166601 (2020).

[ADS](#) [MathSciNet](#) [CAS](#) [Article](#) [Google Scholar](#)

30. 30.

Nomura, K. & MacDonald, A. H. Quantum Hall ferromagnetism in graphene. *Phys. Rev. Lett.* **96**, 256602 (2006).

[ADS](#) [Article](#) [Google Scholar](#)

31. 31.

Young, A. F. et al. Spin and valley quantum Hall ferromagnetism in graphene. *Nat. Phys.* **8**, 550–556 (2012).

[CAS](#) [Article](#) [Google Scholar](#)

32. 32.

Song, Y. J. et al. High-resolution tunnelling spectroscopy of a graphene quartet. *Nature* **467**, 185–189 (2010).

[ADS](#) [CAS](#) [Article](#) [Google Scholar](#)

33. 33.

Feldman, B. E. et al. Observation of a nematic quantum Hall liquid on the surface of bismuth. *Science* **354**, 316–321 (2016).

[ADS](#) [CAS](#) [Article](#) [Google Scholar](#)

34. 34.

Randeria, M. T. et al. Interacting multi-channel topological boundary modes in a quantum Hall valley system. *Nature* **566**, 363–367 (2019).

[ADS](#) [Article](#) [Google Scholar](#)

35. 35.

Středa, P. Theory of quantised Hall conductivity in two dimensions. *J. Phys. C* **15**, L717 (1982).

[ADS](#) [Article](#) [Google Scholar](#)

36. 36.

Spanton, E. M. et al. Observation of fractional Chern insulators in a van der Waals heterostructure. *Science* **360**, 62–66 (2018).

[ADS](#) [CAS](#) [Article](#) [Google Scholar](#)

37. 37.

Tomarken, S. L. et al. Electronic compressibility of magic-angle graphene superlattices. *Phys. Rev. Lett.* **123**, 046601 (2019).

[ADS](#) [CAS](#) [Article](#) [Google Scholar](#)

38. 38.

Abouelkomsan, A., Liu, Z. & Bergholtz, E. J. Particle-hole duality, emergent Fermi liquids, and fractional Chern insulators in moiré

flatbands. *Phys. Rev. Lett.* **124**, 106803 (2020).

[ADS](#) [MathSciNet](#) [CAS](#) [Article](#) [Google Scholar](#)

39. 39.

Ledwith, P. J., Tarnopolsky, G., Khalaf, E. & Vishwanath, A. Fractional Chern insulator states in twisted bilayer graphene: an analytical approach. *Phys. Rev. Res.* **2**, 023237 (2020).

[CAS](#) [Article](#) [Google Scholar](#)

40. 40.

Repelin, C. & Senthil, T. Chern bands of twisted bilayer graphene: fractional Chern insulators and spin phase transition. *Phys. Rev. Res.* **2**, 023238 (2019).

[Article](#) [Google Scholar](#)

41. 41.

Deng, Y. et al. Quantum anomalous Hall effect in intrinsic magnetic topological insulator MnBi_2Te_4 . *Science* **367**, 895–900 (2020).

[ADS](#) [CAS](#) [Article](#) [Google Scholar](#)

42. 42.

Liu, C. et al. Helical Chern insulator phase with broken time-reversal symmetry in MnBi_2Te_4 . Preprint at <https://arxiv.org/abs/2001.08401> (2020).

43. 43.

Zhang, Y. H., Mao, D., Cao, Y., Jarillo-Herrero, P. & Senthil, T. Nearly flat Chern bands in moiré superlattices. *Phys. Rev. B* **99**, 075127 (2019).

[ADS](#) [CAS](#) [Article](#) [Google Scholar](#)

[Download references](#)

Acknowledgements

We thank S. Wu, B. Jaeck, X. Liu, K. Hejazi, N. Yuan and L. Fu for discussions. This work was primarily supported by the Gordon and Betty Moore Foundation's EPiQS initiative grants GBMF4530, GBMF9469 and DOE-BES grant DE-FG02-07ER46419 to A.Y. Other support for the experimental work was provided by NSF-MRSEC through the Princeton Center for Complex Materials NSF-DMR-1420541, NSF-DMR-1904442, ExxonMobil through the Andlinger Center for Energy and the Environment at Princeton, and the Princeton Catalysis Initiative. K.W. and T.T. acknowledge support from the Elemental Strategy Initiative conducted by MEXT, Japan, grant JPMXP0112101001, JSPS KAKENHI grant JP20H00354, and CREST (JPMJCR15F3), JST. B.L. acknowledges support from the Princeton Center for Theoretical Science at Princeton University. B.A.B. acknowledges support from the Department of Energy DE-SC0016239, Simons Investigator Award, the Packard Foundation, the Schmidt Fund for Innovative Research, NSF EAGER grant DMR-1643312, NSF-MRSEC DMR1420541, BSF Israel US foundation number 2018226, ONR number N00014-20-1-2303, and the Princeton Global Network Funds.

Author information

Author notes

1. These authors contributed equally: Kevin P. Nuckolls, Myungchul Oh, Dillon Wong

Affiliations

1. Joseph Henry Laboratories and Department of Physics, Princeton University, Princeton, NJ, USA

Kevin P. Nuckolls, Myungchul Oh, Dillon Wong, B. Andrei Bernevig & Ali Yazdani

2. Princeton Center for Theoretical Science, Princeton University, Princeton, NJ, USA

Biao Lian

3. Research Center for Functional Materials, National Institute for Materials Science, Tsukuba, Japan

Kenji Watanabe

4. International Center for Materials Nanoarchitectonics, National Institute for Materials Science, Tsukuba, Japan

Takashi Taniguchi

Authors

1. Kevin P. Nuckolls

[View author publications](#)

You can also search for this author in [PubMed](#) [Google Scholar](#)

2. Myungchul Oh

[View author publications](#)

You can also search for this author in [PubMed](#) [Google Scholar](#)

3. Dillon Wong

[View author publications](#)

You can also search for this author in [PubMed](#) [Google Scholar](#)

4. Biao Lian

[View author publications](#)

You can also search for this author in [PubMed](#) [Google Scholar](#)

5. Kenji Watanabe

[View author publications](#)

You can also search for this author in [PubMed](#) [Google Scholar](#)

6. Takashi Taniguchi

[View author publications](#)

You can also search for this author in [PubMed](#) [Google Scholar](#)

7. B. Andrei Bernevig

[View author publications](#)

You can also search for this author in [PubMed](#) [Google Scholar](#)

8. Ali Yazdani

[View author publications](#)

You can also search for this author in [PubMed](#) [Google Scholar](#)

Contributions

K.P.N., M.O., D.W. and A.Y. designed the experiment. K.P.N., D.W. and M.O. fabricated samples, carried out STM/STS measurements and performed the data analysis. B.L. and B.A.B. performed the theoretical calculations. K.W. and T.T. synthesized the hBN crystals. All authors discussed the results and contributed to the writing of the manuscript.

Corresponding author

Correspondence to [Ali Yazdani](#).

Ethics declarations

Competing interests

The authors declare no competing interests.

Additional information

Peer review information *Nature* thanks Vincent Renard, Yayu Wang and the other, anonymous, reviewer(s) for their contribution to the peer review of this work.

Publisher's note Springer Nature remains neutral with regard to jurisdictional claims in published maps and institutional affiliations.

Supplementary information

Supplementary Information

This file contains Supplementary Text, Supplementary References and Supplementary Figures 1–14.

Rights and permissions

Reprints and Permissions

About this article



Check for
updates

Cite this article

Nuckolls, K.P., Oh, M., Wong, D. *et al.* Strongly correlated Chern insulators in magic-angle twisted bilayer graphene. *Nature* **588**, 610–615 (2020).
<https://doi.org/10.1038/s41586-020-3028-8>

Download citation

- Received: 03 July 2020

- Accepted: 19 October 2020
- Published: 14 December 2020
- Issue Date: 24 December 2020
- DOI: <https://doi.org/10.1038/s41586-020-3028-8>

Comments

By submitting a comment you agree to abide by our [Terms](#) and [Community Guidelines](#). If you find something abusive or that does not comply with our terms or guidelines please flag it as inappropriate.

[Access through your institution](#)

[Change institution](#)

[Buy or subscribe](#)

This article was downloaded by **calibre** from <https://www.nature.com/articles/s41586-020-3028-8>

| [Section menu](#) | [Main menu](#) |

- Article
- [Published: 23 December 2020](#)

Plasmonic topological quasiparticle on the nanometre and femtosecond scales

- [Yanan Dai](#) [ORCID: orcid.org/0000-0002-0192-1480](#)^{1,2},
- [Zhikang Zhou](#)^{1,2},
- [Atreyie Ghosh](#)^{1,2},
- [Roger S. K. Mong](#)^{1,2},
- [Atsushi Kubo](#)³,
- [Chen-Bin Huang](#) [ORCID: orcid.org/0000-0002-5824-3318](#)⁴ &
- [Hrvoje Petek](#) [ORCID: orcid.org/0000-0001-9605-2590](#)^{1,2}

[Nature](#) volume **588**, pages616–619(2020)[Cite this article](#)

- 1030 Accesses
- 82 Altmetric
- [Metrics details](#)

Subjects

- [Nanometrology](#)
- [Nanophotonics and plasmonics](#)
- [Ultrafast photonics](#)

Abstract

At the interface of classical and quantum physics, the Maxwell and Schrödinger equations describe how optical fields drive and control electronic phenomena to enable lightwave electronics at terahertz or petahertz frequencies and on ultrasmall scales^{1,2,3,4,5}. The electric field of light striking a metal interacts with electrons and generates light–matter quasiparticles, such as excitons⁶ or plasmons⁷, on an attosecond timescale. Here we create and image a quasiparticle of topological plasmonic spin texture in a structured silver film. The spin angular momentum components of linearly polarized light interacting with an Archimedean coupling structure with a designed geometric phase generate plasmonic waves with different orbital angular momenta. These plasmonic fields undergo spin–orbit interaction and their superposition generates an array of plasmonic vortices. Three of these vortices can form spin textures that carry non-trivial topological charge⁸ resembling magnetic meron quasiparticles⁹. These spin textures are localized within a half-wavelength of light, and exist on the timescale of the plasmonic field. We use ultrafast nonlinear coherent photoelectron microscopy to generate attosecond videos of the spatial evolution of the vortex fields; electromagnetic simulations and analytic theory confirm the presence of plasmonic meron quasiparticles. The quasiparticles form a chiral field, which breaks the time-reversal symmetry on a nanometre spatial scale and a 20-femtosecond timescale (the ‘nano-femto scale’). This transient creation of non-trivial spin angular momentum topology pertains to cosmological structure creation and topological phase transitions in quantum matter^{10,11,12}, and may transduce quantum information on the nano-femto scale^{13,14}.

[Access through your institution](#)

[Change institution](#)

[Buy or subscribe](#)

Access options

Subscribe to Journal

Get full journal access for 1 year

\$199.00

only \$3.83 per issue

[Subscribe](#)

All prices are NET prices.
VAT will be added later in the checkout.

Rent or Buy article

Get time limited or full article access on ReadCube.
from \$8.99

[Rent or Buy](#)

All prices are NET prices.

Additional access options:

- [Log in](#)
- [Access through your institution](#)
- [Learn about institutional subscriptions](#)

Fig. 1: The plasmonic meron SAM texture.

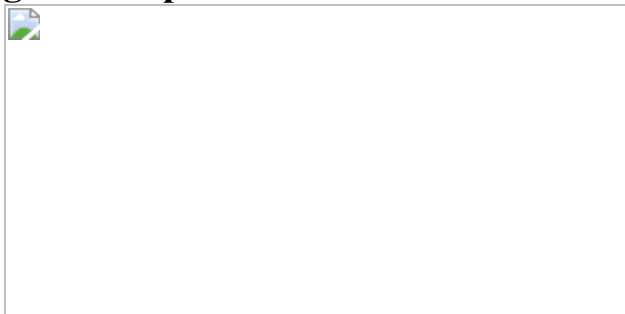


Fig. 2: Ultrafast microscopy of the SPP vortex.

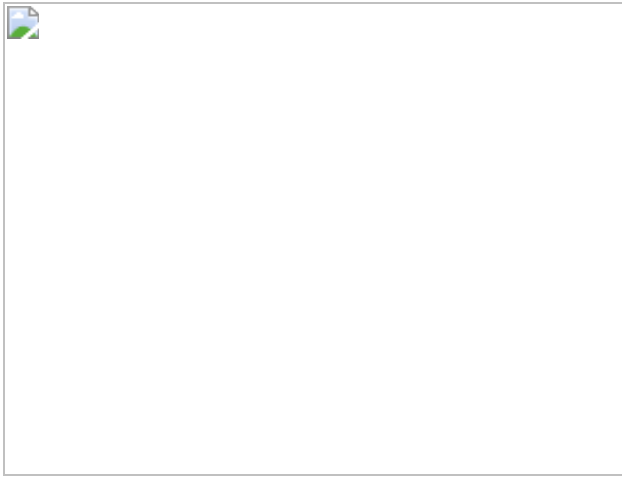


Fig. 3: The origin of the topological SAM texture.

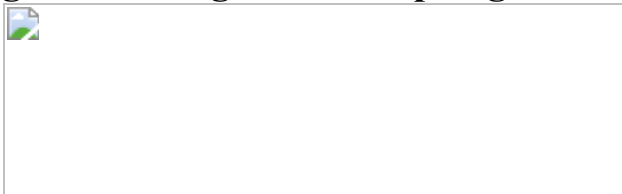


Fig. 4: The topological charge.



Data availability

The data that support the reported findings of this study are available from the corresponding authors on reasonable request.

References

1. 1.

Corkum, P. B. & Krausz, F. Attosecond science. *Nat. Phys.* **3**, 381–387 (2007).

[CAS](#) [Google Scholar](#)

2. 2.

Langer, F. et al. Lightwave-driven quasiparticle collisions on a subcycle timescale. *Nature* **533**, 225–229 (2016).

[ADS](#) [CAS](#) [PubMed](#) [PubMed Central](#) [Google Scholar](#)

3. 3.

Higuchi, T., Heide, C., Ullmann, K., Weber, H. B. & Hommelhoff, P. Light-field-driven currents in graphene. *Nature* **550**, 224–228 (2017).

[ADS](#) [Google Scholar](#)

4. 4.

Ciappina, M. F. et al. Attosecond physics at the nanoscale. *Rep. Prog. Phys.* **80**, 054401 (2017).

[ADS](#) [CAS](#) [Google Scholar](#)

5. 5.

Reimann, J. et al. Subcycle observation of lightwave-driven Dirac currents in a topological surface band. *Nature* **562**, 396–400 (2018).

[ADS](#) [CAS](#) [Google Scholar](#)

6. 6.

Silkin, V. M., Lazić, P., Došlić, N., Petek, H. & Gumhalter, B. Ultrafast electronic response of Ag(111) and Cu(111) surfaces: from early excitonic transients to saturated image potential. *Phys. Rev. B* **92**, 155405 (2015).

[ADS](#) [Google Scholar](#)

7. 7.

Pitarke, J. M., Silkin, V. M., Chulkov, E. V. & Echenique, P. M. Theory of surface plasmons and surface-plasmon polaritons. *Rep. Prog. Phys.* **70**, 1–87 (2007).

[ADS](#) [CAS](#) [Google Scholar](#)

8. 8.

Anderson, P. W. When the electron falls apart. *Phys. Today* **50**, 42–47 (1997).

[CAS](#) [Google Scholar](#)

9. 9.

Nagaosa, N. & Tokura, Y. Topological properties and dynamics of magnetic skyrmions. *Nat. Nanotechnol.* **8**, 899–911 (2013).

[ADS](#) [CAS](#) [Google Scholar](#)

10. 10.

Haldane, F. & Duncan, M. Nobel lecture: topological quantum matter. *Rev. Mod. Phys.* **89**, 040502 (2017).

[ADS](#) [MathSciNet](#) [Google Scholar](#)

11. 11.

Zurek, W. H. Cosmological experiments in condensed matter systems. *Phys. Rep.* **276**, 177–221 (1996).

[ADS](#) [CAS](#) [Google Scholar](#)

12. 12.

Kibble, T. W. Some implications of a cosmological phase transition. *Phys. Rep.* **67**, 183–199 (1980).

[ADS](#) [MathSciNet](#) [CAS](#) [Google Scholar](#)

13. 13.

Rubinsztein-Dunlop, H. et al. Roadmap on structured light. *J. Opt.* **19**, 013001 (2017).

[ADS](#) [Google Scholar](#)

14. 14.

Bliokh, K. Y., Rodríguez-Fortuño, F. J., Nori, F. & Zayats, A. V. Spin-orbit interactions of light. *Nat. Photon.* **9**, 796–808 (2015); erratum **11**, 137 (2017).

[ADS](#) [CAS](#) [Google Scholar](#)

15. 15.

Hopfield, J. J. Theory of the contribution of excitons to the complex dielectric constant of crystals. *Phys. Rev.* **112**, 1555–1567 (1958).

[ADS](#) [CAS](#) [MATH](#) [Google Scholar](#)

16. 16.

Echenique, P. M., Pitarke, J. M., Chulkov, E. V. & Rubio, A. Theory of inelastic lifetimes of low-energy electrons in metals. *Chem. Phys.* **251**, 1–35 (2000).

[CAS](#) [Google Scholar](#)

17. 17.

Skyrme, T. H. R. A unified field theory of mesons and baryons. *Nucl. Phys.* **31**, 556–569 (1962).

[MathSciNet](#) [CAS](#) [Google Scholar](#)

18. 18.

Yu, X. Z. et al. Real-space observation of a two-dimensional skyrmion crystal. *Nature* **465**, 901–904 (2010).

[ADS](#) [CAS](#) [Google Scholar](#)

19. 19.

Lin, S.-Z. et al. Topological defects as relics of emergent continuous symmetry and Higgs condensation of disorder in ferroelectrics. *Nat. Phys.* **10**, 970–977 (2014).

[CAS](#) [Google Scholar](#)

20. 20.

Davis, T. J. et al. Ultrafast vector imaging of plasmonic skyrmion dynamics with deep subwavelength resolution. *Science* **368**, eaba6415 (2020).

[CAS](#) [Google Scholar](#)

21. 21.

Du, L., Yang, A., Zayats, A. V. & Yuan, X. Deep-subwavelength features of photonic skyrmions in a confined electromagnetic field with orbital angular momentum. *Nat. Phys.* **15**, 650–654 (2019).

[CAS](#) [Google Scholar](#)

22. 22.

Tsesses, S. et al. Optical skyrmion lattice in evanescent electromagnetic fields. *Science* **361**, 993–996 (2018).

[ADS](#) [MathSciNet](#) [CAS](#) [MATH](#) [Google Scholar](#)

23. 23.

Bliokh, K. Y. & Nori, F. Transverse and longitudinal angular momenta of light. *Phys. Rep.* **592**, 1–38 (2015).

[ADS](#) [MathSciNet](#) [MATH](#) [Google Scholar](#)

24. 24.

Bliokh, K. Y., Smirnova, D. & Nori, F. Quantum spin Hall effect of light. *Science* **348**, 1448–1451 (2015).

[ADS](#) [MathSciNet](#) [CAS](#) [MATH](#) [Google Scholar](#)

25. 25.

Van Mechelen, T. & Jacob, Z. Universal spin-momentum locking of evanescent waves. *Optica* **3**, 118–126 (2016).

[ADS](#) [Google Scholar](#)

26. 26.

Kim, H. et al. Synthesis and dynamic switching of surface plasmon vortices with plasmonic vortex lens. *Nano Lett.* **10**, 529–536 (2010).

[ADS](#) [CAS](#) [Google Scholar](#)

27. 27.

Ohno, T. & Miyanishi, S. Study of surface plasmon chirality induced by Archimedes' spiral grooves. *Opt. Express* **14**, 6285–6290 (2006).

[ADS](#) [Google Scholar](#)

28. 28.

Spektor, G. et al. Revealing the subfemtosecond dynamics of orbital angular momentum in nanoplasmonic vortices. *Science* **355**, 1187–

1191 (2017).

[ADS](#) [CAS](#) [Google Scholar](#)

29. 29.

Barnett, S. M. et al. On the natures of the spin and orbital parts of optical angular momentum. *J. Opt.* **18**, 064004 (2016).

[ADS](#) [Google Scholar](#)

30. 30.

Kubo, A., Pontius, N. & Petek, H. Femtosecond microscopy of surface plasmon polariton wave packet evolution at the silver/vacuum interface. *Nano Lett.* **7**, 470–475 (2007).

[ADS](#) [CAS](#) [Google Scholar](#)

31. 31.

Fösel, T., Peano, V. & Marquardt, F. L lines, C points and Chern numbers: understanding band structure topology using polarization fields. *New J. Phys.* **19**, 115013 (2017).

[ADS](#) [MathSciNet](#) [Google Scholar](#)

32. 32.

Horn, B. K. P. & Schunck, B. G. Determining optical flow. *Artif. Intell.* **17**, 185–203 (1981).

[Google Scholar](#)

33. 33.

Dai, Y. et al. Ultrafast microscopy of a plasmonic spin skyrmion. Preprint at <http://arXiv.org/abs/1912.03826> (2019).

34. 34.

Van Mechelen, T. & Jacob, Z. Photonic Dirac monopoles and skyrmions: spin-1 quantization. *Opt. Mater. Express* **9**, 95–111 (2019).

[ADS](#) [Google Scholar](#)

35. 35.

Kimel, A. V. et al. Ultrafast non-thermal control of magnetization by instantaneous photomagnetic pulses. *Nature* **435**, 655–657 (2005).

[ADS](#) [CAS](#) [Google Scholar](#)

36. 36.

Xiao, D., Liu, G.-B., Feng, W., Xu, X. & Yao, W. Coupled spin and valley physics in monolayers of MoS₂ and other group-VI dichalcogenides. *Phys. Rev. Lett.* **108**, 196802 (2012).

[ADS](#) [Google Scholar](#)

37. 37.

Bauer, E. *Surface Microscopy with Low Energy Electrons* (Springer, 2014).

38. 38.

Dąbrowski, M., Dai, Y. & Petek, H. Ultrafast microscopy: imaging light with photoelectrons on the nano–femto scale. *J. Phys. Chem. Lett.* **8**, 4446–4455 (2017).

[Google Scholar](#)

39. 39.

Dąbrowski, M., Dai, Y. & Petek, H. Ultrafast photoemission electron microscopy: imaging plasmons in space and time. *Chem. Rev.* **120**,

6247–6287 (2020).

[Google Scholar](#)

40. 40.

Podbiel, D. et al. Imaging the nonlinear plasmoemission dynamics of electrons from strong plasmonic fields. *Nano Lett.* **17**, 6569–6574 (2017).

[ADS](#) [CAS](#) [Google Scholar](#)

41. 41.

Kahl, P. et al. Normal-incidence photoemission electron microscopy (NI-PEEM) for imaging surface plasmon polaritons. *Plasmonics* **9**, 1401–1407 (2014).

[CAS](#) [Google Scholar](#)

42. 42.

Cardano, F., Karimi, E., Marrucci, L., de Lisio, C. & Santamato, E. Generation and dynamics of optical beams with polarization singularities. *Opt. Express* **21**, 8815–8820 (2013).

[ADS](#) [Google Scholar](#)

43. 43.

Petek, H. & Ogawa, S. Femtosecond time-resolved two-photon photoemission studies of electron dynamics in metals. *Prog. Surf. Sci.* **56**, 239–310 (1997).

[ADS](#) [CAS](#) [Google Scholar](#)

44. 44.

Reutzel, M., Li, A., Wang, Z. & Petek, H. Coherent multidimensional photoelectron spectroscopy of ultrafast quasiparticle dressing by light. *Nat. Commun.* **11**, 2230 (2020).

[ADS](#) [CAS](#) [PubMed](#) [PubMed Central](#) [Google Scholar](#)

45. 45.

Li, C. M., Urbach, L. E. & Dai, H. L. Second-harmonic generation from a Ag(111) surface at the interband transition region: role of the dielectric function. *Phys. Rev. B* **49**, 2104–2112 (1994).

[ADS](#) [CAS](#) [Google Scholar](#)

46. 46.

Spektor, G. et al. Mixing the light spin with plasmon orbit by nonlinear light-matter interaction in gold. *Phys. Rev. X* **9**, 021031 (2019).

[CAS](#) [Google Scholar](#)

47. 47.

Rosch, A. Magnetic skyrmions: particles or waves. *Nat. Mater.* **15**, 1231–1232 (2016).

[ADS](#) [CAS](#) [Google Scholar](#)

48. 48.

Vuong, L. T. et al. Experiments showing orbital angular momentum exchange with optical vortices. In *International Quantum Electronics Conference 2007* IG2_3 (OSA, 2007).

49. 49.

Computer Vision Toolbox, MATLAB (MathWorks, 2018).

[Download references](#)

Acknowledgements

This research was supported by the NSF Center for Chemical Innovation on Chemistry at the Space-Time Limit, grant CHE-1414466. The authors thank L. Vuong for advice on the plasmonic flow analysis, A. Kosowsky for illuminating discussion of the role of phase transitions in cosmological structure formation and J. Chen at the Peterson Institute of NanoScience and Engineering for help in sample preparation.

Author information

Affiliations

1. Department of Physics and Astronomy, University of Pittsburgh,
Pittsburgh, PA, USA

Yanan Dai, Zhikang Zhou, Atreyie Ghosh, Roger S. K.
Mong & Hrvoje Petek
2. Pittsburgh Quantum Institute, University of Pittsburgh, Pittsburgh, PA,
USA

Yanan Dai, Zhikang Zhou, Atreyie Ghosh, Roger S. K.
Mong & Hrvoje Petek
3. Division of Physics, Faculty of Pure and Applied Sciences, University
of Tsukuba, Tsukuba-shi, Japan

Atsushi Kubo
4. Institute of Photonics Technologies, National Tsing Hua University,
Hsinchu, Taiwan

Chen-Bin Huang

Authors

1. Yanan Dai

[View author publications](#)

You can also search for this author in [PubMed](#) [Google Scholar](#)

2. Zhikang Zhou

[View author publications](#)

You can also search for this author in [PubMed](#) [Google Scholar](#)

3. Atreyie Ghosh

[View author publications](#)

You can also search for this author in [PubMed](#) [Google Scholar](#)

4. Roger S. K. Mong

[View author publications](#)

You can also search for this author in [PubMed](#) [Google Scholar](#)

5. Atsushi Kubo

[View author publications](#)

You can also search for this author in [PubMed](#) [Google Scholar](#)

6. Chen-Bin Huang

[View author publications](#)

You can also search for this author in [PubMed](#) [Google Scholar](#)

7. Hrvoje Petek

[View author publications](#)

You can also search for this author in [PubMed](#) [Google Scholar](#)

Contributions

Y.D. performed the experiments and simulations, processed and analysed the data, and generated the figures; Z.Z. helped with the sample preparation

and performing the experiments; Y.D., Z.Z. and A.G. developed the analytical model for topological quasiparticles; R.S.K.M. advised on the topological properties of quasiparticles; A.K. explained the PEEM imaging of plasmonic phenomena; C.-B.H. supervised the research on plasmonic vortices, performed simulations of experiments and participated in the data interpretation, H.P. guided interpretation of the data as a realization of topological quasiparticles, wrote the manuscript and supervised the research; all authors contributed to the discussion.

Corresponding authors

Correspondence to [Yanan Dai](#) or [Hrvoje Petek](#).

Ethics declarations

Competing interests

The authors declare no competing interests.

Additional information

Publisher's note Springer Nature remains neutral with regard to jurisdictional claims in published maps and institutional affiliations.

Extended data figures and tables

[Extended Data Fig. 1 Diagram of the nonlinear two-photon photoelectron emission process that forms the PEEM images.](#)

The recorded photoelectron count images are created by electrons absorbing two energy quanta ($2\hbar\omega_L$) from the total electric fields at the surface, $\mathbf{E}_L + \mathbf{E}_{\text{long}} + \mathbf{E}_z$, exciting them above E_{vac} (left). The light quanta can be supplied either from a single pulse, or from a coherent superposition of fields from a pump–probe pulse pair with a variable time delay; the PEEM records the spatial distribution of photoelectrons excited by the total field.

Right, the superposition of \mathbf{E}_L (shown as solid (dotted) grey lines) with wavelength λ_L and the parallel (anti-parallel) \mathbf{E}_{long} (the tangential component of the SPP field at the vacuum/Ag interface, which oscillates between the \mathbf{E}_z and \mathbf{E}_{long} character; the solid and dotted curved lines signify a change in the SPP field sign in the same sense as for \mathbf{E}_L) fields with wavelength λ_{SPP} creates the total in-plane field with a modulation period of λ_{SPP} , as shown by the green curve. The PEEM signal is integrated over many excitation cycles, so the experimental time resolution is encoded by how interferences evolve with the pump–probe delay.

Extended Data Fig. 2 Raw static PEEM image of the plasmonic vortex.

Top, image presented on a logarithmic colour scale. The vertical dashed lines approximately delineate the regions dominated by self-interference and SPP interference, as described in the text. Bottom, the horizontal line intensity profile shows the vertically integrated signal within the white rectangle centred on the vortex. The interferences occur with λ_{SPP} and $\lambda_{\text{SPP}}/2$ periods.

Extended Data Fig. 3 Interferograms of photoemission (PE) yields.

a, 2PP yields recorded at single pixels from selected regions within the vortex (inset). The reference 2PP signal is recorded from a flat Ag surface region. The scans are translated vertically for easier viewing. **b**, Phase distribution (the red and blue colours signify opposite phases) of the y component of \mathbf{E}_{long} relative to the excitation field. **c**, Fourier transform of the 2PP yield, as a function of polarization energy, which is defined by $\hbar\omega_L$. The square filtering function of 1 eV width centred at $1\hbar\omega_L$ indicates the selected energy range for the inverse Fourier transformation to obtain Supplementary Video 2. A second-order correlation process also includes the $2\hbar\omega_L$ signal, which is not evaluated. The vertical scale is normalized at the $0\hbar\omega_L$ peak maximum. Scale bars in **a** and **b**, λ_{SPP} .

Extended Data Fig. 4 ITR-PEEM images of the SPP vortex corresponding to the same time delays as in Fig. 2d.

The time delay increases from τ (leftmost image) to $\tau + 0.9$ fs (rightmost image). **a**, The raw PEEM data; **b**, absolute values of the phase-independent $0\hbar\omega_L$ Fourier component. **c**, The real part (amplitude) of the E_y component of the SPP field from the inverse Fourier transform of the $1\hbar\omega_L$ signal. The asterisk and white lines mark the evolution of two components with the opposite phase as $\Delta\tau$ is advanced. Scale bars, λ_{SPP} .

Extended Data Fig. 5 The FDTD simulated field evolution in 1/2 an optical cycle at the SPP vortex excited by 550-nm y -polarized light.

The fields from top to bottom represent E_z and y and x components of E_{long} . For an $m = 2$ Archimedean spiral structure, the optical phase evolves by π from left to right. Note that the stronger E_z component is plotted with a different colour scale than the x and y components. Scale bars, $\lambda_{SPP}/2$.

Extended Data Fig. 6 Topological properties of plasmonic vortex system.

a, L-line map of a $2 \mu\text{m} \times 2 \mu\text{m}$ region about the central vortex. The central domains are surrounded by apple-shaped toroids that are delimited by dashed lines and repeat with an approximate periodicity of λ_{SPP} (along the y direction) to infinity. Different domains of interest are coloured and labelled with the corresponding topological charge. Black dots mark the phase singularities, within these regions. **b**, Normalized spin texture overlapped by the L-line map in **a**. The colour map and arrows indicate the spin components, as in Supplementary Fig. 3b. **c**, **d**, Enlarged spin textures at side phase singularities indicated by the square shading in **c**. **e**, **f**, Spin texture in the same region as in **c**, **d**, but with the sign of positive S_z reversed, while conserving the topological charge. Black dots in **c**, **d** indicate positions of the phase singularities.

Extended Data Fig. 7 Phase change of the E_z associated with the phase singularities.

a, Phase change of E_z around the central and the two side phase singularities at $y = 0$ and $\pm\lambda_{\text{SPP}}/2$ in the dumb-bell region. **b**, Phase change of E_z around of the phase singularities along the x and y axes shown in Extended Data Fig. 6c,d. The opposite phase change along the x and y axes results from the opposite vorticity causing the topological charges of apple toroid domains to be zero.

Extended Data Fig. 8 Selected slices of the experimental plasmonic flow illustrating L-line formation, persistence and decay.

The delay times given at the top of each panel are normalized by the optical cycle. They are obtained from ITR-PEEM images with the probe pulse interacting with the sample before, during and after the generation of the plasmonic vortex (labelled ‘Pre-vortex’, ‘Established vortex’ and ‘After vortex’, respectively).

Supplementary information

Supplementary Information

This file contains (A) Analytical formalism of the Plasmonic Vortex Fields; (B) Formalism of the Topological SAM Textures; Supplementary References; and Supplementary Figure 1-3.

Supplementary Video 1

. Raw ITR-PEEM movie of plasmonic vortex The experimental ITR-PEEM data showing the spatial distribution of the 2PP signal from the SPP plasmonic vortex; PEEM images are taken in pump-probe delay increments between identical pulses of ~ 100 as.

Supplementary Video 2

. Fourier filtered plasmon vortex at 1ω The component of the Fourier transformed signal (absolute value) from Video 1 at the laser driving frequency, $1\omega_L$, is inverse Fourier transformed. This extracts the interference signal between the SPP and the probe optical pulse fields at the sample, enabling imaging of the vortex gyration about the vortex core. This SPP field gyration generates the spin angular momentum meron texture.

Supplementary Video 3

. The L-line singularity distribution The L-line distribution for a single pulse generated at the optical vortex. The bright contrast corresponds to high ellipticity of the x,y polarized SPP field, where the polarization is nearly linear and SAM points in the x,y plane orthogonal to the propagation k -vector. The central hourglass domain and the dumbbell region that are constant on ± 20 fs time scale contain the meron-like SAM texture, and define the integration boundaries that obtain the topological charge of $+1/2$ /per domain or $+3/2$ total. Time zero corresponds to maximum in the SPP vortex field.

Supplementary Video 4

. SAM quasiparticle density distribution. The video shows the evolution of SAM quasiparticle density. Integrating the density within the specified L-line domains in Video 3, gives topological charges of $+1/2$ and $+3/2$, respectively.

Rights and permissions

Reprints and Permissions

About this article



Cite this article

Dai, Y., Zhou, Z., Ghosh, A. *et al.* Plasmonic topological quasiparticle on the nanometre and femtosecond scales. *Nature* **588**, 616–619 (2020).
<https://doi.org/10.1038/s41586-020-3030-1>

[Download citation](#)

- Received: 11 February 2019
- Accepted: 02 October 2020
- Published: 23 December 2020
- Issue Date: 24 December 2020
- DOI: <https://doi.org/10.1038/s41586-020-3030-1>

Comments

By submitting a comment you agree to abide by our [Terms](#) and [Community Guidelines](#). If you find something abusive or that does not comply with our terms or guidelines please flag it as inappropriate.

[Access through your institution](#)

[Change institution](#)

[Buy or subscribe](#)

This article was downloaded by **calibre** from <https://www.nature.com/articles/s41586-020-3030-1>

- Article
- [Published: 23 December 2020](#)

Xolography for linear volumetric 3D printing

- [Martin Regehly](#) [ORCID: orcid.org/0000-0002-7547-787X¹](#),
- [Yves Garmshausen²](#),
- [Marcus Reuter²](#),
- [Niklas F. König²](#),
- [Eric Israel³](#),
- [Damien P. Kelly²](#),
- [Chun-Yu Chou²](#),
- [Klaas Koch²](#),
- [Baraa Asfari¹](#) &
- [Stefan Hecht](#) [ORCID: orcid.org/0000-0002-6124-0222^{4,5,6}](#)

[Nature](#) volume 588, pages620–624(2020) [Cite this article](#)

- 2017 Accesses
- 63 Altmetric
- [Metrics details](#)

Subjects

- [Design, synthesis and processing](#)
- [Materials chemistry](#)
- [Photochemistry](#)

Abstract

The range of applications for additive manufacturing is expanding quickly, including mass production of athletic footwear parts¹, dental ceramics² and aerospace components³ as well as fabrication of microfluidics⁴, medical devices⁵, and artificial organs⁶. The light-induced additive manufacturing techniques⁷ used are particularly successful owing to their high spatial and temporal control, but such techniques still share the common motifs of pointwise or layered generation, as do stereolithography⁸, laser powder bed fusion⁹, and continuous liquid interface production¹⁰ and its successors^{11,12}. Volumetric 3D printing^{13,14,15,16,17,18,19,20} is the next step onward from sequential additive manufacturing methods. Here we introduce xolography, a dual colour technique using photoswitchable photoinitiators to induce local polymerization inside a confined monomer volume upon linear excitation by intersecting light beams of different wavelengths. We demonstrate this concept with a volumetric printer designed to generate three-dimensional objects with complex structural features as well as mechanical and optical functions. Compared to state-of-the-art volumetric printing methods, our technique has a resolution about ten times higher than computed axial lithography without feedback optimization, and a volume generation rate four to five orders of magnitude higher than two-photon photopolymerization. We expect this technology to transform rapid volumetric production for objects at the nanoscopic to macroscopic length scales.

[Access through your institution](#)

[Change institution](#)

[Buy or subscribe](#)

Access options

Subscribe to Journal

Get full journal access for 1 year

\$199.00

only \$3.83 per issue

Subscribe

All prices are NET prices.
VAT will be added later in the checkout.

Rent or Buy article

Get time limited or full article access on ReadCube.

from \$8.99

Rent or Buy

All prices are NET prices.

Additional access options:

- [Log in](#)
- [Access through your institution](#)
- [Learn about institutional subscriptions](#)

Fig. 1: Xolography 3D printing technology.

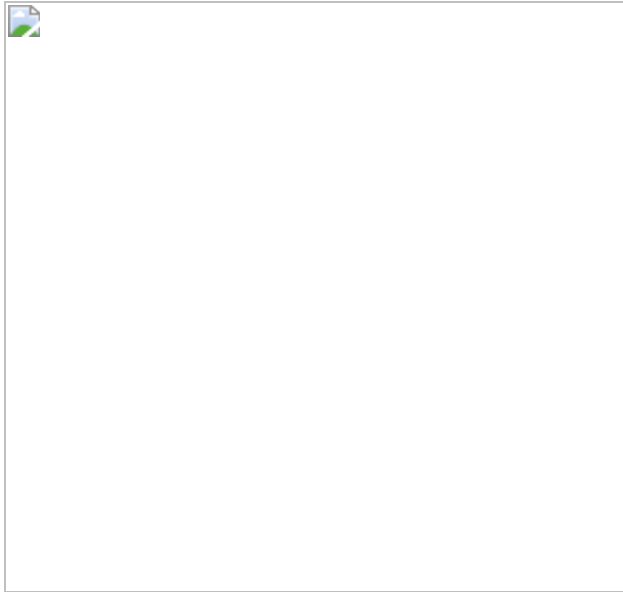


Fig. 2: Volumetric digital manufacturing.

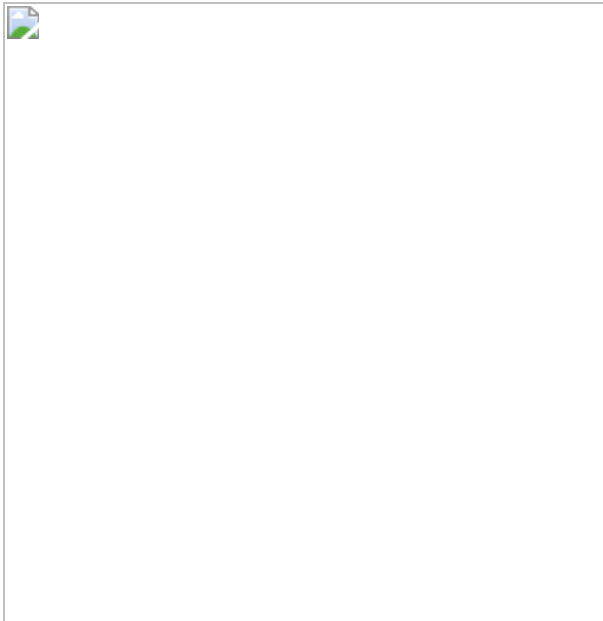
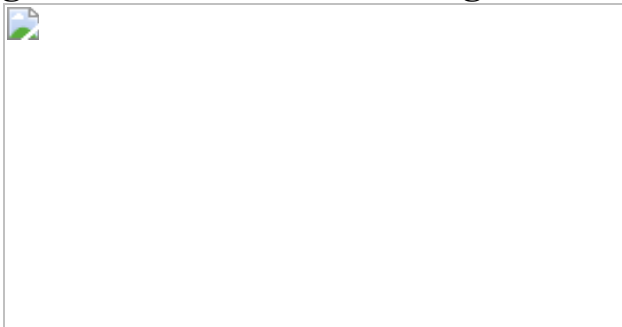


Fig. 3: Characterization of high-resolution object features.



Data availability

The data that support the findings of this study are available within the paper and Supplementary Information. Additional supporting data generated during the present study are available from the corresponding authors upon reasonable request.

References

1. 1.

- Zastrow, M. 3D printing gets bigger, faster and stronger. *Nature* **578**, 20–23 (2020).

[ADS](#) [CAS](#) [Article](#) [Google Scholar](#)

2. 2.

Galante, R., Figueiredo-Pina, C. G. & Serro, A. P. Additive manufacturing of ceramics for dental applications: a review. *Dent. Mater. J.* **35**, 825–846 (2019).

[CAS](#) [Article](#) [Google Scholar](#)

3. 3.

Najmon, J. C., Raeisi, S. & Tovar, A. Review of additive manufacturing technologies and applications in the aerospace industry. In *Additive Manufacturing for the Aerospace Industry* (eds Froes, F. & Boyer, R.) (Elsevier, 2019).

4. 4.

Ahmadi, A. et al. Additive manufacturing of laminar flow cells for single-molecule experiments. *Sci. Rep.* **9**, 16784 (2019).

[ADS](#) [Article](#) [Google Scholar](#)

5. 5.

Douroumis, D. 3D printing of pharmaceutical and medical applications: a new era. *Pharm. Res.* **36**, 42 (2019).

[Article](#) [Google Scholar](#)

6. 6.

Lee, A. et al. 3D bioprinting of collagen to rebuild components of the human heart. *Science* **365**, 482–487 (2019).

[ADS](#) [CAS](#) [Article](#) [Google Scholar](#)

7. 7.

Jung, K. et al. Designing with light: advanced 2D, 3D, and 4D materials. *Adv. Mater.* **32**, 1903850 (2020).

[CAS](#) [Article](#) [Google Scholar](#)

8. 8.

Hull, C. W. Apparatus for production of three-dimensional objects by stereolithography. US Patent 4,575,330 (1986).

9. 9.

Zhang, D. et al. Additive manufacturing of ultrafine-grained high-strength titanium alloys. *Nature* **576**, 91–95 (2019).

[ADS](#) [CAS](#) [Article](#) [Google Scholar](#)

10. 10.

Tumbleston, J. et al. Additive manufacturing. Continuous liquid interface production of 3D objects. *Science* **347**, 1349–1352 (2015).

[ADS](#) [CAS](#) [Article](#) [Google Scholar](#)

11. 11.

Walker, D. A., Hedrick, J. L. & Mirkin, C. A. Rapid, large-volume, thermally controlled 3D printing using a mobile liquid interface. *Science* **366**, 360–364 (2019).

[ADS](#) [CAS](#) [Article](#) [Google Scholar](#)

12. 12.

de Beer, M. P. et al. Rapid, continuous additive manufacturing by volumetric polymerisation inhibition patterning. *Sci. Adv.* **5**, eaau8723 (2019).

[ADS](#) [Article](#) [Google Scholar](#)

13. 13.

Shusteff, M. et al. One-step volumetric additive manufacturing of complex polymer structures. *Sci. Adv.* **3**, eaa05496 (2017).

[Article](#) [Google Scholar](#)

14. 14.

Kelly, B. E. et al. Volumetric additive manufacturing via tomographic reconstruction. *Science* **363**, 1075–1079 (2019).

[ADS](#) [CAS](#) [Article](#) [Google Scholar](#)

15. 15.

Loterie, D., Delrot, P. & Moser, C. High-resolution volumetric additive manufacturing. *Nat. Commun.* **11**, 852 (2020).

[ADS](#) [CAS](#) [Article](#) [Google Scholar](#)

16. 16.

Baldachini, T. *Three-Dimensional Microfabrication Using Two-Photon Polymerisation: Fundamentals, Technology and Applications* (Elsevier, 2019).

17. 17.

Zheng, L. et al. Nanofabrication of high-resolution periodic structures with a gap size below 100 nm by two-photon polymerisation. *Nanoscale Res. Lett.* **14**, 134 (2019).

[ADS](#) [Article](#) [Google Scholar](#)

18. 18.

Geng, Q., Wang, D. & Chen, P. Ultrafast multi-focus 3-D nano-fabrication based on two-photon polymerisation. *Nat. Commun.* **10**,

2179 (2019).

[ADS](#) [Article](#) [Google Scholar](#)

19. 19.

Saha, S. et al. Scalable submicrometer additive manufacturing. *Science* **366**, 105–109 (2019).

[ADS](#) [CAS](#) [Article](#) [Google Scholar](#)

20. 20.

Bernal, P. N. et al. Volumetric bioprinting of complex living-tissue constructs within seconds. *Adv. Mater.* **31**, 1970302 (2019).

[Article](#) [Google Scholar](#)

21. 21.

Swainson, W. K. Method, medium and apparatus for producing three-dimensional figure product. US patent US4041476A (1977).

22. 22.

Scott, T., Kowalski, B., Sullivan, A., Bowman, C. & Mcleod, R. Two-color single-photon photoinitiation and photoinhibition for subdiffraction photolithography. *Science* **324**, 913–917 (2009).

[ADS](#) [CAS](#) [Article](#) [Google Scholar](#)

23. 23.

Liaros, N. & Fourkas, J. T. Ten years of two-color photolithography. *Opt. Mater. Express* **9**, 3006–3020 (2019).

[ADS](#) [CAS](#) [Article](#) [Google Scholar](#)

24. 24.

van der Laan, H. L., Burns, M. A. & Scott, T. F. Volumetric photopolymerisation confinement through dual-wavelength photoinitiation and photoinhibition. *ACS Macro Lett.* **8**, 899–904 (2019).

[Article](#) [Google Scholar](#)

25. 25.

Goulet-Hanssens, A., Eisenreich, F. & Hecht, S. Enlightening materials with photoswitches. *Adv. Mater.* **32**, 1905966 (2020).

[CAS Article](#) [Google Scholar](#)

26. 26.

Patel, S., Cao, J. & Lippert, A. A volumetric three-dimensional digital light photoactivatable dye display. *Nat. Commun.* **8**, 15239 (2017).

[ADS](#) [CAS Article](#) [Google Scholar](#)

27. 27.

Jeudy, M. J. & Robillard, J. J. Spectral photosensitisation of a variable index material for recording phase holograms with high efficiency. *Opt. Commun.* **13**, 25–28 (1975).

[ADS](#) [CAS Article](#) [Google Scholar](#)

28. 28.

Ichimura, K. & Sakuragi, M. A. Spiropyran-iodonium salt system as a two photon radical photoinitiator. *J. Polym. Sci. C* **26**, 185–189 (1988).

[CAS Article](#) [Google Scholar](#)

29. 29.

Lee, S.-K. & Neckers, D. Two-photon radical-photoinitiator system based on iodinated benzospiropyrans. *Chem. Mater.* **3**, 858–864 (1991).

[CAS Article](#) [Google Scholar](#)

30. 30.

Born, M. & Wolf, E. *Principles of Optics: Electromagnetic Theory of Propagation, Interference and Diffraction of Light* (Cambridge Univ. Press, 1999).

31. 31.

OSIRIX DICOM Image Library <http://www.osirix-viewer.com/resources/dicom-image-library> (accessed 2 April 2020).

32. 32.

Kikinis, R., Pieper, S. D. & Vosburgh, K. G. 3D Slicer: a platform for subject-specific image analysis, visualisation, and clinical support. In *Intraoperative Imaging and Image-Guided Therapy* (ed. Jolesz, F.) (Springer, 2014).

33. 33.

Aloui, F. et al. Refractive index evolution of various commercial acrylic resins during photopolymerisation. *Express Polym. Lett.* **12**, 966–971 (2018).

[CAS Article](#) [Google Scholar](#)

34. 34.

Liu, Y. et al. Improvement of the diffraction properties in holographic polymer dispersed liquid crystal Bragg gratings. *Opt. Commun.* **218**, 27–32 (2003).

[ADS](#) [CAS Article](#) [Google Scholar](#)

35. 35.

Saleh, B. E. A. et al. *Fundamentals of Photonics* (John Wiley & Sons, 2019).

36. 36.

Zhou, X. et al. Rayleigh scattering of linear alkylbenzene in large liquid scintillator detectors. *Rev. Sci. Instrum.* **86**, 073310 (2015).

[ADS](#) [Article](#) [Google Scholar](#)

37. 37.

Coumou, D. J., Mackor, E. L. & Hijmans, J. Isotropic light-scattering in pure liquids. *Trans. Faraday Soc.* **60**, 1539 (1964).

[CAS](#) [Article](#) [Google Scholar](#)

38. 38.

Fandiño, O., Comuñas, M. J. P., Lugo, L., López, E. R. & Fernández, J. Density measurements under pressure for mixtures of pentaerythritol ester lubricants. Analysis of a density–viscosity relationship. *J. Chem. Eng. Data* **52**, 1429–1436 (2007).

[Article](#) [Google Scholar](#)

39. 39.

Fandiño, O., Pensado, A. S., Lugo, L., Comuñas, M. J. P. & Fernández, J. Compressed liquid densities of squalane and pentaerythritol tetra(2-ethylhexanoate). *J. Chem. Eng. Data* **50**, 939–946 (2005).

[Article](#) [Google Scholar](#)

40. 40.

Fandiño, O., Pensado, A. S., Lugo, L., Comuñas, M. J. P. & Fernández, J. Volumetric behaviour of the environmentally compatible lubricants pentaerythritol tetraheptanoate and pentaerythritol tetranonanoate at high pressures. *Green Chem.* **7**, 775–783 (2005).

[Article](#) [Google Scholar](#)

[Download references](#)

Acknowledgements

We thank D. Radzinski for continuous support, F. Pinno and N. Wandel for SEM measurements, P. Fengler and A. F. Thünemann as well as J. Müller and A. Gurlo for help with material property measurements, S. Schneider and M. Dinter for 3D visualization of the printing zone, A. Steinbach for CAD modelling of the optical setup, and M. Vollmer for proofreading the manuscript.

Author information

Affiliations

1. Technology Department, Brandenburg University of Applied Science, Brandenburg, Germany

Martin Regehly & Baraa Asfari

2. xolo GmbH, Berlin, Germany

Yves Garmshausen, Marcus Reuter, Niklas F. König, Damien P. Kelly, Chun-Yu Chou & Klaas Koch

3. Institute of Materials Science, TU Dresden, Dresden, Germany

Eric Israel

4. Department of Chemistry and IRIS Adlershof, Humboldt-Universität zu Berlin, Berlin, Germany

Stefan Hecht

5. DWI—Leibniz Institute for Interactive Materials, Aachen, Germany

Stefan Hecht

6. Institute of Technical and Macromolecular Chemistry, RWTH Aachen University, Aachen, Germany

Stefan Hecht

Authors

1. Martin Regehly

[View author publications](#)

You can also search for this author in [PubMed](#) [Google Scholar](#)

2. Yves Garmshausen

[View author publications](#)

You can also search for this author in [PubMed](#) [Google Scholar](#)

3. Marcus Reuter

[View author publications](#)

You can also search for this author in [PubMed](#) [Google Scholar](#)

4. Niklas F. König

[View author publications](#)

You can also search for this author in [PubMed](#) [Google Scholar](#)

5. Eric Israel

[View author publications](#)

You can also search for this author in [PubMed](#) [Google Scholar](#)

6. Damien P. Kelly

[View author publications](#)

You can also search for this author in [PubMed](#) [Google Scholar](#)

7. Chun-Yu Chou

[View author publications](#)

You can also search for this author in [PubMed](#) [Google Scholar](#)

8. Klaas Koch

[View author publications](#)

You can also search for this author in [PubMed](#) [Google Scholar](#)

9. Baraa Asfari

[View author publications](#)

You can also search for this author in [PubMed](#) [Google Scholar](#)

10. Stefan Hecht

[View author publications](#)

You can also search for this author in [PubMed](#) [Google Scholar](#)

Contributions

M. Regehly and S.H. designed the research and wrote the paper. Y.G. designed the spiropyran photoinitiator. Synthesis and characterization was performed by Y.G. and M. Reuter. Theoretical work and simulations by M. Regehly. Volumetric printer development was done by M. Regehly, M. Reuter, D.P.K. and C.-Y.C. 3D data processing was done by M. Reuter, E.I. and M. Regehly. Development of resin formulations, characterization and post-processing were performed by N.F.K., E.I. and Y.G. Software development was done by K.K. and B.A.

Corresponding authors

Correspondence to [Martin Regehly](#) or [Stefan Hecht](#).

Ethics declarations

Competing interests

Two patents (DE 10 2019 115 336 and DE 10 2019 129 868) have been filed related to the topic covered in this publication.

Additional information

Peer review information *Nature* thanks Cyrille Boyer, Robert McLeod and the other, anonymous, reviewer(s) for their contribution to the peer review of this work. Peer reviewer reports are available.

Publisher's note Springer Nature remains neutral with regard to jurisdictional claims in published maps and institutional affiliations.

Extended data figures and tables

[Extended Data Fig. 1 Synthesis of DCPI.](#)

MeI, methyl iodide (CH_3I).

[Extended Data Fig. 2 \$^1\text{H}\$ NMR \(500 MHz, \$\text{CDCl}_3\$ \) of DCPI](#)

[Extended Data Fig. 3 \$^{13}\text{C}\$ NMR \(126 MHz, \$\text{CDCl}_3\$ \) of DCPI](#)

Extended Data Fig. 4 ^{19}F NMR (471 MHz, CDCl_3) of DCPI

Extended Data Fig. 5 Optical design and characterization of the light sheet generator.

a, Schematic representation of the optical setup. L1, Powell lens. L2, L3, cylindrical lenses. S, beamsplitter. M, mirrors. A, linear axis. C, cuvette. **b**, Partial image of the light sheet in one arm at waist position. **c**, Horizontal lineout of the light sheet intensity distribution.

Extended Data Fig. 6 Results of the calibration procedure.

a, Diagram showing an array of tested irradiance/velocity combinations, which are used to identify the parameter space for xolography 3D printing. **b**, Photograph of the automated testing procedure in a 1-cm cuvette containing resin 1.

Extended Data Fig. 7 Optimal light sheet waist widths.

The plot shows the FWHM waist sizes d_{FWHM} of the light sheet against volume depth D for different values of the homogeneity factor β . The simulation has been performed for the design wavelength of $\lambda = 375$ nm and assumed refractive index of the resin of $n = 1.56$ (375 nm).

Extended Data Fig. 8 Simulation of light sheet intensity distributions.

a, Exponential intensity decrease along the 1-cm volume depth for single-side illumination. **b**, Double-sided illumination leads to a nearly homogenous distribution for 1-cm depth. **c**, Maximum deviation from the average intensity in percentage for volume depths of up to 10 cm.

Extended Data Fig. 9 Mechanical characterization of printed and post-processed test specimen.

a, Stress–strain curve obtained at a nominal strain rate of $4 \times 10^{-2} \text{ s}^{-1}$. The inset shows the sample mounted to the holder of the tensile testing machine.
b, Modulus–temperature behaviour acquired using a 1 K min^{-1} heating ramp rate and an amplitude of $30 \mu\text{m}$ at an oscillation frequency of 1 Hz. The inset shows the sample mounted to the stage of the dynamic mechanical analyser.

Supplementary information

Peer Review File

Video 1

: Xolography volumetric 3D printing. Video of the printing process in 1, 3 and 5 cm volume depth. Solidified objects are highly transparent and only visible via diffuse light scattering.

Video 2

: Function test of the printed flowcell. A simple example of multicomponent systems with mechanical functionalities made by volumetric 3D printing in one step without the need for subsequent assembly.

Video 3

| Stability demonstration of the anatomical model. If required, xolography creates objects with similar mechanical stability compared to conventional point-by-point or layer-by-layer production processes.

Rights and permissions

[Reprints and Permissions](#)

About this article



Check for
updates

Cite this article

Regehly, M., Garmshausen, Y., Reuter, M. *et al.* Xolography for linear volumetric 3D printing. *Nature* **588**, 620–624 (2020).

<https://doi.org/10.1038/s41586-020-3029-7>

[Download citation](#)

- Received: 05 June 2020
- Accepted: 02 November 2020
- Published: 23 December 2020
- Issue Date: 24 December 2020
- DOI: <https://doi.org/10.1038/s41586-020-3029-7>

Comments

By submitting a comment you agree to abide by our [Terms](#) and [Community Guidelines](#). If you find something abusive or that does not comply with our terms or guidelines please flag it as inappropriate.

[Access through your institution](#)

[Change institution](#)

[Buy or subscribe](#)

Associated Content

Nature | News & Views

[High-resolution 3D printing in seconds](#)

- Cameron Darkes-Burkey
- & Robert F. Shepherd

This article was downloaded by **calibre** from <https://www.nature.com/articles/s41586-020-3029-7>

| [Section menu](#) | [Main menu](#) |

- Article
- [Published: 16 December 2020](#)

Maximizing US nitrate removal through wetland protection and restoration

- [F. Y. Cheng](#) [ORCID: orcid.org/0000-0002-8674-9383¹](#) na1,
- [K. J. Van Meter](#) [ORCID: orcid.org/0000-0002-3698-7850²](#) na1,
- [D. K. Byrnes¹](#) &
- [N. B. Basu](#) [ORCID: orcid.org/0000-0002-8867-8523^{1,3,4}](#)

Nature volume **588**, pages625–630(2020) [Cite this article](#)

- 2265 Accesses
- 256 Altmetric
- [Metrics details](#)

Subjects

- [Element cycles](#)
- [Hydrology](#)
- [Limnology](#)

Abstract

Growing populations and agricultural intensification have led to raised riverine nitrogen (N) loads, widespread oxygen depletion in coastal zones (coastal hypoxia)¹ and increases in the incidence of algal blooms. Although

recent work has suggested that individual wetlands have the potential to improve water quality^{[2](#),[3](#),[4](#),[5](#),[6](#),[7](#),[8](#),[9](#)}, little is known about the current magnitude of wetland N removal at the landscape scale. Here we use National Wetland Inventory data and 5-kilometre grid-scale estimates of N inputs and outputs to demonstrate that current N removal by US wetlands (about 860 ± 160 kilotonnes of nitrogen per year) is limited by a spatial disconnect between high-density wetland areas and N hotspots. Our model simulations suggest that a spatially targeted increase in US wetland area by 10 per cent (5.1 million hectares) would double wetland N removal. This increase would provide an estimated 54 per cent decrease in N loading in nitrate-affected watersheds such as the Mississippi River Basin. The costs of this increase in area would be approximately 3.3 billion US dollars annually across the USA—nearly twice the cost of wetland restoration on non-agricultural, undeveloped land—but would provide approximately 40 times more N removal. These results suggest that water quality improvements, as well as other types of ecosystem services such as flood control and fish and wildlife habitat, should be considered when creating policy regarding wetland restoration and protection.

[Access through your institution](#)

[Change institution](#)

[Buy or subscribe](#)

Access options

Subscribe to Journal

Get full journal access for 1 year

\$199.00

only \$3.83 per issue

[Subscribe](#)

All prices are NET prices.

VAT will be added later in the checkout.

Rent or Buy article

Get time limited or full article access on ReadCube.

from \$8.99

[Rent or Buy](#)

All prices are NET prices.

Additional access options:

- [Log in](#)
- [Access through your institution](#)
- [Learn about institutional subscriptions](#)

Fig. 1: Our approach to estimating wetland N removal across the USA.

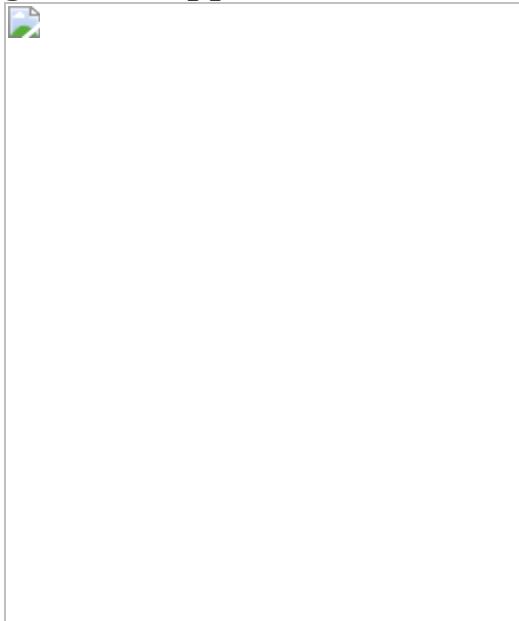


Fig. 2: Wetland densities, N surplus magnitudes and wetland N removal across the contiguous US.

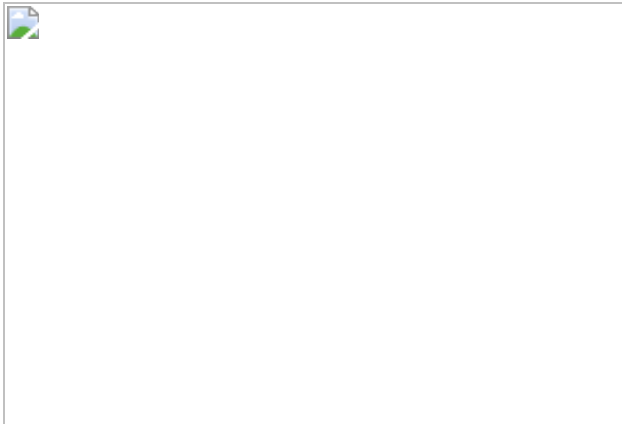


Fig. 3: Spatial relationships between N source areas and existing wetlands.

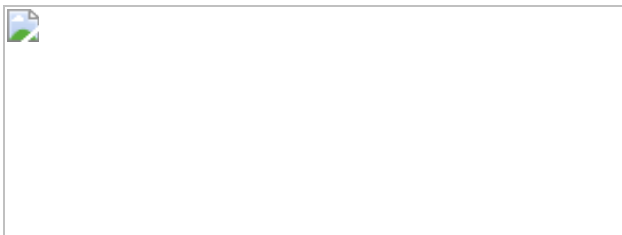
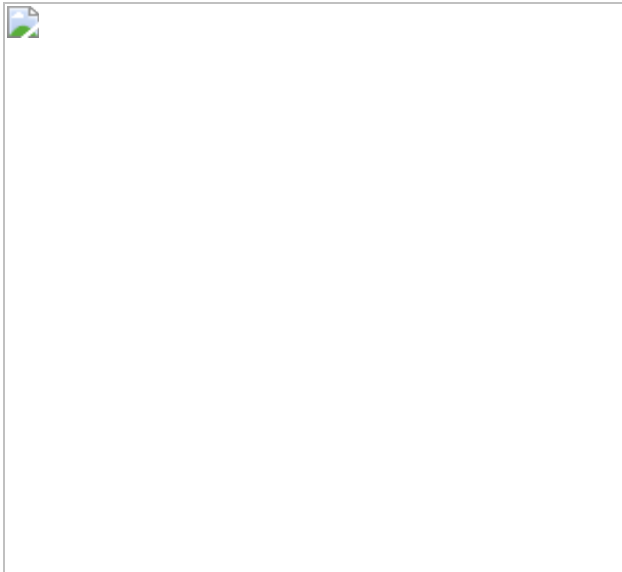


Fig. 4: Estimated N mass removal and costs for the three wetland restoration scenarios.



Fig. 5: Wetland restoration simulation results for a 10% increase in wetland area.



Data availability

Nitrogen mass balance data were obtained from the TREND-nitrogen dataset, available through the PANGAEA Data Publisher (<https://doi.org/10.1594/PANGAEA.917583>). The National Wetlands Inventory dataset was retrieved from US-FWS (<https://www.fws.gov/wetlands>). The Watershed Boundary Data set used for HUC-8 boundaries was retrieved from the USGS website <https://www.usgs.gov/core-science-systems/ngp/ngtoc/watershed-boundary-dataset>. USGS water quality data were retrieved from Oelsner et al.⁵⁴. [Source data](#) are provided with this paper.

Code availability

The MATLAB software used for the present analysis is available from Mathworks (<https://www.mathworks.com/>); R (version 3.5.2) used for geospatial analysis is available from the R Core Team (<https://www.r-project.org/>). Codes for the estimation of current wetland N removal, wetland restoration scenarios and cost analysis are available at https://github.com/landscape-ecohydrology/optimizing_wetland_restoration_in_nature.

References

1. 1.

Díaz, R. J. & Rosenberg, R. Introduction to environmental and economic consequences of hypoxia. *Int. J. Water Resour. Dev.* **27**, 71–82 (2011).

[Article](#) [Google Scholar](#)

2. 2.

Van Meter, K. J., Basu, N. B. & Van Cappellen, P. Two centuries of nitrogen dynamics: legacy sources and sinks in the Mississippi and Susquehanna river basins. *Global Biogeochem. Cy.* **31**, 2016GB005498 (2017).

[Google Scholar](#)

3. 3.

Cheng, F. Y. & Basu, N. B. Biogeochemical hotspots: role of small water bodies in landscape nutrient processing. *Wat. Resour. Res.* **53**, 5038–5056 (2017).

[ADS](#) [CAS](#) [Article](#) [Google Scholar](#)

4. 4.

Mitsch, W. J. et al. Reducing nitrogen loading to the Gulf of Mexico from the Mississippi River Basin: strategies to counter a persistent ecological problem. *Bioscience* **51**, 373–388 (2001).

[Article](#) [Google Scholar](#)

5. 5.

Mitsch, W. J. & Day, J. W. Restoration of wetlands in the Mississippi–Ohio–Missouri (MOM) River Basin: experience and needed research. *Ecol. Eng.* **26**, 55–69 (2006).

[Article](#) [Google Scholar](#)

6. 6.

Verhoeven, J. T. A., Arheimer, B., Yin, C. & Hefting, M. M. Regional and global concerns over wetlands and water quality. *Trends Ecol. Evol.* **21**, 96–103 (2006).

[Article](#) [Google Scholar](#)

7. 7.

Cohen, M. J. et al. Do geographically isolated wetlands influence landscape functions? *Proc. Natl Acad. Sci. USA* **113**, 1978–1986 (2016).

[ADS](#) [CAS](#) [Article](#) [Google Scholar](#)

8. 8.

Thorslund, J. et al. Wetlands as large-scale nature-based solutions: status and challenges for research, engineering and management. *Ecol. Eng.* **108**, 489–497 (2017).

[Article](#) [Google Scholar](#)

9. 9.

Fennessy, S. & Craft, C. Agricultural conservation practices increase wetland ecosystem services in the Glaciated Interior Plains. *Ecol. Appl.* **21**, S49–S64 (2011).

[Article](#) [Google Scholar](#)

10. 10.

Altieri, A. H. et al. Tropical dead zones and mass mortalities on coral reefs. *Proc. Natl Acad. Sci. USA* **114**, 3660–3665 (2017).

[CAS](#) [Article](#) [Google Scholar](#)

11. 11.

Fennel, K. & Testa, J. M. Biogeochemical controls on coastal hypoxia. *Annu. Rev. Mar. Sci.* **11**, 105–130 (2019).

[ADS](#) [Article](#) [Google Scholar](#)

12. 12.

Creed, I. F. et al. Enhancing protection for vulnerable waters. *Nat. Geosci.* **10**, 809–815 (2017).

[ADS](#) [CAS](#) [Article](#) [Google Scholar](#)

13. 13.

Golden, H. E. et al. Integrating geographically isolated wetlands into land management decisions. *Front. Ecol. Environ.* **15**, 319–327 (2017).

[Article](#) [Google Scholar](#)

14. 14.

Marton, J. M. et al. Geographically isolated wetlands are important biogeochemical reactors on the landscape. *Bioscience* **65**, 408–418 (2015).

[Article](#) [Google Scholar](#)

15. 15.

Hansen, L. et al. *Targeting Investments to Cost Effectively Restore and Protect*. Report No. 183

https://www.ers.usda.gov/webdocs/publications/45347/51895_err183.pdf?v=0 (United States Department of Agriculture, 2015).

16. 16.

Brinson, M. M. & Eckles, S. D. U. S. Department of Agriculture conservation program and practice effects on wetland ecosystem services: a synthesis. *Ecol. Appl.* **21**, S116–S127 (2011).

[Article](#) [Google Scholar](#)

17. 17.

Zedler, J. B. Wetlands at your service: reducing impacts of agriculture at the watershed scale. *Front. Ecol. Environ.* **1**, 65–72 (2003).

[Article](#) [Google Scholar](#)

18. 18.

Zimmerman, E. K., Tyndall, J. C. & Schulte, L. A. Using spatially targeted conservation to evaluate nitrogen reduction and economic opportunities for best management practice placement in agricultural landscapes. *Environ. Manage.* **64**, 313–328 (2019).

[ADS](#) [Article](#) [Google Scholar](#)

19. 19.

Moreno-Mateos, D., Power, M. E., Comín, F. A. & Yockteng, R. Structural and functional loss in restored wetland ecosystems. *PLoS Biol.* **10**, e1001247 (2012).

[CAS](#) [Article](#) [Google Scholar](#)

20. 20.

Golden, H. E. et al. Non-floodplain wetlands affect watershed nutrient dynamics. *Crit. Rev. Environ. Sci. Technol.* **53**, 7203–7214 (2019).

[ADS](#) [CAS](#) [Article](#) [Google Scholar](#)

21. 21.

Jordan, S. J., Stoffer, J. & Nestlerode, J. A. Wetlands as sinks for reactive nitrogen at continental and global scales: a meta-analysis. *Ecosystems* **14**, 144–155 (2011).

[CAS](#) [Article](#) [Google Scholar](#)

22. 22.

Czuba, J. A., Hansen, A. T., Foufoula-Georgiou, E. & Finlay, J. C. Contextualizing wetlands within a river network to assess nitrate removal and inform watershed management. *Wat. Resour. Res.* **54**, 1312–1337 (2018).

[ADS](#) [CAS](#) [Article](#) [Google Scholar](#)

23. 23.

Hansen, A. T., Dolph, C. L., Foufoula-Georgiou, E. & Finlay, J. C. Contribution of wetlands to nitrate removal at the watershed scale. *Nat. Geosci.* (2018).

24. 24.

Czuba, J. A. & Foufoula-Georgiou, E. A network-based framework for identifying potential synchronizations and amplifications of sediment delivery in river basins. *Wat. Resour. Res.* **50**, 3826–3851 (2014).

[ADS](#) [Article](#) [Google Scholar](#)

25. 25.

Van Cleemput, O., Boeckx, P., Lindgren, P.-E. & Tonderski, K. in *Biology of the Nitrogen Cycle* 359–367 (Elsevier, 2007).

26. 26.

Ferris, J. & Siikamäki, J. *Conservation Reserve Program and Wetland Reserve Program: Primary Land Retirement Programs for Promoting Farmland Conservation* https://media.rff.org/documents/RFF-BCK-ORRG_CRP_and_WRP.pdf (Resources for the Future, 2009).

27. 27.

Rabotyagov, S. S. et al. Cost-effective targeting of conservation investments to reduce the northern Gulf of Mexico hypoxic zone. *Proc. Natl Acad. Sci. USA* **111**, 18530–18535 (2014).

[ADS](#) [CAS](#) [Article](#) [Google Scholar](#)

28. 28.

Van Meter, K. J., Van Cappellen, P. & Basu, N. B. Legacy nitrogen may prevent achievement of water quality goals in the Gulf of Mexico. *Science* **360**, 427–430 (2018).

[ADS](#) [Article](#) [Google Scholar](#)

29. 29.

Van Meter, K. J., Van Cappellen, P. & Basu, N. B. Response to Comment on “Legacy nitrogen may prevent achievement of water quality goals in the Gulf of Mexico”. *Science* **365**, eaav3851 (2019).

[Article](#) [Google Scholar](#)

30. 30.

Hayes, D. J., Kling, C. L. & Lawrence, J. D. *Economic Evaluation of Governor Branstad's Water Quality Initiative*. Report No. 16-PB 19 <https://governor.iowa.gov/sites/default/files/documents/ISU%20CARD%20Economic%20Evaluation.pdf> (Center for Agricultural and Rural Development, 2016).

31. 31.

Jones, C. S., Nielsen, J. K., Schilling, K. E. & Weber, L. J. Iowa stream nitrate and the Gulf of Mexico. *PLoS One* **13**, e0195930 (2018).

[Article](#) [Google Scholar](#)

32. 32.

Dahl, T. E. *Wetlands Losses in the United States, 1780's to 1980's*. <https://www.fws.gov/wetlands/documents/Wetlands-Losses-in-the-United-States-1780s-to-1980s.pdf> (U.S. Department of the Interior, Fish and Wildlife Service, 1990).

33. 33.

Ward, A. S. New Clean Water Act rule leaves U.S. waters vulnerable. *Eos* <https://eos.org/opinions/new-clean-water-act-rule-leaves-u-s-waters-vulnerable> (2020).

34. 34.

Tomer, M. D. & Nelson, J. A. Measurements of landscape capacity for water detention and wetland restoration practices can inform watershed planning goals and implementation strategies. *J. Soil Water Conserv.* (2020).

35. 35.

Salo, T. & Turtola, E. Nitrogen balance as an indicator of nitrogen leaching in Finland. *Agric. Ecosyst. Environ.* **113**, 98–107 (2006).

[CAS](#) [Article](#) [Google Scholar](#)

36. 36.

Bouwman, A. F., Van Drecht, G. & Van der Hoek, K. W. Global and regional surface nitrogen balances in intensive agricultural production systems for the period 1970-2030. *Pedosphere* **15**, 137–155 (2005).

[Google Scholar](#)

37. 37.

Byrnes, D. K., Van Meter, K. J. & Basu, N. B. Trajectories nutrient dataset for nitrogen (TREND-nitrogen). *PANGAEA* <https://doi.org/10.1594/PANGAEA.917583> (2020).

38. 38.

Byrnes, D. K., Van Meter, K. J. & Basu, N. B. Long-term shifts in U.S. nitrogen sources and sinks revealed by the new TREND-nitrogen dataset (1930–2017). *Glob. Biogeochem. Cycles* (2020).

39. 39.

USDA – National Agricultural Statistics Service. Census of Agriculture. www.nass.usda.gov/AgCensus (2017).

40. 40.

NADP Total Deposition Science Committee. NADP total deposition maps. *National Atmospheric Deposition Program* <http://nadp.slh.wisc.edu/committees/tdep/tdepmaps/> (2018).

41. 41.

USDA ERS. Fertilizer use and price. <https://www.ers.usda.gov/data-products/fertilizer-use-and-price.aspx> (2018).

42. 42.

Brakebill, J. W. & Gronberg, J. M. *County-Level Estimates of Nitrogen and Phosphorus from Commercial Fertilizer for the Conterminous United States, 1987–2012*. <https://www.sciencebase.gov/catalog/item/5851b2d1e4b0f99207c4f238> (USGS, 2019).

43. 43.

U.S. Fish and Wildlife Service. *National Wetlands Inventory* <https://www.fws.gov/wetlands/Data/Data-Download.html> (2019).

44. 44.

Land, M. et al. How effective are created or restored freshwater wetlands for nitrogen and phosphorus removal? A systematic review. *Environ. Evid.* **5**, 9 (2016).

[Article](#) [Google Scholar](#)

45. 45.

Fisher, J. & Acreman, M. C. Wetland nutrient removal: a review of the evidence. *Hydrol. Earth Syst. Sci.* **8**, 673–685 (2004).

[ADS](#) [CAS](#) [Article](#) [Google Scholar](#)

46. 46.

Spieles, D. J. & Mitsch, W. J. The effects of season and hydrologic and chemical loading on nitrate retention in constructed wetlands: a comparison of low- and high-nutrient riverine systems. *Ecol. Eng.* **14**, 77–91 (1999).

[Article](#) [Google Scholar](#)

47. 47.

Barton, L., McLay, C. D. A., Schipper, L. A. & Smith, C. T. Annual denitrification rates in agricultural and forest soils: a review. *Soil Res.* **37**, 1073–1094 (1999).

[Article](#) [Google Scholar](#)

48. 48.

Wu, Q. & Lane, C. R. Delineating wetland catchments and modeling hydrologic connectivity using lidar data and aerial imagery. *Hydrol.*

Earth Syst. Sci. **21**, 3579–3595 (2017).

[ADS](#) [Article](#) [Google Scholar](#)

49. 49.

Mishra, S. Uncertainty and sensitivity analysis techniques for hydrologic modeling. *J. Hydroinform.* **11**, 282–296 (2009).

[Article](#) [Google Scholar](#)

50. 50.

Muleta, M. K. & Nicklow, J. W. Sensitivity and uncertainty analysis coupled with automatic calibration for a distributed watershed model. *J. Hydrol.* **306**, 127–145 (2005).

[ADS](#) [Article](#) [Google Scholar](#)

51. 51.

Van Meter, K. J. & Basu, N. B. Signatures of human impact: size distributions and spatial organization of wetlands in the Prairie Pothole landscape. *Ecol. Appl.* **25**, 451–465 (2015).

[Article](#) [Google Scholar](#)

52. 52.

Theriot, J. M., Conkle, J. L., Reza Pezeshki, S., DeLaune, R. D. & White, J. R. Will hydrologic restoration of Mississippi River riparian wetlands improve their critical biogeochemical functions? *Ecol. Eng.* **60**, 192–198 (2013).

[Article](#) [Google Scholar](#)

53. 53.

Tyndall, J. & Bowman, T. *Nutrient Reduction Strategy Decision Support Tool* <https://www.nrem.iastate.edu/bmpcosttools/> (Iowa State Univ., 2016).

54. 54.

Oelsner, G. P. et al. *Water-Quality Trends in the Nation's Rivers and Streams, 1972–2012—Data Preparation, Statistical Methods, and Trend Results*. Report No. 2017-5006
<https://pubs.er.usgs.gov/publication/sir20175006> (USGS, 2017).

[Download references](#)

Acknowledgements

The present work was financially supported by a Natural Sciences and Engineering Research Council of Canada (NSERC) grant (reference number 386129293) for F.Y.C. and N.B.B., an NSERC graduate scholarship for F.Y.C., an NSERC Discovery Grant and an Ontario Early Researcher Award for N.B.B. and D.K.B., and by startup funds from the University of Illinois at Chicago for K.J.V.M. Additional funding support was received through the Global Water Futures project Lake Futures for N.B.B.

Author information

Author notes

1. These authors contributed equally: F. Y. Cheng, K. J. Van Meter

Affiliations

1. Department of Civil and Environmental Engineering, University of Waterloo, Waterloo, Ontario, Canada

F. Y. Cheng, D. K. Byrnes & N. B. Basu

2. Department of Earth and Environmental Sciences, University of Illinois at Chicago, Chicago, IL, USA

K. J. Van Meter

3. Department of Earth and Environmental Sciences, University of Waterloo, Waterloo, Ontario, Canada

N. B. Basu

4. Water Institute, University of Waterloo, Waterloo, Ontario, Canada

N. B. Basu

Authors

1. F. Y. Cheng

[View author publications](#)

You can also search for this author in [PubMed](#) [Google Scholar](#)

2. K. J. Van Meter

[View author publications](#)

You can also search for this author in [PubMed](#) [Google Scholar](#)

3. D. K. Byrnes

[View author publications](#)

You can also search for this author in [PubMed](#) [Google Scholar](#)

4. N. B. Basu

[View author publications](#)

You can also search for this author in [PubMed](#) [Google Scholar](#)

Contributions

N.B.B., K.J.V.M. and F.Y.C. conceived the study. N.B.B., F.Y.C. and K.J.V.M. developed the wetland N removal models. F.Y.C. ran simulations for current wetland N removal, and K.J.V.M. carried out the wetland restoration simulations and cost analysis. D.K.B., K.J.V.M. and N.B.B. provided N input data for the model simulations. K.J.V.M. wrote the paper with direct contributions from N.B.B., F.Y.C. and D.K.B.

Corresponding author

Correspondence to [N. B. Basu](#).

Ethics declarations

Competing interests

The authors declare no competing interests.

Additional information

Peer review information *Nature* thanks Jacques Finlay, Patrick Inglett, John Tyndall and the other, anonymous, reviewer(s) for their contribution to the peer review of this work. Peer reviewer reports are available.

Publisher's note Springer Nature remains neutral with regard to jurisdictional claims in published maps and institutional affiliations.

Extended data figures and tables

[Extended Data Fig. 1 Nitrogen surplus distributions across US hydrologic regions.](#)

a, Histograms of N surplus by hydrologic region. The counts in the histograms refer to individual HUC-8 watersheds within the hydrologic regions. **b**, Map of hydrologic regions defined by the USGS. Boundaries of the Mississippi River Basin are drawn in yellow.

Extended Data Fig. 2 Modelled N removal by hydrologic region.

The counts in the histograms refer to individual HUC-8 watersheds within the corresponding hydrologic regions. See Extended Data Fig. 1b for region locations.

Extended Data Fig. 3 Analysis of empirical data used by Cheng & Basu³ to develop the $k-\tau$ relationship used in our study.

a, N removed at the individual wetland scale. Data were obtained from a global meta-analysis of 178 wetlands. **b**, N removal efficiency, ρ , calculated as the ratio between N removal and N inputs to the wetland. **c**, N removal-rate constant, k , estimated as a function of ρ and empirically based estimates of wetland residence times, τ , assuming that N removal within the wetland follows first-order kinetics. **d**, A strong inverse relationship was found between k and wetland residence time τ . This relationship between size and N removal-rate constants allows us, in this work, to more accurately upscale to the continental US scale than has previously been achieved.

Extended Data Fig. 4 Costs of wetland restoration.

a, b, Estimated costs for restoration of a 1-ha wetland in 48 states across the contiguous US on cropland (**a**) and pastureland (**b**). Whereas construction and maintenance costs are considered to be constant across states, land rental costs vary by state and by land use. Costs are annualized over a 50-year management horizon.

Extended Data Table 1 N surplus and wetland N removal magnitudes for a subset of nitrate-affected watersheds

[Full size table](#)

Extended Data Table 2 Ranges of parameters used in the Monte Carlo simulations of wetland N removal

[Full size table](#)

Supplementary information

Peer Review File

Source data

[Source Data Fig. 2](#)

[Source Data Fig. 3](#)

[Source Data Fig. 4](#)

Rights and permissions

[Reprints and Permissions](#)

About this article



Check for
updates

Cite this article

Cheng, F.Y., Van Meter, K.J., Byrnes, D.K. *et al.* Maximizing US nitrate removal through wetland protection and restoration. *Nature* **588**, 625–630 (2020). <https://doi.org/10.1038/s41586-020-03042-5>

[Download citation](#)

- Received: 10 March 2020
- Accepted: 28 October 2020
- Published: 16 December 2020
- Issue Date: 24 December 2020

- DOI: <https://doi.org/10.1038/s41586-020-03042-5>

Comments

By submitting a comment you agree to abide by our [Terms](#) and [Community Guidelines](#). If you find something abusive or that does not comply with our terms or guidelines please flag it as inappropriate.

[Access through your institution](#)

[Change institution](#)

[Buy or subscribe](#)

Associated Content

Nature | News & Views

[Targeted wetland restoration could greatly reduce nitrogen pollution](#)

- Jacques C. Finlay

This article was downloaded by **calibre** from <https://www.nature.com/articles/s41586-020-03042-5>

| [Section menu](#) | [Main menu](#) |

- Article
- [Published: 25 November 2020](#)

A network of grassroots reserves protects tropical river fish diversity

- [Aaron A. Koning](#) ORCID: [orcid.org/0000-0002-1222-8972^{1,2,3}](https://orcid.org/0000-0002-1222-8972),
- [K. Martin Perales](#) ORCID: [orcid.org/0000-0003-3394-5716¹](https://orcid.org/0000-0003-3394-5716),
- [Etienne Fluet-Chouinard](#) ORCID: [orcid.org/0000-0003-4380-2153^{1,4}](https://orcid.org/0000-0003-4380-2153)
&
- [Peter B. McIntyre^{1,5}](#)

[Nature](#) volume **588**, pages631–635(2020) [Cite this article](#)

- 1358 Accesses
- 2 Citations
- 149 Altmetric
- [Metrics details](#)

Subjects

- [Conservation biology](#)
- [Freshwater ecology](#)

Abstract

Intensive fisheries have reduced fish biodiversity and abundance in aquatic ecosystems worldwide^{1,2,3}. ‘No-take’ marine reserves have become a cornerstone of marine ecosystem-based fisheries management^{4,5,6}, and their

benefits for adjacent fisheries are maximized when reserve design fosters synergies among nearby reserves^{7,8}. The applicability of this marine reserve network paradigm to riverine biodiversity and inland fisheries remains largely untested. Here we show that reserves created by 23 separate communities in Thailand's Salween basin have markedly increased fish richness, density, and biomass relative to adjacent areas. Moreover, key correlates of the success of protected areas in marine ecosystems—particularly reserve size and enforcement—predict differences in ecological benefits among riverine reserves. Occupying a central position in the network confers additional gains, underscoring the importance of connectivity within dendritic river systems. The emergence of network-based benefits is remarkable given that these reserves are young (less than 25 years old) and arose without formal coordination. Freshwater ecosystems are under-represented among the world's protected areas⁹, and our findings suggest that networks of small, community-based reserves offer a generalizable model for protecting biodiversity and augmenting fisheries as the world's rivers face unprecedented pressures^{10,11}.

[Access through your institution](#)

[Change institution](#)

[Buy or subscribe](#)

Access options

Subscribe to Journal

Get full journal access for 1 year

\$199.00

only \$3.83 per issue

[Subscribe](#)

All prices are NET prices.

VAT will be added later in the checkout.

Rent or Buy article

Get time limited or full article access on ReadCube.

from \$8.99

[Rent or Buy](#)

All prices are NET prices.

Additional access options:

- [Log in](#)
- [Access through your institution](#)
- [Learn about institutional subscriptions](#)

Fig. 1: Riverine reserve network within the Mae Ngao basin.

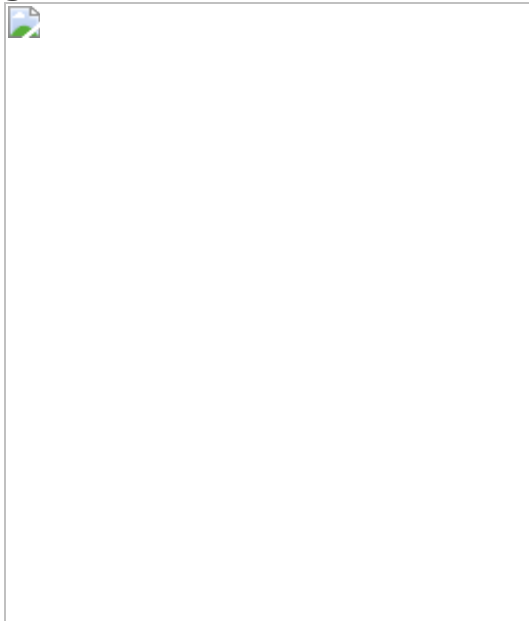


Fig. 2: Fish responses to protection in reserves.

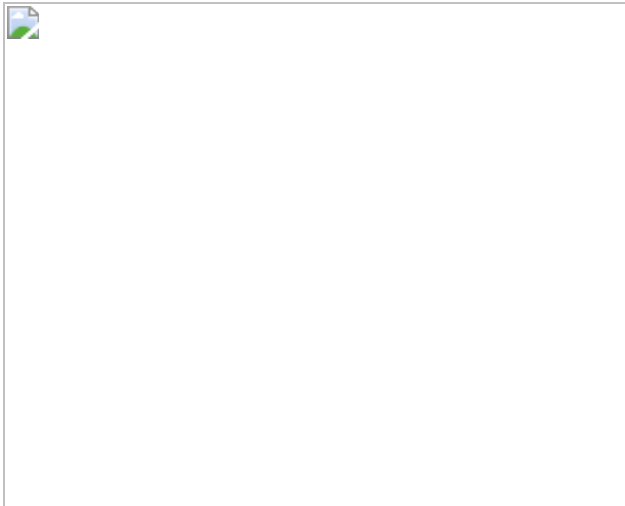


Fig. 3: Reserve features vary in benefits for fish.



Fig. 4: Scaling of benefits with key reserve features.

Data availability

The datasets used and/or analysed during the current study are available in the Environmental Data Initiative repository (<https://portal.edirepository.org/nis/mapbrowse?packageid=edi.513.1>).

Code availability

The R code used for the analyses presented here is available from GitHub (https://github.com/aakoning/riv_res_2020).

References

1. 1.

Worm, B. et al. Rebuilding global fisheries. *Science* **325**, 578–585 (2009).

[ADS](#) [CAS](#) [Article](#) [Google Scholar](#)

2. 2.

Costello, C. et al. Global fishery prospects under contrasting management regimes. *Proc. Natl Acad. Sci. USA* **113**, 5125–5129 (2016).

[ADS](#) [CAS](#) [PubMed](#) [PubMed Central](#) [Google Scholar](#)

3. 3.

Allan, J. D. et al. Overfishing of inland waters. *Bioscience* **55**, 1041–1051 (2005).

[Google Scholar](#)

4. 4.

Lester, S. E. et al. Biological effects within no-take marine reserves: a global synthesis. *Mar. Ecol. Prog. Ser.* **384**, 33–46 (2009).

[ADS](#) [Google Scholar](#)

5. 5.

Halpern, B. S., Lester, S. E. & McLeod, K. L. Placing marine protected areas onto the ecosystem-based management seascape. *Proc.*

Natl Acad. Sci. USA **107**, 18312–18317 (2010).

[ADS](#) [CAS](#) [PubMed](#) [PubMed Central](#) [Google Scholar](#)

6. 6.

Carr, M. H. et al. Marine protected areas exemplify the evolution of science and policy. *Oceanography (Wash. D.C.)* **32**, 94–103 (2019).

[Google Scholar](#)

7. 7.

Gaines, S. D., White, C., Carr, M. H. & Palumbi, S. R. Designing marine reserve networks for both conservation and fisheries management. *Proc. Natl Acad. Sci. USA* **107**, 18286–18293 (2010).

[ADS](#) [CAS](#) [PubMed](#) [PubMed Central](#) [Google Scholar](#)

8. 8.

Edgar, G. J. et al. Global conservation outcomes depend on marine protected areas with five key features. *Nature* **506**, 216–220 (2014).

[ADS](#) [CAS](#) [PubMed](#) [PubMed Central](#) [Google Scholar](#)

9. 9.

Abell, R., Lehner, B., Thieme, M. & Linke, S. Looking beyond the fenceline: assessing protection gaps for the world's rivers. *Conserv. Lett.* **10**, 384–394 (2017).

[Google Scholar](#)

10. 10.

Grill, G. et al. Mapping the world's free-flowing rivers. *Nature* **569**, 215–221 (2019).

[ADS](#) [CAS](#) [Google Scholar](#)

11. 11.

Vörösmarty, C. J. et al. Global threats to human water security and river biodiversity. *Nature* **467**, 555–561 (2010).

[ADS](#) [Google Scholar](#)

12. 12.

McIntyre, P. B., Reidy Liermann, C. A. & Revenga, C. Linking freshwater fishery management to global food security and biodiversity conservation. *Proc. Natl Acad. Sci. USA* **113**, 12880–12885 (2016).

[CAS](#) [Google Scholar](#)

13. 13.

Fluet-Chouinard, E., Funge-Smith, S. & McIntyre, P. B. Global hidden harvest of freshwater fish revealed by household surveys. *Proc. Natl Acad. Sci. USA* **115**, 7623–7628 (2018).

[CAS](#) [Google Scholar](#)

14. 14.

Golden, C. D. et al. Nutrition: Fall in fish catch threatens human health. *Nature* **534**, 317–320 (2016).

[ADS](#) [Google Scholar](#)

15. 15.

Botsford, L. W., Micheli, F. & Hastings, A. Principles for the design of marine reserves. *Ecol. Appl.* **13**, 25–31 (2003).

[Google Scholar](#)

16. 16.

Gell, F. R. & Roberts, C. M. Benefits beyond boundaries: the fishery effects of marine reserves. *Trends Ecol. Evol.* **18**, 448–455 (2003).

[Google Scholar](#)

17. 17.

Hastings, A. & Botsford, L. W. Comparing designs of marine reserves for fisheries and for biodiversity. *Ecol. Appl.* **13**, 65–70 (2003).

[Google Scholar](#)

18. 18.

Pendleton, L. H. et al. Debating the effectiveness of marine protected areas. *ICES J. Mar. Sci.* **75**, 1156–1159 (2018).

[Google Scholar](#)

19. 19.

Chessman, B. C. Do protected areas benefit freshwater species? A broad-scale assessment for fish in Australia’s Murray–Darling Basin. *J. Appl. Ecol.* **50**, 969–976 (2013).

[Google Scholar](#)

20. 20.

Lawrence, D. J. et al. National parks as protected areas for U.S. freshwater fish diversity. *Conserv. Lett.* **4**, 364–371 (2011).

[Google Scholar](#)

21. 21.

Abell, R. et al. Concordance of freshwater and terrestrial biodiversity. *Conserv. Lett.* **4**, 127–136 (2011).

[Google Scholar](#)

22. 22.

Hilborn, R. Policy: Marine biodiversity needs more than protection. *Nature* **535**, 224–226 (2016).

[ADS](#) [CAS](#) [Google Scholar](#)

23. 23.

Halpern, B. S. et al. Achieving the triple bottom line in the face of inherent trade-offs among social equity, economic return, and conservation. *Proc. Natl Acad. Sci. USA* **110**, 6229–6234 (2013).

[ADS](#) [CAS](#) [Google Scholar](#)

24. 24.

Gill, D. A. et al. Capacity shortfalls hinder the performance of marine protected areas globally. *Nature* **543**, 665–669 (2017).

[ADS](#) [CAS](#) [Google Scholar](#)

25. 25.

Baird, I. G., Flaherty, M. S. & Baird, I. G. Mekong River fish conservation zones in southern Laos: assessing effectiveness using local ecological knowledge. *Environ. Manage.* **36**, 439–454 (2005).

[Google Scholar](#)

26. 26.

Loury, E. K. et al. Salty stories, fresh spaces: lessons for aquatic protected areas from marine and freshwater experiences. *Aquat.*

Conserv. **28**, 485–500 (2018).

[Google Scholar](#)

27. 27.

McCann, K. S. et al. Food webs and the sustainability of indiscriminate fisheries. *Can. J. Fish. Aquat. Sci.* **73**, 656–665 (2016).

[CAS](#) [Google Scholar](#)

28. 28.

Gutiérrez, N. L., Hilborn, R. & Defeo, O. Leadership, social capital and incentives promote successful fisheries. *Nature* **470**, 386–389 (2011).

[ADS](#) [Google Scholar](#)

29. 29.

Kramer, D. L. & Chapman, M. R. Implications of fish home range size and relocation for marine reserve function. *Environ. Biol. Fishes* **55**, 65–79 (1999).

[Google Scholar](#)

30. 30.

Morrison, S. A. A framework for conservation in a human-dominated world. *Conserv. Biol.* **29**, 960–964 (2015).

[PubMed](#) [PubMed Central](#) [Google Scholar](#)

31. 31.

Campos-Silva, J. V. & Peres, C. A. Community-based management induces rapid recovery of a high-value tropical freshwater fishery. *Sci. Rep.* **6**, 34745 (2016).

[ADS](#) [CAS](#) [PubMed](#) [PubMed Central](#) [Google Scholar](#)

32. 32.

Castello, L., Viana, J. P., Watkins, G., Pinedo-Vasquez, M. & Luzadis, V. A. Lessons from integrating fishers of arapaima in small-scale fisheries management at the Mamirauá Reserve, Amazon. *Environ. Manage.* **43**, 197–209 (2009).

[ADS](#) [PubMed](#) [PubMed Central](#) [Google Scholar](#)

33. 33.

Pinho, P. F., Orlove, B. & Lubell, M. Overcoming barriers to collective action in community-based fisheries management in the Amazon. *Hum. Organ.* **71**, 99–109 (2012).

[Google Scholar](#)

34. 34.

Thompson, P. M., Sultana, P. & Islam, N. Lessons from community based management of floodplain fisheries in Bangladesh. *J. Environ. Manage.* **69**, 307–321 (2003).

[PubMed](#) [PubMed Central](#) [Google Scholar](#)

35. 35.

Alexander, S. M., Epstein, G., Bodin, Ö., Armitage, D. & Campbell, D. Participation in planning and social networks increase social monitoring in community-based conservation. *Conserv. Lett.* **11**, e12562 (2018).

[Google Scholar](#)

36. 36.

Ostrom, E. A general framework for analyzing sustainability of social-ecological systems. *Science* **325**, 419–422 (2009).

[ADS](#) [MathSciNet](#) [CAS](#) [PubMed](#) [PubMed Central](#) [MATH](#) [Google Scholar](#)

37. 37.

Halpern, B. S., Lester, S. E. & Kellner, J. B. Spillover from marine reserves and the replenishment of fished stocks. *Environ. Conserv.* **36**, 268–276 (2009).

[Google Scholar](#)

38. 38.

Campbell Grant, E. H., Lowe, W. H. & Fagan, W. F. Living in the branches: population dynamics and ecological processes in dendritic networks. *Ecol. Lett.* **10**, 165–175 (2007).

[PubMed](#) [PubMed Central](#) [Google Scholar](#)

39. 39.

Palumbi, S. R. Population genetics, demographic connectivity, and the design of marine reserves. *Ecol. Appl.* **13**, 146–158 (2003).

[Google Scholar](#)

40. 40.

Tilman, D., May, R. M., Lehman, C. L. & Nowak, M. A. Habitat destruction and the extinction debt. *Nature* **371**, 65–66 (1994).

[ADS](#) [Google Scholar](#)

41. 41.

McIntyre, P. B. et al. in *Conservation of Freshwater Fishes* (eds Closs, G. P. et al.) 324–360 (Cambridge Univ. Press, 2015).

42. 42.

Dudgeon, D. et al. Freshwater biodiversity: importance, threats, status and conservation challenges. *Biol. Rev. Camb. Philos. Soc.* **81**, 163–182 (2006).

[PubMed](#) [PubMed Central](#) [Google Scholar](#)

43. 43.

Roberts, C. M. et al. Marine reserves can mitigate and promote adaptation to climate change. *Proc. Natl Acad. Sci. USA* **114**, 6167–6175 (2017).

[ADS](#) [CAS](#) [PubMed](#) [PubMed Central](#) [Google Scholar](#)

44. 44.

Koning, A. A., Moore, J., Suttidate, N., Hannigan, R. & McIntyre, P. B. Aquatic ecosystem impacts of land sharing versus sparing: nutrient loading to Southeast Asian rivers. *Ecosystems (N. Y.)* **20**, 393–405 (2017).

[CAS](#) [Google Scholar](#)

45. 45.

Froese, R. & Pauly, D. (eds) *FishBase* <http://www.fishbase.org> (2019).

46. 46.

Lamberti, G. A. & Hauer, F. R. *Methods in Stream Ecology* (Academic, 2017).

47. 47.

Jari Oksanen, F. et al. vegan: Community Ecology Package. R package version 2.5-6 <https://CRAN.R-project.org/package=vegan> (2019).

48. 48.

R Core Team. *R: A Language and Environment for Statistical Computing* <https://www.R-project.org/> (R Foundation for Statistical Computing, 2019).

49. 49.

Google Earth (November, 2015). Mae Ngao, Thailand.
<https://www.google.co.uk/earth/> (2020).

50. 50.

Environmental Systems Research Institute (ESRI). *ArcGIS Release 10.3* (2015).

51. 51.

Yamazaki, D. et al. A high-accuracy map of global terrain elevations. *Geophys. Res. Lett.* **44**, 5844–5853 (2017).

[ADS](#) [Google Scholar](#)

52. 52.

Robin, X. et al. pROC: an open-source package for R and S+ to analyze and compare ROC curves. *BMC Bioinformatics* **12**, 77 (2011).

[PubMed](#) [PubMed Central](#) [Google Scholar](#)

53. 53.

Jordán, F., Liu, W. C. & Andrew, J. D. Topological keystone species: measures of positional importance in food webs. *Oikos* **112**, 535–546 (2006).

[Google Scholar](#)

54. 54.

Bates, D., Maechler, M. & Ben Bolker, S. W. Fitting linear mixed-effects models using lme4. *J. Stat. Softw.* **67**, 1–48 (2015).

[Google Scholar](#)

55. 55.

Claudet, J. et al. Marine reserves: size and age do matter. *Ecol. Lett.* **11**, 481–489 (2008).

[Google Scholar](#)

56. 56.

Claudet, J. et al. Marine reserves: fish life history and ecological traits matter. *Ecol. Appl.* **20**, 830–839 (2010).

[CAS Google Scholar](#)

57. 57.

Johnson, J. B. & Omland, K. S. Model selection in ecology and evolution. *Trends Ecol. Evol.* **19**, 101–108 (2004).

[Google Scholar](#)

58. 58.

Barton, K. MuMIn: Multi-Model Inference. R package version 1.43.6
<https://CRAN.R-project.org/package=MuMIn> (2019).

[Download references](#)

Acknowledgements

We thank the communities of the Mae Ngao River basin for their participation in and support of this research, and the International Sustainable Development Studies Institute (Chiang Mai) for logistical support. Earlier drafts of the manuscript were improved by the McIntyre laboratory groups at the University of Wisconsin-Madison and Cornell University, and by comments from I. Baird, B. Peckarsky, K. Winemiller, E. Stanley, T. Ives, R. Abell and M. Thieme. Funding was provided by National Science Foundation grants DGE-0718123, DGE-1144752, and DEB-15011836 to A.A.K. and DGE-1144752 to K.M.P., a Harvey Fellowship and a Cornell Atkinson Center for Sustainability Postdoctoral Fellowship to A.A.K., and a David and Lucille Packard Fellowship to P.B.M. Additional funding provided by USAID's 'Wonders of the Mekong' Cooperative Agreement No: AID-OAA-A-16-00057.

Author information

Affiliations

1. Center for Limnology, University of Wisconsin-Madison, Madison, WI, USA

Aaron A. Koning, K. Martin Perales, Etienne Fluet-Chouinard & Peter B. McIntyre

2. Cornell Atkinson Center for Sustainability, Cornell University, Ithaca, NY, USA

Aaron A. Koning

3. Global Water Center, Department of Biology, University of Nevada, Reno, Reno, NV, USA

Aaron A. Koning

4. Department of Earth System Science, Stanford University, Stanford, CA, USA

Etienne Fluet-Chouinard

5. Department of Natural Resources, Cornell University, Ithaca, NY,
USA

Peter B. McIntyre

Authors

1. Aaron A. Koning

[View author publications](#)

You can also search for this author in [PubMed](#) [Google Scholar](#)

2. K. Martin Perales

[View author publications](#)

You can also search for this author in [PubMed](#) [Google Scholar](#)

3. Etienne Fluet-Chouinard

[View author publications](#)

You can also search for this author in [PubMed](#) [Google Scholar](#)

4. Peter B. McIntyre

[View author publications](#)

You can also search for this author in [PubMed](#) [Google Scholar](#)

Contributions

A.A.K. conceptualized the research, acquired funding, performed fieldwork, conducted analyses, and wrote the manuscript. K.M.P. performed fieldwork, assisted in methodological development, and edited the manuscript. E.F.-C. conducted analyses, contributed to creating figures, and edited the manuscript. P.B.M. contributed to research conceptualization and methodological development, and edited the manuscript.

Corresponding author

Correspondence to [Aaron A. Koning](#).

Ethics declarations

Competing interests

The authors declare no competing interests.

Additional information

Peer review information *Nature* thanks Edward Allison and the other, anonymous, reviewer(s) for their contribution to the peer review of this work.

Publisher's note Springer Nature remains neutral with regard to jurisdictional claims in published maps and institutional affiliations.

Extended data figures and tables

[**Extended Data Fig. 1 Frequency distribution of species-level maximum observed body length for the fish fauna of the study area of the Salween River basin.**](#)

The natural break at 20 cm (blue dashed line) was used to classify each species as relatively large (≥ 20 cm) versus smaller (< 20 cm).

[**Extended Data Fig. 2 Average total fish biomass measures in paired reserve \(red points\) and non-reserve \(blue points\) of varying ages.**](#)

Dotted lines correspond to nonlinear least squares estimates for reserves and non-reserves showing gains in both reserves and adjacent fished areas

over time.

Extended Data Fig. 3 Partial residual plots for all best averaged models of richness (R_r), density (D_r), and biomass (B_r) responses to no-take reserves.

Symbology indicates alternative groupings of fish species by body size and trophic group at each site ($n = 23$). The box and whisker plot shows the minimum and maximum values (excluding outliers) as ends of hashed lines, upper and lower quartiles as the upper and lower bounds of the box, the median as the bold line, and outliers (values exceeding 1.5 times the interquartile range) as points for reserves having no explicit penalty (No; $n = 4$) and those with an explicit penalty (Yes; $n = 19$). Full model results are found in Extended Data Tables [1–3](#).

Extended Data Table 1 Results of model averaging for richness reserve response (R_r)

[Full size table](#)

Extended Data Table 2 Results of model averaging for density reserve response (D_r)

[Full size table](#)

Extended Data Table 3 Results of model averaging for biomass reserve response (B_r)

[Full size table](#)

Supplementary information

Supplementary Information

The file contains additional text providing details of the cultural context in which the network of reserves studied here arose. Supplementary Figure 1. Shoaling fish in a reserve in Mae Ngao River, northern Thailand.

Reporting Summary

Rights and permissions

[Reprints and Permissions](#)

About this article



Cite this article

Koning, A.A., Perales, K.M., Fluet-Chouinard, E. *et al.* A network of grassroots reserves protects tropical river fish diversity. *Nature* **588**, 631–635 (2020). <https://doi.org/10.1038/s41586-020-2944-y>

[Download citation](#)

- Received: 14 January 2020
- Accepted: 05 October 2020
- Published: 25 November 2020
- Issue Date: 24 December 2020
- DOI: <https://doi.org/10.1038/s41586-020-2944-y>

Further reading

- [**River conservation by an Indigenous community**](#)
 - Edward H. Allison
 - & Violet Cho

Nature (2020)

- [Identifying Indicators to Evaluate Community-Managed Freshwater Protected Areas in the Lower Mekong Basin: A Review of Marine and Freshwater Examples](#)

- Erin K. Loury
- & Shaara M. Ainsley

Water (2020)

Comments

By submitting a comment you agree to abide by our [Terms](#) and [Community Guidelines](#). If you find something abusive or that does not comply with our terms or guidelines please flag it as inappropriate.

[Access through your institution](#)

[Change institution](#)

[Buy or subscribe](#)

Associated Content

Nature | News & Views

[River conservation by an Indigenous community](#)

- Edward H. Allison
- & Violet Cho

This article was downloaded by **calibre** from <https://www.nature.com/articles/s41586-020-2944-y>.

- Article
- [Published: 09 December 2020](#)

Impacts of speciation and extinction measured by an evolutionary decay clock

- [Jennifer F. Royal Cuthill](#) ORCID: [orcid.org/0000-0002-3139-9750^{1,2,3,4}](https://orcid.org/0000-0002-3139-9750),
- [Nicholas Guttenberg^{3,5,6}](#) &
- [Graham E. Budd](#) ORCID: [orcid.org/0000-0001-9007-4369⁷](https://orcid.org/0000-0001-9007-4369)

Nature volume **588**, pages636–641(2020) [Cite this article](#)

- 3964 Accesses
- 249 Altmetric
- [Metrics details](#)

Subjects

- [Machine learning](#)
- [Palaeontology](#)

Abstract

The hypothesis that destructive mass extinctions enable creative evolutionary radiations (creative destruction) is central to classic concepts of macroevolution^{1,2}. However, the relative impacts of extinction and radiation on the co-occurrence of species have not been directly

quantitatively compared across the Phanerozoic eon. Here we apply machine learning to generate a spatial embedding (multidimensional ordination) of the temporal co-occurrence structure of the Phanerozoic fossil record, covering 1,273,254 occurrences in the Paleobiology Database for 171,231 embedded species. This facilitates the simultaneous comparison of macroevolutionary disruptions, using measures independent of secular diversity trends. Among the 5% most significant periods of disruption, we identify the ‘big five’ mass extinction events², seven additional mass extinctions, two combined mass extinction–radiation events and 15 mass radiations. In contrast to narratives that emphasize post-extinction radiations^{1,3}, we find that the proportionally most comparable mass radiations and extinctions (such as the Cambrian explosion and the end-Permian mass extinction) are typically decoupled in time, refuting any direct causal relationship between them. Moreover, in addition to extinctions⁴, evolutionary radiations themselves cause evolutionary decay (modelled co-occurrence probability and shared fraction of species between times approaching zero), a concept that we describe as destructive creation. A direct test of the time to over-threshold macroevolutionary decay⁴ (shared fraction of species between two times ≤ 0.1), counted by the decay clock, reveals saw-toothed fluctuations around a Phanerozoic mean of 18.6 million years. As the Quaternary period began at a below-average decay-clock time of 11 million years, modern extinctions further increase life’s decay-clock debt.

[Access through your institution](#)

[Change institution](#)

[Buy or subscribe](#)

Access options

Subscribe to Journal

Get full journal access for 1 year

\$199.00

only \$3.83 per issue

Subscribe

All prices are NET prices.
VAT will be added later in the checkout.

Rent or Buy article

Get time limited or full article access on ReadCube.

from \$8.99

Rent or Buy

All prices are NET prices.

Additional access options:

- [Log in](#)
- [Access through your institution](#)
- [Learn about institutional subscriptions](#)

Fig. 1: Time structure of the fossil record.

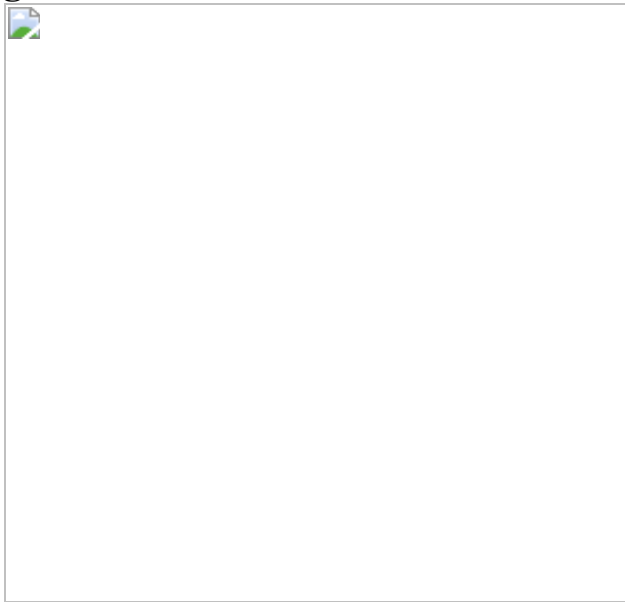


Fig. 2: Macroevolutionary decay.

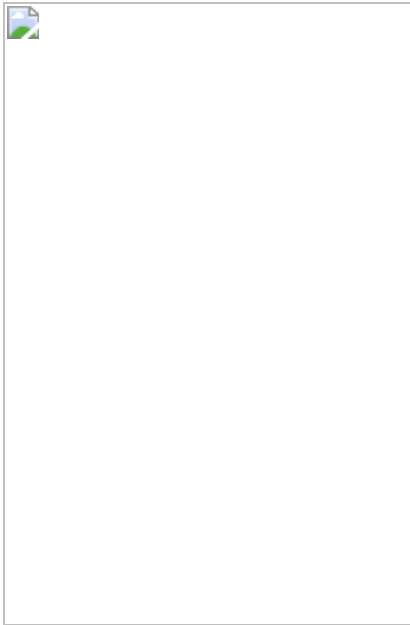
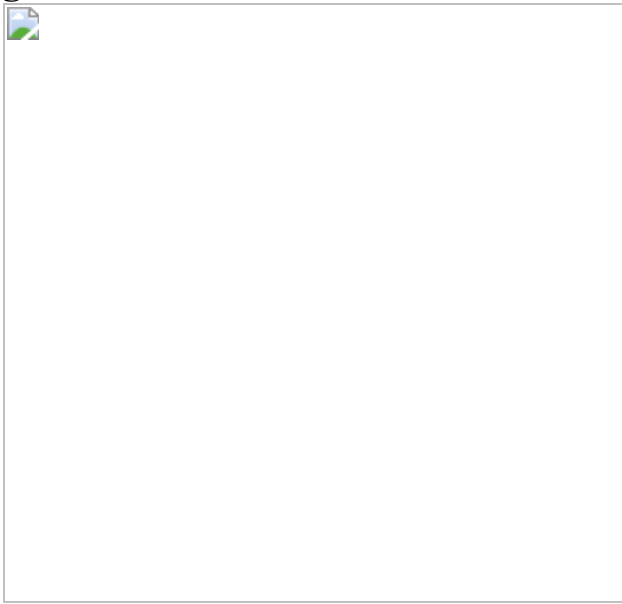


Fig. 3: Balance between mass radiation and extinction.



Data availability

Raw data are publicly available in the Paleobiology Database at <https://paleobiodb.org>. Additional source data for Figs. 1–3 are provided in the Dryad data repository (<https://doi.org/10.5061/dryad.b8gtht79t>). Additional data are provided as Extended Data Figs. 1–7.

Code availability

Custom computer code is provided as Supplementary Computer Code Code [1–6](#).

References

1. 1.

Simpson, G. G. *Tempo and Mode in Evolution* (Columbia Univ. Press, 1944).

2. 2.

Raup, D. M. The role of extinction in evolution. *Proc. Natl Acad. Sci. USA* **91**, 6758–6763 (1994).

[ADS](#) [CAS](#) [Article](#) [Google Scholar](#)

3. 3.

Hull, P. M., Darroch, S. A. F. & Erwin, D. H. Rarity in mass extinctions and the future of ecosystems. *Nature* **528**, 345–351 (2015).

[ADS](#) [CAS](#) [Article](#) [Google Scholar](#)

4. 4.

Van Valen, L. A new evolutionary law. *Evol. Theory* **1**, 1–30 (1973).

[Google Scholar](#)

5. 5.

Jablonski, D. Extinctions: a paleontological perspective. *Science* **253**, 754–757 (1991).

[ADS](#) [CAS](#) [Article](#) [Google Scholar](#)

6. 6.

Jablonski, D. Lessons from the past: evolutionary impacts of mass extinctions. *Proc. Natl Acad. Sci. USA* **98**, 5393–5398 (2001).

[ADS](#) [CAS](#) [Article](#) [Google Scholar](#)

7. 7.

Budd, G. E. & Mann, R. P. History is written by the victors: the effect of the push of the past on the fossil record. *Evolution* **72**, 2276–2291 (2018).

[Article](#) [Google Scholar](#)

8. 8.

Lehman, J. & Miikkulainen, R. Extinction events can accelerate evolution. *PLoS One* **10**, e0132886 (2015).

[Article](#) [Google Scholar](#)

9. 9.

Sepkoski, J. J. A kinetic model of Phanerozoic taxonomic diversity. III. Post-Paleozoic families and mass extinctions. *Paleobiology* **10**, 246–267 (1984).

[Article](#) [Google Scholar](#)

10. 10.

Stroud, J. T. & Losos, J. B. Ecological opportunity and adaptive radiation. *Annu. Rev. Ecol. Evol. Syst.* **47**, 507–532 (2016).

[Article](#) [Google Scholar](#)

11. 11.

Field, D. J., Benito, J., Chen, A., Jagt, J. W. M. & Ksepka, D. T. Late Cretaceous neornithine from Europe illuminates the origins of crown

birds. *Nature* **579**, 397–401 (2020).

[ADS](#) [CAS](#) [Article](#) [Google Scholar](#)

12. 12.

Wood, R. et al. Integrated records of environmental change and evolution challenge the Cambrian Explosion. *Nat. Ecol. Evol.* **3**, 528–538 (2019).

[Article](#) [Google Scholar](#)

13. 13.

Fan, J. X. et al. A high-resolution summary of Cambrian to Early Triassic marine invertebrate biodiversity. *Science* **367**, 272–277 (2020).

[ADS](#) [CAS](#) [Article](#) [Google Scholar](#)

14. 14.

Muscente, A. D. et al. Quantifying ecological impacts of mass extinctions with network analysis of fossil communities. *Proc. Natl Acad. Sci. USA* **115**, 5217–5222 (2018).

[ADS](#) [CAS](#) [Article](#) [Google Scholar](#)

15. 15.

Alroy, J. Are Sepkoski's evolutionary faunas dynamically coherent? *Evol. Ecol. Res.* **6**, 1–32 (2004).

[Google Scholar](#)

16. 16.

Brett, C. E., Ivany, L. C. & Schopf, K. M. Coordinated stasis: an overview. *Palaeogeogr. Palaeoclimatol. Palaeoecol.* **127**, 1–20 (1996).

[Article](#) [Google Scholar](#)

17. 17.

Blanchet, F. G., Cazelles, K. & Gravel, D. Co-occurrence is not evidence of ecological interactions. *Ecol. Lett.* **23**, 1050–1063 (2020).

[Article](#) [Google Scholar](#)

18. 18.

Sepkoski, J. J., Jr. Rates of speciation in the fossil record. *Phil. Trans. R. Soc. Lond. B* **353**, 315–326 (1998).

[Article](#) [Google Scholar](#)

19. 19.

Sadler, P. M. Quantitative biostratigraphy—achieving finer resolution in global correlation. *Annu. Rev. Earth Planet. Sci.* **32**, 187–213 (2004).

[ADS](#) [CAS](#) [Article](#) [Google Scholar](#)

20. 20.

Alroy, J. et al. Phanerozoic trends in the global diversity of marine invertebrates. *Science* **321**, 97–100 (2008).

[ADS](#) [CAS](#) [Article](#) [Google Scholar](#)

21. 21.

Na, L. & Kiessling, W. Diversity partitioning during the Cambrian radiation. *Proc. Natl Acad. Sci. USA* **112**, 4702–4706 (2015).

[ADS](#) [CAS](#) [Article](#) [Google Scholar](#)

22. 22.

Kearsey, T. I. et al. The terrestrial landscapes of tetrapod evolution in earliest Carboniferous seasonal wetlands of SE Scotland. *Palaeogeogr. Palaeoclimatol. Palaeoecol.* **457**, 52–69 (2016).

[Article](#) [Google Scholar](#)

23. 23.

Van Valen, L. Adaptive zones and the orders of mammals. *Evolution* **25**, 420–428 (1971).

[Article](#) [Google Scholar](#)

24. 24.

Benton, M. J. The Red Queen and the Court Jester: species diversity and the role of biotic and abiotic factors through time. *Science* **323**, 728–732 (2009).

[ADS](#) [CAS](#) [Article](#) [Google Scholar](#)

25. 25.

Newman, M. E. J. & Eble, G. J. Decline in extinction rates and scale invariance in the fossil record. *Paleobiology* **25**, 434–439 (1999).

[Article](#) [Google Scholar](#)

26. 26.

Fischer, A. G. & Arthur, M. A. in *Deep Water Carbonate Environments* (eds Cook, H. E. & Enos, P. E.) 10–50 (Society of Economic Paleontologists and Mineralogists, 1977).

27. 27.

Raup, D. M. & Sepkoski, J. J. Jr. Periodicity of extinctions in the geologic past. *Proc. Natl Acad. Sci. USA* **81**, 801–805 (1984).

[ADS](#) [CAS](#) [Article](#) [Google Scholar](#)

28. 28.

Gilinsky, N. L. Volatility and the Phanerozoic decline of background extinction intensity. *Paleobiology* **20**, 445–458 (1994).

[Article](#) [Google Scholar](#)

29. 29.

Pimiento, C. et al. The Pliocene marine megafauna extinction and its impact on functional diversity. *Nat. Ecol. Evol.* **1**, 1100–1106 (2017).

[Article](#) [Google Scholar](#)

30. 30.

Gradstein, F. M., Ogg, J. G. & Smith, A. G. *A Geologic Time Scale 2004* (Cambridge Univ. Press, 2004).

31. 31.

Ross, R. J., Adler, F. J., Amsden, T. W., Bergstrom, D. & Bergström, S. M. *The Ordovician System in the United States: Correlation Chart and Explanatory Note* (International Union of Geological Scientists, 1982).

32. 32.

Walker, J. D., Geissman, J. W., Bowring, S. A. & Babcock, L. E. The Geological Society of America geologic time scale. *Geol. Soc. Am. Bull.* **125**, 259–272 (2013).

[ADS](#) [CAS](#) [Article](#) [Google Scholar](#)

33. 33.

Gilinsky, N. L. & Bambach, R. K. Asymmetrical patterns of origination and extinction in higher taxa. *Paleobiology* **13**, 427–445 (1987).

[Article](#) [Google Scholar](#)

34. 34.

Peters, S. E. & McClenen, M. The Paleobiology Database application programming interface. *Paleobiology* **42**, 1–7 (2016).

[Article](#) [Google Scholar](#)

35. 35.

Caswell, B. A. & Frid, C. L. J. Learning from the past: functional ecology of marine benthos during eight million years of aperiodic hypoxia, lessons from the Late Jurassic. *Oikos* **122**, 1687–1699 (2013).

[Article](#) [Google Scholar](#)

36. 36.

van der Maaten, L. & Hinton, G. Visualizing data using t-SNE. *J. Mach. Learn. Res.* **9**, 2579–2605 (2008).

[MATH](#) [Google Scholar](#)

37. 37.

Mikolov, T., Chen, K., Corrado, G. S. & Dean, J. A. Efficient estimation of word representations in vector space.. Preprint at <https://arxiv.org/abs/1301.3781> (2013).

38. 38.

Schroff, F., Kalenichenko, D. & Philbin, J. in *Proceedings of the IEEE Conference on Computer Vision and Pattern Recognition* 815–823 (Institute of Electrical and Electronics, 2015).

39. 39.

Hoyal Cuthill, J. F., Guttenberg, N., Ledger, S., Crowther, R. & Huertas, B. Deep learning on butterfly phenotypes tests evolution's oldest mathematical model. *Sci. Adv.* **5**, eaaw4967 (2019).

[ADS](#) [Article](#) [Google Scholar](#)

40. 40.

Ruder, S. An overview of gradient descent optimization algorithms. Preprint at <https://arxiv.org/abs/1609.04747> (2017).

41. 41.

Dietterich, T. Overfitting and undercomputing in machine learning. *ACM Comput. Surv.* **27**, 326–327 (1995).

[Article](#) [Google Scholar](#)

42. 42.

Goldberg, Y. & Levy, O. word2vec explained: deriving Mikolov et al.'s negative-sampling word-embedding method. Preprint at <https://arxiv.org/abs/1402.3722> (2014).

43. 43.

Heim, N. A. & Peters, S. E. Covariation in macrostratigraphic and macroevolutionary patterns in the marine record of North America. *Geol. Soc. Am. Bull.* **123**, 620–630 (2011).

[ADS](#) [Article](#) [Google Scholar](#)

44. 44.

Bacaro, G. & Ricotta, C. A spatially explicit measure of beta diversity. *Community Ecol.* **8**, 41–46 (2007).

[Article](#) [Google Scholar](#)

[Download references](#)

Acknowledgements

This research was supported by funding from an IADS Research Fellowship (J.F.H.C.), EON Research Fellowship (J.F.H.C.) at the Tokyo Institute of Technology (supported by a grant from the John Templeton Foundation), Earth–Life Science Institute Research Interactions Committee Visitor Fund (N.G. and J.F.H.C.) and Swedish Research Council (VR grant no. 2015-04726, G.E.B.). We thank S. Newman and L. Schalkwyk for computing time and support, S. Conway Morris and E. Mitchell for highly constructive comments on the manuscript.

Author information

Affiliations

1. Institute of Analytics and Data Science, University of Essex, Colchester, UK

Jennifer F. Hoyal Cuthill

2. School of Life Sciences, University of Essex, Colchester, UK

Jennifer F. Hoyal Cuthill

3. Earth–Life Science Institute, Tokyo Institute of Technology, Tokyo, Japan

Jennifer F. Hoyal Cuthill & Nicholas Guttenberg

4. Department of Earth Sciences, University of Cambridge, Cambridge, UK

Jennifer F. Hoyal Cuthill

5. Cross Labs, Cross Compass Ltd, Tokyo, Japan

Nicholas Guttenberg

6. GoodAI, Prague, Czech Republic

Nicholas Guttenberg

7. Department of Earth Sciences, Palaeobiology Programme, Uppsala University, Uppsala, Sweden

Graham E. Budd

Authors

1. Jennifer F. Hoyal Cuthill

[View author publications](#)

You can also search for this author in [PubMed](#) [Google Scholar](#)

2. Nicholas Guttenberg

[View author publications](#)

You can also search for this author in [PubMed](#) [Google Scholar](#)

3. Graham E. Budd

[View author publications](#)

You can also search for this author in [PubMed](#) [Google Scholar](#)

Contributions

J.F.H.C., N.G and G.E.B. designed research, N.G. and J.F.H.C. wrote computer code and performed analyses and J.F.H.C. wrote the paper with input from all authors.

Corresponding author

Correspondence to [Jennifer F. Hoyal Cuthill](#).

Ethics declarations

Competing interests

The authors declare no competing interests.

Additional information

Peer review information *Nature* thanks Emily Mitchell and the other, anonymous, reviewer(s) for their contribution to the peer review of this work.

Publisher's note Springer Nature remains neutral with regard to jurisdictional claims in published maps and institutional affiliations.

Extended data figures and tables

[Extended Data Fig. 1 Methods graphical summary and effects of computer simulated diversity increases.](#)

a, Graphical summary of the ML method. **b–g**, Computer simulations of secular variation in diversity, testing effects on measures of co-occurrence structure used in this study. **b–g**, Linear (**b–d**) and exponential (**e–g**) diversity increases (Supplementary Computer Code [3](#)). **b, e**, Heatmaps visualizing the machine learnt spatial embedding distance between mean species locations at different times: yellow, closest; purple, farthest. **c, f**, Plot of embedding distances between successive times. **d, g**, Plot of first two principal component axes from the 16-dimensional spatial embedding. ML training times were 3,000 training epochs.

[Extended Data Fig. 2 Bootstrap data-resampling results and shared fraction of species between successive times versus mean embedding distance.](#)

a, Bootstrap data-resampling results: differences in embedding distances for 60 reference fossils, compared within 20 A, B, C triplets over 18 technical replicates of bootstrap data re-sampling and ML embedding training. Error bars, s.d. of the distance absolute(A–B) – absolute(A–C): mean 0.77. We expect the embedding distances to be comparatively stable within the time range over which co-occurrence probability is within the evolutionary decay range (observed to be mean 30 Myr for co-occurrence probability to reach 0.1 in the complete data set). **b, d**, Fraction of species shared between successive times, calculated exhaustively from raw species time ranges (histogram, Extended Data Fig. 6a). **c, e**, Distance in the ML spatial embedding between mean species locations at successive times. Compared times are at increments of 1 Myr. **b, c**, Complete fossil occurrence data set. **d, e**, Taxonomically screened data set. Vertical lines indicate the 5% most significant times of fractional species turnover (Fig. 3, Extended Data Fig. 4): mass extinctions (red), mass radiations (blue) and mixed mass extinction–radiations (magenta).

[Extended Data Fig. 3 Proportions of species originating versus going extinct.](#)

1-Myr increments from 600 to 0 Ma with a threshold of 30% species entry/exit threshold, grey square. This threshold highlights the top 66 times of turnover from 222 total turnover times identified among 600 times included in the analysis. Red, mass extinctions; blue, mass radiations; magenta, mixed mass extinction–radiations.

[Extended Data Fig. 4 Times of greatest fractional species turnover in the Phanerozoic fossil record.](#)

Top 5% most significant proportionate extinction or origination times (corresponding to the 30 labelled and coloured times in Fig. 3, > 42% species entry/exit threshold). Drill plots for focal times (key, top left) comparing stratigraphic ranges of all species occurring within 1 Myr of the focal time, vertically sorted into originations, extinctions and crossing ranges. Colours indicate over threshold mass extinctions (red), mass radiations (blue) and mixed mass extinction–radiations (magenta). Relevant

stratigraphic unit names, dates and corresponding references are those used in the PBDB (*ref. [30](#); **refs. [31,32](#)).

Extended Data Fig. 5 Breakdown by phylum of species extinctions and originations at the top 5% of evolutionary disruption times.

Associated with Fig. [3](#), Extended Data Fig. [4](#). Proportions of species entering (dark blue) or exiting (dark red) the fossil record are shown for the 19 most prevalent phyla in the data set (taxonomically screened data set).

Extended Data Fig. 6 Raw species time ranges and diversity counts and examples of the decay in probability of temporal co-occurrence.

a, Raw species time ranges: time ranges (maximum occurrence – minimum occurrence) for 137,779 fossil species (taxonomically screened data set). Taxonomically screened Phanerozoic data set (535–0 Ma): median = 6.5 Myr, mean = 9.95 Myr, s.d. = 12.86. Complete data set: median 7 Myr, mean 14.4 s.d. = 28.1 Myr. **b**, Raw diversity counts: sampled-in-bin taxonomic diversity of genera (grey dashed line) and families (black line) for the complete data set, output by the PBDB within the default time bin of geological ages (at maximum Ma). **c–f**, Examples of decays in co-occurrence probability (**c, e**) or in shared fraction of species (**d, f**), from base times 1 Myr before versus after major evolutionary disturbance events. Grey dashed lines indicate a value of 0.1. **c, d**, End-Permian mass extinction at 252 Ma. **e, f**, Carboniferous mass radiation at 358 Ma. Following a disturbance event, co-occurrence probabilities and shared fractions of species fall more rapidly to low levels because comparatively few living species co-occur with any species that were present in the past.

Extended Data Fig. 7 Conceptual diagram comparing measures of macroevolutionary decay, decay-clock detail focusing on the last 40 Myr and statistical relationships between measures of macroevolutionary disturbance and time.

a, Set representation of the shared fraction of species between compared times (for example, times t_1 and t_2). This measure is used in this study and is closely conceptually related to the co-occurrence probability calculated using the ML spatial embedding (see [Methods](#) for further details). **b**, Fraction of surviving species, a core concept of standard methods of survivor analysis for example⁴. These measures (**a**, **b**) will be equal if no new species have originated by time t_2 (scenario in **c**). Where new species have instead originated by time t_2 , their effect will be picked up by the measures used in this study (**a**), whereas the impact of new species would not be considered by measures only of the fraction of survivors from t_1 (**b**). **d**, Vertical lines indicate times of evolutionary disturbance (blue, mass radiations; red, mass extinctions, corresponding to Fig. [3](#); grey, turnover events below the mass-event threshold). **e**, (1), measures of disturbance to co-occurrence structure calculated between consecutive time windows are largely independent of Phanerozoic time (over which there have been secular trends in raw diversity²⁰). The shared fraction of species shows no significant relationship with time (taxonomically screened data set). The embedding distance (complete data set) shows a weak relationship across the whole Phanerozoic that is removed when Cenozoic data are excluded (data excluded in order to isolate hypothesized effect after initial data analysis), consistent with a weak effect on Cenozoic embedding distance from fossils with ranges extending to 0 Ma (which are particularly abundant in the data set). (2), proportions of species exiting or entering the fossil record within 1 Myr of a given time show no significant relationship with time (taxonomically screened data set). All statistical tests are two-tailed.

Supplementary information

[Reporting Summary](#)

[Supplementary Data](#)

This zip folder contains Supplementary Computer Code 1-6, with Python program files supplied in py or ipynb file format and in pdf format. Descriptions of each code are included in an accompanying text file.

Rights and permissions

[Reprints and Permissions](#)

About this article



Check for
updates

Cite this article

Hoyal Cuthill, J.F., Guttenberg, N. & Budd, G.E. Impacts of speciation and extinction measured by an evolutionary decay clock. *Nature* **588**, 636–641 (2020). <https://doi.org/10.1038/s41586-020-3003-4>

[Download citation](#)

- Received: 21 May 2020
- Accepted: 16 September 2020
- Published: 09 December 2020
- Issue Date: 24 December 2020
- DOI: <https://doi.org/10.1038/s41586-020-3003-4>

Comments

By submitting a comment you agree to abide by our [Terms](#) and [Community Guidelines](#). If you find something abusive or that does not comply with our terms or guidelines please flag it as inappropriate.

[Access through your institution](#)

[Change institution](#)

Buy or subscribe

This article was downloaded by **calibre** from <https://www.nature.com/articles/s41586-020-3003-4>

| [Section menu](#) | [Main menu](#) |

- Article
- [Published: 11 November 2020](#)

Transcriptome and translatome co-evolution in mammals

- [Zhong-Yi Wang¹](#) na1,
- [Evgeny Leushkin](#) 1 na1,
- [Angélica Liechti](#) [ORCID: orcid.org/0000-0002-0166-0639](#)²,
- [Svetlana Ovchinnikova¹](#),
- [Katharina Mößinger¹](#),
- [Thoomke Brüning¹](#),
- [Coralie Rummel²](#),
- [Frank Grützner](#) [ORCID: orcid.org/0000-0002-3088-7314](#)³,
- [Margarida Cardoso-Moreira](#) [ORCID: orcid.org/0000-0001-6639-3597](#)¹,
- [Peggy Janich](#) [ORCID: orcid.org/0000-0003-1045-7365](#)²,
- [David Gatfield](#) [ORCID: orcid.org/0000-0001-5114-2824](#)²,
- [Boubou Diagouraga⁴](#) nAff7,
- [Bernard de Massy⁴](#),
- [Mark E. Gill⁵](#),
- [Antoine H. F. M. Peters](#) [ORCID: orcid.org/0000-0002-0311-1887](#)^{5,6},
- [Simon Anders](#) [ORCID: orcid.org/0000-0003-4868-1805](#)¹ &
- [Henrik Kaessmann](#) [ORCID: orcid.org/0000-0001-7563-839X](#)¹

[Nature](#) volume **588**, pages642–647(2020) [Cite this article](#)

- 9223 Accesses
- 201 Altmetric
- [Metrics details](#)

Subjects

- [Gene expression](#)
- [Molecular evolution](#)

Abstract

Gene-expression programs define shared and species-specific phenotypes, but their evolution remains largely uncharacterized beyond the transcriptome layer¹. Here we report an analysis of the co-evolution of translatomes and transcriptomes using ribosome-profiling and matched RNA-sequencing data for three organs (brain, liver and testis) in five mammals (human, macaque, mouse, opossum and platypus) and a bird (chicken). Our within-species analyses reveal that translational regulation is widespread in the different organs, in particular across the spermatogenic cell types of the testis. The between-species divergence in gene expression is around 20% lower at the translatome layer than at the transcriptome layer owing to extensive buffering between the expression layers, which especially preserved old, essential and housekeeping genes. Translational upregulation specifically counterbalanced global dosage reductions during the evolution of sex chromosomes and the effects of meiotic sex-chromosome inactivation during spermatogenesis. Despite the overall prevalence of buffering, some genes evolved faster at the translatome layer —potentially indicating adaptive changes in expression; testis tissue shows the highest fraction of such genes. Further analyses incorporating mass spectrometry proteomics data establish that the co-evolution of transcriptomes and translatomes is reflected at the proteome layer. Together, our work uncovers co-evolutionary patterns and associated selective forces across the expression layers, and provides a resource for understanding their interplay in mammalian organs.

[Access through your institution](#)

[Change institution](#)

[Buy or subscribe](#)

Access options

[Subscribe to Journal](#)

Get full journal access for 1 year

\$199.00

only \$3.83 per issue

[Subscribe](#)

All prices are NET prices.

VAT will be added later in the checkout.

Rent or Buy article

Get time limited or full article access on ReadCube.

from \$8.99

[Rent or Buy](#)

All prices are NET prices.

Additional access options:

- [Log in](#)
- [Access through your institution](#)
- [Learn about institutional subscriptions](#)

Fig. 1: Regulatory dynamics across expression layers.

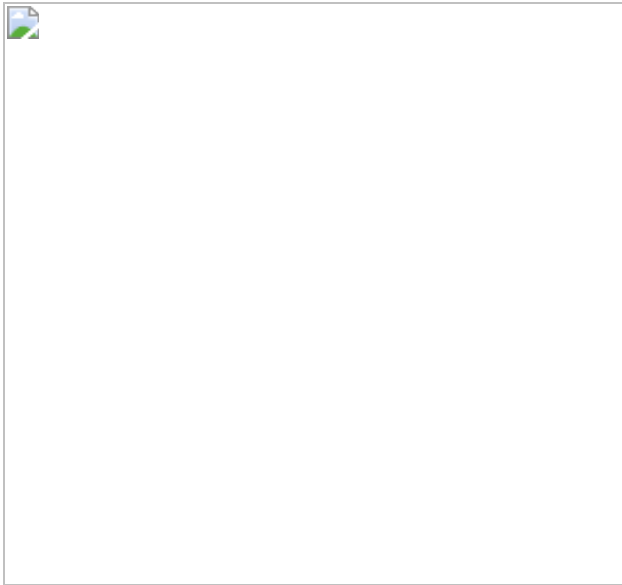


Fig. 2: Evolution of gene expression across expression layers.

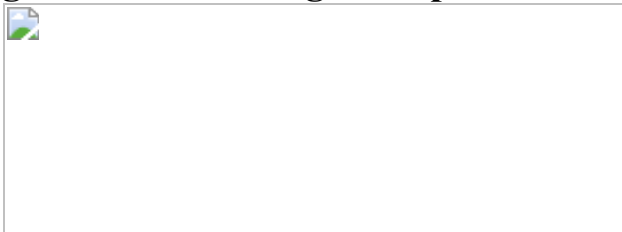


Fig. 3: Co-evolution of expression layers across gene classes.

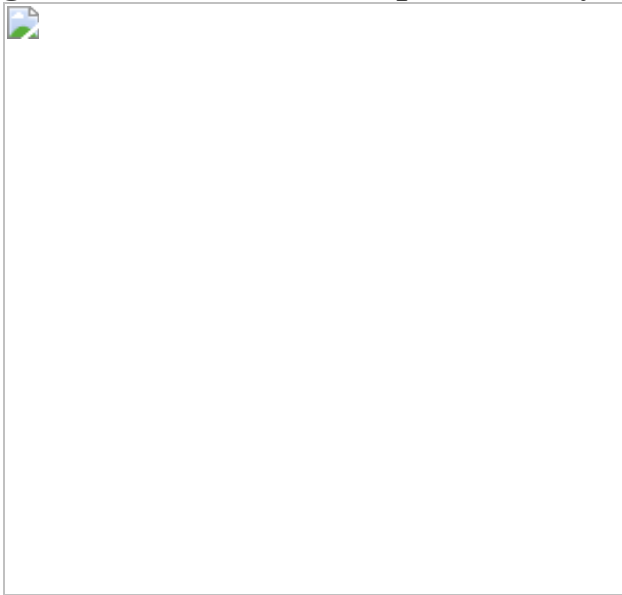
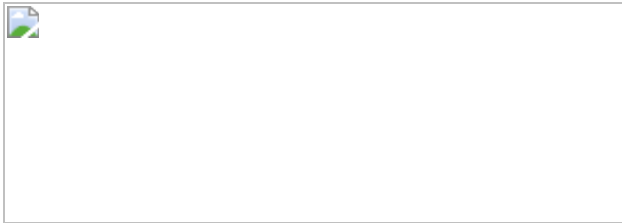


Fig. 4: Compensatory evolution of X-linked genes.



Data availability

Raw and processed Ribo-seq and RNA-seq data are available from ArrayExpress with accession number [E-MTAB-7247](#). All other data are available as supplementary information or are available upon request. The interactive data resource we created, *Ex²plorer*, is publicly available at <https://ex2plorer.kaessmannlab.org/>.

Code availability

Custom R scripts used to generate the results reported in the manuscript and processed data are available at
<https://github.com/evgenyleushkin/translatome>.

References

1. 1.

Necsulea, A. & Kaessmann, H. Evolutionary dynamics of coding and non-coding transcriptomes. *Nat. Rev. Genet.* **15**, 734–748 (2014).

[CAS](#) [PubMed](#) [Google Scholar](#)

2. 2.

Vogel, C. & Marcotte, E. M. Insights into the regulation of protein abundance from proteomic and transcriptomic analyses. *Nat. Rev. Genet.* **13**, 227–232 (2012).

[CAS](#) [PubMed](#) [PubMed Central](#) [Google Scholar](#)

3. 3.

Khan, Z. et al. Primate transcript and protein expression levels evolve under compensatory selection pressures. *Science* **342**, 1100–1104 (2013).

[ADS](#) [CAS](#) [PubMed](#) [PubMed Central](#) [Google Scholar](#)

4. 4.

Brar, G. A. & Weissman, J. S. Ribosome profiling reveals the what, when, where and how of protein synthesis. *Nat. Rev. Mol. Cell Biol.* **16**, 651–664 (2015).

[CAS](#) [PubMed](#) [PubMed Central](#) [Google Scholar](#)

5. 5.

Ingolia, N. T., Ghaemmaghami, S., Newman, J. R. & Weissman, J. S. Genome-wide analysis *in vivo* of translation with nucleotide resolution using ribosome profiling. *Science* **324**, 218–223 (2009).

[ADS](#) [CAS](#) [PubMed](#) [PubMed Central](#) [Google Scholar](#)

6. 6.

McManus, J., May, G., Spealman, P. & Shteyman, A. Ribosome profiling reveals post-transcriptional buffering of divergent gene expression in yeast. *Genome Res.* **24**, 422–430 (2014).

[CAS](#) [PubMed](#) [PubMed Central](#) [Google Scholar](#)

7. 7.

Artieri, C. G. & Fraser, H. B. Evolution at two levels of gene expression in yeast. *Genome Res.* **24**, 411–421 (2014).

[CAS](#) [PubMed](#) [PubMed Central](#) [Google Scholar](#)

8. 8.

Stadler, M. & Fire, A. Conserved translatome remodeling in nematode species executing a shared developmental transition. *PLoS Genet.* **9**, e1003739 (2013).

[PubMed](#) [PubMed Central](#) [Google Scholar](#)

9. 9.

Albert, F. W., Muzzey, D., Weissman, J. S. & Kruglyak, L. Genetic influences on translation in yeast. *PLoS Genet.* **10**, e1004692 (2014).

[PubMed](#) [PubMed Central](#) [Google Scholar](#)

10. 10.

Wang, Z. et al. Evolution of gene regulation during transcription and translation. *Genome Biol. Evol.* **7**, 1155–1167 (2015).

[CAS](#) [PubMed](#) [PubMed Central](#) [Google Scholar](#)

11. 11.

Wang, S. H., Hsiao, C. J., Khan, Z. & Pritchard, J. K. Post-translational buffering leads to convergent protein expression levels between primates. *Genome Biol.* **19**, 83 (2018).

[PubMed](#) [PubMed Central](#) [Google Scholar](#)

12. 12.

Hou, J. et al. Extensive allele-specific translational regulation in hybrid mice. *Mol. Syst. Biol.* **11**, 825 (2015).

[PubMed](#) [PubMed Central](#) [Google Scholar](#)

13. 13.

Csárdi, G., Franks, A., Choi, D. S., Airoldi, E. M. & Drummond, D. A. Accounting for experimental noise reveals that mRNA levels, amplified by post-transcriptional processes, largely determine steady-state protein levels in yeast. *PLoS Genet.* **11**, e1005206 (2015).

[PubMed](#) [PubMed Central](#) [Google Scholar](#)

14. 14.

Kleene, K. C. A possible meiotic function of the peculiar patterns of gene expression in mammalian spermatogenic cells. *Mech. Dev.* **106**, 3–23 (2001).

[CAS](#) [PubMed](#) [Google Scholar](#)

15. 15.

Kleene, K. C. Patterns, mechanisms, and functions of translation regulation in mammalian spermatogenic cells. *Cytogenet. Genome Res.* **103**, 217–224 (2003).

[CAS](#) [PubMed](#) [Google Scholar](#)

16. 16.

Iguchi, N., Tobias, J. W. & Hecht, N. B. Expression profiling reveals meiotic male germ cell mRNAs that are translationally up- and down-regulated. *Proc. Natl Acad. Sci. USA* **103**, 7712–7717 (2006).

[ADS](#) [CAS](#) [PubMed](#) [Google Scholar](#)

17. 17.

Brawand, D. et al. The evolution of gene expression levels in mammalian organs. *Nature* **478**, 343–348 (2011).

[ADS](#) [CAS](#) [PubMed](#) [Google Scholar](#)

18. 18.

Ramm, S. A., Schärer, L., Ehmcke, J. & Wistuba, J. Sperm competition and the evolution of spermatogenesis. *Mol. Hum. Reprod.* **20**, 1169–1179 (2014).

[CAS](#) [PubMed](#) [Google Scholar](#)

19. 19.

Lareau, L. F., Inada, M., Green, R. E., Wengrod, J. C. & Brenner, S. E. Unproductive splicing of SR genes associated with highly conserved and ultraconserved DNA elements. *Nature* **446**, 926–929 (2007).

[ADS](#) [CAS](#) [PubMed](#) [Google Scholar](#)

20. 20.

Zarate, Y. A. & Fish, J. L. SATB2-associated syndrome: mechanisms, phenotype, and practical recommendations. *Am. J. Med. Genet. A.* **173**, 327–337 (2017).

[PubMed](#) [Google Scholar](#)

21. 21.

Sharma, K. et al. Cell type- and brain region-resolved mouse brain proteome. *Nat. Neurosci.* **18**, 1819–1831 (2015).

[CAS](#) [PubMed](#) [Google Scholar](#)

22. 22.

Wang, D. et al. A deep proteome and transcriptome abundance atlas of 29 healthy human tissues. *Mol. Syst. Biol.* **15**, e8503 (2019).

[PubMed](#) [PubMed Central](#) [Google Scholar](#)

23. 23.

Bartha, I., di Julio, J., Venter, J. C. & Telenti, A. Human gene essentiality. *Nat. Rev. Genet.* **19**, 51–62 (2018).

[CAS](#) [PubMed](#) [Google Scholar](#)

24. 24.

Eisenberg, E. & Levanon, E. Y. Human housekeeping genes, revisited. *Trends Genet.* **29**, 569–574 (2013).

[CAS](#) [PubMed](#) [Google Scholar](#)

25. 25.

Cardoso-Moreira, M. et al. Gene expression across mammalian organ development. *Nature* **571**, 505–509 (2019).

[CAS](#) [PubMed](#) [PubMed Central](#) [Google Scholar](#)

26. 26.

Chen, W. H., Trachana, K., Lercher, M. J. & Bork, P. Younger genes are less likely to be essential than older genes, and duplicates are less likely to be essential than singletons of the same age. *Mol. Biol. Evol.* **29**, 1703–1706 (2012).

[CAS](#) [PubMed](#) [PubMed Central](#) [Google Scholar](#)

27. 27.

Graves, J. A. Evolution of vertebrate sex chromosomes and dosage compensation. *Nat. Rev. Genet.* **17**, 33–46 (2016).

[CAS](#) [PubMed](#) [Google Scholar](#)

28. 28.

Julien, P. et al. Mechanisms and evolutionary patterns of mammalian and avian dosage compensation. *PLoS Biol.* **10**, e1001328 (2012).

[CAS](#) [PubMed](#) [PubMed Central](#) [Google Scholar](#)

29. 29.

Marin, R. et al. Convergent origination of a *Drosophila*-like dosage compensation mechanism in a reptile lineage. *Genome Res.* **27**, 1974–1987 (2017).

[CAS](#) [PubMed](#) [PubMed Central](#) [Google Scholar](#)

30. 30.

Turner, J. M. Meiotic silencing in mammals. *Annu. Rev. Genet.* **49**, 395–412 (2015).

[CAS](#) [PubMed](#) [Google Scholar](#)

31. 31.

Soumillon, M. et al. Cellular source and mechanisms of high transcriptome complexity in the mammalian testis. *Cell Rep.* **3**, 2179–2190 (2013).

[CAS](#) [PubMed](#) [Google Scholar](#)

32. 32.

Faucillion, M. L. & Larsson, J. Increased expression of X-linked genes in mammals is associated with a higher stability of transcripts and an increased ribosome density. *Genome Biol. Evol.* **7**, 1039–1052 (2015).

[CAS](#) [PubMed](#) [PubMed Central](#) [Google Scholar](#)

33. 33.

Chen, X. & Zhang, J. No X-chromosome dosage compensation in human proteomes. *Mol. Biol. Evol.* **32**, 1456–1460 (2015).

[CAS](#) [PubMed](#) [PubMed Central](#) [Google Scholar](#)

34. 34.

Bader, D. M. et al. Negative feedback buffers effects of regulatory variants. *Mol. Syst. Biol.* **11**, 785 (2015).

[PubMed](#) [PubMed Central](#) [Google Scholar](#)

35. 35.

Schaefke, B., Sun, W., Li, Y. S., Fang, L. & Chen, W. The evolution of posttranscriptional regulation. *Wiley Interdiscip. Rev. RNA* **9**, e1485 (2018).

[Google Scholar](#)

36. 36.

Ingolia, N. T., Brar, G. A., Rouskin, S., McGeachy, A. M. & Weissman, J. S. The ribosome profiling strategy for monitoring translation in vivo by deep sequencing of ribosome-protected mRNA fragments. *Nat. Protoc.* **7**, 1534–1550 (2012).

[CAS](#) [PubMed](#) [PubMed Central](#) [Google Scholar](#)

37. 37.

Yates, A. et al. Ensembl 2016. *Nucleic Acids Res.* **44**, D710–D716 (2016).

[CAS](#) [PubMed](#) [Google Scholar](#)

38. 38.

Martin, M. Cutadapt removes adapter sequences from high-throughput sequencing reads. *EMBnet.journal* **17**, 10–12 (2011).

[Google Scholar](#)

39. 39.

Kim, D. et al. TopHat2: accurate alignment of transcriptomes in the presence of insertions, deletions and gene fusions. *Genome Biol.* **14**, R36 (2013).

[PubMed](#) [PubMed Central](#) [Google Scholar](#)

40. 40.

Pertea, M. et al. StringTie enables improved reconstruction of a transcriptome from RNA-seq reads. *Nat. Biotechnol.* **33**, 290–295 (2015).

[CAS](#) [PubMed](#) [PubMed Central](#) [Google Scholar](#)

41. 41.

Trapnell, C. et al. Transcript assembly and quantification by RNA-seq reveals unannotated transcripts and isoform switching during cell differentiation. *Nat. Biotechnol.* **28**, 511–515 (2010).

[CAS](#) [PubMed](#) [PubMed Central](#) [Google Scholar](#)

42. 42.

Tress, M. L., Abascal, F. & Valencia, A. Alternative splicing may not be the key to proteome complexity. *Trends Biochem. Sci.* **42**, 98–110 (2017).

[CAS](#) [PubMed](#) [Google Scholar](#)

43. 43.

Gonzàlez-Porta, M., Frankish, A., Rung, J., Harrow, J. & Brazma, A. Transcriptome analysis of human tissues and cell lines reveals one dominant transcript per gene. *Genome Biol.* **14**, R70 (2013).

[PubMed](#) [PubMed Central](#) [Google Scholar](#)

44. 44.

Quast, C. et al. The SILVA ribosomal RNA gene database project: improved data processing and web-based tools. *Nucleic Acids Res.* **41**, D590–D596 (2013).

[CAS](#) [PubMed](#) [Google Scholar](#)

45. 45.

Chan, P. P. & Lowe, T. M. GtRNAdb 2.0: an expanded database of transfer RNA genes identified in complete and draft genomes. *Nucleic Acids Res.* **44**, D184–D189 (2016).

[CAS](#) [PubMed](#) [Google Scholar](#)

46. 46.

Langmead, B. & Salzberg, S. L. Fast gapped-read alignment with Bowtie 2. *Nat. Methods* **9**, 357–359 (2012).

[CAS](#) [PubMed](#) [PubMed Central](#) [Google Scholar](#)

47. 47.

R Core Team. R: a language and environment for statistical computing (R Foundation for Statistical Computing, 2012).

48. 48.

Yanai, I. et al. Genome-wide midrange transcription profiles reveal expression level relationships in human tissue specification. *Bioinformatics* **21**, 650–659 (2005).

[CAS](#) [PubMed](#) [Google Scholar](#)

49. 49.

Futschik, M. E. & Carlisle, B. Noise-robust soft clustering of gene expression time-course data. *J. Bioinform. Comput. Biol.* **3**, 965–988 (2005).

[CAS](#) [PubMed](#) [Google Scholar](#)

50. 50.

Alexa, A., Rahnenführer, J. & Lengauer, T. Improved scoring of functional groups from gene expression data by decorrelating GO graph structure. *Bioinformatics* **22**, 1600–1607 (2006).

[CAS](#) [PubMed](#) [Google Scholar](#)

51. 51.

Love, M. I., Huber, W. & Anders, S. Moderated estimation of fold change and dispersion for RNA-seq data with DESeq2. *Genome Biol.* **15**, 550 (2014).

[PubMed](#) [PubMed Central](#) [Google Scholar](#)

52. 52.

Bedford, T. & Hartl, D. L. Optimization of gene expression by natural selection. *Proc. Natl Acad. Sci. USA* **106**, 1133–1138 (2009).

[ADS](#) [CAS](#) [PubMed](#) [Google Scholar](#)

53. 53.

Paradis, E. & Schliep, K. ape 5.0: an environment for modern phylogenetics and evolutionary analyses in R. *Bioinformatics* **35**, 526–528 (2019).

[CAS](#) [PubMed](#) [Google Scholar](#)

54. 54.

Benjamini, Y. & Hochberg, Y. Controlling the false discovery rate: a practical and powerful approach to multiple testing. *J. R. Stat. Soc. B* **57**, 289–300 (1995).

[MathSciNet](#) [MATH](#) [Google Scholar](#)

55. 55.

Lek, M. et al. Analysis of protein-coding genetic variation in 60,706 humans. *Nature* **536**, 285–291 (2016).

[CAS](#) [PubMed](#) [PubMed Central](#) [Google Scholar](#)

56. 56.

Shihab, H. A., Rogers, M. F., Campbell, C. & Gaunt, T. R. HiPred: an integrative approach to predicting haploinsufficient genes. *Bioinformatics* **33**, 1751–1757 (2017).

[CAS](#) [PubMed](#) [PubMed Central](#) [Google Scholar](#)

57. 57.

Shao, Y. et al. GenTree, an integrated resource for analyzing the evolution and function of primate-specific coding genes. *Genome Res.* **29**, 682–696 (2019).

[CAS](#) [PubMed](#) [PubMed Central](#) [Google Scholar](#)

58. 58.

Yang, Z. PAML: a program package for phylogenetic analysis by maximum likelihood. *Comput. Appl. Biosci.* **13**, 555–556 (1997).

[CAS](#) [PubMed](#) [Google Scholar](#)

[Download references](#)

Acknowledgements

We thank K. Harshman and the Lausanne Genomics Technology Facility for high-throughput sequencing support; I. Xenarios and the Vital-IT

computational facility for computational support; M. Baumann and S. Richling from the Heidelberg University Computational Center (Universitätsrechenzentrum, URZ) for supporting our computational work on the bwForCluster; M. Sanchez-Delgado for figure assistance; J. VandeBerg for opossum samples; P. Khaitovich for human and macaque samples; P. Jensen and A. Fallahshahroudi for red junglefowl samples; and A. B. Arpat and the Kaessmann group for discussions. This work was primarily supported by a grant (KA 1710/3-1) to H.K. from the German Research Council (DFG) and a European Research Council grant (615253, OntoTransEvol) to H.K. We acknowledge computational support by the state of Baden-Württemberg through bwHPC and the German Research Foundation (DFG) through grant INST 35/1134-1 FUGG. D.G. acknowledges funding through the National Centre of Competence in Research (NCCR) RNA & Disease; F.G. is supported by an Australian Research Council Fellowship; S.O. was supported by the DFG (CRC 1366); S.A. was supported by the DFG (SFB 1036); M.E.G. and A.H.F.M.P acknowledge funding from the Swiss National Science Foundation (31003A_146293) and the Novartis Research Foundation; and B.d.M. was funded by grants from the Centre National pour la Recherche Scientifique (CNRS) and the European Research Council (ERC) Executive Agency under the European Community's Seventh Framework Programme (FP7/2007-2013 Grant Agreement no. 322788).

Author information

Author notes

1. Boubou Diagouraga

Present address: Centre de Biochimie Structurale (CBS), CNRS, INSERM, Université de Montpellier, Montpellier, France

2. These authors contributed equally: Zhong-Yi Wang, Evgeny Leushkin

Affiliations

1. Center for Molecular Biology of Heidelberg University (ZMBH),
DKFZ-ZMBH Alliance, Heidelberg, Germany

Zhong-Yi Wang, Evgeny Leushkin, Svetlana Ovchinnikova, Katharina Mößinger, Thoomke Brüning, Margarida Cardoso-Moreira, Simon Anders & Henrik Kaessmann

2. Center for Integrative Genomics, University of Lausanne, Lausanne, Switzerland

Angélica Liechti, Coralie Rummel, Peggy Janich & David Gatfield

3. Robinson Research Institute, School of Biological Sciences, University of Adelaide, Adelaide, South Australia, Australia

Frank Grützner

4. Institute of Human Genetics, Centre National de la Recherche Scientifique, Université de Montpellier, Montpellier, France

Boubou Diagouraga & Bernard de Massy

5. Friedrich Miescher Institute for Biomedical Research, Basel, Switzerland

Mark E. Gill & Antoine H. F. M. Peters

6. Faculty of Sciences, University of Basel, Basel, Switzerland

Antoine H. F. M. Peters

Authors

1. Zhong-Yi Wang
[View author publications](#)

You can also search for this author in [PubMed](#) [Google Scholar](#)

2. Evgeny Leushkin

[View author publications](#)

You can also search for this author in [PubMed](#) [Google Scholar](#)

3. Angélica Liechti

[View author publications](#)

You can also search for this author in [PubMed](#) [Google Scholar](#)

4. Svetlana Ovchinnikova

[View author publications](#)

You can also search for this author in [PubMed](#) [Google Scholar](#)

5. Katharina Mößinger

[View author publications](#)

You can also search for this author in [PubMed](#) [Google Scholar](#)

6. Thoomke Brüning

[View author publications](#)

You can also search for this author in [PubMed](#) [Google Scholar](#)

7. Coralie Rummel

[View author publications](#)

You can also search for this author in [PubMed](#) [Google Scholar](#)

8. Frank Grützner

[View author publications](#)

You can also search for this author in [PubMed](#) [Google Scholar](#)

9. Margarida Cardoso-Moreira

[View author publications](#)

You can also search for this author in [PubMed](#) [Google Scholar](#)

10. Peggy Janich

[View author publications](#)

You can also search for this author in [PubMed](#) [Google Scholar](#)

11. David Gatfield

[View author publications](#)

You can also search for this author in [PubMed](#) [Google Scholar](#)

12. Boubou Diagouraga

[View author publications](#)

You can also search for this author in [PubMed](#) [Google Scholar](#)

13. Bernard de Massy

[View author publications](#)

You can also search for this author in [PubMed](#) [Google Scholar](#)

14. Mark E. Gill

[View author publications](#)

You can also search for this author in [PubMed](#) [Google Scholar](#)

15. Antoine H. F. M. Peters

[View author publications](#)

You can also search for this author in [PubMed](#) [Google Scholar](#)

16. Simon Anders

[View author publications](#)

You can also search for this author in [PubMed](#) [Google Scholar](#)

17. Henrik Kaessmann

[View author publications](#)

You can also search for this author in [PubMed](#) [Google Scholar](#)

Contributions

H.K. conceived and designed the original study. The work was supervised by H.K. and E.L. Z.-Y.W. and E.L. processed all data and performed the analyses; A.L., K.M., T.B. and C.R. performed all experimental work. F.G. provided platypus samples and related biological expertise. M.C.-M. provided key analytical ideas and discussions. B.D., B.d.M., M.E.G. and A.H.F.M.P provided purified mouse spermatogenic cell samples. P.J. and D.G. helped to establish the original ribosome-profiling method for solid tissues. D.G. provided key experimental input and guidance during the data production and initial analysis phase. S.O. developed the *Ex²plorer* app. S.A. provided key statistical advice. Z.-Y.W., E.L. and H.K. wrote the manuscript, with input from all authors.

Corresponding authors

Correspondence to [Evgeny Leushkin](#) or [Henrik Kaessmann](#).

Ethics declarations

Competing interests

The authors declare no competing interests.

Additional information

Peer review information *Nature* thanks Hunter Fraser, Bo Xia, Itai Yanai and the other, anonymous, reviewer(s) for their contribution to the peer review of this work.

Publisher's note Springer Nature remains neutral with regard to jurisdictional claims in published maps and institutional affiliations.

Extended data figures and tables

Extended Data Fig. 1 Information on generated RNA-seq and Ribo-seq data.

a, Ribosome footprint length distributions across Ribo-seq libraries (nt, nucleotides). **b**, Fractions of Ribo-seq and RNA-seq reads mapped to 5'-untranslated regions (5'-UTRs), coding sequences (CDSs) and 3' untranslated regions (3'-UTRs), respectively. **c**, Distribution of Ribo-seq and RNA-seq reads across the three reading frames in the CDS of dominant splicing isoforms (frame 1: canonical reading frame). **d**, Mean normalized density of footprints along the coding region of the dominant isoforms of protein-coding genes for the brain Ribo-seq data. The Ribo-seq read (A-site) density for each position is plotted relative to the first nucleotide position of the start codon. **e–h**, Spearman's correlation coefficient (ρ) of read counts for protein-coding genes with a mean read count > 1 between the two technical replicates for mouse liver Ribo-seq (**e**) and RNA-seq (**f**) data, and for chicken liver Ribo-seq (**g**) and RNA-seq (**h**) data. **i**, Correlations between biological replicates for Ribo-seq and RNA-seq data. Each dot corresponds to Spearman's correlation coefficient (ρ) in pairs of biological replicates for every species-organ combination. Only one replicate (therefore no pairs) is available for the human liver transcriptome, only two replicates (one pair) are available for the human testis transcriptome and translatome, and only two replicates (one pair) are available for the platypus brain transcriptome. The correlation coefficients between the replicates are similar for the two data types and statistically indistinguishable ($P = 0.159$) in a Mann–Whitney U test (two-sided). **j**, Comparisons of gene-expression (rank) changes between the three expression layers. Changes in gene-expression ranks were calculated between expression layers (that is, from transcriptome to translatome, from transcriptome to proteome, and from translatome to proteome), and Spearman's ρ was calculated to estimate the similarity of rank changes between the different pairs of expression layers. **k–n**, PCA based on 5,060 robustly expressed (median FPKM > 1 across organ libraries) 1:1 amniote orthologues. Factorial maps represent the relations of PC2 versus PC1 (**k**), PC3 versus PC1 (**l**) and PC4 versus PC1 (**m**). The scree plot (**n**) indicates the percentage of variance explained by each of the first 10 PCs. **o**, Expression variation at the two expression layers across mammalian organs for downsampled data. For this analysis data were downsampled to 2.5

million reads in each library. See Fig. [1d](#) for the analysis of the full dataset. Organ and species icons are from a previous study^{[25](#)}.

[Extended Data Fig. 2 Correlations of gene-expression levels between sequenced libraries.](#)

The heat map of the pairwise Spearman's correlation coefficient (ρ) is based on the set of 5,060 robustly expressed (median FPKM > 1 across organ libraries) 1:1 amniote orthologues for perfectly aligned regions (see [Methods](#)). It represents the degree of similarity of gene-expression profiles between data types (translatome, transcriptome), species (human, macaque, mouse, opossum, platypus, chicken) and tissues (brain, liver, testis).

[Extended Data Fig. 3 Quality assessment and analysis of mouse spermatogenesis data.](#)

a, Ribosome footprint length distributions across Ribo-seq libraries (nt, nucleotides). **b**, Fractions of Ribo-seq and RNA-seq reads mapped to 5'-UTRs, CDSs and 3'-UTRs, respectively. **c**, Distribution of Ribo-seq and RNA-seq reads across the three reading frames in the CDS of dominant splicing isoforms (frame 1: canonical reading frame). **d**, PCA based on 11,057 genes robustly expressed (median FPKM > 1) across mouse spermatogenesis libraries. The scree plot (inset) indicates the percentage of variance explained by each of the first 10 PCs. **e**, Expression variation at the translatome layer calculated for simulated scenarios with different amounts of translational contribution (see [Methods](#) for details). Dashed line corresponds to IQR calculated at the transcriptome layer. **f**, **g**, Spearman's ρ between transcription abundance and translational efficiency was calculated for 5,060 robustly expressed (median FPKM > 1 across organ libraries) 1:1 amniote orthologues in bulk testis across the amniotes (**f**) and across spermatogenesis stages in mouse (**g**). **h**, **i**, Translational efficiency (**h**) and translational shift (**i**) for clusters of genes (gene numbers in parentheses) with distinct translational efficiency patterns (Mfuzz clustering). Arrows indicate translational efficiency increases or decreases compared to the respective global pattern (Fig. [1e](#)). * indicates a cluster of genes, which

escape expression repression and delay at the translatome layer. **j**, Expression of individual genes, representing each of the five translational efficiency clusters, at the transcriptome and translatome layers (left column); shift in expression timing between expression layers for the corresponding genes (right column) with crosses representing the centres of mass of gene expression across spermatogenesis. **k**, Tissue-specificity (tissue Tau) across translational efficiency clusters. Cluster I, highlighted in colour, is dominated by testis-specific genes. Box plots represent the median \pm 25th and 75th percentiles; whiskers are at $1.5 \times$ IQR. **l**, Gene-expression divergence at the two expression layers for genes with stage-specific expression across spermatogenesis among 8,109 1:1 orthologues robustly expressed ($\text{FPKM} > 1$) in macaque, mouse and opossum.

Extended Data Fig. 4 GO enrichment analyses.

a–d, Top five significantly enriched GO terms among genes with high (**a**, **b**) and low (**c**, **d**) translational efficiency for brain (**a**, **c**; blue) and liver (**b**, **d**; green) in mouse. **e**, Top ten significantly enriched GO terms for each of the mouse spermatogenesis translational efficiency trajectory cluster (Extended Data Fig. [3h–k](#)). **f–h**, Significantly enriched GO terms (biological processes) among genes that changed significantly more at the translatome compared to the transcriptome layer in brain (**f**), liver (**g**) and testis (**h**). Significance was estimated in Fisher's exact test ($P < 0.05$), with P values adjusted for multiple testing using the Benjamini–Hochberg method.

Extended Data Fig. 5 Normalization procedures in the evolutionary expression analyses.

a, Illustration of the normalization approach used in our study to globally assess gene-expression evolution. In this approach, evolutionary changes in gene expression are based on the assessment of expression differences across 1:1 orthologues between species. Specifically, we quantify the differences across orthologues as the variance (var) of their \log_2 -transformed fold expression changes between species (left column), which is then divided (normalized) by the expression variation, calculated as the

variance (var) of expression levels across genes, averaged across all studied species (right column). This procedure provides the expression divergence estimate (d). We note that the variance is similar across species for a given organ and expression layer (Fig. 1d). The example shown illustrates changes between human and each of the other five species in brain at the transcriptome layer. b, Illustration of the normalization procedure used to assess the expression evolution of individual genes. The normalization coefficient k is calculated as the ratio of the variances (var) across genes between the translatome and the transcriptome layer. The brain is shown as an example. Organ and species icons are from a previous study²⁵.

Extended Data Fig. 6 Simulation of gene-expression divergence across expression layers.

a, Simulation of gene-expression divergence across different evolutionary scenarios. Expression divergence at the translatome layer between macaque and mouse brain was modelled over parameters of compensation and translational efficiency change (see ‘Modelling gene-expression divergence’ section in the Methods for details). Red (blue) corresponds to simulated scenarios with expression divergence higher (lower) than in actual data. Black line corresponds to simulated scenarios demonstrating expression divergence values observed in actual data. b, Contrast in evolutionary rates between the two expression layers for simulated data. Δ was calculated for simulated datasets with different amounts of compensation and different amounts of θ , corresponding to expression variation between individuals and measurement errors (see [Methods](#) for details).

Extended Data Fig. 7 Contrast in evolution between transcriptome and translatome layers for individual genes in downsampled data.

a–c, Δ was calculated on the basis of datasets downsampled to 0.5 million in each library for brain (a), liver (b) and testis (c). See Fig. 2e–f in the main text for the analysis of the full dataset.

Extended Data Fig. 8 Screenshot of the *SATB2* gene in our *Ex2plorer* application.

SATB2 is an example of a gene that changes significantly less at the translational layer compared to the transcriptional layer in mammalian brain. Organ icons are from a previous study²⁵.

Extended Data Fig. 9 Evolution at the proteome layer between human and mouse brain for genes with slower or faster evolution at the translatome compared to the transcriptome layer.

Absolute rank changes of proteome expression levels were calculated for genes with slower (olive) and faster (purple) evolution at the translatome compared to the transcriptome layer. The difference of the distributions between the two gene sets is statistically significant (***/*P < 0.0001, Mann–Whitney *U* test, two-sided). Box plots represent the median ± 25th and 75th percentiles; whiskers are at 1.5 × IQR.

Extended Data Fig. 10 Mammalian lineage-specific changes between expression layers.

a–c, Number of genes with lineage-specific patterns of slower (olive) or faster (purple) evolution at the translational layer, potentially driven by stabilizing and directional selection, respectively, for brain (**a**), liver (**b**) and testis (**c**). Owing to the lack of a biological replicate, the branch leading to human was omitted in the liver phylogeny for the transcriptional layer. **d, e**, Examples of individual genes with potential patterns of stabilizing (**d**) or directional (**e**) evolution. Species names with significant changes are marked by corresponding colours. Organ and species icons are from a previous study²⁵.

Extended Data Fig. 11 Compensatory evolution of X-linked genes.

a, b, Examples of upregulation for the dosage reduction at the transcriptome layer. Species affected by upregulation are shown in olive, with arrows representing compensatory changes at the translatome layer. **c**, Median ratio of X-linked gene-expression values in mouse spermatogenic cell types to expression values of their 1:1 orthologues in chicken testis. In all cases \log_2 ratio at the translatome layer is significantly ($P < 0.05$, Mann–Whitney U test, two-sided) higher than at the transcriptome layer (marked in bold). Solid vertical lines correspond to expression levels expected under no dosage reduction (that is, \log_2 ratio = −1). **d**, Median present-day to ancestral gene-expression ratios at two expression layers for 1:1 orthologous autosomal genes located on chromosome 4 in chicken for brain, liver and testis. Chicken orthologues were used as a proxy for ancestral expression. See Fig. 4a and main text for details. **e**, Normalized translational efficiencies for 1:1 orthologues of eutherian X-linked and autosomal genes across amniote organs. Mann–Whitney U tests (two-sided) were performed for statistical comparisons (non-significant, ns: $P > 0.05$, *** $P = 0.00003$, **** $P < 0.0001$). P values were adjusted for multiple testing using Bonferroni method. Box plots represent the median ± 25th and 75th percentiles; whiskers are at $1.5 \times$ IQR. Organ and species icons are from a previous study²⁵.

Supplementary information

Supplementary Tables

This file contains Supplementary Tables 1-10.

Reporting Summary

Rights and permissions

Reprints and Permissions

About this article



Check for
updates

Cite this article

Wang, ZY., Leushkin, E., Liechti, A. *et al.* Transcriptome and translatome co-evolution in mammals. *Nature* **588**, 642–647 (2020).
<https://doi.org/10.1038/s41586-020-2899-z>

[Download citation](#)

- Received: 30 November 2018
- Accepted: 14 August 2020
- Published: 11 November 2020
- Issue Date: 24 December 2020
- DOI: <https://doi.org/10.1038/s41586-020-2899-z>

Comments

By submitting a comment you agree to abide by our [Terms](#) and [Community Guidelines](#). If you find something abusive or that does not comply with our terms or guidelines please flag it as inappropriate.

[Access through your institution](#)

[Change institution](#)

[Buy or subscribe](#)

This article was downloaded by **calibre** from <https://www.nature.com/articles/s41586-020-2899-z>

- Article
- [Published: 11 November 2020](#)

Spatial connectivity matches direction selectivity in visual cortex

- [L. Federico Rossi](#) [ORCID: orcid.org/0000-0001-5831-4860](#)¹,
- [Kenneth D. Harris](#) [ORCID: orcid.org/0000-0002-5930-6456](#)² &
- [Matteo Carandini](#) [ORCID: orcid.org/0000-0003-4880-7682](#)¹

[Nature](#) volume **588**, pages648–652(2020)[Cite this article](#)

- 5254 Accesses
- 98 Altmetric
- [Metrics details](#)

Subjects

- [Neural circuits](#)
- [Striate cortex](#)

Abstract

The selectivity of neuronal responses arises from the architecture of excitatory and inhibitory connections. In the primary visual cortex, the selectivity of a neuron in layer 2/3 for stimulus orientation and direction is thought to arise from intracortical inputs that are similarly selective^{1,2,3,4,5,6,7,8}. However, the excitatory inputs of a neuron can have diverse stimulus preferences^{1,2,3,4,6,7,9}, and inhibitory inputs can be promiscuous¹⁰ and unselective¹¹. Here we show that the excitatory and

inhibitory intracortical connections to a layer 2/3 neuron accord with its selectivity by obeying precise spatial patterns. We used rabies tracing^{1,12} to label and functionally image the excitatory and inhibitory inputs to individual pyramidal neurons of layer 2/3 of the mouse visual cortex. Presynaptic excitatory neurons spanned layers 2/3 and 4 and were distributed coaxial to the preferred orientation of the postsynaptic neuron, favouring the region opposite to its preferred direction. By contrast, presynaptic inhibitory neurons resided within layer 2/3 and favoured locations near the postsynaptic neuron and ahead of its preferred direction. The direction selectivity of a postsynaptic neuron was unrelated to the selectivity of presynaptic neurons, but correlated with the spatial displacement between excitatory and inhibitory presynaptic ensembles. Similar asymmetric connectivity establishes direction selectivity in the retina^{13,14,15,16,17}. This suggests that this circuit motif might be canonical in sensory processing.

[Access through your institution](#)

[Change institution](#)

[Buy or subscribe](#)

Access options

Subscribe to Journal

Get full journal access for 1 year

\$199.00

only \$3.83 per issue

[Subscribe](#)

All prices are NET prices.

VAT will be added later in the checkout.

Rent or Buy article

Get time limited or full article access on ReadCube.

from \$8.99

[Rent or Buy](#)

All prices are NET prices.

Additional access options:

- [Log in](#)
- [Access through your institution](#)
- [Learn about institutional subscriptions](#)

Fig. 1: Tracing the excitatory and inhibitory presynaptic inputs to an L2/3 pyramidal neuron.

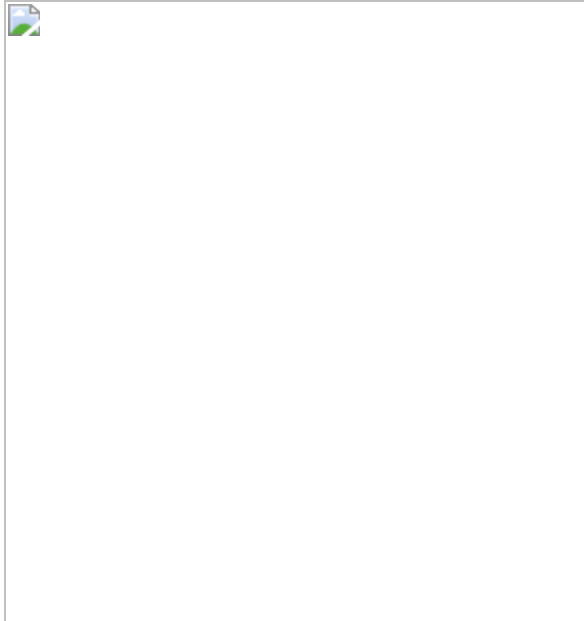


Fig. 2: Excitatory and inhibitory presynaptic ensembles are co-tuned for orientation but not direction.

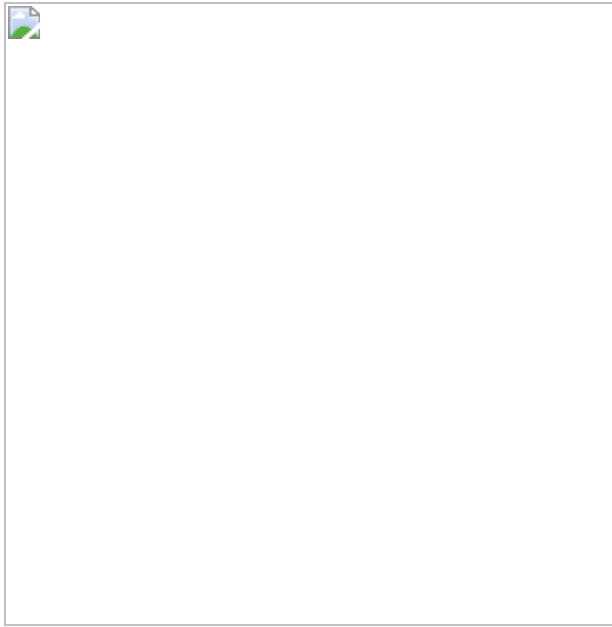
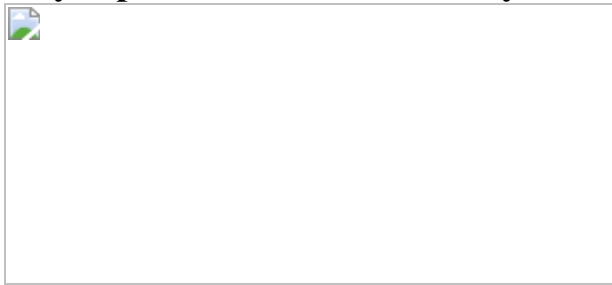


Fig. 3: Elongated excitation and spatially offset inhibition accord with direction selectivity.



Fig. 4: Spatially offset and delayed excitation and inhibition predict postsynaptic direction selectivity.



Data availability

Source data for the figures are deposited at <https://github.com/lfedros/Rossi-et-al-2020>. All other relevant data are available from the corresponding author upon reasonable request.

Code availability

Code used in this study is deposited at <https://github.com/lfedros/Rossi-et-al-2020>.

References

1. 1.

Wertz, A. et al. Single-cell-initiated monosynaptic tracing reveals layer-specific cortical network modules. *Science* **349**, 70–74 (2015).

[ADS](#) [CAS](#) [PubMed](#) [Google Scholar](#)

2. 2.

Ko, H. et al. Functional specificity of local synaptic connections in neocortical networks. *Nature* **473**, 87–91 (2011).

[ADS](#) [CAS](#) [PubMed](#) [PubMed Central](#) [Google Scholar](#)

3. 3.

Iacaruso, M. F., Gasler, I. T. & Hofer, S. B. Synaptic organization of visual space in primary visual cortex. *Nature* **547**, 449–452 (2017).

[CAS](#) [PubMed](#) [PubMed Central](#) [Google Scholar](#)

4. 4.

Lee, W. C. et al. Anatomy and function of an excitatory network in the visual cortex. *Nature* **532**, 370–374 (2016).

[ADS](#) [CAS](#) [PubMed](#) [PubMed Central](#) [Google Scholar](#)

5. 5.

Wilson, D. E., Whitney, D. E., Scholl, B. & Fitzpatrick, D. Orientation selectivity and the functional clustering of synaptic inputs in primary visual cortex. *Nat. Neurosci.* **19**, 1003–1009 (2016).

[CAS](#) [PubMed](#) [PubMed Central](#) [Google Scholar](#)

6. 6.

Cossell, L. et al. Functional organization of excitatory synaptic strength in primary visual cortex. *Nature* **518**, 399–403 (2015).

[ADS](#) [CAS](#) [PubMed](#) [PubMed Central](#) [Google Scholar](#)

7. 7.

Wilson, D. E., Scholl, B. & Fitzpatrick, D. Differential tuning of excitation and inhibition shapes direction selectivity in ferret visual cortex. *Nature* **560**, 97–101 (2018).

[ADS](#) [CAS](#) [PubMed](#) [PubMed Central](#) [Google Scholar](#)

8. 8.

Chen, T. W. et al. Ultrasensitive fluorescent proteins for imaging neuronal activity. *Nature* **499**, 295–300 (2013).

[ADS](#) [CAS](#) [PubMed](#) [PubMed Central](#) [Google Scholar](#)

9. 9.

Jia, H., Rochefort, N. L., Chen, X. & Konnerth, A. Dendritic organization of sensory input to cortical neurons in vivo. *Nature* **464**, 1307–1312 (2010).

[ADS](#) [CAS](#) [PubMed](#) [Google Scholar](#)

10. 10.

Packer, A. M. & Yuste, R. Dense, unspecific connectivity of neocortical parvalbumin-positive interneurons: a canonical microcircuit for inhibition? *J. Neurosci.* **31**, 13260–13271 (2011).

[CAS](#) [PubMed](#) [PubMed Central](#) [Google Scholar](#)

11. 11.

Hofer, S. B. et al. Differential connectivity and response dynamics of excitatory and inhibitory neurons in visual cortex. *Nat. Neurosci.* **14**, 1045–1052 (2011).

[CAS](#) [PubMed](#) [PubMed Central](#) [Google Scholar](#)

12. 12.

Wickersham, I. R. et al. Monosynaptic restriction of transsynaptic tracing from single, genetically targeted neurons. *Neuron* **53**, 639–647 (2007).

[CAS](#) [PubMed](#) [PubMed Central](#) [Google Scholar](#)

13. 13.

Barlow, H. B. & Levick, W. R. The mechanism of directionally selective units in rabbit's retina. *J. Physiol. (Lond.)* **178**, 477–504 (1965).

[CAS](#) [Google Scholar](#)

14. 14.

Fried, S. I., Münch, T. A. & Werblin, F. S. Mechanisms and circuitry underlying directional selectivity in the retina. *Nature* **420**, 411–414 (2002).

[ADS](#) [CAS](#) [PubMed](#) [Google Scholar](#)

15. 15.

Briggman, K. L., Helmstaedter, M. & Denk, W. Wiring specificity in the direction-selectivity circuit of the retina. *Nature* **471**, 183–188 (2011).

[ADS](#) [CAS](#) [PubMed](#) [Google Scholar](#)

16. 16.

Vaney, D. I., Sivyer, B. & Taylor, W. R. Direction selectivity in the retina: symmetry and asymmetry in structure and function. *Nat. Rev. Neurosci.* **13**, 194–208 (2012).

[CAS](#) [PubMed](#) [Google Scholar](#)

17. 17.

Kim, J. S. et al. Space-time wiring specificity supports direction selectivity in the retina. *Nature* **509**, 331–336 (2014).

[CAS](#) [PubMed](#) [PubMed Central](#) [Google Scholar](#)

18. 18.

Alonso, J. M. & Martinez, L. M. Functional connectivity between simple cells and complex cells in cat striate cortex. *Nat. Neurosci.* **1**, 395–403 (1998).

[CAS](#) [PubMed](#) [Google Scholar](#)

19. 19.

Priebe, N. J. Mechanisms of orientation selectivity in the primary visual cortex. *Annu. Rev. Vis. Sci.* **2**, 85–107 (2016).

[PubMed](#) [Google Scholar](#)

20. 20.

Isaacson, J. S. & Scanziani, M. How inhibition shapes cortical activity. *Neuron* **72**, 231–243 (2011).

[CAS](#) [PubMed](#) [PubMed Central](#) [Google Scholar](#)

21. 21.

Liu, B. H. et al. Broad inhibition sharpens orientation selectivity by expanding input dynamic range in mouse simple cells. *Neuron* **71**, 542–554 (2011).

[CAS](#) [PubMed](#) [PubMed Central](#) [Google Scholar](#)

22. 22.

Znamenskiy, P. et al. Functional selectivity and specific connectivity of inhibitory neurons in primary visual cortex. Preprint at <https://doi.org/10.1101/294835> (2018).

23. 23.

Lee, S. H. et al. Activation of specific interneurons improves V1 feature selectivity and visual perception. *Nature* **488**, 379–383 (2012).

[ADS](#) [CAS](#) [PubMed](#) [PubMed Central](#) [Google Scholar](#)

24. 24.

Atallah, B. V., Bruns, W., Carandini, M. & Scanziani, M. Parvalbumin-expressing interneurons linearly transform cortical responses to visual stimuli. *Neuron* **73**, 159–170 (2012).

[CAS](#) [PubMed](#) [PubMed Central](#) [Google Scholar](#)

25. 25.

Wilson, N. R., Runyan, C. A., Wang, F. L. & Sur, M. Division and subtraction by distinct cortical inhibitory networks *in vivo*. *Nature* **488**, 343–348 (2012).

[ADS](#) [CAS](#) [PubMed](#) [PubMed Central](#) [Google Scholar](#)

26. 26.

Ma, W. P. et al. Visual representations by cortical somatostatin inhibitory neurons—selective but with weak and delayed responses. *J. Neurosci.* **30**, 14371–14379 (2010).

[CAS](#) [PubMed](#) [PubMed Central](#) [Google Scholar](#)

27. 27.

Monier, C., Chavane, F., Baudot, P., Graham, L. J. & Frégnac, Y. Orientation and direction selectivity of synaptic inputs in visual cortical neurons: a diversity of combinations produces spike tuning. *Neuron* **37**, 663–680 (2003).

[CAS](#) [PubMed](#) [Google Scholar](#)

28. 28.

Livingstone, M. S. Mechanisms of direction selectivity in macaque V1. *Neuron* **20**, 509–526 (1998).

[CAS](#) [PubMed](#) [Google Scholar](#)

29. 29.

Xu, X. et al. Primary visual cortex shows laminar-specific and balanced circuit organization of excitatory and inhibitory synaptic connectivity. *J. Physiol. (Lond.)* **594**, 1891–1910 (2016).

[CAS](#) [Google Scholar](#)

30. 30.

Adesnik, H. & Scanziani, M. Lateral competition for cortical space by layer-specific horizontal circuits. *Nature* **464**, 1155–1160 (2010).

[ADS](#) [CAS](#) [PubMed](#) [PubMed Central](#) [Google Scholar](#)

31. 31.

Holmgren, C., Harkany, T., Svensenfors, B. & Zilberter, Y. Pyramidal cell communication within local networks in layer 2/3 of rat neocortex. *J. Physiol. (Lond.)* **551**, 139–153 (2003).

[CAS](#) [Google Scholar](#)

32. 32.

Weiler, S. et al. Relationship between input connectivity, morphology and orientation tuning of layer 2/3 pyramidal cells in mouse visual cortex. Preprint at *bioRxiv* <https://doi.org/10.1101/2020.06.03.127191> (2020).

33. 33.

Sun, W., Tan, Z., Mensh, B. D. & Ji, N. Thalamus provides layer 4 of primary visual cortex with orientation- and direction-tuned inputs. *Nat. Neurosci.* **19**, 308–315 (2016).

[CAS](#) [PubMed](#) [Google Scholar](#)

34. 34.

Ringach, D. L. et al. Spatial clustering of tuning in mouse primary visual cortex. *Nat. Commun.* **7**, 12270 (2016).

[ADS](#) [CAS](#) [PubMed](#) [PubMed Central](#) [Google Scholar](#)

35. 35.

Marques, T., Nguyen, J., Fioreze, G. & Petreanu, L. The functional organization of cortical feedback inputs to primary visual cortex. *Nat. Neurosci.* **21**, 757–764 (2018).

[CAS](#) [PubMed](#) [Google Scholar](#)

36. 36.

Bonin, V., Histed, M. H., Yurgenson, S. & Reid, R. C. Local diversity and fine-scale organization of receptive fields in mouse visual cortex. *J. Neurosci.* **31**, 18506–18521 (2011).

[CAS](#) [PubMed](#) [PubMed Central](#) [Google Scholar](#)

37. 37.

Garrett, M. E., Nauhaus, I., Marshel, J. H. & Callaway, E. M. Topography and areal organization of mouse visual cortex. *J. Neurosci.* **34**, 12587–12600 (2014).

[CAS](#) [PubMed](#) [PubMed Central](#) [Google Scholar](#)

38. 38.

Haider, B., Häusser, M. & Carandini, M. Inhibition dominates sensory responses in the awake cortex. *Nature* **493**, 97–100 (2013).

[ADS](#) [PubMed](#) [Google Scholar](#)

39. 39.

Liu, B. H. et al. Intervening inhibition underlies simple-cell receptive field structure in visual cortex. *Nat. Neurosci.* **13**, 89–96 (2010).

[CAS](#) [PubMed](#) [Google Scholar](#)

40. 40.

Li, Y. T., Liu, B. H., Chou, X. L., Zhang, L. I. & Tao, H. W. Strengthening of direction selectivity by broadly tuned and spatiotemporally slightly offset inhibition in mouse visual cortex. *Cereb. Cortex* **25**, 2466–2477 (2015).

[PubMed](#) [Google Scholar](#)

41. 41.

Lien, A. D. & Scanziani, M. Tuned thalamic excitation is amplified by visual cortical circuits. *Nat. Neurosci.* **16**, 1315–1323 (2013).

[CAS](#) [PubMed](#) [PubMed Central](#) [Google Scholar](#)

42. 42.

Li, Y. T., Ibrahim, L. A., Liu, B. H., Zhang, L. I. & Tao, H. W. Linear transformation of thalamocortical input by intracortical excitation. *Nat. Neurosci.* **16**, 1324–1330 (2013).

[CAS](#) [PubMed](#) [PubMed Central](#) [Google Scholar](#)

43. 43.

Hillier, D. et al. Causal evidence for retina-dependent and -independent visual motion computations in mouse cortex. *Nat. Neurosci.* **20**, 960–968 (2017).

[CAS](#) [PubMed](#) [PubMed Central](#) [Google Scholar](#)

44. 44.

Cruz-Martín, A. et al. A dedicated circuit links direction-selective retinal ganglion cells to the primary visual cortex. *Nature* **507**, 358–361 (2014).

45. 45.

Lien, A. D. & Scanziani, M. Cortical direction selectivity emerges at convergence of thalamic synapses. *Nature* **558**, 80–86 (2018).

[ADS](#) [CAS](#) [PubMed](#) [Google Scholar](#)

46. 46.

Thiele, A., Distler, C., Korbmacher, H. & Hoffmann, K. P. Contribution of inhibitory mechanisms to direction selectivity and response normalization in macaque middle temporal area. *Proc. Natl Acad. Sci. USA* **101**, 9810–9815 (2004).

[ADS](#) [CAS](#) [PubMed](#) [Google Scholar](#)

47. 47.

Madisen, L. et al. Transgenic mice for intersectional targeting of neural sensors and effectors with high specificity and performance. *Neuron* **85**, 942–958 (2015).

48. 48.

Wekselblatt, J. B., Flister, E. D., Piscopo, D. M. & Niell, C. M. Large-scale imaging of cortical dynamics during sensory perception and behavior. *J. Neurophysiol.* **115**, 2852–2866 (2016).

[CAS](#) [PubMed](#) [PubMed Central](#) [Google Scholar](#)

49. 49.

Gorski, J. A. et al. Cortical excitatory neurons and glia, but not GABAergic neurons, are produced in the Emx1-expressing lineage. *J. Neurosci.* **22**, 6309–6314 (2002).

[CAS](#) [PubMed](#) [PubMed Central](#) [Google Scholar](#)

50. 50.

Mayford, M. et al. Control of memory formation through regulated expression of a CaMKII transgene. *Science* **274**, 1678–1683 (1996).

[ADS](#) [CAS](#) [PubMed](#) [Google Scholar](#)

51. 51.

Peron, S. P., Freeman, J., Iyer, V., Guo, C. & Svoboda, K. A cellular resolution map of barrel cortex activity during tactile behavior. *Neuron* **86**, 783–799 (2015).

[CAS](#) [PubMed](#) [Google Scholar](#)

52. 52.

Wickersham, I. R., Finke, S., Conzelmann, K. K. & Callaway, E. M. Retrograde neuronal tracing with a deletion-mutant rabies virus. *Nat. Methods* **4**, 47–49 (2007).

[CAS](#) [PubMed](#) [Google Scholar](#)

53. 53.

Marshel, J. H., Mori, T., Nielsen, K. J. & Callaway, E. M. Targeting single neuronal networks for gene expression and cell labeling in vivo. *Neuron* **67**, 562–574 (2010).

[CAS](#) [PubMed](#) [PubMed Central](#) [Google Scholar](#)

54. 54.

Rancz, E. A. et al. Transfection via whole-cell recording in vivo: bridging single-cell physiology, genetics and connectomics. *Nat. Neurosci.* **14**, 527–532 (2011).

[CAS](#) [PubMed](#) [PubMed Central](#) [Google Scholar](#)

55. 55.

Osakada, F. et al. New rabies virus variants for monitoring and manipulating activity and gene expression in defined neural circuits. *Neuron* **71**, 617–631 (2011).

[CAS](#) [PubMed](#) [PubMed Central](#) [Google Scholar](#)

56. 56.

Goldey, G. J. et al. Removable cranial windows for long-term imaging in awake mice. *Nat. Protocols* **9**, 2515–2538 (2014).

[CAS](#) [PubMed](#) [Google Scholar](#)

57. 57.

Judkewitz, B., Rizzi, M., Kitamura, K. & Häusser, M. Targeted single-cell electroporation of mammalian neurons in vivo. *Nat. Protocols* **4**, 862–869 (2009).

[CAS](#) [PubMed](#) [Google Scholar](#)

58. 58.

Kitamura, K., Judkewitz, B., Kano, M., Denk, W. & Häusser, M. Targeted patch-clamp recordings and single-cell electroporation of unlabeled neurons in vivo. *Nat. Methods* **5**, 61–67 (2008).

[CAS](#) [PubMed](#) [Google Scholar](#)

59. 59.

Pologruto, T. A., Sabatini, B. L. & Svoboda, K. ScanImage: flexible software for operating laser scanning microscopes. *Biomed. Eng. Online* **2**, 13 (2003).

[PubMed](#) [PubMed Central](#) [Google Scholar](#)

60. 60.

Kim, E. J., Jacobs, M. W., Ito-Cole, T. & Callaway, E. M. Improved monosynaptic neural circuit tracing using engineered rabies virus glycoproteins. *Cell Rep.* **15**, 692–699 (2016).

[CAS](#) [PubMed](#) [PubMed Central](#) [Google Scholar](#)

61. 61.

Drobizhev, M., Makarov, N. S., Tillo, S. E., Hughes, T. E. & Rebane, A. Two-photon absorption properties of fluorescent proteins. *Nat. Methods* **8**, 393–399 (2011).

[CAS](#) [PubMed](#) [PubMed Central](#) [Google Scholar](#)

62. 62.

Brondi, M., Sato, S. S., Rossi, L. F., Ferrara, S. & Ratto, G. M. Finding a needle in a haystack: identification of EGFP tagged neurons during calcium imaging by means of two-photon spectral separation. *Front. Mol. Neurosci.* **5**, 96 (2012).

[CAS](#) [PubMed](#) [PubMed Central](#) [Google Scholar](#)

63. 63.

Kleiner, M. et al. What's new in psychtoolbox-3. *Perception* **36**, 1–16 (2007).

[Google Scholar](#)

64. 64.

Burgess, C. P. et al. High-yield methods for accurate two-alternative visual psychophysics in head-fixed mice. *Cell Rep.* **20**, 2513–2524 (2017).

[CAS](#) [PubMed](#) [PubMed Central](#) [Google Scholar](#)

65. 65.

Pachitariu, M. et al. Suite2p beyond 10,000 neurons with standard two-photon microscopy. Preprint at <https://doi.org/10.1101/061507> (2016).

66. 66.

Dipoppa, M. et al. Vision and locomotion shape the interactions between neuron types in mouse visual cortex. *Neuron* **98**, 602–615 (2018).

[CAS](#) [PubMed](#) [PubMed Central](#) [Google Scholar](#)

67. 67.

Berens, P. CircStat: a MATLAB toolbox for circular statistics. *J. Stat. Softw.* **31**, 1–21 (2009).

[MathSciNet](#) [Google Scholar](#)

[Download references](#)

Acknowledgements

We thank E. Callaway for sharing viruses via the Salk Institute Vector Core; M. Rizzi for advice on electroporation; M. Krumin for support with microscopy; C. Reddy for help with plasmid production; M. Drobizhev for providing the two-photon cross-section of fluorescent proteins; S. Bugeon for help with histology and anatomical registration; L. Mariotti for help with anatomical reconstructions and cell counting; M. Scanziani for suggestions on the manuscript; and K. Balint, S. Trenholm, B. Roska and M. Tripodi for advice and for genetic materials that we used in pilot studies. This work was supported by the Wellcome Trust (grant 099692 to L.F.R., and grants 205093 and 108726 to K.D.H. and M.C.). M.C. holds the GlaxoSmithKline/Fight for Sight Chair in Visual Neuroscience.

Author information

Affiliations

1. UCL Institute of Ophthalmology, University College London, London, UK

L. Federico Rossi & Matteo Carandini

2. UCL Queen Square Institute of Neurology, University College London, London, UK

Kenneth D. Harris

Authors

1. L. Federico Rossi

[View author publications](#)

You can also search for this author in [PubMed](#) [Google Scholar](#)

2. Kenneth D. Harris

[View author publications](#)

You can also search for this author in [PubMed](#) [Google Scholar](#)

3. Matteo Carandini

[View author publications](#)

You can also search for this author in [PubMed](#) [Google Scholar](#)

Contributions

L.F.R., K.D.H. and M.C. conceived the experiments. L.F.R. refined the techniques, performed the experiments and analysed the data. L.F.R., K.D.H. and M.C. wrote the paper.

Corresponding author

Correspondence to [L. Federico Rossi](#).

Ethics declarations

Competing interests

The authors declare no competing interests.

Additional information

Peer review information *Nature* thanks Hillel Adesnik and the other, anonymous, reviewer(s) for their contribution to the peer review of this work.

Publisher's note Springer Nature remains neutral with regard to jurisdictional claims in published maps and institutional affiliations.

Extended data figures and tables

[Extended Data Fig. 1 Targeted single-neuron electroporation with survival control in vivo.](#)

a, Experimental pipeline: electroporation of the postsynaptic neuron, targeted by shadow-imaging and expression of GCaMP6; imaging of the postsynaptic neuron, labelled by dsRed; injection of the modified rabies virus; imaging and tracing of the presynaptic neurons marked by dsRed. **b–d**, Schematic of the electroporation technique, performed under a two-photon microscope on a transgenic mouse expressing GCaMP6 in cortical excitatory neurons. **b**, A pipette filled with DNA plasmids and Alexa Fluor 594 is targeted to a craniotomy; an 820-nm laser (red) excites Alexa Fluor 594 fluorescence (magenta) and GCaMP6 fluorescence (cyan). The latter is insensitive to neural activity because 820 nm is an isosbestic wavelength, at which calcium-bound and calcium-free isoforms fluoresce approximately equally. **c**, Upon electroporation, DNA plasmids and Alexa Fluor 594 are transferred into a neuron expressing GCaMP6. **d**, A healthy neuron maintains its GCaMP6 concentration and the resulting calcium-insensitive fluorescence (top), whereas a neuron with a damaged membrane bleeds indicator, gradually darkening and disappearing against the surrounding neuropil (bottom). **e**, Time lapse of an electroporation in layer 2/3 of mouse V1, using Alexa Fluor 594 negative contrast and calcium-insensitive GCaMP6 fluorescence imaging: approach (left), electroporation (middle) and pipette withdrawal (right). **f**, The same neuron as in **e**, imaged the next 1–3 days at 920 nm, expressing the electroporated genes for dsRed (red) and maintaining healthy GCaMP6 expression (green). **g**, Average

fluorescence (mean \pm s.e.m.) of somatic Alexa Fluor 594 (magenta) and GCaMP6 (cyan), relative to neuropil background (dashed line represents unity) before and after electroporation (arrow, $n = 10$ neurons). **h, i**, As in **e, f**, but with a slower time lapse of a neuron that survived the procedure. Images in **h** are 30-s-long averages acquired 0–1 min (left), 2–3 min (centre) and 5–6 min (right) after electroporation. **j, k**, As in **h, i**, for a neuron that did not recover from the electroporation. **l**, As in **g**, for GCaMP6 somatic fluorescence (mean \pm s.e.m.) in neurons that did (cyan, $n = 18$) or did not (grey, $n = 10$) survive the procedure. Scale bar, 15 μm (for all fluorescence images).

Extended Data Fig. 2 Photo-ablation of supernumerary postsynaptic neurons before rabies injection.

a, Cartoon of the protocol. The target neuron expresses both GCaMP6 (green) and dsRed (red), whereas surrounding neurons express only GCaMP6. The day after electroporation (day 1), the neuron is targeted with steady two-photon illumination at 820 nm, focused with intensity of approximately 150 mW, for 10–20 s (top). The target neuron is ablated and by the next day (day 2) it has disappeared (bottom). **b**, Time-lapse imaging during the photo-ablation of two neighbouring neurons, lasting approximately 10 min. Imaging at 920 nm shows calcium-sensitive fluorescence of GCaMP6 (top) and fluorescence of dsRed (bottom). Each of the neurons was targeted with two photo-ablation pulses (red triangles). Photo-ablation pulses lasted 20 s, and each neuron was imaged for 30 s afterwards. Each pulse increases cellular damage: localized photo-bleaching after the first pulse; elevated intracellular calcium and cell swelling after the second pulse. Neighbouring cells, not expressing dsRed, resist the photo-damage. **c**, The successful elimination of the target neurons (red, see insets) is confirmed the day following the photo-ablation procedure: by day 2, the target neuron has either disappeared (yellow arrow, top neuron) or gone in apoptosis (yellow arrow, bottom neuron). The surrounding tissue is unaffected, as shown by the normal activity detected in neighbouring neurons using Suite2p (blue-green ROIs and traces; scale bar, 30 s and 10 s.d.). **d**, Effectiveness of photo-ablation as a function of cortical distance from the photo-ablation target neuron ($n = 9$ attempts, mean \pm s.e.m.).

Extended Data Fig. 3 Time course of rabies tracing and recordings.

a, Viability of postsynaptic neurons as a function of day after the rabies virus injection, based on $n = 17$ injections. **b**, Count of observed presynaptic neurons traced over the same period from $n = 17$ postsynaptic neurons (mean \pm s.e.m.). **c**, Fraction of viable presynaptic neurons (red) over the total traced (grey), and worst-case-scenario population mortality of presynaptic neurons (dashed), estimated assuming the viability of each newly labelled presynaptic neuron degrades at the same rate as the viability of the postsynaptic neurons measured in **a**. **d**, Average distribution across mice ($n = 17$, mean \pm s.e.m.) of the imaging sessions used to record the responses of presynaptic neurons, split by cortical layer. The time of imaging did not systematically change across layer (black triangle, median, first and third quartiles), and most of the data were acquired before presynaptic neurons suffered from the toxicity of the rabies virus. **e**, Distribution of responsivity of the presynaptic neurons across days (red violin plot with black median). Responsivity was measured as the maximum average stimulus-triggered response. To compare across sessions, presynaptic responsivity was normalized to the median responsivity of the local population (shaded line). **f**, Longitudinal imaging of presynaptic neurons identified before (left, black ROI) and 5–12 days after (right, red ROI) rabies virus infection. Scale bar, 25 μm . **g**, Average responses to drifting gratings of the same presynaptic neurons before (black) and after (red) the rabies virus infection. Responses (4-s long) were z -scored with the respect to blank trials. Scale bar, 1 s.d. **h**, Preferred orientation of presynaptic neurons recorded before and after the rabies virus infection. At the time of recording used in this study, the preferred orientation of presynaptic neurons is unperturbed by the rabies virus infection ($n = 51$ neurons from $n = 4$ mice, circular correlation 0.76, $P_r = 1.6 \times 10^{-6}$, Z test).

Extended Data Fig. 4 Classification of excitatory and inhibitory presynaptic neurons.

a, Three example excitatory presynaptic neurons showing similar expression of dsRed (left) and decreasing expression of GCaMP6 (middle).

The somatic masks obtained from dsRed and the GCaMP6 signal were used to compute a map of phase correlation in the 5- μm -radius annulus around the somatic centre (right). In the first two examples, the stronger GCaMP6 expression in the soma compared to the surrounding neuropil results in positive peaks of the phase correlation. **b**, As in **a**, for three example inhibitory neurons. The lack of GCaMP6 expression in the soma results in negative peaks of the phase correlation. **c**, For each presynaptic neuron, the central peak of phase correlation is plotted against the s.d. of the phase correlation within the 5- μm annulus centred on the soma (top). Darker dots indicate neurons the identity of which was confirmed by immunostaining. Open dots represent example neurons shown in **a**, **b**. A classification boundary was used to split the clusters of excitatory (red) and inhibitory neurons (blue). This boundary was identified independently for each presynaptic ensemble with a bilinear fit. The average fit across datasets is shown (black line). The histogram (bottom) summarizes the classification across experiments, with the average classification boundary. **d**, Average expression of dsRed (left), GCaMP6 (middle) and map of phase correlation (right) for presynaptic neurons classified as excitatory neurons (top, $n = 584$) or inhibitory neurons (bottom, $n = 426$). **e**, Number of presynaptic neurons classified as inhibitory versus excitatory in experiments in *CaMK2a–GCaMP6* mice (red upward triangles, $n = 13$) and *GAD2–NLS–mCherry* mice (red downward triangles, $n = 4$). A linear fit (blue, $r = 0.6$, $P_r = 2.6 \times 10^{-3}$, linear correlation, *F*-test) shows that the fraction of traced presynaptic neurons that are inhibitory tends towards 30% as the yield of tracing increases; yet, owing to the positive intercept, the fraction of inhibitory neurons may appear as high as 60% in experiments with low tracing yield. In control experiments in which the red marker tdTomato was expressed only in excitatory neurons (*AAV-CaMK2-tomato* in *CaMK2a–GCaMP6* mice, grey circles), the fraction of neurons incorrectly classified as inhibitory was below 5%.

Extended Data Fig. 5 Immunohistochemical verification of presynaptic neuron classification method.

a, Coronal maximum projection from a z -stack acquired in vivo, showing a section through a presynaptic network labelled with RV-dsRed (red) in a *CaMK2a–GCaMP6s* transgenic mouse (green). Scale bar, 50 μm . **b**,

Coronal brain slice matching the section in **a**. We could match $n = 94$ out of the $n = 105$ neurons traced in vivo. **c**, Inset from **b** (dashed) showing the immunostaining for the inhibitory neurons marker GAD (blue). **d**, ROC curve illustrating the sensitivity and specificity of the neuron classification method based on somatic GCaMP6 fluorescence (Extended Data Fig. 4) against the ground-truth measurements obtained by immunostaining against GAD, for a range of classification boundaries. The fitted classification boundary was optimal (blue dot), yielding a specificity of 94% and sensitivity of 91%. **e**, Two example presynaptic neurons classified as excitatory ($n = 49$) from the z-stack in **a**. **f**, Slice immunostaining of the two neurons in **e**. Neurons were confirmed as excitatory if they expressed GCaMP6 and were GAD-negative ($n = 45$). Scale bar, 40 μm . **g**, **h**, As in **e**, **f**, for two example presynaptic neurons classified as inhibitory. Neurons were confirmed as inhibitory if they did not express GCaMP6 and were GAD-positive ($n = 42$).

Extended Data Fig. 6 Spectral unmixing of dsRed and mCherry fluorescence.

a, Emission spectra of GCaMP6, dsRed and mCherry. Shaded areas indicate the emission band captured by the green (G) and red (R) channels of the microscope. The G channel collects mostly GCaMP6 fluorescence, and the R channel captures a mixture of mCherry, dsRed and GCaMP6 fluorescence. Emission spectra were normalized to their peak. **b**, Two-photon action cross-section of dsRed (top, red) and mCherry (bottom, purple). **c**, Ratio between the two-photon action cross-sections of dsRed and mCherry (red) and its inverse (purple). Shaded bands in **b**, **c** indicate the excitation wavelengths used for imaging: 780, 890, 970 and 1,020 nm. The four wavelengths were chosen to maximize the SNR of each fluorophore while ensuring the ratio between the two signals was maximal. **d**, Example field of view imaged at the four excitation wavelengths in the G channel. GCaMP6 was expressed in all neurons with an *AAV2.1-Syn-GCaMP6s* in a *GAD-NLS-mCherry* mouse; a subset of presynaptic neurons was traced with a dsRed rabies virus. **e**, As in **d**, for the R channel. **f**, The fluorescence in the R channel (R_λ) plotted against the fluorescence in the G channel (G_λ) for each pixel, and for each excitation wavelength λ . Because the GCaMP6 labelling was dense and both the dsRed and the mCherry signals were

sparse, and because the contribution of dsRed and mCherry to G_λ was minimal, the GCaMP6 signal contributing to R_λ could be recovered by piecewise robust linear regression ($\alpha G_\lambda + \beta$). **g**, The image representing the linear mix of dsRed or mCherry signals, M_λ , was recovered by subtracting the scaled G_λ from the R_λ . **h**, An iterative algorithm was used to linearly unmix the two source images. Each unmixing iteration was constrained to minimize the quadratic reconstruction error over the data and return maximally uncorrelated sources R_{dsRed} and R_{mCherry} . **i, j**, The two source images R_{dsRed} and R_{mCherry} for the example field of view in **d, e**. The unmixing procedure correctly recovers the nuclear localization of mCherry without any prior. Scale bars, 50 μm . Similar results were obtained for all *GAD–NLS–mCherry* mice ($n = 4$).

Extended Data Fig. 7 Distributions of individual excitatory and inhibitory presynaptic ensembles.

a, Density of excitatory presynaptic neurons around the postsynaptic neuron (black triangle) as a function of cortical depth and radial distance from the postsynaptic neuron. Density was normalized to its maximum for display purposes. Depth marginals are shown on the left of each density map. **b**, As in **a**, for inhibitory presynaptic neurons. **c**, Overlay of excitatory and inhibitory densities shown in **a, b**. Hue indicates the relative proportion of excitatory (red) and inhibitory (blue) inputs, and saturation indicates maximum normalized neuronal density. Data are shown for the 13 experiments that included substantial recordings from L4.

Extended Data Fig. 8 L2/3 neurons receive presynaptic excitation preferentially tuned to their orientation preference.

a, Average tuning across the postsynaptic neurons responding to drifting gratings ($n = 16$, mean \pm s.e.m.), after alignment of their preferred stimulus direction. **b**, Distribution of preferred direction relative to the postsynaptic preferred direction, for excitatory presynaptic ensembles across all layers ($n = 15$, median \pm m.a.d.). **c**, As in **b**, for excitatory presynaptic ensembles within L2/3 (top) and within L4 (bottom). **d**, As in **b**, for inhibitory

presynaptic ensembles. **e**, Average orientation tuning across the postsynaptic neurons responding to drifting gratings ($n = 16$, mean \pm s.e.m.), after alignment of their preferred stimulus orientation. **f**, Average distribution of preferred orientation relative to the postsynaptic preferred orientation, for excitatory presynaptic neurons pooled across all layers ($n = 15$, median \pm m.a.d.). Presynaptic ensembles tuning for orientation ($P_{\text{KW}} = 5 \times 10^{-8}$, two-sided one-way Kruskal–Wallis test) was significantly stronger than expected from random samples of the surrounding population (grey, median \pm m.a.d.). **g**, As in **f**, for presynaptic ensembles within L2/3 (top, $n = 15$, $P_{\text{KW}} = 10^{-7}$) and within L4 (bottom, $n = 13$, $P_{\text{KW}} = 2 \times 10^{-5}$). **h**, As in **f**, for inhibitory presynaptic ensembles ($n = 4$). **i**, The tuning of the distributions of preferred orientation of excitatory presynaptic ensembles across layers plotted against the preferred orientation of their postsynaptic neuron. The co-tuning for orientation ($r = 0.75$, circular correlation, $P_r = 4 \times 10^{-3}$, Z-test; $P_V = 9 \times 10^{-8}$ circular V-test) was stronger than expected from random samples of the local population ($P_{r_rand} < 10^{-4}$ for circular correlation, $P_{V_rand} < 10^{-4}$ for V statistic). Upwards triangles represent experiments in *CaMK2a–GCaMP6* mice ($n = 11$); downward triangles indicate experiments in GAD2–NLS–mCherry mice ($n = 4$). **j**, As in **i**, for excitatory presynaptic ensembles within L2/3 (top, $r = 0.92$, $P_r = 5 \times 10^{-3}$, $P_V = 10^{-5}$, $P_{r_rand} = 2 \times 10^{-4}$, $P_{V_rand} < 10^{-4}$, $n = 15$) and within L4 (bottom, $r = 0.76$, $P_r = 2 \times 10^{-2}$, $P_V = 3 \times 10^{-3}$, $P_{r_rand} = 0.18$, $P_{V_rand} = 3 \times 10^{-3}$, $n = 13$). **k**, As in **i**, for inhibitory presynaptic ensembles. Inhibitory presynaptic ensembles were weakly biased to the orientation preference of the postsynaptic neuron ($P_V = 0.05$, circular V-test, $n = 4$).

Extended Data Fig. 9 Mapping retinotopy using individual neurons versus wide-field signals.

a, The stimulus used for retinotopic mapping was a sparse random pattern of white and black squares on a grey background (top). The fluorescence time-course from the entire field of view was used to compute a global stimulus-triggered average response elicited by changes in luminance at

each position. The centre of mass of this global receptive field (RF) was used to constrain the fits of wide field and neuronal receptive field to the appropriate retinotopic region (dashed rectangle). **b**, Maximal projection from an example field of view. In this example, the field of view was subsampled in a grid of 9×9 regions of interest (ROIs, red squares) to compute wide-field receptive fields. Scale bar, 100 μm . **c**, The wide-field receptive fields calculated for the ROIs in **b**, normalized to their maximum. The wide-field receptive field centres from the grid of ROIs were interpolated to estimate a retinotopic map, assigning a wide-field receptive field to each cortical location, whether it contained a responsive neuron, an unresponsive neuron or neuropil. **d**, Estimation of neuronal receptive fields. ON (red) and OFF (blue) receptive fields were estimated by regularized smooth pseudoinverse regression using either streams of white (ON) or black stimuli (OFF) as predictors, and assuming a common response kernel across neurons. ON and OFF subfields were then combined to estimate the receptive field centre (green dot). Receptive fields were considered significant if the cross validated correlation coefficient between predicted (red trace) and actual response (black trace) was greater than 0.2. **e**, Azimuth of neuron receptive field centre versus wide-field receptive field centre for all excitatory presynaptic neurons (black dots, $n = 113$, $r_{\text{pre}} = 0.89$, $P_{r_{\text{pre}}} = 2.8 \times 10^{-39}$, linear correlation, F -test) and surrounding excitatory neurons (red density, $n = 25,677$, $r_{\text{all}} = 0.88$, $P_{r_{\text{all}}} < 10^{-308}$, linear correlation F -test) across experiments. **f**, As in **e** for elevation ($r_{\text{pre}} = 0.80$, $P_{r_{\text{pre}}} = 9 \times 10^{-27}$; $r_{\text{all}} = 0.85$, $P_{r_{\text{all}}} < 10^{-308}$). **g**, **h**, As in **e**, **f**, for inhibitory presynaptic neurons (black dots, $n = 37$, $r_{\text{pre}} = 0.92$, $P_{r_{\text{pre}}} = 1.3 \times 10^{-15}$, for azimuth; $r_{\text{pre}} = 0.71$, $P_{r_{\text{pre}}} = 9.7 \times 10^{-7}$, for elevation) and all inhibitory neurons ($n = 1,963$, $r_{\text{all}} = 0.95$, $P_{r_{\text{all}}} < 10^{-308}$, for azimuth; $r_{\text{all}} = 0.74$, $P_{r_{\text{all}}} < 10^{-308}$, for elevation).

Extended Data Fig. 10 Spatial connectivity accords with direction selectivity in cortex and across layers.

a, Distribution of excitatory and inhibitory presynaptic neurons in cortex, pooled across experiments ($n = 17$), and polar tuning curves for each postsynaptic neuron (top). The colour hue indicates the average fraction of

local excitatory (red) or inhibitory (blue) presynaptic neurons; the colour saturation indicates the maximum normalized input density, averaged across experiments. **b, c**, As in **a**, plotting the excitatory and inhibitory presynaptic neurons separately. **d**, As in **a**, after rotating each presynaptic cortical distribution to align the postsynaptic preferred direction ($n = 16$). The cortical angle of rotation, corresponding to the postsynaptic preferred direction, was calculated from the local retinotopic gradient at the postsynaptic location. After the alignment, the postsynaptic preferred orientation approximately maps to a line at the postsynaptic location (dashed line). **e**, As in **d**, for excitatory presynaptic neurons. **f**, As in **d**, for inhibitory presynaptic neurons. **g**, As in **d**, for the distribution of L1 and L2/3 excitatory and inhibitory presynaptic neurons in visual space, pooled across experiments after alignment to the preferred direction across postsynaptic neurons ($n = 16$). **h, i**, As in **g**, distinguishing between excitatory and inhibitory presynaptic neurons. **j–l**, As in **g–i**, for presynaptic neurons in L4 and in superficial L5. In all panels, upwards triangles and circles represent *CaMK2a–GCaMP6* datasets; downward triangles and squares indicate *GAD2–NLS–mCherry* datasets.

Supplementary information

[Reporting Summary](#)

Rights and permissions

[Reprints and Permissions](#)

About this article



Check for
updates

Cite this article

Rossi, L.F., Harris, K.D. & Carandini, M. Spatial connectivity matches direction selectivity in visual cortex. *Nature* **588**, 648–652 (2020). <https://doi.org/10.1038/s41586-020-2894-4>

[Download citation](#)

- Received: 29 January 2019
- Accepted: 20 August 2020
- Published: 11 November 2020
- Issue Date: 24 December 2020
- DOI: <https://doi.org/10.1038/s41586-020-2894-4>

Comments

By submitting a comment you agree to abide by our [Terms](#) and [Community Guidelines](#). If you find something abusive or that does not comply with our terms or guidelines please flag it as inappropriate.

[Access through your institution](#)

[Change institution](#)

[Buy or subscribe](#)

This article was downloaded by **calibre** from <https://www.nature.com/articles/s41586-020-2894-4>

- Article
- [Published: 02 December 2020](#)

The neuropeptide Pth2 dynamically senses others via mechanosensation

- [Lukas Anneser](#) [ORCID: orcid.org/0000-0001-5870-5722¹](#),
- [Ivan C. Alcantara¹](#) [nAff3](#),
- [Anja Gemmer](#) [ORCID: orcid.org/0000-0003-0282-9587¹](#),
- [Kristina Mirkes¹](#),
- [Soojin Ryu²](#) [nAff4](#) &
- [Erin M. Schuman](#) [ORCID: orcid.org/0000-0002-7053-1005¹](#)

[Nature](#) volume **588**, pages653–657(2020)[Cite this article](#)

- 3629 Accesses
- 236 Altmetric
- [Metrics details](#)

Subjects

- [Cooperation](#)
- [Neural circuits](#)

Abstract

Species that depend on membership in social groups for survival exhibit changes in neuronal gene expression and behaviour when they face

restricted social interactions or isolation^{1,2,3}. Here we show that, across the lifespan of zebrafish (*Danio rerio*), social isolation specifically decreased the level of transcription of *pth2*, the gene that encodes the vertebrate-specific neuropeptide Pth2. However, 30 minutes of exposure to conspecifics was sufficient to initiate a significant rescue of *pth2* transcript levels in previously isolated zebrafish. Transcription of *pth2* exhibited bidirectional dynamics; following the acute isolation of socially reared fish, a rapid reduction in the levels of *pth2* was observed. The expression of *pth2* tracked not only the presence of other fish but also the density of the group. The sensory modality that controls the expression of *pth2* was neither visual nor chemosensory in origin but instead was mechanical, induced by the movements of neighbouring fish. Chemical ablation of the mechanosensitive neuromast cells within the lateral line of fish prevented the rescue of *pth2* levels that was induced by the social environment. In addition, mechanical perturbation of the water at frequencies similar to the movements of the zebrafish tail was sufficient to rescue the levels of *pth2* in previously isolated fish. These data indicate a previously underappreciated role for the relatively unexplored neuropeptide Pth2 in both tracking and responding to the population density of the social environment of an animal.

[Access through your institution](#)

[Change institution](#)

[Buy or subscribe](#)

Access options

Subscribe to Journal

Get full journal access for 1 year

\$199.00

only \$3.83 per issue

[Subscribe](#)

All prices are NET prices.
VAT will be added later in the checkout.

Rent or Buy article

Get time limited or full article access on ReadCube.

from \$8.99

[Rent or Buy](#)

All prices are NET prices.

Additional access options:

- [Log in](#)
- [Access through your institution](#)
- [Learn about institutional subscriptions](#)

Fig. 1: Transcriptional response to social isolation.

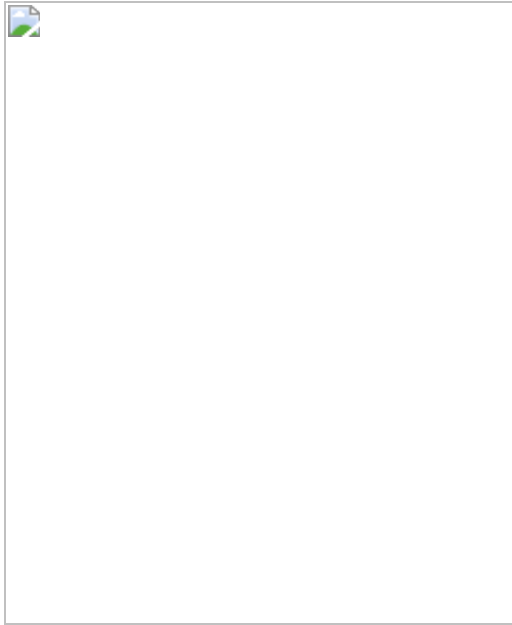


Fig. 2: Transcriptional dynamics of *pth2*.

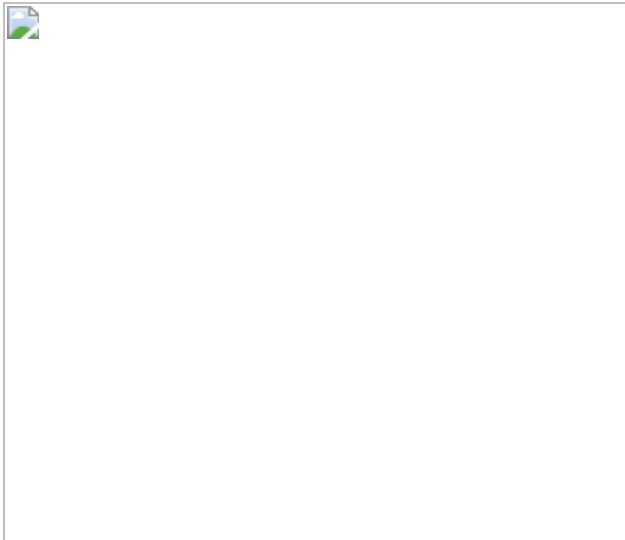


Fig. 3: Sensory perception of conspecifics.

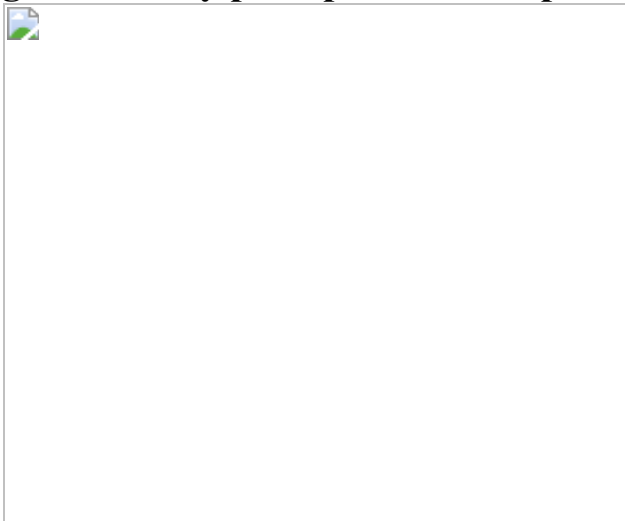
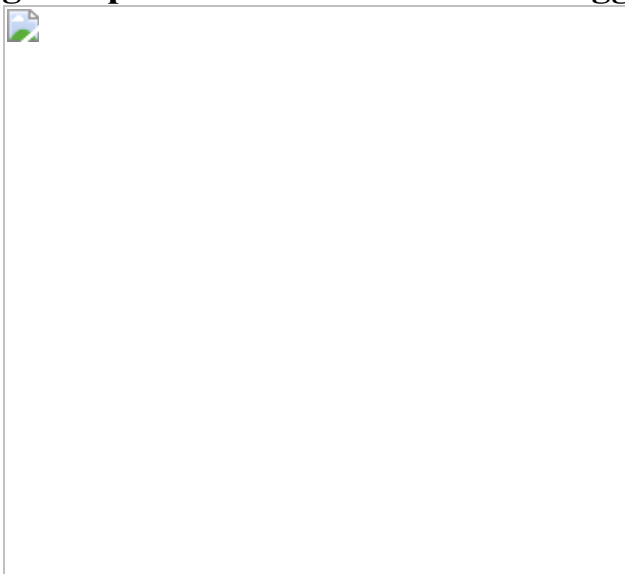


Fig. 4: Specific mechanosensation triggers transcription of *pth2*.



Data availability

All data are provided in this paper or the accompanying Supplementary Information files. All sequencing data have been made available under the Sequence Read Archive BioProject [PRJNA627056](#). Gene annotation was performed using the publicly available ENSEMBL database (<https://www.ensembl.org/Danio rerio/Info/Index>). The Z-Brain atlas can be downloaded from <https://github.com/owenrandlett/Z-Brain>⁶⁰. Gene expression data from Raj et al.²³ are available under the Gene Expression Omnibus accession number [GSE105010](#).

Code availability

All relevant code is available under the public repository <https://github.com/Anneser/SensingOthers/>.

References

1. 1.

Fulcher, N., Tran, S., Shams, S., Chatterjee, D. & Gerlai, R. Neurochemical and behavioral responses to unpredictable chronic mild stress following developmental isolation: the zebrafish as a model for major depression. *Zebrafish* **14**, 23–34 (2017).

[CAS](#) [PubMed](#) [Google Scholar](#)

2. 2.

Slavich, G. M. & Cole, S. W. The emerging field of human social genomics. *Clin. Psychol. Sci.* **1**, 331–348 (2013).

[PubMed](#) [PubMed Central](#) [Google Scholar](#)

3. 3.

Zelikowsky, M. et al. The neuropeptide Tac2 controls a distributed brain state induced by chronic social isolation stress. *Cell* **173**, 1265–1279 (2018).

[CAS](#) [PubMed](#) [PubMed Central](#) [Google Scholar](#)

4. 4.

Harlow, H. F., Dodsworth, R. O. & Harlow, M. K. Total social isolation in monkeys. *Proc. Natl Sci. Acad. USA* **54**, 90–97 (1965).

[ADS](#) [CAS](#) [Google Scholar](#)

5. 5.

Kumari, A., Singh, P., Baghel, M. S. & Thakur, M. K. Social isolation mediated anxiety like behavior is associated with enhanced expression and regulation of BDNF in the female mouse brain. *Physiol. Behav.* **158**, 34–42 (2016).

[CAS](#) [PubMed](#) [Google Scholar](#)

6. 6.

Swerdlow, N. R. et al. Forebrain gene expression predicts deficits in sensorimotor gating after isolation rearing in male rats. *Behav. Brain Res.* **257**, 118–128 (2013).

[CAS](#) [PubMed](#) [PubMed Central](#) [Google Scholar](#)

7. 7.

Angulo, J. A., Printz, D., Ledoux, M. & McEwen, B. S. Isolation stress increases tyrosine hydroxylase mRNA in the locus coeruleus and midbrain and decreases proenkephalin mRNA in the striatum and nucleus accumbens. *Brain Res. Mol. Brain Res.* **11**, 301–308 (1991).

[CAS](#) [PubMed](#) [Google Scholar](#)

8. 8.

Poletto, R., Siegfried, J. M., Steibel, J. P., Coussens, P. M. & Zanella, A. J. Investigation of changes in global gene expression in the frontal cortex of early-weaned and socially isolated piglets using microarray and quantitative real-time RT-PCR. *Brain Res.* **1068**, 7–15 (2006).

[CAS](#) [PubMed](#) [Google Scholar](#)

9. 9.

Yap, E. L. & Greenberg, M. E. Activity-regulated transcription: bridging the gap between neural activity and behavior. *Neuron* **100**, 330–348 (2018).

[CAS](#) [PubMed](#) [PubMed Central](#) [Google Scholar](#)

10. 10.

Sun, X. & Lin, Y. Npas4: linking neuronal activity to memory. *Trends Neurosci.* **39**, 264–275 (2016).

[CAS](#) [PubMed](#) [PubMed Central](#) [Google Scholar](#)

11. 11.

Usdin, T. B. Evidence for a parathyroid hormone-2 receptor selective ligand in the hypothalamus. *Endocrinology* **138**, 831–834 (1997).

[CAS](#) [PubMed](#) [Google Scholar](#)

12. 12.

Coutellier, L., Logemann, A., Rusnak, M. & Usdin, T. B. Maternal absence of the parathyroid hormone 2 receptor affects postnatal pup development. *J. Neuroendocrinol.* **23**, 612–619 (2011).

[CAS](#) [PubMed](#) [PubMed Central](#) [Google Scholar](#)

13. 13.

Cservenák, M. et al. A thalamo-hypothalamic pathway that activates oxytocin neurons in social contexts in female rats. *Endocrinology* **158**, 335–348 (2017).

[PubMed](#) [Google Scholar](#)

14. 14.

Dobolyi, A., Ueda, H., Uchida, H., Palkovits, M. & Usdin, T. B. Anatomical and physiological evidence for involvement of tuberoinfundibular peptide of 39 residues in nociception. *Proc. Natl Acad. Sci. USA* **99**, 1651–1656 (2002).

[ADS](#) [CAS](#) [PubMed](#) [Google Scholar](#)

15. 15.

Guerreiro, P. M., Renfro, J. L., Power, D. M. & Canario, A. V. M. The parathyroid hormone family of peptides: structure, tissue distribution, regulation, and potential functional roles in calcium and phosphate balance in fish. *Am. J. Physiol. Regul. Integr. Comp. Physiol.* **292**, R679–R696 (2007).

[CAS](#) [PubMed](#) [Google Scholar](#)

16. 16.

Bhattacharya, P., Yan, Y. L., Postlethwait, J. & Rubin, D. A. Evolution of the vertebrate pth2 (tip39) gene family and the regulation of PTH type 2 receptor (pth2r) and its endogenous ligand pth2 by hedgehog signaling in zebrafish development. *J. Endocrinol.* **211**, 187–200 (2011).

[CAS](#) [PubMed](#) [PubMed Central](#) [Google Scholar](#)

17. 17.

Usdin, T. B., Gruber, C. & Bonner, T. I. Identification and functional expression of a receptor selectively recognizing parathyroid hormone, the PTH2 receptor. *J. Biol. Chem.* **270**, 15455–15458 (1995).

[CAS](#) [PubMed](#) [Google Scholar](#)

18. 18.

Cservesnák, M. et al. Tuberoinfundibular peptide of 39 residues is activated during lactation and participates in the suckling-induced prolactin release in rat. *Endocrinology* **151**, 5830–5840 (2010).

[PubMed](#) [PubMed Central](#) [Google Scholar](#)

19. 19.

Dobolyi, A., Cservesnák, M. & Young, L. J. Thalamic integration of social stimuli regulating parental behavior and the oxytocin system. *Front. Neuroendocrinol.* **51**, 102–115 (2018).

[CAS](#) [PubMed](#) [PubMed Central](#) [Google Scholar](#)

20. 20.

Sugimura, Y. et al. Centrally administered tuberoinfundibular peptide of 39 residues inhibits arginine vasopressin release in conscious rats. *Endocrinology* **144**, 2791–2796 (2003).

[CAS](#) [PubMed](#) [Google Scholar](#)

21. 21.

Dimitrov, E. & Usdin, T. B. Tuberoinfundibular peptide of 39 residues modulates the mouse hypothalamic–pituitary–adrenal axis via paraventricular glutamatergic neurons. *J. Comp. Neurol.* **518**, 4375–4394 (2010).

[CAS](#) [PubMed](#) [PubMed Central](#) [Google Scholar](#)

22. 22.

Fernandes, A. M., Beddows, E., Filippi, A. & Driever, W. Orthopedia transcription factor *otpa* and *otpB* paralogous genes function during dopaminergic and neuroendocrine cell specification in larval zebrafish. *PLoS One* **8**, e75002 (2013).

[ADS](#) [CAS](#) [PubMed](#) [PubMed Central](#) [Google Scholar](#)

23. 23.

Raj, B. et al. Simultaneous single-cell profiling of lineages and cell types in the vertebrate brain. *Nat. Biotechnol.* **36**, 442–450 (2018).

[CAS](#) [PubMed](#) [PubMed Central](#) [Google Scholar](#)

24. 24.

Vitebsky, A., Reyes, R., Sanderson, M. J., Michel, W. C. & Whitlock, K. E. Isolation and characterization of the laure olfactory behavioral mutant in the zebrafish, *Danio rerio*. *Dev. Dyn.* **234**, 229–242 (2005).

[CAS](#) [PubMed](#) [Google Scholar](#)

25. 25.

Gerlach, G., Hodgins-Davis, A., Avolio, C. & Schunter, C. Kin recognition in zebrafish: a 24-hour window for olfactory imprinting. *Proc. Biol. Sci.* **275**, 2165–2170 (2008).

[PubMed](#) [PubMed Central](#) [Google Scholar](#)

26. 26.

Brockhoff, S. E. Measuring the optokinetic response of zebrafish larvae. *Nat. Protoc.* **1**, 2448–2451 (2006).

[CAS](#) [PubMed](#) [Google Scholar](#)

27. 27.

Neuhauß, S. C. F. Behavioral genetic approaches to visual system development and function in zebrafish. *J. Neurobiol.* **54**, 148–160 (2003).

[CAS](#) [PubMed](#) [Google Scholar](#)

28. 28.

Lloyd, E. et al. Evolutionary shift towards lateral line dependent prey capture behavior in the blind Mexican cavefish. *Dev. Biol.* **441**, 328–337 (2018).

[CAS](#) [PubMed](#) [PubMed Central](#) [Google Scholar](#)

29. 29.

Suli, A., Watson, G. M., Rubel, E. W. & Raible, D. W. Rheotaxis in larval zebrafish is mediated by lateral line mechanosensory hair cells. *PLoS One* **7**, e29727 (2012).

[ADS](#) [CAS](#) [PubMed](#) [PubMed Central](#) [Google Scholar](#)

30. 30.

Butler, J. M. & Maruska, K. P. Mechanosensory signaling as a potential mode of communication during social interactions in fishes. *J. Exp. Biol.* **219**, 2781–2789 (2016).

[PubMed](#) [Google Scholar](#)

31. 31.

Hernández, P. P., Moreno, V., Olivari, F. A. & Allende, M. L. Sub-lethal concentrations of waterborne copper are toxic to lateral line neuromasts in zebrafish (*Danio rerio*). *Hear. Res.* **213**, 1–10 (2006).

[PubMed](#) [Google Scholar](#)

32. 32.

Groneberg, A. H., Herget, U., Ryu, S. & De Marco, R. J. Positive taxis and sustained responsiveness to water motions in larval zebrafish. *Front. Neural Circuits* **9**, 9 (2015).

[PubMed](#) [PubMed Central](#) [Google Scholar](#)

33. 33.

Lush, M. E. & Piotrowski, T. Sensory hair cell regeneration in the zebrafish lateral line. *Dev. Dyn.* **243**, 1187–1202 (2014).

[PubMed](#) [PubMed Central](#) [Google Scholar](#)

34. 34.

Brown, A. D., Mussen, T. D., Sisneros, J. A. & Coffin, A. B. Reevaluating the use of aminoglycoside antibiotics in behavioral studies of the lateral line. *Hear. Res.* **272**, 1–4 (2011).

[CAS](#) [PubMed](#) [Google Scholar](#)

35. 35.

d'Alençon, C. A. et al. A high-throughput chemically induced inflammation assay in zebrafish. *BMC Biol.* **8**, 151 (2010).

[PubMed](#) [PubMed Central](#) [Google Scholar](#)

36. 36.

Kirchner, S. R., Fedoruk, M., Lohmüller, T. & Feldmann, J. Analyzing the movement of the Nauplius '*Artemia salina*' by optical tracking of plasmonic nanoparticles. *J. Vis. Exp.* **89**, 51502 (2014).

[Google Scholar](#)

37. 37.

Müller, U. K. & van Leeuwen, J. L. Swimming of larval zebrafish: ontogeny of body waves and implications for locomotory development. *J. Exp. Biol.* **207**, 853–868 (2004).

[PubMed](#) [Google Scholar](#)

38. 38.

Pan, Y., Liu, Y., Young, K. A., Zhang, Z. & Wang, Z. Post-weaning social isolation alters anxiety-related behavior and neurochemical gene expression in the brain of male prairie voles. *Neurosci. Lett.* **454**, 67–71 (2009).

[CAS](#) [PubMed](#) [PubMed Central](#) [Google Scholar](#)

39. 39.

French, J. A., Taylor, J. H., Mustoe, A. C. & Cavanaugh, J. Neuropeptide diversity and the regulation of social behavior in New World primates. *Front. Neuroendocrinol.* **42**, 18–39 (2016).

[CAS](#) [PubMed](#) [PubMed Central](#) [Google Scholar](#)

40. 40.

Cole, S. W. et al. Myeloid differentiation architecture of leukocyte transcriptome dynamics in perceived social isolation. *Proc. Natl Acad. Sci. USA* **112**, 15142–15147 (2015).

[ADS](#) [CAS](#) [PubMed](#) [Google Scholar](#)

41. 41.

Poletto, R., Steibel, J. P., Siegfard, J. M. & Zanella, A. J. Effects of early weaning and social isolation on the expression of glucocorticoid and mineralocorticoid receptor and 11 β -hydroxysteroid dehydrogenase 1 and 2 mRNAs in the frontal cortex and hippocampus of piglets. *Brain Res.* **1067**, 36–42 (2006).

[CAS](#) [PubMed](#) [Google Scholar](#)

42. 42.

Hermes, G., Li, N., Duman, C. & Duman, R. Post-weaning chronic social isolation produces profound behavioral dysregulation with decreases in prefrontal cortex synaptic-associated protein expression in female rats. *Physiol. Behav.* **104**, 354–359 (2011).

[CAS](#) [PubMed](#) [Google Scholar](#)

43. 43.

Robinson, S. A., Loiacono, R. E., Christopoulos, A., Sexton, P. M. & Malone, D. T. The effect of social isolation on rat brain expression of genes associated with endocannabinoid signaling. *Brain Res.* **1343**, 153–167 (2010).

[CAS](#) [PubMed](#) [Google Scholar](#)

44. 44.

Gellén, B., Zelena, D., Usdin, T. B. & Dobolyi, Á. The parathyroid hormone 2 receptor participates in physiological and behavioral alterations of mother mice. *Physiol. Behav.* **181**, 51–58 (2017).

[PubMed](#) [Google Scholar](#)

45. 45.

Cservenák, M. et al. Thalamic neuropeptide mediating the effects of nursing on lactation and maternal motivation. *Psychoneuroendocrinology* **38**, 3070–3084 (2013).

[PubMed](#) [Google Scholar](#)

46. 46.

Butler, J. M. & Maruska, K. P. The mechanosensory lateral line is used to assess opponents and mediate aggressive behaviors during territorial interactions in an African cichlid fish. *J. Exp. Biol.* **218**, 3284–3294 (2015).

[PubMed](#) [Google Scholar](#)

47. 47.

Simpson, S. J., Despland, E., Hägele, B. F. & Dodgson, T. Gregarious behavior in desert locusts is evoked by touching their back legs. *Proc. Natl Acad. Sci. USA* **98**, 3895–3897 (2001).

[ADS](#) [CAS](#) [PubMed](#) [Google Scholar](#)

48. 48.

McCormick, C. A. *Central Lateral Line Mechanosensory Pathways in Bony Fish. The Mechanosensory Lateral Line* (Springer-Verlag, 1989).

49. 49.

Petersen, C. L. et al. Exposure to advertisement calls of reproductive competitors activates vocal-acoustic and catecholaminergic neurons in the plainfin midshipman fish, *Porichthys notatus*. *PLoS One* **8**, e70474 (2013).

[CAS](#) [PubMed](#) [PubMed Central](#) [Google Scholar](#)

50. 50.

Burmeister, S. S., Rodriguez Moncalvo, V. G. & Pfennig, K. S. Monoaminergic integration of diet and social signals in the brains of juvenile spadefoot toads. *J. Exp. Biol.* **220**, 3135–3141 (2017).

[PubMed](#) [PubMed Central](#) [Google Scholar](#)

51. 51.

Alsop, D. & Vijayan, M. M. Development of the corticosteroid stress axis and receptor expression in zebrafish. *Am. J. Physiol. Regul. Integr. Comp. Physiol.* **294**, R711–R719 (2008).

[CAS](#) [PubMed](#) [Google Scholar](#)

52. 52.

Livak, K. J. & Schmittgen, T. D. Analysis of relative gene expression data using real-time quantitative PCR and the $2^{-\Delta\Delta C_T}$ method. *Methods* **25**, 402–408 (2001).

[CAS](#) [PubMed](#) [PubMed Central](#) [Google Scholar](#)

53. 53.

Dobin, A. et al. STAR: ultrafast universal RNA-seq aligner. *Bioinformatics* **29**, 15–21 (2013).

[CAS](#) [Google Scholar](#)

54. 54.

Liao, Y., Smyth, G. K. & Shi, W. featureCounts: an efficient general purpose program for assigning sequence reads to genomic features. *Bioinformatics* **30**, 923–930 (2014).

[CAS](#) [PubMed](#) [Google Scholar](#)

55. 55.

Durinck, S. et al. BioMart and Bioconductor: a powerful link between biological databases and microarray data analysis. *Bioinformatics* **21**, 3439–3440 (2005).

[CAS](#) [PubMed](#) [Google Scholar](#)

56. 56.

Robinson, M. D., McCarthy, D. J. & Smyth, G. K. edgeR: a Bioconductor package for differential expression analysis of digital gene expression data. *Bioinformatics* **26**, 139–140 (2010).

[CAS](#) [Google Scholar](#)

57. 57.

Benjamini, Y. & Hochberg, Y. Controlling the false discovery rate: a practical and powerful approach to multiple testing. *J. R. Stat. Soc. B* **57**, 289–300 (1995).

[MathSciNet](#) [MATH](#) [Google Scholar](#)

58. 58.

Herget, U., Wolf, A., Wullimann, M. F. & Ryu, S. Molecular neuroanatomy and chemoarchitecture of the neurosecretory preoptic-hypothalamic area in zebrafish larvae. *J. Comp. Neurol.* **522**, 1542–1564 (2014).

[CAS](#) [PubMed](#) [Google Scholar](#)

59. 59.

Ryu, S. et al. Orthopedia homeodomain protein is essential for diencephalic dopaminergic neuron development. *Curr. Biol.* **17**, 873–880 (2007).

[CAS](#) [PubMed](#) [Google Scholar](#)

60. 60.

Randlett, O. et al. Whole-brain activity mapping onto a zebrafish brain atlas. *Nat. Methods* **12**, 1039–1046 (2015).

[CAS](#) [PubMed](#) [PubMed Central](#) [Google Scholar](#)

61. 61.

Jeffery, G. S. X. E. et al. Comprehensive maps of *Drosophila* higher olfactory centers: spatially segregated fruit and pheromone representation. *Cell* **128**, 1187–1203 (2007).

[CAS](#) [PubMed](#) [PubMed Central](#) [Google Scholar](#)

62. 62.

Schindelin, J. et al. Fiji: an open-source platform for biological-image analysis. *Nat. Methods* **9**, 676–682 (2012).

[CAS](#) [PubMed](#) [Google Scholar](#)

63. 63.

Palmér, T. et al. Action sequencing in the spontaneous swimming behavior of zebrafish larvae—implications for drug development. *Sci. Rep.* **7**, 3191 (2017).

[ADS](#) [PubMed](#) [PubMed Central](#) [Google Scholar](#)

64. 64.

Holm, S. A simple sequentially rejective multiple test procedure. *Scand. J. Stat.* **6**, 65–70 (1978).

[MathSciNet](#) [MATH](#) [Google Scholar](#)

65. 65.

Raj, B., Gagnon, J. A. & Schier, A. F. Large-scale reconstruction of cell lineages using single-cell readout of transcriptomes and CRISPR–Cas9 barcodes by scGESTALT. *Nat. Protoc.* **13**, 2685–2713 (2018).

[CAS](#) [PubMed](#) [PubMed Central](#) [Google Scholar](#)

[Download references](#)

Acknowledgements

We thank S. Chanda, J. Glüsing, F. Vollrath and C. Polissen for their contribution to the experiments; A.-Y. Loos for her help with fish husbandry and discussions; and G. Laurent for discussions. S.R. and E.M.S. are funded by DFG CRC 1193: Neurobiology of Resilience. E.M.S. is supported by the Max Planck Society.

Author information

Author notes

1. Ivan C. Alcantara

Present address: Brown University, Providence, RI, USA

2. Soojin Ryu

Present address: Living Systems Institute, College of Medicine and Health, University of Exeter, Exeter, UK

Affiliations

1. Max Planck Institute for Brain Research, Frankfurt, Germany

Lukas Anneser, Ivan C. Alcantara, Anja Gemmer, Kristina Mirkes & Erin M. Schuman

2. Johannes Gutenberg University Medical Center, Mainz, Germany

Soojin Ryu

Authors

1. Lukas Anneser

[View author publications](#)

You can also search for this author in [PubMed](#) [Google Scholar](#)

2. Ivan C. Alcantara

[View author publications](#)

You can also search for this author in [PubMed](#) [Google Scholar](#)

3. Anja Gemmer

[View author publications](#)

You can also search for this author in [PubMed](#) [Google Scholar](#)

4. Kristina Mirkes

[View author publications](#)

You can also search for this author in [PubMed](#) [Google Scholar](#)

5. Soojin Ryu

[View author publications](#)

You can also search for this author in [PubMed](#) [Google Scholar](#)

6. Erin M. Schuman

[View author publications](#)

You can also search for this author in [PubMed](#) [Google Scholar](#)

Contributions

L.A. and E.M.S. conceived the project. L.A., A.G., S.R. and E.M.S. designed the experiments. L.A., I.C.A., A.G. and K.M. conducted the experiments. L.A. wrote the code for data acquisition, analysis and modelling. L.A. and E.M.S. wrote the manuscript.

Corresponding author

Correspondence to [Erin M. Schuman](#).

Ethics declarations

Competing interests

The authors declare no competing interests.

Additional information

Peer review information *Nature* thanks Iain Couzin, Allen Mensinger and Ted Usdin for their contribution to the peer review of this work. Peer reviewer reports are available.

Publisher's note Springer Nature remains neutral with regard to jurisdictional claims in published maps and institutional affiliations.

Extended data figures and tables

[Extended Data Fig. 1 Extended analysis of transcriptional responses to social isolation.](#)

a, Experimental scheme. Beginning at 2 dpf, larval zebrafish were raised in an isolated or social (with four conspecifics) environment for 5, 8, 14 or 21 days. After the specified periods, RNA was obtained from whole brains and next-generation sequencing (NGS) was conducted. 6 biological replicates were obtained for 5 and 8 dpf, 5 replicates for 14 dpf, and 4 replicates for 21 dpf. **b**, Box plots depicting the fold change of gene expression between isolated and social groups (5 dpf) for all members of the pth-family in zebrafish. Only *pth2* showed a significant change. Values are expressed relative to the isolated condition ($n = 10$ for all experiments, paired *t*-test, one-sided, Benjamini-Hochberg-corrected: *pth2*, $p_t = 9.82 < 0.001$, *pthla*, $p_t = -0.52 = 0.62$, *pthlb*, *pth1a*, $p_t = -2.55 = 0.09$, *pth1b*, $p_t = 1.55 = 0.31$, $p_t = -0.92 = 0.57$, *pth4*, $p_t = 0.51 = 0.62$). **c**, Gene expression data of previously described stress-responsive genes, *StAR*: steroidogenic acute regulatory protein; *nr3c1*: nuclear receptor subfamily 3, group C, member 1; *avp*: arginine vasopressin; *pomca*: proopiomelanocortin a; *pomcb*:

proopiomelanocortin b; and *oxt: oxytocin* ($n = 6$ for all genes, FDR-corrected quasi-likelihood F-test implemented in edgeR, *StAR*: $P = 0.99$, *nr3c1*: $P = 0.99$, *avp*: $P = 0.99$, *pomca*: 0.99 , *pomcb*: $P = 0.99$, *oxt*: $P = 0.99$). **d**, Validation of gene expression analysis by qPCR for *StAR* and *nr3c1* after short exposure of previously isolated fish to conspecifics for 3 h. Box plots show expression relative to mean levels of isolated animals. Paired, one-sided *t*-tests, $n = 6$ for both genes. For *StAR*, $p_{t=0.37} = 0.71$, for *nr3c1*, $p_{t=-0.45} = 0.66$. Box plots in **b** and **d** represent the median (black line), the lower and upper quartile (box) with the whiskers indicating at most $1.5 \times$ the interquartile range. Significance is reported as follows: *** $P < 0.001$.

Extended Data Fig. 2 Registration and morphology of *pth2*[±] cells.

a, Maximum-intensity projection (dorsal view) of the averaged Elavl3-H2BRFP stack from the z-brain atlas overlaid with the manually annotated position of *pth2*⁺ cells. **b**, Lateral view of the same stack. **c**, Number of *pth2*⁺ cells in each of the bilateral clusters. Stacks from 7 different 5 dpf larvae were counted. In the left cluster, 9.4 ± 2.4 cells were found, in the right one 10.9 ± 1.7 (mean \pm standard deviation). Box plots represent the median (black line), the lower and upper quartile (box) with the whiskers indicating at most $1.5 \times$ the interquartile range. **d**, Depth-encoded (0 – 184 μm) Z-projection of whole-mount immunostaining against *pth2* (5 dpf). White box shows area magnified in **e–g**. **e**, Single frame on the level of the *pth2*⁺ cell bodies. **f**, Magnification of a single frame on the level of the posterior projections. **g**, Single frame on the depth of the anterior projections of the *pth2*⁺ cells, forming a dense neuropil in the telencephalon. Scale bar indicates 100 μm .

Extended Data Fig. 3 Localization of *pth2*[±] cells.

a, *pth2*⁺ cell bodies form bilateral clusters at the edge of the *otpa* domain in the diencephalon. More ventrally, *pth2*⁺ cell projections were closely apposed to the *otpa* domain and enter the telencephalon. 18 animals were

imaged across 4 different experiments. All scale bars indicate 100 µm. **b**, The *pth2*⁺ cells were found dorsolateral to the main *TH*⁺ cell clusters in the diencephalon. The rostral projections of the *pth2* clusters were found caudal to the telencephalic dopaminergic neurites. 14 animals were imaged across 3 different experiments. **c**, *pth2*⁺ cell bodies were slightly more dorsally located than the more rostrally situated *OXT*⁺ neurons. Their telencephalic projections formed a dense neuropil structure rostral to the neurosecretory hypothalamic preoptic area, where *OXT*⁺ neurons were found. 4 different animals were imaged.

Extended Data Fig. 4 Evidence for widespread expression of the Pth2 receptor, *pth2r*.

a, Clustering of cell types reproduced from a previous study⁶⁵. Data were used as provided under Gene Expression Omnibus accession number GSE105010 and analysed using the Seurat pipeline. **b**, Distribution of *pth2r*-expressing cells. Grey points correspond to cells in which *pth2r* was not detected, the intensity of blue indicates how many reads were detected. **c**, Distribution of oxytocin receptor (*oxtr*)-expressing cells. **d**, Distribution of *avpr2aa*-expressing cells. Four receptors of *avp* were detected in the data set, we show the one that was most widely expressed. **e**, Barplots show the percentage of *pth2r*⁺ cells within each cluster (“measured”). For each cluster, we also provide a bootstrapped estimation of what percentage would be expected by random sampling of cells, with numbers of bootstrapped cells being equal to cells belonging to the given cluster. In addition, we show the percentage of *pth2r*⁺ cells across the entire population (“all”) **f**, Barplots show percentage of *avpr2aa*⁺ cells within each cluster, same as in e. For *oxtr*⁺ cells, an insufficient number of cells were identified in this data set to perform this kind of comparison.

Extended Data Fig. 5 The effect of sex and density on *pth2* expression in adult zebrafish.

a, Male and female adult zebrafish (3 mpf) were sampled from the same tank. Box plots show *pth2* levels in relation to the mean level of male gene expression. Unpaired, one-sided *t*-test, $p_{(n=4, t=0.40)} = 0.69$. **b**, Box plots

show *pth2* levels in adult zebrafish that were kept at densities of 5 and 35 per 3.5 l for one week, respectively. Expression levels were normalized to the mean level at the lower density. Unpaired, one-sided *t*-test, $p_{(n=6, t=2.44)} = 3.4\text{E-}2$. Box plots in **a** and **b** represent the median (black line), the lower and upper quartile (box) with the whiskers indicating at most $1.5 \times$ the interquartile range. Significance is reported as follows: * $P < 0.05$.

Extended Data Fig. 6 The effect of genotype on *pth2* transcription.

a, Box plot shows the difference in *pth2* levels between socially reared and isolated Nacre (*mitfa*^{-/-}) larvae (5 dpf). 6 replicates were obtained, a paired, one-sided *t*-test showed that $p_t = 7.98 = 2.1\text{E-}4$. **b**, Same experiment as shown in Fig. 3d. Here, *pth2* levels of KN larvae were assessed and Nacre (*mitfa*^{-/-}) animals used as stooges. The impact of visual and physical access as well as the interaction of both was evaluated using a 2-way ANOVA. For all groups, $n = 6$. For visual access, $p_F = 0.83 = 0.37$, physical access, $p_F = 144.96 = 1.3\text{E-}10$, visual-physical interaction, $p_F = 2.41 = 0.14$. Box plots in **a** and **b** represent the median (black line), the lower and upper quartile (box) with the whiskers indicating at most $1.5 \times$ the interquartile range. Significance is reported as follows: *** $P < 0.001$.

Extended Data Fig. 7 The effect of experimental conditions on locomotion.

a, Box plot shows the average velocity of 5 dpf animals that were raised either in isolation or with conspecifics. Unpaired, one-sided *t*-test, $n = 14$ for isolation-reared fish, $n = 11$ for socially-reared fish, $p_t = 0.28 = 0.78$. **b**, Box plot depicts average velocity of isolation-reared animals when swimming alone or together with 14 conspecifics. Unpaired, one-sided *t*-test, $n = 8$ for both conditions, $p_t = 0.32 = 0.75$. **c**, Scheme of the open field used in **d**. Animals were placed in a rectangular dish, which contained an adjacent compartment separated by a transparent barrier (indicated by dashed line), where (in some experiments) conspecifics were placed. **d**, Box plot shows the average velocity of animals at different developmental

stages after rearing in isolation or with conspecifics. Visual access indicates whether conspecifics were placed in the adjacent compartment. An ANOVA revealed that visual access did not lead to differences between the groups ($p_{F=0.21} = 0.65$). Speed increased with age ($p_{F=333.62} = 4.1\text{E-}47$), and was influenced by raising condition ($p_{F=16.81} = 5.7\text{E-}5$), although one-sided post hoc *t*-tests corrected with Holm's method indicated no consistent influence on locomotion for the different age groups. Interaction effects were not observed. At 7 dpf without visual access (v.a.) and socially reared: $N = 15$, isolation-reared: $N = 17$, $p_t = 4.71 = 2.1\text{E-}4$; $N = 16$ with v.a. and socially reared; $N = 18$ isolation-reared, $p_t = 2.38 = 6.9\text{E-}2$; at 14 dpf without v.a., socially reared: $N = 17$ and isolation-reared: $N = 16$, $p_t = 1.55 = 0.19$; with v.a. and socially reared $N = 18$ and isolation-reared $N = 15$, $p_t = 1.79 = 0.17$; at 21 dpf, without v.a., socially reared: $N = 18$, isolation-reared: $N = 17$, $p_t = 3.47 = 5.2\text{E-}3$; with v.a. and socially reared $N = 16$ and isolation-reared $N = 13$, $p_t = 0.06 = 0.82$; at 28 dpf, isolation-reared: $N = 9$ for both cases, without v.a., socially reared: $N = 15$, $p_t = 0.23 = 0.82$; with v.a. $N = 18$, $p_t = 2.25 = 8.3\text{E-}2$. Box plots in **a**, **b** and **d** represent the median (black line), the lower and upper quartile (box) with the whiskers indicating at most $1.5 \times$ the interquartile range. **e**, Graph depicts the bout onset of larvae in response to piezo stimulation as explained in Fig. [4d, e](#). Bout onsets are displayed as relative frequencies, data from individual fish are shown in grey with the mean (smoothed with a rolling window of length 0.05 s) overlaid in purple.

Extended Data Fig. 8 Artificial mechanical stimulation.

a, Experimental scheme for artificial mechanical perturbation. A randomized series of stimulation and pause periods was drawn from two distributions using a custom-written Matlab script. Periods of activity were propagated via an Arduino board to gate a frequency generator. The output signal was amplified before activating a piezo actuator transferring specific frequencies to a well in a 12-well dish with an isolated fish. **b**, Scatter plot indicating *pth2* levels relative to isolated animals (dashed line) after 3 h of different stimulation paradigms (either continuous stimulation or short bouts of stimulation interrupted by pauses of the same length). Paired, one-

sided *t*-tests with BH-correction were used. Single piezo element: for continuous stimulation, $p_{(n=6, t=-0.65)} = 0.54$, for continuous stimulation in the presence of kin-imbued water, $n = 2$. Two piezo elements: for periodic stimulation at 300 ms intervals, $p_{(n=3, t=-0.18)} = 0.87$, at 5 s intervals, $n = 2$. Two piezo elements with appendages: for periodic stimulation at 300 ms intervals, $p_{(n=3, t=-0.68)} = 0.57$, at 500 ms intervals, $n = 2$, at 700 ms, $p_{(n=3, t=-0.82)} = 0.50$, at 800 ms intervals, $p_{(n=5, t=-0.85)} = 0.44$. **c**, Larval zebrafish (5 dpf) were recorded for 10 min during a free exploration in 10 cm diameter dishes. Trajectories were used to extract behavioural features. **d**, Locomotion of larval fish occurs in discrete bouts, facilitating the extraction of interbout-intervals (IBIs). In total, we extracted 16.326 IBIs from 25 fish. **e**, Distribution of all IBIs is shown as a histogram, overlaid with a log-logarithmic distribution fit to the data. **f**, Table displays all distribution types that were fitted to the IBI data set and shows the corresponding Akaike information criterion.

Supplementary information

Reporting Summary

Supplementary Table 1

Table listing all genes identified as differentially expressed at the different developmental stages tested. Provided are ENSEMBL gene ID, external gene name, entrezgene ID, Log-fold change, logCPM, P-value, FDR. P-values are derived using a quasi-likelihood F-test.

Supplementary Table 2

Table listing all Δ Ct values obtained in our qPCR experiments for all figures.

Peer Review File

Rights and permissions

[Reprints and Permissions](#)

About this article



Check for
updates

Cite this article

Anneser, L., Alcantara, I.C., Gemmer, A. *et al.* The neuropeptide Pth2 dynamically senses others via mechanosensation. *Nature* **588**, 653–657 (2020). <https://doi.org/10.1038/s41586-020-2988-z>

[Download citation](#)

- Received: 21 April 2020
- Accepted: 15 September 2020
- Published: 02 December 2020
- Issue Date: 24 December 2020
- DOI: <https://doi.org/10.1038/s41586-020-2988-z>

Comments

By submitting a comment you agree to abide by our [Terms](#) and [Community Guidelines](#). If you find something abusive or that does not comply with our terms or guidelines please flag it as inappropriate.

[Access through your institution](#)

[Change institution](#)

[Buy or subscribe](#)

This article was downloaded by **calibre** from <https://www.nature.com/articles/s41586-020-2988-z>

| [Section menu](#) | [Main menu](#) |

- Article
- [Published: 14 October 2020](#)

The NAD⁺-mediated self-inhibition mechanism of pro-neurodegenerative SARM1

- [Yuefeng Jiang](#) ORCID: orcid.org/0000-0003-3985-2027¹,
- [Tingting Liu](#)¹,
- [Chia-Hsueh Lee](#)²,
- [Qing Chang](#)³,
- [Jing Yang](#) ORCID: orcid.org/0000-0002-2048-735X¹ &
- [Zhe Zhang](#) ORCID: orcid.org/0000-0002-4932-4343¹

Nature volume **588**, pages658–663(2020)[Cite this article](#)

- 8184 Accesses
- 2 Citations
- 37 Altmetric
- [Metrics details](#)

Subjects

- [Cryoelectron microscopy](#)
- [Neuroscience](#)

Abstract

Pathological degeneration of axons disrupts neural circuits and represents one of the hallmarks of neurodegeneration^{1,2,3,4}. Sterile alpha and Toll/interleukin-1 receptor motif-containing protein 1 (SARM1) is a central regulator of this neurodegenerative process^{5,6,7,8}, and its Toll/interleukin-1 receptor (TIR) domain exerts its pro-neurodegenerative action through NADase activity^{9,10}. However, the mechanisms by which the activation of SARM1 is stringently controlled are unclear. Here we report the cryo-electron microscopy structures of full-length SARM1 proteins. We show that NAD⁺ is an unexpected ligand of the armadillo/heat repeat motifs (ARM) domain of SARM1. This binding of NAD⁺ to the ARM domain facilitated the inhibition of the TIR-domain NADase through the domain interface. Disruption of the NAD⁺-binding site or the ARM–TIR interaction caused constitutive activation of SARM1 and thereby led to axonal degeneration. These findings suggest that NAD⁺ mediates self-inhibition of this central pro-neurodegenerative protein.

[Access through your institution](#)

[Change institution](#)

[Buy or subscribe](#)

Access options

Subscribe to Journal

Get full journal access for 1 year

\$199.00

only \$3.83 per issue

[Subscribe](#)

All prices are NET prices.

VAT will be added later in the checkout.

Rent or Buy article

Get time limited or full article access on ReadCube.

from \$8.99

[Rent or Buy](#)

All prices are NET prices.

Additional access options:

- [Log in](#)
- [Access through your institution](#)
- [Learn about institutional subscriptions](#)

Fig. 1: SARM1^{TIR} is maintained in the inactive state by interacting with SARM1^{ARM}.

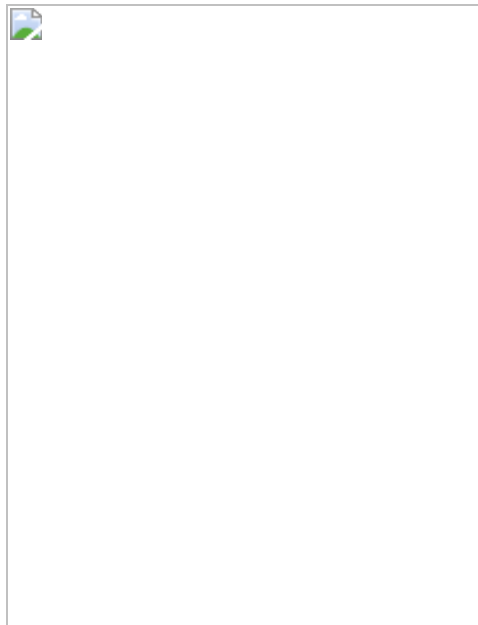


Fig. 2: Functional verification of the self-inhibitory interaction between SARM1^{ARM} and SARM1^{TIR}.

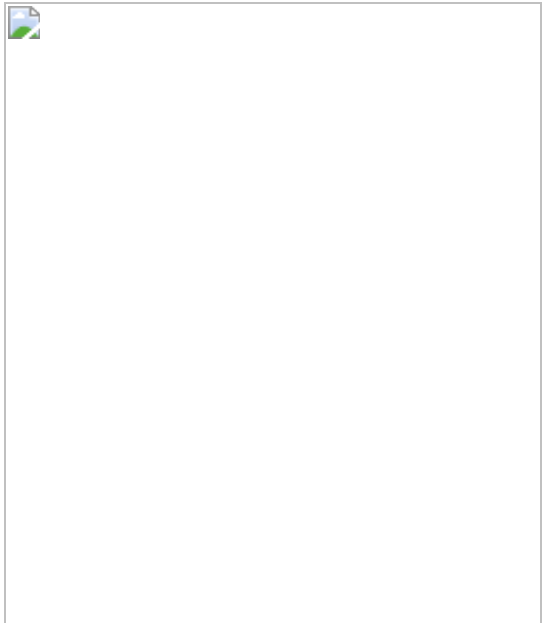


Fig. 3: The NAD⁺-binding site within SARM1^{ARM}.

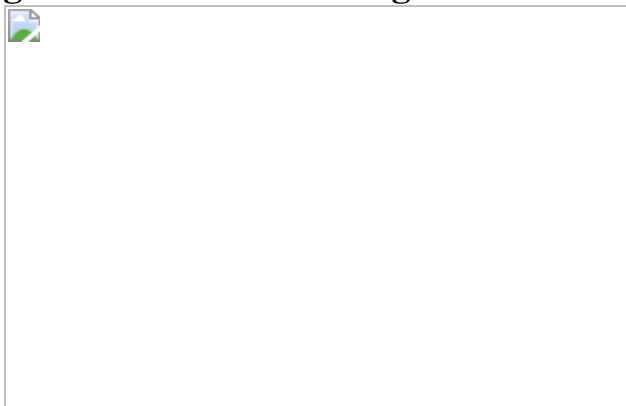
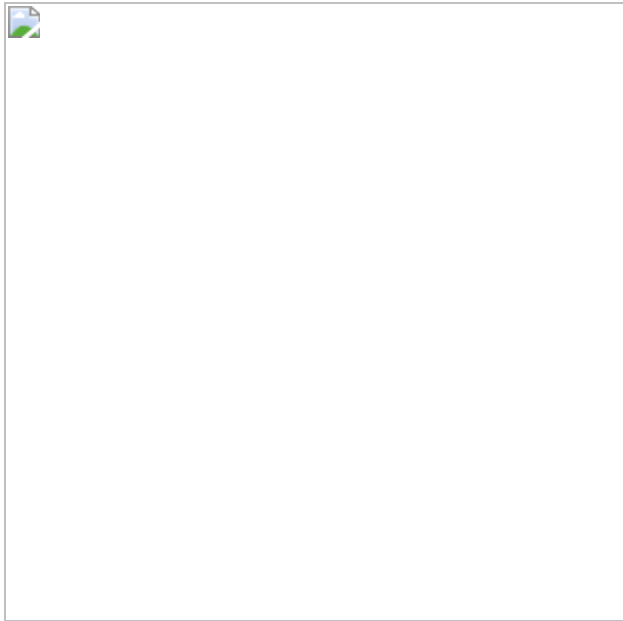


Fig. 4: The binding of NAD⁺ to SARM1^{ARM} facilitates the self-inhibition of SARM1.



Data availability

Cryo-EM density maps of SARM1, NAD⁺-bound SARM1 and NAD⁺-bound SARM1(E642A) have been deposited in the Electron Microscopy Data Bank (EMDB) under the accession codes EMD-30401, EMD-30402 and EMD-30403. Their atomic coordinates have been deposited in the Protein Data Bank (PDB) under the accession codes 7CM5, 7CM6 and 7CM7. All of the structural models used in this study are accessible in the Protein Data Bank under the following codes: SARM1^{SAM} (6O0S and 6QWV), SARM1^{TIR} (6O0Q), SARM1^{TIR}(G601P) (6O0V), importin- α (1IAL), β -catenin (2BCT), RRS1/RPS4 heterodimer (4C6T) and TLR10 homodimer (2J67). [Source data](#) are provided with this paper.

References

1. 1.

Coleman, M. P. & Freeman, M. R. Wallerian degeneration, Wld^S, and Nmnat. *Annu. Rev. Neurosci.* **33**, 245–267 (2010).

[CAS](#) [PubMed](#) [PubMed Central](#) [Google Scholar](#)

2. 2.

Conforti, L., Gilley, J. & Coleman, M. P. Wallerian degeneration: an emerging axon death pathway linking injury and disease. *Nat. Rev. Neurosci.* **15**, 394–409 (2014).

[CAS](#) [Google Scholar](#)

3. 3.

Freeman, M. R. Signaling mechanisms regulating Wallerian degeneration. *Curr. Opin. Neurobiol.* **27**, 224–231 (2014).

[CAS](#) [PubMed](#) [Google Scholar](#)

4. 4.

Coleman, M. P. & Höke, A. Programmed axon degeneration: from mouse to mechanism to medicine. *Nat. Rev. Neurosci.* **21**, 183–196 (2020).

[CAS](#) [PubMed](#) [Google Scholar](#)

5. 5.

Osterloh, J. M. et al. dSarm/Sarm1 is required for activation of an injury-induced axon death pathway. *Science* **337**, 481–484 (2012).

[CAS](#) [PubMed](#) [PubMed Central](#) [ADS](#) [Google Scholar](#)

6. 6.

Gerdts, J., Summers, D. W., Sasaki, Y., DiAntonio, A. & Milbrandt, J. Sarm1-mediated axon degeneration requires both SAM and TIR interactions. *J. Neurosci.* **33**, 13569–13580 (2013).

[CAS](#) [PubMed](#) [PubMed Central](#) [Google Scholar](#)

7. 7.

Yang, J. et al. Pathological axonal death through a MAPK cascade that triggers a local energy deficit. *Cell* **160**, 161–176 (2015).

[CAS](#) [PubMed](#) [PubMed Central](#) [Google Scholar](#)

8. 8.

Walker, L. J. et al. MAPK signaling promotes axonal degeneration by speeding the turnover of the axonal maintenance factor NMNAT2. *eLife* **6**, e22540 (2017).

[PubMed](#) [PubMed Central](#) [Google Scholar](#)

9. 9.

Essuman, K. et al. The SARM1 Toll/interleukin-1 receptor domain possesses intrinsic NAD⁺ cleavage activity that promotes pathological axonal degeneration. *Neuron* **93**, 1334–1343 (2017).

[CAS](#) [PubMed](#) [PubMed Central](#) [Google Scholar](#)

10. 10.

Gerdts, J., Brace, E. J., Sasaki, Y., DiAntonio, A. & Milbrandt, J. SARM1 activation triggers axon degeneration locally via NAD⁺ destruction. *Science* **348**, 453–457 (2015).

[CAS](#) [PubMed](#) [PubMed Central](#) [ADS](#) [Google Scholar](#)

11. 11.

Figley, M. D. & DiAntonio, A. The SARM1 axon degeneration pathway: control of the NAD⁺ metabolome regulates axon survival in health and disease. *Curr. Opin. Neurobiol.* **63**, 59–66 (2020).

[CAS](#) [PubMed](#) [Google Scholar](#)

12. 12.

Gerdts, J., Summers, D. W., Milbrandt, J. & DiAntonio, A. Axon self-destruction: new links among SARM1, MAPKs, and NAD⁺ metabolism. *Neuron* **89**, 449–460 (2016).

[CAS](#) [PubMed](#) [PubMed Central](#) [Google Scholar](#)

13. 13.

Mack, T. G. et al. Wallerian degeneration of injured axons and synapses is delayed by a Ube4b/Nmnat chimeric gene. *Nat. Neurosci.* **4**, 1199–1206 (2001).

[CAS](#) [PubMed](#) [Google Scholar](#)

14. 14.

Lunn, E. R., Perry, V. H., Brown, M. C., Rosen, H. & Gordon, S. Absence of Wallerian degeneration does not hinder regeneration in peripheral nerve. *Eur. J. Neurosci.* **1**, 27–33 (1989).

[CAS](#) [PubMed](#) [Google Scholar](#)

15. 15.

Babetto, E. et al. Targeting NMNAT1 to axons and synapses transforms its neuroprotective potency in vivo. *J. Neurosci.* **30**, 13291–13304 (2010).

[CAS](#) [PubMed](#) [PubMed Central](#) [Google Scholar](#)

16. 16.

Sasaki, Y., Vohra, B. P., Baloh, R. H. & Milbrandt, J. Transgenic mice expressing the Nmnat1 protein manifest robust delay in axonal degeneration in vivo. *J. Neurosci.* **29**, 6526–6534 (2009).

[CAS](#) [PubMed](#) [PubMed Central](#) [Google Scholar](#)

17. 17.

Horsefield, S. et al. NAD⁺ cleavage activity by animal and plant TIR domains in cell death pathways. *Science* **365**, 793–799 (2019).

[CAS](#) [PubMed](#) [ADS](#) [Google Scholar](#)

18. 18.

Chuang, C. F. & Bargmann, C. I. A Toll-interleukin 1 repeat protein at the synapse specifies asymmetric odorant receptor expression via ASK1 MAPKKK signaling. *Genes Dev.* **19**, 270–281 (2005).

[CAS](#) [PubMed](#) [PubMed Central](#) [Google Scholar](#)

19. 19.

Sporny, M. et al. Structural evidence for an octameric ring arrangement of SARM1. *J. Mol. Biol.* **431**, 3591–3605 (2019).

[CAS](#) [PubMed](#) [Google Scholar](#)

20. 20.

Kobe, B. Autoinhibition by an internal nuclear localization signal revealed by the crystal structure of mammalian importin alpha. *Nat. Struct. Biol.* **6**, 388–397 (1999).

[CAS](#) [PubMed](#) [Google Scholar](#)

21. 21.

Huber, A. H., Nelson, W. J. & Weis, W. I. Three-dimensional structure of the armadillo repeat region of beta-catenin. *Cell* **90**, 871–882 (1997).

[CAS](#) [PubMed](#) [Google Scholar](#)

22. 22.

Xu, Y. et al. Structural basis for signal transduction by the Toll/interleukin-1 receptor domains. *Nature* **408**, 111–115 (2000).

[CAS](#) [PubMed](#) [ADS](#) [Google Scholar](#)

23. 23.

Summers, D. W., Gibson, D. A., DiAntonio, A. & Milbrandt, J. SARM1-specific motifs in the TIR domain enable NAD⁺ loss and regulate injury-induced SARM1 activation. *Proc. Natl Acad. Sci. USA* **113**, E6271–E6280 (2016).

[CAS](#) [PubMed](#) [Google Scholar](#)

24. 24.

Williams, S. J. et al. Structural basis for assembly and function of a heterodimeric plant immune receptor. *Science* **344**, 299–303 (2014).

[CAS](#) [PubMed](#) [ADS](#) [Google Scholar](#)

25. 25.

Nyman, T. et al. The crystal structure of the human toll-like receptor 10 cytoplasmic domain reveals a putative signaling dimer. *J. Biol. Chem.* **283**, 11861–11865 (2008).

[CAS](#) [PubMed](#) [Google Scholar](#)

26. 26.

Kim, Y. et al. MyD88-5 links mitochondria, microtubules, and JNK3 in neurons and regulates neuronal survival. *J. Exp. Med.* **204**, 2063–2074 (2007).

[CAS](#) [PubMed](#) [PubMed Central](#) [Google Scholar](#)

27. 27.

Chai, J. & Shi, Y. Apoptosome and inflammasome: conserved machineries for caspase activation. *Natl Sci. Rev.* **1**, 101–118 (2014).

[CAS](#) [Google Scholar](#)

28. 28.

Bratkowski, M. et al. Structural and mechanistic regulation of the pro-degenerative NAD hydrolase SARM1. *Cell Rep.* **32**, 107999 (2020).

[CAS](#) [PubMed](#) [Google Scholar](#)

29. 29.

Sporny, M. et al. The structural basis for SARM1 inhibition, and activation under energetic stress. Preprint at *bioRxiv* <https://doi.org/10.1101/2020.08.05.238287> (2020).

30. 30.

Yang, H. et al. Nutrient-sensitive mitochondrial NAD⁺ levels dictate cell survival. *Cell* **130**, 1095–1107 (2007).

[CAS](#) [PubMed](#) [PubMed Central](#) [Google Scholar](#)

31. 31.

Yang, Y., Mohammed, F. S., Zhang, N. & Sauve, A. A. Dihydronicotinamide riboside is a potent NAD⁺ concentration enhancer *in vitro* and *in vivo*. *J. Biol. Chem.* **294**, 9295–9307 (2019).

[CAS](#) [PubMed](#) [PubMed Central](#) [Google Scholar](#)

32. 32.

Gilley, J., Orsomando, G., Nascimento-Ferreira, I. & Coleman, M. P. Absence of SARM1 rescues development and survival of NMNAT2-deficient axons. *Cell Rep.* **10**, 1974–1981 (2015).

[CAS](#) [PubMed](#) [PubMed Central](#) [Google Scholar](#)

33. 33.

Gilley, J., Adalbert, R., Yu, G. & Coleman, M. P. Rescue of peripheral and CNS axon defects in mice lacking NMNAT2. *J. Neurosci.* **33**, 13410–13424 (2013).

[CAS](#) [PubMed](#) [PubMed Central](#) [Google Scholar](#)

34. 34.

Loreto, A., Di Stefano, M., Gering, M. & Conforti, L. Wallerian degeneration is executed by an NMN-SARM1-dependent late Ca^{2+} influx but only modestly influenced by mitochondria. *Cell Rep.* **13**, 2539–2552 (2015).

[CAS](#) [PubMed](#) [Google Scholar](#)

35. 35.

Zhao, Z. Y. et al. A cell-permeant mimetic of NMN activates SARM1 to produce cyclic ADP-ribose and induce non-apoptotic cell death. *iScience* **15**, 452–466 (2019).

[CAS](#) [PubMed](#) [PubMed Central](#) [ADS](#) [Google Scholar](#)

36. 36.

Di Stefano, M. et al. A rise in NAD precursor nicotinamide mononucleotide (NMN) after injury promotes axon degeneration. *Cell Death Differ.* **22**, 731–742 (2015).

[Google Scholar](#)

37. 37.

Di Stefano, M. et al. NMN deamidase delays Wallerian degeneration and rescues axonal defects caused by NMNAT2 deficiency *in vivo*.

Curr. Biol. **27**, 784–794 (2017).

[PubMed](#) [Google Scholar](#)

38. 38.

Sasaki, Y., Nakagawa, T., Mao, X., DiAntonio, A. & Milbrandt, J. NMNAT1 inhibits axon degeneration via blockade of SARM1-mediated NAD⁺ depletion. *eLife* **5**, e19749 (2016).

[PubMed](#) [PubMed Central](#) [Google Scholar](#)

39. 39.

Goehring, A. et al. Screening and large-scale expression of membrane proteins in mammalian cells for structural studies. *Nat. Protoc.* **9**, 2574–2585 (2014).

[CAS](#) [PubMed](#) [PubMed Central](#) [Google Scholar](#)

40. 40.

Mastronarde, D. N. Automated electron microscope tomography using robust prediction of specimen movements. *J. Struct. Biol.* **152**, 36–51 (2005).

[Google Scholar](#)

41. 41.

Zheng, S. Q. et al. MotionCor2: anisotropic correction of beam-induced motion for improved cryo-electron microscopy. *Nat. Methods* **14**, 331–332 (2017).

[CAS](#) [PubMed](#) [PubMed Central](#) [Google Scholar](#)

42. 42.

Zhang, K. Gctf: real-time CTF determination and correction. *J. Struct. Biol.* **193**, 1–12 (2016).

[CAS](#) [PubMed](#) [PubMed Central](#) [ADS](#) [Google Scholar](#)

43. 43.

Fernandez-Leiro, R. & Scheres, S. H. W. A pipeline approach to single-particle processing in RELION. *Acta Crystallogr. D* **73**, 496–502 (2017).

[CAS](#) [Google Scholar](#)

44. 44.

Punjani, A., Rubinstein, J. L., Fleet, D. J. & Brubaker, M. A. cryoSPARC: algorithms for rapid unsupervised cryo-EM structure determination. *Nat. Methods* **14**, 290–296 (2017).

[CAS](#) [Google Scholar](#)

45. 45.

Pettersen, E. F. et al. UCSF Chimera—a visualization system for exploratory research and analysis. *J. Comput. Chem.* **25**, 1605–1612 (2004).

[CAS](#) [Google Scholar](#)

46. 46.

Emsley, P., Lohkamp, B., Scott, W. G. & Cowtan, K. Features and development of Coot. *Acta Crystallogr. D* **66**, 486–501 (2010).

[CAS](#) [PubMed](#) [Google Scholar](#)

47. 47.

Adams, P. D. et al. PHENIX: a comprehensive Python-based system for macromolecular structure solution. *Acta Crystallogr. D* **66**, 213–221 (2010).

[CAS](#) [PubMed](#) [Google Scholar](#)

48. 48.

Brown, A. et al. Tools for macromolecular model building and refinement into electron cryo-microscopy reconstructions. *Acta Crystallogr. D* **71**, 136–153 (2015).

[CAS](#) [PubMed](#) [Google Scholar](#)

49. 49.

Davis, I. W. et al. MolProbity: all-atom contacts and structure validation for proteins and nucleic acids. *Nucleic Acids Res.* **35**, W375–W383 (2007).

[PubMed](#) [PubMed Central](#) [ADS](#) [Google Scholar](#)

50. 50.

Dolinsky, T. J. et al. PDB2PQR: expanding and upgrading automated preparation of biomolecular structures for molecular simulations. *Nucleic Acids Res.* **35**, W522–W525 (2007).

[PubMed](#) [PubMed Central](#) [Google Scholar](#)

51. 51.

Schneider, C. A., Rasband, W. S. & Eliceiri, K. W. NIH Image to ImageJ: 25 years of image analysis. *Nat. Methods* **9**, 671–675 (2012).

[CAS](#) [PubMed](#) [PubMed Central](#) [Google Scholar](#)

52. 52.

Sohal, V. S., Zhang, F., Yizhar, O. & Deisseroth, K. Parvalbumin neurons and gamma rhythms enhance cortical circuit performance. *Nature* **459**, 698–702 (2009).

[CAS](#) [PubMed](#) [PubMed Central](#) [ADS](#) [Google Scholar](#)

[Download references](#)

Acknowledgements

We thank the Cryo-EM platform and the School of Life Sciences of Peking University for cryo-EM data collection. We are grateful to Z. Guo, G. Wang, B. Shao, X. Pei and N. Gao for their help in the cryo-EM experiments and discussion. We thank the National Center for Protein Sciences at Peking University for assistance with the initial exploration of the SARM1–NAD⁺ binding assay, the liquid chromatography–mass spectrometry experiment and the HPLC analysis. We are indebted to X. Li for critical comments on the manuscript. The computation was supported by the High-Performance Computing Platform of Peking University. This research was funded by the Center for Life Sciences, School of Life Sciences of Peking University and the State Key Laboratory of Membrane Biology of China. The study was also supported by the National Natural Science Foundation of China (to J.Y., nos. 31522024, 31771111 and 31970974).

Author information

Affiliations

1. State Key Laboratory of Membrane Biology, Center for Life Sciences, School of Life Sciences, Peking University, Beijing, China

Yuefeng Jiang, Tingting Liu, Jing Yang & Zhe Zhang

2. Department of Structural Biology, St. Jude Children's Research Hospital, Memphis, TN, USA

Chia-Hsueh Lee

3. Beijing Advanced Innovation Center for Structural Biology, Tsinghua University, Beijing, China

Qing Chang

Authors

1. Yuefeng Jiang

[View author publications](#)

You can also search for this author in [PubMed](#) [Google Scholar](#)

2. Tingting Liu

[View author publications](#)

You can also search for this author in [PubMed](#) [Google Scholar](#)

3. Chia-Hsueh Lee

[View author publications](#)

You can also search for this author in [PubMed](#) [Google Scholar](#)

4. Qing Chang

[View author publications](#)

You can also search for this author in [PubMed](#) [Google Scholar](#)

5. Jing Yang

[View author publications](#)

You can also search for this author in [PubMed](#) [Google Scholar](#)

6. Zhe Zhang

[View author publications](#)

You can also search for this author in [PubMed](#) [Google Scholar](#)

Contributions

Y.J. and Z.Z. performed all of the cloning and cell cultures. Y.J. prepared all of the protein samples, performed data collection for cryo-EM samples and carried out the NAD⁺ cleavage assay. Z.Z. processed the cryo-EM data, and built and refined the structural models. Z.Z. and C.-H.L. analysed the structures. J.Y. and T.L. performed the experiments with cultured neurons. Q.C. carried out the MST analysis. Z.Z., J.Y. and C.-H.L. wrote and revised the manuscript with input and support from all co-authors.

Corresponding authors

Correspondence to [Jing Yang](#) or [Zhe Zhang](#).

Ethics declarations

Competing interests

The authors declare no competing interests.

Additional information

Peer review information *Nature* thanks Andrew Bowie, Liang Tong and the other, anonymous, reviewer(s) for their contribution to the peer review of this work. Peer reviewer reports are available.

Publisher's note Springer Nature remains neutral with regard to jurisdictional claims in published maps and institutional affiliations.

Extended data figures and tables

[Extended Data Fig. 1 Cryo-EM data processing of the wild-type SARM1 dataset. Workflow for the sample preparation and cryo-EM data processing of the wild-type SARM1 dataset](#)

Extended Data Fig. 2 Data and model quality assessment for the wild-type SARM1 dataset.

a, Angular distributions for all the particles used in the final refinement. Red and higher cylinders represent more particles assigned to a particular orientation, while blue and shorter cylinders represent less. **b**, Local resolution estimation calculated by RELION. **c**, Fourier shell correlation (FSC) curves between two half maps are plotted in black. For cross-validation, the FSC curves are calculated between the refined structure and three maps (full map: green; half-1 map: red; half-2 map: blue). **d**, Local cryo-EM densities and fitted atomic models for representative regions of the structure.

Extended Data Fig. 3 Cryo-EM data processing of the NAD⁺-bound wild-type SARM1 dataset.

a, Flowchart of the data processing. **b**, Angular distributions for all the particles used in the final refinement. Red and higher cylinders represent more particles assigned to a particular orientation, while blue and shorter cylinders represent less. **c**, Local resolution estimation calculated by RELION. **d**, FSC curves between two half maps are plotted in black. For cross-validation, the FSC curves are calculated between the refined structure and three maps (full map: green; half-1 map: red; half-2 map: blue). **e**, Local cryo-EM densities and fitted atomic models for representative regions of the structure.

Extended Data Fig. 4 Cryo-EM data processing of the NAD⁺-bound SARM1(E642A) dataset.

a, Flowchart of the data processing. **b**, Angular distributions for all the particles used in the final refinement. Red and higher cylinders represent more particles assigned to a particular orientation, while blue and shorter cylinders represent less. **c**, Local resolution estimation calculated by RELION. **d**, FSC curves between two half maps are plotted in black. For

cross-validation, the FSC curves are calculated between the refined structure and three maps (full map: green; half-1 map: red; half-2 map: blue). **e**, Local cryo-EM densities and fitted atomic models for representative regions of the structure.

Extended Data Fig. 5 Analysis of the SARM1 assembly.

a, Structural comparison of the three full-length SARM1 structures. Yellow: SARM1; green: SARM1+NAD⁺; pink: SARM1(E642A)+NAD⁺. **b**, Superimposition of three different SARM1^{SAM} octamers. Blue: SARM1^{SAM} in the structure of the NAD⁺-bound full-length SARM1(E642A); green (PDB code: 6QWV) and yellow (PDB code: 6O0S): two reported structures of SARM1^{SAM} alone. **c**, Assembly of the SARM1 octamer. Each protomer interacts with four adjacent ones. For instance, protomer A (red) interacts with protomers B (yellow), C (green), G (pink), and H (cyan). SARM1^{SAM} and SARM1^{TIR} within one protomer are linked with a stick to show the domain assignment. The density of detergent micelles is also shown. All the panels are shown in orthogonal views.

Extended Data Fig. 6 SARM1^{TIR} is restricted in the inactive state through interactions with SARM1^{ARM}.

a, Structural comparison of the ARM domains in SARM1, importin- α (PDB code: 1IAL), and β -catenin (PDB code: 2BCT). ARM1-8 of SARM1^{ARM}, ARM3-10 of importin- α , and ARM5-12 of β -catenin are shown. The ARM motifs in the middle adopt the similar conformation and are coloured in grey. However, the conformations of ARM motifs on both ends of SARM1^{ARM} (ARM1, ARM7-8, and the last helix of ARM6; coloured in green) are different from those of the corresponding ARM motifs in importin- α (ARM3, ARM9-10, and the last helix of ARM8; coloured in yellow) or β -catenin (ARM5, ARM11-12, and the last helix of ARM10; coloured in pink). The last helix of ARM6 in SARM1^{ARM} and its corresponding helices in importin- α and β -catenin are marked out with dashed circles. Their orientations are indicated with arrows. **b**, Detailed

interactions between the two neighbouring SARM1^{ARM} (green box), and between SARM1^{ARM} and the two closely packed SARM1^{SAM} (pink boxes). **c**, Cryo-EM densities (black mesh) of the BB-loop in the NAD⁺-bound SARM1(E642A) structure. Atomic models of α A and BB-loop are coloured in wheat and red, respectively. Relevant residues are shown with side chains. **d**, Cryo-EM densities of the BB-loop in SARM1 (blue mesh) and NAD⁺-bound SARM1 (green mesh) structures. The atomic model of the BB-loop in NAD⁺-bound SARM1(E642A) structure is shown as a reference. The contour levels of the maps in **c** and **d** are 6.0. **e**, The inactive conformation of SARM1^{TIR} is designated by its interactions with the two adjacent SARM1^{ARM}. **f**, The α A helix and BB-loop of different TIR domains are prone to mediate protein–protein interactions. The RRS1/RPS4 heterodimer (PDB code: 4C6T) is formed through interactions between their α A helices (in wheat), and the TLR10 homodimer (PDB code: 2J67) is assembled via the BB-loop interaction (in red). Two subunits are coloured in cyan and green, respectively.

Extended Data Fig. 7 Sequence alignment of the SARM1 ARM motifs among several representative species.

a, Sequence alignment of ARM5. The positions of three helices (H1, H2, and H3) are indicated with green cylinders. The residues involved in SARM1^{ARM}-SARM1^{TIR} interaction are denoted by black arrowheads. **b**, Sequence alignment of ARM1-3. The residues participating in NAD⁺ binding are denoted by green (group 1) or yellow (group 2) arrowheads.

Extended Data Fig. 8 Purification of different SARM1 mutant proteins.

a, b, Gel filtration profiles (**a**) and SDS-PAGE gels (**b**) of different SARM1 mutant proteins used in the NADase assay in Fig. 2. **c, d**, Gel filtration profiles (**c**) and SDS-PAGE gels (**d**) of different SARM1^{ARM+SAM} mutant proteins used for the microscale thermophoresis (MST) assay. The asterisk denotes the protein band of HSP70, as identified by LC-MS (liquid chromatography–mass spectrometry). **e, f**, Gel filtration profiles (**e**) and SDS-PAGE gels (**f**) of different SARM1 mutant proteins used for the

NADase assay in Fig. 4. The SDS–PAGE gels were stained with Coomassie blue. All the experiments were independently repeated three times. Each band of the molecular marker contains about 1–2 µg protein. For gel source data, see Supplementary Fig. 1.

Extended Data Fig. 9 The NAD⁺-binding site within SARM1^{ARM}.

a–c, Cryo-EM densities around the NAD⁺-binding site in three structures. NAD⁺ density is present in both the SARM1+NAD⁺ (**b**: blue mesh) and SARM1(E642A)+NAD⁺ (**c**: green mesh) structures but not the apo one (**a**). NAD⁺ is shown as magenta sticks. The density and atomic model of SARM1^{ARM} are shown as surface and ribbon, respectively. **d,e**, Cryo-EM densities for the residues of SARM1^{ARM} involved in the NAD⁺ binding. The densities of the SARM1+NAD⁺ structure are shown as orange mesh (**d**), and those of the SARM1(E642A)+NAD⁺ structure are shown as blue mesh (**e**). The residues are shown as sticks and coloured in green. The six residues interacting with NAD⁺ through their side chains are labelled. The contour levels of the maps in **a–e** are 6.0. **f, g**, The NAD⁺ affinity to SARM1(E642A) (**f**) and SARM1^{ARM+TIR}(WQH to A) (**g**). The experiments were biologically replicated twice and analysed ($n = 2$). The values of calculated K_d are presented as mean ± s.d. **h, i**, The HPLC analysis of the NADase kinetics of SARM1(RRK to A) (**h**) and SARM1^{SAM+TIR} (**i**). The background degradation of NAD⁺ was subtracted from each reaction. All the experiments were biologically replicated three times ($n = 3$). The kinetics of SARM1^{SAM+TIR} in **i** was fitted to the Michaelis–Menten equation. **j**, The NMN affinity to SARM1^{ARM+SAM}. The experiments were biologically replicated three times and analysed ($n = 3$). The value of calculated K_d is presented as mean ± s.d. [Source data](#)

Extended Data Table 1 Cryo-EM data collection, refinement and validation statistics

[Full size table](#)

Supplementary information

[Supplementary Figure 1](#)

Uncropped TLC images for Fig. 2b and all the other TLC replicates used for the statistical analysis in Figs. 2c and 4c, together with the uncropped and replicated SDS-PAGE gels for Extended Data Fig. 8b, d, f. The cropping regions are indicated as red boxes.

[Reporting Summary](#)

[Peer Review File](#)

Source data

[Source Data Fig. 2](#)

[Source Data Fig. 4](#)

[Source Data Extended Data Fig. 9](#)

Rights and permissions

[Reprints and Permissions](#)

About this article



Check for
updates

Cite this article

Jiang, Y., Liu, T., Lee, CH. *et al.* The NAD⁺-mediated self-inhibition mechanism of pro-neurodegenerative SARM1. *Nature* **588**, 658–663 (2020). <https://doi.org/10.1038/s41586-020-2862-z>

[Download citation](#)

- Received: 08 May 2020
- Accepted: 08 October 2020
- Published: 14 October 2020
- Issue Date: 24 December 2020
- DOI: <https://doi.org/10.1038/s41586-020-2862-z>

Further reading

- [**Vincristine- and bortezomib-induced neuropathies – from bedside to bench and back**](#)
 - Stefanie Geisler
- [**Structural basis for SARM1 inhibition and activation under energetic stress**](#)
 - Michael Sporny
 - , Julia Guez-Haddad
 - , Tami Khazma
 - , Avraham Yaron
 - , Moshe Dessau
 - , Yoel Shkolnisky
 - , Carsten Mim
 - , Michail N Isupov
 - , Ran Zalk

- , Michael Hons
- & Yarden Opatowsky

eLife (2020)

Comments

By submitting a comment you agree to abide by our [Terms](#) and [Community Guidelines](#). If you find something abusive or that does not comply with our terms or guidelines please flag it as inappropriate.

[Access through your institution](#)

[Change institution](#)

[Buy or subscribe](#)

Associated Content

Nature Structural & Molecular Biology | News & Views

[How to diSARM the executioner of axon degeneration](#)

- Liang Tong

This article was downloaded by **calibre** from <https://www.nature.com/articles/s41586-020-2862-z>

- Article
- [Published: 16 December 2020](#)

Creation of bladder assembloids mimicking tissue regeneration and cancer

- [Eunjee Kim¹](#),
- [Seoyoung Choi¹](#),
- [Byunghee Kang^{1,2}](#),
- [JungHo Kong¹](#),
- [Yubin Kim¹](#),
- [Woong Hee Yoon²](#),
- [Hwa-Rim Lee³](#),
- [SungEun Kim¹](#),
- [Hyo-Min Kim](#) [ORCID: orcid.org/0000-0002-2667-3719^{1,2}](#),
- [HyeSun Lee⁴](#),
- [Chorong Yang²](#),
- [You Jeong Lee](#) [ORCID: orcid.org/0000-0002-6786-6955²](#),
- [Minyong Kang^{5,6,7}](#),
- [Tae-Young Roh](#) [ORCID: orcid.org/0000-0001-5833-0844^{1,2}](#),
- [Sungjune Jung](#) [ORCID: orcid.org/0000-0001-9258-0572^{2,3}](#),
- [Sanguk Kim](#) [ORCID: orcid.org/0000-0002-3449-3814¹](#),
- [Ja Hyeon Ku](#) [ORCID: orcid.org/0000-0002-0391-2342⁴](#) &
- [Kunyoo Shin](#) [ORCID: orcid.org/0000-0002-1519-9839¹](#)

[Nature](#) volume **588**, pages664–669(2020)[Cite this article](#)

- 4159 Accesses

- 52 Altmetric
- [Metrics details](#)

Subjects

- [Adult stem cells](#)
- [Cancer microenvironment](#)

Abstract

Current organoid models are limited by their inability to mimic mature organ architecture and associated tissue microenvironments^{1,2}. Here we create multilayer bladder ‘assembloids’ by reconstituting tissue stem cells with stromal components to represent an organized architecture with an epithelium surrounding stroma and an outer muscle layer. These assembloids exhibit characteristics of mature adult bladders in cell composition and gene expression at the single-cell transcriptome level, and recapitulate *in vivo* tissue dynamics of regenerative responses to injury. We also develop malignant counterpart tumour assembloids to recapitulate the *in vivo* pathophysiological features of urothelial carcinoma. Using the genetically manipulated tumour-assembloid platform, we identify tumoural FOXA1, induced by stromal bone morphogenetic protein (BMP), as a master pioneer factor that drives enhancer reprogramming for the determination of tumour phenotype, suggesting the importance of the FOXA1–BMP–hedgehog signalling feedback axis between tumour and stroma in the control of tumour plasticity.

[Access through your institution](#)

[Change institution](#)

[Buy or subscribe](#)

Access options

Subscribe to Journal

Get full journal access for 1 year

\$199.00

only \$3.83 per issue

[Subscribe](#)

All prices are NET prices.

VAT will be added later in the checkout.

Rent or Buy article

Get time limited or full article access on ReadCube.

from \$8.99

[Rent or Buy](#)

All prices are NET prices.

Additional access options:

- [Log in](#)
- [Access through your institution](#)
- [Learn about institutional subscriptions](#)

Fig. 1: Generation of 3D reconstituted bladder assembloids.

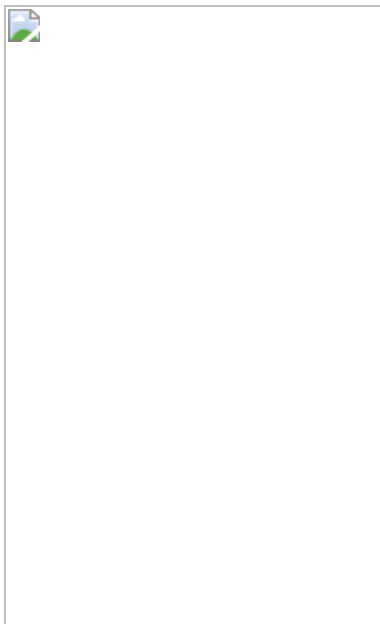


Fig. 2: Bladder assembloids mimicking the functionality of adult bladder and human UTI.

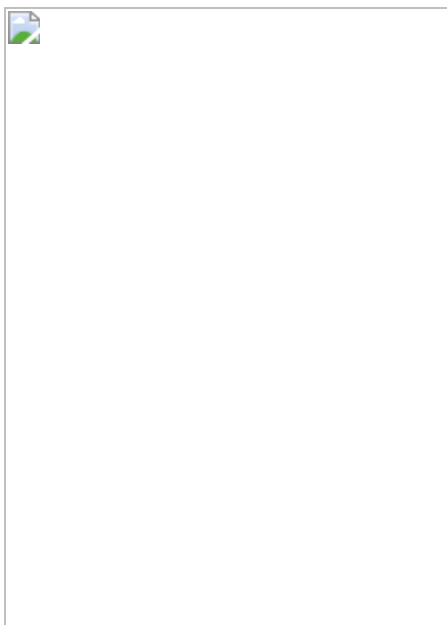


Fig. 3: Generation of tumour assembloids recapitulating the pathophysiology of human urothelial carcinomas.

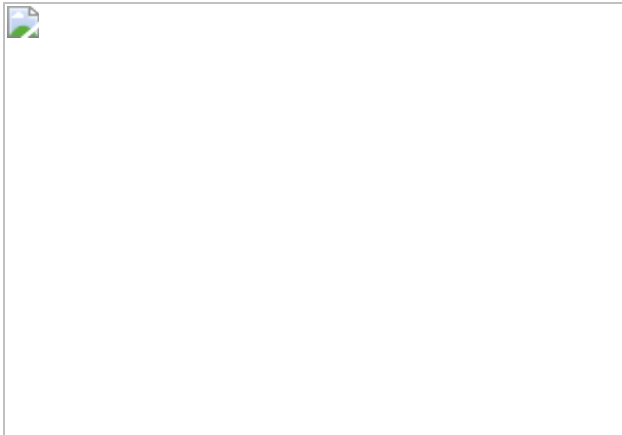


Fig. 4: Subtype plasticity of human urothelial carcinomas is determined by the FOXA1–BMP–hedgehog axis.



Data availability

All relevant data are included in this Article and its Supplementary Information files. RNA-seq, ChIP-seq, ATAC-seq and scRNA-seq data have been uploaded to the Gene Expression Omnibus with accession codes [GSE141356](#) and [GSE141348](#), respectively. These data (RNA-seq, ChIP-seq, ATAC-seq and scRNA-seq) are also available on the Korean Nucleotide Archive with accession ID PRKJA200011 upon request to the corresponding authors. WES data have been uploaded to the Sequence Read Archive with accession code [PRJNA647991](#). The MSigDB v.7.0 is available at <https://www.gsea-msigdb.org/gsea/msigdb>. Source data are provided with this paper.

Code availability

The code used for data analysis is available at
<https://github.com/sysgenlab/BladderAssembloid>.

References

1. 1.

de Souza, N. Organoids. *Nat. Methods* **15**, 23–23 (2018).

[Google Scholar](#)

2. 2.

Rossi, G., Manfrin, A. & Lutolf, M. P. Progress and potential in organoid research. *Nat. Rev. Genet.* **19**, 671–687 (2018).

[CAS](#) [PubMed](#) [Google Scholar](#)

3. 3.

Lancaster, M. A. & Knoblich, J. A. Organogenesis in a dish: modeling development and disease using organoid technologies. *Science* **345**, 1247125 (2014).

[PubMed](#) [Google Scholar](#)

4. 4.

Dutta, D., Heo, I. & Clevers, H. Disease modeling in stem cell-derived 3D organoid systems. *Trends Mol. Med.* **23**, 393–410 (2017).

[CAS](#) [PubMed](#) [Google Scholar](#)

5. 5.

Shin, K. et al. Hedgehog/Wnt feedback supports regenerative proliferation of epithelial stem cells in bladder. *Nature* **472**, 110–114 (2011).

[CAS](#) [PubMed](#) [PubMed Central](#) [ADS](#) [Google Scholar](#)

6. 6.

Santos, C. P. et al. Urothelial organoids originating from Cd49f^{high} mouse stem cells display Notch-dependent differentiation capacity. *Nat. Commun.* **10**, 4407 (2019).

[PubMed](#) [PubMed Central](#) [ADS](#) [Google Scholar](#)

7. 7.

Andersson, K.-E. & Arner, A. Urinary bladder contraction and relaxation: physiology and pathophysiology. *Physiol. Rev.* **84**, 935–986 (2004).

[CAS](#) [PubMed](#) [Google Scholar](#)

8. 8.

Mysorekar, I. U., Isaacson-Schmid, M., Walker, J. N., Mills, J. C. & Hultgren, S. J. Bone morphogenetic protein 4 signaling regulates epithelial renewal in the urinary tract in response to uropathogenic infection. *Cell Host Microbe* **5**, 463–475 (2009).

[CAS](#) [PubMed](#) [PubMed Central](#) [Google Scholar](#)

9. 9.

Hisha, H. et al. Establishment of a novel lingual organoid culture system: generation of organoids having mature keratinized epithelium from adult epithelial stem cells. *Sci. Rep.* **3**, 3224 (2013).

[PubMed](#) [PubMed Central](#) [Google Scholar](#)

10. 10.

Rinkevich, Y., Lindau, P., Ueno, H., Longaker, M. T. & Weissman, I. L. Germ-layer and lineage-restricted stem/progenitors regenerate the

mouse digit tip. *Nature* **476**, 409–413 (2011).

[CAS](#) [PubMed](#) [ADS](#) [Google Scholar](#)

11. 11.

Yanai, H., Tanaka, T. & Ueno, H. Multicolor lineage tracing methods and intestinal tumors. *J. Gastroenterol.* **48**, 423–433 (2013).

[CAS](#) [PubMed](#) [PubMed Central](#) [Google Scholar](#)

12. 12.

Lee, S. H. et al. Tumor evolution and drug response in patient-derived organoid models of bladder cancer. *Cell* **173**, 515–528 (2018).

[CAS](#) [PubMed](#) [PubMed Central](#) [Google Scholar](#)

13. 13.

Kim, S. et al. Epigenetic regulation of mammalian Hedgehog signaling to the stroma determines the molecular subtype of bladder cancer. *eLife* **8**, e43024 (2019).

[PubMed](#) [PubMed Central](#) [Google Scholar](#)

14. 14.

Shin, K. et al. Hedgehog signaling restrains bladder cancer progression by eliciting stromal production of urothelial differentiation factors. *Cancer Cell* **26**, 521–533 (2014).

[CAS](#) [PubMed](#) [PubMed Central](#) [Google Scholar](#)

15. 15.

Spiekerkoetter, E. et al. FK506 activates BMPR2, rescues endothelial dysfunction, and reverses pulmonary hypertension. *J. Clin. Invest.* **123**, 3600–3613 (2013).

[CAS](#) [PubMed](#) [PubMed Central](#) [Google Scholar](#)

16. 16.

McConkey, D. J. et al. A prognostic gene expression signature in the molecular classification of chemotherapy-naïve urothelial cancer is predictive of clinical outcomes from neoadjuvant chemotherapy: a phase 2 trial of dose-dense methotrexate, vinblastine, doxorubicin, and cisplatin with bevacizumab in urothelial cancer. *Eur. Urol.* **69**, 855–862 (2016).

[CAS](#) [PubMed](#) [Google Scholar](#)

17. 17.

Seiler, R. et al. Impact of molecular subtypes in muscle-invasive bladder cancer on predicting response and survival after neoadjuvant chemotherapy. *Eur. Urol.* **72**, 544–554 (2017).

[CAS](#) [PubMed](#) [Google Scholar](#)

18. 18.

Neesse, A. et al. Stromal biology and therapy in pancreatic cancer. *Gut* **60**, 861–868 (2011).

[PubMed](#) [Google Scholar](#)

19. 19.

Öhlund, D. et al. Distinct populations of inflammatory fibroblasts and myofibroblasts in pancreatic cancer. *J. Exp. Med.* **214**, 579–596 (2017).

[PubMed](#) [PubMed Central](#) [Google Scholar](#)

20. 20.

Olive, K. P. et al. Inhibition of Hedgehog signaling enhances delivery of chemotherapy in a mouse model of pancreatic cancer. *Science* **324**, 1457–1461 (2009).

[CAS](#) [PubMed](#) [PubMed Central](#) [ADS](#) [Google Scholar](#)

21. 21.

Rhim, A. D. et al. Stromal elements act to restrain, rather than support, pancreatic ductal adenocarcinoma. *Cancer Cell* **25**, 735–747 (2014).

[CAS](#) [PubMed](#) [PubMed Central](#) [Google Scholar](#)

22. 22.

Shin, K. et al. Cellular origin of bladder neoplasia and tissue dynamics of its progression to invasive carcinoma. *Nat. Cell Biol.* **16**, 469–478 (2014).

[CAS](#) [PubMed](#) [PubMed Central](#) [Google Scholar](#)

23. 23.

Dijkstra, K. K. et al Generation of tumor-reactive T cells by co-culture of peripheral blood lymphocytes and tumor organoids. *Cell* **174**, 1586–1598 (2018).

[CAS](#) [PubMed](#) [PubMed Central](#) [Google Scholar](#)

24. 24.

Robertson, A. G. et al. Comprehensive molecular characterization of muscle-invasive bladder cancer. *Cell* **171**, 540–556 (2017).

[Google Scholar](#)

25. 25.

Choi, W. et al. Identification of distinct basal and luminal subtypes of muscle-invasive bladder cancer with different sensitivities to frontline chemotherapy. *Cancer Cell* **25**, 152–165 (2014).

[CAS](#) [PubMed](#) [PubMed Central](#) [Google Scholar](#)

26. 26.

McConkey, D. J. & Choi, W. Molecular subtypes of bladder cancer. *Curr. Oncol. Rep.* **20**, 77 (2018).

[PubMed](#) [Google Scholar](#)

27. 27.

Wang, Q. et al. Androgen receptor regulates a distinct transcription program in androgen-independent prostate cancer. *Cell* **138**, 245–256 (2009).

[CAS](#) [PubMed](#) [PubMed Central](#) [Google Scholar](#)

28. 28.

Cirillo, L. A. et al. Opening of compacted chromatin by early developmental transcription factors HNF3 (FoxA) and GATA-4. *Mol. Cell* **9**, 279–289 (2002).

[CAS](#) [PubMed](#) [Google Scholar](#)

29. 29.

Roe, J. S. et al. Enhancer reprogramming promotes pancreatic cancer metastasis. *Cell* **170**, 875–888 (2017).

[CAS](#) [PubMed](#) [PubMed Central](#) [Google Scholar](#)

30. 30.

Jozwik, K. M., Chernukhin, I., Serandour, A. A., Nagarajan, S. & Carroll, J. S. FOXA1 directs H3K4 monomethylation at enhancers via recruitment of the methyltransferase MLL3. *Cell Rep.* **17**, 2715–2723 (2016).

[CAS](#) [PubMed](#) [PubMed Central](#) [Google Scholar](#)

31. 31.

Lupien, M. et al. FoxA1 translates epigenetic signatures into enhancer-driven lineage-specific transcription. *Cell* **132**, 958–970 (2008).

[CAS](#) [PubMed](#) [PubMed Central](#) [Google Scholar](#)

32. 32.

Warrick, J. I. et al. FOXA1, GATA3 and PPAR γ cooperate to drive luminal subtype in bladder cancer: a molecular analysis of established human cell lines. *Sci. Rep.* **6**, 38531 (2016).

[CAS](#) [PubMed](#) [PubMed Central](#) [ADS](#) [Google Scholar](#)

33. 33.

Varley, C. L., Bacon, E. J., Holder, J. C. & Southgate, J. FOXA1 and IRF-1 intermediary transcriptional regulators of PPARgamma-induced urothelial cytodifferentiation. *Cell Death Differ.* **16**, 103–114 (2009).

[CAS](#) [PubMed](#) [Google Scholar](#)

34. 34.

Osei-Ampensa, V. et al. Hypermethylation of FOXA1 and allelic loss of PTEN drive squamous differentiation and promote heterogeneity in bladder cancer. *Oncogene* **39**, 1302–1317 (2020).

[CAS](#) [PubMed](#) [Google Scholar](#)

35. 35.

Reddy, O. L. et al. Loss of FOXA1 drives sexually dimorphic changes in urothelial differentiation and is an independent predictor of poor prognosis in bladder cancer. *Am. J. Pathol.* **185**, 1385–1395 (2015).

[CAS](#) [PubMed](#) [PubMed Central](#) [Google Scholar](#)

36. 36.

DeGraff, D. J. et al. When urothelial differentiation pathways go wrong: implications for bladder cancer development and progression. *Urol. Oncol.* **31**, 802–811 (2013).

[CAS](#) [PubMed](#) [Google Scholar](#)

37. 37.

Park, I. H., Lerou, P. H., Zhao, R., Huo, H. & Daley, G. Q. Generation of human-induced pluripotent stem cells. *Nat. Protocols* **3**, 1180–1186 (2008).

[CAS](#) [PubMed](#) [Google Scholar](#)

38. 38.

Kim, E., Choi, S. & Shin, K. Creation of bladder assembloids by reconstituting tissue stem cell/tumour cell-derived organoids with multiple stromal components. *Protoc. Exch.* <https://doi.org/10.21203/rs.3.pex-1174/v1> (2020).

39. 39.

Qian, X. et al. Brain-region-specific organoids using mini-bioreactors for modeling ZIKV exposure. *Cell* **165**, 1238–1254 (2016).

[CAS](#) [PubMed](#) [PubMed Central](#) [Google Scholar](#)

40. 40.

Wan, Q. et al. Urothelium with barrier function differentiated from human urine-derived stem cells for potential use in urinary tract reconstruction. *Stem Cell Res. Ther.* **9**, 304 (2018).

[CAS](#) [PubMed](#) [PubMed Central](#) [Google Scholar](#)

41. 41.

Cai, A. et al. Mutated BCR-ABL generates immunogenic T-cell epitopes in CML patients. *Clin. Cancer Res.* **18**, 5761–5772 (2012).

[CAS](#) [PubMed](#) [PubMed Central](#) [ADS](#) [Google Scholar](#)

42. 42.

Rajasagi, M. et al. Systematic identification of personal tumor-specific neoantigens in chronic lymphocytic leukemia. *Blood* **124**, 453–462 (2014).

[CAS](#) [PubMed](#) [PubMed Central](#) [Google Scholar](#)

43. 43.

Combes, A. N., Zappia, L., Er, P. X., Oshlack, A. & Little, M. H. Single-cell analysis reveals congruence between kidney organoids and human fetal kidney. *Genome Med.* **11**, 3 (2019).

[PubMed](#) [PubMed Central](#) [Google Scholar](#)

44. 44.

Stuart, T. et al. Comprehensive integration of single-cell data. *Cell* **177**, 1888–1902 (2019).

[CAS](#) [PubMed](#) [PubMed Central](#) [Google Scholar](#)

45. 45.

Waltman, L. & van Eck, N. J. A smart local moving algorithm for large-scale modularity-based community detection. *Eur. Phys. J. B* **86**, 471 (2013).

[ADS](#) [Google Scholar](#)

46. 46.

Ashburner, M. et al.; The Gene Ontology Consortium. Gene ontology: tool for the unification of biology. *Nat. Genet.* **25**, 25–29 (2000).

[CAS](#) [PubMed](#) [PubMed Central](#) [Google Scholar](#)

47. 47.

Subramanian, A. et al. Gene set enrichment analysis: A knowledge-based approach for interpreting genome-wide expression profiles. *Proc. Natl Acad. Sci. USA* **102**, 15545–15550 (2005).

[CAS](#) [PubMed](#) [PubMed Central](#) [ADS](#) [Google Scholar](#)

48. 48.

Zhang, X. et al. CellMarker: a manually curated resource of cell markers in human and mouse. *Nucleic Acids Res.* **47** (D1), D721–D728 (2019).

[CAS](#) [PubMed](#) [PubMed Central](#) [Google Scholar](#)

49. 49.

Franzén, O., Gan, L. M. & Björkegren, J. L. M. PanglaoDB: a web server for exploration of mouse and human single-cell RNA sequencing data. *Database* **2019**, baz046 (2019).

[PubMed](#) [PubMed Central](#) [Google Scholar](#)

50. 50.

Li, H. & Durbin, R. Fast and accurate short read alignment with Burrows-Wheeler transform. *Bioinformatics* **25**, 1754–1760 (2009).

[CAS](#) [PubMed](#) [PubMed Central](#) [Google Scholar](#)

51. 51.

DePristo, M. A. et al. A framework for variation discovery and genotyping using next-generation DNA sequencing data. *Nat. Genet.* **43**, 491–498 (2011).

[CAS](#) [PubMed](#) [PubMed Central](#) [Google Scholar](#)

52. 52.

McKenna, A. et al. The genome analysis toolkit: a MapReduce framework for analyzing next-generation DNA sequencing data. *Genome Res.* **20**, 1297–1303 (2010).

[CAS](#) [PubMed](#) [PubMed Central](#) [Google Scholar](#)

53. 53.

Cibulskis, K. et al. Sensitive detection of somatic point mutations in impure and heterogeneous cancer samples. *Nat. Biotechnol.* **31**, 213–219 (2013).

[CAS](#) [PubMed](#) [PubMed Central](#) [Google Scholar](#)

54. 54.

Karczewski, K. J. et al. The mutational constraint spectrum quantified from variation in 141,456 humans. *Nature* **581**, 434–443 (2020).

[CAS](#) [PubMed](#) [PubMed Central](#) [ADS](#) [Google Scholar](#)

55. 55.

Cingolani, P. et al. A program for annotating and predicting the effects of single nucleotide polymorphisms, SnpEff: SNPs in the genome of *Drosophila melanogaster* strain w1118; iso-2; iso-3. *Fly* **6**, 80–92 (2012).

[CAS](#) [PubMed](#) [PubMed Central](#) [Google Scholar](#)

56. 56.

Choe, M. K., Hong, C. P., Park, J., Seo, S. H. & Roh, T. Y. Functional elements demarcated by histone modifications in breast cancer cells. *Biochem. Biophys. Res. Commun.* **418**, 475–482 (2012).

[CAS](#) [PubMed](#) [Google Scholar](#)

57. 57.

Langmead, B. & Salzberg, S. L. Fast gapped-read alignment with Bowtie 2. *Nat. Methods* **9**, 357–359 (2012).

[CAS](#) [PubMed](#) [PubMed Central](#) [Google Scholar](#)

58. 58.

Martin, M. Cutadapt removes adapter sequences from high-throughput sequencing reads. *EMBnet* **17**, 10–12 (2011).

[Google Scholar](#)

59. 59.

Li, H. et al. The Sequence Alignment/Map format and SAMtools. *Bioinformatics* **25**, 2078–2079 (2009).

[PubMed](#) [PubMed Central](#) [Google Scholar](#)

60. 60.

Quinlan, A. R. & Hall, I. M. BEDTools: a flexible suite of utilities for comparing genomic features. *Bioinformatics* **26**, 841–842 (2010).

[CAS](#) [PubMed](#) [PubMed Central](#) [Google Scholar](#)

61. 61.

Zhang, Y. et al. Model-based analysis of ChIP-Seq (MACS). *Genome Biol.* **9**, R137 (2008).

[PubMed](#) [PubMed Central](#) [Google Scholar](#)

62. 62.

Buenrostro, J. D., Wu, B., Chang, H. Y. & Greenleaf, W. J. ATAC-seq: a method for assaying chromatin accessibility genome-wide. *Curr Protoc Mol Biol.* **109**, 21–29 (2015).

[PubMed](#) [PubMed Central](#) [Google Scholar](#)

63. 63.

Buenrostro, J. D., Giresi, P. G., Zaba, L. C., Chang, H. Y. & Greenleaf, W. J. Transposition of native chromatin for fast and sensitive epigenomic profiling of open chromatin, DNA-binding proteins and nucleosome position. *Nat. Methods* **10**, 1213–1218 (2013).

[CAS](#) [PubMed](#) [PubMed Central](#) [Google Scholar](#)

64. 64.

Dobin, A. et al. STAR: ultrafast universal RNA-seq aligner. *Bioinformatics* **29**, 15–21 (2013).

[CAS](#) [Google Scholar](#)

65. 65.

Li, B. & Dewey, C. N. RSEM: accurate transcript quantification from RNA-seq data with or without a reference genome. *BMC Bioinformatics* **12**, 323 (2011).

[CAS](#) [PubMed](#) [PubMed Central](#) [Google Scholar](#)

66. 66.

Love, M. I., Huber, W. & Anders, S. Moderated estimation of fold change and dispersion for RNA-seq data with DESeq2. *Genome Biol.* **15**, 550 (2014).

[PubMed](#) [PubMed Central](#) [Google Scholar](#)

67. 67.

Heinz, S. et al. Simple combinations of lineage-determining transcription factors prime cis-regulatory elements required for macrophage and B cell identities. *Mol. Cell* **38**, 576–589 (2010).

[CAS](#) [PubMed](#) [PubMed Central](#) [Google Scholar](#)

68. 68.

Bailey, T. L., Johnson, J., Grant, C. E. & Noble, W. S. The MEME suite. *Nucleic Acids Res.* **43** (W1), W39–W49 (2015).

[CAS](#) [PubMed](#) [PubMed Central](#) [Google Scholar](#)

69. 69.

Zhou, Y. et al. Metascape provides a biologist-oriented resource for the analysis of systems-level datasets. *Nat. Commun.* **10**, 1523 (2019).

[PubMed](#) [PubMed Central](#) [ADS](#) [Google Scholar](#)

70. 70.

Liberzon, A. et al. Molecular signatures database (MSigDB) 3.0. *Bioinformatics* **27**, 1739–1740 (2011).

[CAS](#) [PubMed](#) [PubMed Central](#) [Google Scholar](#)

71. 71.

Ramírez, F. et al. deepTools2: a next generation web server for deep-sequencing data analysis. *Nucleic Acids Res.* **44** (W1), W160–W165 (2016).

[PubMed](#) [PubMed Central](#) [Google Scholar](#)

[Download references](#)

Acknowledgements

We thank I. Weissman at Stanford University for their generous provision of the Rainbow mouse. This research was supported by grants from the National Research Foundation of Korea (NRF-2020R1A2B5B01001490, NRF-2017M3C7A104787521, NRF-2017R1A5A101536614 and NRF-2014M3C9A3064548), Gyeongbuk Science and Technology Promotion Center of Korea (SF317001A), POSCO (2018Y060), and the BK21 Plus and BK21 FOUR Research Fellowship.

Author information

Affiliations

1. Department of Life Sciences, Pohang University of Science and Technology, Pohang, South Korea

Eunjee Kim, Seoyoung Choi, Byunghee Kang, JungHo Kong, Yubin Kim, SungEun Kim, Hyo-Min Kim, Tae-Young Roh, Sanguk Kim & Kunyoo Shin

2. Department of Integrative Biosciences and Biotechnology, Pohang University of Science and Technology, Pohang, South Korea

Byunghee Kang, Woong Hee Yoon, Hyo-Min Kim, Chorong Yang, You Jeong Lee, Tae-Young Roh & Sungjune Jung

3. Department of Creative IT Engineering, Pohang University of Science and Technology, Pohang, South Korea

Hwa-Rim Lee & Sungjune Jung

4. Department of Urology, Seoul National University Hospital, Seoul, South Korea

HySun Lee & Ja Hyeon Ku

5. Department of Urology, Samsung Medical Center, Sungkyunkwan University School of Medicine, Seoul, South Korea

Minyong Kang

6. Department of Health Sciences and Technology, SAIHST, Sungkyunkwan University, Seoul, South Korea

Minyong Kang

7. Department of Digital Health, SAIHST, Sungkyunkwan University, Seoul, South Korea

Minyong Kang

Authors

1. Eunjee Kim

[View author publications](#)

You can also search for this author in [PubMed](#) [Google Scholar](#)

2. Seoyoung Choi

[View author publications](#)

You can also search for this author in [PubMed](#) [Google Scholar](#)

3. Byunghee Kang

[View author publications](#)

You can also search for this author in [PubMed](#) [Google Scholar](#)

4. JungHo Kong

[View author publications](#)

You can also search for this author in [PubMed](#) [Google Scholar](#)

5. Yubin Kim

[View author publications](#)

You can also search for this author in [PubMed](#) [Google Scholar](#)

6. Woong Hee Yoon

[View author publications](#)

You can also search for this author in [PubMed](#) [Google Scholar](#)

7. Hwa-Rim Lee

[View author publications](#)

You can also search for this author in [PubMed](#) [Google Scholar](#)

8. SungEun Kim

[View author publications](#)

You can also search for this author in [PubMed](#) [Google Scholar](#)

9. Hyo-Min Kim

[View author publications](#)

You can also search for this author in [PubMed](#) [Google Scholar](#)

10. HyeSun Lee

[View author publications](#)

You can also search for this author in [PubMed](#) [Google Scholar](#)

11. Chorong Yang

[View author publications](#)

You can also search for this author in [PubMed](#) [Google Scholar](#)

12. You Jeong Lee

[View author publications](#)

You can also search for this author in [PubMed](#) [Google Scholar](#)

13. Minyong Kang

[View author publications](#)

You can also search for this author in [PubMed](#) [Google Scholar](#)

14. Tae-Young Roh

[View author publications](#)

You can also search for this author in [PubMed](#) [Google Scholar](#)

15. Sungjune Jung

[View author publications](#)

You can also search for this author in [PubMed](#) [Google Scholar](#)

16. Sanguk Kim

[View author publications](#)

You can also search for this author in [PubMed](#) [Google Scholar](#)

17. Ja Hyeon Ku

[View author publications](#)

You can also search for this author in [PubMed](#) [Google Scholar](#)

18. Kunyoo Shin

[View author publications](#)

You can also search for this author in [PubMed](#) [Google Scholar](#)

Contributions

E.K. and K.S. conceived ideas and experimental design. E.K., S.C., Y.K. and S.E.K. performed the overall experiments. B.K., H.-M.K., E.K. and T.-Y.R. performed RNA-seq, ATAC-seq, ChIP-seq and scRNA-seq analysis and wrote the relevant Methods. J.K., E.K. and S.K. analysed data from WES and scRNA-seq. W.H.Y., H.-R.L. and S.J. performed the 3D printing experiments. S.J. provided advice on 3D bioprinting. C.Y. and Y.J.L. helped with FACS analysis. T.-Y.R. and S.K. provided advice on bioinformatic analyses. H.S.L., M.K. and J.H.K. provided patient specimens and helped analyse data. E.K. and K.S. wrote the manuscript.

Corresponding authors

Correspondence to [Tae-Young Roh](#) or [Ja Hyeon Ku](#) or [Kunyoo Shin](#).

Ethics declarations

Competing interests

The authors declare no competing interests.

Additional information

Peer review information *Nature* thanks Andrew Adey, David McConkey and the other, anonymous, reviewer(s) for their contribution to the peer review of this work.

Publisher's note Springer Nature remains neutral with regard to jurisdictional claims in published maps and institutional affiliations.

Extended data figures and tables

Extended Data Fig. 1 Single-cell-derived bladder organoids were maintained for over a year by short-term serial passaging or long-term culture.

a, Schematic diagram illustrating the experimental strategies for the short- and long-term culture of mouse normal bladder organoids. **b**, Time-course images showing that single urothelial cells successfully generated a bladder organoid. Scale bar, 100 µm. **c**, Quantification of organoid size when cultured for 9 days at each passage. **d**, Quantification of the organoid-forming efficiency at each passage. **e**, Bright-field images of serially passaged short-term (day 9) bladder organoids from passage 1 to 20. Scale bars, 100 µm. **f**, Representative images of serially passaged short-term (day 18) bladder organoids analysed by bright-field images and immunostaining. Scale bars, 100 µm. **g**, Average size of long-term cultured bladder organoids at indicated day. **h**, Representative images of bladder organoids at indicated times during long-term culture, analysed by bright-field images and immunostaining. Scale bars, 100 µm. **i**, Short-term (day 14) and long-term (day 81) organoids compared with embryonic (E16) bladders and adult (p8week) bladders. Dotted lines demarcate the border between epithelium and stroma (white arrowheads, umbrella cells). Scale bars, 20 µm. **j**, The relative expression of *Upk2*, *Upk1a*, *Foxa1*, and *Gata3* in short-term (day 14) organoids, as compared to long-term (day 81) organoids. Data are mean ± s.e.m. For details on statistics, sample sizes (*n*), and numbers of replications, see ‘Statistics and reproducibility’ (Methods). [Source data](#)

Extended Data Fig. 2 Bladder assembloids recapitulate tissue architecture of in vivo bladders.

a, Experimental scheme for reconstituting mouse and human bladder assembloids. **b**, Representative photos of 3D printed, 12-well spinning bioreactor. **c**, Representative images of the urothelial organoid compared with the reconstituted bladder organoid with stroma. Dotted lines demarcate the border between epithelium and stroma. Scale bars, 100 µm. **d**, **e**, Bladder organoids (**d**) or reconstituted bladder organoids with stroma (**e**)

were analysed by immunostaining. Dotted lines demarcate the border between epithelium and stroma (L, lumen). Scale bars, 100 µm. **f, g**, Bladder assembloids (**f**) or wild-type bladders (**g**) were analysed by immunostaining. Dotted lines demarcate the borders between epithelium and stroma in the left panels, and stroma and muscle in the right panels (L, lumen; S, stroma; M, muscle). Scale bars, 100 µm. **h**, Representative images of human bladder organoids and human reconstituted bladder organoid with stroma. Dotted lines demarcate the border between epithelium and stroma. Scale bars, 100 µm. **i**, Representative images of normal fibroblasts derived from the P-9 benign urothelial samples (left) and iPSCs generated from the P-9 normal fibroblasts (right). Scale bars, 100 µm. **j**, Experimental strategy for stepwise differentiation of hiPSCs derived from human fibroblasts into contractile human smooth muscle cells (hSMCs). Representative images at indicated times during stepwise differentiation process are shown. Scale bar, 100 µm. **k**, hSMCs differentiated from hiPSCs at day 14 were analysed by immunostaining. Scale bar, 100 µm. For details on statistics, sample sizes (*n*), and numbers of replications, see ‘Statistics and reproducibility’ (Methods).

Extended Data Fig. 3 scRNA-seq and functional analysis of bladder assembloids.

a, *t*-SNE plots of human cells (HULECs) in 1-day and 7-day bladder assembloids. **b**, Heat map representation of gene expression for the top 15 markers expressed in wild-type endothelial cell cluster A3 and A5 compared with human endothelial cell (HULECs) cluster of 1-day and 7-day bladder assembloids. Gene expression of HULECs in bladder assembloids are represented by orthologous genes (the list of orthologous genes is from ENSEMBL BioMart database). **c**, Split dot plot showing gene expression for the top 15 markers expressed in endothelial cell cluster A3 or A5 of wild-type bladder compared with endothelial clusters of 1-day or 7-day assembloid (circle size, proportion of cells; degree of shading, expression level). **d**, Comparative analysis between wild-type bladder and bladder assembloids for the proportions of individual cell types. **e**, Hierarchical clustering of distinct cell types shared by wild-type bladder, 1-day-old, and 7-day-old bladder assembloids using cell type-specific top 50 genes. **f**, Heat map representation of gene expression between clusters in

four individual cell populations for top 15 markers expressed in wild-type bladder. **g**, Re-clustering of epithelial cell populations in 1-day and 7-day bladder assembloids from Fig. 2a identified five and four epithelial sub-clusters, respectively. **h**, The proportions of each cluster of 1-day and 7-day bladder assembloids shown in panel g. **i**, Violin plots for selected eight basal and luminal markers in each cell cluster shown in panel g. **j**, Bladder assembloids treated with acetylcholine (Ach) or noradrenaline (NA) were analysed using bright-field images and immunostaining. Scale bars, 100 μm . **k**, Transmission electron microscopy (TEM) and immunostaining analysis for tight junctions and urothelial plaques in bladder assembloids compared with wild-type bladder (black and white arrowheads, tight junctions; L, lumen; UP, urothelial plaques). Scale bars, 1 μm (TEM) or 10 μm (immunostaining). **l**, Immunostaining of ZO-1 for tight junctions in human bladder assembloids (white arrowheads, tight junctions; L, lumen). Scale bars, 20 μm . For details on statistics, sample sizes (n), and numbers of replications, see ‘Statistics and reproducibility’ (Methods). [Source data](#)

Extended Data Fig. 4 Bladder assembloids mimic the pathophysiology and represent tissue dynamics during urinary tract infection.

a, Schematic diagram for establishment of in vivo and in vitro models of UTI. **b**, UTI89 labelled with the fluorescent protein, AmCyan, was microinjected into the lumen bladder assembloids. Scale bars, 100 μm . **c**, **d**, Wild-type bladders (**c**) and bladder assembloids (**d**) were analysed by immunostaining. Scale bars, 50 μm . **e**, Wild-type bladders and bladder assembloids were analysed by immunostaining (white arrowheads, intracellular bacterial aggregates within superficial cells). Scale bars, 50 μm . **f**, Wild-type bladders and bladder assembloids were immunostained for KRT5, KRT18 and vimentin to highlight basal epithelial cells, luminal epithelial cells, and stromal cells, respectively. Scale bars, 100 μm . **g**, **h**, Bladder assembloids reconstituted with different cell types from *Col1a2^{CreER};Smo^{fl/fl}* mice (**g**, wild-type Smo; **h**, Smo ablated) analysed by immunostaining. The quantification of epithelial and stromal cell proliferations is shown in the right panels. Scale bars, 100 μm . **i**, Schematic representation of the Rainbow allele. After Cre-mediated excision of three lox sites (lox2272, loxN, and loxP) induced by tamoxifen (TM), each cell

expresses either EGFP (before recombination) or mCerulean, mOrange, or mCherry (after recombination). **j**, Single-cell-labelled normal bladder or bladder organoid from Rainbow mouse after TM treatment. Scale bars, 100 µm. **k**, Experimental scheme for *in vivo* and *in vitro* lineage tracing of KRT5-expressing basal epithelial cells. **l**, Bladders from TM-injected *Krt5*^{CreERT2}; *Rosa26*^{RainbowWT} mice and bladder assembloids derived from *Krt5*^{CreERT2}; *Rosa26*^{RainbowWT} mice treated with 4-OHT were analysed before (UPEC day 0) and after (UPEC day 7) bacterial injection using four-colour fluorescence. Scale bars, 100 µm. **m**, Model for clonal relationship during UTI-induced urothelial regeneration. For details on statistics, sample sizes (*n*), and numbers of replications, see ‘Statistics and reproducibility’ (Methods). [Source data](#)

Extended Data Fig. 5 Generation of bladder tumour assembloids recapitulating the histopathology, genomic alterations and tumour subtypes of human urothelial carcinomas.

a, Eight bladder tumour organoid lines were established from patient-derived invasive urothelial carcinoma samples. Resulting tumour organoids were analysed by H&E staining and immunostaining to mark basal (KRT5) and luminal (KRT18) cells. Scale bars, 100 µm. **b–i**, The relative expressions of luminal (UPK1A, UPK2, ERBB2, FOXA1, and GATA3) and basal (KRT5, KRT14, CDH3, and KRT6A) markers in eight patient-derived bladder tumour organoids. **j**, Summary of molecular subtypes of eight bladder tumour organoids based on gene expression analysis. **k**, Experimental scheme for reconstituting patient-derived bladder tumour assembloids. **l, m**, Histopathology of tumour organoids, tumour assembloids, xenografts, and parental tumours derived from P-3 and P-6 were analysed by H&E staining and immunostaining. Scale bars, 100 µm. **n**, Bladder tumour assembloids derived from P-1 were analysed by immunostaining to mark tumour cells, CAFs, and endothelial cells (arrowheads, interconnected regions). Scale bars, 100 µm. **o**, Tumour growth was quantified by measuring tumour areas using the Image J program. **p**, Bladder tumour assembloids reconstituted without or with endothelial cells were analysed by immunostaining. Scale bars, 100 µm. **q**,

Comparative analysis for mutations detected by WES of parental tumours, tumour organoids, and tumour assembloids. **r**, Parental tumours, tumour organoids at late passages (late organoid), and tumour assembloids at late passages (late assembloid) were analysed by immunostaining. Scale bars, 50 µm. **s**, Relative expression of luminal (UPK1A, UPK2, ERBB2, FOXA1, and GATA3) and basal (KRT5, KRT14, CDH3, and KRT6A) markers in parental tumours, late organoids, and late assembloids. Data are mean ± s.e.m. For details on statistics, sample sizes (*n*), and numbers of replications, see ‘Statistics and reproducibility’ (Methods). [Source data](#)

Extended Data Fig. 6 3D bioprinting-based, reconstituted bladder tumour assembloids recapitulate the pathophysiology of patient-derived urothelial carcinoma.

a, Schematic diagram for 3D bioprinting-based reconstitution of patient-derived bladder tumour assembloids. **b**, **c**, 3D bioprinted bladder tumour organoids and assembloids derived from the P-1 (**b**) or P-3 (**c**) lines were analysed by H&E staining and immunostaining. Scale bars, 100 µm. **d**, **e**, 3D bioprinted bladder tumour assembloids treated with SAG, FK506, or vehicle control were analysed by immunostaining for KRT18 (luminal subtype; **d**) or KRT5 (basal subtype; **e**), and vimentin, which was compared with bladder tumour organoids. Quantification of tumour cell number is shown. Scale bars, 100 µm. **f**, **g**, 3D bioprinted bladder tumour assembloids treated with cisplatin were analysed by caspase 3, which was compared with bladder tumour organoids. Quantification of tumour cell apoptosis is shown. Scale bars, 100 µm. **h**, Experimental strategy for stepwise differentiation of human ES cells into contractile hSMCs. Representative images at indicated times during stepwise differentiation process are shown. Scale bar, 100 µm. **i**, hSMCs differentiated from human ES cells at day 14 were analysed by immunostaining. Scale bar, 100 µm. **j**, Experimental scheme to create bladder tumour assembloids containing an outer muscle layer. **k**, Bladder tumour assembloids containing outer muscle layer derived from P-7 and P-3 were analysed by immunostaining. Dotted lines demarcate the border between the stromal and muscle layer. Scale bar, 100 µm. Data are mean ± s.e.m. For details on statistics, sample sizes (*n*), and numbers of replications, see ‘Statistics and reproducibility’ (Methods).

[Source data](#)

Extended Data Fig. 7 Bladder tumour assembloids mimic the pathophysiology of bladder tumours and show the CD8 T cell-mediated tumour cytotoxicity.

a, Experimental scheme for reconstituting mouse bladder tumour assembloids. **b**, Tumour organoids derived from BBN-induced mouse bladder tumours, reconstituted bladder tumour assembloids, and endogenous BBN-induced mouse bladder tumours were analysed by H&E staining and immunostaining. Scale bars, 100 µm. **c**, Mouse bladder tumour organoids and tumour assembloids treated with SAG, FK506, or vehicle control were analysed by immunostaining. Tumour growth was quantified by measuring tumour areas using the Image J program. Scale bars, 100 µm. **d**, Experimental strategy for generating tumour-reactive T cells. **e**, Gating strategy to analyse CD8 T cells (B220-CD11b-TCR β +CD4-CD8+) shown in panel **f**. **f**, Flow cytometry plots gated on tumour-reactive CD8 T cells expressing CD69 and IFN γ . **g**, Experimental strategy for generating bladder tumour assembloids containing tumour-reactive T cells. **h**, Bladder tumour assembloids containing tumour-reactive T cells were analysed by bright-field imaging (dotted lines, tumour areas) and immunostaining. Scale bars, 100 µm. **i**, Schematic representation for the strategy to systematically discover tumour neoantigens and test tumour reactivity within the tumour-assembloid platform. Tumour-specific mutations in BBN-induced mouse tumours were detected by WES and identified through application of mutation calling algorithms (Mutect). Candidate neoepitopes were predicted using well-validated algorithms (NetMHCpan) and selected based on binding affinity to H-2-Db and H-2-Kb molecules. Tumour reactivity of selected neoantigen-specific T cells was validated by increased *Ifng* expression. These candidate neoantigen-specific T cells were further reconstituted to test their ability to stimulate tumour-specific T cell responses within the assembloid platform. **j**, The list of putative neoantigens considered to bind strongly to H-2-Db (left) or H-2-Kb (right). Top 10 neoantigen candidates are displayed in order of binding affinity of mutant peptide relative to wt peptide. Only one mutant, LGFSNYPEL (Olfr512 mutant), is predicted to bind strongly to both H-2-Db and H-2-Kb. **k**, Relative expression of *Ifng* in T cells stimulated with wt-Olfr512 peptide compared with the mutant-Olfr512 peptide. **l**, Bladder tumour assembloids containing neoantigen-reactive T cells were analysed by bright-field images

(dotted lines, tumour areas) and immunostaining. Quantifications of tumour size and tumour cell apoptosis are shown. Scale bars, 100 µm. Data are mean ± s.e.m. For details on statistics, sample sizes (*n*), and numbers of replications, see ‘Statistics and reproducibility’ (Methods). [Source data](#)

Extended Data Fig. 8 Prospective model for the development of next-generation assembloids.

Our study provides a conceptual framework for development of multilayered, functional organoids derived from tissue stem cells or tumour cells that mimic the biology of native tissues. These miniature tissues, assembloids, could serve as model systems for various diseases, including cancers and degenerative diseases. With 3D bioprinting technology, this platform may facilitate the establishment of an *in vitro* organoid system for high-throughput drug screening or repositioning to develop precise and personalized therapies.

Extended Data Fig. 9 Genetically manipulated tumour assembloids show differential epigenomic landscape of chromatin accessibility and enhancer activity between basal and luminal tumours.

a, Basal tumour organoids and luminal tumour organoids were reconstituted with patient-derived CAFs, followed by shaking incubation in a spinning bioreactor. **b**, Basal tumour organoids infected with lentivirus to overexpress FOXA1 were reconstituted with CAFs. Luminal tumour organoids infected with lentivirus to knockout FOXA1 were reconstituted with CAF. **c**, Basal tumour organoids were reconstituted with CAFs manipulated to overexpress BMP4 and BMP5. Luminal tumour organoids were reconstituted with CAFs manipulated to knockout BMP4 and BMP5. **d**, Basal tumour organoids infected with lentivirus to knockout FOXA1 were reconstituted with CAFs manipulated to overexpress BMP4 and BMP5 and were cultured by shaking incubation. Luminal tumour organoids infected with lentivirus to overexpress FOXA1 were reconstituted with CAFs manipulated to knockout BMP4 and BMP5 and were cultured by shaking incubation. **e, f**, Relative expression of *FOXA1* in FOXA1-

overexpressing basal tumour organoids was analysed by RT–qPCR. KO, knockout; OE, overexpression. **g, h**, Relative expression of *FOXA1* in *FOXA1*-knocked out luminal tumour organoids was analysed by RT–qPCR. **i, j**, Relative expression of *BMP4* or *BMP5* in *BMP4/BMP5*-overexpressing CAFs was analysed by RT–qPCR. **k, l**, Relative expression of *BMP4* or *BMP5* in *BMP4/BMP5*-knocked out CAFs was analysed by RT–qPCR. **m**, Sequences of guide RNAs and target genes for knockout of *BMP4*, *BMP5*, and *FOXA1* (PAM sequences are marked in red). **n, p**, Heat map representation of regions with increased chromatin accessibility/H3K27ac signals in luminal (**n**) or basal (**p**) in four assembloids (L1 = P-1; L2 = P-6; B1 = P-2; B2 = P-3). Each row; individual line ($n = 4$). Each column; single region (centre \pm 5Kb). **o, q**, Pie chart showing the genomic annotations of regions with increased chromatin accessibility/H3K27ac signals in luminal (**o**) or basal (**q**) according to the location of a given peak. TSS, “–1-kb to +100-bp” of transcription start sites. TTS, “–100-bp to +1-Kb” of transcription termination sites. **r**, Top 5 enriched de novo motifs and transcription factors with best matched binding motifs in regions with increased chromatin accessibility/H3K27ac signals in luminal. The most enriched motif shows high similarity with Forkhead box transcription factor binding motifs. **s**, Representative ATAC-seq, H3K27ac ChIP-seq, and *FOXA1* ChIP-seq profiles of the regions at ISX loci in the indicated samples. **t**, Pathway analysis for genes associated with increased chromatin accessibility/H3K27ac signals in luminal. Only top 10 GO terms ranked by their significance are shown. Data are mean \pm s.e.m. For details on statistics, sample sizes (n), and numbers of replications, see ‘Statistics and reproducibility’ (Methods). [Source data](#)

Extended Data Fig. 10 FOXA1-mediated enhancer reprogramming confers tumour subtype plasticity of urothelial carcinomas through a FOXA1–BMP–hedgehog signalling feedback axis between the epithelial tumour and stroma.

a, c, Heat maps of ATAC-seq, H3K27ac ChIP-seq, and RNA-seq for GAIN/LOSS regions/genes from indicated samples. Hierarchical clustering was performed on ATAC-seq and H3K27ac ChIP-seq. **b, d**, GSEA of indicated samples to assess differential enrichment of GAIN genes (left)

and signature genes for cell differentiation (right). NES, normalized enrichment score. Nominal p value is shown **e**, **f**, Relative expression of *FOXA1* in basal tumour organoid B1 (**e**) and B2 (**f**), treated with BMP4, BMP5, or BMP4 and BMP5 together. Data are mean \pm s.e.m. **g**, **h**, Representative ATAC-seq, H3K27ac ChIP-seq, and *FOXA1* ChIP-seq profiles of the regions at IRX2 loci in the indicated samples. **i**, **j**, Molecular subtypes of indicated samples were analysed using the BASE47 together with MDACC classifiers. Heat maps show the normalized gene expression profile organized by the luminal and basal classifier genes. **k**, **l**, Heat map representation of unsupervised hierarchical clustering from ATAC-seq (**k**) or H3K27ac ChIP-seq (**l**) data for tumour assembloids in each experiment summarized in Extended Data Fig. [9a–d](#). Samples were clustered based on the Spearman correlation coefficient with single linkage. **m**, Principal components analysis from RNA-seq data for tumour assembloids in each experiment summarized in Extended Data Fig. [9a–d](#). **n**, Representation of motifs enriched at the regions with increased chromatin accessibility/H3K27ac signals in basal. **o**, Top 5 enriched de novo motifs and transcription factors with best matched binding motifs in regions with increased chromatin accessibility/H3K27ac signals in basal. The most enriched motif shows high similarity with AP-1 transcription factor binding motifs. For details on statistics, sample sizes (n), and numbers of replications, see ‘Statistics and reproducibility’ (Methods). [Source data](#)

Supplementary information

Supplementary Table 1

Patient sources of human invasive urothelial carcinoma samples. Invasive urothelial carcinoma samples were obtained from TURB or radical cystectomy patients with disease and treatment histories as shown.

Reporting Summary

Supplementary Video 1.

Plate-making process for the spinning bioreactor using a 3D printer.

Supplementary Video 2.

Gear-making process for the spinning bioreactor using a 3D printer.

Supplementary Video 3.

Operation of 3D-printed spinning bioreactor.

Supplementary Video 4.

Incubation of reconstituted assembloids with shaking in a 3D-printed spinning bioreactor.

Supplementary Video 5.

Microinjection of UPEC into the lumen of reconstituted bladder assembloids.

Supplementary Video 6.

3D bioprinting-based reconstitution of patient-derived bladder tumour assembloids.

Source data

[Source Data Fig. 1](#)

[Source Data Fig. 2](#)

[Source Data Fig. 3](#)

[Source Data Fig. 4](#)

[Source Data Extended Data Fig. 1](#)

[Source Data Extended Data Fig. 3](#)

[Source Data Extended Data Fig. 4](#)

[Source Data Extended Data Fig. 5](#)

[Source Data Extended Data Fig. 6](#)

[Source Data Extended Data Fig. 7](#)

[Source Data Extended Data Fig. 9](#)

[Source Data Extended Data Fig. 10](#)

Rights and permissions

[Reprints and Permissions](#)

About this article



Cite this article

Kim, E., Choi, S., Kang, B. *et al.* Creation of bladder assembloids mimicking tissue regeneration and cancer. *Nature* **588**, 664–669 (2020). <https://doi.org/10.1038/s41586-020-3034-x>

[Download citation](#)

- Received: 12 May 2019
- Accepted: 13 October 2020
- Published: 16 December 2020
- Issue Date: 24 December 2020
- DOI: <https://doi.org/10.1038/s41586-020-3034-x>

Comments

By submitting a comment you agree to abide by our [Terms](#) and [Community Guidelines](#). If you find something abusive or that does not comply with our terms or guidelines please flag it as inappropriate.

[Access through your institution](#)

[Change institution](#)

[Buy or subscribe](#)

Associated Content

Collection

Cancer at Nature Research

This article was downloaded by **calibre** from <https://www.nature.com/articles/s41586-020-3034-x>

| [Section menu](#) | [Main menu](#) |

Progenitor identification and SARS-CoV-2 infection in human distal lung organoids
[Download PDF](#)

- Article
- [Published: 25 November 2020](#)

Progenitor identification and SARS-CoV-2 infection in human distal lung organoids

- [Ameen A. Salahudeen](#) [ORCID: orcid.org/0000-0001-9037-3481](#)^{1 na1 nAff19},
- [Shannon S. Choi](#)^{1 na1},
- [Arjun Rustagi](#) [ORCID: orcid.org/0000-0002-6921-1012](#)²,
- [Junjie Zhu](#) [ORCID: orcid.org/0000-0001-7177-8694](#)³,
- [Vincent van Unen](#) [ORCID: orcid.org/0000-0001-9339-8430](#)^{4,5},
- [Sean M. de la O](#)¹,
- [Ryan A. Flynn](#) [ORCID: orcid.org/0000-0001-5013-0442](#)^{6,7},
- [Mar Margalef-Català](#) [ORCID: orcid.org/0000-0002-6259-4348](#)⁸,
- [António J. M. Santos](#)¹,
- [Jihang Ju](#)¹,
- [Arpit Batish](#)¹,
- [Tatsuya Usui](#)¹,
- [Grace X. Y. Zheng](#)⁹,
- [Caitlin E. Edwards](#) [ORCID: orcid.org/0000-0003-4228-2192](#)¹⁰,
- [Lisa E. Wagar](#)^{4,5},
- [Vincent Luca](#)¹¹,
- [Benedict Anchang](#)¹²,
- [Monica Nagendran](#)¹³,
- [Khanh Nguyen](#)¹⁴,
- [Daniel J. Hart](#)¹,
- [Jessica M. Terry](#)⁹,
- [Phillip Belgrader](#)⁹,
- [Solongo B. Ziraldo](#)⁹,
- [Tarjei S. Mikkelsen](#)⁹,
- [Pehr B. Harbury](#)¹⁵,

- [Jeffrey S. Glenn](#)^{4,14},
- [K. Christopher Garcia](#) ORCID: orcid.org/0000-0001-9273-0278^{11,16},
- [Mark M. Davis](#) ORCID: orcid.org/0000-0001-6868-657X^{4,5,16},
- [Ralph S. Baric](#) ORCID: orcid.org/0000-0001-6827-8701^{10,17},
- [Chiara Sabatti](#)¹²,
- [Manuel R. Amieva](#)^{4,8},
- [Catherine A. Blish](#) ORCID: orcid.org/0000-0001-6946-7627^{2,18},
- [Tushar J. Desai](#) ORCID: orcid.org/0000-0002-8794-5319¹³ &
- [Calvin J. Kuo](#) ORCID: orcid.org/0000-0002-7427-5985¹

[Nature](#) volume 588, pages670–675(2020) [Cite this article](#)

- 16k Accesses
- 154 Altmetric
- [Metrics details](#)

Subjects

- [Adult stem cells](#)
- [Influenza virus](#)
- [SARS-CoV-2](#)

Abstract

The distal lung contains terminal bronchioles and alveoli that facilitate gas exchange. Three-dimensional in vitro human distal lung culture systems would strongly facilitate the investigation of pathologies such as interstitial lung disease, cancer and coronavirus disease 2019 (COVID-19) pneumonia caused by severe acute respiratory syndrome coronavirus 2 (SARS-CoV-2). Here we describe the development of a long-term feeder-free, chemically defined culture system for distal lung progenitors as organoids derived from single adult human alveolar epithelial type II (AT2) or KRT5⁺ basal cells. AT2 organoids were able to differentiate into AT1 cells, and basal cell organoids developed lumens lined with differentiated club and ciliated cells. Single-cell analysis of KRT5⁺ cells in basal organoids revealed a distinct population of *ITGA6*⁺*ITGB4*⁺ mitotic cells, whose offspring further segregated into a *TNFRSF12A*^{hi} subfraction that comprised about ten per cent of KRT5⁺ basal cells. This subpopulation formed clusters within terminal bronchioles and exhibited enriched clonogenic organoid growth activity. We created distal lung organoids with apical-out polarity to present ACE2 on the exposed external surface, facilitating infection of AT2 and basal

cultures with SARS-CoV-2 and identifying club cells as a target population. This long-term, feeder-free culture of human distal lung organoids, coupled with single-cell analysis, identifies functional heterogeneity among basal cells and establishes a facile in vitro organoid model of human distal lung infections, including COVID-19-associated pneumonia.

[Download PDF](#)

Main

The distal lung performs essential respiratory functions that can be compromised by inflammatory, neoplastic or infectious disorders such as COVID-19 pneumonia. The study of these conditions would be facilitated by robust in vitro models based on human cells. The identities of the stem cells that regenerate distal lung epithelium *in vivo* over the human lifespan have been inferred from mouse studies, despite differences between these species¹. In humans, basal stem cells span the entire airway tree, whereas in mouse, club cells² and/or secretoglobin 1A1 (SCGB1A1)-expressing non-club cells³ renew the distal bronchioles during ageing. In the gas exchange region, mouse alveolar epithelial type II (AT2) cells generate AT1 and AT2 cells during homeostasis^{4,5}, and additional progenitors are recruited in response to severe injury^{3,6,7,8,9}. The presence and/or roles of facultative progenitors in human lung are unknown. Human AT2 cells can be differentiated into AT1 cells, but these cultures are short-lived and do not demonstrate long-term self-renewal or enable expansion for disease modelling^{4,10,11}; furthermore, their requirements for feeder cells impede the definition of specific niche components^{12,13}. We have established long-term organoid culture of distal human lung, including AT2 and basal stem cells, and used this system to validate functional progenitor cells and model SARS-CoV-2 infection.

Clonogenic alveolar and basal organoids

We empirically defined medium conditions to support the clonal expansion of distal human lung progenitors from 136 individuals in collagen/laminin extracellular matrix (ECM) (Fig. 1a, Supplementary Table 1). Together, EGF and the BMP antagonist NOGGIN supported growth of disaggregated distal lung cells or purified epithelial fractions thereof (Extended Data Fig. 1a–c). Single cells (Extended Data Fig. 1d–g) expanded into either SFTPC⁺HTII-280⁺ AT2 cystic organoids (Fig. 1b–e) or KRT5⁺ solid organoids expressing the basal cell marker KRT5 (Fig. 1b, f–h).

Fig. 1: Clonogenic expansion of human distal lung organoids.

 **figure1**

- a.** Human distal lung D14 (day 14) organoid cultures contain cystic and solid organoids. Bottom left, brightfield; right, haematoxylin and eosin (H&E). Scale bar, 100 µm. **b**, Whole-mount immunofluorescence with anti-KRT5 (basal cell), anti-SFTPC (AT2 cell) and anti-SCGB1A1 (club cell) antibodies. Scale bar, 100 µm. **c–e**, Alveolar organoids on D32. **c**, Cystic AT2 organoid. H&E; scale bar, 25 µm. **d**, Whole-mount immunofluorescence for anti-SFTPC, anti-HTII-280, phalloidin (Ph) and DAPI; scale bar, 50 µm. **e**, Anti-KI67 and DAPI fluorescence of an adjacent section to **d**. **f–h**, Basal organoids on D32. **f**, H&E; scale bar, 50 µm. **g**, Whole-mount immunofluorescence for anti-KRT5 and DAPI; scale bar, 100 µm. **h**, Anti-KI67 and DAPI immunostaining of adjacent section to **g**. **i–k**, Single-cell RNA-seq of total distal lung organoids at D28. **i**, t-Distributed stochastic neighbour embedding (t-SNE) plot of 7,285 individual cells demonstrating AT2, basal, and club populations. **j**, Expression of *SFTPC* (AT2), *KRT5* (basal) and *SCGB1A1* (club). **k**, Feature plots for expression of *SFTPC* (AT2), *KRT5* (basal) and *SCGB1A1* (club). **l–p**, Clonogenic AT2 organoid culture. **l**, Brightfield microscopy of AT2 organoids at D180; scale bar, 200 µm. **m**, H&E staining from culture as in **l**; scale bar, 50 µm. **n**, Transmission electron microscopy of AT2 organoid at D32. LB, lamellar body; scale bar, 5 µm. **o**, **p**, Immunofluorescence of AT2 organoid at D32 (**o**); culture on glass for 10 additional

days induces differentiation into AT1 cells (**p**). Immunofluorescence for anti-HTI-56 (AT1) and anti-HTII-280 (AT2); scale bar, 50 μ m. **q**, scRNA-seq feature plots of 2,780 AT2 organoid cells on D89 of cumulative culture.

[Full size image](#)

Single cell RNA sequencing (scRNA-seq) of distal lung organoids confirmed the presence of populations of *SFTPC*⁺ AT2 cells, *KRT5*⁺ basal cells and *SCGB1A1*⁺ club cells (Fig. [1i,j](#), Extended Data Fig. [2](#)). Cells that co-expressed *KRT5* and *SCGB1A1* were found in both basal and club cell populations, suggesting a transitional state (Fig. [1j,k](#), Extended Data Fig. [2](#)) that was supported by the results of SPADE^{[14](#)} and Monocle^{[15](#)} trajectory analysis (Extended Data Fig. [3](#), Supplementary Table [2](#)).

Characterization of human AT2 cell organoids

We generated pure AT2 organoids from mixed cultures via uptake of lysosomal dyes into lamellar bodies (Extended Data Fig. [4a,b](#), Supplementary Fig. [1](#)).

EPCAM⁺Lysotracker⁺ AT2 cells expanded clonally for up to 180 days (Fig. [1l,m](#), Extended Data Fig. [4c,d](#)). Chemically defined EGF/NOGGIN medium was sufficient for baseline clonal proliferation of AT2 organoids, which was attenuated by blocking global endogenous WNT biosynthesis (Extended Data Fig. [4e](#)), consistent with the requirement for autocrine WNT signalling in mouse AT2 cells^{[16](#)}. Growth was enhanced by adding fibroblast conditioned medium containing serum and WNT agonists (Extended Data Fig. [4f](#)). Transmission electron microscopy revealed microvilli and lamellar bodies characteristic of mature AT2 cells (Fig. [1n](#), Extended Data Fig. [4g](#)). AT2 organoids showed upregulation of AT1 markers when cultured on glass with serum (Fig. [1o,p](#)).

Single-cell RNA-seq of mixed distal lung organoids or purified alveolar organoids revealed uniformly high expression of canonical AT2 cell markers in alveolar populations (Fig. [1i-k,q](#), Extended Data Fig. [2](#), Supplementary Data [1](#)). AT2 cell subsets were not readily observed, and cell cycle-related mRNAs did not localize to a specific AT2 subpopulation (Fig. [1q](#), Supplementary Data [1](#), Supplementary Table [3](#)).

Differentiation of human basal organoids

Basal cell organoids in mixed distal lung culture grew more rapidly than alveolar organoids and initially formed solid KRT5⁺ spheroids (Fig. [1a,b,f-h](#)). However, by one month of culture, about 50% of organoids had developed single or occasionally multiple lumens (Fig. [2a,b](#), Extended Data Fig. [5a-c](#)) with club (*SCGB1A1*⁺*KRT5*⁻) and ciliated (*AcTUB*⁺*KRT5*⁻) cells lining the interior surface (Fig. [2a,b](#)). Basal

cultures purified by density sedimentation exhibited serial clonal outgrowth, dependence on EGF and NOGGIN, and cavitation lined by luminal SCGB1A1⁺ club and AcTUB⁺ ciliated cells (Fig. 2c, d, Extended Data Fig. 5d–h, Supplementary Videos 1, 2). Similar differentiation occurred when organoids were transferred into 2D air–liquid interface (ALI) cultures (Fig. 2e).

Fig. 2: Basal organoid differentiation and TNFRSF12A^{hi} progenitor discovery.



a, b, Immunofluorescence showing basal organoid differentiation in mixed culture. Lumens are lined with acetylated tubulin⁺ (AcTUB) ciliated cells, which express the SARS-CoV-2 receptor ACE2 but lack KRT5 (**a**), and SCGB1A1⁺ club cells (**b**). Scale bar, 20 μ m. **c–e,** Sedimented basal organoid culture. **c,** Club cell differentiation in purified basal organoids after 38 days in 3D clonogenic culture, shown by whole-mount fluorescence for anti-SCGB1A1 (red), phalloidin (white), and DAPI (blue); scale bar, 50 μ m. **d,** Ciliated differentiation of organoids as in **c**. Confocal transmission image; scale bar, 20 μ m. White box in inset expanded to main image; arrowheads denote cilia. **e,** Immunofluorescence showing AcTUB⁺ ciliated and SCGB1A1⁺ club cells in an organoid that has been replated in 2D ALI culture. Scale bar, 50 μ m. **f, g,** Single-cell RNA-seq of KRT5⁺ basal cells from Fig. 1i. **f,** t-SNE plots showing Basal 1 and Basal 2 subclusters. Basal 1 is subdivided into Basal 1.1 and 1.2, with the latter expressing the proliferative mRNAs *CDK1* and *PCNA*. **g,** Differential gene expression in Basal 1 and Basal 2 subclusters from a total of 2,303 basal cells. **h,** Basal marker transcript t-SNE overlays of **f** (\log_{10} number of unique molecular identifiers (UMI)). **i,**

Relative gene expression kinetic plots of **f** and **g** across the pseudotime trajectory ($n = 3,721$ cells). **j**, FACS isolation of TNFRSF12A^{hi} versus TNFRSF12A^{neg} cells from mixed distal lung organoids, pre-gated on live singlets. **k**, Brightfield image of organoid culture of cells from **j** at D14. **l**, Quantification of **k** (number of organoids per 1,000 cells); *** $P < 0.001$ ($P = 1.0 \times 10^{-4}$), two-tailed Student's *t*-test. Data in **j**, **k** represent $n = 5$ independent experiments for each TNFRSF12A population.

[Source data](#)

[Full size image](#)

Distinct subtypes of airway basal cells

Single-cell RNA-seq clustering of organoid *KRT5*⁺ basal cells from multiple individuals reproducibly identified two populations: Basal 1 and Basal 2 (Fig. 2f,g, Extended Data Fig. 6a, Supplementary Data 1). Basal 1 included an actively cycling subpopulation (Basal 1.2) that was enriched in proliferation markers (*PCNA*, *CDKI*) and gene cell enrichment analysis (GSEA) cell-cycle-related processes (Fig. 2f,g, Extended Data Fig. 6a–c, Supplementary Table 3). Basal 1, but not Basal 2, expressed canonical lung basal cell mRNAs such as *TP63*¹⁷, integrin- α_6 (*ITGA6*) and integrin- β_4 (*ITGB4*, which encodes a binding partner of *ITGA6*¹⁸ and marks mouse lineage-negative epithelial progenitors (LNEPs))⁷ (Fig. 2h). Basal 2 was enriched in expression of genes related to vesicular transport, endoplasmic reticulum processes and squamous markers (Fig. 2g, Supplementary Table 3).

Characterization of TNFRSF12A⁺ progenitors

We examined the differentially expressed Basal 1 gene *TNFRSF12A* (also known as *Fn14*, *TWEAKR*), which encodes a membrane receptor (Fig. 2g,h, Supplementary Table 4) because of its potential utility for fluorescence-activated cell sorting (FACS) isolation and its homology to the intestinal stem cell marker *TNFRSF19*¹⁹. Unbiased pseudotime analysis revealed a continuous single-cell trajectory connecting *KRT5*⁺ Basal 1 cells to *SCGB1A1*⁺ club cells, with *TNFRSF12A* mRNA being strongly associated with the proliferation marker gene *MKI67* (Fig. 2i, Extended Data Fig. 3e). When Basal 1 cells co-expressing *EPCAM*, *ITGA6* and *ITGB4* were divided into three fractions (expressing low, medium and high levels of *TNFRSF12A* mRNA), a proliferative gene module²⁰ was significantly enriched in the highest (*TNFRSF12A*^{hi}) versus lowest fraction (*TNFRSF12A*^{lo}) (Extended Data Fig. 6d–f). To determine whether this enrichment reflected intrinsic proliferative potential, we fractionated total distal lung organoids by FACS into *EPCAM*⁺*ITGA6*⁺*ITGB4*⁺ Basal 1 cells and then

into TNFRSF12A^{hi} and TNFRSF12A^{neg} subsets (Fig. 2j). When cultured, the TNFRSF12A^{hi} subset showed 4–12 times greater clonogenic organoid-forming capacity than the TNFRSF12A^{neg} subset (Fig. 2k,l).

We examined lineage relationships between Basal 1 and Basal 2 by fractionating density-sedimented KRT5⁺ basal organoids by FACS into EPCAM⁺ITGA6⁺ITGB4⁺TNFRSF12A^{hi} (Basal 1) and EPCAM⁺ITGA6⁻ITGB4⁻TNFRSF12A^{neg} (Basal 2) populations (Extended Data Fig. 7a). Clonogenic organoid formation was strongly enriched in Basal 1 versus Basal 2 from three separate individuals (Extended Data Fig. 7b–d). The basal 2-enriched genes *SPRR1B* and *TMSB4X* (Fig. 2g, Supplementary Table 3) were transiently induced in Basal 1 cell organoids (Extended Data Fig. 7e,f), suggesting that Basal 2 cells might differentiate from Basal 1.

The NOTCH target gene *HES1* was one of the most differentially expressed loci in Basal 1 organoids, in which gene networks included *NOTCH1*, *NOTCH2* and *JAG1* (Fig. 2g, Supplementary Table 3). Inhibition of NOTCH significantly increased basal organoid proliferation from TNFRSF12A^{hi}EPCAM⁺ITGA6⁺ITGB4⁺ cells (Extended Data Fig. 7g,h), suggesting that NOTCH signalling restrains growth in these cells. Conversely, NOTCH agonism did not affect proliferation, but did induce expression of *SCGB1A1*, similar to upper airway cells^{21,22} (Extended Data Fig. 7i).

Characterization of TNFRSF12A⁺ cells in distal lung

Immunostaining of human distal lung tissue showed TNFRSF12A⁺ basal cells that were enriched intermittently at the tips or bases of bronchiolar furrows (Fig. 3a, Extended Data Fig. 8a,b); the latter are recognized as a goblet cell niche²³. We found TNFRSF12A in diverse lung stromal and epithelial cells, but it clearly marked a minor population of KRT5⁺ and p63⁺ basal cells (Fig. 3a, Extended Data Fig. 8a–c). The TNFRSF12A⁺ subset of KRT5⁺ basal cells had a higher mitotic index than total KRT5⁺ cells in vivo (Fig. 3b,c), consistent with the results of organoid scRNA-seq (Fig. 2i). FACS analysis of human distal lung cells confirmed that TNFRSF12A was expressed in 10.9% of basal cells (Extended Data Fig. 8d, top).

Fig. 3: Characterization of TNFRSF12A^{hi} Basal 1 cells from intact human lung.

 **figure3**

a, Left, anti-KRT5 and anti-TNFRSF12A immunofluorescence of human distal lung. Yellow boxed area is expanded with (middle) and without (right) DAPI. Scale bars, 100 µm. **b**, Immunofluorescence of distal airway TNFRSF12A⁺ basal cell proliferation showing KRT5, TNFRSF12A, KI67 and DAPI. Scale bar, 100 µm. **c**, Mitotic index of TNFRSF12A⁺KRT5⁺ cells from **b**; three independent experiments. K5⁺, total KRT5⁺; K5⁺T⁺, TNFRSF12A⁺KRT5⁺. Box plots represent first quartile, median and third quartile; whiskers show minimum and maximum. ** $P < 0.01$ ($P = 4.4 \times 10^{-3}$), two-tailed Student's *t*-test. **d**, Brightfield and anti-KRT5 immunofluorescence of FACS-isolated TNFRSF12A^{neg} and TNFRSF12A^{hi} organoid cultures at D14; scale bars, 500 µm. **e**, Quantification of **d** (number of organoids per 1,000 cells); data represent $n = 5$ independent experiments for each TNFRSF12A population. Box plots represent first quartile, median and third quartile; whiskers show minimum and maximum. $P = 1.1 \times 10^{-3}$, two-tailed Student's *t*-test. **f**, H&E and anti-KRT5, anti-TNFRSF12A, anti-SCGB1A1, and anti-AcTUB immunostaining of organoids from the TNFRSF12A^{hi} fraction of FACS-sorted EPCAM⁺ITGA6⁺ITGB4⁺ distal lung cells. Scale bars, 50 µm. **g**, H&E and anti-SCGB1A1 and anti-AcTUB immunofluorescence of 2D ALI cultures from basal cell organoids from TNFRSF12A^{hi} basal cells as in **f**. Scale bars, 50 µm.

[Source data](#)

[Full size image](#)

Upon prospective culture directly from human lung without an organoid intermediate, FACS-isolated EPCAM⁺ITGA6⁺ITGB4⁺TNFRSF12A^{hi} cells (TNFRSF12A^{hi} Basal 1 cells; Extended Data Fig. 8d, bottom) showed a 15-fold increase in KRT5⁺ organoid formation compared with EPCAM⁺ITGA6⁺ITGB4⁺TNFRSF12A^{neg} cells (TNFRSF12^{neg} Basal 1 cells; Fig. 3d,e). TNFRSF12A^{hi} basal organoids also differentiated into SCGB1A1⁺ club and AcTUB⁺ ciliated cells in prolonged culture (Fig. 3f) or when grown as 2D ALI monolayers (Fig. 3g).

SARS-CoV-2 and H1N1 infection of organoids

Influenza virus H1N1 avidly infected distal lung organoids, which also expressed influenza receptors (Extended Data Fig. 9a-d), similar to proximal airway organoids^{24,25}. Infection of organoids with influenza H1N1 PR8 was inhibited by nucleoside analogues, consistent with previous studies²⁶ (Extended Data Fig. 9e), and screening of diverse antiviral compound classes in 48-well format revealed differential activity (Extended Data Fig. 9f), suggesting that this system could be used for scalable therapeutics discovery.

In COVID-19 pneumonia, severe SARS-CoV-2 infection of the distal lung induces alveolar damage and respiratory failure²⁷. Organoid scRNA-seq at time points before ciliated differentiation identified expression of the SARS-CoV-2 receptor ACE2 and processing protease TMPRSS2 mRNAs predominantly in club and AT2 cells (Extended Data Fig. 10a), consistent with expression of ACE2 in KRT5⁻ differentiated interior luminal cells (Fig. 2a). To facilitate access of SARS-CoV-2 to ACE2-expressing luminal cells, we adapted an apical-out suspension culture polarization method²⁸ to distal lung organoids (Extended Data Fig. 10b). Within 48 h in suspension, organoids reorganized into apical-out epithelial spheroids with microvilli, apical junctions, and motile cilia facing the organoid exterior. Differentiation of outwardly oriented ciliated cells accelerated over five days and progressed over weeks (Fig. 4a, Extended Data Fig. 10c-f, Supplementary Video 3). Apical-out basal organoids also showed an increase in outwardly facing club cells with apical secretory granules (Fig. 4a, Extended Data Fig. 10g), and apical-out AT2 organoids showed differentiation into AT1 cells (Extended Data Fig. 10h-j). Crucially, in apical-out organoids, ACE2 localized to apical cell membranes on the external organoid surface (Fig. 4b, Extended Data Fig. 10k).

Fig. 4: SARS-CoV-2 infection of apical-out distal lung organoids.

 **figure4**

a, Immunofluorescence comparing polarization and surface localization of SCGB1A1⁺ club cells (green) and AcTUB⁺ ciliated cells (white) upon ECM-embedded non-polarized growth (left) or apical-out suspension culture (right). **b**, Transverse sections of apical-out basal organoid as in **a** stained with anti-ACE2, anti-SCGB1A1 and DAPI. **c**, Quantitative PCR for SARS-CoV-2 unspliced genomic RNA (gRNA, left) and spliced sgRNA (right) in apical-out distal lung organoids, 72 h post-infection (hpi), normalized to U3 snoRNA; $n = 2$ independent experiments. **d**, Anti-dsRNA immunofluorescence of apical-out human distal lung organoids, either mock-infected or infected with SARS-CoV-2, 48 hpi. **e**, Immunofluorescence for SARS-CoV-2 nucleocapsid protein (NP) in infected or mock-infected apical-out organoids at 96 hpi. **f**, Immunofluorescence of SARS-CoV-2-infected apical-out AT2 organoids with the indicated antibodies at 96 hpi. **g**, Immunofluorescence colocalization of SARS-CoV-2

NP and SCGB1A1 in apical-out distal lung basal organoids at 96 hpi. **h**, Immunofluorescence showing cell-type specificity in SARS-CoV-2-infected apical-out organoids. Inf, SARS-CoV-2 infected cell. In **c–h**, organoids were in suspension for 6–10 days (basal) or 3 days (AT2) before infection. Scale bars, 20 μ m except for **f, h** (10 μ m).

[Full size image](#)

SARS-CoV-2 infected apical-out mixed distal lung organoids, with induction of unspliced SARS-CoV-2 genomic RNA reaching levels similar to those of the abundantly expressed U3 small nucleolar RNA (Fig. [4c](#), left). In addition, infected organoids showed replication-specific SARS-CoV-2 spliced subgenomic RNA (sgRNA; Fig. [4c](#), right) and production of infectious virions with VeroE6 cell plaque formation (35 PFU ml⁻¹ from organoid lysates and 65 PFU ml⁻¹ from organoid supernatants). In basal organoids infected with SARS-CoV-2, double-stranded RNA (dsRNA) appeared by 48 h after infection (Fig. [4d](#)) and SARS-CoV-2 nucleocapsid protein (NP) by 96 h (Fig. [4e](#)). Approximately 10% of AT2 organoids displayed prominent SARS-CoV-2 NP expression in SFTPC⁺ cells; the remaining organoids were devoid of infection (Fig. [4f](#)). Similarly, SARS-CoV-2 infected about 10% of basal organoids. In 2,621 total distal airway basal cells representing cultures from four individuals (Supplementary Table [5](#)), SARS-CoV-2 infection was not detected in KRT5⁺ basal or AcTUB⁺ ciliated cells (odds ratio 0, $P < 0.05$), in contrast to infection of upper airway ciliated cells by SARS-CoV-2 in 2D ALI culture^{[29,30](#)}. However, SARS-CoV-2 NP and dsRNA immunofluorescence were primarily present in SCGB1A1⁺ club cells (Fig. [4g,h](#)) which were strongly associated with and accounted for 79% of NP- or dsRNA-positive cells (odds ratio 19.33, $P < 0.0001$); 21% of infected cells lacked SCGB1A1 (Fig. [4g,h](#), Supplementary Table [5](#)). Overall, these studies indicate that AT2 cells were directly infected by SARS-CoV-2, and suggest that club cells are a distal lung target population.

Discussion

We have applied long-term human distal lung organoid cultures to progenitor discovery and modelling of infectious disease. Our findings extend upon earlier short-term and feeder-dependent adult lung culture methods^{[4,10,11](#)} and present an alternative to techniques involving the differentiation of inducible pluripotent stem cells^{[31,32,33,34](#)}. Organoids contained two related subtypes of KRT5⁺ human distal lung basal cells—Basal 1 and Basal 2. Notably, the TNFRSF12A-expressing Basal 1 fraction possessed enriched clonogenic progenitor activity, establishing functional precedent for a proliferation-enriched basal cell subtype. Although TNFRSF12A is by no means exclusively present in basal cells, within the basal layer it often localizes to a

postulated niche in airway furrow bases and tips²³, extending recent notions that the lung epithelium shows spatial specialization³⁵. It is possible that TNFRSF12A or analogous markers could distinguish basal cell progenitor subsets in other tissues. Our organoids also enable facile exploration of SARS-CoV-2 distal lung infection, which is relevant to COVID-19-associated pneumonia²⁷, and implicate SCGB1A1⁺ club cells as a target whose infection could compromise protective lung glycosaminoglycans and precipitate a vicious infection cycle. We did not observe infection of ciliated cells, in contrast to 2D ALI lung studies^{29,30}; this could require alternative culture conditions. SCGB1A1-negative populations were also infected and are under further investigation; for example, bronchial transient secretory cells express *ACE2* and *TMPRSS2*³⁶.

Overall, single-cell analysis of organoid cultures, as described here, may represent a general strategy for identifying and functionally validating candidate stem cells in slowly proliferating tissues. The culture of progenitors for all adult human distal lung epithelial lineages, including alveoli, should substantially enable the modelling of diseases such as neoplastic and interstitial lung conditions¹² and allow tissue engineering and precision medicine applications. Finally, this organoid system should facilitate diverse investigations of pulmonary pathogens, including the SARS-CoV-2 distal lung infection that is associated with fulminant respiratory failure.

Methods

Additional experimental details are in the [Supplementary Methods](#). No statistical methods were used to predetermine sample size. The experiments were not randomized and the investigators were not blinded to allocation during experiments and outcome assessment.

Human tissue procurement and processing

All experiments performed in this work were approved by the Stanford University School of Medicine Institutional Review Board and performed under protocol no. 28908. Standard informed consent for research was obtained in writing from all patients who contributed to this study before tissue procurement and all experiments followed relevant guidelines and regulations. Peripheral lung tissue within 1 cm of the visceral pleura was obtained from discarded surgical tissue from lobectomies. For patients with suspected lung cancer, cases with clinical T4 (American Joint Cancer Committee 6th edition) disease (for example, features such as bronchial invasion or parenchymal satellite nodule/metastases) were deferred. Normal tissue was removed from the lung margin most anatomically distal to palpably well-defined lesions, or from uninvolved lobes in the case of pneumonectomies. Samples with tumours

containing ill-defined margins were deferred. Tissue was either processed fresh or stored at 4 °C overnight and processed the following morning.

Mixed distal lung organoid culture

To isolate distal airway cells, lung parenchyma from 1 cm from the visceral pleura was mechanically dissociated with Castro scissors, washed and incubated with 5 units per ml porcine elastase (Worthington), 100 Kunitz units per ml DNase I (Worthington), and Normocin (InvivoGen), and resuspended in two tissue volumes of lung organoid medium, comprising advanced DMEM/F12 (Invitrogen) supplemented with 10 mM nicotinamide, *N*-acetyl cysteine, 1× B27 supplement minus vitamin A, recombinant human NOGGIN (100 ng ml⁻¹, R&D Systems), recombinant human EGF (50 ng ml⁻¹, R&D Systems), and TGF-β inhibitor A83-01 (100 nM, Tocris). This lung organoid medium was used for all experiments except for those shown in Extended Data Fig. 4f. The tissue was then agitated for 1 h at 37 °C and the resultant cell suspension was filtered through 100–40-μm cell strainers and subjected to ammonium chloride red blood cell lysis. The cell pellet was then washed and resuspended in 10 volumes of reduced growth factor Basement Membrane Extract II (Trevigen). Cells in matrix were then plated in 24-well plates in 50-μl droplets, and warm medium was added after the droplets had solidified for 10 min at room temperature. Medium was changed every 3–4 days and organoids were passaged every 3–4 weeks by dissociation with TrypLE. Passaging was based on ECM durability and integrity and estimated organoid confluence, judged by estimated organoid volume to volume of the ECM droplet. Distal lung organoids could be passaged for about 6 months with basal organoids initially exhibiting 6–7 doublings every 2 weeks. Alveolar organoids expanded more slowly with an initial rate of 3–4 doublings every 2 weeks but predominated over basal organoids after several months. Calculated from initial cell division rates, the upper limits of basal and alveolar expansion were 2¹⁹ (524,288-fold) and 2¹⁶ (65,536-fold), respectively. To rule out contamination by malignant cells, long-term cultures were systematically evaluated for the presence of dysplasia or carcinoma by a board-certified pathologist. In addition, five long-term organoid cultures (2–6 months) underwent targeted next generation sequencing to exclude pathogenic nucleotide variants (see below). Full details are provided in the [Supplementary Methods](#).

Tandem MACS stromal depletion and EPCAM purification of distal lung cells

Distal lung was dissociated as above, and all incubation steps were carried out on ice. We incubated 10⁷ cells with Fc Block (Biolegend 422301) and diluted them 1:100 in FACS buffer (2 mM EDTA and 0.2% fetal calf serum in 1× PBS, pH 7.4), for 10 min.

The cells were then mixed with APC-conjugated anti-CD45 antibodies at 1 µg ml⁻¹ in FACS buffer for 30 min, washed, and subjected to two rounds of depletion with magnetic beads according to the manufacturer's protocol (Miltenyi: anti-human fibroblast 130-050-601, anti-CD31 130-091-935, anti-APC 130-090-855, LS column 130-042-401). Unlabelled cells were then centrifuged at 300g and labelled with a cocktail of 1 µg ml⁻¹ of PerCP-Cy5.5 anti-EPCAM antibody and Zombie Aqua viability stain (Biolegend 423101) diluted 1:400 from stock concentration in FACS buffer.

Organoid cryopreservation and recovery

For cryopreservation and recovery, ECM droplets were dissociated by pipetting in three volumes of PBS with 5 mM EDTA and then incubated on ice for 1 h. Cells were pelleted at 300g for 5 min and resuspended in freezing medium (fetal calf serum (Gibco), 10% v/v DMSO), placed into cryovials and then into Mr. Frosty (Thermo Fisher) containers and stored at -80 °C overnight, followed by transfer to liquid nitrogen vapour phase for long-term storage. Organoids were recovered by quick thaw in a 37 °C water bath followed by washing in organoid medium and plating in ECM with organoid medium plus 10 µM ROCK inhibitor Y-27632 (Tocris).

Screening exogenous growth factors in organoid culture

Distal airway cells were isolated and plated as above with the following exceptions: advanced DMEM/F12 was used instead of organoid medium during elastase digestion of lung tissue, and cells were serially diluted and filtered through a 40-µm cell strainer and counted with a haemocytometer. One thousand viable epithelial cells (by Trypan blue exclusion, size, and morphology) per µl ECM were plated per 5 µl Matrigel droplet per well. Base medium consisted of organoid medium lacking A83-01, EGF, NOGGIN, WNT3A or RSPO1. EGF (final 50 ng ml⁻¹, R&D), NOGGIN (final 100 ng ml⁻¹, R&D), WNT3A (final 100 ng ml⁻¹, R&D), RSPO1 (final 500 ng ml⁻¹, Peprotech) or the PORCUPINE inhibitor C59 (final 1 µM, Biogems) were added singly or in combination to base medium. Images were obtained ten days after primary plating with an inverted light microscope at 5× magnification. Each condition was plated in quadruplicate and organoid formation was quantified using the analyse particle (threshold, 490² pixels) plugin in ImageJ (see [Supplementary Methods](#)).

Single-cell RNA-seq of unfractionated organoid cultures

Lung organoid cultures from separate individuals were dissociated 4 weeks after primary plating and subjected to droplet-based scRNA-seq with the 10x Genomics Single Cell 3' platform with a 5-nucleotide UMI, according to the manufacturer's

protocol. Cell capture, library preparation, and sequencing were performed as previously described³⁷. For scRNA-seq analysis in Fig. 1k, a modified Kruskal–Wallis rank sum test was performed to determine the significance of differential marker gene expression for AT2 (*SFTPC*), basal (*KRT5*), and club (*SCGB1A1*) cells, with all $P < 0.001$. Principal component analysis, t-SNE, unsupervised graph-based clustering, statistical testing, and the pseudotime trajectory for all scRNA-seq analyses are described in [Supplementary Methods](#) and Supplementary Data 1.

Single-cell RNA-seq of purified AT2 organoid cultures

LysoTracker⁺ AT2 cells³⁸ from unfractionated organoids were purified by FACS and cultured for two months with one passage. These were dissociated and subjected to droplet-based scRNA-seq with the 10x Genomics Chromium Single Cell 3' platform v2 according to the manufacturer's protocol. The library was sequenced using paired-end sequencing (26 bp read 1 and 98 bp read 2) with a single sample index (8 bp) on an Illumina NextSeq 500. Data preprocessing and principal component analysis were carried out with CellRanger v1.2. Subsequent analysis is described in [Supplementary Methods](#) and Supplementary Data 1.

Electron microscopy

Organoid cultures were fixed in ECM with 2.5% glutaraldehyde in 0.1 M cacodylate buffer (pH 7.4), dehydrated, embedded in epoxy resin and visualized with a JEOL (model JEM1400) transmission-electron microscope with a LaB6 emitter at 120 kV.

Histology and immunocytochemistry

Organoids were fixed with 2% paraformaldehyde at 4 °C overnight, paraffin embedded and sectioned (10–20 µm) as previously described³⁷. Sections were deparaffinized and stained with H&E for histological analysis. Antibodies used for immunocytochemistry staining following standard staining protocols³⁹ are listed in [Supplementary Methods](#) and images were acquired on a Leica-SP8 confocal microscope.

RNA fluorescent in situ hybridization

RNA in situ hybridization was performed as described⁴⁰ and probe sequences are provided in [Supplementary Methods](#).

Whole-mount organoid confocal immunofluorescence microscopy

Intact, uninfected organoids were fixed in 2% paraformaldehyde in 100 mM phosphate buffer (pH 7.4) (4% paraformaldehyde for infected organoids) for 1 h at room temperature, washed with PBS with 100 mM glycine, permeabilized in 0.5% Triton X-100 in PBS for 1 h, then incubated in staining buffer (4% BSA, 0.05% Tween-20 in PBS pH 7.4, 10% goat/donkey serum) for an additional hour, followed by incubation with primary antibody for 24 h at room temperature in staining buffer. Whole mounts were then washed with PBS-T and incubated with fluorescent secondary antibodies, phalloidin and DAPI, for 4 h at room temperature in staining buffer. Following additional washes, whole mounts were submerged in mounting medium (Vectashield, Vector Laboratories) and mounted on chambered coverslips for imaging in four channels using Zeiss LSM 700 or 900 confocal microscopes. 3D rendering of confocal image stacks was performed using Volocity Image Analysis software (Quorum Technologies Inc., Guelph, Ontario). For Fig. [4h](#), which required five colours, cilia were distinguished by staining with two fluorescent secondary antibodies and merging the colocalized voxels into a pseudocoloured channel using Volocity software. Lectin staining (FITC-Sambuca Nigrin, Vector Labs FL-1301; Biotin-Maackia Amurensis, Vector Labs FL-1301) was carried out according to the manufacturer's protocol after fixation of organoids with 0.1% paraformaldehyde in PBS for 1 h at room temperature followed by blocking with avidin/biotin (Vector Labs SP-2001). Biotin-Maackia Amurensis lectin was labelled with streptavidin–PE conjugate (Thermo Fisher SA10041) and after washing lectin staining was imaged in a Keyence BZ-X700.

Next generation sequencing of organoid cultures

Ten organoid cultures were sequenced using a commercial targeted resequencing assay with end-to-end coverage of 131 cancer genes and companion software (TOMA COMPASS Tumour Mutational Profiling System, Foster City, CA) to determine the presence of oncogenic mutations in long-term organoid cultures. Libraries were sequenced on an Illumina NextSeq 500. Nonsynonymous variants are listed in Supplementary Table 6. Variant call files are provided in Supplementary Data 2.

Density sedimentation of basal cells

Organoid cultures within 2–3 weeks of primary plating were dissociated with 1 U ml⁻¹ neutral protease (Worthington, Cat LS02100) and 100 KU DNase I in lung organoid medium. Basal organoids were then collected by gravity sedimentation and the supernatant was either aspirated or collected for downstream use. Basal organoids were then further fractionated on a custom Ficoll-Paque gradient (4 vol Ficoll-Paque to 1 vol PBS) and centrifuged at 300g for 10 min at room temperature. Supernatant was aspirated and the organoid pellet was resuspended in 10 ml PBS in a 15-ml conical tube, collected by gravity sedimentation, and plated into ECM as described above.

FACS isolation and culture of AT2 cells

Organoids were dissociated with TrypLE followed by neutralization with 10% volume fetal calf serum, subjected to DNase at 100 KU ml⁻¹, washed with lung organoid medium and then incubated with 100 cell pellet volumes of lung organoid medium with 10 nM LysoTracker Red DND-99 (Thermo Fisher L7528) at 37 °C for 30 min. Cells were then washed and resuspended in FACS buffer as described above, incubated with Fc block, and then incubated on ice with labelling cocktail consisting of 1 µg ml⁻¹ of PerCP-Cy5.5 anti-EPCAM antibody and Zombie Aqua viability stain (Biolegend 423101) diluted 1:400 from stock concentration in FACS buffer. EPCAM^{hi} and LysoTracker^{hi} cells were sorted into lung organoid medium with 10 µM Y-27632 (Tocris 1254) and cultured in ECM and lung organoid medium with Y-27632 for 24 h, followed by lung organoid medium without Y-27632. Pure AT2 organoid growth was enhanced by the addition of 1:1

vol:vol serum-containing L-cell conditioned medium (L-WRN CM) containing WNT3A, R-SPONDIN3 and NOGGIN and supplemented with recombinant EGF⁴¹. The full gating strategy is provided in Supplementary Fig. 1. All FACS antibodies were purchased from Biolegend. Qualitatively identical results could also be obtained with anti-HTII-280 (AT2 marker, Terrace Biotech) FACS purification in lieu of LysoTracker. AT2 organoid cells were transdifferentiated into AT1 cells by TrypLE dissociation from ECM and seeding onto chambered glass coverslips followed by culturing with advanced DMEM/F12 and 5% fetal calf serum⁴².

Colour mixing studies with lentivirally transduced GFP and mCherry

FACS EPCAM⁺ stroma-depleted organoids at D14 were infected with lentivirus at an estimated MOI of 0.9 as described previously⁴³ with third-generation lentiviral vectors (PGK-GFP T2A Puro, SBI cat. no. CD550A-1; mCherry modified from pLentiCRISPRv1 (Addgene no. 49545) to incorporate an EF-1a-mCherry P2A Puro cassette, a gift from Paul Rack). Ninety-six hours after infection, organoids were treated with puromycin at a concentration of 600 ng ml⁻¹ for 48 h to select for transduced cells. Two weeks after selection, GFP-expressing organoids or mCherry-expressing organoids were dissociated into single cells and mixed in a 1:1 ratio and scored as monochromatic or mixed after 28 days of each passage. The same approach was employed for purified AT2 and basal cultures after respective isolation strategies from an initial FACS-purified, EPCAM⁺, stroma-depleted organoid starter culture.

Flow cytometry analysis of resident basal cells from adult human lung

Adult human lung tissue was procured and dissociated as above but cells were labelled with Zombie Aqua live:dead stain as above, washed with FACS buffer, and then fixed in 2% PFA in PBS overnight at 4 °C. Cells were then stained using the whole-mount procedure as described above with the omission of PBS-glycine washing. Fixed and permeabilized cells were then incubated with 1:400 dilution of Alexa Fluor 647 conjugated

mouse anti-human cytokeratin 5 antibody (Abcam) for 24 h at 4 °C in permeabilization buffer. Cells were then washed with FACS buffer and labelled with PE conjugated mouse anti-human TNFRSF12A antibody (clone ITEM-4, Biolegend) for 30 min on ice, followed by washing and analysis on a BD Aria Fusion instrument. The full gating strategy and qPCR validation of the ITEM-4 antibody are detailed in Supplementary Fig. 1.

FACS isolation of TNFRSF12A^{hi} and TNFRSF12A^{neg} basal cells

Single-cell suspensions from either fresh human distal lung or primary organoid culture at approximately 4 weeks of culture were dissociated as above, treated with Fc Block (BioLegend), and incubated in FACS buffer with Zombie Aqua 1:400, 1 µg ml⁻¹ PerCP-Cy5.5 anti-human EpCAM (CD326), 1 µg ml⁻¹ APC anti-human ITGA6 (CD49f), 2 µg ml⁻¹ FITC anti-human ITGB4 (CD104), and 1 µg ml⁻¹ PE anti-human TNFRSF12A (CD266). Thirty minutes after labelling, the cells were washed twice with FACS buffer and sorted for EPCAM^{hi}, ITGA6/ITGB4^{hi}, TNFRSF12A^{hi} and TNFRSF12A^{neg}. The full gating strategy is provided in Supplementary Fig. 1. More than 5,000 cells were sorted into Eppendorf tubes with lung organoid medium and 10 µM ROCK inhibitor Y-27632. All FACS antibodies were purchased from Biolegend.

Culture of TNFRSF12A^{hi} and TNFRSF12A^{neg} basal cells

Cells were seeded in ECM and submerged in lung organoid medium with 10 µM ROCK inhibitor Y-27632. The seeding density for cells FACS-isolated from organoid culture was 1,000 cells per well at a density of 100 cells per µl ECM. The seeding density for cells FACS-isolated from fresh human distal lung was 3,000 cells per well at a density of 300 cells per µl ECM. After 24 h, the medium was changed to remove ROCK inhibitor, thereafter it was changed every 72 h. Organoid formation was manually quantified 14 days after plating by two independent observers.

H1N1 organoid influenza assay

Unfractionated cultures containing AT2, basal, and club cell types at 2–3 weeks were infected in triplicate with H1N1 strain PR8 modified to express GFP upon viral replication⁴⁴ after 24 h of pretreatment with antiviral compounds. ECM was dispersed by addition of 5 mM EDTA in PBS, followed by washing and inoculation with PR8-H1N1–GFP reporter virus at an estimated MOI of 1 in medium containing either vehicle or antivirals. After 12 h (one influenza infection cycle), intact organoid GFP expression was either visualized by fluorescence microscopy with a Keyence BZ-X700 automated microscope, or dissociated to single cells and fixed with 0.1% PFA in PBS followed by FACS quantification of GFP⁺ cells (gating strategy is provided in Supplementary Fig. 1). Antiviral dose response curves were generated using four-parameter nonlinear regression curve fitting with GraphPad Prism 7 (GraphPad Software, San Diego, CA). H1N1 tropism was assessed in a manner similar to above with the exception that Ficoll-sedimented basal cell fraction versus non-basal fractions were dissociated into single cells, counted, and infected with an estimated MOI of 1 in organoid medium for 1 h at 37 °C, followed by washing and reseeding into ECM, culturing for 16 h, and then being subjected to dissociation and FACS as above.

Suspension culture to generate apical-out polarity in lung organoids

Lung organoids grown embedded in 50 µl ECM droplets were transferred to suspension culture as described²⁸ with modifications. In brief, ECM-embedded organoids were dislodged gently by pipetting using sterile LoBind tips (Eppendorf 22493008) and placed in 15 ml LoBind conical tubes (Eppendorf 30122216) containing ice-cold 5 mM EDTA in PBS. Five millilitres of EDTA solution was used per ECM droplet (3 ECM droplets per 15-ml conical tube) rotating for 1 h at 4 °C on a rotating platform. Organoids were centrifuged at 200g for 3 min at 4 °C and the supernatant was removed. The pellet was resuspended in growth medium in ultra-low attachment six-well tissue culture plates (Corning Costar 3471). Suspended organoids were incubated at 37 °C with 5% CO₂ for different times (range 0–30 days) to characterize apical-out polarity, ciliogenesis and

differentiation, and to prepare apical-out organoids for infection experiments with SARS-CoV-2.

SARS-CoV2 infection of human distal lung organoids

VeroE6 cells were obtained from ATCC as mycoplasma-free stocks and maintained in supplemented DMEM with 10% FBS. SARS-CoV-2 (USA-WA1/2020) was passaged in VeroE6 cells in DMEM with 2% FBS. Titres were determined by plaque assay on VeroE6 cells using Avicel (FMC Biopolymer) and crystal violet (Sigma), the viral genome sequence was verified, and all infections were performed with passage 3 virus. Organoids were counted and passaged into suspension medium for 6–8 days and then resuspended in virus medium or an equal volume of mock medium at an MOI of 1 relative to total organoid cells in the sample, and then incubated at 37 °C under 5% CO₂ for 2 h. Organoids were then plated in suspension in lung organoid medium (apical-out organoids). At the indicated time points, apical-out organoids were washed with lung organoid medium and PBS and resuspended in TRIzol LS (Thermo Fisher), freshly-made 4% PFA in PBS, or 250 µl lung organoid medium. Cells resuspended in lung organoid medium were lysed by freezing at –80 °C. Culture supernatants were preserved in TRIzol LS or added directly to plaque assay monolayers. All SARS-CoV-2 work was performed in a class II biosafety cabinet under BSL3 conditions at Stanford University.

qPCR analysis of SARS-CoV-2 RNA

RNA from SARS-CoV-2-infected organoids was extracted by adding 750 µl TRIzol (Thermo Fisher Scientific), incubating at 55 °C for 5 min and then adding 150 µl chloroform. After mixing each sample by vortexing for 7 s, the samples were incubated at 25 °C for 5 min and then centrifuged at 12,000 rpm for 15 min at 4 °C. The aqueous layer was carefully removed from each sample, mixed with two volumes of 100% ethanol and purified using an RNA Clean & Concentrator-25 kit (Zymo Research) as per the manufacturer's instructions. All RNA samples were treated with DNase (Turbo DNA-free kit, Thermo Fisher Scientific). The Brilliant II SYBR Green QRT-PCR 1-Step Master Mix (VWR) was used to convert RNA into cDNA and to amplify specific RNA regions on the CFX96 Touch real-time

PCR detection system (Bio-Rad). The reverse transcription reaction was performed for 30 min at 50 °C, 10 min at 95 °C, followed by two-step qPCR with 95 °C for 10 s and 55 °C for 30 s, for a total of 40 cycles. Two primer sets were used to amplify either non-spliced SARS-CoV-2 genomic RNA (gRNA) spanning nucleotide positions 14221–14306, or spliced SARS-CoV-2 sgRNA³⁰. Primer sequences are in Supplementary Table 7.

TNFRSF12A immunostaining of intact distal lung

Optimal staining of human distal lung tissue was achieved from specimens fixed within 30 min of primary surgical resections in 4% paraformaldehyde in PBS. Specimens were incubated in fixative overnight at 4 °C, transferred to 30% sucrose, and embedded into OCT. Frozen sections were cut at 10 µm, subjected to citrate-based antigen retrieval (Vector Labs) at 70 °C for 30 min, and then blocked for 1 h with 10% goat serum in IF wash buffer as described above. Mouse anti-TNFRSF12A (clone ITEM-4, Biolegend) was used for Fig. 3a and polyclonal rabbit anti-TNFRSF12A (ThermoFisher PA5-20275) was used for Fig. 3b, f and Extended Data Fig. 8⁴⁵.

Live-imaging and confocal microscopy of immobilized apical-out lung organoids

Live organoids were held between two coverslips in a viewing chamber (Lab-Tek II two-chambered coverglass) and filmed using a Nikon TE2000E microscope using differential interference contrast (DIC) microscopy with a 63× objective. Samples were kept at 37 °C with 5% CO₂ during imaging. Digital videos were collected by a Hamamatsu high-resolution ORCA-285 digital camera and rendered using OpenLab 5.5.2 software (Improvision). After recording, samples were fixed and stained without removal from the chambers and transferred to the confocal microscope for immunofluorescence microscopy.

Statistics and reproducibility

Unless stated otherwise, all data are representative of at least two independent experiments with each independent experiment carried out

using an organoid culture derived from one individual. Box plot bounds span first through third quartiles, horizontal lines represent median values, and whiskers represent data range minima or maxima or, in the case of outliers, 1.5 times the interquartile range with outliers represented by data points. *t*-tests were two-tailed and *P* values are denoted as **P* < 0.05, ***P* ≤ 0.01, and ****P* ≤ 0.001. Full details are provided in [Supplementary Methods](#).

Reporting summary

Further information on research design is available in the [Nature Research Reporting Summary](#) linked to this paper.

Data availability

scRNA-seq data sets have been deposited in Gene Expression Omnibus with the accession code [GSE106850](#). [Source data](#) are provided with this paper.

Code availability

Scripts to perform analyses of scRNA-seq data are provided with this paper. Custom code is available on GitHub (https://github.com/ameen-salahudeen/lung_organoid).

References

1. 1.

Hogan, B. & Tata, P. R. Cellular organization and biology of the respiratory system. *Nat. Cell Biol.* <https://doi.org/10.1038/s41556-019-0357-7> (2019).

2. 2.

Rawlins, E. L. et al. The role of Scgb1a1^+ Clara cells in the long-term maintenance and repair of lung airway, but not alveolar, epithelium. *Cell Stem Cell* **4**, 525–534 (2009).

[CAS](#) [PubMed](#) [PubMed Central](#) [Google Scholar](#)

3. 3.

Kathiriya, J. J., Brumwell, A. N., Jackson, J. R., Tang, X. & Chapman, H. A. Distinct airway epithelial stem cells hide among club cells but mobilize to promote alveolar regeneration. *Cell Stem Cell* **26**, 346–358.e4 (2020).

[CAS](#) [PubMed](#) [Google Scholar](#)

4. 4.

Barkauskas, C. E. et al. Type 2 alveolar cells are stem cells in adult lung. *J. Clin. Invest.* **123**, 3025–3036 (2013).

[CAS](#) [PubMed](#) [PubMed Central](#) [Google Scholar](#)

5. 5.

Desai, T. J., Brownfield, D. G. & Krasnow, M. A. Alveolar progenitor and stem cells in lung development, renewal and cancer. *Nature* **507**, 190–194 (2014).

[ADS](#) [CAS](#) [PubMed](#) [PubMed Central](#) [Google Scholar](#)

6. 6.

Liu, Q. et al. Lung regeneration by multipotent stem cells residing at the bronchioalveolar-duct junction. *Nat. Genet.* **51**, 728–738 (2019).

[CAS](#) [PubMed](#) [Google Scholar](#)

7. 7.

Vaughan, A. E. et al. Lineage-negative progenitors mobilize to regenerate lung epithelium after major injury. *Nature* **517**, 621–625 (2015).

[ADS](#) [CAS](#) [PubMed](#) [Google Scholar](#)

8. 8.

Zuo, W. et al. p63⁺Krt5⁺ distal airway stem cells are essential for lung regeneration. *Nature* **517**, 616–620 (2015).

[ADS](#) [CAS](#) [PubMed](#) [Google Scholar](#)

9. 9.

Juul, N. H., Stockman, C. A. & Desai, T. J. Niche cells and signals that regulate lung alveolar stem cells in vivo. *Cold Spring Harb. Perspect. Biol.* <https://doi.org/10.1101/cshperspect.a035717> (2020).

10. 10.

Sucre, J. M. S. et al. Successful establishment of primary type II alveolar epithelium with 3D organotypic coculture. *Am. J. Respir. Cell Mol. Biol.* **59**, 158–166 (2018).

[CAS](#) [PubMed](#) [PubMed Central](#) [Google Scholar](#)

11. 11.

Zacharias, W. J. et al. Regeneration of the lung alveolus by an evolutionarily conserved epithelial progenitor. *Nature* **555**, 251–255 (2018).

[ADS](#) [CAS](#) [PubMed](#) [PubMed Central](#) [Google Scholar](#)

12. 12.

Nikolić, M. Z. & Rawlins, E. L. Lung organoids and their use to study cell-cell interaction. *Curr. Pathobiol. Rep.* **5**, 223–231 (2017).

[PubMed](#) [PubMed Central](#) [Google Scholar](#)

13. 13.

Evans, K. V. & Lee, J. H. Alveolar wars: the rise of in vitro models to understand human lung alveolar maintenance, regeneration, and disease. *Stem Cells Transl. Med.* **9**, 867–881 (2020).

[PubMed](#) [PubMed Central](#) [Google Scholar](#)

14. 14.

Anchang, B. et al. Visualization and cellular hierarchy inference of single-cell data using SPADE. *Nat. Protoc.* **11**, 1264–1279 (2016).

[CAS](#) [PubMed](#) [Google Scholar](#)

15. 15.

Cao, J. et al. The single-cell transcriptional landscape of mammalian organogenesis. *Nature* **566**, 496–502 (2019).

[ADS](#) [CAS](#) [PubMed](#) [PubMed Central](#) [Google Scholar](#)

16. 16.

Nabhan, A. N., Brownfield, D. G., Harbury, P. B., Krasnow, M. A. & Desai, T. J. Single-cell Wnt signaling niches maintain stemness of alveolar type 2 cells. *Science* **359**, 1118–1123 (2018).

[ADS](#) [CAS](#) [PubMed](#) [PubMed Central](#) [Google Scholar](#)

17. 17.

Rock, J. R. et al. Basal cells as stem cells of the mouse trachea and human airway epithelium. *Proc. Natl Acad. Sci. USA* **106**, 12771–12775 (2009).

[ADS](#) [CAS](#) [PubMed](#) [Google Scholar](#)

18. 18.

Kajiji, S., Tamura, R. N. & Quaranta, V. A novel integrin (alpha E beta 4) from human epithelial cells suggests a fourth family of integrin adhesion receptors. *EMBO J.* **8**, 673–680 (1989).

[CAS](#) [PubMed](#) [PubMed Central](#) [Google Scholar](#)

19. 19.

Stange, D. E. et al. Differentiated *Troy*⁺ chief cells act as reserve stem cells to generate all lineages of the stomach epithelium. *Cell* **155**, 357–368 (2013).

[CAS](#) [PubMed](#) [PubMed Central](#) [Google Scholar](#)

20. 20.

Whitfield, M. L., George, L. K., Grant, G. D. & Perou, C. M. Common markers of proliferation. *Nat. Rev. Cancer* **6**, 99–106 (2006).

[CAS](#) [PubMed](#) [Google Scholar](#)

21. 21.

Rock, J. R. et al. Notch-dependent differentiation of adult airway basal stem cells. *Cell Stem Cell* **8**, 639–648 (2011).

[CAS](#) [PubMed](#) [PubMed Central](#) [Google Scholar](#)

22. 22.

Pardo-Saganta, A. et al. Injury induces direct lineage segregation of functionally distinct airway basal stem/progenitor cell subpopulations. *Cell Stem Cell* **16**, 184–197 (2015).

[CAS](#) [PubMed](#) [PubMed Central](#) [Google Scholar](#)

23. 23.

Quinton, P. M. Both ways at once: keeping small airways clean. *Physiology (Bethesda)* **32**, 380–390 (2017).

[CAS](#) [Google Scholar](#)

24. 24.

Zhou, J. et al. Differentiated human airway organoids to assess infectivity of emerging influenza virus. *Proc. Natl Acad. Sci. USA* **115**, 6822–6827 (2018).

[CAS](#) [PubMed](#) [Google Scholar](#)

25. 25.

Imai, M. & Kawaoka, Y. The role of receptor binding specificity in interspecies transmission of influenza viruses. *Curr. Opin. Virol.* **2**, 160–167 (2012).

[CAS](#) [PubMed](#) [PubMed Central](#) [Google Scholar](#)

26. 26.

Kumaki, Y., Day, C. W., Smee, D. F., Morrey, J. D. & Barnard, D. L. In vitro and in vivo efficacy of fluorodeoxycytidine analogs against highly pathogenic avian influenza H5N1, seasonal, and pandemic H1N1 virus infections. *Antiviral Res.* **92**, 329–340 (2011).

[CAS](#) [PubMed](#) [PubMed Central](#) [Google Scholar](#)

27. 27.

Zhu, N. et al. A novel coronavirus from patients with pneumonia in China, 2019. *N. Engl. J. Med.* **382**, 727–733 (2020).

[CAS](#) [PubMed](#) [PubMed Central](#) [Google Scholar](#)

28. 28.

Co, J. Y. et al. Controlling epithelial polarity: a human enteroid model for host-pathogen interactions. *Cell Rep.* **26**, 2509–2520.e4 (2019).

[CAS](#) [PubMed](#) [PubMed Central](#) [Google Scholar](#)

29. 29.

Lamers, M. M. et al. SARS-CoV-2 productively infects human gut enterocytes. *Science* **369**, 50–54 (2020).

[ADS](#) [CAS](#) [PubMed](#) [PubMed Central](#) [Google Scholar](#)

30. 30.

Hou, Y. J. et al. SARS-CoV-2 reverse genetics reveals a variable infection gradient in the respiratory tract. *Cell* **182**, 429–446.e14 (2020).

[CAS](#) [PubMed](#) [PubMed Central](#) [Google Scholar](#)

31. 31.

Dye, B. R. et al. In vitro generation of human pluripotent stem cell derived lung organoids. *eLife* **4**, e05098 (2015).

[PubMed Central](#) [Google Scholar](#)

32. 32.

Chen, Y. W. et al. A three-dimensional model of human lung development and disease from pluripotent stem cells. *Nat. Cell Biol.* **19**, 542–549 (2017).

[CAS](#) [PubMed](#) [PubMed Central](#) [Google Scholar](#)

33. 33.

Jacob, A. et al. Differentiation of human pluripotent stem cells into functional lung alveolar epithelial cells. *Cell Stem Cell* **21**, 472–

488.e10 (2017).

[CAS](#) [PubMed](#) [PubMed Central](#) [Google Scholar](#)

34. 34.

Yamamoto, Y., Korogi, Y., Hirai, T. & Gotoh, S. A method of generating alveolar organoids using human pluripotent stem cells. *Methods Cell Biol.* **159**, 115–141 (2020).

[PubMed](#) [Google Scholar](#)

35. 35.

Montoro, D. T. et al. A revised airway epithelial hierarchy includes CFTR-expressing ionocytes. *Nature* **560**, 319–324 (2018).

[ADS](#) [CAS](#) [PubMed](#) [PubMed Central](#) [Google Scholar](#)

36. 36.

Lukassen, S. et al. SARS-CoV-2 receptor ACE2 and TMPRSS2 are primarily expressed in bronchial transient secretory cells. *EMBO J.* **39**, e105114 (2020).

[CAS](#) [PubMed](#) [PubMed Central](#) [Google Scholar](#)

37. 37.

Yan, K. S. et al. Non-equivalence of Wnt and R-spondin ligands during Lgr5⁺ intestinal stem-cell self-renewal. *Nature* **545**, 238–242 (2017).

[ADS](#) [CAS](#) [PubMed](#) [PubMed Central](#) [Google Scholar](#)

38. 38.

Van der Velden, J. L., Bertoncello, I. & McQualter, J. L. Lysotracker is a marker of differentiated alveolar type II cells. *Respir. Res.* **14**, 123 (2013).

[PubMed](#) [PubMed Central](#) [Google Scholar](#)

39. 39.

Chang, J. et al. Gpr124 is essential for blood-brain barrier integrity in central nervous system disease. *Nat. Med.* **23**, 450–460 (2017).

[CAS](#) [PubMed](#) [PubMed Central](#) [Google Scholar](#)

40. 40.

Nagendran, M., Riordan, D. P., Harbury, P. B. & Desai, T. J. Automated cell-type classification in intact tissues by single-cell molecular profiling. *eLife* **7**, e30510 (2018).

[PubMed](#) [PubMed Central](#) [Google Scholar](#)

41. 41.

Neal, J. T. et al. Organoid modeling of the tumor immune microenvironment. *Cell* **175**, 1972–1988.e16 (2018).

[CAS](#) [PubMed](#) [PubMed Central](#) [Google Scholar](#)

42. 42.

Dobbs, L. G., Williams, M. C. & Brandt, A. E. Changes in biochemical characteristics and pattern of lectin binding of alveolar type II cells with time in culture. *Biochim. Biophys. Acta* **846**, 155–166 (1985).

[CAS](#) [PubMed](#) [Google Scholar](#)

43. 43.

Van Lidth de Jeude, J. F., Vermeulen, J. L., Montenegro-Miranda, P. S., Van den Brink, G. R. & Heijmans, J. A protocol for lentiviral transduction and downstream analysis of intestinal organoids. *J. Vis. Exp.* **98**, e52531 (2015).

[Google Scholar](#)

44. 44.

Manicassamy, B. et al. Analysis of in vivo dynamics of influenza virus infection in mice using a GFP reporter virus. *Proc. Natl Acad. Sci. USA* **107**, 11531–11536 (2010).

[ADS](#) [CAS](#) [PubMed](#) [Google Scholar](#)

45. 45.

Karaca, G. et al. TWEAK/Fn14 signaling is required for liver regeneration after partial hepatectomy in mice. *PLoS ONE* **9**, e83987 (2014).

[ADS](#) [PubMed](#) [PubMed Central](#) [Google Scholar](#)

[Download references](#)

Acknowledgements

We thank members of the Kuo and Desai laboratories for discussions; the Stanford Tissue Bank, J. Shrager, M. Berry and W. Trope for tissue acquisition; S. Plevritis for trajectory analysis; and the Stanford Stem Cell FACS Facility, P. Chu, A. McCormick, D. Mendoza, F. de la Vega and J. Zengel for technical expertise. SARS-Related Coronavirus 2, Isolate USA-WA1/2020, NR-52281 was deposited by the CDC and obtained through BEI Resources, NIAID, NIH. Fellowships supporting authors are as follows: A.A.S.: A.P. Giannini, ECOG-ACRIN, P. Carbone, Stanford Cancer Institute; S.S.C.: Stanford Medical Scientist Training Program grant T32 GM007365-44; J.Z.: Stanford Graduate Fellowship.; S.M.d.I.O.: CIRM Bridges. Funding support is as follows: A.R.: NIH grant T32 AI007502-23; R.A.F.: Damon Runyon Cancer Research Foundation (DRG-2286-17); V.v.U.: Netherlands Organization for Scientific Research Rubicon grant (452181214); C.S. and J.Z.: NSF DMS 1712800 and the Stanford Discovery Innovation Fund; K.C.G. and M.M.D.: Howard Hughes Medical

Institute; C.A.B.: Burroughs Wellcome Fund Investigators in the Pathogenesis of Infectious Disease Grant 1016687. This work was also supported by CIRM DISC2-09637 to C.J.K. and T.J.D.: Bill and Melinda Gates Foundation OPP1113682 to C.J.K., M.R.A., and C.A.B.; Novo Nordisk Foundation Challenge Grant to M.R.A and M.M.-C.; Mathers Foundation Covid Fund to K.C.G.; and NIH grants K08DE027730 to A.A.S., U19AI057229 to M.M.D., R56AI111460 to J.S.G., 5R01HL14254902 to T.J.D., DK11572802 to C.J.K. and K.C.G., R01AI157155 to R.S.B., and U19AI116484, U01DK085527, U01CA217851, U01CA176299 and U01DE025188 to C.J.K.. C.A.B is the Tashia and John Morgridge Faculty Scholar and Chan Zuckerberg Biohub Investigator. T.J.D. is the Woods Family Endowed Faculty Scholar in Pediatric Translational Medicine. C.J.K. is the Maureen Lyles D'Ambrogio Professor of Medicine.

Author information

Author notes

1. Ameen A. Salahudeen

Present address: Division of Hematology and Oncology, Department of Medicine, University of Illinois at Chicago College of Medicine, Chicago, IL, USA

2. These authors contributed equally: Ameen A. Salahudeen, Shannon S. Choi

Affiliations

1. Division of Hematology, Department of Medicine, Stanford University School of Medicine, Stanford, CA, USA

Ameen A. Salahudeen, Shannon S. Choi, Sean M. de la O, António J. M. Santos, Jihang Ju, Arpit Batish, Tatsuya Usui, Daniel J. Hart & Calvin J. Kuo

2. Division of Infectious Disease and Geographic Medicine, Department of Medicine, Stanford University School of Medicine, Stanford, CA, USA

Arjun Rustagi & Catherine A. Blish

3. Stanford University School of Engineering, Department of Electrical Engineering, Stanford, CA, USA

Junjie Zhu

4. Department of Microbiology and Immunology, Stanford University School of Medicine, Stanford, CA, USA

Vincent van Unen, Lisa E. Wagar, Jeffrey S. Glenn, Mark M. Davis & Manuel R. Amieva

5. Stanford Institute of Immunity, Transplantation and Infection, Stanford University School of Medicine, Stanford, CA, USA

Vincent van Unen, Lisa E. Wagar & Mark M. Davis

6. Stanford ChEM-H, Stanford University, Stanford, CA, USA

Ryan A. Flynn

7. Department of Chemistry, Stanford University, Stanford, CA, USA

Ryan A. Flynn

8. Department of Pediatrics, Stanford University School of Medicine, Stanford, CA, USA

Mar Margalef-Català & Manuel R. Amieva

9. 10x Genomics, Pleasanton, CA, USA

Grace X. Y. Zheng, Jessica M. Terry, Phillip Belgrader, Solongo B. Ziraldo & Tarjei S. Mikkelsen

10. Department of Epidemiology, University of North Carolina at Chapel Hill, Chapel Hill, NC, USA

Caitlin E. Edwards & Ralph S. Baric

11. Department of Molecular and Cellular Physiology, Stanford University School of Medicine, Stanford, CA, USA

Vincent Luca & K. Christopher Garcia

12. Division of Biomedical Data Science, Department of Medicine, Stanford University School of Medicine, Stanford, CA, USA

Benedict Anchang & Chiara Sabatti

13. Division of Pulmonary, Allergy and Critical Care, Department of Medicine, Stanford University School of Medicine, Stanford, CA, USA

Monica Nagendran & Tushar J. Desai

14. Division of Gastroenterology, Department of Medicine, Stanford University School of Medicine, Stanford, CA, USA

Khanh Nguyen & Jeffrey S. Glenn

15. Department of Biochemistry, Stanford University School of Medicine, Stanford, CA, USA

Pehr B. Harbury

16. Howard Hughes Medical Institute, Stanford University School of Medicine, Stanford, CA, USA

K. Christopher Garcia & Mark M. Davis

17. Department of Microbiology and Immunology, University of North Carolina at Chapel Hill, Chapel Hill, NC, USA

Ralph S. Baric

18. Chan Zuckerberg Biohub, San Francisco, CA, USA

Catherine A. Blish

Authors

1. Ameen A. Salahudeen

[View author publications](#)

You can also search for this author in [PubMed](#) [Google Scholar](#)

2. Shannon S. Choi

[View author publications](#)

You can also search for this author in [PubMed](#) [Google Scholar](#)

3. Arjun Rustagi

[View author publications](#)

You can also search for this author in [PubMed](#) [Google Scholar](#)

4. Junjie Zhu

[View author publications](#)

You can also search for this author in [PubMed](#) [Google Scholar](#)

5. Vincent van Unen

[View author publications](#)

You can also search for this author in [PubMed](#) [Google Scholar](#)

6. Sean M. de la O

[View author publications](#)

You can also search for this author in [PubMed](#) [Google Scholar](#)

7. Ryan A. Flynn

[View author publications](#)

You can also search for this author in [PubMed](#) [Google Scholar](#)

8. Mar Margalef-Català

[View author publications](#)

You can also search for this author in [PubMed](#) [Google Scholar](#)

9. António J. M. Santos

[View author publications](#)

You can also search for this author in [PubMed](#) [Google Scholar](#)

10. Jihang Ju

[View author publications](#)

You can also search for this author in [PubMed](#) [Google Scholar](#)

11. Arpit Batish

[View author publications](#)

You can also search for this author in [PubMed](#) [Google Scholar](#)

12. Tatsuya Usui

[View author publications](#)

You can also search for this author in [PubMed](#) [Google Scholar](#)

13. Grace X. Y. Zheng

[View author publications](#)

You can also search for this author in [PubMed](#) [Google Scholar](#)

14. Caitlin E. Edwards

[View author publications](#)

You can also search for this author in [PubMed](#) [Google Scholar](#)

15. Lisa E. Wagar

[View author publications](#)

You can also search for this author in [PubMed](#) [Google Scholar](#)

16. Vincent Luca

[View author publications](#)

You can also search for this author in [PubMed](#) [Google Scholar](#)

17. Benedict Anchang

[View author publications](#)

You can also search for this author in [PubMed](#) [Google Scholar](#)

18. Monica Nagendran

[View author publications](#)

You can also search for this author in [PubMed](#) [Google Scholar](#)

19. Khanh Nguyen

[View author publications](#)

You can also search for this author in [PubMed](#) [Google Scholar](#)

20. Daniel J. Hart

[View author publications](#)

You can also search for this author in [PubMed](#) [Google Scholar](#)

21. Jessica M. Terry

[View author publications](#)

You can also search for this author in [PubMed](#) [Google Scholar](#)

22. Phillip Belgrader

[View author publications](#)

You can also search for this author in [PubMed](#) [Google Scholar](#)

23. Solongo B. Ziraldo

[View author publications](#)

You can also search for this author in [PubMed](#) [Google Scholar](#)

24. Tarjei S. Mikkelsen

[View author publications](#)

You can also search for this author in [PubMed](#) [Google Scholar](#)

25. Pehr B. Harbury

[View author publications](#)

You can also search for this author in [PubMed](#) [Google Scholar](#)

26. Jeffrey S. Glenn

[View author publications](#)

You can also search for this author in [PubMed](#) [Google Scholar](#)

27. K. Christopher Garcia

[View author publications](#)

You can also search for this author in [PubMed](#) [Google Scholar](#)

28. Mark M. Davis

[View author publications](#)

You can also search for this author in [PubMed](#) [Google Scholar](#)

29. Ralph S. Baric

[View author publications](#)

You can also search for this author in [PubMed](#) [Google Scholar](#)

30. Chiara Sabatti

[View author publications](#)

You can also search for this author in [PubMed](#) [Google Scholar](#)

31. Manuel R. Amieva

[View author publications](#)

You can also search for this author in [PubMed](#) [Google Scholar](#)

32. Catherine A. Blish

[View author publications](#)

You can also search for this author in [PubMed](#) [Google Scholar](#)

33. Tushar J. Desai

[View author publications](#)

You can also search for this author in [PubMed](#) [Google Scholar](#)

34. Calvin J. Kuo

[View author publications](#)

You can also search for this author in [PubMed](#) [Google Scholar](#)

Contributions

A.A.S. and S.S.C. conceived, designed, and performed experiments, analysed data, and wrote the manuscript. A.R. designed and performed SARS-CoV-2 infections. J.Z., V.v.U. and C.S. designed and interpreted single-cell RNA-seq studies. R.A.F. performed qRT–PCR. M.M.-C., S.M.d.l.O., A.J.M.S., T.U., D.J.H., J.J. and A.B. performed organoid culture and analysis. L.E.W. and M.M.D. designed FACS panels. V.L. and K.C.G. contributed the DLL4 E12 mutant. B.A. performed SPADE analysis. K.N. and J.S.G. designed and executed influenza studies. G.X.Y.Z., J.M.T., P.B., S.B.Z. and T.S.M. designed and executed single-cell RNA-seq experiments. C.E.E. and R.S.B. advised on SARS-CoV-2 studies. M.N. and P.B.H. provided in situ hybridization protocols. M.R.A., C.A.B., T.J.D. and C.J.K. conceived and designed experiments, analysed data and wrote the manuscript.

Corresponding authors

Correspondence to [Catherine A. Blish](#) or [Tushar J. Desai](#) or [Calvin J. Kuo](#).

Ethics declarations

Competing interests

C.J.K., A.A.S., S.S.C., C.A.B., A.R., M.R.A., M.M.-C., S.M.d.l.O. and T.U. are listed as inventors on provisional patent 63/053,079 describing the methods in this paper. C.J.K. is a founder of Surrozen Inc. All other authors declare no competing interests.

Additional information

Peer review information *Nature* thanks the anonymous reviewers for their contribution to the peer review of this work.

Publisher's note Springer Nature remains neutral with regard to jurisdictional claims in published maps and institutional affiliations.

Extended data figures and tables

Extended Data Fig. 1 Optimization of human distal lung organoid culture.

a, Schematic of culture initiation from human distal lung. **b**, Brightfield microscopy evaluation of required exogenous growth factors and automated organoid quantitation after day 10 of chemically defined organoid culture with specified recombinant growth factors, N = Noggin, E = EGF, W = WNT3A, R = RSPO1, n = 4 per condition, data are mean \pm s.e.m., * = $P < 0.05$, two-tailed student's t -test, scale bar = 500 μm . **c**, Top, purification schema to isolate epithelial cells from distal human lung involving negative MACS bead depletion of CD45 $^+$ haematopoietic cells, endothelial cells and fibroblasts, followed by positive FACS selection for EPCAM $^+$ epithelium. Bottom left, representative FACS demonstrating >99.9% EPCAM $^+$ purity (orange) upon re-analysis versus unstained controls (grey). Bottom right, proliferation of EPCAM $^+$ cells purified from distal lung cultures after day 10 of organoid culture with specified growth factors, N = Noggin, E = EGF, W = WNT3A, R = RSPO1, n = 3 per condition, data are mean \pm s.e.m., ** = $P < 0.01$, two-tailed student's t -test. **d**, Time lapse transmission confocal images of solid and cystic organoids originating from single dissociated human distal lung cells, scale bar = 100 μm . **e-g**, Clonality mixing studies. **e**, Schema of mixing studies of lentivirus-GFP- and lentivirus-mCherry-expressing cells to determine clonality. **f**, Representative live fluorescent imaging of resultant green and red organoids from (e), scale bar = 500 μm . **g**, Quantitation of red, green, or chimaeric, distal lung organoid cultures from two individuals (1, 2) after initial and serial passaging (P1 = passage 1). [Source data](#)

Extended Data Fig. 2 scRNA-seq of human distal lung organoids cultured from three individuals reveals reproducible basal, club, and AT2 populations.

a–c, Unsupervised clustering of total cell populations demonstrates consistency in top differentially expressed genes corresponding to basal (*KRT5/6*), club (*SCGB1A1*), and AT2 (*SFTPC*) cells. The epithelial fraction from these cultures ranged from approximately 90–99% of all cells with the remainder being either fibroblasts (VIM^+) or mononuclear cells (HLA-DR+, likely alveolar macrophages). **d–f**, t-SNE visualization and violin plots for marker genes corresponding to each population. Note, a unique population enriched for SPRR genes, which have been described to mark squamous metaplasia, were exclusively found in the organoid culture of Lung 3, derived from an individual who was an active smoker.

Extended Data Fig. 3 Trajectory inference with SPADE and pseudotime.

a, SPADE plot of pooled cells where each point represents cell states that are more related on the same or adjacent branches of a minimum spanning tree. Note: AT2 cells exist on a branch distal to basal and club cells, suggesting no lineage hierarchy between AT2, basal, and club cells. **b**, SPADE plots of pooled scRNA-seq samples after excluding AT2, VIM^+ and HLA-DR⁺ cells support lineage relationships between basal (blue) and club (red) populations by club cell branches emanating from basal cells. **c**, SPADE plots of Basal 1, Basal 2, and club populations. **d**, Left, gene expression of *SCGB1A1* shows higher expression in club versus basal cell lineages (left) as compared to *KRT5* (middle). Right, median gene expression of *TNFRSF12A*, showing a high (orange outline) and a low (blue outline) within basal cell branches and inferring a potential lineage relationship. **e**, Monocle 3 pseudotime trajectory analysis of single cell transcriptomes of Basal 1 connected to club cells depicted with UMAP (cell number, $n = 3,721$), colored by (left) cell cluster and (right) pseudotime gradient.

Extended Data Fig. 4 Human AT2 organoid characterization.

a, Left, confocal images of a live AT2 organoid at 67 days of culture labelled with Hoescht nuclear stain and LysoTracker Red DND-99. Top right, isolation of purified AT2 organoids. Representative FACS plots

showing LysoTracker Red AT2 purification from unfractionated organoid cultures. Bottom right, immunostaining of cytospin of LysoTracker-sorted AT2 cells show high purity (100/100 cells SPC⁺ SCGB1A1⁻ KRT5); scale bar = 50 μ m). **b**, Schema of FACS isolation of AT2 cells from human mixed distal lung organoids as EPCAM⁺LysoTracker⁺ AT2 cells followed by long-term clonogenic organoid culture. **c**, Representative image of clonal mixing studies from stroma-depleted, EPCAM⁺LysoTracker⁺, lentivirally-marked AT2 cells demonstrating presence of completely mCherry⁺ or GFP⁺ but not chimaeric organoids carried out as in Extended Data Fig. 1e-g, passage 1 after lentiviral infection, scale bar = 200 μ m. **d**, Quantitation of red, green, or chimaeric AT2 organoid cultures as in (c) from two individuals (1, 2) after initial and serial passaging (P1 = passage 1). **e**, AT2 organoid proliferation with differing combinations of recombinant niche factors and PORCUPINE inhibitor C59 (1 mM), NOGGIN (N), EGF (E), WNT3A (W), R-SPONDIN1 (R). n = 3 per condition, data are mean \pm s.e.m., * = P < 0.05, *** = P < 0.001, two-tailed student's *t*-test. **f**, Brightfield microscopy comparing pure AT2 organoid growth enhancement in chemically defined lung organoid media (EN) versus serum-containing L-cell conditioned media containing WNT3A, NOGGIN, and R-SPONDIN3 (L-WRN CM) supplemented with recombinant EGF, one experiment. Scale bar = 200 μ m. **g**, Transmission electron microscopy image of representative AT2 organoid at 28 days of culture. Note apical microvilli (black arrows) and lamellar bodies (red arrows); scale bar = 10 μ m. [Source data](#)

Extended Data Fig. 5 Characterization of basal organoids.

a-c, Basal organoids in mixed culture progressively form internal lumens, which is not associated with apoptosis. **a**, KRT5 IF, day 26 culture, scale bar = 200 μ m. **b**, Lumen quantitation, d12 versus d26 culture, single determination. **c**, Absence of apoptosis in d26 basal cell organoid internal lumen, cleaved caspase IF, from Fig. 2b, scale bar = 20 μ m. **d**, **e**, Isolation of purified basal cell organoids via differential sedimentation in Ficoll. **d**, Schema and enrichment to >90% KRT5⁺ cells as measured by intracellular KRT5 FACS of sedimented basal organoid cells; scale bar = 100 μ m. **e**, Serial time lapse microscopy of sedimented basal organoids reveals spontaneous cavitation within two weeks post passage or within four weeks of culture initiation; scale bar = 25 μ m. **f**, **g**, Clonal mixing studies from

stroma-depleted, Ficoll-purified and lentivirally-marked basal organoid cells demonstrating fully mCherry⁺ or GFP⁺ but not chimaeric organoids as in Extended Data Fig. 1f, passage 1 after lentiviral infection, scale bar = 200 μ m. f, Representative clonal mixing image study. g, Quantitation. h, Growth factor evaluation for basal organoids after d14 sedimentation, enzymatic dissociation and clonogenic culture. Growth was not affected by the PORCUPINE inhibitor C59 (1 μ M). n = 4 per condition, data are mean \pm s.e.m., *** = P < 0.001, two-tailed student's t-test. [Source data](#)

Extended Data Fig. 6 scRNA-seq identifies an active basal cell subpopulation across three individual patient organoid cultures.

a, High resolution clustering analysis identifies a reproducible active basal cell subpopulation with significantly higher expression of mRNAs for *TNFRSF12A*, the NOTCH pathway marker *HES1*, and the proliferation marker *MKI67*. Modified Kruskal–Wallis Rank Sum Test two tail p-values: *TNFRSF12A* 4.15×10^{-8} ; *HES1* 2.4×10^{-10} ; *MKI67* 3.4×10^{-3} . b, Fine resolution clustering of KRT5⁺ populations identifies two Basal 1 sub-clusters, Basal 1.1 and 1.2. c, Gene Ontology PANTHER overrepresentation of differentially expressed genes enriched in Basal 1.2 versus 1.1 show the majority of Basal 1.2 processes involve cell cycle (asterisks). Complete analysis is provided in Supplementary Table 3. d, Violin plot of scRNA-seq analysis for Fig. 2f–h depicting *KRT5* mRNA expression among triply *EPCAM*⁺*ITGA6*⁺*ITGB4*⁺ mRNA-expressing single cells (purple, that is, tandem mRNA expression of all three genes) versus the remainder of cells (grey), P < 0.001 two tailed Kruskal–Wallis Rank Sum Test. e, t-SNE visualization of *TNFRSF12A* and *ITGA6* expression from d among cells with *EPCAM*⁺*ITGA6*⁺*ITGB4*⁺ gene expression and subdivision by high (top quartile, orange), medium (pink) and low (bottom quartile, navy blue) mRNA expression. f, Proliferation-associated gene expression is progressively enriched for scRNA-seq cell fractions of in *EPCAM*⁺*ITGA6*⁺*ITGB4*⁺ cells that are stratified for low, medium, or high expression of *TNFRSF12A* mRNA as in e. Data in f represent cell population fractions from a single experiment. *** = P < 0.001, two tailed Chi-square test.

Extended Data Fig. 7 Evaluation of Basal 1 lineage relationship to Basal 2 and the influence of NOTCH signalling on Basal 1 renewal and differentiation.

a, Isolation of Basal 1 and Basal 2 via differential sedimentation of KRT5⁺ cells followed by FACS sorting of EPCAM⁺ITGA6⁺ITGB4⁺TNFRSF12A⁺ (Basal 1) versus EPCAM⁻ITGA6⁻ITGB4⁻TNFRSF12A⁻ (Basal 2). **b**, Intracellular FACS measurement of KRT5 protein expression in Basal 1 and 2 fractions from **a**. **c**, Representative brightfield of day 14 organoid cultures from **a**, **b**. **d**, Quantitation of 3 independent experiments from **a–c**, box plot represents first quartile, median, third quartile, and whiskers represent minimum and maximum. *** $P < 0.001$, two tailed student's *t*-test. **e**, qPCR measurement of two differentially upregulated Basal 2 genes from the three scRNA-seq biological replicates (Extended Data Fig. 6, *SPRR1B*, *TMSB4X*) after prolonged culture of FACS isolated Basal 1 cells. Data are relative mean \pm s.e.m. of cultures from three independent experiments, ** = $P < 0.01$, two tailed student's *t*-test. **f**, RNA FISH demonstrating *TMSB4X* and *SPRR1B* cellular transcripts within organoids originating from Basal 1 cells (arrows), scale bar = 25 μ m. **g**, KRT5 immunostaining and *SFTPC* and *SCGB1A1* RNA FISH of FACS isolated TNFRSF12A^{hi} Basal 1 cells under vehicle, NOTCH agonism (JAG1 peptide), or NOTCH antagonism with the Delta-like ligand mutant 4 (DLL4^{E12}; E12) or the gamma secretase inhibitor DBZ; scale bar = 50 μ m. **h**, Fluorescent quantitation of resazurin dye reduction to estimate relative cellular proliferation in **g**, data are normalized to vehicle (V) and represent mean \pm s.e.m. from five independent experiments, * $P < 0.05$, two tailed student's *t*-test. **i**, Quantitation of *SCGB1A1* and *SFTPC* gene expression by RNA FISH in the context of NOTCH agonism or antagonism from three independent experiments, ** $P < 0.01$, *** $P < 0.001$, two tailed student's *t*-test. *SFTPC* mRNA upregulation was not accompanied by lamellar body or SFTPC protein production (data not shown). [Source data](#)

Extended Data Fig. 8 TNFRSF12A marks a subset of distal airway basal cells in vivo.

a, b, Immunostaining of KRT5 and TNFRSF12A in human distal airways from two individuals, scale bar = 100 μm . **c**, Immunostaining of KRT5, TNFRSF12A, and p63 in human distal airway, scale bar = 100 μm . **d**, FACS analysis from freshly fixed human distal lung with anti-KRT5 (intracellular) and monoclonal anti-TNFRSF12A (cell surface) (top), or sequential FACS isolation from freshly dissociated human distal lung of EPCAM $^+$ ITGA6 $^+$ ITGB4 $^+$ cells followed by fractionation into TNFRSF12A $^{\text{hi}}$ or TNFRSF12A $^{\text{neg}}$ subsets (bottom), pre-gated on live singlets and used for culture experiments in Fig. [3d–g](#).

Extended Data Fig. 9 Influenza infection modelling in mixed distal lung organoid cultures.

a, b, Distal lung organoid modelling of H1N1 influenza infection. **a**, Merged transmission and GFP confocal images of purified basal (left) and purified AT2 organoids (right) 12 h after infection with PR8-GFP H1N1 influenza virus, quantified by FACS for % GFP $^+$ cells. Bar plot represents the mean percentage of infected cells from three technical replicates, $P = 0.57$, Chi-square test. Scale bars = 50 μm . **b**, Viral genome quantitation over time of mixed distal lung organoid culture supernatants subjected to initial infection of wild-type H1N1 at an estimated multiplicity of infection (MOI) of 0.01, qRT–PCR, data represent the mean of three independent experiments \pm s.e.m. **c, d**, Lectin staining with *M. amurensis* (a2-3) and *S. nigra* (a2-6) lectins or no lectin negative controls to characterize sialic acid residues which serve as surface molecules for influenza virus host cell entry. AT2 organoids (c) and basal organoids (d). Scale bar = 25 μm . **e**, Dose response curves for two different classes of antiviral drugs on influenza infectivity and replication. The nucleoside analogue FdC demonstrated dose dependent activity with IC $_{50}$ of 340 nM as compared to neuraminidase inhibitor zanamivir, which only impairs viral shedding but not infectivity and replication. $n = 3$ per condition, data represents mean \pm s.e.m. **f**, Fluorescence micrograph of multiwell screening of selected various antiviral agents after H1N1 PR8-GFP organoid infection in 48 well format. FdC = nucleoside analogue 2'-deoxy-2'-fluorocytidine.
Cpd = compound #. [Source data](#)

Extended Data Fig. 10 Apical-out polarization and multi-lineage differentiation of distal lung organoids upon suspension culture.

a, scRNA-seq plots of *ACE2* and *TPRSS2* gene expression in ECM-embedded mixed distal lung organoids as in Fig. 1a–h. **b**, Diagram of ECM removal and suspension culture leading to apical-out polarity of lung organoids. **c**, Representative confocal microscopy showing reorganization of microfilaments (phalloidin) and acetylated microtubules (AcTUB) upon ECM removal. Scale bar = 10 μ m. **d–f**, Polarization and accelerated ciliary differentiation of apical-out basal organoids. **d**, Confocal 3D sections (top panels) and surface reconstructions (bottom panels) of apical-out lung organoids at different days after ECM removal. At day 0 (d0) microfilament (green, phalloidin) and microtubule (red, acetylated tubulin) organization is not polarized while junctional strands (ZO-1, white) are polarized. By day 2 in suspension (d2) ZO-1 (white) forms junctional rings in the apical periphery of each cell facing the external side of the organoids and the actin cytoskeleton forms microvilli (green) facing outward (apical-out polarity). Also, at d2 some cells initiate microtubule polarization. By day 5 (d5) many more cells have motile cilia facing outwards. Mature motile cilia can be observed for several weeks, example at day 14 (d14). **e**, 3D confocal reconstruction of an organoid embedded in ECM consisting mostly of basal stem cells ($KRT5^+$, white). **f**, As apical-out polarity is established in suspension culture and ciliogenesis begins, $KRT5^+$ basal cells are found underneath the polarized epithelium. **g**, $SCGB1A1^+$ Club cells with apical-out polarity are present on the exterior surface. In all panels nuclei are stained blue with DAPI, and actin microfilament organization visualized with phalloidin (green). Scale bars = 10 μ m. **h–j**, Prolonged suspension culture of AT2 organoids (day 10 post-suspension) induces apical-out polarization and AT1 differentiation. **h**, Optical sections through alveolar-derived organoids after 10 days in suspension culture show decreased abundance of AT2 cells while individual cuboidal cells begin to express the AT1 marker HTI-56 (red), a transmembrane protein specific to the apical membrane of alveolar type 1 pneumocytes (AT1). Scale bars = 10 μ m. **i, j**, Side views of alveolar organoids after 10 days of suspension culture reveal thin AT1 cells with phalloidin-reactive apical junctional complexes facing

outwards (apical-out) (**i**) and expression of HTI-56 on the apical membrane (**j**). Scale bars = 10 μ m. **k**, Representative confocal microscopy immunofluorescence of apical-out human basal organoid after 10 days in suspension expressing SARS-CoV-2 receptor ACE2 (green), cilia (AcTUB, red) and DAPI (blue). Scale bar = 20 μ m.

Supplementary information

[This file contains Supplementary Methods and associated references.](#)

[Reporting Summary](#)

[Supplementary Figure 1](#)

Gating strategies. **a**, EPCAM $^+$ Lysotracker $^+$ gating strategy to purify AT2 cells. Purity was confirmed with 100/100 sorted cells staining positive for SFTPC protein (corresponding to Extended Data Fig. 4a). **b**, EPCAM $^+$ ITGA6 $^+$ ITGB4 $^+$ TNFRSF12A $^{\text{hi/neg}}$ gating strategy. Purity was confirmed with 100/100 pooled sorted cells staining positive for KRT5 protein (corresponding to Fig. 2j-k). **c**, Gating strategy to analyze KRT5 $^+$ cells and corresponding TNFRSF12A $^+$ populations within cells freshly dissociated from distal human lungs (corresponding to Extended Data Fig. 8d). **d**, RT-PCR correlation of TNFRSF12A and other mRNAs from cells sorted by FACS into TNFRSF12A neg, med, and hi fractions (Fig. 3d). **e**, Gating strategy to estimate H1N1 PR8 GFP infectivity in human lung organoids (corresponding to Extended Data Fig. 9a).

[Supplementary Table 1](#)

Clinical demographics of 136 lung tissue donors used in this study. Each row corresponds to a unique individuals from whom normal lung was obtained and columns correspond to features such as age, sex, and lung anatomic location.

Supplementary Table 2

Genes used for SPADE analysis. Genes were utilized in SPADE based on graph-based clustering annotation of cells from scRNA-seq analysis of three individuals. Full SPADE details are provided in Supplementary Methods.

Supplementary Table 3

Gene Set Enrichment Analysis (GSEA) of top differentially expressed genes from scRNA-seq populations. Populations correspond to Basal 1, Basal 2, Basal 1.1, Basal 1.2, and Cluster 1 of purified AT2 scRNA-seq data sets. Top differentially expressed genes for each population are listed in each tab. Bold = genes used for GSEA analysis (Panther overrepresentation test, with Bonferroni correction, p values are two tailed).

Supplementary Table 4

List of Basal 1 membrane protein genes. Genes were identified by ontology analysis of top differentially expressed Basal 1 genes with GO term 0031224, (intrinsic component of membrane).

Supplementary Table 5

Analysis of SARS-CoV-2-infection in lung organoid cultures. Positively infected cells were quantified by dsRNA and SARS-CoV-2 NP staining among KRT5⁺ basal cells, SCGB1A1⁺ club cells, and AcTUB⁺ ciliated cells using confocal microscopy. Statistical analysis (chi-square or Fisher's exact test) were performed as indicated.

Supplementary Table 6

Next Generation Sequencing of five distal lung organoid cultures. Summary and annotations of nonsynonymous variants with allele frequency > 0.10 for 130 cancer genes using the TOMA Tumor Profiling System (TOMA, Foster City, CA).

Supplementary Table 7

Tables of reagents. Individual tables of organoid media components, immunostaining and fluorescence microscopy reagents, RT-PCR reagents, RT-PCR primers, and RNA hybridization probes used in this study.

Supplementary Data 1

Guide to lung organoid scRNA-seq analysis. scRNA-seq analysis for lungs 1, 2, 3 and purified AT2 organoids provided in .rmd and .html format.

Supplementary Data 2

Lung organoid culture sequencing. Next Generation Sequencing data for each of five distal lung organoid cultures (TOMA Tumor Profiling System) are provided in Variant Call Format.

Supplementary Video 1

Differentiated basal organoids have functional cilia, Part 1. Transmission confocal microscopy video of beating cilia (25X magnification).

Supplementary Video 2

Differentiated basal organoids have functional cilia, Part 2. Bright-field microscopy video of beating cilia (10x magnification).

Supplementary Video 3

Apical-out differentiated basal organoids have functional cilia. DIC and 3D confocal microscopy video of motile cilia in apical-out basal organoids at suspension culture day 5 and 14.

Source data

Source Data Fig. 2

[Source Data Fig. 3](#)

[Source Data Extended Data Fig. 1](#)

[Source Data Extended Data Fig. 4](#)

[Source Data Extended Data Fig. 5](#)

[Source Data Extended Data Fig. 7](#)

[Source Data Extended Data Fig. 9](#)

Rights and permissions

[Reprints and Permissions](#)

About this article



Check for
updates

Cite this article

Salahudeen, A.A., Choi, S.S., Rustagi, A. *et al.* Progenitor identification and SARS-CoV-2 infection in human distal lung organoids. *Nature* **588**, 670–675 (2020). <https://doi.org/10.1038/s41586-020-3014-1>

[Download citation](#)

- Received: 08 November 2017
- Accepted: 18 November 2020
- Published: 25 November 2020

- Issue Date: 24 December 2020
- DOI: <https://doi.org/10.1038/s41586-020-3014-1>

Comments

By submitting a comment you agree to abide by our [Terms](#) and [Community Guidelines](#). If you find something abusive or that does not comply with our terms or guidelines please flag it as inappropriate.

[Download PDF](#)

Associated Content

Collection

[Coronavirus](#)

This article was downloaded by **calibre** from <https://www.nature.com/articles/s41586-020-3014-1>

| [Section menu](#) | [Main menu](#) |

- Article
- [Published: 02 December 2020](#)

Highly multiplexed spatial mapping of microbial communities

- [Hao Shi](#) ORCID: [orcid.org/0000-0002-9658-2847¹](https://orcid.org/0000-0002-9658-2847),
- [Qiaojuan Shi¹](#),
- [Benjamin Grodner¹](#),
- [Joan Sesing Lenz¹](#),
- [Warren R. Zipfel¹](#),
- [Ilana Lauren Brito](#) ORCID: [orcid.org/0000-0002-2250-3480¹](https://orcid.org/0000-0002-2250-3480) &
- [Iwijn De Vlaminck](#) ORCID: [orcid.org/0000-0001-6085-7311¹](https://orcid.org/0000-0001-6085-7311)

[Nature](#) volume **588**, pages676–681(2020)[Cite this article](#)

- 10k Accesses
- 1 Citations
- 241 Altmetric
- [Metrics details](#)

Subjects

- [Antimicrobials](#)
- [Microbial communities](#)
- [Imaging](#)

Abstract

Mapping the complex biogeography of microbial communities *in situ* with high taxonomic and spatial resolution poses a major challenge because of the high density¹ and rich diversity² of species in environmental microbiomes and the limitations of optical imaging technology^{3,4,5,6}. Here we introduce high-phylogenetic-resolution microbiome mapping by fluorescence *in situ* hybridization (HiPR-FISH), a versatile technology that uses binary encoding, spectral imaging and decoding based on machine learning to create micrometre-scale maps of the locations and identities of hundreds of microbial species in complex communities. We show that 10-bit HiPR-FISH can distinguish between 1,023 isolates of *Escherichia coli*, each fluorescently labelled with a unique binary barcode. HiPR-FISH, in conjunction with custom algorithms for automated probe design and analysis of single-cell images, reveals the disruption of spatial networks in the mouse gut microbiome in response to treatment with antibiotics, and the longitudinal stability of spatial architectures in the human oral plaque microbiome. Combined with super-resolution imaging, HiPR-FISH shows the diverse strategies of ribosome organization that are exhibited by taxa in the human oral microbiome. HiPR-FISH provides a framework for analysing the spatial ecology of environmental microbial communities at single-cell resolution.

[Access through your institution](#)

[Change institution](#)

[Buy or subscribe](#)

Access options

Subscribe to Journal

Get full journal access for 1 year

\$199.00

only \$3.83 per issue

[Subscribe](#)

All prices are NET prices.
VAT will be added later in the checkout.

Rent or Buy article

Get time limited or full article access on ReadCube.

from \$8.99

[Rent or Buy](#)

All prices are NET prices.

Additional access options:

- [Log in](#)
- [Access through your institution](#)
- [Learn about institutional subscriptions](#)

Fig. 1: Working principle of HiPR-FISH.

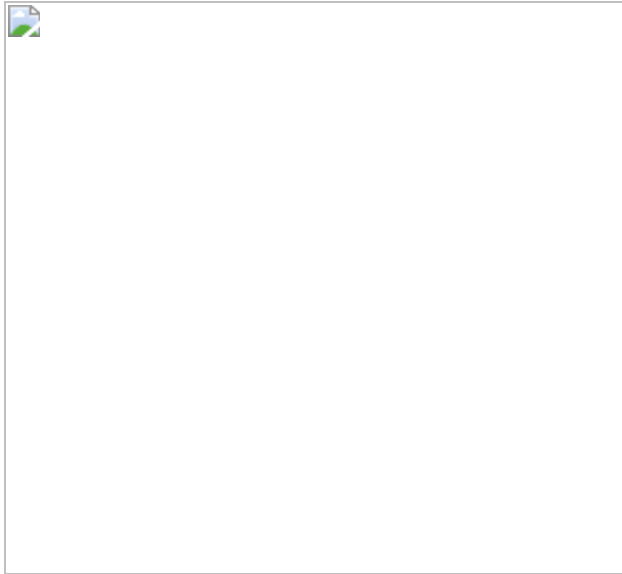


Fig. 2: Algorithm for single-cell segmentation.

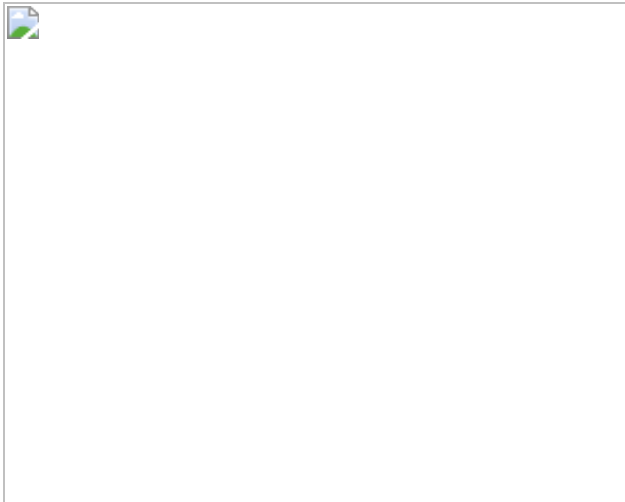
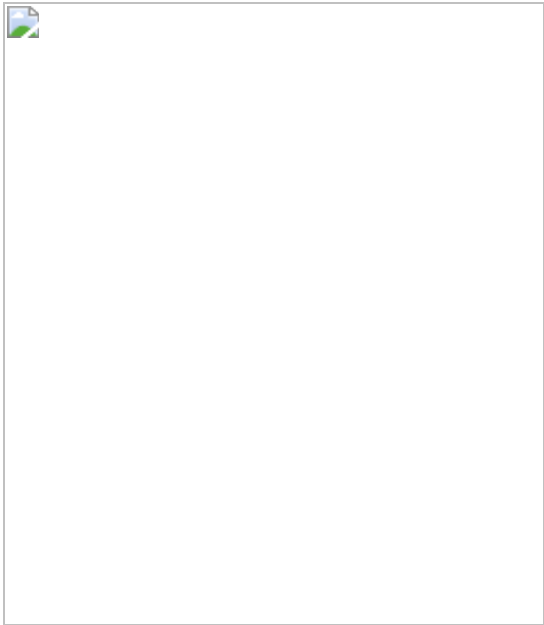


Fig. 3: Antibiotic treatments disrupt the spatial organization of the mouse gut microbiome.



Fig. 4: Biogeography of human oral biofilms.



Data availability

PacBio sequencing data are available at the NCBI Sequence Read Archive (SRA) with accession number [PRJNA665727](#). Metagenomic sequencing data of laser-capture-microdissected tissue samples are available at the NCBI SRA with accession number [PRJNA665536](#). All microscopy data have been deposited to Zenodo. A full list of DOIs is provided in the Supplementary Information. [Source data](#) are provided with this paper.

Code availability

All code is available on GitHub at <https://github.com/proudquartz/hiprfish>.

References

1. 1.

Donaldson, G. P., Lee, S. M. & Mazmanian, S. K. Gut biogeography of the bacterial microbiota. *Nat. Rev. Microbiol.* **14**, 20–32 (2016).

[CAS](#) [Article](#) [Google Scholar](#)

2. 2.

The Human Microbiome Project Consortium. Structure, function and diversity of the healthy human microbiome. *Nature* **486**, 207–214 (2012).

[ADS](#) [Article](#) [Google Scholar](#)

3. 3.

Tropini, C., Earle, K. A., Huang, K. C. & Sonnenburg, J. L. The gut microbiome: connecting spatial organization to function. *Cell Host Microbe* **21**, 433–442 (2017).

[CAS](#) [Article](#) [Google Scholar](#)

4. 4.

Mark Welch, J. L., Rossetti, B. J., Rieken, C. W., Dewhirst, F. E. & Borisy, G. G. Biogeography of a human oral microbiome at the micron scale. *Proc. Natl Acad. Sci. USA* **113**, E791–E800 (2016).

[ADS](#) [CAS](#) [Article](#) [Google Scholar](#)

5. 5.

Valm, A. M. et al. Systems-level analysis of microbial community organization through combinatorial labeling and spectral imaging. *Proc. Natl Acad. Sci. USA* **108**, 4152–4157 (2011).

[ADS](#) [CAS](#) [Article](#) [Google Scholar](#)

6. 6.

Valm, A. M., Mark Welch, J. L. & Borisy, G. G. CLASI-FISH: principles of combinatorial labeling and spectral imaging. *Syst. Appl. Microbiol.* **35**, 496–502 (2012).

[CAS](#) [Article](#) [Google Scholar](#)

7. 7.

De Weirdt, R. & Van De Wiele, T. Micromanagement in the gut: Microenvironmental factors govern colon mucosal biofilm structure and functionality. *npj Biofilms and Microbiomes* **1**, 15026 (2015).

[Article](#) [Google Scholar](#)

8. 8.

Thaiss, C. A. et al. Microbiota diurnal rhythmicity programs host transcriptome oscillations. *Cell* **167**, 1495–1510 (2016).

[CAS](#) [Article](#) [Google Scholar](#)

9. 9.

Valm, A. M., Oldenbourg, R. & Borisy, G. G. Multiplexed spectral imaging of 120 different fluorescent labels. *PLoS ONE* **11**, e0158495 (2016).

[Article](#) [Google Scholar](#)

10. 10.

Mark Welch, J. L., Hasegawa, Y., McNulty, N. P., Gordon, J. I. & Borisy, G. G. Spatial organization of a model 15-member human gut microbiota established in gnotobiotic mice. *Proc. Natl Acad. Sci. USA* **114**, E9105–E9114 (2017).

[CAS](#) [Article](#) [Google Scholar](#)

11. 11.

Earle, K. A. et al. Quantitative imaging of gut microbiota spatial organization. *Cell Host Microbe* **18**, 478–488 (2015).

[CAS](#) [Article](#) [Google Scholar](#)

12. 12.

Dagher, M., Kleinman, M., Ng, A. & Juncker, D. Ensemble multicolour FRET model enables barcoding at extreme FRET levels. *Nat. Nanotechnol.* **13**, 925–932 (2018).

[ADS](#) [CAS](#) [Article](#) [Google Scholar](#)

13. 13.

Otsu, N. A threshold selection method from gray-level histograms. *IEEE Trans. Syst. Man Cybern.* **9**, 62–66 (1979).

[Article](#) [Google Scholar](#)

14. 14.

Sauvola, J. & Pietikäinen, M. Adaptive document image binarization. *Pattern Recognit.* **33**, 225–236 (2000).

[Article](#) [Google Scholar](#)

15. 15.

Francino, M. P. Antibiotics and the human gut microbiome: dysbioses and accumulation of resistances. *Front. Microbiol.* **6**, 1543 (2016).

[Article](#) [Google Scholar](#)

16. 16.

Samad, T., Co, J. Y., Witten, J. & Ribbeck, K. Mucus and mucin environments reduce the efficacy of polymyxin and fluoroquinolone antibiotics against *Pseudomonas aeruginosa*. *ACS Biomater. Sci. Eng.* **5**, 1189–1194 (2019).

[CAS](#) [Article](#) [Google Scholar](#)

17. 17.

Antonopoulos, D. A. et al. Reproducible community dynamics of the gastrointestinal microbiota following antibiotic perturbation. *Infect. Immun.* **77**, 2367–2375 (2009).

[CAS Article](#) [Google Scholar](#)

18. 18.

Panda, S. et al. Short-term effect of antibiotics on human gut microbiota. *PLoS ONE* **9**, e95476 (2014).

[ADS Article](#) [Google Scholar](#)

19. 19.

Li, J. et al. Probiotics modulated gut microbiota suppresses hepatocellular carcinoma growth in mice. *Proc. Natl Acad. Sci. USA* **113**, E1306–E1315 (2016).

[CAS Article](#) [Google Scholar](#)

20. 20.

Scheiman, J. et al. Meta-omics analysis of elite athletes identifies a performance-enhancing microbe that functions via lactate metabolism. *Nat. Med.* **25**, 1104–1109 (2019).

[CAS Article](#) [Google Scholar](#)

21. 21.

Dewhirst, F. E. et al. The human oral microbiome. *J. Bacteriol.* **192**, 5002–5017 (2010).

[CAS Article](#) [Google Scholar](#)

22. 22.

Rasiah, I. A., Wong, L., Anderson, S. A. & Sissons, C. H. Variation in bacterial DGGE patterns from human saliva: over time, between individuals and in corresponding dental plaque microcosms. *Arch. Oral Biol.* **50**, 779–787 (2005).

[CAS](#) [Article](#) [Google Scholar](#)

23. 23.

Costello, E. K. et al. Bacterial community variation in human body habitats across space and time. *Science* **326**, 1694–1697 (2009).

[ADS](#) [CAS](#) [Article](#) [Google Scholar](#)

24. 24.

Li, K., Bihan, M. & Methé, B. A. Analyses of the stability and core taxonomic memberships of the human microbiome. *PLoS ONE* **8**, e63139 (2013).

[ADS](#) [CAS](#) [Article](#) [Google Scholar](#)

25. 25.

Zhou, Y. et al. Biogeography of the ecosystems of the healthy human body. *Genome Biol.* **14**, R1 (2013).

[Article](#) [Google Scholar](#)

26. 26.

Baddour, L. M. et al. Infective endocarditis in adults: diagnosis, antimicrobial therapy, and management of complications: a scientific statement for healthcare professionals from the American Heart Association. *Circulation* **132**, 1435–1486 (2015).

[CAS](#) [Article](#) [Google Scholar](#)

27. 27.

Hedberg, M. E. et al. *Lachnoanaerobaculum* gen. nov., a new genus in the *Lachnospiraceae*: characterization of *Lachnoanaerobaculum umeaense* gen. nov., sp. nov., isolated from the human small intestine, and *Lachnoanaerobaculum orale* sp. nov., isolated from saliva, and reclassification of *Eubacterium saburreum* (Prevot 1966) Holdeman and Moore 1970 as *Lachnoanaerobaculum saburreum* comb. nov. *Int. J. Syst. Evol. Microbiol.* **62**, 2685–2690 (2012).

[Article](#) [Google Scholar](#)

28. 28.

Stracy, M. et al. Live-cell superresolution microscopy reveals the organization of RNA polymerase in the bacterial nucleoid. *Proc. Natl Acad. Sci. USA* **112**, E4390–E4399 (2015).

[CAS](#) [Article](#) [Google Scholar](#)

29. 29.

Sanamrad, A. et al. Single-particle tracking reveals that free ribosomal subunits are not excluded from the *Escherichia coli* nucleoid. *Proc. Natl Acad. Sci. USA* **111**, 11413–11418 (2014).

[ADS](#) [CAS](#) [Article](#) [Google Scholar](#)

30. 30.

Smid, M. C., Dotters-Katz, S. K., Plongla, R. & Boggess, K. A. *Leptotrichia buccalis*: a novel cause of chorioamnionitis. *Infect. Dis. Rep.* **7**, 5801 (2015).

[Article](#) [Google Scholar](#)

31. 31.

Hou, H., Chen, Z., Tian, L. & Sun, Z. *Leptotrichia trevisanii* bacteremia in a woman with systemic lupus erythematosus receiving high-dose chemotherapy. *BMC Infect. Dis.* **18**, 661 (2018).

[Article](#) [Google Scholar](#)

32. 32.

Kraatz, M., Wallace, R. J. & Svensson, L. *Olsenella umbonata* sp. nov., a microaerotolerant anaerobic lactic acid bacterium from the sheep rumen and pig jejunum, and emended descriptions of *Olsenella*, *Olsenella uli* and *Olsenella profusa*. *Int. J. Syst. Evol. Microbiol.* **61**, 795–803 (2011).

[CAS](#) [Article](#) [Google Scholar](#)

33. 33.

Moffitt, J. R. & Zhuang, X. RNA imaging with multiplexed error-robust fluorescence in situ hybridization (MERFISH). *Methods Enzymol.* **572**, 1–49 (2016).

[CAS](#) [Article](#) [Google Scholar](#)

34. 34.

Chen, K. H., Boettiger, A. N., Moffitt, J. R., Wang, S. & Zhuang, X. Spatially resolved, highly multiplexed RNA profiling in single cells. *Science* **348**, aaa6090 (2015).

[Article](#) [Google Scholar](#)

35. 35.

Singer, E. et al. High-resolution phylogenetic microbial community profiling. *ISME J.* **10**, 2020–2032 (2016).

[Article](#) [Google Scholar](#)

36. 36.

Manz, W., Amann, R., Ludwig, W., Wagner, M. & Schleifer, K.-H. Phylogenetic oligodeoxynucleotide probes for the major subclasses of

proteobacteria: problems and solutions. *Syst. Appl. Microbiol.* **15**, 593–600 (1992).

[Article](#) [Google Scholar](#)

37. 37.

Randall, J. T. & Jackson, S. F. Fine structure and function in *Stentor polymorphus*. *J. Biophys. Biochem. Cytol.* **4**, 807–830 (1958).

[CAS](#) [Article](#) [Google Scholar](#)

[Download references](#)

Acknowledgements

We thank R. M. Williams and J. M. Dela Cruz for assistance with microscopy; A. Douglas, J. McMullen, T. Doerr, J. Peters and M. Petassi for providing materials; and P. S. Burnham, A. P. Cheng, T. Lan and E. Michel for discussions and feedback. This work was supported by an instrumentation grant from the Kavli Institute at Cornell and by US National Institutes of Health (NIH) grants 1DP2AI138242 to I.D.V. and 1R33CA235302 to I.D.V., W.Z. and I.L.B. Imaging data were acquired in the Cornell Biotechnology Resource Center Imaging Facility using the shared, NYSTEM (CO29155)- and NIH (S10OD018516)-funded Zeiss LSM880 confocal and multiphoton microscope.

Author information

Affiliations

1. Nancy E. and Peter C. Meinig School of Biomedical Engineering, Cornell University, Ithaca, NY, USA

Hao Shi, Qiaojuan Shi, Benjamin Grodner, Joan Seling Lenz, Warren R. Zipfel, Ilana Lauren Brito & Iwijn De Vlaminck

Authors

1. Hao Shi

[View author publications](#)

You can also search for this author in [PubMed](#) [Google Scholar](#)

2. Qiaojuan Shi

[View author publications](#)

You can also search for this author in [PubMed](#) [Google Scholar](#)

3. Benjamin Grodner

[View author publications](#)

You can also search for this author in [PubMed](#) [Google Scholar](#)

4. Joan Sesing Lenz

[View author publications](#)

You can also search for this author in [PubMed](#) [Google Scholar](#)

5. Warren R. Zipfel

[View author publications](#)

You can also search for this author in [PubMed](#) [Google Scholar](#)

6. Ilana Lauren Brito

[View author publications](#)

You can also search for this author in [PubMed](#) [Google Scholar](#)

7. Iwijn De Vlaminck

[View author publications](#)

You can also search for this author in [PubMed](#) [Google Scholar](#)

Contributions

H.S. and I.D.V. conceived the study. H.S., W.Z., I.L.B. and I.D.V. contributed to the study design. H.S., performed the *E. coli* experiments. H.S. and J.L.S performed the multispecies community experiments. Q.S. and I.L.B. performed mouse experiments. H.S. performed PacBio sequencing experiments and analysed data. H.S. and B.G. performed HiPR-FISH experiments in mice. H.S. performed HiPR-FISH experiments on the human oral microbiome. H.S. and I.D.V. analysed the data. H.S., W.Z., I.L.B. and I.D.V. wrote the manuscript.

Corresponding authors

Correspondence to [Hao Shi](#) or [Iwijn De Vlaminck](#).

Ethics declarations

Competing interests

H.S. and I.D.V. are inventors on the patent WO 2019/173555, which was filed in September 2019 by Cornell University Center for Technology Licensing and which covers the technical aspects of the manuscript.

Additional information

Peer review information *Nature* thanks Arjun Raj, Carolina Tropini and the other, anonymous, reviewer(s) for their contribution to the peer review of this work.

Publisher's note Springer Nature remains neutral with regard to jurisdictional claims in published maps and institutional affiliations.

Extended data figures and tables

[**Extended Data Fig. 1 Workflow of HiPR-FISH experiments.**](#)

Environmental microbial consortia are first split into two samples. One sample is used to generate full-length 16S amplicon sequences using PCR and PacBio sequencing. The resulting sequence file is used to generate a list of probes, which are purchased from a commercial vendor. The other sample is used for imaging experiments. Fixed samples are hybridized using an encoding hybridization buffer containing the amplified complex probes and read out using a readout hybridization buffer containing fluorescently labelled readout probes. Samples are then embedded and imaged on a standard confocal microscope in the spectral imaging mode. Resulting raw images are registered and segmented. The spectra of individual cells are measured using the raw image and the segmentation image and classified using a machine learning algorithm. Finally, classified images are used for downstream quantitative measurements of microbial spatial associations.

Extended Data Fig. 2 Spectra construction and classification.

a, Fluorescence spectra measured using each laser are concatenated for classification. **b**, Example spectra for two different barcodes. The combined spectra can contain distinct peaks or broad peaks, depending on the fluorophores used for each barcode. **c**, Spectra for the 10 fluorophores used in this study. **d**, Classification algorithm for barcode assignment. Concatenated spectra are projected using UMAP before classified using support vector machines.

Extended Data Fig. 3 Classification accuracy for *E. coli* 1,023-plex barcoding experiment.

a, Classification frequency as a function of Hamming distance for all 1,023 barcodes. Insets show barcodes with detectable error (in orange) and an example of a barcode with no detectable error (in blue). **b**, **c**, Photon counting measurements for Alexa 488 for each pixel (**b**) and across each cell (**c**). **d**, Signal-to-noise ratio calculated using Poisson statistics for the *E. coli* cells under nominal experimental imaging conditions. **e**, Simulated classification error as a function of ribosomal density within individual cells. In box plots (**b**, **c**), the centre lines show the median value, the bounds

of the boxes correspond to the 25th and 75th percentiles and the whiskers extend to $1.5 \times \text{IQR}$.

Extended Data Fig. 4 Probe design pipeline and amplification strategy.

a, Full-length 16S sequences are first grouped by taxa. The consensus sequence for each taxon is used to design probes. Each probe within each taxon is then blasted against the database of full-length 16S sequences. Several probe quality metrics are calculated on the basis of the blast results and are used to select probes. All selected probes are conjugated to the appropriate readout sequences and blasted against the database of full-length 16S sequences to remove probes with any potential mis-hybridization sites owing to the conjugation of the readout sequences. **b**, Schematic for probe synthesis. Complex oligo pools are amplified using limited-cycle PCR. The T7 promoter introduced during PCR allows the templates to be in-vitro-transcribed. Reverse transcription then converts RNA to cDNA. Finally, alkaline hydrolysis removes the RNA strand to generate the final single-stranded DNA probe pool.

Extended Data Fig. 5 Classification accuracy in synthetic communities.

Classification accuracy as a function of Hamming distance for each species of bacteria measured using different barcodes.

Extended Data Fig. 6 Image segmentation workflow and comparison to other methods.

a, A typical raw image of a human plaque biofilm sample averaged along the spectral axis was enhanced using the LNE algorithm before segmentation using the watershed algorithm. Spectra of segmented cells were then used to generate the identification image. Scale bars, 25 μm . **b**, Examples of segmentation comparisons between LNE and existing methods. Scale bars, 25 μm . **c**, Enlarged views highlight advantages of LNE over existing methods at segmenting closely packed cells. Scale bars, 5 μm .

Extended Data Fig. 7 LNE can segment objects with diverse shapes in images collected using different modalities.

a, Raw (left) and segmented (right) images of a longitudinal section of a km fibre³⁷ in a partially contracted *Stentor coeruleus* cell imaged using transmission electron microscopy. **b**, Raw (left) and segmented (right) images of fluorescently labelled actin bundles from chicken muscle imaged using total internal reflection microscopy. Source images are from the Cell Image Library.

Extended Data Fig. 8 Spatio-spectral deconvolution accuracy of simulated merged objects.

a, Heat map of merger detection rates across all 10-bit barcode combinations. Barcode–neighbour combinations not detected in the 1,023-plex *E. coli* mixing experiment are shown in orange. The diagonal corresponds to the correct identification of merged objects with the same barcode as single objects. **b**, Merger detection rate as a function of Hamming distance. The spatio-spectral deconvolution approach can detect 99.6% of all objects with spatially varying barcodes that are more than 1 bit away.

Extended Data Fig. 9 Additional analysis of the gut microbiome images.

a, Heat map of the Pearson correlation between maximum average intensity for all detected barcodes from different FFPE sections of the same mouse gut, with 15 FOVs per FFPE section. **b**, Heat map of Pearson correlation between maximum average intensity for all detected barcodes from different mice, with 14 to 15 FOVs per mouse. **c**, Comparison of imaging and sequencing measurements on mouse gut FFPE tissue sections. **d**, Phylum abundance measurements from images of a clindamycin-treated mouse compared to a control mouse. The clindamycin-treated mouse shows a lower Bacteroidetes to Firmicutes ratio than the control mouse. **e**, Measured Shannon diversity is lower in the clindamycin-treated mouse than the control mouse. The centre lines show the median value, the bounds of

the boxes correspond to the 25th and 75th percentiles and the whiskers extend to $1.5 \times \text{IQR}$. **f**, β -diversity as a function of patch size shows similar trends in the clindamycin-treated mouse and the control mouse. The boxes correspond to 25th and 75th quartile, and the whiskers extend to the most extreme data points. **g**, Bray–Curtis dissimilarity increases as a function of intra-patch distance in both the clindamycin-treated and the control mice. **h**, Volcano plot of significance versus spatial association fold change between ciprofloxacin-treated mice and control mice. Altered spatial associations that are statistically significant after Bonferroni correction are listed.

[Extended Data Fig. 10 Reproducible and recurrent microarchitectures in the oral microbiome.](#)

a, Clusters of *Lautropia* cells observed using different panels of probes. **b**, Two-dimensional UMAP projections of the physical properties of *Lautropia* cells observed using different probe panels overlap in the reduced dimensions. **c**, Additional observed instances of the *Pseudopropionibacterium–Cardiobacterium–Schwartzia* consortium.

Supplementary information

[Supplementary Information](#)

This file contains data access information as well as Supplementary Tables related to fluorescent probes information, cultured cell information, relevant software versions, and image acquisition conditions.

[Reporting Summary](#)

Source data

[Source Data Fig. 3](#)

[Source Data Fig. 4](#)

Rights and permissions

[Reprints and Permissions](#)

About this article



Cite this article

Shi, H., Shi, Q., Grodner, B. *et al.* Highly multiplexed spatial mapping of microbial communities. *Nature* **588**, 676–681 (2020).
<https://doi.org/10.1038/s41586-020-2983-4>

[Download citation](#)

- Received: 24 September 2019
- Accepted: 06 October 2020
- Published: 02 December 2020
- Issue Date: 24 December 2020
- DOI: <https://doi.org/10.1038/s41586-020-2983-4>

Further reading

- [**Bacterial species singled out from a diverse crowd**](#)
 - Jen Nguyen
 - & Carolina Tropini

Nature (2020)

Comments

By submitting a comment you agree to abide by our [Terms](#) and [Community Guidelines](#). If you find something abusive or that does not comply with our terms or guidelines please flag it as inappropriate.

[Access through your institution](#)

[Change institution](#)

[Buy or subscribe](#)

Associated Content

Nature | News & Views

[Bacterial species singled out from a diverse crowd](#)

- Jen Nguyen
- & Carolina Tropini

This article was downloaded by **calibre** from <https://www.nature.com/articles/s41586-020-2983-4>

| [Section menu](#) | [Main menu](#) |

SARS-CoV-2 neutralizing antibody structures inform therapeutic strategies
[Download PDF](#)

- Article
- [Published: 12 October 2020](#)

SARS-CoV-2 neutralizing antibody structures inform therapeutic strategies

- [Christopher O. Barnes](#)¹,
- [Claudia A. Jette](#)¹,
- [Morgan E. Abernathy](#)¹,
- [Kim-Marie A. Dam](#) [ORCID: orcid.org/0000-0002-1416-4757](#)¹,
- [Shannon R. Esswein](#) [ORCID: orcid.org/0000-0002-5142-0190](#)¹,
- [Harry B. Gristick](#)¹,
- [Andrey G. Malyutin](#)²,
- [Naima G. Sharaf](#)³,
- [Kathryn E. Huey-Tubman](#)¹,
- [Yu E. Lee](#)¹,
- [Davide F. Robbiani](#)⁴ nAff⁶,
- [Michel C. Nussenzweig](#)^{4,5},
- [Anthony P. West Jr](#)¹ &
- [Pamela J. Bjorkman](#) [ORCID: orcid.org/0000-0002-2277-3990](#)¹

[Nature](#) volume 588, pages682–687(2020)[Cite this article](#)

- 33k Accesses
- 8 Citations
- 479 Altmetric
- [Metrics details](#)

Subjects

- [Antibodies](#)
- [Cryoelectron microscopy](#)

- [SARS-CoV-2](#)

Abstract

The coronavirus disease 2019 (COVID-19) pandemic presents an urgent health crisis. Human neutralizing antibodies that target the host ACE2 receptor-binding domain (RBD) of the severe acute respiratory syndrome coronavirus-2 (SARS-CoV-2) spike protein^{1,2,3,4,5} show promise therapeutically and are being evaluated clinically^{6,7,8}. Here, to identify the structural correlates of SARS-CoV-2 neutralization, we solved eight new structures of distinct COVID-19 human neutralizing antibodies⁵ in complex with the SARS-CoV-2 spike trimer or RBD. Structural comparisons allowed us to classify the antibodies into categories: (1) neutralizing antibodies encoded by the *VH3-53* gene segment with short CDRH3 loops that block ACE2 and bind only to ‘up’ RBDs; (2) ACE2-blocking neutralizing antibodies that bind both up and ‘down’ RBDs and can contact adjacent RBDs; (3) neutralizing antibodies that bind outside the ACE2 site and recognize both up and down RBDs; and (4) previously described antibodies that do not block ACE2 and bind only to up RBDs⁹. Class 2 contained four neutralizing antibodies with epitopes that bridged RBDs, including a VH3-53 antibody that used a long CDRH3 with a hydrophobic tip to bridge between adjacent down RBDs, thereby locking the spike into a closed conformation. Epitope and paratope mapping revealed few interactions with host-derived *N*-glycans and minor contributions of antibody somatic hypermutations to epitope contacts. Affinity measurements and mapping of naturally occurring and in vitro-selected spike mutants in 3D provided insight into the potential for SARS-CoV-2 to escape from antibodies elicited during infection or delivered therapeutically. These classifications and structural analyses provide rules for assigning current and future human RBD-targeting antibodies into classes, evaluating avidity effects and suggesting combinations for clinical use, and provide insight into immune responses against SARS-CoV-2.

[Download PDF](#)

Main

Neutralizing antibodies (Nabs) against SARS-CoV-2 protect against infection in animal models^{1,3,4,10,11} and are being evaluated for prophylaxis and as therapeutic agents in humans^{7,8}. These antibodies target the SARS-CoV-2 spike (S) trimer^{3,5,10,12,13,14,15,16,17}, a viral glycoprotein that mediates binding to the angiotensin-converting enzyme 2 (ACE2) receptor^{18,19}. The S trimer comprises three copies of an S1 subunit that contains the RBD and three copies of S2, which includes the fusion peptide and transmembrane regions^{20,21}. The RBDs of SARS-CoV-2 and other

coronaviruses exhibit flexibility, such that they bind to ACE2 only when they are in an ‘up’ conformation, compared with the ‘down’ RBD conformation of the closed, prefusion S trimer^{20,21,22,23,24,25}.

Many human NAbs isolated from COVID-19-convalescent donors target the RBD, binding to distinct, sometimes non-overlapping, epitopes^{3,4,5,10,12,13,14,17}. A subset of these antibodies blocks viral entry by binding to the ACE2-binding site on the RBD^{6,11,13,15,26,27}. A family of recurrent ACE2-blocking human NAbs is composed of heavy chains encoded by the *VH3-53* or *VH3-66* gene segment^{3,12,13,16,17,27,28,29}, most of which are known or predicted^{15,26,28,30,31} to exhibit a common RBD binding mode that results from the use of germline-encoded residues within the complementarity-determining regions 1 and 2 (CDRH1 and CDRH2) and a CDRH3 that is shorter than the average length (15 amino acids; IMGT³² complementarity-determining region (CDR) definition) in human antibodies³³. Other SARS-CoV-2 RBD-binding antibodies are encoded by *VH3-30*⁵, and these have also been isolated from donors infected with SARS-CoV³⁴, and antibodies with a variety of the other Vh gene segments^{3,5,10,12,13,14,15,16,17}.

To classify commonalities and differences among RBD-binding human NAbs isolated from COVID-19-convalescent individuals⁵, we solved complexes of NAbs with stabilized (2P and 6P versions)^{35,36} soluble S trimer. Subsequently, we used high-resolution details of the binding orientations of NAb encoded by the *VH1-2*, *VH1-46*, *VH3-30*, *VH3-53*, *VH4-34* and *VH5-51* gene segments to determine rules for binding by four distinct anti-RBD antibody classes (Supplementary Table 2). The NAb chosen for structures are highly potent, achieving 90% neutralization in pseudotype virus assays at concentrations ranging from 22 to 140 ng ml⁻¹ (ref. 5), and thus our structural analyses and classifications directly relate to understanding mechanisms of neutralization and potency differences between human NAb.

Class 1 VH3-53 NAb block ACE2 and bind to up RBDs

We solved Fab and Fab–RBD crystal structures of C102 (Supplementary Table 1), which we compared to our previous²⁶ cryo-electron microscopy (cryo-EM) structure of S trimer complexed with the related human NAb C105 (Extended Data Figs. 1, 2). Both C102 and C105 are VH3-53 NAb with short (11 and 12 residues, respectively) CDRH3 loops (Extended Data Fig. 1g) that were isolated from the same donor⁵. They share structural similarities with each other and with other *VH3-53*-encoded short CDRH3 human NAb structures solved as complexes with RBDs^{12,30,37,38} (Extended Data Fig. 2a). Notably, the C102–RBD structure resembled the analogous portion of the C105–S structure²⁶ (Extended Data Fig. 2a). These results establish that Fab–RBD structures can reproduce interactions with RBDs in the context of an S trimer;

however, Fab–RBD structures do not reveal the state(s) of the antibody-bound RBD in the complex (up versus down) or the potential inter-protomer contacts by Fabs.

Because the C105 Fab bound to either two or three up RBDs on S with no observed interactions with down RBDs or with adjacent RBDs²⁶ (Extended Data Fig. 1f), we used the higher-resolution C102 Fab–RBD structure to deduce a more accurate epitope and paratope than was possible using the C105–S cryo-EM structure with flexible up RBDs (Extended Data Fig. 1a–e). Buried surface area calculations showed that the C102 CDRH3 region had a relatively minor role in the paratope: of 1,045 Å² of buried surface area on the antibody (786 Å² on the heavy chain; 259 Å² on the light chain), CDRH3 accounted for only 254 Å² (Extended Data Fig. 2b). This contrasts with most antibodies in which CDRH3 contributes equally or more to the interface with antigen than the sum of CDRH1 and CDRH2 contributions³⁹. The epitopes on RBD for all available *VH3-53*-encoded short CDRH3 human NAb span the ACE2-binding site^{15,26,28,30,31} and show common RBD-binding interactions, represented by the C102 epitope (Extended Data Fig. 1b–e), which buried 1,017 Å² on RBD (Extended Data Fig. 2b). The ACE2-blocking epitope for these NAb is sterically occluded in the RBD down conformation (Fig. 1b, Extended Data Fig. 1f); therefore, class 1 NAb can only bind to up RBDs, as observed in the C105–S structure²⁶, and as previously discussed, IgGs in this class could crosslink adjacent RBDs within a single trimer to achieve tighter binding through avidity effects²⁶.

Fig. 1: Cryo-EM structure of the C144–S complex illustrates a distinct VH3-53 NAb binding mode.

 **figure1**

a, 3.2 Å cryo-EM density for the C144–S trimer complex revealing C144 binding to a closed (three down RBDs) spike conformation. LC, light chain; HC, heavy chain. **b**, Overlay of C102 Fab (from C102–RBD crystal structure) (Extended Data Fig. 1) and C144 Fab (from C144–S structure) aligned on a RBD monomer. RBD residues

corresponding to the ACE2 epitope (orange-red cartoon) are shown on the same RBD for reference. C144 adopts a distinct conformation relative to the C102-like *VH3-53*-encoded short CDRH3 NAb class, allowing binding to the down RBD conformation on trimeric spike, whereas C102-like NAbs can only bind to up RBDs. **c**, Quaternary epitope of C144 involving bridging between adjacent RBDs via the CDRH3 loop (illustrated as thicker ribbon). **d, e**, Close-up view of CDRH3-mediated contacts on adjacent protomer RBD (dark grey). C144 CDRH3 residues F100_D and W100_E are buried in a hydrophobic pocket comprising the RBD α 1 helix, residue F374_{RBD} and the N343_{RBD} glycan. **f**, Surface representation of C144 epitope (light blue) across two adjacent RBDs. RBD epitope residues (defined as residues containing atom(s) within 4 Å of a Fab atom) are labelled in black.

[Full size image](#)

Class 2 NAbs recognize ‘up’ and ‘down’ RBDs

In addition to the recurrent *VH3-53*-encoded short CDRH3 NAb structures, a small subset of potently neutralizing *VH3-53*-encoded antibodies use longer CDRH3 regions^{5,12} (more than 15 residues, IMGT definition³²) (Extended Data Fig. 1g). A recent structure of a RBD complexed with a *VH3-53*-encoded long CDRH3 human NAb (COVA2-39) revealed a different RBD binding mode³⁸, thus confirming predictions that binding with a C102-like interaction requires a short CDRH3^{26,30}. To further determine molecular mechanisms for binding of *VH3-53*-encoded long CDRH3 human NAbs, we solved a 3.2 Å cryo-EM structure of C144 (encoded by the *VH3-53* and *VL2-14* gene segments; 25-residue CDRH3) bound to an S trimer³⁶ (Extended Data Fig. 3). Despite the ability of ligand-free stabilized S trimers to adopt up RBD conformations³⁶ and modelling suggesting the C144 binding site would be accessible on up RBDs (Fig. 1b), the C144–S structure revealed three C144 Fabs bound to a completely closed S with three down RBDs (Fig. 1a). The C144 binding mode differs from class 1 NAbs, the binding orientation of which is incompatible with down RBD conformations (Fig. 1b). In addition, the binding orientation observed for C144 differs from the binding described for COVA2-39, the RBD epitope of which is predicted to be accessible only on up RBDs³⁸ owing to steric hindrances imposed on the light chain by the N343_{RBD}-associated glycan on the adjacent RBD (Extended Data Fig. 1h). Despite differences in orientation, the RBD epitopes of C144, C102 and COVA2-39 overlap with the ACE2-binding site, which suggests a neutralization mechanism that involves direct competition with ACE2 (Fig. 1b).

Despite overlapping with the ACE2-binding site on up RBDs, an interesting feature of C144 binding is that its long CDRH3 bridges between adjacent down RBDs to lock the spike glycoprotein into a closed, prefusion conformation, providing an additional

neutralization mechanism in which S cannot open to engage ACE2 (Fig. 1c, d). The formation of the C144 quaternary epitope is driven by sandwiching CDRH3 residues F100_D and W100_E (in which subscripts denote numbering of the CDRH3 loop) into a hydrophobic RBD cavity at the base of an N-linked glycan attached to N343_{RBD}. The cavity comprises the RBD α 1 helix (337–344), α 2 helix (364–371), and hydrophobic residues (F374_{RBD} and W436_{RBD}) at the edge of the RBD five-stranded β -sheet (Fig. 1e, f). In contrast to the CDRH3s of class 1 *VH3-53*-encoded short CDRH3 NAbs, the C144 CDRH3 contributed to most (approximately 60%) of the paratope and buried 330 Å² of surface area on the adjacent RBD (Extended Data Fig. 2b), rationalizing observed escape at L455_{RBD} (Fig. 1f) in C144 selection experiments⁴⁰. Despite adjacent CDRH3 hydrophobic residues (F100_D and W100_E) likely to be solvent-exposed before antigen binding, C144 IgG showed no evidence of non-specific binding in a polyreactivity assay (Extended Data Fig. 1i).

Given the unusual binding characteristics of C144, we investigated whether antibodies that showed similar S binding orientations in low-resolution negative-stain electron microscopy reconstructions⁵ use similar neutralization mechanisms. We characterized Fab–S cryo-EM structures (overall resolutions from 3.4 to 3.8 Å) of potent NAbs (C002, C104, C119 and C121) predicted to compete with ACE2 binding⁵, which varied in their use of V gene segments and CDRH3 lengths (Fig. 2, Extended Data Figs. 3, 4, Extended Data Table 1). Fab–S cryo-EM structures of these class 2 NAb showed bound RBDs in both up or down conformations, consistent with observations of similar human NAb from negative-stain electron microscopy^{5,12} and single-particle cryo-EM studies^{10,34,41}. By contrast, the C144–S structure showed Fabs bound only to down RBDs (Fig. 1), which suggests that C144 binding requires recognition of the closed S trimer, or that C144 Fab(s) initially bound to up RBD(s) could trap the closed (three RBDs down) S conformation through CDRH3-mediated interactions between adjacent RBDs.

Fig. 2: Cryo-EM structures of class 2 C002 and C121 NAb show binding to up and down RBDs.

 **figure2**

a, b, Cryo-EM densities for C002–S (**a**; 3.4 Å) and C121–S (**b**; 3.7 Å) complexes, revealing binding of C002 or C121 to both down and up RBDs. Inset, alignment of C002 and C121 Fabs on the same RBD. ACE2 is represented as a green surface for reference. **c, d**, Surface representations of C002 epitope (orange, **c**) and C121 epitope (purple, **d**) on the RBD surface (grey). RBD epitope residues (defined as residues containing atom(s) within 4 Å of a Fab atom) are labelled in black. **e**, C002 forms inter-protomer contacts via binding to an adjacent up RBD conformation on the surface of the trimer spike (also observed for class 2 C121–S, C119–S and C104–S structures) (Extended Data Fig. 5). Red box shows close-up of adjacent up RBD and C002 light-chain interface.

[Full size image](#)

To understand commonalities of class 2 RBD epitopes better, we further analysed two additional potent human NAbs, C002 (encoded by *VH3-30* and *VK1-39* gene segments; 17-residue CDRH3, half-maximal inhibitory concentration (IC_{50}) = 8.0 ng ml⁻¹)⁵ and C121 (encoded by *VH1-2* and *VL2-23* gene segments; 23-residue CDRH3, IC_{50} = 6.7 ng ml⁻¹)⁵, for which cryo-EM Fab–S structures were solved to 3.4 Å and 3.6 Å, respectively (Fig. 2a, b), using crystal structures of unbound C002 and C121 Fabs for fitting (Supplementary Table 1). The C002 and C121 RBD epitopes are focused on the receptor-binding ridge, overlapping with polar and hydrophobic residues along the flat face of the RBD responsible for ACE2 interactions (Fig. 2c–e). Similar to C144, NAb C002 and C121 buried most of their RBD epitopes against heavy-chain CDR loops, with light-chain CDR loops engaging the receptor-binding ridge (Fig. 3). Notably, Fab–S structures of C002, C121, C119 and C104 revealed a quaternary epitope involving an adjacent RBD (Extended Data Figs. 3, 4, 5a–c), albeit distinct from the quaternary binding of C144 (Fig. 1c–e). The C002/C121/C119/C104 type of secondary interaction was only observed when a Fab was bound to a down RBD and adjacent to an up RBD. The extent of secondary interactions varied depending on the antibody pose (Extended Data Fig. 5a–c). Bridging interactions between adjacent up and down RBDs would not allow the two Fabs of a single IgG to bind simultaneously to an S trimer. However, this class of antibodies could support bivalent interactions between two adjacent down RBDs (Extended Data Fig. 5h, Extended Data Table 1).

Fig. 3: Details of common RBD interactions among class 2 human NAbs.

 **figure3**

a–l, Conserved interactions between the RBD and CDRs of class 2 NAbs as observed for C144 (HC, cyan; LC, sky blue) (**a–d**), C002 (HC, dark orange; LC, light orange) (**e–h**), and C121 (HC, purple; LC, pink) (**i–l**). Primary and secondary epitopes on adjacent down RBDs are shown for C144. Secondary epitopes for C002 and C121, which require adjacent up RBDs, are shown in Extended Data Fig. [5](#). RBDs are grey; potential hydrogen bonds and π – π stacking interactions (**d**, Y33_{LC} and F486_{RBD}; **h**, Y92_{LC} and F486_{RBD}; **l**, Y91_{LC} and F486_{RBD}) are indicated by dashed lines.

[Full size image](#)

Characterization of the highest resolution interface (C002–S structure) showed C002 light-chain framework regions 1 and 2 (FWR1 and FWR2) interfaced with the RBD residues comprising the five-stranded β -sheet and α -helix that spans residues 440–444 (Fig. [2e](#)), which is typically located near the three-fold axis of a closed S trimer. In addition to contacting neighbouring RBDs, inter-protomer engagement with the N165_{NTD}-associated glycan in the N-terminal domain (NTD) was observed for the class 2 NAb BD23^{[13](#)}. If fully processed, the N165_{NTD} glycan could adopt a

conformation that would allow interactions with the heavy-chain FWR3 and CDRH1 (Fig. 2e). However, in the structures reported here, we did not observe N165_{NTD} glycan density beyond the initial *N*-acetylglucosamine.

Given differences in class 2 human NAb V gene segments, CDRH3 lengths and antibody poses, we investigated sequence features that drive conserved interactions. Sequence differences between SARS-CoV-2 and SARS-CoV RBD, including at positions 486_{RBD} and 493_{RBD} (F and Q, respectively, in SARS-CoV-2), in the ACE2 receptor-binding motif allowed more favourable ACE2 binding to the SARS-CoV-2 RBD⁴². Analysis of interactions by C144, C002 and C121 revealed common interactions with these residues and also for E484_{RBD} by both antibody heavy-chain and light-chain residues (Fig. 3). In particular, class 2 NAb interactions with F486_{RBD} mimicked ACE2 interactions, in that F486_{RBD} buries into a hydrophobic pocket typically involving CDRL1 or CDRL3 tyrosine residues⁴³ (Fig. 3d, h, l). Mimicking of the ACE2 F486 binding pocket by SARS-CoV-2 human Nabs was observed across different light-chain V gene segments (Extended Data Table 1), which suggests that there is no restriction in light-chain V gene segment usage for class 2 Nabs. Notably, a germline-encoded feature described for VH3-53-encoded short CDRH3 class 1 Nabs, the CDRH2 SXXS motif, is also found in other class 2 Nabs (for example, C121 and C119) despite different Vh gene segment usage. Similar to VH3-53 Nabs C144 and COVA2-39, the C121 CDRH2 SXXS motif forms a potential hydrogen-bond network with E484_{RBD} (Fig. 3b, j).

Overall, these results suggest a convergent mode of recognition by germline-encoded residues across diverse Vh/Vl gene segments for SARS-CoV-2, which may contribute to low levels of somatic hypermutation observed for these human Nabs (Extended Data Fig. 4i–n, Extended Data Table 1).

Class 3 NAbs bind outside the ACE2-binding site

C135 is a potent NAb that showed distinct binding properties from class 1, 2 and 4 Nabs, the latter of which bind a highly conserved buried epitope that is only accessible in up RBD conformations (Extended Data Table 1). To evaluate the mechanism of C135-mediated neutralization of SARS-CoV-2, we solved the cryo-EM structure of a C135–S complex to 3.5 Å (Fig. 4a, Extended Data Fig. 6), using an unbound C135 crystal structure for fitting (Supplementary Table 1). The structure revealed three C135 Fabs bound to an S trimer with two down and one up RBD, although the C135-bound up RBD conformation was weakly resolved and therefore not modelled. C135 recognizes a similar glycopeptidic epitope to the cross-reactive SARS-CoV NAb S309³⁴, focusing on a region of the RBD near the N343 glycan and non-overlapping with the ACE2-binding site (Fig. 4b, Extended Data Fig. 6c, d).

Despite differences in binding orientations between C135 and S309, targeting of the RBD epitope was mainly Vh-mediated (the surface area buried by RBD on the C135 heavy chain represented approximately 480 \AA^2 of the 700 \AA^2 total buried surface area) and included interactions with the core fucose moiety of the N343_{RBD} glycan. The smaller C135 footprint relative to S309 (approximately 700 \AA^2 versus $1,150 \text{ \AA}^2$ buried surface area, respectively) (Extended Data Fig. [6c, d](#)) focused on interactions with R346_{RBD} and N440_{RBD}, which are engaged by residues from heavy-chain and light-chain CDRs (Fig. [4c, d](#)) and are not conserved between SARS-CoV-2 and SARS-CoV RBDs, rationalizing the lack of SARS-CoV cross-reactivity observed for C135⁵.

Fig. 4: Cryo-EM structure of S complexed with the class 3 (non-ACE2 blocking) human NAb C135.



a, 3.5 Å cryo-EM density of C135–S complex. **b**, Composite model of C135–RBD (blue and grey, respectively) overlaid with the SARS-CoV-2 NAb S309 (sand; PDB code 6WPS) and soluble ACE2 (green; PDB code 6M0J). The model was generated by aligning on 188 RBD Ca atoms. **c**, **d**, C135 CDRH (dark blue) and CDRL (light blue) interactions with R346_{RBD} (**c**) and N440_{RBD} (**d**). Potential π–π stacking interactions (**c**) and hydrogen bonds (**c**, **d**) are illustrated by dashed black lines. **e**, **f**, Model of RBD interactions of NAbs C135 (class 3) and C144 (class 2), demonstrating that both Fabs can bind simultaneously to a single monomeric RBD (**e**), but would clash if bound to adjacent down RDBs on S trimer (**f**). Steric clashes indicated by a red and yellow star in **f**. **g**, **h**, Model of RBD interaction of NAbs C135 (class 3) and C119 (class 2) demonstrating that both Fabs cannot bind simultaneously to a single monomeric RBD (**g**), but do not clash if bound to adjacent down RDBs on S trimer (**h**). Steric clashes indicated by a red and yellow star in **g**.

[Full size image](#)

The discovery of class 3 NAbs such as C135 and S309 that were raised during SARS-CoV-2 or SARS-CoV natural infections, respectively, and bind outside of the ACE2-binding site, provides the potential for additive neutralization effects when combined with NAbs that block ACE2, while also limiting viral escape^{1,40}. A pair of antibodies in human clinical trials that includes REGN10987⁸, a human NAb that binds distal to the ACE2-binding site, prevented SARS-CoV-2 viral escape in vitro, but did not show synergistic neutralization⁶. Comparison of C135 and REGN10987 interactions with S showed similarities in epitopes (interactions focused on R346_{RBD} and N440_{RBD}) (Extended Data Fig. [7c,f](#)). However, REGN10987 binding would sterically hinder ACE2 interactions, whereas C135 binding does not (Fig. [4b](#), Extended Data Fig. [6b](#)). Notably, a structure of S complexed with C110 (encoded by the *VH5-51* and *VK1-5* gene segments), isolated from the same donor as the C102 and C105 (class 1) and C119 and C121 (class 2) NAbs⁵, showed a binding pose that resembled that of REGN10987 (Extended Data Fig. [6b,e,f](#)). The C110 epitope showed similarities with both class 3 and class 2 NAbs, binding distal to the ACE2-binding motif, but like REGN10987, could potentially sterically interfere with ACE2 (Extended Data Fig. [7](#)). For each of these class 3 NAbs, the Fab binding pose suggests that inter-protomer crosslinking by a single IgG is not possible (Extended Data Table [1](#)).

Class 3 human NAbs add to the anti-SARS-CoV-2 antibody repertoire and could probably be effectively used in therapeutic combinations with class 1 or 2 NAbs. However, when using structures to predict whether NAbs have overlapping epitopes, it is sometimes not sufficient to only examine Fab–RBD structures or even static images of the S trimer because of the dynamic nature of the spike. Thus, what might appear to be non-overlapping epitopes on an isolated RBD could overlap in some (Fig. [4e,f](#)), but not all (Extended Data Fig. [7](#)), scenarios on a spike trimer, complicating

interpretation of competition experiments using monomeric RBDs and S trimers. The opposite can also be true; that is, two Fabs predicted to be accommodated on a trimer could clash on an RBD monomer (Fig. 4g,h). Finally, adjacent monomers in different orientations could accommodate different antibodies that target overlapping sites (Extended Data Fig. 7).

RBD substitutions affect NAb binding

Vesicular stomatitis virus (VSV) reporter viruses pseudotyped with the SARS-CoV-2 S protein can escape by mutation(s) from the C121, C135 or C144 NAbs⁴⁰ that we used for structural studies. RBD mutations that were selected in response to antibody pressure correlated with the epitopes mapped from the structures of their Fabs complexed with the S trimer (Figs. 1, 2, 4).

To further assess the effects of these mutations and other RBD substitutions, we assayed NAbs for which we obtained structural information (eight from this study; C105–S complex previously described²⁶) for binding to mutated RBD proteins. The RBD mutants included two that induced escape from the class 3 hNAb C135 (R346S and N440K)⁴⁰ (Fig. 4c,d), one found in circulating isolates⁴⁴ that conferred partial resistance to C135 (N439K)⁴⁰ (Fig. 4d), a circulating variant (A475V) that conferred resistance to class 1 and 2 VH3-53 NAbs⁴⁴, two that induced escape from C121 or C144 (E484K and Q493R)⁴⁰ (Fig. 3), and a circulating variant that conferred partial resistance to C121 (V483A)⁴⁰. Kinetic and equilibrium constants for the original and mutant RBDs were derived from surface plasmon resonance (SPR) binding assays in which RBDs were injected over immobilized IgGs. Loss of binding affinity was consistent with RBD mutations that conferred escape (Extended Data Fig. 8). Comparing effects of point mutations between NAb classes showed that point mutations leading to a loss of binding for NAbs within one class did not affect NAbs in a different class, indicating that antibody pressure that leads to escape from one NAb class would be unlikely to affect a different class. These results suggest a therapeutic strategy involving human NAbs of different classes for monoclonal NAb treatment of individuals infected with SARS-CoV-2.

Conclusions

Here we report structural, biophysical and bioinformatics analyses of SARS-CoV-2 NAbs (Extended Data Fig. 9), providing information for interpreting correlates of protection for clinical use. The structures reveal a wealth of unexpected interactions of NAbs with the spike protein, including five antibodies that reach between adjacent RBDs on the protomers of a single trimer. A notable example of bridging between spike protomers involved the human C144 NAb that uses a long CDRH3 with a

hydrophobic tip to reach across to an adjacent RBD, resulting in all three RBDs on the spike trimer being locked into a closed conformation. This example, and four other NAbs that contact adjacent RBDs, demonstrates that crystal structures of Fab–monomeric RBD complexes, although informative for defining primary epitopes on one RBD, do not reveal how antibodies recognize the flexible up or down RBD conformations on the spike trimer that are targeted for neutralization on a virus. Indeed, our cryo-EM structures of Fab–spike trimer complexes showed all possible up and down combinations of recognized RBDs, with structures showing either three or two Fabs bound per trimer. By analysing approach angles of Fabs bound to RBDs on spike trimers, we predicted whether an IgG can bind to a single spike trimer to gain potency through avidity, which would also render the antibody more resistant to spike mutations. In addition, structural information allowed us to assess RBD mutants that arose in circulating viral isolates and/or were obtained by *in vitro* selection. Together, this study provides a blueprint for the design of antibody cocktails for therapeutic agents and potential spike-based immunogens for vaccines.

Methods

No statistical methods were used to predetermine sample size. The experiments were not randomized, and investigators were not blinded to allocation during experiments and outcome assessment.

Cell lines

Expi293F cells (GIBCO) for protein expression were maintained at 37 °C and 8% CO₂ in Expi293 Expression medium (GIBCO), transfected using Expi293 Expression System Kit (GIBCO) and maintained under shaking at 130 rpm. Cell lines were not specifically authenticated, but lines tested negative for contamination with mycoplasma.

Protein expression

Expression and purification of SARS-CoV-2 ectodomains were conducted as previously described²⁶. In brief, constructs encoded the SARS-CoV-2 S ectodomain (residues 16–1206 of the early SARS-CoV-2 GenBank MN985325.1 sequence isolate with 2P³⁵ or 6P³⁶ stabilizing mutations, a mutated furin cleavage site between S1 and S2, a C-terminal TEV site, foldon trimerization motif, octa-His tag, and AviTag) were used to express soluble SARS-CoV-2 S ectodomains. Constructs encoding the SARS-CoV-2 RBD from GenBank MN985325.1 (residues 331–524 with C-terminal octa-His tag and AviTag) and mutant RBDs were made as described²⁶, SARS-CoV-2 2P S, 6P S, and RBD proteins were purified from the supernatants of transiently transfected

Expi293F cells (Gibco) by nickel affinity and size-exclusion chromatography²⁶. Peak fractions were identified by SDS-PAGE, and fractions corresponding to S trimers or monomeric RBDs were pooled and stored at 4 °C. Fabs and IgGs were expressed, purified, and stored as previously described^{45,46}.

X-ray crystallography

Crystallization trials were carried out at room temperature using the sitting drop vapour diffusion method by mixing equal volumes of a Fab or Fab–RBD complex and reservoir using a TTP LabTech Mosquito robot and commercially available screens (Hampton Research). Crystals were obtained in 0.2 M ammonium sulfate, 20% (w/v) PEG 3350 (C102 Fab), 0.2 M sodium citrate tribasic, 20% (w/v) PEG 3350 (C102–RBD), 0.2 M lithium sulfate monohydrate, 20% (w/v) PEG 3350 (C002 Fab), 0.04 M potassium phosphate, 16% (w/v) PEG 8000, 20% (v/v) glycerol (C135 Fab), 0.2 M ammonium citrate pH 5.1, 20% PEG 3350 (C121 Fab), or 0.2 M sodium tartrate dibasic dihydrate pH 7.3, 20% (w/v) PEG 3350 (C110 Fab). A C135 Fab crystal was directly looped and cryopreserved in liquid nitrogen. Other crystals were quickly cryoprotected in a mixture of well solution with 20% glycerol and then cryopreserved in liquid nitrogen.

X-ray diffraction data were collected for Fabs and the Fab–RBD complex at the Stanford Synchrotron Radiation Lightsource (SSRL) beamline 12-1 on a Eiger X 16 M pixel detector (Dectris) at a wavelength of 1.0 Å. Data from single crystals of C121 Fab and C110 Fab were indexed and integrated in XDS⁴⁷ and merged using AIMLESS v.0.7.4 in CCP4⁴⁸ v.7.0.6 (Supplementary Table 1). Data from single crystals of C102 Fab, C135 Fab and C002 Fab were indexed and integrated using XDS⁴⁷ and merged in Phenix⁴⁹ (v.1.18). Data from a single crystal of C102 Fab–RBD complex were indexed and integrated using XIA2⁵⁰ v.0.3.8 implementing DIALS^{51,52} v.2.2 and merged using AIMLESS in CCP4⁴⁸. For C110 Fab and C121 Fabs, structures were determined by molecular replacement in PHASER⁵³ v.2.8.2 using the coordinates for B38 (PDB 7BZ5) or an inferred germline form of the HIV-1 NAb IOMA⁵⁴ inferred germline (unpublished), respectively, after removing CDR loops as a search model. For C002 Fab, C102 Fab, C102 Fab–RBD and C135 Fab, structures were determined by molecular replacement in PHASER⁵³ using B38 Fab coordinates (PDB 7BZ5) after trimming heavy and light chain variable domains using Sculptor⁵⁵ v.2.0 (and for the C102 Fab–RBD data, also RBD coordinates from PDB code 7BZ5) as search models. Coordinates were refined using Phenix⁴⁹ and cycles of manual building in Coot⁵⁶ (Supplementary Table 1).

Cryo-EM sample preparation

Purified Fabs were mixed with the SARS-CoV-2 S 2P trimer³⁵ or SARS-CoV-2 S 6P trimer³⁶ (1.1:1 molar ratio Fab per protomer) to a final Fab–S complex concentration of 2–3 mg ml⁻¹ and incubated on ice for 30 min. Immediately before deposition of 3 µl of complex onto a 300 mesh, 1.2/1.3 UltrAuFoil grid (Electron Microscopy Sciences) that had been freshly glow-discharged for 1 min at 20 mA using a PELCO easiGLOW (Ted Pella), a 0.5% (w/v) octyl-maltoside, fluorinated solution (Anatrace) was added to each sample to a final concentration of 0.02%. Samples were vitrified in 100% liquid ethane using a Mark IV Vitrobot (Thermo Fisher) after blotting at 22 °C and 100% humidity for 3 s with Whatman No. 1 filter paper.

Cryo-EM data collection and processing

Single-particle cryo-EM data were collected on a Titan Krios transmission electron microscope (Thermo Fisher) operating at 300 kV for all Fab–S complexes except for C144–S, which was collected on a Talos Arctica (Thermo Fisher) operating at 200 kV. Movies were collected using SerialEM v.3.7 automated data collection software⁵⁷ with beam-image shift over a 3-by-3 pattern of 1.2 µm holes with 1 exposure per hole. Movies were recorded in super-resolution mode on a K3 camera (Gatan) for the C144–S dataset on the Arctica (0.435 Å per pixel) or on a K3 behind BioQuantum energy filter (Gatan) with a 20 eV slit on the Krios (0.418 Å per pixel) for all other datasets. Data collections parameters are summarized in Supplementary Table 2. In general, the data-processing workflow described below was performed for all datasets in cryoSPARC v.2.15⁵⁸.

Cryo-EM movies were patch motion corrected for beam-induced motion including dose weighting within cryoSPARC⁵⁸ after binning super-resolution movies. The non-dose-weighted images were used to estimate CTF parameters using CTFFIND4⁵⁹ v.4.1.14 or with cryoSPARC implementation of the Patch CTF job, and micrographs with power spectra that showed poor CTF fits or signs of crystalline ice were discarded. A

subset of images were randomly selected and used for reference-free particle picking using Blob picker in cryoSPARC⁵⁸. Particles were subjected to 2D classification and the best class averages that represented different views were used to generate 3 ab initio models. The particles from the best classes were used in another 2D classification job, and the best set of unique views was used as templates for particle picking on the full set of images. Initial particle stacks were extracted, downsampled twice, and used in heterogeneous refinement against the three ab initio volumes generated with the smaller dataset (ab initio volumes used were interpreted as a Fab–S complex, free Fab or dissociated S protomers, and junk/noise class). Particles assigned to the Fab–S volume were further cleaned via iterative rounds of 2D classification to select class averages that displayed unique views and secondary structural elements. Resulting particle stacks were homogenously refined before being split into nine individual exposure groups based upon collection holes. Per particle CTF and aberration corrections were performed and the resulting particles further 3D refined. Additional processing details are summarized in Supplementary Table 2.

Given the known heterogeneity of spike trimers^{20,21}, homogenously refined particles were used for 3D classification in cryoSPARC⁵⁸ (ab initio job: $k = 4$ classes, class similarity = 0.3). This typically resulted in one or two majority Fab–S complexes, with the other minority populated classes representing junk or unbound S trimer. Particles from the good class(es) were further subjected to 3D classification (ab initio job: $k = 4$, class similarity = 0.7) to attempt to separate various Fab–S complex states. If several states were identified (as observed for the C002–S and C121–S complexes), particles were heterogeneously refined, followed by re-extraction without binning (0.836 Å per pixel) before homogeneous refinement of individual states. For all other datasets, most particles represented one state that was homogenously refined after re-extraction without binning.

Particle stacks for individual states were non-uniform refined with C1 symmetry and a dynamic mask. To improve resolution at the Fab–RBD interfaces, volumes were segmented in Chimera⁶⁰ and the regions corresponding to the NTD and RBD domains of the S1 subunit and the Fab Vh–Vl domains were extracted and used to generate a soft mask (5-pixel

extension, 10-pixel soft cosine edge). Local refinements with the mask resulted in modest improvements of the Fab–RBD interface, which allowed for fitting and refinement of this region. The particles were then subjected to CTF refinement and aberration correction, followed by a focused, non-uniform refinement with polished particles imposing *C*1 symmetry (except for the C144–S complex, in which *C*3 symmetry was used). Final overall resolutions were according to the gold-standard FSC⁶¹. Details of overall resolution and locally refined resolutions according to the gold-standard FSC⁶¹ can be found in Supplementary Table 2.

Cryo-EM structure modelling and refinement

Coordinates for initial complexes were generated by docking individual chains from reference structures into cryo-EM density using UCSF Chimera⁶² v.1.13. The following coordinates were used: SARS-CoV-2 S trimers: PDB codes 6VXX, 6VYB and 6XKL, up RBD conformations: PDB codes 7BZ5 or 6W41, and unbound C102, C002, C110, C121, C135 Fab structures (this study) (Supplementary Table 1). Initial models were then refined into cryo-EM maps using one round of rigid body refinement followed by real space refinement. Sequence-updated models were built manually in Coot⁵⁶ v.0.8.9 and then refined using iterative rounds of refinement in Coot⁵⁶ and Phenix⁴⁹. Glycans were modelled at potential *N*-linked glycosylation sites in Coot⁵⁶ using ‘blurred’ maps processed with a variety of B-factors⁶³. Validation of model coordinates was performed using MolProbity⁶⁴ (Supplementary Table 2).

Structural analyses

CDR lengths were calculated based on IMGT definitions³². Structure figures were made with PyMOL (v.2.2 Schrodinger, LLC) or UCSF ChimeraX⁶⁰ v.1.0. Local resolution maps were calculated using cryoSPARC v.2.15⁵⁸. Buried surface areas were calculated using PDBePISA v.1.48⁶⁵ and a 1.4 Å probe. Potential hydrogen bonds were assigned as interactions that were less than 4.0 Å and with an A-D-H angle above 90°. Potential van der Waals interactions between atoms were assigned as interactions that were less than 4.0 Å. Hydrogen bond and van der Waals interaction

assignments are tentative due to resolution limitations. r.m.s.d. calculations following pairwise C α alignments were done in PyMOL without rejecting outliers. Criteria for epitope assignments are described in figure legends.

To evaluate whether intra-spike crosslinking by an IgG binding to a single spike trimer was possible (Extended Data Table 1), we first measured the C α distance between a pair of residues near the C termini of adjacent Fab Ch1 domains (residue 222 of the heavy chain on each Fab) (Extended Data Fig. 5h). We compared this distance to the analogous distances in crystal structures of intact IgGs (42 Å, PDB code 1HZH; 48 Å, PDB code 1IGY; 52 Å, PDB code 1IGT). To account for potential influences of crystal packing in these measurements, as well as flexibility in the Vh–Vl/Ch1–Cl elbow bend angle and uncertainties in Ch1–Cl domain placement in Fab–S cryo-EM structures, we set a cut-off of ≤ 65 Å for this measured distance as possibly allowing for a single IgG to include both Fabs. Entries in the ‘potential IgG intra-spike binding’ column in Extended Data Table 1 are marked ‘no’ if all of the adjacent Fabs in cryo-EM classes of that structure are separated by more than 65 Å for this measured distance. Entries in the ‘potential IgG intra-spike binding’ column in Extended Data Table 1 are marked as ‘yes’ if at least one pair of the adjacent Fabs in cryo-EM classes of that structure are separated by ≤ 65 Å for this measured distance.

SPR binding experiments

SPR experiments were performed using a Biacore T200 instrument (GE Healthcare). IgGs were immobilized on a CM5 chip by primary amine chemistry (Biacore manual) to a final response level of approximately 3,000 resonance units. Concentration series of the original SARS-CoV-2 RBD and RBD mutants (six fourfold dilutions starting from a top concentration of 1,000 nM) were injected at a flow rate of 30 μ l min over immobilized IgGs for a contact time of 60 s, followed by an injection of 0.01 M HEPES, pH 7.4, 0.15 M NaCl, 3 mM EDTA, 0.005% (v/v) surfactant P20 buffer for a dissociation time of 300 s. Binding reactions were allowed to reach equilibrium, and K_d values were calculated from the ratio of association and dissociation rates ($K_d = k_d/k_a$) derived from a 1:1 binding model (C002, C102, C105, C110 and C119 (except for C119 mutant E484K)), C121, C135 and C144), or from a two-state binding model

($K_d = k_{d1}/k_{a1} \times k_{d2}/[k_{d2} + k_{a2}]$) (C104 and C119 mutant E484K). Kinetic constants were calculated using Biacore T200 Evaluation Software v.3.2 using a global fit to all curves in each dataset. Flow cells were regenerated with 10 mM glycine, pH 2.0, at a flow rate of 90 $\mu\text{l min}^{-1}$.

Polyreactivity assays

IgGs were evaluated for off-target interactions by measuring binding to baculovirus extracts containing non-specific proteins and lipids as described⁵⁹. The assays were automated on a Tecan Evo2 liquid handling robot fitted with a Tecan Infinite M1000 plate reader capable of reading luminescence. Maxisorb 384-well plates (Nunc) were adsorbed overnight with a 1% preparation of recombinant baculovirus particles generated in Sf9 insect cells⁶⁶. The adsorbed plate was blocked with 0.5% bovine serum albumin (BSA) in PBS, then incubated with 20 μl of a 1.0 $\mu\text{g ml}^{-1}$ solution of IgG in PBS for 3 h. Polyreactivity was quantified by detecting bound IgG using an HRP-conjugated anti-human IgG secondary antibody (SouthernBiotech) at a 1:5,000 dilution and SuperSignal ELISA Femto Maximum Sensitivity Substrate (Thermo Scientific). RLU values were measured at 475 nm in the integrated plate reader. Engineered human anti-HIV-1 IgGs previously demonstrated to exhibit high levels of polyreactivity (NIH45-46(G54W) and 45-46m2)^{60,61} were used as positive controls. NIH45-46, which exhibited intermediate polyreactivity⁶², was also evaluated for comparisons. Negative control IgGs with low polyreactivity included the human HIV-1 antibodies N6⁶³ and 3BNC117⁶² and BSA. RLU values were plotted in GraphPad Prism v8.4.3 and presented as the mean and standard deviation of triplicate measurements ($n = 3$ biological replicates) with results for individual experiments shown as circles in Extended Data Fig. 1i.

Reporting summary

Further information on research design is available in the [Nature Research Reporting Summary](#) linked to this paper.

Data availability

The atomic models generated from X-ray crystallographic studies of the C102–RBD complex, C102 Fab, C002 Fab, C110 Fab, C121 Fab and C135 Fab have been deposited at the Protein Data Bank (PDB) under accession codes [7K8M](#), [7K8N](#), [7K8O](#), [7K8P](#), [7K8Q](#) and [7K8R](#), respectively. The atomic models and cryo-EM maps generated from cryo-EM studies of the C002–S 2P (state 1), C002–S 2P (state 2), C104–S 2P, C110–S 2P, C119–S 2P, C121–S 2P (state 1), C121–S 2P (state 2), C135–S 2P and C144–S 6P complexes have been deposited at the PDB and the Electron Microscopy Data Bank (EMDB) under the following accession codes: PDB [7K8S](#), [7K8T](#), [7K8U](#), [7K8V](#), [7K8W](#), [7K8X](#), [7K8Y](#), [7K8Z](#) and [7K90](#); EMD [EMD-22729](#), [EMD-22730](#), [EMD-22731](#), [EMD-22372](#), [EMD-22733](#), [EMD-22734](#), [EMD-22735](#), [EMD-22736](#) and [EMD-22737](#).

References

1. 1.

Baum, A. et al. REGN-COV2 antibody cocktail prevents and treats SARS-CoV-2 infection in rhesus macaques and hamsters. *Science* <https://doi.org/10.1126/science.abe2402> (2020).

2. 2.

Baum, A. et al. Antibody cocktail to SARS-CoV-2 spike protein prevents rapid mutational escape seen with individual antibodies. *Science* **369**, 1014–1018 (2020).

[CAS](#) [PubMed](#) [Google Scholar](#)

3. 3.

Rogers, T. F. et al. Isolation of potent SARS-CoV-2 neutralizing antibodies and protection from disease in a small animal model. *Science* **369**, 956–963 (2020).

[CAS](#) [PubMed](#) [PubMed Central](#) [Google Scholar](#)

4. 4.

Zost, S. J. et al. Potently neutralizing and protective human antibodies against SARS-CoV-2. *Nature* **584**, 443–449 (2020).

[CAS](#) [PubMed](#) [Google Scholar](#)

5. 5.

Robbiani, D. F. et al. Convergent antibody responses to SARS-CoV-2 in convalescent individuals. *Nature* **584**, 437–442 (2020).

[CAS](#) [PubMed](#) [PubMed Central](#) [Google Scholar](#)

6. 6.

Hansen, J. et al. Studies in humanized mice and convalescent humans yield a SARS-CoV-2 antibody cocktail. *Science* **369**, 1010–1014 (2020).

[CAS](#) [PubMed](#) [PubMed Central](#) [Google Scholar](#)

7. 7.

US National Library of Medicine. A study of LY3819253 (LY-CoV555) in preventing SARS-CoV-2 infection and COVID-19 in nursing home residents and staff (BLAZE-2). ClinicalTrials.gov <https://clinicaltrials.gov/ct2/show/NCT04497987> (2020).

8. 8.

NIH. Clinical trials of monoclonal antibodies to prevent COVID-19 now enrolling. <https://www.nih.gov/news-events/news-releases/clinical-trials-monoclonal-antibodies-prevent-covid-19-now-enrolling> (2020).

9. 9.

Yuan, M. et al. A highly conserved cryptic epitope in the receptor binding domains of SARS-CoV-2 and SARS-CoV. *Science* **368**, 630–633 (2020).

[ADS](#) [CAS](#) [PubMed](#) [PubMed Central](#) [Google Scholar](#)

10. 10.

Liu, L. et al. Potent neutralizing antibodies against multiple epitopes on SARS-CoV-2 spike. *Nature* **584**, 450–456 (2020).

[CAS](#) [Google Scholar](#)

11. 11.

Kreye, J. et al. A SARS-CoV-2 neutralizing antibody protects from lung pathology in a COVID-19 hamster model. Preprint at <https://doi.org/10.1101/2020.08.15.252320> (2020).

12. 12.

Brouwer, P. J. M. et al. Potent neutralizing antibodies from COVID-19 patients define multiple targets of vulnerability. *Science* **369**, 643–650 (2020).

[CAS](#) [PubMed](#) [PubMed Central](#) [Google Scholar](#)

13. 13.

Cao, Y. et al. Potent neutralizing antibodies against SARS-CoV-2 identified by high-throughput single-cell sequencing of convalescent patients' B cells. *Cell* **182**, 73–84 (2020).

[CAS](#) [PubMed](#) [PubMed Central](#) [Google Scholar](#)

14. 14.

Kreer, C. et al. Longitudinal isolation of potent near-germline SARS-CoV-2-neutralizing antibodies from COVID-19 patients. *Cell* **182**, 843–854 (2020).

[CAS](#) [PubMed](#) [PubMed Central](#) [Google Scholar](#)

15. 15.

Shi, R. et al. A human neutralizing antibody targets the receptor-binding site of SARS-CoV-2. *Nature* **584**, 120–124 (2020).

[ADS](#) [CAS](#) [PubMed](#) [Google Scholar](#)

16. 16.

Zost, S. J. et al. Rapid isolation and profiling of a diverse panel of human monoclonal antibodies targeting the SARS-CoV-2 spike protein. *Nat. Med.* **26**, 1422–1427 (2020).

[CAS](#) [PubMed](#) [Google Scholar](#)

17. 17.

Seydoux, E. et al. Analysis of a SARS-CoV-2-infected individual reveals development of potent neutralizing antibodies with limited somatic mutation. *Immunity* **53**, 98–105 (2020).

[CAS](#) [PubMed](#) [PubMed Central](#) [Google Scholar](#)

18. 18.

Hoffmann, M. et al. SARS-CoV-2 cell entry depends on ACE2 and TMPRSS2 and is blocked by a clinically proven protease inhibitor. *Cell* **181**, 271–280 (2020).

[CAS](#) [PubMed](#) [PubMed Central](#) [Google Scholar](#)

19. 19.

Wang, Q. et al. Structural and functional basis of SARS-CoV-2 entry by using human ACE2. *Cell* **181**, 894–904 (2020).

[CAS](#) [PubMed](#) [PubMed Central](#) [Google Scholar](#)

20. 20.

Walls, A.C. et al. Structure, function, and antigenicity of the SARS-CoV-2 spike glycoprotein. *Cell* **181**, 281–292 (2020).

[CAS](#) [PubMed](#) [PubMed Central](#) [Google Scholar](#)

21. 21.

Wrapp, D. et al. Cryo-EM structure of the 2019-nCoV spike in the prefusion conformation. *Science* **367**, 1260–1263 (2020).

[ADS](#) [CAS](#) [PubMed](#) [PubMed Central](#) [Google Scholar](#)

22. 22.

Walls, A. C. et al. Cryo-electron microscopy structure of a coronavirus spike glycoprotein trimer. *Nature* **531**, 114–117 (2016).

[ADS](#) [CAS](#) [PubMed](#) [PubMed Central](#) [Google Scholar](#)

23. 23.

Yuan, Y. et al. Cryo-EM structures of MERS-CoV and SARS-CoV spike glycoproteins reveal the dynamic receptor binding domains. *Nat. Commun.* **8**, 15092 (2017).

[ADS](#) [CAS](#) [PubMed](#) [PubMed Central](#) [Google Scholar](#)

24. 24.

Kirchdoerfer, R. N. et al. Pre-fusion structure of a human coronavirus spike protein. *Nature* **531**, 118–121 (2016).

[ADS](#) [CAS](#) [PubMed](#) [PubMed Central](#) [Google Scholar](#)

25. 25.

Li, Z. et al. The human coronavirus HCoV-229E S-protein structure and receptor binding. *eLife* **8**, e51230 (2019).

[CAS](#) [PubMed](#) [PubMed Central](#) [Google Scholar](#)

26. 26.

Barnes, C.O. et al. Structures of human antibodies bound to SARS-CoV-2 spike reveal common epitopes and recurrent features of antibodies. *Cell* **182**, 828–842 (2020).

[CAS](#) [PubMed](#) [PubMed Central](#) [Google Scholar](#)

27. 27.

Ju, B. et al. Human neutralizing antibodies elicited by SARS-CoV-2 infection. *Nature* **584**, 115–119 (2020).

[ADS](#) [CAS](#) [PubMed](#) [Google Scholar](#)

28. 28.

Wu, Y. et al. A noncompeting pair of human neutralizing antibodies block COVID-19 virus binding to its receptor ACE2. *Science* **368**, 1274–1278 (2020).

[ADS](#) [CAS](#) [PubMed](#) [PubMed Central](#) [Google Scholar](#)

29. 29.

Chi, X. et al. A neutralizing human antibody binds to the N-terminal domain of the Spike protein of SARS-CoV-2. *Science* **369**, 650–655 (2020).

[CAS](#) [PubMed](#) [PubMed Central](#) [Google Scholar](#)

30. 30.

Yuan, M. et al. Structural basis of a shared antibody response to SARS-CoV-2. *Science* **369**, 1119–1123 (2020).

[CAS](#) [PubMed](#) [Google Scholar](#)

31. 31.

Hurlburt, N. K. et al. Structural basis for potent neutralization of SARS-CoV-2 and role of antibody affinity maturation. Preprint at <https://doi.org/10.1101/2020.06.12.148692> (2020).

32. 32.

Lefranc, M. P. et al. IMGT®, the international ImMunoGeneTics information system® 25 years on. *Nucleic Acids Res.* **43**, D413–D422 (2015).

[CAS](#) [PubMed](#) [Google Scholar](#)

33. 33.

Briney, B., Inderbitzin, A., Joyce, C. & Burton, D. R. Commonality despite exceptional diversity in the baseline human antibody repertoire. *Nature* **566**, 393–397 (2019).

[ADS](#) [PubMed](#) [PubMed Central](#) [Google Scholar](#)

34. 34.

Pinto, D. et al. Cross-neutralization of SARS-CoV-2 by a human monoclonal SARS-CoV antibody. *Nature* **583**, 290–295 (2020).

35. 35.

Pallesen, J. et al. Immunogenicity and structures of a rationally designed prefusion MERS-CoV spike antigen. *Proc. Natl Acad. Sci. USA* **114**, E7348–E7357 (2017).

[CAS](#) [PubMed](#) [Google Scholar](#)

36. 36.

Hsieh, C. L. et al. Structure-based design of prefusion-stabilized SARS-CoV-2 spikes. *Science* **369**, 1501–155 (2020).

[CAS](#) [PubMed](#) [Google Scholar](#)

37. 37.

Wu, F. et al. Neutralizing antibody responses to SARS-CoV-2 in a COVID-19 recovered patient cohort and their implications. Preprint at <https://doi.org/10.1101/2020.03.30.20047365> (2020).

38. 38.

Wu, N. C. et al. An alternative binding mode of IGHV3-53 antibodies to the SARS-CoV-2 receptor binding domain. *Cell Rep.* <https://doi.org/10.1016/j.celrep.2020.108274> (2020).

39. 39.

Marillet, S., Lefranc, M. P., Boudinot, P. & Cazals, F. Novel structural parameters of Ig-Ag complexes yield a quantitative description of interaction specificity and binding affinity. *Front. Immunol.* **8**, 34 (2017).

[PubMed](#) [PubMed Central](#) [Google Scholar](#)

40. 40.

Weisblum, Y. et al. Escape from neutralizing antibodies by SARS-CoV-2 spike protein variants. Preprint at <https://doi.org/10.1101/2020.07.21.214759> (2020).

41. 41.

Wang, B. et al. Bivalent binding of a fully human IgG to the SARS-CoV-2 spike proteins reveals mechanisms of potent neutralization. Preprint at <https://doi.org/10.1101/2020.07.14.203414> (2020).

42. 42.

Shang, J. et al. Structural basis of receptor recognition by SARS-CoV-2. *Nature* **581**, 221–224 (2020).

[ADS](#) [CAS](#) [PubMed](#) [PubMed Central](#) [Google Scholar](#)

43. 43.

Yan, R. et al. Structural basis for the recognition of SARS-CoV-2 by full-length human ACE2. *Science* **367**, 1444–1448 (2020).

[ADS](#) [CAS](#) [PubMed](#) [PubMed Central](#) [Google Scholar](#)

44. 44.

Li, Q. et al. The impact of mutations in SARS-CoV-2 spike on viral infectivity and antigenicity. *Cell* **182**, 1284–1294.e9 (2020).

[CAS](#) [PubMed](#) [PubMed Central](#) [Google Scholar](#)

45. 45.

Scharf, L. et al. Broadly neutralizing antibody 8ANC195 recognizes closed and open states of HIV-1 Env. *Cell* **162**, 1379–1390 (2015).

[CAS](#) [PubMed](#) [PubMed Central](#) [Google Scholar](#)

46. 46.

Schoofs, T. et al. Broad and potent neutralizing antibodies recognize the silent face of the HIV envelope. *Immunity* **50**, 1513–1529 (2019).

[CAS](#) [PubMed](#) [PubMed Central](#) [Google Scholar](#)

47. 47.

Kabsch, W. XDS. *Acta Crystallogr. D* **66**, 125–132 (2010).

[CAS](#) [Google Scholar](#)

48. 48.

Winn, M. D. et al. Overview of the CCP4 suite and current developments. *Acta Crystallogr. D* **67**, 235–242 (2011).

[CAS](#) [Google Scholar](#)

49. 49.

Adams, P. D. et al. PHENIX: a comprehensive Python-based system for macromolecular structure solution. *Acta Crystallogr. D* **66**, 213–221 (2010).

[CAS](#) [PubMed](#) [Google Scholar](#)

50. 50.

Winter, G. xia2: an expert system for macromolecular crystallography data reduction. *J. Appl. Crystallogr.* **43**, 186–190 (2010).

[CAS](#) [Google Scholar](#)

51. 51.

Beilsten-Edmands, J. et al. Scaling diffraction data in the DIALS software package: algorithms and new approaches for multi-crystal scaling. *Acta Crystallogr. D* **76**, 385–399 (2020).

[CAS](#) [Google Scholar](#)

52. 52.

Winter, G. et al. DIALS: implementation and evaluation of a new integration package. *Acta Crystallogr. D* **74**, 85–97 (2018).

[CAS](#) [Google Scholar](#)

53. 53.

McCoy, A. J. et al. Phaser crystallographic software. *J. Appl. Crystallogr.* **40**, 658–674 (2007).

[CAS](#) [PubMed](#) [PubMed Central](#) [Google Scholar](#)

54. 54.

Gristick, H. B. et al. Natively glycosylated HIV-1 Env structure reveals new mode for antibody recognition of the CD4-binding site. *Nat. Struct. Mol. Biol.* **23**, 906–915 (2016).

[CAS](#) [PubMed](#) [PubMed Central](#) [Google Scholar](#)

55. 55.

Bunkóczki, G. & Read, R. J. Improvement of molecular-replacement models with Sculptor. *Acta Crystallogr. D* **67**, 303–312 (2011).

[PubMed](#) [Google Scholar](#)

56. 56.

Emsley, P., Lohkamp, B., Scott, W. G. & Cowtan, K. Features and development of Coot. *Acta Crystallogr. D* **66**, 486–501 (2010).

[CAS](#) [PubMed](#) [Google Scholar](#)

57. 57.

Mastronarde, D. N. Automated electron microscope tomography using robust prediction of specimen movements. *J. Struct. Biol.* **152**, 36–51 (2005).

[Google Scholar](#)

58. 58.

Punjani, A., Rubinstein, J. L., Fleet, D. J. & Brubaker, M. A. cryoSPARC: algorithms for rapid unsupervised cryo-EM structure determination. *Nat. Methods* **14**, 290–296 (2017).

[CAS](#) [Google Scholar](#)

59. 59.

Rohou, A. & Grigorieff, N. CTFFIND4: fast and accurate defocus estimation from electron micrographs. *J. Struct. Biol.* **192**, 216–221 (2015).

[PubMed](#) [PubMed Central](#) [Google Scholar](#)

60. 60.

Goddard, T. D. et al. UCSF ChimeraX: meeting modern challenges in visualization and analysis. *Protein Sci.* **27**, 14–25 (2018).

[CAS](#) [Google Scholar](#)

61. 61.

Bell, J. M., Chen, M., Baldwin, P. R. & Ludtke, S. J. High resolution single particle refinement in EMAN2.1. *Methods* **100**, 25–34 (2016).

[CAS](#) [PubMed](#) [PubMed Central](#) [Google Scholar](#)

62. 62.

Goddard, T. D., Huang, C. C. & Ferrin, T. E. Visualizing density maps with UCSF Chimera. *J. Struct. Biol.* **157**, 281–287 (2007).

[CAS](#) [PubMed](#) [Google Scholar](#)

63. 63.

Terwilliger, T. C., Adams, P. D., Afonine, P. V. & Sobolev, O. V. A fully automatic method yielding initial models from high-resolution cryo-electron microscopy maps. *Nat. Methods* **15**, 905–908 (2018).

[CAS](#) [PubMed](#) [PubMed Central](#) [Google Scholar](#)

64. 64.

Chen, V. B. et al. MolProbity: all-atom structure validation for macromolecular crystallography. *Acta Crystallogr. D* **66**, 12–21 (2010).

[CAS](#) [Google Scholar](#)

65. 65.

Krissinel, E. & Henrick, K. Inference of macromolecular assemblies from crystalline state. *J. Mol. Biol.* **372**, 774–797 (2007).

[CAS](#) [PubMed](#) [Google Scholar](#)

66. 66.

Davis, M. I., Bennett, M. J., Thomas, L. M. & Bjorkman, P. J. Crystal structure of prostate-specific membrane antigen, a tumor marker and peptidase. *Proc. Natl Acad. Sci. USA* **102**, 5981–5986 (2005).

[ADS](#) [CAS](#) [PubMed](#) [Google Scholar](#)

67. 67.

Liu, H. et al. Cross-neutralization of a SARS-CoV-2 antibody to a functionally conserved site is mediated by avidity. Preprint at <https://doi.org/10.1101/2020.08.02.233536> (2020).

68. 68.

Zhou, D. et al. Structural basis for the neutralization of SARS-CoV-2 by an antibody from a convalescent patient. *Nat. Struct. Mol. Biol.* **27**, 950–958 (2020).

[CAS](#) [PubMed](#) [Google Scholar](#)

69. 69.

Piccoli, L. et al. Mapping neutralizing and immunodominant sites on the SARS-CoV-2 spike receptor-binding domain by structure-guided

high-resolution serology. *Cell* **183**, 1024–1042 (2020).

[Article](#) [PubMed](#) [PubMed Central](#) [Google Scholar](#)

70. 70.

Dunbar, J. et al. SAbDab: the structural antibody database. *Nucleic Acids Res.* **42**, D1140–D1146 (2014).

[CAS](#) [PubMed](#) [Google Scholar](#)

[Download references](#)

Acknowledgements

We thank J. Vielmetter, P. Hoffman, and the Protein Expression Center in the Beckman Institute at Caltech for expression assistance, J. Vielmetter and J. Keeffe for setting up automated polyreactivity assays, J. Keeffe for construct design, and N. Koranda for help with cloning and protein purification. Electron microscopy was performed in the Caltech Beckman Institute Resource Center for Transmission Electron Microscopy with assistance from S. Chen. We thank the Gordon and Betty Moore and Beckman Foundations for gifts to Caltech to support the Molecular Observatory (J. Kaiser, director), and S. Russi, A. Cohen and C. Smith and the beamline staff at SSRL for data collection assistance. Use of the Stanford Synchrotron Radiation Lightsource, SLAC National Accelerator Laboratory, is supported by the US Department of Energy, Office of Science, Office of Basic Energy Sciences under contract no. DE-AC02-c76SF00515. The SSRL Structural Molecular Biology Program is supported by the DOE Office of Biological and Environmental Research, and by the National Institutes of Health, National Institute of General Medical Sciences (P41GM103393). The contents of this publication are solely the responsibility of the authors and do not necessarily represent the official views of NIGMS or NIH. This work was supported by NIH grant P01-AI138938-S1 (P.J.B. and M.C.N.), the Caltech Merkin Institute for Translational Research (P.J.B.), NIH grant P50 8 P50 AI150464-13 (P.J.B.), and a George Mason University Fast Grant (P.J.B.). C.O.B was supported

by the Hanna Gray Fellowship Program from the Howard Hughes Medical Institute and the Postdoctoral Enrichment Program from the Burroughs Wellcome Fund. M.C.N. is a Howard Hughes Medical Institute Investigator.

Author information

Author notes

1. Davide F. Robbiani

Present address: Institute for Research in Biomedicine, Università della Svizzera Italiana, Bellinzona, Switzerland

Affiliations

1. Division of Biology and Biological Engineering, California Institute of Technology, Pasadena, CA, USA

Christopher O. Barnes, Claudia A. Jette, Morgan E. Abernathy, Kim-Marie A. Dam, Shannon R. Esswein, Harry B. Gristick, Kathryn E. Huey-Tubman, Yu E. Lee, Anthony P. West Jr & Pamela J. Bjorkman

2. Beckman Institute, California Institute of Technology, Pasadena, CA, USA

Andrey G. Malyutin

3. Division of Chemistry and Chemical Engineering, California Institute of Technology, Pasadena, CA, USA

Naima G. Sharaf

4. Laboratory of Molecular Immunology, The Rockefeller University, New York, NY, USA

Davide F. Robbiani & Michel C. Nussenzweig

5. Howard Hughes Medical Institute, Chevy Chase, MD, USA

Michel C. Nussenzweig

Authors

1. Christopher O. Barnes

[View author publications](#)

You can also search for this author in [PubMed](#) [Google Scholar](#)

2. Claudia A. Jette

[View author publications](#)

You can also search for this author in [PubMed](#) [Google Scholar](#)

3. Morgan E. Abernathy

[View author publications](#)

You can also search for this author in [PubMed](#) [Google Scholar](#)

4. Kim-Marie A. Dam

[View author publications](#)

You can also search for this author in [PubMed](#) [Google Scholar](#)

5. Shannon R. Esswein

[View author publications](#)

You can also search for this author in [PubMed](#) [Google Scholar](#)

6. Harry B. Gristick

[View author publications](#)

You can also search for this author in [PubMed](#) [Google Scholar](#)

7. Andrey G. Malyutin

[View author publications](#)

You can also search for this author in [PubMed](#) [Google Scholar](#)

8. Naima G. Sharaf

[View author publications](#)

You can also search for this author in [PubMed](#) [Google Scholar](#)

9. Kathryn E. Huey-Tubman

[View author publications](#)

You can also search for this author in [PubMed](#) [Google Scholar](#)

10. Yu E. Lee

[View author publications](#)

You can also search for this author in [PubMed](#) [Google Scholar](#)

11. Davide F. Robbiani

[View author publications](#)

You can also search for this author in [PubMed](#) [Google Scholar](#)

12. Michel C. Nussenzweig

[View author publications](#)

You can also search for this author in [PubMed](#) [Google Scholar](#)

13. Anthony P. West Jr

[View author publications](#)

You can also search for this author in [PubMed](#) [Google Scholar](#)

14. Pamela J. Bjorkman

[View author publications](#)

You can also search for this author in [PubMed](#) [Google Scholar](#)

Contributions

C.O.B., M.C.N., A.P.W. and P.J.B. conceived the study and analysed data; D.F.R. and M.C.N. provided monoclonal antibody sequences and plasmids

derived from COVID-19-convalescent donors. C.O.B. and K.H.T. performed protein purifications and C.O.B. assembled complexes for cryo-EM and X-ray crystallography studies. C.O.B. performed cryo-EM and interpreted structures with assistance from M.E.A., K.A.D., S.R.E., A.G.M. and N.G.S. C.A.J. and C.O.B. performed and analysed crystallographic structures, with refinement assistance from M.E.A. and K.M.D. Y.E.L. performed polyreactivity assays. H.B.G. performed and analysed SPR experiments. A.P.W. analysed antibody sequences. C.O.B., M.C.N., A.P.W. and P.J.B. wrote the paper with contributions from other authors.

Corresponding author

Correspondence to [Pamela J. Bjorkman](#).

Ethics declarations

Competing interests

The Rockefeller University has filed a provisional patent application in connection with this work on which D.F.R. and M.C.N. are inventors (US 63/021,387).

Additional information

Peer review information *Nature* thanks the anonymous reviewer(s) for their contribution to the peer review of this work.

Publisher's note Springer Nature remains neutral with regard to jurisdictional claims in published maps and institutional affiliations.

Extended data figures and tables

[Extended Data Fig. 1 X-ray structure and epitope mapping of VH3-53 NAb C102.](#)

a, X-ray structure of the C102 Fab–RBD_{331–518} complex. **b**, C102 CDR loops mapped on the RBD surface. **c**, Surface representation of C102 epitope coloured by C102 heavy chain (dark green) and light chain (light green) interactions. **d**, **e**, CDRH1, CDRH2 (**d**) and CDRH3 (**e**) interactions with RBD residues. Potential hydrogen-bond contacts are illustrated as dashed lines. **f**, Left, overlay of C102–RBD crystal structure (cartoon) with C105–S trimer cryoEM density (PDB 6XCM, EMD-22127) illustrating conserved binding to RBD epitope in an up conformation. Right, the C102 epitope is sterically occluded when aligned to a down RBD conformation

(red and yellow star). SARS-CoV-2 S domains are dark grey (S2 domain) and light grey (S1 domain); the C105 Fab is yellow-green. **g**, Alignment of selected CDRH3 sequences for *VH3-53*- or *VH3-66*-encoded SARS-CoV-2 neutralizing antibodies (IMGT definition³²). **h**, Overlay of NAb COVA2-39 Fab³⁸ (lime green and lemon, from COVA2-39–RBD structure, PDB 7JMP) and C144 Fab (blue, from C144–S structure) aligned on a RBD_A of C144 epitope. COVA2-39 adopts a distinct conformation relative to the C102-like *VH3-53*-encoded short CDRH3 NAb class and to C144, recognizing its RBD epitope only in an up RBD conformations owing to steric clashes (red and yellow star) with the N343-associated glycan on the adjacent RBD. **i**, Polyreactivity assay. IgGs were evaluated for binding to baculovirus extracts to assess non-specific binding. Polyreactive positive control IgGs were NIH45-46, 45-46^{G54W} and 45-46m2. Negative controls were bovine serum albumin (BSA) and IgGs N6 and 3BNC117. Relative light unit (RLU) values are presented as the mean and s.d. of triplicate measurements ($n = 3$ biological replicates) with results for individual experiments shown as circles.

Extended Data Fig. 2 Overview of *VH3-53/VH3-66*-encoded human NAb structures.

a, Superimposition of Vh and Vl domains of C102 with other *VH3-53*- or *VH3-66*-encoded NAbs (top) and root mean square deviation (r.m.s.d.) calculations (bottom). **b**, Buried surface area comparisons for the indicated Fab–RBD structures. Buried surface areas were calculated using PDBePISA⁶⁵ and a 1.4 Å probe. **c**, **d**, Heavy-chain buried surface areas of anti-SARS-CoV-2 antibodies plotted as CDRH1 (IMGT residues 27–38) plus CDRH2 (residues 56–67*) versus CDRH3 (residues 105–117) (**c**), and V gene segment region (residues 1–105) versus CDRH3 (residues 106*–117) (**d**, asterisk indicates differences from IMGT definition). Blue data points represent 501 human antibodies complexed with protein antigens. IMGT-numbered structures (resolutions of 3.5 Å or better) were downloaded from the Structural Antibody Database (SAbDab)⁷⁰ and buried surface area were calculated using PISA⁶⁵. Buried surface areas from antibody structures with identical or near-identical heavy chain sequences were averaged to give a single point on the graph.

Extended Data Fig. 3 Cryo-EM data processing and validation for C144–S, C002–S and C121–S complexes.

a–i, Representative micrograph selected from total dataset (Supplementary Table 2), 2D class averages, gold-standard Fourier shell correlation (FSC) plots, and local resolution estimations for C144–S 6P (**a–c**), C002–S 2P (**d–f**) and C121–S 2P (**g–i**). Scale bars, 100 nm. For the C002–S dataset, two classes were resolved: state 1, C002 Fabs bound to three down RBDs, and state 2, C002 Fabs bound to two down and one up RBD. For the C121–S 2P dataset, two classes were resolved: state 1, C121 Fabs bound to two down and one up RBD and state 2, C121 Fabs bound to one down, two up RBDs.

Extended Data Fig. 4 Cryo-EM processing, validation and reconstruction for C119–S and C104–S complexes.

a, 3.6 Å cryo-EM reconstruction for a C119–S trimer complex. **b**, 3.7 Å cryo-EM reconstruction for a C104–S trimer complex. Representative micrograph selected from the total dataset (Supplementary Table 2), 2D class averages, gold-standard FSC plot, and local resolution estimation for C119–S2P (**c–e**) and C104–S (**f–h**). Scale bars, 100 nm. Both complexes revealed binding of Fabs to both down and up RBD conformations. **i–n**, Somatic hypermutations in heavy- and light-chain V gene segments for C002 (**i**), C121 (**j**), C119 (**k**), C144 (**l**), C102 (**m**) and C135 (**n**) are shown as spheres on the antibody V_h and V_l domains (ribbon representations). The primary RBD epitope is shown as a light grey surface; secondary RBD epitope for C144 is in dark grey.

Extended Data Fig. 5 Primary and secondary epitopes of class 2 human NAbs.

a–c, Primary epitopes for C002 (**a**), C121 (**b**), and C119 (**c**) on down RBD. A secondary epitope is observed if a Fab is bound to an adjacent up RBD for these NAbs. Antibody paratopes are represented as cartoons. A similar interaction in the C104–S structure is not shown owing to low local resolution on the up RBD. **d–g**, Primary epitopes for C119 (**d**), C104 (**e**), P2B-2F6 (**f**; PDB 7BWJ), and BD23 (**g**; PDB 7BYR). The existence of

secondary epitopes for P2B-2F6 and BD23 cannot be determined because the P2B-2F6 epitope was determined from a crystal structure with an RBD²⁷, and the BD23–S cryo-EM structure showed only one bound Fab¹³. **h**, Measurement of C α distance between the C termini of adjacent C121 Ch1 domains (residue 222 of the heavy chain on each Fab). Measurements of this type were used to evaluate whether intra-spike crosslinking by an IgG binding to a single spike trimer was possible for human NAbs in Extended Data Table 1.

Extended Data Fig. 6 Cryo-EM structure of C110–S complex and epitope mapping.

a, 3.8 Å cryo-EM reconstruction of the C110–S trimer complex. **b**, Composite model of C110–RBD (purple and grey, respectively) overlaid with the SARS-CoV-2 NAb REGN-10987 (yellow, PDB 6XDG) and soluble ACE2 (green, PDB 6M0J). Model was generated by aligning structures on 188 RBD C α atoms. **c–f**, Surface representation of RBD epitopes for C135 (blue) (**c**), S309 (brown, PDB 6WSP) (**d**), C110 (purple) (**e**) and REGN-10987 (yellow, PDB 6XDG) (**f**). Given the low resolution of the antibody–RBD interface, epitopes were assigned by selection of any RBD residue within 7 Å of any antibody C α atom. Mutation sites found in sequence isolates⁴⁴ (green) and in laboratory selection assays⁴⁰ (red) are shown. Representative micrograph selected from total dataset (Supplementary Table 2), 2D class averages, gold-standard FSC plot, and local resolution estimation for C135–S 2P (**g–i**) and C110–S 2P (**j–l**). Scale bars, 100 nm. Both complexes revealed binding of Fabs to both two-down and one-up RBD conformations.

Extended Data Fig. 7 Possibilities for simultaneous engagement of C144 and C135 on spikes with different combinations of up and down RBDs.

Modelling of C144 (light blue) and C135 (dark blue) Vh–VI domains on different RBD conformations. Steric clashes are shown as a red and yellow star.

Extended Data Fig. 8 SPR binding data for NAbs.

a–c, Kinetic and equilibrium constants for binding to unaltered RBD (indicated as wild type, wt) and mutant RBDs are shown in tables beside structures of a representative NAb–RBD complex for each class. Residues that were mutated are highlighted as coloured side chains on a grey RBD surface. Antibody Vh–Vl domains are shown as cartoons. Kinetic and equilibrium constants for NAbs that contact adjacent RBDs on the S trimer (C144, C002, C119 and C121) do not account for contacts to a secondary RBD because binding was assayed by injected monomeric RBDs over immobilized IgGs. Asterisk indicates kinetic constants determined from a two-state binding model.

Extended Data Fig. 9 Summary of NAbs.

a, Structural depiction of a representative NAb from each class binding its RBD epitope. **b**, Composite model illustrating non-overlapping epitopes of NAbs from each class bound to a RBD monomer. **c**, Epitopes for SARS-CoV-2 NAbs. RBD residues involved in ACE2 binding are boxed in green. Diamonds represent RBD residues contacted by the indicated antibody.

Extended Data Table 1 Classification and structural properties of SARS-CoV-2 RBD-specific antibodies

[Full size table](#)

Supplementary information

Supplementary Tables

This file contains Supplementary Tables 1-2 which include X-ray crystallography and cryo-EM data collection and refinement statistics.

Reporting Summary

Rights and permissions

[Reprints and Permissions](#)

About this article



Check for
updates

Cite this article

Barnes, C.O., Jette, C.A., Abernathy, M.E. *et al.* SARS-CoV-2 neutralizing antibody structures inform therapeutic strategies. *Nature* **588**, 682–687 (2020). <https://doi.org/10.1038/s41586-020-2852-1>

[Download citation](#)

- Received: 30 August 2020
- Accepted: 06 October 2020
- Published: 12 October 2020
- Issue Date: 24 December 2020
- DOI: <https://doi.org/10.1038/s41586-020-2852-1>

Further reading

- [**COVID-19 antibody development fueled by HIV-1 broadly neutralizing antibody research**](#)
 - Pilar Mendoza
 - , Julio C.C. Lorenzi
 - & Christian Gaebler

Current Opinion in HIV and AIDS (2021)

- Neutralizing antibodies targeting SARS-CoV-2 spike protein
 - Shi Xiaojie
 - , Li Yu
 - , Yan lei
 - , Yang Guang
 - & Qiang Min
- COVID-19: The Effect of Host Genetic Variations on Host–Virus Interactions
 - Suvobrata Chakravarty
- Diamond Light Source: contributions to SARS-CoV-2 biology and therapeutics
 - Martin A. Walsh
 - , Jonathan M. Grimes
 - & David I. Stuart
- Vaccine formulations in clinical development for the prevention of severe acute respiratory syndrome coronavirus 2 infection
 - Cole J. Batty
 - , Mark T. Heise
 - , Eric M. Bachelder
 - & Kristy M. Ainslie

Comments

By submitting a comment you agree to abide by our [Terms](#) and [Community Guidelines](#). If you find something abusive or that does not comply with our terms or guidelines please flag it as inappropriate.

[Download PDF](#)

This article was downloaded by **calibre** from <https://www.nature.com/articles/s41586-020-2852-1>

| [Section menu](#) | [Main menu](#) |

- Article
- [Published: 02 December 2020](#)

Galactosaminogalactan activates the inflammasome to provide host protection

- [Benoit Briard](#) ORCID: [orcid.org/0000-0002-1496-9408¹](#),
- [Thierry Fontaine²](#),
- [Parimal Samir](#) ORCID: [orcid.org/0000-0001-7655-5713¹](#),
- [David E. Place](#) ORCID: [orcid.org/0000-0002-1904-4164¹](#),
- [Laetitia Muszkieta²](#),
- [R. K. Subbarao Malireddi](#) ORCID: [orcid.org/0000-0001-8855-9447¹](#),
- [Rajendra Karki](#) ORCID: [orcid.org/0000-0003-4436-9128¹](#),
- [Shelbi Christgen](#) ORCID: [orcid.org/0000-0003-1145-4430¹](#),
- [Perrine Bomme³](#),
- [Peter Vogel](#) ORCID: [orcid.org/0000-0002-7535-0545⁴](#),
- [Rémi Beau²](#),
- [Emilia Mellado⁵](#),
- [Oumaima Ibrahim-Granet⁶](#),
- [Bernard Henrissat](#) ORCID: [orcid.org/0000-0002-3434-8588^{7,11}](#),
- [Ravi C. Kalathur](#) ORCID: [orcid.org/0000-0002-4889-8003⁸](#),
- [Cam Robinson](#) ORCID: [orcid.org/0000-0002-7277-692X⁹](#),
- [Jean-Paul Latgé²](#) nAff10 &
- [Thirumala-Devi Kanneganti](#) ORCID: [orcid.org/0000-0002-6395-6443¹](#)

[Nature](#) volume 588, pages688–692(2020)Cite this article

- 3839 Accesses

- 113 Altmetric
- [Metrics details](#)

Subjects

- [Fungi](#)
- [Infection](#)
- [Inflammasome](#)
- [NOD-like receptors](#)

A [Publisher Correction](#) to this article was published on 21 December 2020

This article has been [updated](#)

Abstract

Inflammasomes are important sentinels of innate immune defence that are activated in response to diverse stimuli, including pathogen-associated molecular patterns (PAMPs)¹. Activation of the inflammasome provides host defence against aspergillosis^{2,3}, which is a major health concern for patients who are immunocompromised. However, the *Aspergillus fumigatus* PAMPs that are responsible for inflammasome activation are not known. Here we show that the polysaccharide galactosaminogalactan (GAG) of *A. fumigatus* is a PAMP that activates the NLRP3 inflammasome. The binding of GAG to ribosomal proteins inhibited cellular translation machinery, and thus activated the NLRP3 inflammasome. The galactosamine moiety bound to ribosomal proteins and blocked cellular translation, which triggered activation of the NLRP3 inflammasome. In mice, a GAG-deficient *Aspergillus* mutant ($\Delta gt4c$) did not elicit protective activation of the inflammasome, and this strain exhibited enhanced virulence. Moreover, administration of GAG protected mice from colitis induced by dextran sulfate sodium in an inflammasome-dependent manner.

Thus, ribosomes connect the sensing of this fungal PAMP to the activation of an innate immune response.

[Access through your institution](#)

[Change institution](#)

[Buy or subscribe](#)

Access options

Subscribe to Journal

Get full journal access for 1 year

\$199.00

only \$3.83 per issue

[Subscribe](#)

All prices are NET prices.

VAT will be added later in the checkout.

Rent or Buy article

Get time limited or full article access on ReadCube.

from \$8.99

[Rent or Buy](#)

All prices are NET prices.

Additional access options:

- [Log in](#)
- [Access through your institution](#)
- [Learn about institutional subscriptions](#)

Fig. 1: *Aspergillus fumigatus* GT4C regulates GAG synthesis.

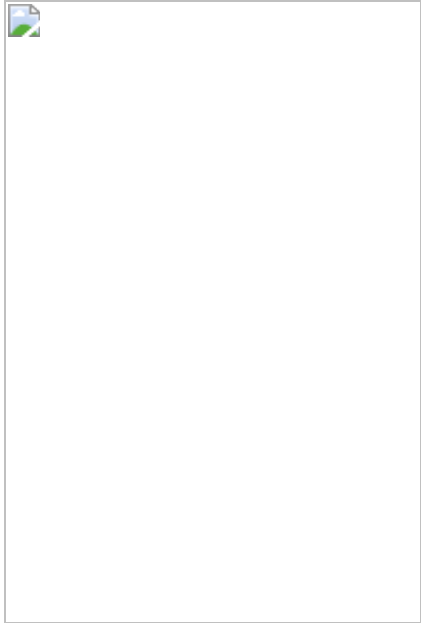


Fig. 2: GT4C potentiates *A.-fumigatus*-induced inflammasome activation.

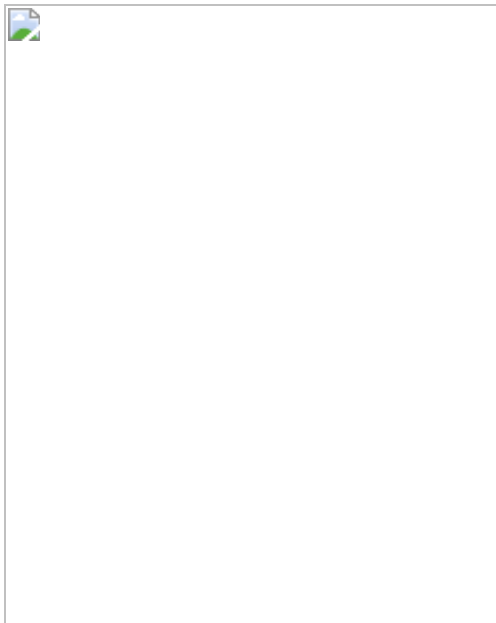


Fig. 3: The galactosamine of GAG interacts with ribosomes, inhibits translation and induces NLRP3 inflammasome activation.

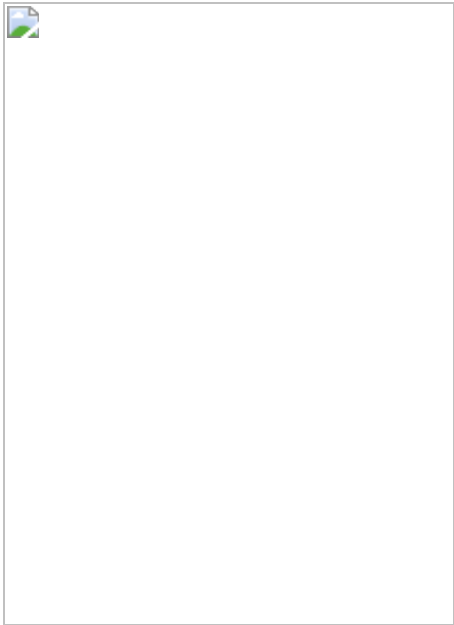


Fig. 4: GAG-induced activation of the inflammasome provides host protection against aspergillosis and DSS-induced colitis.



Data availability

The datasets generated and analysed in this study are contained within the Article, and its Supplementary Information; any other relevant data are available from the corresponding author upon reasonable request. [Source data](#) are provided with this paper.

Change history

- **21 December 2020**

A Correction to this paper has been published:
<https://doi.org/10.1038/s41586-020-03088-5>

References

1. 1.

Man, S. M., Karki, R. & Kanneganti, T. D. Molecular mechanisms and functions of pyroptosis, inflammatory caspases and inflammasomes in infectious diseases. *Immunol. Rev.* **277**, 61–75 (2017).

[CAS](#) [PubMed](#) [PubMed Central](#) [Google Scholar](#)

2. 2.

Briard, B. et al. Fungal ligands released by innate immune effectors promote inflammasome activation during *Aspergillus fumigatus* infection. *Nat. Microbiol.* **4**, 316–327 (2019).

[CAS](#) [PubMed](#) [Google Scholar](#)

3. 3.

Karki, R. et al. Concerted activation of the AIM2 and NLRP3 inflammasomes orchestrates host protection against *Aspergillus* infection. *Cell Host Microbe* **17**, 357–368 (2015).

[CAS](#) [PubMed](#) [PubMed Central](#) [Google Scholar](#)

4. 4.

Saïd-Sadier, N., Padilla, E., Langsley, G. & Ojcius, D. M. *Aspergillus fumigatus* stimulates the NLRP3 inflammasome through a pathway

requiring ROS production and the Syk tyrosine kinase. *PLoS ONE* **5**, e10008 (2010).

[ADS](#) [PubMed](#) [PubMed Central](#) [Google Scholar](#)

5. 5.

Latgé, J. P., Beauvais, A. & Chamilos, G. The cell wall of the human fungal pathogen *Aspergillus fumigatus*: biosynthesis, organization, immune response, and virulence. *Annu. Rev. Microbiol.* **71**, 99–116 (2017).

[PubMed](#) [Google Scholar](#)

6. 6.

Fontaine, T. et al. Galactosaminogalactan, a new immunosuppressive polysaccharide of *Aspergillus fumigatus*. *PLoS Pathog.* **7**, e1002372 (2011).

[CAS](#) [PubMed](#) [PubMed Central](#) [Google Scholar](#)

7. 7.

Gravelat, F. N. et al. *Aspergillus* galactosaminogalactan mediates adherence to host constituents and conceals hyphal β -glucan from the immune system. *PLoS Pathog.* **9**, e1003575 (2013).

[CAS](#) [PubMed](#) [PubMed Central](#) [Google Scholar](#)

8. 8.

Hua, K. F. et al. Capsular polysaccharide is Involved in NLRP3 inflammasome activation by *Klebsiella pneumoniae* serotype K1. *Infect. Immun.* **83**, 3396–3409 (2015).

[CAS](#) [PubMed](#) [PubMed Central](#) [Google Scholar](#)

9. 9.

Wolf, A. J. et al. Hexokinase is an innate immune receptor for the detection of bacterial peptidoglycan. *Cell* **166**, 624–636 (2016).

[CAS](#) [PubMed](#) [PubMed Central](#) [Google Scholar](#)

10. 10.

Briard, B., Muszkieta, L., Latgé, J. P. & Fontaine, T. Galactosaminogalactan of *Aspergillus fumigatus*, a bioactive fungal polymer. *Mycologia* **108**, 572–580 (2016).

[CAS](#) [PubMed](#) [Google Scholar](#)

11. 11.

Lee, M. J. et al. Deacetylation of fungal exopolysaccharide mediates adhesion and biofilm formation. *MBio* **7**, e00252-16 (2016).

[CAS](#) [PubMed](#) [PubMed Central](#) [Google Scholar](#)

12. 12.

Tzianabos, A. O. Polysaccharide immunomodulators as therapeutic agents: structural aspects and biologic function. *Clin. Microbiol. Rev.* **13**, 523–533 (2000).

[CAS](#) [PubMed](#) [PubMed Central](#) [Google Scholar](#)

13. 13.

Zhou, X., Liao, W. J., Liao, J. M., Liao, P. & Lu, H. Ribosomal proteins: functions beyond the ribosome. *J. Mol. Cell Biol.* **7**, 92–104 (2015).

[CAS](#) [PubMed](#) [PubMed Central](#) [Google Scholar](#)

14. 14.

Vyleta, M. L., Wong, J. & Magun, B. E. Suppression of ribosomal function triggers innate immune signaling through activation of the NLRP3 inflammasome. *PLoS One* **7**, e36044 (2012).

[ADS](#) [CAS](#) [PubMed](#) [PubMed Central](#) [Google Scholar](#)

15. 15.

Bronner, D. N. et al. Endoplasmic reticulum stress activates the inflammasome via NLRP3- and caspase-2-driven mitochondrial damage. *Immunity* **43**, 451–462 (2015).

[CAS](#) [PubMed](#) [PubMed Central](#) [Google Scholar](#)

16. 16.

Hetz, C. The unfolded protein response: controlling cell fate decisions under ER stress and beyond. *Nat. Rev. Mol. Cell Biol.* **13**, 89–102 (2012).

[CAS](#) [PubMed](#) [Google Scholar](#)

17. 17.

Samir, P. et al. DDX3X acts as a live-or-die checkpoint in stressed cells by regulating NLRP3 inflammasome. *Nature* **573**, 590–594 (2019).

[ADS](#) [CAS](#) [PubMed](#) [PubMed Central](#) [Google Scholar](#)

18. 18.

Man, S. M. et al. Differential roles of caspase-1 and caspase-11 in infection and inflammation. *Sci. Rep.* **7**, 45126 (2017).

[ADS](#) [CAS](#) [PubMed](#) [Google Scholar](#)

19. 19.

Dupaul-Chicoine, J. et al. Control of intestinal homeostasis, colitis, and colitis-associated colorectal cancer by the inflammatory caspases. *Immunity* **32**, 367–378 (2010).

[CAS](#) [PubMed](#) [Google Scholar](#)

20. 20.

Zaki, M. H. et al. The NLRP3 inflammasome protects against loss of epithelial integrity and mortality during experimental colitis. *Immunity* **32**, 379–391 (2010).

[CAS](#) [PubMed](#) [PubMed Central](#) [Google Scholar](#)

21. 21.

Chadani, Y. et al. Intrinsic ribosome destabilization underlies translation and provides an organism with a strategy of environmental sensing. *Mol. Cell* **68**, 528–539.e5 (2017).

[CAS](#) [PubMed](#) [Google Scholar](#)

22. 22.

van der Horst, S., Filipovska, T., Hanson, J. & Smeekens, S. Metabolite control of translation by conserved peptide uORFs: the ribosome as a metabolite multisensor. *Plant Physiol.* **182**, 110–122 (2020).

[PubMed](#) [Google Scholar](#)

23. 23.

Menu, P. et al. ER stress activates the NLRP3 inflammasome via an UPR-independent pathway. *Cell Death Dis.* **3**, e261 (2012).

[CAS](#) [PubMed](#) [PubMed Central](#) [Google Scholar](#)

24. 24.

Chen, J. & Chen, Z. J. PtdIns4P on dispersed trans-Golgi network mediates NLRP3 inflammasome activation. *Nature* **564**, 71–76 (2018).

[ADS](#) [CAS](#) [PubMed](#) [Google Scholar](#)

25. 25.

Muñoz-Planillo, R. et al. K⁺ efflux is the common trigger of NLRP3 inflammasome activation by bacterial toxins and particulate matter. *Immunity* **38**, 1142–1153 (2013).

[PubMed](#) [PubMed Central](#) [Google Scholar](#)

26. 26.

Topf, U. et al. Quantitative proteomics identifies redox switches for global translation modulation by mitochondrially produced reactive oxygen species. *Nat. Commun.* **9**, 324 (2018).

[ADS](#) [PubMed](#) [PubMed Central](#) [Google Scholar](#)

27. 27.

Willi, J. et al. Oxidative stress damages rRNA inside the ribosome and differentially affects the catalytic center. *Nucleic Acids Res.* **46**, 1945–1957 (2018).

[CAS](#) [PubMed](#) [PubMed Central](#) [Google Scholar](#)

28. 28.

Lamarre, C. et al. Galactofuranose attenuates cellular adhesion of *Aspergillus fumigatus*. *Cell. Microbiol.* **11**, 1612–1623 (2009).

[CAS](#) [PubMed](#) [Google Scholar](#)

29. 29.

da Silva Ferreira, M. E. et al. The *akuB*^{KU80} mutant deficient for nonhomologous end joining is a powerful tool for analyzing pathogenicity in *Aspergillus fumigatus*. *Eukaryot. Cell* **5**, 207–211 (2006).

[PubMed](#) [PubMed Central](#) [Google Scholar](#)

30. 30.

Kayagaki, N. et al. Non-canonical inflammasome activation targets caspase-11. *Nature* **479**, 117–121 (2011).

[ADS](#) [CAS](#) [PubMed](#) [Google Scholar](#)

31. 31.

Kanneganti, T. D. et al. Bacterial RNA and small antiviral compounds activate caspase-1 through cryopyrin/Nalp3. *Nature* **440**, 233–236 (2006).

[ADS](#) [CAS](#) [PubMed](#) [Google Scholar](#)

32. 32.

Jones, J. W. et al. Absent in melanoma 2 is required for innate immune recognition of *Francisella tularensis*. *Proc. Natl Acad. Sci. USA* **107**, 9771–9776 (2010).

[ADS](#) [CAS](#) [PubMed](#) [Google Scholar](#)

33. 33.

Karki, R. et al. IRF8 regulates transcription of Naips for NLRC4 inflammasome activation. *Cell* **173**, 920–933 (2018).

[CAS](#) [PubMed](#) [PubMed Central](#) [Google Scholar](#)

34. 34.

Hartmann, T. et al. Validation of a self-excising marker in the human pathogen *Aspergillus fumigatus* by employing the β -rec/six site-specific recombination system. *Appl. Environ. Microbiol.* **76**, 6313–6317 (2010).

[CAS](#) [PubMed](#) [PubMed Central](#) [Google Scholar](#)

35. 35.

Briard, B. et al. Dirhamnolipids secreted from *Pseudomonas aeruginosa* modify anjpegunal susceptibility of *Aspergillus fumigatus* by inhibiting β 1,3 glucan synthase activity. *ISME J.* **11**, 1578–1591 (2017).

[CAS](#) [PubMed](#) [PubMed Central](#) [Google Scholar](#)

36. 36.

Muszkieta, L. et al. Deciphering the role of the chitin synthase families 1 and 2 in the in vivo and in vitro growth of *Aspergillus fumigatus* by multiple gene targeting deletion. *Cell. Microbiol.* **16**, 1784–1805 (2014).

[CAS](#) [PubMed](#) [Google Scholar](#)

37. 37.

Dubois, M., Gilles, K., Hamilton, J. K., Rebers, P. A. & Smith, F. A colorimetric method for the determination of sugars. *Nature* **168**, 167 (1951).

[ADS](#) [CAS](#) [PubMed](#) [Google Scholar](#)

38. 38.

Stalhberger, T. et al. Chemical organization of the cell wall polysaccharide core of *Malassezia restricta*. *J. Biol. Chem.* **289**, 12647–12656 (2014).

[CAS](#) [PubMed](#) [PubMed Central](#) [Google Scholar](#)

39. 39.

Plassard, C. S., Mousain, D. G. & Salsac, L. E. Estimation of mycelial growth of basidiomycetes by means of chitin determination. *Phytochemistry* **21**, 345–348 (1982).

[CAS](#) [Google Scholar](#)

40. 40.

Fontaine, T., Talmont, F., Dutton, G. G. S. & Fournet, B. Analysis of pyruvic acid acetal containing polysaccharides by methanolysis and reductive cleavage methods. *Anal. Biochem.* **199**, 154–161 (1991).

[CAS](#) [PubMed](#) [Google Scholar](#)

41. 41.

Gressler, M. et al. Definition of the anti-inflammatory oligosaccharides derived from the galactosaminogalactan (GAG) from *Aspergillus fumigatus*. *Front. Cell. Infect. Microbiol.* **9**, 365 (2019).

[CAS](#) [PubMed](#) [PubMed Central](#) [Google Scholar](#)

42. 42.

Samir, P. et al. Identification of changing ribosome protein compositions using mass spectrometry. *Proteomics* **18**, 1800217 (2018).

[Google Scholar](#)

43. 43.

Werner, J. L. et al. Requisite role for the dectin-1 β -glucan receptor in pulmonary defense against *Aspergillus fumigatus*. *J. Immunol.* **182**, 4938–4946 (2009).

[CAS](#) [PubMed](#) [PubMed Central](#) [Google Scholar](#)

44. 44.

Gresnigt, M. S. et al. A polysaccharide virulence factor from *Aspergillus fumigatus* elicits anti-inflammatory effects through induction of interleukin-1 receptor antagonist. *PLoS Pathog.* **10**, e1003936 (2014).

[PubMed](#) [PubMed Central](#) [Google Scholar](#)

45. 45.

Schindelin, J. et al. Fiji: an open-source platform for biological-image analysis. *Nat. Methods* **9**, 676–682 (2012).

[CAS](#) [PubMed](#) [Google Scholar](#)

46. 46.

Mouyna, I. et al. GH16 and GH81 family β-(1,3)-glucanases in *Aspergillus fumigatus* are essential for conidial cell wall morphogenesis. *Cell. Microbiol.* **18**, 1285–1293 (2016).

[CAS](#) [PubMed](#) [Google Scholar](#)

[Download references](#)

Acknowledgements

We thank members of the Kanneganti laboratory for their comments, suggestions and technical assistance; R. Tweedell for scientific editing of the manuscript; the St Jude Children's Research Hospital Veterinary Pathology Core, SJCRH Center for Proteomics and Metabolomics and SJCRH Cell and Tissue Imaging Center (supported by the NCI P30 CA021765); D. Sheppard for sharing the *A. fumigatus* deletion mutant Δagd ; and V. M. Dixit and N. Kayagaki for the *CaspI*^{-/-}*CaspII*^{-/-} mutant mouse strain. T.-D.K. is supported by NIH grants AI101935, AI124346,

AR056296 and CA253095 and by the American Lebanese Syrian Associated Charities. The content is solely the responsibility of the authors and does not necessarily represent the official views of the National Institutes of Health. J.-P.L. is supported by the Aviesan project Aspergillus, the French Government's Investissement d'Avenir program, Laboratoire d'Excellence 'Integrative Biology of Emerging Infectious Diseases' (grant number ANR-10-LABX-62-IBEID) and la Fondation pour la Recherche Médicale (DEQ20150331722 LATGE Equipe FRM 2015).

Author information

Author notes

1. Jean-Paul Latgé

Present address: Institute of Molecular Biology and Biotechnology, Foundation for Research and Technology, Heraklion, Greece

Affiliations

1. Department of Immunology, St Jude Children's Research Hospital, Memphis, TN, USA

Benoit Briard, Parimal Samir, David E. Place, R. K. Subbarao Malireddi, Rajendra Karki, Shelbi Christgen & Thirumala-Devi Kanneganti

2. Unité des Aspergillus, Institut Pasteur, Paris, France

Thierry Fontaine, Laetitia Muszkieta, Rémi Beau & Jean-Paul Latgé

3. Ultrastructural Bio Imaging Unit, C2RT, Institut Pasteur, Paris, France

Perrine Bomme

4. Animal Resources Center and the Veterinary Pathology Core, St Jude Children's Research Hospital, Memphis, TN, USA

Peter Vogel

5. Mycology Reference Laboratory, Centro Nacional de Microbiología, Instituto de Salud Carlos III, Madrid, Spain

Emilia Mellado

6. Unité des Cytokines et Inflammation, Institut Pasteur, Paris, France

Oumaima Ibrahim-Granet

7. AFMB, UMR 7257 CNRS, Aix-Marseille Université, Marseille, France

Bernard Henrissat

8. Department of Structural Biology, St Jude Children's Research Hospital, Memphis, TN, USA

Ravi C. Kalathur

9. Cell and Tissue Imaging Center, St Jude Children's Research Hospital, Memphis, TN, USA

Cam Robinson

10. Department of Biological Sciences, King Abdulaziz University, Jeddah, Saudi Arabia

Bernard Henrissat

Authors

1. Benoit Briard

[View author publications](#)

You can also search for this author in [PubMed](#) [Google Scholar](#)

2. Thierry Fontaine

[View author publications](#)

You can also search for this author in [PubMed](#) [Google Scholar](#)

3. Parimal Samir

[View author publications](#)

You can also search for this author in [PubMed](#) [Google Scholar](#)

4. David E. Place

[View author publications](#)

You can also search for this author in [PubMed](#) [Google Scholar](#)

5. Laetitia Muszkieta

[View author publications](#)

You can also search for this author in [PubMed](#) [Google Scholar](#)

6. R. K. Subbarao Malireddi

[View author publications](#)

You can also search for this author in [PubMed](#) [Google Scholar](#)

7. Rajendra Karki

[View author publications](#)

You can also search for this author in [PubMed](#) [Google Scholar](#)

8. Shelbi Christgen

[View author publications](#)

You can also search for this author in [PubMed](#) [Google Scholar](#)

9. Perrine Bomme

[View author publications](#)

You can also search for this author in [PubMed](#) [Google Scholar](#)

10. Peter Vogel

[View author publications](#)

You can also search for this author in [PubMed](#) [Google Scholar](#)

11. Rémi Beau

[View author publications](#)

You can also search for this author in [PubMed](#) [Google Scholar](#)

12. Emilia Mellado

[View author publications](#)

You can also search for this author in [PubMed](#) [Google Scholar](#)

13. Oumaima Ibrahim-Granet

[View author publications](#)

You can also search for this author in [PubMed](#) [Google Scholar](#)

14. Bernard Henrissat

[View author publications](#)

You can also search for this author in [PubMed](#) [Google Scholar](#)

15. Ravi C. Kalathur

[View author publications](#)

You can also search for this author in [PubMed](#) [Google Scholar](#)

16. Cam Robinson

[View author publications](#)

You can also search for this author in [PubMed](#) [Google Scholar](#)

17. Jean-Paul Latgé

[View author publications](#)

You can also search for this author in [PubMed](#) [Google Scholar](#)

18. Thirumala-Devi Kanneganti

[View author publications](#)

You can also search for this author in [PubMed](#) [Google Scholar](#)

Contributions

B.B. and T.-D.K. conceptualized the study and designed the experiments. B.B., P.S., D.E.P., R.K.S.M., R.K. and S.C. performed the in vitro experiments with BMDMs. B.B., D.E.P., R.K. and S.C. performed the in vivo experiments. T.F., L.M., P.B., R.B., E.M., O.I.-G. and B.H. generated and biochemically characterized the $\Delta gt4c$ *Aspergillus* strain. P.V. analysed the in vivo pathology. B.B., P.S. and R.C.K. performed the polysome profiling. P.B. and C.R. performed the electron microscopy. B.B., T.F., J.-P.L. and T.-D.K. analysed the data. B.B. and T.-D.K. wrote the paper. T.-D.K. and J.-P.L. obtained funding. T.-D.K. supervised the study.

Corresponding author

Correspondence to [Thirumala-Devi Kanneganti](#).

Ethics declarations

Competing interests

The authors declare no competing interests.

Additional information

Peer review information *Nature* thanks Gordon D. Brown, Osamu Takeuchi and the other, anonymous, reviewer(s) for their contribution to the peer review of this work.

Publisher's note Springer Nature remains neutral with regard to jurisdictional claims in published maps and institutional affiliations.

Extended data figures and tables

Extended Data Fig. 1 Identification of *A. fumigatus* GAG synthase.

a, Schematic of GAG synthase cluster. **b**, RNA sequencing analysis during *A. fumigatus* growth (0, 4 and 8 h) from ref. 46; gene expression is represented by mean of normalized read count per gene for the *GT4C* cluster. $n = 3$ biologically independent samples. Data are mean \pm s.e.m. **c**, Heat map showing differential gene expression of *A. fumigatus* at 4 h (swollen conidia) and 8 h (germinated conidia) compared to 0 h (resting conidia). **d**, Schematic of the *GT4C* protein with transmembrane regions (black), α -glycosyltransferase domains (green) and major facilitator superfamily domain (MFS) predicted from amino acid sequence with InterProScan 5. **e**, Schematic of wild-type (WT) and $\Delta gt4c$ locus with NcoI restriction sites and Southern blot probe used to control the *GT4C* gene deletion. **f**, Southern blot using *GT4C* probe with WT and $\Delta gt4c$ purified DNA from one experiment. **g**, RT–PCR analysis of *GT4C*, *AGD3*, *EGA3*, *SPH3* and *UGE3* *A. fumigatus* genes in WT and $\Delta gt4c$ strains (8 h in LB medium, 37 °C and 250 rpm) presented relative to that of *TEF1*. n.d., not detected. $n = 3$ biologically independent samples. Data are mean \pm s.e.m.

[Source data](#)

Extended Data Fig. 2 Absence of GAG does not affect release of non-inflammasome dependent cytokines.

a, b, Release of IL-6 (**a**) and TNF (**b**) from unprimed BMDMs left uninfected (med.) or assessed 20 h after infection with *A. fumigatus* wild type (WT) or $\Delta gt4c$ strain (MOI of 10). $n = 3$ independent biological samples. Data are mean \pm s.e.m. [Source data](#)

Extended Data Fig. 3 *UGE3* potentiates *A. fumigatus*-induced inflammasome activation.

a, Assessment of biofilm formation on an abiotic surface with *A. fumigatus* (*A. f*) wild type (WT) and deletion mutant strain $\Delta uge3$. **b**, Immunoblot

analysis of pro-caspase 1 (pro-Casp1; p45) and the active caspase 1 subunit (p20) from unprimed BMDMs left untreated (medium alone (med.)) or measured 20 h after infection with the indicated *A. fumigatus* live resting conidia (MOI of 10). Representative images. $n \geq 3$ independent experiments. **c**, Immunoblot analysis of phospho-I κ B α and total I κ B α (t-I κ B α) or phospho-ERK1/2 (p-ERK) and total ERK1/2 (t-ERK) from unprimed WT BMDMs 0–8 h after infection with WT or Δ *uge3* mutant *A. fumigatus* live resting conidia (MOI of 10). Representative images. $n \geq 3$ independent experiments. **d**, Immunoblot analysis of pro-IL-1 β from unprimed BMDMs 0–8 h after infection with WT or Δ *uge3* mutant *A. fumigatus* live resting conidia (MOI of 10). Representative images. $n \geq 3$ independent experiments. **e–g**, RT–PCR analysis of *Nlrp3*, *Il1b* and *Tnf* genes from WT BMDMs 0–8 h after infection with WT or Δ *uge3* mutant *A. fumigatus* live resting conidia presented relative to that of the gene encoding β -actin. $n = 4$ biologically independent samples. Data are mean \pm s.e.m. [Source data](#)

Extended Data Fig. 4 Over-synthesis of GAG induces hyper-inflammasome activation.

a, Immunofluorescence staining of *A. fumigatus* GAG (green) and BMDM nuclei (blue) in unprimed BMDMs 4 h after infection with *A. fumigatus* wild-type (WT) or Δ *ugm1* resting conidia (MOI of 10). Scale bars, 10 μ m. Representative images. $n \geq 3$ independent experiments. **b**, Immunoblot analysis of pro-caspase 1 (pro-Casp1; p45) and the active caspase 1 subunit (p20) of unprimed BMDMs left untreated (medium alone (med.)) or assessed 20 h after infection with the indicated live *A. fumigatus* resting conidia genotype (WT or *A. fumigatus* deletion mutant Δ *ugm1*) (MOI of 10). Representative image. $n \geq 3$ independent experiments. **c**, Release of IL-1 β from unprimed BMDMs left uninfected (med.) or assessed 20 h after infection with *A. fumigatus* (MOI of 10). ** $P = 0.0046$. Unpaired two-tailed *t*-test. $n = 4$ biologically independent samples. Data are mean \pm s.e.m. [Source data](#)

Extended Data Fig. 5 GAG induces caspase 1 cleavage in a dose- and charge-charge interaction-dependent manner and

interacts with ribosomes.

a, Representative images of BMDMs in medium (med.) or during treatment with DOTAP alone (green fluorescence corresponds to Sytox green nuclei, and Sytox green-positive nuclei are marked with a red circle). Scale bars, 10 µm. Representative images. $n \geq 3$ independent experiments. **b**, Immunoblot analysis of pro-caspase 1 (pro-Casp1; p45) and the active caspase 1 subunit (p20) of BMDMs left untreated (medium alone (med.)) or assessed 3 h after transfection with increasing concentrations of GAG or vehicle alone (DOTAP). Representative image. $n \geq 3$ independent experiments. **c**, Immunoblot analysis of caspase 1 during transfection with GAG in wild-type (WT) and *Gsdmd*^{-/-} BMDMs. Representative image. $n \geq 3$ independent experiments. **d**, Volcano plot of the polysaccharide pull-down mass spectrometry analysis of the β-glucan interactome with BMDM cytosolic proteins versus control. Proteins with $P < 0.005$ are highlighted in orange and proteins with $P < 0.005$ and \log_2 -transformed fold change > 7 compared to control are highlighted in red (none identified); P value was determined by the *G* test; exact P values are presented in Supplementary Table 1. **e**, Immunoblot analysis of ribosomal proteins interacting with GAG, Ac-GAG, d-GAG or β-glucan or vehicle with or without NaCl. Representative images. $n \geq 3$ independent experiments. **f**, Immunoblot analysis of caspase 1 from BMDMs assessed after 3 h incubation with GAG, Ac-GAG or d-GAG, with or without NaCl. Representative image. $n \geq 3$ independent experiments. **g, h**, Measurement of cell death by Sytox green staining during GAG and d-GAG treatment, with or without NaCl. $n = 3$ biologically independent samples. Data are mean ± s.e.m. **i**, Electron microscopy pictures of ribosomes, GAG + ribosomes and chitin + ribosomes with negative staining; data from one experiment. Scale bars, 100 nm. [Source data](#)

Extended Data Fig. 6 GAG inhibits translation and induces endoplasmic stress.

a–c Immunoblot analysis of translation rate in BMDMs by puromycin integration into proteins during vehicle (DOTAP) or PBS incubation (**a**), poly(dA:dT) transfection (**b**) or *A. fumigatus* infection and pro-caspase 1

(pro-Casp1; p45) and the active caspase 1 subunit (p20) during *A. fumigatus* infection (**c**). Representative images. $n \geq 2$ independent experiments. **d**, Polysome profiling during DOTAP or DOTAP + GAG treatments. **e**, Immunoblot analysis of the cell pellet after polysome profiling. Representative images. $n \geq 2$ independent experiments. **f**, Polysome:monosome ratio during DOTAP or DOTAP + GAG treatments. Data are mean \pm s.e.m. * $P = 0.0366$. Paired two-tailed *t*-test. $n = 3$ biologically independent samples. **g–i**, Immunoblot analysis of pro-caspase 1 and the active caspase 1 subunit of wild-type (WT) or *Nlrp3*^{-/-} BMDMs assessed after 16 h incubation with 25 µg ml⁻¹ anisomycin (aniso) (**g**), 50 µg ml⁻¹ puromycin (puro) (**h**) or 50 µg ml⁻¹ cycloheximide (CHX) (**i**). Representative images. $n \geq 2$ independent experiments. **j, k**, Immunoblot analysis of PERK activation (p-PERK) and IRE1α induction during GAG transfection (**j**) or PERK activation during treatment with translation inhibitors (**k**). Representative images. $n \geq 2$ independent experiments. **l**, Immunoblot analysis of proteins ubiquitinated during GAG transfection. Representative images. $n \geq 2$ independent experiments. **m**, Immunoblot analysis of caspase 1 of BMDMs left untreated (medium alone (med.)) or assessed 3 h after transfection with DOTAP alone, GAG or GAG with MG132 treatment. Representative image. $n \geq 2$ independent experiments. [Source data](#)

Extended Data Fig. 7 Stress granules are not induced by GAG.

a, Immunofluorescence staining of G3BP1 (green), DDX3X (red) and BMDM nuclei (blue) in unprimed BMDMs 40 min after transfection with GAG or incubation with arsenite (Ars). Representative images. $n \geq 2$ independent experiments. **b**, Quantification of the percentage of stress-granule-positive cells after transfection with GAG, vehicle (DOTAP) alone or Ars. $n > 10$ biologically independent fields of cells. Data are mean \pm s.e.m. **c**, Immunofluorescence staining of G3BP1 (green), DDX3X (red) and BMDM nuclei (blue) in unprimed BMDMs 15 h after infection with *A. fumigatus*. Representative images. $n \geq 2$ independent experiments. **d, e**, Immunoblot analysis of pro-caspase 1 (pro-Casp1; p45) and the active caspase 1 subunit (p20) of BMDMs assessed 3 h after transfection with vehicle (DOTAP), GAG (**d**) or d-GAG (**e**). Representative images. $n \geq 2$ independent experiments. **f**, Immunoblot analysis of caspase 1 from

BMDMs left untreated (medium alone (med.)) or infected with *A. fumigatus* wild-type (WT) or deletion mutant $\Delta gt4c$ (MOI of 10). Representative image. $n \geq 2$ independent experiments. Scale bars, 10 μm (**a, c**). [Source data](#)

Extended Data Fig. 8 GAG-induced pro-inflammatory cytokine secretion during aspergillosis and DSS-induced colitis.

a, b, Level of IL-1 β (**a**) and IL-18 (**b**) in bronchioalveolar lavage 2 days after infection with wild-type (WT) or $\Delta ugml$ strains of *A. fumigatus*. **a**, * $P = 0.036$. Unpaired two-tailed *t*-test. $n = 6$ independent samples. Data are mean \pm s.e.m. **c**, Survival of 7–8-week-old immunocompetent WT mice infected intravenously with 1×10^6 *A. fumigatus* resting conidia (WT or $\Delta ugml$). ** $P = 0.0014$. Log-rank (Mantel–Cox) test. **d, e**, Levels of IL-1 β (**d**) and IL-18 (**e**) in liver homogenates after infection with WT or $\Delta gt4c$ strains. **d**, * $P = 0.0209$; **e**, ** $P = 0.0041$. Unpaired two-tailed *t*-test. $n = 5$ independent samples. Data are mean \pm s.e.m. **f–k**, Concentration of cytokines in colon homogenates after DSS water supplementation and treatment with GAG or vehicle (vehicle and GAG, $n = 10$ mice each). **f**, * $P = 0.0336$; **g**, * $P = 0.0181$; **h**, * $P = 0.0188$; **i**, * $P = 0.0115$; **j**, ** $P = 0.0066$; **k**, * $P = 0.0154$. Unpaired two-tailed *t*-test. Data are mean \pm s.e.m. [Source data](#)

Extended Data Table 1 Primer list

[Full size table](#)

Extended Data Table 2 Exact *P* values

[Full size table](#)

Supplementary information

Supplementary Table

Supplementary Table 1: Spectral count comparison of proteins identified from the Control and GAG-treated samples. *P* values were determined by the G-test.

Reporting Summary

Supplementary Figure

Supplementary Figure 1: Uncropped blots with molecular weight and size markers and an indication of how the images were cropped.

Source data

Source Data Fig. 1

Source Data Fig. 2

Source Data Fig. 3

Source Data Fig. 4

Source Data Extended Data Fig. 1

Source Data Extended Data Fig. 2

Source Data Extended Data Fig. 3

Source Data Extended Data Fig. 4

Source Data Extended Data Fig. 5

Source Data Extended Data Fig. 6

Source Data Extended Data Fig. 7

Source Data Extended Data Fig. 8

Rights and permissions

Reprints and Permissions

About this article



Cite this article

Briard, B., Fontaine, T., Samir, P. *et al.* Galactosaminogalactan activates the inflammasome to provide host protection. *Nature* **588**, 688–692 (2020). <https://doi.org/10.1038/s41586-020-2996-z>

Download citation

- Received: 04 March 2020
- Accepted: 23 September 2020
- Published: 02 December 2020
- Issue Date: 24 December 2020
- DOI: <https://doi.org/10.1038/s41586-020-2996-z>

Comments

By submitting a comment you agree to abide by our [Terms](#) and [Community Guidelines](#). If you find something abusive or that does not comply with our terms or guidelines please flag it as inappropriate.

[Access through your institution](#)

[Change institution](#)

[Buy or subscribe](#)

| [Section menu](#) | [Main menu](#) |

- Article
- [Published: 11 November 2020](#)

Inhibition of PCSK9 potentiates immune checkpoint therapy for cancer

- [Xinjian Liu](#)^{1,2} na1,
- [Xuhui Bao](#)¹ na1,
- [Mengjie Hu](#)¹,
- [Hanman Chang](#)¹,
- [Meng Jiao](#)¹,
- [Jin Cheng](#)³,
- [Liyi Xie](#)⁴,
- [Qian Huang](#)³,
- [Fang Li](#)¹ &
- [Chuan-Yuan Li](#) [ORCID: orcid.org/0000-0002-0418-6231](#)^{1,5,6}

[Nature](#) volume **588**, pages693–698(2020) [Cite this article](#)

- 14k Accesses
- 1 Citations
- 131 Altmetric
- [Metrics details](#)

Subjects

- [Cancer immunotherapy](#)

- [Cancer microenvironment](#)
- [Cancer therapeutic resistance](#)

Abstract

Despite its success in achieving the long-term survival of 10–30% of treated individuals, immune therapy is still ineffective for most patients with cancer^{1,2}. Many efforts are therefore underway to identify new approaches that enhance such immune ‘checkpoint’ therapy^{3,4,5} (so called because its aim is to block proteins that inhibit checkpoint signalling pathways in T cells, thereby freeing those immune cells to target cancer cells). Here we show that inhibiting PCSK9—a key protein in the regulation of cholesterol metabolism^{6,7,8}—can boost the response of tumours to immune checkpoint therapy, through a mechanism that is independent of PCSK9’s cholesterol-regulating functions. Deleting the *PCSK9* gene in mouse cancer cells substantially attenuates or prevents their growth in mice in a manner that depends on cytotoxic T cells. It also enhances the efficacy of immune therapy that is targeted at the checkpoint protein PD1. Furthermore, clinically approved PCSK9-neutralizing antibodies synergize with anti-PD1 therapy in suppressing tumour growth in mouse models of cancer.

Inhibiting PCSK9—either through genetic deletion or using PCSK9 antibodies—increases the expression of major histocompatibility protein class I (MHC I) proteins on the tumour cell surface, promoting robust intratumoral infiltration of cytotoxic T cells. Mechanistically, we find that PCSK9 can disrupt the recycling of MHC I to the cell surface by associating with it physically and promoting its relocation and degradation in the lysosome. Together, these results suggest that inhibiting PCSK9 is a promising way to enhance immune checkpoint therapy for cancer.

[Access through your institution](#)

[Change institution](#)

[Buy or subscribe](#)

Access options

Subscribe to Journal

Get full journal access for 1 year

\$199.00

only \$3.83 per issue

[Subscribe](#)

All prices are NET prices.

VAT will be added later in the checkout.

Rent or Buy article

Get time limited or full article access on ReadCube.

from \$8.99

[Rent or Buy](#)

All prices are NET prices.

Additional access options:

- [Log in](#)
- [Access through your institution](#)
- [Learn about institutional subscriptions](#)

Fig. 1: PCSK9 depletion attenuates tumour growth in syngeneic mice.

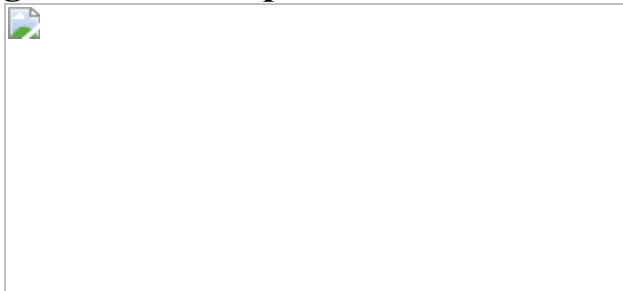


Fig. 2: Inhibition of PCSK9 overcomes tumour resistance to anti-PD1 therapy.

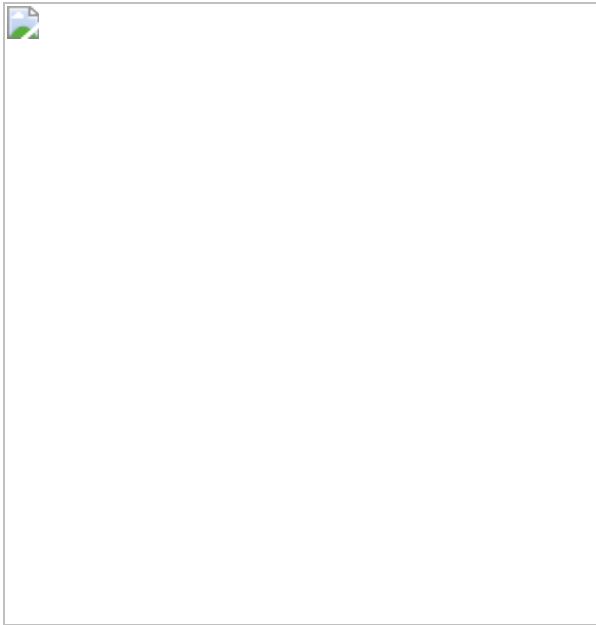
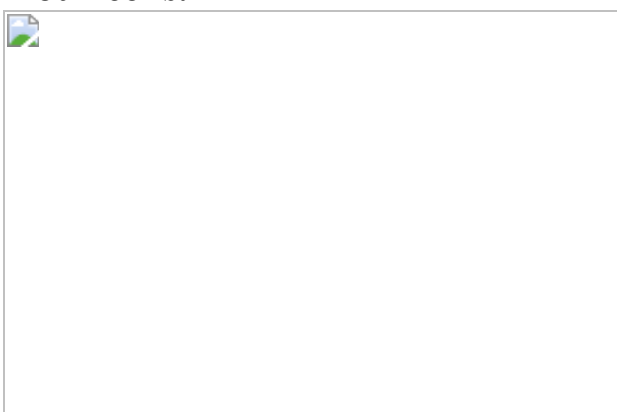


Fig. 3: Depletion of PCSK9 enhances intratumoral T-cell infiltration.



Fig. 4: PCSK9 promotes lysosome-mediated degradation of MHC I in tumour cells.



Data availability

PCSK9 and *CD8A* mRNA expression data from various human cancers were downloaded from the GENT (<http://gent2.appex.kr/gent2/>) database⁴³. *PCSK9* mRNA expression and overall survival data were from TCGA data sets included in cBioportal^{44,45} (<https://www.cbiopal.org/>) in November 2018. Western blot source data are provided in Supplementary Fig. 1. Source data for the quantitative graphs are provided for Figs. 1–4 and Extended Data Figs. 1–9. Other data in support of this study are available from the corresponding author upon reasonable request. [Source data](#) are provided with this paper.

References

1. 1.

Topalian, S. L. et al. Safety, activity, and immune correlates of anti-PD-1 antibody in cancer. *N. Engl. J. Med.* **366**, 2443–2454 (2012).

[CAS](#) [PubMed](#) [PubMed Central](#) [Google Scholar](#)

2. 2.

Brahmer, J. R. et al. Safety and activity of anti-PD-L1 antibody in patients with advanced cancer. *N. Engl. J. Med.* **366**, 2455–2465 (2012).

[CAS](#) [PubMed](#) [PubMed Central](#) [Google Scholar](#)

3. 3.

Manguso, R. T. et al. In vivo CRISPR screening identifies Ptpn2 as a cancer immunotherapy target. *Nature* **547**, 413–418 (2017).

[CAS](#) [PubMed](#) [PubMed Central](#) [Google Scholar](#)

4. 4.

Pan, D. et al. A major chromatin regulator determines resistance of tumor cells to T cell-mediated killing. *Science* **359**, 770–775 (2018).

[ADS](#) [CAS](#) [PubMed](#) [PubMed Central](#) [Google Scholar](#)

5. 5.

Patel, S. J. et al. Identification of essential genes for cancer immunotherapy. *Nature* **548**, 537–542 (2017).

[ADS](#) [CAS](#) [PubMed](#) [PubMed Central](#) [Google Scholar](#)

6. 6.

Abifadel, M. et al. Mutations in PCSK9 cause autosomal dominant hypercholesterolemia. *Nat. Genet.* **34**, 154–156 (2003).

[CAS](#) [PubMed](#) [Google Scholar](#)

7. 7.

Cohen, J. et al. Low LDL cholesterol in individuals of African descent resulting from frequent nonsense mutations in PCSK9. *Nat. Genet.* **37**, 161–165 (2005); corrigendum **37**, 328 (2005).

[CAS](#) [PubMed](#) [Google Scholar](#)

8. 8.

Cohen, J. C., Boerwinkle, E., Mosley, T. H., Jr & Hobbs, H. H. Sequence variations in PCSK9, low LDL, and protection against coronary heart disease. *N. Engl. J. Med.* **354**, 1264–1272 (2006).

[CAS](#) [PubMed](#) [Google Scholar](#)

9. 9.

Yang, W. et al. Potentiating the antitumour response of CD8⁺ T cells by modulating cholesterol metabolism. *Nature* **531**, 651–655 (2016).

[ADS](#) [CAS](#) [PubMed](#) [PubMed Central](#) [Google Scholar](#)

10. 10.

Ma, X. et al. Cholesterol negatively regulates IL-9-producing CD8⁺ T cell differentiation and antitumor activity. *J. Exp. Med.* **215**, 1555–1569 (2018).

[CAS](#) [PubMed](#) [PubMed Central](#) [Google Scholar](#)

11. 11.

Naslavsky, N., Weigert, R. & Donaldson, J. G. Characterization of a nonclathrin endocytic pathway: membrane cargo and lipid requirements. *Mol. Biol. Cell* **15**, 3542–3552 (2004).

[CAS](#) [PubMed](#) [PubMed Central](#) [Google Scholar](#)

12. 12.

Benjannet, S. et al. NARC-1/PCSK9 and its natural mutants: zymogen cleavage and effects on the low density lipoprotein (LDL) receptor and LDL cholesterol. *J. Biol. Chem.* **279**, 48865–48875 (2004).

[CAS](#) [PubMed](#) [Google Scholar](#)

13. 13.

Maxwell, K. N., Fisher, E. A. & Breslow, J. L. Overexpression of PCSK9 accelerates the degradation of the LDLR in a post-endoplasmic reticulum compartment. *Proc. Natl Acad. Sci. USA* **102**, 2069–2074 (2005).

[ADS](#) [CAS](#) [PubMed](#) [Google Scholar](#)

14. 14.

Zhang, D. W. et al. Binding of proprotein convertase subtilisin/kexin type 9 to epidermal growth factor-like repeat A of low density

lipoprotein receptor decreases receptor recycling and increases degradation. *J. Biol. Chem.* **282**, 18602–18612 (2007).

[CAS](#) [PubMed](#) [Google Scholar](#)

15. 15.

Lagace, T. A. et al. Secreted PCSK9 decreases the number of LDL receptors in hepatocytes and in livers of parabiotic mice. *J. Clin. Invest.* **116**, 2995–3005 (2006).

[CAS](#) [PubMed](#) [PubMed Central](#) [Google Scholar](#)

16. 16.

Poirier, S. et al. Dissection of the endogenous cellular pathways of PCSK9-induced low density lipoprotein receptor degradation: evidence for an intracellular route. *J. Biol. Chem.* **284**, 28856–28864 (2009).

[CAS](#) [PubMed](#) [PubMed Central](#) [Google Scholar](#)

17. 17.

Poirier, S. et al. The proprotein convertase PCSK9 induces the degradation of low density lipoprotein receptor (LDLR) and its closest family members VLDLR and ApoER2. *J. Biol. Chem.* **283**, 2363–2372 (2008).

[CAS](#) [PubMed](#) [Google Scholar](#)

18. 18.

Canuel, M. et al. Proprotein convertase subtilisin/kexin type 9 (PCSK9) can mediate degradation of the low density lipoprotein receptor-related protein 1 (LRP-1). *PLoS One* **8**, e64145 (2013).

[ADS](#) [CAS](#) [PubMed](#) [PubMed Central](#) [Google Scholar](#)

19. 19.

Demers, A. et al. PCSK9 induces CD36 degradation and affects long-chain fatty acid uptake and triglyceride metabolism in adipocytes and in mouse liver. *Arterioscler. Thromb. Vasc. Biol.* **35**, 2517–2525 (2015).

[CAS](#) [PubMed](#) [Google Scholar](#)

20. 20.

Jonas, M. C., Costantini, C. & Puglielli, L. PCSK9 is required for the disposal of non-acetylated intermediates of the nascent membrane protein BACE1. *EMBO Rep.* **9**, 916–922 (2008).

[CAS](#) [PubMed](#) [PubMed Central](#) [Google Scholar](#)

21. 21.

Blom, D. J. et al. A 52-week placebo-controlled trial of evolocumab in hyperlipidemia. *N. Engl. J. Med.* **370**, 1809–1819 (2014).

[CAS](#) [PubMed](#) [Google Scholar](#)

22. 22.

Robinson, J. G. et al. Efficacy and safety of alirocumab in reducing lipids and cardiovascular events. *N. Engl. J. Med.* **372**, 1489–1499 (2015).

[CAS](#) [PubMed](#) [Google Scholar](#)

23. 23.

Cong, L. et al. Multiplex genome engineering using CRISPR/Cas systems. *Science* **339**, 819–823 (2013).

[ADS](#) [CAS](#) [PubMed](#) [PubMed Central](#) [Google Scholar](#)

24. 24.

Ran, F. A. et al. Genome engineering using the CRISPR-Cas9 system. *Nat. Protocols* **8**, 2281–2308 (2013).

[CAS](#) [PubMed](#) [Google Scholar](#)

25. 25.

Ishibashi, S. et al. Hypercholesterolemia in low density lipoprotein receptor knockout mice and its reversal by adenovirus-mediated gene delivery. *J. Clin. Invest.* **92**, 883–893 (1993).

[CAS](#) [PubMed](#) [PubMed Central](#) [Google Scholar](#)

26. 26.

Wolchok, J. D. et al. Nivolumab plus ipilimumab in advanced melanoma. *N. Engl. J. Med.* **369**, 122–133 (2013).

[CAS](#) [PubMed](#) [PubMed Central](#) [Google Scholar](#)

27. 27.

Kühnast, S. et al. Alirocumab inhibits atherosclerosis, improves the plaque morphology, and enhances the effects of a statin. *J. Lipid Res.* **55**, 2103–2112 (2014).

[PubMed](#) [PubMed Central](#) [Google Scholar](#)

28. 28.

Chan, J. C. et al. A proprotein convertase subtilisin/kexin type 9 neutralizing antibody reduces serum cholesterol in mice and nonhuman primates. *Proc. Natl Acad. Sci. USA* **106**, 9820–9825 (2009).

[ADS](#) [CAS](#) [PubMed](#) [Google Scholar](#)

29. 29.

Kim, K. et al. Eradication of metastatic mouse cancers resistant to immune checkpoint blockade by suppression of myeloid-derived cells. *Proc. Natl Acad. Sci. USA* **111**, 11774–11779 (2014).

[ADS](#) [CAS](#) [PubMed](#) [Google Scholar](#)

30. 30.

Chandramohan, V. et al. Improved efficacy against malignant brain tumors with EGFRwt/EGFRvIII targeting immunotoxin and checkpoint inhibitor combinations. *J. Immunother. Cancer* **7**, 142 (2019).

[PubMed](#) [PubMed Central](#) [Google Scholar](#)

31. 31.

Hogquist, K. A. et al. T cell receptor antagonist peptides induce positive selection. *Cell* **76**, 17–27 (1994).

[CAS](#) [PubMed](#) [Google Scholar](#)

32. 32.

Shan, L. et al. PCSK9 binds to multiple receptors and can be functionally inhibited by an EGF-A peptide. *Biochem. Biophys. Res. Commun.* **375**, 69–73 (2008).

[CAS](#) [PubMed](#) [Google Scholar](#)

33. 33.

Fasano, T., Sun, X. M., Patel, D. D. & Soutar, A. K. Degradation of LDLR protein mediated by ‘gain of function’ PCSK9 mutants in normal and ARH cells. *Atherosclerosis* **203**, 166–171 (2009).

[CAS](#) [PubMed](#) [Google Scholar](#)

34. 34.

Duff, C. J. et al. Antibody-mediated disruption of the interaction between PCSK9 and the low-density lipoprotein receptor. *Biochem. J.* **419**, 577–584 (2009).

[CAS](#) [PubMed](#) [PubMed Central](#) [Google Scholar](#)

35. 35.

Yu, Y. Y. et al. Definition and transfer of a serological epitope specific for peptide-empty forms of MHC class I. *Int. Immunol.* **11**, 1897–1906 (1999).

[CAS](#) [PubMed](#) [Google Scholar](#)

36. 36.

Zhang, L. et al. Intratumoral T cells, recurrence, and survival in epithelial ovarian cancer. *N. Engl. J. Med.* **348**, 203–213 (2003).

[CAS](#) [PubMed](#) [Google Scholar](#)

37. 37.

Carstens, J. L. et al. Spatial computation of intratumoral T cells correlates with survival of patients with pancreatic cancer. *Nat. Commun.* **8**, 15095 (2017).

[ADS](#) [PubMed](#) [PubMed Central](#) [Google Scholar](#)

38. 38.

Labun, K. et al. CHOPCHOP v3: expanding the CRISPR web toolbox beyond genome editing. *Nucleic Acids Res.* **47** (W1), W171–W174 (2019).

[CAS](#) [PubMed](#) [PubMed Central](#) [Google Scholar](#)

39. 39.

Shalem, O. et al. Genome-scale CRISPR-Cas9 knockout screening in human cells. *Science* **343**, 84–87 (2014).

[ADS](#) [CAS](#) [PubMed](#) [PubMed Central](#) [Google Scholar](#)

40. 40.

Borowicz, S. et al. The soft agar colony formation assay. *J. Vis. Exp.* **92**, e51998 (2014).

[Google Scholar](#)

41. 41.

Moore, M. W., Carbone, F. R. & Bevan, M. J. Introduction of soluble protein into the class I pathway of antigen processing and presentation. *Cell* **54**, 777–785 (1988).

[CAS](#) [PubMed](#) [Google Scholar](#)

42. 42.

Curtsinger, J. M., Lins, D. C. & Mescher, M. F. CD8+ memory T cells (CD44high, Ly-6C+) are more sensitive than naive cells to (CD44low, Ly-6C-) to TCR/CD8 signaling in response to antigen. *J. Immunol.* **160**, 3236–3243 (1998).

[CAS](#) [PubMed](#) [Google Scholar](#)

43. 43.

Park, S. J., Yoon, B. H., Kim, S. K. & Kim, S. Y. GENT2: an updated gene expression database for normal and tumor tissues. *BMC Med. Genomics* **12** (Suppl 5), 101 (2019).

[PubMed](#) [PubMed Central](#) [Google Scholar](#)

44. 44.

Cerami, E. et al. The cBio cancer genomics portal: an open platform for exploring multidimensional cancer genomics data. *Cancer Discov.* **2**, 401–404 (2012).

[Google Scholar](#)

45. 45.

Gao, J. et al. Integrative analysis of complex cancer genomics and clinical profiles using the cBioPortal. *Sci. Signal.* **6**, pl1 (2013).

[PubMed](#) [PubMed Central](#) [Google Scholar](#)

[Download references](#)

Acknowledgements

We thank J. M. Cook and colleagues at the Flow Cytometry Facility of Duke University School of Medicine for their assistance. We also thank the Duke University Light Microscopy Core Facility for professional help with confocal microscopy. We thank I. Li for proofreading our manuscript. We also thank S. Coffman of MedMedia Solutions for help with illustrations. C.-Y.L. is supported by US National Institutes of Health (NIH) grants ES024015, CA208852 and CA216876, and by a Cancer Center Support Grant (CCSG, CA014236) to Duke University. X.L. is supported by Guangdong Basic and Applied Basic Research Foundation grant 2020B1515020054 and Shenzhen Science and Technology Program grant JCYJ20190807154813511.

Author information

Author notes

1. These authors contributed equally: Xinjian Liu, Xuhui Bao

Affiliations

1. Department of Dermatology, Duke University Medical Center, Durham, NC, USA

Xinjian Liu, Xuhui Bao, Mengjie Hu, Hanman Chang, Meng Jiao, Fang Li & Chuan-Yuan Li

2. Department of Biochemistry, Molecular Cancer Research Center, School of Medicine, Sun Yat-sen University, Shenzhen, Guangdong, China

Xinjian Liu

3. Molecular Diagnostic Laboratory of Cancer Center, Shanghai General Hospital, Shanghai Jiaotong University School of Medicine, Shanghai, China

Jin Cheng & Qian Huang

4. Department of Radiation Oncology, Fudan University Shanghai Cancer Center, Shanghai, China

Liyi Xie

5. Department of Pharmacology and Cancer Biology, Duke University Medical Center, Durham, NC, USA

Chuan-Yuan Li

6. Duke Cancer Institute, Duke University Medical Center, Durham, NC, USA

Chuan-Yuan Li

Authors

1. Xinjian Liu

[View author publications](#)

You can also search for this author in [PubMed](#) [Google Scholar](#)

2. Xuhui Bao

[View author publications](#)

You can also search for this author in [PubMed](#) [Google Scholar](#)

3. Mengjie Hu

[View author publications](#)

You can also search for this author in [PubMed](#) [Google Scholar](#)

4. Hanman Chang

[View author publications](#)

You can also search for this author in [PubMed](#) [Google Scholar](#)

5. Meng Jiao

[View author publications](#)

You can also search for this author in [PubMed](#) [Google Scholar](#)

6. Jin Cheng

[View author publications](#)

You can also search for this author in [PubMed](#) [Google Scholar](#)

7. Liyi Xie

[View author publications](#)

You can also search for this author in [PubMed](#) [Google Scholar](#)

8. Qian Huang

[View author publications](#)

You can also search for this author in [PubMed](#) [Google Scholar](#)

9. Fang Li

[View author publications](#)

You can also search for this author in [PubMed](#) [Google Scholar](#)

10. Chuan-Yuan Li

[View author publications](#)

You can also search for this author in [PubMed](#) [Google Scholar](#)

Contributions

X.L., X.B. and C.-Y.L. designed the study. X.L., X.B. and H.C. carried out CRISPR–Cas9-mediated gene knockouts in tumour cells. X.L., X.B. and H.C. performed western blot analyses. X.L. generated PCSK9 and H2-K1 mutants and carried out immunoprecipitation/western blot experiments. X.L., X.B. and M.H. carried out mouse tumour-growth experiments. X.L. and X.B. characterized tumour cells in vitro and in vivo and intratumoral lymphocytes in vivo using flow cytometry. X.B. maintained OVA-specific T-cell culture, performed CTL assays and analysed the results. X.B., L.X. and X.L. analysed TCGA data for PCSK9 expression and its relationship to the expression of *CD8A* and prognosis of patients with cancer. M.H., M.J., J.C. and Q. H. carried out immunofluorescence and immunohistochemistry analyses. F.L. advised on CRISPR knockouts and provided material support. X.L., X.B. and C.L. wrote the manuscript with help from all co-authors. C.-Y.L. provided funding and study supervision.

Corresponding author

Correspondence to [Chuan-Yuan Li](#).

Ethics declarations

Competing interests

X.L. and C.-Y.L. are inventors on a patent application filed by Duke University that covers the use of anti-PCSK9 antibodies in cancer immunotherapy. The other authors declare no competing interests.

Additional information

Peer review information *Nature* thanks the anonymous reviewers for their contribution to the peer review of this work.

Publisher's note Springer Nature remains neutral with regard to jurisdictional claims in published maps and institutional affiliations.

Extended data figures and tables

[Extended Data Fig. 1 CRISPR–Cas9-mediated knockout of PCSK9 and its effect on tumour-cell growth in vitro and in vivo.](#)

a, Western blot analysis of the expression of PCSK9 in murine tumour lines (B16F10, 4T1, MC38 and CT26) with and without PCSK9 knockout (PCSK9KO). GAPDH was used as a protein loading control. The analysis was done twice with biologically independent samples. α GAPDH, anti-GAPDH antibody; α PCSK9, anti-PCSK9 antibody. **b**, Cell growth of vector control or PCSK9KO B16F10 tumour cells. Results (means \pm s.e.m.) are from five biologically independent samples; *P*-values were calculated by unpaired two-sided *t*-test. **c**, Soft agar analysis of the colony-formation ability of B16F10 tumour cells transduced with vector control or PCSK9 sgRNA. **d**, Quantitative representation of soft agar formation in **c**. $n = 4$ biologically independent samples, showing means \pm s.e.m; *P*-values calculated by unpaired two-sided *t*-test. **e**, Details of the in vivo competition assay. **f**, Change in ratios of mixed control–tdTomato and PCSK9KO–EGFP B16F10 cells after 12 days of growth in vivo (subcutaneously) in C57BL/6 mice, as determined by flow cytometry. **g**, Quantitative representation of the flow analysis in **f**, showing means \pm s.e.m. $n = 2$ and 4 biologically independent tumour samples for in vitro and in vivo groups, respectively. *P*-values determined by unpaired two-sided *t*-test. [Source data](#)

[Extended Data Fig. 2 Effect of PCSK9 re-expression and the host immune system on tumour formation by PCSK9-knockout cells.](#)

a, Western blot analysis of the expression of exogenously transduced, HA-tagged PCSK9 in PCSK9KO B16F10 cells. The analysis was done once. **b**, **c**. Tumour formation from B16F10 PCSK9KO cells transduced with either vector control or *PCSK9* (**b**), and Kaplan–Meier survival curves of host mice (**c**). About 2×10^5 tumour cells were injected subcutaneously into C57BL/6 mice and observed for tumour formation. $n = 5$ tumours per group. Error bars show means \pm s.e.m.; P -values were determined by two-way ANOVA in **b** and log-rank test in **c**. **d–i**, Growth rate (**d**, **g**), host survival (**e**, **h**) and endpoint tumour weight (**f**, **i**) of vector control and PCSK9KO 4T1 (**d–f**) and B16F10 (**g–i**) tumours. In each case, about 1×10^5 tumour cells were injected subcutaneously and observed for tumour formation in NCG mice. $n = 6$ mice for **d**, **e**, **g**, **h**; and $n = 5$ tumours for **f**, **i**. Error bars in **d**, **f**, **g**, **i** represent means \pm s.e.m.; ns, not significant, as determined by two-way ANOVA (**d**, **g**), log-rank test (**e**, **h**), or unpaired two-sided *t*-test (**f**, **i**). **j**, **k**, Tumour growth from vector control and PCSK9KO B16F10 cells in *Rag1^{−/−}* C57BL/6 mice (**j**) and Kaplan–Meier survival curve of tumour-bearing host mice (**k**). About 1×10^5 vector control or PCSK9KO B16F10 tumour cells were injected into *Rag1^{−/−}* C57BL/6 mice and observed for tumour formation. $n = 5$ tumours per group. Error bars in **j** show means \pm s.e.m. P -values were calculated by two-way ANOVA in **j** and by log-rank test in **k**. [Source data](#)

Extended Data Fig. 3 The influence of tumour or host cell LDLR and host cholesterol levels on tumour growth from control or PCSK9KO tumour cells in immunocompetent hosts.

a, Western blot analysis of CRISPR–Cas9-mediated knockdown (KD) of LDLR in B16F10 cells. The analysis was done once. **b**, Tumour growth from vector control and LDLR KD B16F10 cells in C57BL/6 mice. $n = 5$ tumours per group. Error bars show means \pm s.e.m. P -values were calculated by two-way ANOVA. **c**, Kaplan–Meier survival curve of mice (from **b**) bearing control and LDLR KD B16F10 tumours. $n = 5$ mice per group. P -values calculated by log-rank test. **d**, Tumour growth from vector control and PCSK9-knockout B16F10 cells in wild-type (C57) and LDLR^{−/−} mice fed on a high-fat diet. $n = 12$, 12, 5 and 5 tumours in, respectively, wild-type mice inoculated with control or PCSK9KO tumour cells, and in

$\text{LDLR}^{-/-}$ mice inoculated with control and PCSK9KO tumour cells. Error bars show means \pm s.e.m. P -values were calculated by two-way ANOVA with multiple comparisons. **e**, Kaplan–Meier survival curve for wild-type and $\text{LDLR}^{-/-}$ mice (from **d**) bearing vector control and PCSK9-knockout tumours. P -values were calculated by log-rank test. [Source data](#)

Extended Data Fig. 4 Additional data on anti-PD1 treatment in murine tumours.

a, Treatment schedule for PCSK9KO 4T1 cells. Balb/c mice were implanted subcutaneously with PCSK9KO 4T1 tumour cells, treated with an anti-PD1 antibody at the indicated times, and observed for tumour formation. Animals that were implanted with PCSK9KO 4T1 tumour cells but did not form visible tumours by day 9 after inoculation were excluded from treatment with anti-PD1 antibodies. **b**, Tumour-growth delay in mice bearing PCSK9KO 4T1 tumours with or without anti-PD1 treatment. $n = 5$ tumours per group. Error bars show means \pm s.e.m. P -values were calculated by two-way ANOVA. **c**, Kaplan–Meier survival curves for tumour-bearing mice from **b**. P -values were calculated by log-rank test. **d**, Treatment schedule for PCSK9KO CT26 tumours. Balb/c mice were implanted subcutaneously with PCSK9KO CT26 tumour cells, treated with an anti-PD1 antibody at the indicated times, and observed for tumour formation. **e**, Tumour-growth delay in mice bearing PCSK9KO CT26 tumours with or without anti-PD1 treatment. $n = 5$ tumours per group. Error bars show means \pm s.e.m. P -values were determined by two-way ANOVA. **f**, Kaplan–Meier survival curves for tumour-bearing mice from **e**. Error bars show means \pm s.e.m. P -values were determined by log-rank test. **g**, A scheme to develop anti-PD1-resistant MC38R tumour cells. **h**, Scheme for treating anti-PD1-resistant MC38R tumours with evolocumab and an anti-PD1 antibody. **i**, Tumour growth kinetics from anti-PD1-resistant MC38R tumours treated with anti-PD1 antibody and/or evolocumab. $n = 5$ tumours per group. Error bars show means \pm s.e.m. P -values were determined by two-way ANOVA. **j**, Kaplan–Meier survival curve for mice bearing MC38R tumours from **i**. P -values were determined by log-rank test. **k**, Treatment schedule for PCSK9KO MC38 tumours. **l**, **m**, Tumour growth delay (**l**) and host mouse survival (**m**) among isotype (iso)- or evolocumab-treated mice bearing MC38-PCSK9KO tumours. $n = 5$ tumours per group.

P-values were calculated by two-way ANOVA test in **I** and log-rank test in **m**. [Source data](#)

Extended Data Fig. 5 Rechallenge of mice that were tumour free after initial tumour inoculation, and gating strategy for intratumoral immune effector cells.

a–c, Treatment scheme (**a**), tumour growth (**b**) and survival of host mice (**c**) after rechallenge with wild-type 4T1 tumour cells in Balb/c mice that remained tumour-free 43 days after initial challenge with PCSK9-knockout 4T1 cells. The control group consisted of tumour-naive Balb/c mice challenged with wild-type 4T1 cells. $n = 5$ and 12 mice for naive and rechallenged groups, respectively. Error bars in **b** show means \pm s.e.m. *P*-values in **b**, **c** were calculated by two-way ANOVA test and log-rank test, respectively. **d–f**, Treatment scheme (**d**), tumour growth (**e**) and survival of host mice (**f**) after rechallenge with wild-type B16F10 tumour cells in C57BL/6 mice that remained tumour-free 26 days after initial challenge with PCSK9-knockout B16F10 cells and treatment with anti-PD1 antibody. The control group consisted of tumour-naive C57BL/6 mice challenged with wild-type B16F10 cells. $n = 5$ and 13 mice for tumour-naive and rechallenge groups, respectively. Error bars in **e** show means \pm s.e.m. *P*-values in **e**, **f** were calculated by two-way ANOVA and log-rank test, respectively. **g–i**, Treatment scheme (**g**), tumour growth (**h**) and survival of host mice (**i**) after rechallenge with parental MC38 tumour cells in C57BL/6 mice that remained tumour-free 34 days after initial challenge with PCSK9-knockout MC38 cells and treatment with anti-PD1 antibody. The control group consisted of tumour-naive C57BL/6 mice challenged with wild-type MC38 cells. $n = 5$ mice per group. Error bars in **h** show means \pm s.e.m. *P*-values were calculated by two-way ANOVA (**h**) and log-rank test (**i**). **j**, Representative flow-cytometry gating strategy for quantifying the numbers of various immune effector cell subsets in murine tumours.

Extended Data Fig. 6 Additional data on the characterization of lymphocyte infiltration into murine tumours.

a, Immunofluorescence staining (left) and quantitative estimates (right) of CD45⁺ leukocytes in control and PCSK9KO tumours grown in syngeneic C57BL/6 mice. Scale bar, 50 µm; $n = 3$ biologically independent samples; four fluorescent fields for each of the three samples were counted. Error bars show means ± s.e.m.; P -values were calculated using unpaired two-sided t -tests. **b**, Immunofluorescence staining (left) and quantitative estimates (right) of CD8a⁺ cells in control and PCSK9KO B16F10 tumours. Scale bar, 20 µm. $n = 3$ biologically independent samples; four fluorescent fields for each of the three samples were counted; error bars show means ± s.e.m.; P -values were calculated using unpaired two-sided t -tests. **c**, Quantitative estimates of CD4⁺ and CD8⁺ T cells in the spleens of mice bearing control and PCSK9KO B16F10 tumours, as determined by flow cytometry. $n = 3$ mice per group; error bars show means ± s.e.m.; P -values were calculated using unpaired two-sided t -tests. **d**, Flow-cytometric determination of the percentage of intratumoral CD8⁺ T cells that expressed IFN- γ . $n = 6$, 5 tumours in the two groups. Error bars show means ± s.e.m.; P -values were calculated by unpaired two-sided t -test. **e**, **f**, qRT-PCR analysis of intratumoural *IFNG* (**e**) and *GZMB* (**f**) mRNA levels in control and PCSK9KO tumours. $n = 3$ and 4 tumours for *IFNG* and *GZMB* groups, respectively. Error bars show means ± s.e.m.; P -values were determined by unpaired two-sided t -test. **g–i**, Flow-cytometric characterization of the cell-surface expression levels of exhaustion markers for intratumoral CD8⁺ T cells in vector control and PCSK9KO tumours. $n = 6$ and 5 tumours for control and PCSK9-knockout conditions. Error bars show means ± s.e.m.; P -values were determined by unpaired two-sided t -test. **j**, Schedule for treating Balb/c mice, injected with 4T1 tumour cells, with evolocumab (α PCSK9 Ab) and anti-PD1 antibodies. **k**, Growth of 4T1 tumours treated with anti-PD1 antibodies and/or evolocumab. $n = 5$ mice per group. P -values were determined by two-way ANOVA. **l**, Kaplan-Meier survival curves for mice in **k**. P -values were determined by log-rank tests. **m**, Frequency of CD8⁺ T cells in 4T1 tumours treated with anti-PD1 antibodies and/or evolocumab. $n = 5$ tumours per group. Error bars show means ± s.e.m.; P values were determined by unpaired two-sided t -test. **n**, Frequency of IFN γ ⁺ CD8⁺ T cells in 4T1 tumours treated with anti-PD1 antibodies and/or evolocumab. $n = 5$ tumours per group. Error bars show

means \pm s.e.m.; P -values were determined by unpaired two-sided t -test.

[Source data](#)

Extended Data Fig. 7 Additional data on the effect of PCSK9 inhibition on immune effector function and antigen presentation.

a, Injection schedule for antibody-mediated depletion of CD4 $^{+}$, CD8 $^{+}$ and natural killer (NK) immune cells. **b**, **c**, Growth rates (**b**) and host mouse survival (**c**) for PCSK9KO tumours in mice administered with control or anti-CD4 antibodies. $n = 5$ tumours per group. Error bars show means \pm s.e.m.; P -values were determined by two-way ANOVA (**b**) and log-rank test (**c**). **d**, **e**, Growth rates (**d**) and host mouse survival (**e**) for PCSK9KO tumours in mice administered with control or anti-NK1.1 antibody. $n = 5$ tumours per group. Error bars show means \pm s.e.m.; P -values were determined by two-way ANOVA (**d**) and log-rank test (**e**). **f**, Fluorescence images of tdTomato-labelled tumour cells with or without the OVA antigen in the presence or absence of OVA-specific T cells. The experiments were repeated twice with similar results. Scale bar, 200 μ m. **g**, Enhanced presentation of OVA antigen (SIINFEKL) by MHC I in cultured B16F10 cells following PCSK9 deficiency. Control and PCSK9KO B16F10 cells transduced with the OVA gene were treated with IFN- γ and assayed for the amount of cell-surface H-2K b -SIINFEKL complex using flow cytometry. Shown are representative results from analyses of four sets of biologically independent samples. **h**, **i**, Flow-cytometric analysis of MHC II (**h**) and PD-L1(**i**) expression in control and PCSK9KO B16F10 cells. $n = 5$ and 4 biologically independent samples, respectively. P -values were determined by unpaired two-sided t -test. **j**, Western blot analysis of PCSK9 expression in control or PCSK9KO MDA-MB-231 cells. The analyses were carried out twice. **k**, Effects of evolocumab and alirocumab on HLA-ABC expression on the surface of MDA-MB-231 human breast cancer cells. $n = 6$, 6 and 5 biologically independent samples from left to right. Data represent means \pm s.e.m.; P -values were determined by unpaired two-sided t -test. **l**, H2-K d /D d expression levels for 4T1 tumour cells that were exposed to anti-PD1 antibodies and/or evolocumab *in vivo*. $n = 5$ mice per group.

Error bars show means \pm s.e.m.; P -values were determined by unpaired two-sided t -test. [Source data](#)

Extended Data Fig. 8 Additional data on the analysis of PCSK9, H2-K1 and LDLR in murine tumour cells.

a, Lentivirus-mediated overexpression of HA-tagged H2-K1 in B16F10 cells as determined by western blot analysis. The analysis was done once. **b**, **c**, Tumour-growth delay (**b**) and Kaplan–Meier survival curve (**c**) of tumour-bearing C57BL/6 mice implanted with vector control or H2-K1-overexpressing B16F10 cells. Error bars show means \pm s.e.m.; $n = 5$ tumours in each group; P -values were determined by two-way ANOVA (**b**) and log-rank test (**c**). **d**, **e**, Tumour-growth delay (**d**) and Kaplan–Meier survival curves (**e**) in mice injected with vector control, H2-K1-knockdown, PCSK9-knockout, or PCSK9-knockout plus H2-K1-knockdown B16F10 cells. $n = 5$ mice per group. Error bars show means \pm s.e.m.; P -values were determined by two-way ANOVA (**d**) and log-rank test (**e**). **f**, Western blot analysis of LDLR knockdown in control and PCSK9KO B16F10 tumour cells. The analysis was done once. **g**, **h**, Tumour-growth delay (**g**) and Kaplan–Meier survival curves (**h**) from LDLR KD and LDLR KD/PCSK9KO B16F10 tumours. $n = 5$ mice per group. Error bars show means \pm s.e.m.; P values were determined by two-way ANOVA (**h**) and log-rank test (**i**). **i**, Flow-cytometric analysis of MHC I expression in tumours formed from tdTomato-labelled control and LDLRKD B16F10 cells. $n = 6$ biologically independent tumours. Error bars show means \pm s.e.m.; P -values were calculated by unpaired two-sided t -test. **j**, Flow-cytometric analysis of MHC I expression in tumours formed from tdTomato-labelled LDLR KD ($n = 6$) and LDLR KD/PCSK9KO cells ($n = 4$). Error bars show means \pm s.e.m.; P -values were calculated by unpaired two-sided t -test. [Source data](#)

Extended Data Fig. 9 Additional data on the mapping and functional characterization of interacting domains in PCSK9 and MHC I, and on the association of PCSK9 expression with the prognosis of TCGA cohorts.

a, Domain structure of mouse PCSK9. Catalytic, catalytic domain; CRD; C-terminal domain; Pro, propeptide; SP, signal peptide. **b**, Immunoprecipitation/western blot analysis of the interaction between full-length FLAG-labelled H2-K1 and full-length or partially deleted mouse HA-labelled PCSK9. Plasmids encoding the two genes were transfected into 293T cells in pairs, and lysates from transduced cells were immunoprecipitated with an anti-HA antibody and probed with an anti-FLAG antibody by western blot analysis. The analyses were repeated twice with biologically independent samples with similar results. **c**, Immunoprecipitation/western blot analysis of the interaction between full-length HA-labelled mouse PCSK9 and full-length or partially deleted FLAG-labelled H2-K1 (amino acids 66–202) ($\alpha 1$ – $\alpha 2$ domains). The analyses were repeated twice with biologically independent samples, with similar results. **d**, Immunoprecipitation/western blot analysis of the interaction of HA-labelled mouse PCSK9 with full-length H2-K1 or H2-K1 with more limited deletions (amino acids 66–100, $\alpha 1$ domain; or amino acids 68–70). The analyses were repeated twice with biologically independent samples, with similar results. **e**, **f**, Tumour growth rates (**e**) and Kaplan–Meier survival curves (**f**) for mice inoculated with PCSK9KO B16F10 tumour cells, with re-expressed wild-type or partially ($\Delta M2$) deleted PCSK9. $n = 5$ tumours per group. Error bars show means \pm s.e.m.; P -values were determined by two-way ANOVA (**e**) and log-rank test (**f**). **g**, **h**, Tumour growth rates (**g**) and Kaplan–Meier survival curve (**h**) for mice inoculated with H2-K1KO or H2-K1/PCSK9 double-knockout (DKO) B16F10 tumour cells re-expressed with wild-type or partially deleted ($\Delta 68$ –70) *H2-K1*. $n = 5$ tumours per group. Error bars show means \pm s.e.m.; P -values were determined by two-way ANOVA (**g**) and log-rank test (**h**). **i**, Higher levels of *PCSK9* expression correlate with worse survival in nine cohorts of patients with cancer, including liver hepatocellular carcinoma (LIHC), pancreatic adenocarcinoma (PAAD), skin cutaneous melanoma (SKCM), uveal melanoma (UVM), bladder urothelial carcinoma (BLCA), lung adenocarcinoma (LUAD), kidney renal clear cell carcinoma (KIRC), kidney renal papillary cell carcinoma (KIRP) and ovarian carcinoma (OV). P -values were calculated by log-rank test. Data are from TCGA data sets.

[Source data](#)

Extended Data Fig. 10 Diagram illustrating PCSK9-mediated degradation of MHC I in the lysosome.

Left, in the presence of PCSK9, MHC I is transported into lysosomes and degraded. Right, in the absence of PCSK9 (through genetic deletion or antibody-mediated neutralization), MHC I levels on the surface remain high and can thus present tumour-specific peptide antigens more efficiently to T cells. Illustration by S. Coffman.

Supplementary information

Supplementary Information

This file contains Supplementary Figure 1. Raw images of immunoblots. Uncropped images of scanned immunoblots shown in Fig. 4g, Fig 4i, Fig. 4j, Fig 4k, and 4l, Extended Data Fig. 1a, Extended Data Fig. 2a, Extended Data Fig. 3a, Extended Data 7j, Extended Data Fig. 8a, Extended Data Fig. 8f, Extended Data Fig. 9b, Extended Data Fig. 9c, and Extended Data Fig. 9d.

Reporting Summary

Source data

Source Data Fig. 1

Source Data Fig. 2

Source Data Fig. 3

Source Data Fig. 4

Source Data Extended Data Fig. 1

Source Data Extended Data Fig. 2

[**Source Data Extended Data Fig. 3**](#)

[**Source Data Extended Data Fig. 4**](#)

[**Source Data Extended Data Fig. 6**](#)

[**Source Data Extended Data Fig. 7**](#)

[**Source Data Extended Data Fig. 8**](#)

[**Source Data Extended Data Fig. 9**](#)

Rights and permissions

[Reprints and Permissions](#)

About this article



Check for
updates

Cite this article

Liu, X., Bao, X., Hu, M. *et al.* Inhibition of PCSK9 potentiates immune checkpoint therapy for cancer. *Nature* **588**, 693–698 (2020).
<https://doi.org/10.1038/s41586-020-2911-7>

[Download citation](#)

- Received: 24 December 2018
- Accepted: 24 August 2020
- Published: 11 November 2020

- Issue Date: 24 December 2020
- DOI: <https://doi.org/10.1038/s41586-020-2911-7>

Further reading

- **[Blocking PCSK9 enhances immune checkpoint therapy](#)**

- Sarah Crunkhorn

Nature Reviews Drug Discovery (2020)

Comments

By submitting a comment you agree to abide by our [Terms](#) and [Community Guidelines](#). If you find something abusive or that does not comply with our terms or guidelines please flag it as inappropriate.

[Access through your institution](#)

[Change institution](#)

[Buy or subscribe](#)

This article was downloaded by **calibre** from <https://www.nature.com/articles/s41586-020-2911-7>

- Article
- [Published: 18 November 2020](#)

MFSD12 mediates the import of cysteine into melanosomes and lysosomes

- [Charles H. Adelmann](#)^{1,2,3,4,5},
- [Anna K. Traunbauer](#)^{1,2,3,4,5},
- [Brandon Chen](#) [ORCID: orcid.org/0000-0002-6319-2228](#)^{1,2,3,4,5},
- [Kendall J. Condon](#)^{1,2,3,4,5},
- [Sze Ham Chan](#)¹,
- [Tenzin Kunchok](#)¹,
- [Caroline A. Lewis](#) [ORCID: orcid.org/0000-0003-1787-5084](#)¹ &
- [David M. Sabatini](#) [ORCID: orcid.org/0000-0002-1446-7256](#)^{1,2,3,4,5}

[Nature](#) volume 588, pages699–704(2020) [Cite this article](#)

- 5463 Accesses
- 93 Altmetric
- [Metrics details](#)

Subjects

- [Metabolic disorders](#)
- [Metabolomics](#)
- [Organelles](#)

Abstract

Dozens of genes contribute to the wide variation in human pigmentation. Many of these genes encode proteins that localize to the melanosome—the organelle, related to the lysosome, that synthesizes pigment—but have unclear functions^{1,2}. Here we describe MelanoIP, a method for rapidly isolating melanosomes and profiling their labile metabolite contents. We use this method to study MFSD12, a transmembrane protein of unknown molecular function that, when suppressed, causes darker pigmentation in mice and humans^{3,4}. We find that MFSD12 is required to maintain normal levels of cystine—the oxidized dimer of cysteine—in melanosomes, and to produce cysteinyldopas, the precursors of pheomelanin synthesis made in melanosomes via cysteine oxidation^{5,6}. Tracing and biochemical analyses show that MFSD12 is necessary for the import of cysteine into melanosomes and, in non-pigmented cells, lysosomes. Indeed, loss of MFSD12 reduced the accumulation of cystine in lysosomes of fibroblasts from patients with cystinosis, a lysosomal-storage disease caused by inactivation of the lysosomal cystine exporter cystinosin^{7,8,9}. Thus, MFSD12 is an essential component of the cysteine importer for melanosomes and lysosomes.

[Access through your institution](#)

[Change institution](#)

[Buy or subscribe](#)

Access options

Subscribe to Journal

Get full journal access for 1 year

\$199.00

only \$3.83 per issue

[Subscribe](#)

All prices are NET prices.

VAT will be added later in the checkout.

Rent or Buy article

Get time limited or full article access on ReadCube.

from \$8.99

[Rent or Buy](#)

All prices are NET prices.

Additional access options:

- [Log in](#)
- [Access through your institution](#)
- [Learn about institutional subscriptions](#)

Fig. 1: MelanoIP enables the rapid isolation of pure melanosomes.



Fig. 2: MFSD12 is necessary to maintain melanosomal cystine levels and produce cysteinyl dopas.

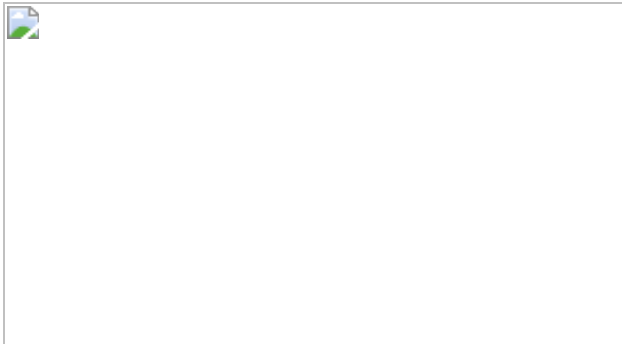


Fig. 3: MFSD12 is necessary to maintain lysosomal cystine and cysteine levels.

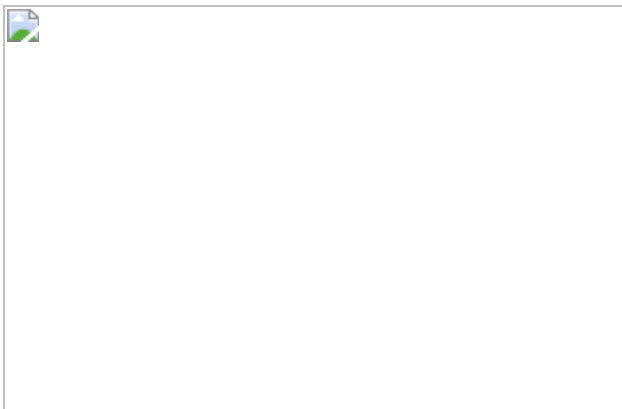
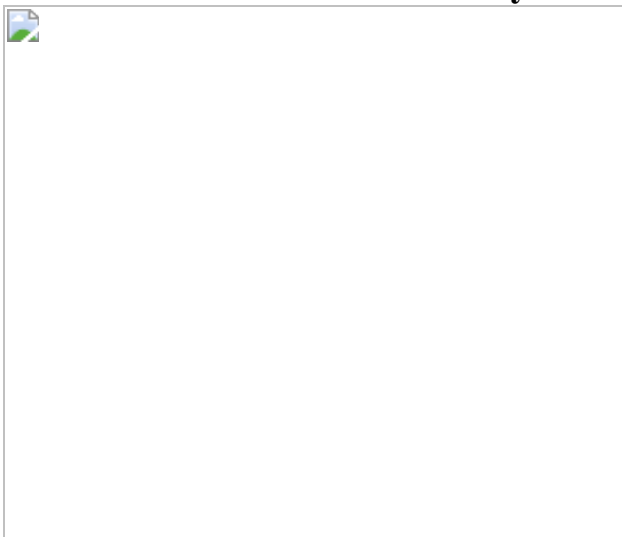


Fig. 4: MFSD12 is necessary and probably sufficient for the import of cysteine into melanosomes and lysosomes.



Data availability

Fig. 3a and Extended Data Fig. 3a were generated from FANTOM5 expression data, accessed via the Human Protein Atlas^{20,21} from

<https://www.proteinatlas.org/about/assays+annotation#fantom>. Raw values from this accession are included in the source data for Fig. 3a and Extended Data Fig. 3a. Unique biological materials in the form of plasmids available from Addgene. Unique biological materials in the form of cell lines are available from the authors by request. [Source data](#) are provided with this paper.

References

1. 1.

Basrur, V. et al. Proteomic analysis of early melanosomes: identification of novel melanosomal proteins. *J. Proteome Res.* **2**, 69–79 (2003).

[ADS](#) [CAS](#) [Article](#) [Google Scholar](#)

2. 2.

Sturm, R. A. Molecular genetics of human pigmentation diversity. *Hum. Mol. Genet.* **18** (R1), R9–R17 (2009).

[CAS](#) [Article](#) [Google Scholar](#)

3. 3.

Adhikari, K. et al. A GWAS in Latin Americans highlights the convergent evolution of lighter skin pigmentation in Eurasia. *Nat. Commun.* **10**, 358 (2019).

[ADS](#) [Article](#) [Google Scholar](#)

4. 4.

Crawford, N. G. et al. Loci associated with skin pigmentation identified in African populations. *Science* **358**, eaan8433 (2017).

[Article](#) [Google Scholar](#)

5. 5.

D'Alba, L. & Shawkey, M. D. Melanosomes: biogenesis, properties, and evolution of an ancient organelle. *Physiol. Rev.* **99**, 1–19 (2019).

[Article](#) [Google Scholar](#)

6. 6.

Prota, G. *Melanins and Melanogenesis* (Academic, 1992).

7. 7.

Gahl, W. A., Bashan, N., Tietze, F., Bernardini, I. & Schulman, J. D. Cystine transport is defective in isolated leukocyte lysosomes from patients with cystinosis. *Science* **217**, 1263–1265 (1982).

[ADS](#) [CAS](#) [Article](#) [Google Scholar](#)

8. 8.

Jonas, A. J., Smith, M. L. & Schneider, J. A. ATP-dependent lysosomal cystine efflux is defective in cystinosis. *J. Biol. Chem.* **257**, 13185–13188 (1982).

[CAS](#) [PubMed](#) [Google Scholar](#)

9. 9.

Town, M. et al. A novel gene encoding an integral membrane protein is mutated in nephropathic cystinosis. *Nat. Genet.* **18**, 319–324 (1998).

[CAS](#) [Article](#) [Google Scholar](#)

10. 10.

Watabe, H., Kushimoto, T., Valencia, J. C. & Hearing, V. J. in *Current Protocols in Cell Biology* (eds J. S. Bonifacino et al.) (John Wiley & Sons, 2005).

11. 11.

Abu-Remaileh, M. et al. Lysosomal metabolomics reveals V-ATPase- and mTOR-dependent regulation of amino acid efflux from lysosomes. *Science* **358**, 807–813 (2017).

[ADS](#) [CAS](#) [Article](#) [Google Scholar](#)

12. 12.

Chen, W. W., Freinkman, E., Wang, T., Birsoy, K. & Sabatini, D. M. Absolute quantification of matrix metabolites reveals the dynamics of mitochondrial metabolism. *Cell* **166**, 1324–1337 (2016).

[CAS](#) [Article](#) [Google Scholar](#)

13. 13.

Ray, G. J. et al. A PEROXO-tag enables rapid isolation of peroxisomes from human cells. *iScience* **23**, 101109 (2020).

[ADS](#) [CAS](#) [Article](#) [Google Scholar](#)

14. 14.

Bruder, J. M. et al. Melanosomal dynamics assessed with a live-cell fluorescent melanosomal marker. *PLoS ONE* **7**, e43465 (2012).

[ADS](#) [CAS](#) [Article](#) [Google Scholar](#)

15. 15.

Diment, S., Eidelman, M., Rodriguez, G. M. & Orlow, S. J. Lysosomal hydrolases are present in melanosomes and are elevated in melanizing cells. *J. Biol. Chem.* **270**, 4213–4215 (1995).

[CAS](#) [Article](#) [Google Scholar](#)

16. 16.

Bissig, C., Rochin, L. & van Niel, G. PMEL amyloid fibril formation: the bright steps of pigmentation. *Int. J. Mol. Sci.* **17**, 1438 (2016).

[Article](#) [Google Scholar](#)

17. 17.

Reddy, V. S., Shlykov, M. A., Castillo, R., Sun, E. I. & Saier, M. H. Jr. The major facilitator superfamily (MFS) revisited. *FEBS J.* **279**, 2022–2035 (2012).

[CAS](#) [Article](#) [Google Scholar](#)

18. 18.

Bloom, J. L. & Falconer, D. S. ‘Grizzled’, a mutant in linkage group X of the mouse. *Genet. Res.* **7**, 159–167 (1966).

[Article](#) [Google Scholar](#)

19. 19.

Potterf, S. B. et al. Cysteine transport in melanosomes from murine melanocytes. *Pigment Cell Res.* **12**, 4–12 (1999).

[CAS](#) [Article](#) [Google Scholar](#)

20. 20.

Kawaji, H., Kasukawa, T., Forrest, A., Carninci, P. & Hayashizaki, Y. The FANTOM5 collection, a data series underpinning mammalian transcriptome atlases in diverse cell types. *Sci. Data* **4**, 170113 (2017).

[CAS](#) [Article](#) [Google Scholar](#)

21. 21.

Uhlén, M. et al. Tissue-based map of the human proteome. *Science* **347**, 1260419 (2015).

[Article](#) [Google Scholar](#)

22. 22.

Pisoni, R. L., Acker, T. L., Lisowski, K. M., Lemons, R. M. & Thoene, J. G. A cysteine-specific lysosomal transport system provides a major route for the delivery of thiol to human fibroblast lysosomes: possible role in supporting lysosomal proteolysis. *J. Cell Biol.* **110**, 327–335 (1990).

[CAS](#) [Article](#) [Google Scholar](#)

23. 23.

Gahl, W. A., Thoene, J. G. & Schneider, J. A. Cystinosis. *N. Engl. J. Med.* **347**, 111–121 (2002).

[Article](#) [Google Scholar](#)

24. 24.

Oshima, R. G., Rhead, W. J., Thoene, J. G. & Schneider, J. A. Cystine metabolism in human fibroblasts. Comparison of normal, cystinotic, and gamma-glutamylcysteine synthetase-deficient cells. *J. Biol. Chem.* **251**, 4287–4293 (1976).

[CAS](#) [PubMed](#) [Google Scholar](#)

25. 25.

Sato, H., Tamba, M., Ishii, T. & Bannai, S. Cloning and expression of a plasma membrane cystine/glutamate exchange transporter composed of two distinct proteins. *J. Biol. Chem.* **274**, 11455–11458 (1999).

[CAS](#) [Article](#) [Google Scholar](#)

26. 26.

Wilbrandt, W. & Rosenberg, T. The concept of carrier transport and its corollaries in pharmacology. *Pharmacol. Rev.* **13**, 109–183 (1961).

[CAS](#) [PubMed](#) [Google Scholar](#)

27. 27.

Behnke, J., Eskelinen, E.-L., Saftig, P. & Schröder, B. Two dileucine motifs mediate late endosomal/lysosomal targeting of transmembrane protein 192 (TMEM192) and a C-terminal cysteine residue is responsible for disulfide bond formation in TMEM192 homodimers. *Biochem. J.* **434**, 219–231 (2011).

[CAS](#) [Article](#) [Google Scholar](#)

28. 28.

Lloyd, J. B. Disulphide reduction in lysosomes. The role of cysteine. *Biochem. J.* **237**, 271–272 (1986).

[CAS](#) [Article](#) [Google Scholar](#)

29. 29.

Mego, J. L. Role of thiols, pH and cathepsin D in the lysosomal catabolism of serum albumin. *Biochem. J.* **218**, 775–783 (1984).

[CAS](#) [Article](#) [Google Scholar](#)

30. 30.

Tsui, C. K. et al. CRISPR–cas9 screens identify regulators of antibody-drug conjugate toxicity. *Nat. Chem. Biol.* **15**, 949–958 (2019).

[CAS](#) [Article](#) [Google Scholar](#)

31. 31.

Gahl, W. A. et al. Cysteamine therapy for children with nephropathic cystinosis. *N. Engl. J. Med.* **316**, 971–977 (1987).

[CAS Article](#) [Google Scholar](#)

32. 32.

Thoene, J. G., Oshima, R. G., Crawhall, J. C., Olson, D. L. & Schneider, J. A. Cystinosis. Intracellular cystine depletion by aminothiols in vitro and in vivo. *J. Clin. Invest.* **58**, 180–189 (1976).

[CAS Article](#) [Google Scholar](#)

33. 33.

Mujahid, N. et al. A UV-independent topical small-molecule approach for melanin production in human skin. *Cell Rep.* **19**, 2177–2184 (2017).

[CAS Article](#) [Google Scholar](#)

34. 34.

Djoumbou-Feunang, Y. et al. CFM-ID 3.0: significantly improved ESI-MS/MS prediction and compound identification. *Metabolites* **9**, 72 (2019).

[CAS Article](#) [Google Scholar](#)

35. 35.

Wishart, D. S. et al. HMDB: the Human Metabolome Database. *Nucleic Acids Res.* **35**, D521–D526 (2007).

[CAS Article](#) [Google Scholar](#)

36. 36.

Guan, X., Hoffman, B., Dwivedi, C. & Matthees, D. P. A simultaneous liquid chromatography/mass spectrometric assay of glutathione, cysteine, homocysteine and their disulfides in biological samples. *J. Pharm. Biomed. Anal.* **31**, 251–261 (2003).

[CAS Article](#) [Google Scholar](#)

37. 37.

Martin, G. B. et al. Development of a mass spectrometry method for the determination of a melanoma biomarker, 5-S-cysteinylldopa, in human plasma using solid phase extraction for sample clean-up. *J. Chromatogr. A* **1156**, 141–148 (2007).

[CAS Article](#) [Google Scholar](#)

38. 38.

Ito, S. & Prota, G. A facile one-step synthesis of cysteinyldopas using mushroom tyrosinase. *Experientia* **33**, 1118–1119 (1977).

[CAS Article](#) [Google Scholar](#)

39. 39.

Graham, J. M. Isolation of lysosomes from tissues and cells by differential and density gradient centrifugation. *Curr. Protoc. Cell Biol.* **Ch. 3**, Unit 3.6 (2001).

[Google Scholar](#)

40. 40.

Goldman, R. & Kaplan, A. Rupture of rat liver lysosomes mediated by l-amino acid esters. *Biochim. Biophys. Acta* **318**, 205–216 (1973).

[CAS Article](#) [Google Scholar](#)

41. 41.

Verdon, Q. et al. SNAT7 is the primary lysosomal glutamine exporter required for extracellular protein-dependent growth of cancer cells. *Proc. Natl Acad. Sci. USA* **114**, E3602–E3611 (2017).

[CAS Article](#) [Google Scholar](#)

[Download references](#)

Acknowledgements

We thank P. Budde, M. Abu-Remaileh, W. W. Chen, L. Bar-Peled and J. G. Bryan, as well as all current members of the Sabatini laboratory for helpful insights. This work was supported by grants from the Leo Foundation (LF18057) and NIH (R01 CA103866, R01 CA129105 and R01 AI047389), fellowship support from the NIH (NRSA F31 CA228241-01) to C.H.A., Marshall Plan Foundation to A.K.T., HHMI XROP to B.C., and NSF (2016197106) to K.J.C. D.M.S. is an investigator of the Howard Hughes Medical Institute and an American Cancer Society Research Professor.

Author information

Affiliations

1. Whitehead Institute for Biomedical Research, Massachusetts Institute of Technology, Cambridge, MA, USA

Charles H. Adelmann, Anna K. Traunbauer, Brandon Chen, Kendall J. Condon, Sze Ham Chan, Tenzin Kunchok, Caroline A. Lewis & David M. Sabatini

2. Department of Biology, Massachusetts Institute of Technology, Cambridge, MA, USA

Charles H. Adelmann, Anna K. Traunbauer, Brandon Chen, Kendall J. Condon & David M. Sabatini

3. Howard Hughes Medical Institute, Department of Biology,
Massachusetts Institute of Technology, Cambridge, MA, USA

Charles H. Adelmann, Anna K. Traunbauer, Brandon Chen, Kendall J. Condon & David M. Sabatini

4. Koch Institute for Integrative Cancer Research, Massachusetts Institute of Technology, Cambridge, MA, USA

Charles H. Adelmann, Anna K. Traunbauer, Brandon Chen, Kendall J. Condon & David M. Sabatini

5. Broad Institute of Harvard and Massachusetts Institute of Technology, Cambridge, MA, USA

Charles H. Adelmann, Anna K. Traunbauer, Brandon Chen, Kendall J. Condon & David M. Sabatini

Authors

1. Charles H. Adelmann

[View author publications](#)

You can also search for this author in [PubMed](#) [Google Scholar](#)

2. Anna K. Traunbauer

[View author publications](#)

You can also search for this author in [PubMed](#) [Google Scholar](#)

3. Brandon Chen

[View author publications](#)

You can also search for this author in [PubMed](#) [Google Scholar](#)

4. Kendall J. Condon

[View author publications](#)

You can also search for this author in [PubMed](#) [Google Scholar](#)

5. Sze Ham Chan

[View author publications](#)

You can also search for this author in [PubMed](#) [Google Scholar](#)

6. Tenzin Kunchok

[View author publications](#)

You can also search for this author in [PubMed](#) [Google Scholar](#)

7. Caroline A. Lewis

[View author publications](#)

You can also search for this author in [PubMed](#) [Google Scholar](#)

8. David M. Sabatini

[View author publications](#)

You can also search for this author in [PubMed](#) [Google Scholar](#)

Contributions

C.H.A. and D.M.S. initiated the project and designed the research plan. C.H.A. performed the experiments and analysed the data with help from A.K.T., B.C. and K.J.C. The LC–MS platform was operated by S.H.C., T.K. and C.A.L., who also had a critical role in method development for LC–MS-based assays for cysteine and cysteinyldopas. C.H.A. wrote the manuscript and D.M.S. edited it.

Corresponding author

Correspondence to [David M. Sabatini](#).

Ethics declarations

Competing interests

The authors declare no competing interests.

Additional information

Peer review information *Nature* thanks Edmund Kunji and the other, anonymous, reviewer(s) for their contribution to the peer review of this work.

Publisher's note Springer Nature remains neutral with regard to jurisdictional claims in published maps and institutional affiliations.

Extended data figures and tables

[Extended Data Fig. 1 MelanoIP analysis detects changes in *Tyr*-dependent melanosomal metabolites.](#)

a, Schematic of melanin synthesis. The common pathway elements for eumelanin and pheomelanin synthesis have a grey backdrop. The brown and red backdrops highlight unique portions of eumelanin and pheomelanin synthesis, respectively. Enzymes proposed to catalyse each step are shown in green. Synthetic intermediates annotated and validated in biological samples in this study are in blue. **b**, Follow-up analysis with standard validated *m/z* and internal normalization of ‘proteogenic amino acids’ highlighted in untargeted metabolite profiling of wild-type and *Tyr*-knockout melanosomes (Fig. 1d). Amino acids are presented in order of increasing retention time (*n* = 3 independently prepared extracts, ^a*P* = 3.9×10^{-2} , ^b*P* = 2.0×10^{-3} , ^c*P* = 6.5×10^{-3} , ^d*P* = 3.8×10^{-2} , ^e*P* = 1.9×10^{-2}). Error bars are mean \pm s.e.m., *P* values by two-sided Student’s *t*-test. [Source data](#)

[Extended Data Fig. 2 In vitro synthesis and biological detection of cysteinyl dopas.](#)

a, Cysteinyl dopas were synthesized according to an adapted protocol from Ito and Prota, 1977³⁸. Two species, distinguished by retention time, were

generated at the expected *m/z* for cysteinyldopas. It has been shown that 5'-cysteinyldopa is produced in greater abundance than 2'-cysteinyldopa in this reaction. Taking MS1 peak intensity to approximate abundance, we putatively annotate the ‘Minor Isomer’ as 2’ substituted, and the ‘Major Isomer’ as 5’ substituted. **b**, Mirror plot of ddMS2 data comparing 2’- and 5’-cysteinyldopa in synthetic cysteinyldopas. **c,d**, Mirror plots of ddMS2 peaks displaying similarities in ddMS2 spectra of 2’- and 5’-cysteinyldopa species in biological samples (B16F10 extracts) and synthetic standards.

[Source data](#)

[Extended Data Fig. 3 MFSD12 maintains lysosomal cystine in non-pigmented cells.](#)

a, FANTOM5 CAGE profiling data accessed via Human Protein Atlas^{20,21}. Six representative pigmentation genes, including *MFSD12*, are shown. **b**, Metabolite profiling of LysoIP samples from HEK 293T cells comparing lysosomes from wild-type and *MFSD12*-knockout cells. ‘Accumulates upon inhibition of’ has been previously reported¹¹ (*n* = 4 independently prepared metabolite extracts, ^a*P* = 7.0×10^{-4} , ^b*P* = 3.0×10^{-3} , ^c*P* = 4.1×10^{-2} , ^d*P* = 4.2×10^{-2} , ^e*P* = 1.7×10^{-4}). **c**, Lentiviral shRNA knock-down of *MFSD12* quantified via qPCR and normalized to *ACTB* levels (*n* = 3 assays on independently prepared cDNA libraries, ^a*P* = 1.97×10^{-3} , ^b*P* = 3.0×10^{-3}). Error bars are mean ± s.e.m., *P* values by two-sided Student’s *t*-test. [Source data](#)

[Extended Data Fig. 4 MFSD12 mediated cysteine transport is cysteine specific.](#)

a, Test of lysosomal counter-transport. Lysosomes were purified by differential centrifugation and incubated with water or 1 mM cysteine methyl ester before washing, resuspension, and incubated for 5 min with 20 μ M cysteine and trace amounts of [³⁵S]cysteine (*n* = 3 independently performed assays per condition, ^a*P* = 2.5×10^{-3} , ^b*P* = 3.3×10^{-2} , NS = not significant). **b**, Lysosomal import of [¹⁴C]cystine. Lysosomes were purified by differential centrifugation and incubated for 10 min with 1 μ M [¹⁴C]cystine, either untreated (Unreduced) or pre-treated with 10 mM DTT

(Reduced, $n = 6$ independently performed assays per condition, ${}^aP = 2.1 \times 10^{-7}$, ${}^bP = 1.3 \times 10^{-6}$, ${}^cP = 3.8 \times 10^{-8}$). **c**, Competition for [^{35}S]cysteine transport. Lysosomes were purified by differential centrifugation and incubated for 10 min with 20 μM cysteine and trace amounts of [^{35}S]cysteine with 500 μM competitor where indicated ($n = 3$ independently performed assays per condition, P values compare competition condition versus water control condition (red), ${}^aP = 2.7 \times 10^{-4}$, ${}^bP = 2.5 \times 10^{-4}$, ${}^cP = 3.2 \times 10^{-4}$). Error bars are mean \pm s.e.m., P values by two-sided Student's *t*-test. [Source data](#)

Supplementary information

[Supplementary Figure 1](#)

Uncropped blots for Fig 1c.

[Reporting Summary](#)

Source data

[Source Data Fig. 1](#)

[Source Data Fig. 2](#)

[Source Data Fig. 3](#)

[Source Data Fig. 4](#)

[Source Data Extended Data Fig. 1](#)

[Source Data Extended Data Fig. 2](#)

[Source Data Extended Data Fig. 3](#)

[Source Data Extended Data Fig. 4](#)

Rights and permissions

[Reprints and Permissions](#)

About this article



Check for
updates

Cite this article

Adelmann, C.H., Traunbauer, A.K., Chen, B. *et al.* MFSD12 mediates the import of cysteine into melanosomes and lysosomes. *Nature* **588**, 699–704 (2020). <https://doi.org/10.1038/s41586-020-2937-x>

[Download citation](#)

- Received: 09 December 2019
- Accepted: 28 August 2020
- Published: 18 November 2020
- Issue Date: 24 December 2020
- DOI: <https://doi.org/10.1038/s41586-020-2937-x>

Comments

By submitting a comment you agree to abide by our [Terms](#) and [Community Guidelines](#). If you find something abusive or that does not comply with our terms or guidelines please flag it as inappropriate.

[Access through your institution](#)

[Change institution](#)

[Buy or subscribe](#)

This article was downloaded by **calibre** from <https://www.nature.com/articles/s41586-020-2937-x>

| [Section menu](#) | [Main menu](#) |

- Article
- [Published: 09 December 2020](#)

Lymphoangiocrine signals promote cardiac growth and repair

- [Xiaolei Liu¹](#),
- [Ester De la Cruz²](#),
- [Xiaowu Gu](#) [ORCID: orcid.org/0000-0003-2266-5516³](#),
- [Laszlo Balint](#) [ORCID: orcid.org/0000-0002-3142-4071^{4,5}](#),
- [Michael Oxendine-Burns](#) [ORCID: orcid.org/0000-0002-8054-0757¹](#),
- [Tamara Terrones⁶](#),
- [Wanshu Ma¹](#),
- [Hui-Hsuan Kuo](#) [ORCID: orcid.org/0000-0001-8266-7105⁷](#),
- [Connor Lantz](#) [ORCID: orcid.org/0000-0003-3317-6486⁸](#),
- [Trisha Bansal¹](#),
- [Edward Thorp](#) [ORCID: orcid.org/0000-0003-1387-7058⁸](#),
- [Paul Burridge](#) [ORCID: orcid.org/0000-0001-9616-0006⁷](#),
- [Zoltán Jakus](#) [ORCID: orcid.org/0000-0002-6304-2369^{4,5}](#),
- [Joachim Herz^{6,9,10}](#),
- [Ondine Cleaver³](#),
- [Miguel Torres](#) [ORCID: orcid.org/0000-0003-0906-4767²](#) &
- [Guillermo Oliver](#) [ORCID: orcid.org/0000-0003-3984-7615¹](#)

[Nature](#) volume **588**, pages 705–711(2020) [Cite this article](#)

- 3572 Accesses
- 76 Altmetric
- [Metrics details](#)

Subjects

- [Disease model](#)
- [Lymphangiogenesis](#)

Abstract

Recent studies have suggested that lymphatics help to restore heart function after cardiac injury^{1,2,3,4,5,6}. Here we report that lymphatics promote cardiac growth, repair and cardioprotection in mice. We show that a lymphoangiocrine signal produced by lymphatic endothelial cells (LECs) controls the proliferation and survival of cardiomyocytes during heart development, improves neonatal cardiac regeneration and is cardioprotective after myocardial infarction. Embryos that lack LECs develop smaller hearts as a consequence of reduced cardiomyocyte proliferation and increased cardiomyocyte apoptosis. Culturing primary mouse cardiomyocytes in LEC-conditioned medium increases cardiomyocyte proliferation and survival, which indicates that LECs produce lymphoangiocrine signals that control cardiomyocyte homeostasis. Characterization of the LEC secretome identified the extracellular protein reelin (RELN) as a key component of this process. Moreover, we report that LEC-specific *Reln*-null mouse embryos develop smaller hearts, that RELN is required for efficient heart repair and function after neonatal myocardial infarction, and that cardiac delivery of RELN using collagen patches improves heart function in adult mice after myocardial infarction by a cardioprotective effect. These results highlight a lymphoangiocrine role of LECs during cardiac development and injury response, and identify RELN as an important mediator of this function.

[Access through your institution](#)

[Change institution](#)

[Buy or subscribe](#)

Access options

Subscribe to Journal

Get full journal access for 1 year

\$199.00

only \$3.83 per issue

[Subscribe](#)

All prices are NET prices.

VAT will be added later in the checkout.

Rent or Buy article

Get time limited or full article access on ReadCube.

from \$8.99

[Rent or Buy](#)

All prices are NET prices.

Additional access options:

- [Log in](#)
- [Access through your institution](#)
- [Learn about institutional subscriptions](#)

Fig. 1: Lymphatics are required for embryonic heart growth.



Fig. 2: Lymphatics are required for CM proliferation and survival.



Fig. 3: LEC-secreted RELN promotes CM proliferation and survival.

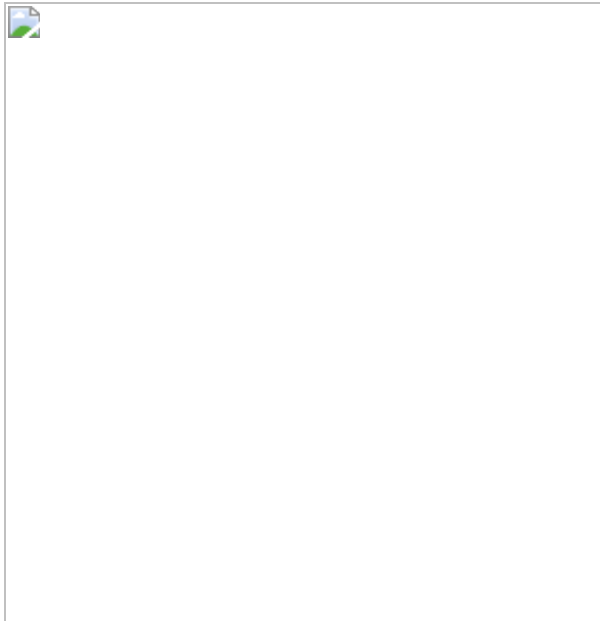


Fig. 4: RELN improves neonatal and adult cardiac function after myocardial infarction.



Data availability

All data from the manuscript are available from the corresponding author on request. RNA-seq raw data have been deposited to the Gene Expression Omnibus (GEO) repository with accession number [GSE158504](#). [Source data](#) are provided with this paper.

References

1. 1.

Oliver, G., Kipnis, J., Randolph, G. J. & Harvey, N. L. The lymphatic vasculature in the 21st century: novel functional roles in homeostasis and disease. *Cell* **182**, 270–296 (2020).

[CAS Article](#) [Google Scholar](#)

2. 2.

Klotz, L. et al. Cardiac lymphatics are heterogeneous in origin and respond to injury. *Nature* **522**, 62–67 (2015).

[ADS](#) [CAS Article](#) [Google Scholar](#)

3. 3.

Vuorio, T., Tirronen, A. & Ylä-Herttula, S. Cardiac lymphatics - a new avenue for therapeutics? *Trends Endocrinol. Metab.* **28**, 285–296 (2017).

[CAS Article](#) [Google Scholar](#)

4. 4.

Henri, O. et al. Selective stimulation of cardiac lymphangiogenesis reduces myocardial edema and fibrosis leading to improved cardiac function following myocardial infarction. *Circulation* **133**, 1484–1497 (2016).

[CAS Article](#) [Google Scholar](#)

5. 5.

Vieira, J. M. et al. The cardiac lymphatic system stimulates resolution of inflammation following myocardial infarction. *J. Clin. Invest.* **128**,

3402–3412 (2018).

[Article](#) [Google Scholar](#)

6. 6.

Harrison, M. R. et al. Late developing cardiac lymphatic vasculature supports adult zebrafish heart function and regeneration. *eLife* **8**, e42762 (2019).

[Article](#) [Google Scholar](#)

7. 7.

Harvey, N. L. et al. Lymphatic vascular defects promoted by *Prox1* haploinsufficiency cause adult-onset obesity. *Nat. Genet.* **37**, 1072–1081 (2005).

[CAS](#) [Article](#) [Google Scholar](#)

8. 8.

Wigle, J. T. & Oliver, G. *Prox1* function is required for the development of the murine lymphatic system. *Cell* **98**, 769–778 (1999).

[CAS](#) [Article](#) [Google Scholar](#)

9. 9.

Johnson, N. C. et al. Lymphatic endothelial cell identity is reversible and its maintenance requires *Prox1* activity. *Genes Dev.* **22**, 3282–3291 (2008).

[CAS](#) [Article](#) [Google Scholar](#)

10. 10.

Sörensen, I., Adams, R. H. & Gossler, A. DLL1-mediated Notch activation regulates endothelial identity in mouse fetal arteries. *Blood* **113**, 5680–5688 (2009).

[Article](#) [Google Scholar](#)

11. 11.

Zhang, L. et al. VEGFR-3 ligand-binding and kinase activity are required for lymphangiogenesis but not for angiogenesis. *Cell Res.* **20**, 1319–1331 (2010).

[ADS](#) [CAS](#) [Article](#) [Google Scholar](#)

12. 12.

Hsieh, P. C. H., Davis, M. E., Lisowski, L. K. & Lee, R. T. Endothelial–cardiomyocyte interactions in cardiac development and repair. *Annu. Rev. Physiol.* **68**, 68–51 (2006).

[Article](#) [Google Scholar](#)

13. 13.

Brutsaert, D. L. & Cotran, R. S. Cardiac endothelial-myocardial signaling: its role in cardiac growth, contractile performance, and rhythmicity. *Physiol. Rev.* **83**, 59–115 (2003).

[CAS](#) [Article](#) [Google Scholar](#)

14. 14.

Jossin, Y. Neuronal migration and the role of reelin during early development of the cerebral cortex. *Mol. Neurobiol.* **30**, 225–251 (2004).

[CAS](#) [Article](#) [Google Scholar](#)

15. 15.

D'Arcangelo, G. Reelin in the years: controlling neuronal migration and maturation in the mammalian brain. *Adv. Neurosci. (Hindawi)* **2014**, 1–19 (2014).

[Article](#) [Google Scholar](#)

16. 16.

Lutter, S., Xie, S., Tatin, F. & Makinen, T. Smooth muscle-endothelial cell communication activates Reelin signaling and regulates lymphatic vessel formation. *J. Cell Biol.* **197**, 837–849 (2012).

[CAS](#) [Article](#) [Google Scholar](#)

17. 17.

D'Arcangelo, G. et al. A protein related to extracellular matrix proteins deleted in the mouse mutant reeler. *Nature* **374**, 719–723 (1995).

[ADS](#) [Article](#) [Google Scholar](#)

18. 18.

Lane-Donovan, C. et al. Reelin protects against amyloid β toxicity in vivo. *Sci. Signal.* **8**, ra67–ra67 (2015).

[Article](#) [Google Scholar](#)

19. 19.

Srinivasan, R. S. et al. Lineage tracing demonstrates the venous origin of the mammalian lymphatic vasculature. *Genes Dev.* **21**, 2422–2432 (2007).

[CAS](#) [Article](#) [Google Scholar](#)

20. 20.

Trommsdorff, M. et al. Reeler/Disabled-like disruption of neuronal migration in knockout mice lacking the VLDL receptor and ApoE receptor 2. *Cell* **97**, 689–701 (1999).

[CAS](#) [Article](#) [Google Scholar](#)

21. 21.

Hiesberger, T. et al. Direct binding of Reelin to VLDL receptor and ApoE receptor 2 induces tyrosine phosphorylation of disabled-1 and modulates tau phosphorylation. *Neuron* **24**, 481–489 (1999).

[CAS](#) [Article](#) [Google Scholar](#)

22. 22.

Lin, L. et al. Reelin promotes the adhesion and drug resistance of multiple myeloma cells via integrin β 1 signaling and STAT3. *Oncotarget* **7**, 9844–9858 (2016).

[Article](#) [Google Scholar](#)

23. 23.

Dulabon, L. et al. Reelin binds α 3 β 1 integrin and inhibits neuronal migration. *Neuron* **27**, 33–44 (2000).

[CAS](#) [Article](#) [Google Scholar](#)

24. 24.

Beffert, U. et al. Reelin-mediated signaling locally regulates protein kinase B/Akt and glycogen synthase kinase 3 β . *J. Biol. Chem.* **277**, 49958–49964 (2002).

[CAS](#) [Article](#) [Google Scholar](#)

25. 25.

Jossin, Y. & Goffinet, A. M. Reelin signals through phosphatidylinositol 3-kinase and Akt to control cortical development and through mTor to regulate dendritic growth. *Mol. Cell. Biol.* **27**, 7113–7124 (2007).

[CAS](#) [Article](#) [Google Scholar](#)

26. 26.

Ieda, M. et al. Cardiac fibroblasts regulate myocardial proliferation through β 1 integrin signaling. *Dev. Cell* **16**, 233–244 (2009).

[CAS](#) [Article](#) [Google Scholar](#)

27. 27.

Porrello, E. R. et al. Transient regenerative potential of the neonatal mouse heart. *Science* **331**, 1078–1080 (2011).

[ADS](#) [CAS](#) [Article](#) [Google Scholar](#)

28. 28.

Wei, K. et al. Epicardial FSTL1 reconstitution regenerates the adult mammalian heart. *Nature* **525**, 479–485 (2015).

[ADS](#) [CAS](#) [Article](#) [Google Scholar](#)

29. 29.

Serpooshan, V. et al. The effect of bioengineered acellular collagen patch on cardiac remodeling and ventricular function post myocardial infarction. *Biomaterials* **34**, 9048–9055 (2013).

[CAS](#) [Article](#) [Google Scholar](#)

30. 30.

Karkkainen, M. J. et al. A model for gene therapy of human hereditary lymphedema. *Proc. Natl Acad. Sci. USA* **98**, 12677–12682 (2001).

[ADS](#) [CAS](#) [Article](#) [Google Scholar](#)

31. 31.

Burridge, P. W. et al. Chemically defined generation of human cardiomyocytes. *Nat. Methods* **11**, 855–860 (2014).

[CAS](#) [Article](#) [Google Scholar](#)

32. 32.

Burridge, P. W., Holmström, A. & Wu, J. C. Chemically defined culture and cardiomyocyte differentiation of human pluripotent stem cells. *Curr. Prot. Human Genet.* **87**, 21.3.1–21.3.15 (2015).

[Google Scholar](#)

33. 33.

Liu, X. et al. Rasip1 controls lymphatic vessel lumen maintenance by regulating endothelial cell junctions. *Development* **145**, dev165092 (2018).

[Article](#) [Google Scholar](#)

[Download references](#)

Acknowledgements

This work was supported by NIH grant (RO1HL073402-16) to G.O., AHA grant (18CDA34110356) to X.L., 5T32HL134633 to W.M., FPU grant from the Spanish Ministry of Education, Culture and Sports and EMBO Short-Term Fellowship to E.D.C., Leducq TNE-17CVD and RD16/0011/0019 (ISCIII) from the Spanish Ministry of Science, Innovation, and Universities to M.T., NIH T32 GM008061 to C.L., HL63762, and NS093382 to J.H. We

thank G. M. Rune and B. Brunne for the *Reln*^{+/−} strain. RNA-seq work was supported by the Northwestern University NUSeq Core Facility. We thank the Robert H. Lurie Cancer Center Flow Cytometry facility supported by NCI CCSG P30 CA060553 for their invaluable assistance. Flow Cytometry Cell Sorting was performed on a BD FACSaria SORP system and BD FACSymphony S6 SORP system, purchased through the support of NIH 1S10OD011996-01 and 1S10OD026814-01. Imaging work was performed at the Northwestern University Center for Advanced Microscopy supported by NCI CCSG P30 CA060553 awarded to the Robert H Lurie Comprehensive Cancer Center. Spinning disk confocal microscopy was performed on an Andor XDI Revolution microscope, purchased through the support of NCRR 1S10 RR031680-01. Proteomics services were performed by the Northwestern Proteomics Core Facility supported by NCI CCSG P30 CA060553 awarded to the Robert H Lurie Comprehensive Cancer Center, instrumentation award (S10OD025194) from NIH Office of Director, and the National Resource for Translational and Developmental Proteomics supported by P41 GM108569. We thank the George M. O'Brien Kidney Research Core Center (NU GoKidney, supported by a P30 DK114857 award from NIDDK) for the use of the Echocardiography machine. The myocardial infarction surgeries were performed by the comprehensive Transplant Center Microsurgery Core, partially supported by NIH NIAID P01AI112522. We thank J. Jin and P. Liu for help with the ELISA reagents and data analysis, R. Ma for help with DNA ploidy analysis, A. Shi for the MEF2C antibodies, M. Dellinger for the *Prox1-creER*^{T2} mice and H. Ardehali for the *Myh6-cre* mice. We specially thank B. Sosa-Pineda for advice and suggestions and P. Ruiz-Lozano for sharing her expertise in the preparation of the collagen patches.

Author information

Affiliations

1. Center for Vascular and Developmental Biology, Feinberg Cardiovascular and Renal Research Institute, Feinberg School of Medicine, Northwestern University, Chicago, IL, USA

Xiaolei Liu, Michael Oxendine-Burns, Wanshu Ma, Trisha Bansal & Guillermo Oliver

2. Cardiovascular Development Program, Centro Nacional de Investigaciones Cardiovasculares, CNIC, Madrid, Spain

Ester De la Cruz & Miguel Torres

3. Department of Molecular Biology, University of Texas Southwestern Medical Center, Dallas, TX, USA

Xiaowu Gu & Ondine Cleaver

4. Department of Physiology, Semmelweis University School of Medicine, Budapest, Hungary

Laszlo Balint & Zoltán Jakus

5. MTA-SE “Lendulet” Lymphatic Physiology Research Group of the Hungarian Academy of Sciences and the Semmelweis University, Department of Physiology, Semmelweis University School of Medicine, Budapest, Hungary

Laszlo Balint & Zoltán Jakus

6. Department of Molecular Genetics, University of Texas Southwestern Medical Center, Dallas, TX, USA

Tamara Terrones & Joachim Herz

7. Department of Pharmacology, Feinberg School of Medicine, Northwestern University, Chicago, IL, USA

Hui-Hsuan Kuo & Paul Burridge

8. Department of Pathology, Feinberg School of Medicine, Northwestern University, Chicago, IL, USA

Connor Lantz & Edward Thorp

9. Department of Neuroscience, University of Texas Southwestern Medical Center, Dallas, TX, USA

Joachim Herz

10. Department of Neurology & Neurotherapeutics, University of Texas Southwestern Medical Center, Dallas, TX, USA

Joachim Herz

Authors

1. Xiaolei Liu

[View author publications](#)

You can also search for this author in [PubMed](#) [Google Scholar](#)

2. Ester De la Cruz

[View author publications](#)

You can also search for this author in [PubMed](#) [Google Scholar](#)

3. Xiaowu Gu

[View author publications](#)

You can also search for this author in [PubMed](#) [Google Scholar](#)

4. Laszlo Balint

[View author publications](#)

You can also search for this author in [PubMed](#) [Google Scholar](#)

5. Michael Oxendine-Burns

[View author publications](#)

You can also search for this author in [PubMed](#) [Google Scholar](#)

6. Tamara Terrones

[View author publications](#)

You can also search for this author in [PubMed](#) [Google Scholar](#)

7. Wanshu Ma

[View author publications](#)

You can also search for this author in [PubMed](#) [Google Scholar](#)

8. Hui-Hsuan Kuo

[View author publications](#)

You can also search for this author in [PubMed](#) [Google Scholar](#)

9. Connor Lantz

[View author publications](#)

You can also search for this author in [PubMed](#) [Google Scholar](#)

10. Trisha Bansal

[View author publications](#)

You can also search for this author in [PubMed](#) [Google Scholar](#)

11. Edward Thorp

[View author publications](#)

You can also search for this author in [PubMed](#) [Google Scholar](#)

12. Paul Burridge

[View author publications](#)

You can also search for this author in [PubMed](#) [Google Scholar](#)

13. Zoltán Jakus

[View author publications](#)

You can also search for this author in [PubMed](#) [Google Scholar](#)

14. Joachim Herz

[View author publications](#)

You can also search for this author in [PubMed](#) [Google Scholar](#)

15. Ondine Cleaver

[View author publications](#)

You can also search for this author in [PubMed](#) [Google Scholar](#)

16. Miguel Torres

[View author publications](#)

You can also search for this author in [PubMed](#) [Google Scholar](#)

17. Guillermo Oliver

[View author publications](#)

You can also search for this author in [PubMed](#) [Google Scholar](#)

Contributions

X.L. and G.O. designed the experiments and analysed the data. X.L. performed most of the experiments and data analysis. E.D.C. performed the neonate myocardial infarction and acquired data. T.T. and J.H. provided the *Reln* conditional mouse strain and generated some of the conditional crosses. X.G. helped with the generation, isolation and data analysis of *Reln* conditional embryos. C.L. and E.T. provided valuable advice with the neonate myocardial infarction and Echo data protocols. Z.J. and L.B. generated the *Vegfr3^{kd/kd}* embryos and analysed that data. M.O.-B. and W.M. helped with the generation of mouse lines, histology and discussions. H.K. and P.B. generated the iPS cell-derived CMs. T.B. helped with the primary cell culture experiments and qPCR analysis. O.C. helped to obtain and generate some of the mutant strains. M.T. provided valuable experimental advice and critical reading of the manuscript. X.L. and G.O. wrote the manuscript.

Corresponding author

Correspondence to [Guillermo Oliver](#).

Ethics declarations

Competing interests

J.H. is a shareholder of Reelin Therapeutics and a co-inventor on a pending US patent application filed by his institution (UT Southwestern; application number 15/763,047 and publication number 20180273637, title “Methods and Compositions for Treatment of Atherosclerosis”; Inventors: J.H., Y. Ding, X. Xian, L. Huang, C. Mineo, P. Shaul and L. Calvier). This patent application covers no aspects of the current manuscript. Findings regarding the potential applications and methods for using RELN to treat cardiac diseases are the subject of provisional patent application (US63/091,558) owned by Northwestern University and list X.L. and G.O. as inventors. All other authors declare no competing interests.

Additional information

Peer review information *Nature* thanks Kristy Red-Horse and the other, anonymous, reviewer(s) for their contribution to the peer review of this work.

Publisher’s note Springer Nature remains neutral with regard to jurisdictional claims in published maps and institutional affiliations.

Extended data figures and tables

[Extended Data Fig. 1 E17.5 \$Prox1^{ΔLEC/ΔLEC}\$ hearts lack LECs and have a reduced number of CMs.](#)

a, Whole-mount immunostaining with anti-PROX1 antibody shows that cardiac lymphatics are missing in E17.5 $Prox1^{ΔLEC/ΔLEC}$ hearts (TAM injected at E13.5 and E14.5). Squared areas are shown in larger magnification in the adjacent images. $n = 3$ embryos per group from two litters. **b**, Co-immunostaining of E17.5 control and $Prox1^{ΔLEC/ΔLEC}$ heart sections with anti- α -actinin and F-actin antibodies show that cardiac muscle

is not affected in *Prox1*^{ΔLEC/ΔLEC} embryos (TAM injected at E13.5 and E14.5). $n = 3$ per group. **c**, Flow cytometry analysis shows reduced CM numbers in E17.5 *Prox1*^{ΔLEC/ΔLEC} hearts (TAM injected at E13.5 and E14.5). **d**, Hoechst 33342 labelling shows no significant differences in CMs ploidy between control and *Prox1*^{ΔLEC/ΔLEC} hearts. $n = 3$ (control) and $n = 4$ (*Prox1*^{ΔLEC/ΔLEC}) embryos from the same litter used in **c** and **d**. Data are mean \pm s.e.m. ** $P = 0.001$, unpaired two-tailed Student's *t*-test. n.s., not significant. **e–g**, The percentage of multinucleated CMs in E17.5 mutant hearts is increased (**e**, **f**), and no global differences in CM size were detected (**e**, **g**) after CM dissociation and overnight plating. $n = 3$ embryo per genotype from the same litter. White arrows indicate CMs and yellow arrows indicate a bi-nucleated CM (**g**). The average cell size was calculated from 25 cTnC⁺ CMs per culture (1 whole heart per culture; 3 cultures per genotype). $n = 75$ (control CMs) and $n = 75$ (*Prox1*^{ΔLEC/ΔLEC} CMs). Data are mean \pm s.e.m. * $P = 0.023$, unpaired two-tailed Student's *t*-test. Scale bars, 500 μm (**a**), 25 μm (**b**, **e**). Flow cytometry gating strategy is included in Supplementary Fig. 10. [Source Data](#)

Extended Data Fig. 2 CM proliferation is reduced in E17.5 *Prox1*^{ΔLEC/ΔLEC} hearts.

a, EdU labelling shows an overall reduction in the number of EdU⁺ cells in sections of E17.5 *Prox1*^{ΔLEC/ΔLEC} hearts. Dashed boxes indicate the corresponding areas of the heart that are shown at higher magnification in **b–e**. **b–e**, Immunostaining results show the presence of PROX1⁺LYVE1⁺ cardiac lymphatics (white arrows) in sections of control hearts (**b**, **c**), and lack of lymphatics in *Prox1*^{ΔLEC/ΔLEC} hearts (**d**, **e**). Yellow arrows indicate LYVE1⁺ PROX1[−] macrophages. $n = 3$ embryos per genotype from three separate litters. **f**, CM proliferation is reduced in the myocardium of the left ventricle (LV) area, the right ventricle (RV) area and the septum. $n = 4$ embryos per genotype from three separate litters. At least three images per region and three separate regions per heart were quantified. Data are mean \pm s.e.m. * $P = 0.01$, ** $P = 0.003$, 0.006 and 0.02 (top); *** $P = 0.0001$, ** $P = 0.004$, 0.002 and 0.005 (middle); ** $P = 0.001$, 0.001, * $P = 0.01$ and ** $P = 0.002$ (bottom), unpaired two-tailed Student's *t*-test. **g**, Immunostaining with antibodies against vimentin (fibroblasts), PECAM1

(blood endothelial cells), CD68 (macrophages), SIX2 (nephron progenitors) or HNF4A (hepatocytes) together with EdU labelling (white arrows) shows no differences in proliferation in those cell types between E17.5 *Prox1^{ΔLEC}* and control hearts (TAM injected at E13.5 and E14.5). *P* values by unpaired two-tailed Student's *t*-test. *n* = 3 embryos per genotype from three separate litters. Control are TAM-treated *cre*[−] embryos and *cre*⁺; *Prox1*^{+/+} littermates. Data are mean ± s.e.m. Scale bars, 200 µm (a), 100 µm (b–e), 25 µm (g). [Source Data](#)

Extended Data Fig. 3 *Vegfr3^{kd/kd}* embryos lack cardiac lymphatics and have smaller hearts.

a, Bright-field images of whole E17.5 *Vegfr3^{kd/kd}* and wild-type embryos and hearts. Quantification of organ weight (heart, liver and kidney) relative to body length indicates that the heart is smaller and the liver and kidney have comparable sizes between *Vegfr3^{kd/kd}* and control embryos. *n* = 10 (WT) and *n* = 8 (*Vegfr3^{kd/kd}*). Embryos are from three different litters.

P* = 0.019. **b, LYVE1 whole-mount immunostaining shows that ventral and dorsal sides of the heart lack lymphatics in *Vegfr3^{kd/kd}* embryos. *n* = 3 per genotype. **c–f**, Co-immunostaining using antibodies against cell proliferation markers (EdU, pH3, Ki67 and auroraB) and antibodies against CM markers (cTnC, PROX1, α-actinin and/or MEF2C) shows reduced CM proliferation in *Vegfr3^{kd/kd}* hearts compared to wild-type hearts at E17.5. Arrows indicate representative proliferating CMs. **g**, Quantification shows significantly reduced percentage of EdU⁺ and Ki67⁺ CMs and significantly reduce number of pH3⁺ and auroraB⁺ CMs in *Vegfr3^{kd/kd}* hearts compared to controls. *n* = 4 embryos per genotype from three separate litters.

***P* = 0.005 (EdU), ***P* = 0.001 (Ki67, pH3), **P* = 0.02 (auroraB). **h**, Active CASP3⁺ immunostaining shows increased CM apoptosis (white arrows) in *Vegfr3^{kd/kd}* hearts compared to wild-type hearts at E17.5. Right, quantitative data showing significantly increased percentage of active caspase-3⁺ CMs (PROX1⁺) in *Vegfr3^{kd/kd}* hearts compared to wild-types. *n* = 4 embryos per genotype from three separate litters. **P* = 0.032. **i**, Co-immunostaining with antibodies against vimentin, PECAM1, CD68, SIX2 and HNF4A, together with EdU labelling shows comparable proliferation

of cardiac fibroblasts, blood endothelial cells and macrophages, and of nephron progenitors and hepatocytes between wild-type and *Vegfr3*^{kd/kd} embryos at E17.5. White arrows indicate EdU⁺ proliferating cells. Right, quantification of the proliferation for each cell type. $n = 3$ embryos per genotype from three separate litters. Data are mean \pm s.e.m. P values were determined by unpaired two-tailed Student's *t*-test. Scale bars, 1 mm (**a**), 500 μ m (**b**), 25 μ m (**c–f, h**), 25 μ m (**i**). Lower magnification images for **c–e** and **h** are included in Supplementary Fig. 4. [Source Data](#)

Extended Data Fig. 4 Heart size and CM proliferation is normal in E17.5 *Prox1*^{ΔLEC/+} embryos and E14.5 *Prox1*^{ΔLEC/ΔLEC} embryos.

a, Bright-field images of whole embryos and hearts show no difference in heart size in E17.5 *Prox1*^{ΔLEC/+} embryos (TAM injected at E13.5 and E14.5). White arrows indicate oedema in the *Prox1*^{ΔLEC/+} embryo. **b**, Whole-mount immunostaining shows that LYVE1⁺ cardiac lymphatics are present in both dorsal and ventral sides of *Prox1*^{ΔLEC/+} hearts. Lymphatics are less branched (arrows). **c**, Cardiac lymphatic density is significantly reduced on the ventral surface of the heart but not on the dorsal one in *Prox1*^{ΔLEC/+} embryos. This difference may be because cardiac lymphatics on the dorsal side and the ventral side originate from two different lineages during embryonic development. $n = 3$ embryos per genotype from three separate litters. * $P = 0.027$. **d**, Heart size is normal in E17.5 *Prox1*^{ΔLEC/+} embryos. $n = 13$ (controls) and $n = 9$ (*Prox1*^{ΔLEC/+}) embryos from three separate litters. **e**, Quantification of the immunostaining analysis shows no significant differences in CM proliferation between E17.5 *Prox1*^{ΔLEC/+} hearts and controls, as indicated by the percentage of EdU⁺ and Ki67⁺ CMs and the number of pH3⁺ and auroraB⁺ CMs. $n = 4$ embryos per genotype from three separate litters. Controls are TAM-treated *cre*[−] embryos and *cre*⁺;*Prox1*^{+/+} littermates. **f**, Bright field images of whole embryos and hearts show no difference in cardiac size between E14.5 wild-type and *Prox1*^{ΔLEC/ΔLEC} embryos (TAM injected at E10.5 and E11.5). White arrows indicate severe oedema. $n = 6$ embryos per genotype from two separate litters. Control embryos are TAM-treated *cre*[−] embryos and *cre*⁺;*Prox1*^{+/+}

littermates. **g**, Whole-mount staining of skin shows efficient PROX1 deletion as indicated by the lack of PROX1⁺ or NRP2⁺ lymphatics at E14.5 in *Prox1^{ΔLEC/ΔLEC}* embryos. $n = 3$ embryos per genotype from same litter. **h**, Co-immunostaining against cell proliferation markers (EdU, Ki67, pH3 and auroraB) together with CM markers (cTnC, PROX1, α -actinin and/or MEF2C). Quantification of those immunostainings shows no differences in CM proliferation between wild-type and *Prox1^{ΔLEC/ΔLEC}* hearts at E14.5. Squares indicate proliferating CMs. $n = 3$ embryos per genotype from the same litter. Data are mean \pm s.e.m. P values determined by unpaired two-tailed Student's *t*-test. Scale bars, 1 mm (**a, f**), 500 μ m (**b**), 25 μ m (**g, h**).

[Source Data](#)

Extended Data Fig. 5 Pathways related to cell cycle are downregulated in E17.5 *Prox1^{ΔLEC/ΔLEC}* embryos and LEC-conditioned medium promotes CM proliferation and survival in vitro.

a, Gene set expression analysis shows downregulation of cell cycle pathways and upregulation of cell death pathways in *Prox1^{ΔLEC/ΔLEC}* hearts. $n = 4$ per genotype from the same litter. **b**, qPCR analysis confirmed the upregulation of pro-apoptotic genes (*Bcl2l11*, *Pdcd4*, *Trp53inp1*, *Stat1* and *P21* (also known as *Cdkn1a*)) and downregulation of cell cycle related genes (*Cdc6*, *E2f1*, *Pcna*, *Mcm5* and *Ccne2*) in *Prox1^{ΔLEC/ΔLEC}* hearts. $n = 3$ per genotype from the same litter. TAM was injected at E13.5 and E14.5. Control embryos are TAM-treated *cre*⁻ embryos and *cre*⁺; *Prox1*^{+/+} littermates. * $P = 0.02$ (*Bcl2l11*), ** $P = 0.001$ (*Pdcd4*), 0.005 (*Trp53inp1*), * $P = 0.01$ (*Stat1*), 0.03 (*P21*), 0.04 (*Cdc6*), 0.02 (*E2f1*), 0.01 (*Pcna*), 0.02 (*Mcm5*) and 0.03 (*Ccne2*). **c**, Co-immunostaining against the proliferation marker Ki67 and the CM markers α -actinin and PROX1 shows that LEC-conditioned medium increases primary CM proliferation. Arrows indicate proliferating CMs. Percentage of CM proliferation was quantified by the number of Ki67⁺ PROX1⁺ CMs relative to total number of PROX1⁺ CMs. $n = 3$. ** $P = 0.001$. **d**, Co-immunostaining against the apoptotic marker active CASP3⁺ and the CM markers α -actinin and PROX1 shows reduced primary CM apoptosis upon LEC-conditioned medium treatment under

CoCl₂-induced hypoxia. Arrows indicate apoptotic CMs. Percentage of apoptotic CMs was quantified by the number of active CASP3⁺ CMs relative to PROX1⁺ CMs. $n = 3$. ** $P = 0.003$. Data are mean \pm s.e.m. P values were determined by unpaired two-tailed Student's *t*-test Scale bar, 25 μm (**c, d**). [Source Data](#)

Extended Data Fig. 6 E17.5 *Reln*^{-/-} embryos develop smaller hearts.

a, qPCR analysis shows reduced *Reln* expression in E17.5 *Prox1*^{ΔLEC/ΔLEC} hearts (TAM injected at E13.5 and E14.5). $n = 3$ embryos per genotype from the same litter. Control embryos are TAM treated *cre*⁻ embryos and *cre*⁺; *Prox1*^{+/+} littermates. * $P = 0.014$. **b**, qPCR analysis validates the expression of candidates from the LECs secretome (*Serpine1*, *Fn1*, *Reln*, *Hspg2*, *Mmrn1*, *Lama4*, *Fstl1* and *Thbs1*). Experiments were repeated three times using different batches of LECs. Gene expression is normalized as a fold change relative to 100× *Gapdh*. **c**, RELN protein can be detected in three different batches of LEC-conditioned medium and the relative RELN level is quantified by ELISA according to the absorbance value at 450 nm ($A_{450\text{ nm}}$). **d, e**, Immunostaining of sections of E17.5 wild-type hearts shows RELN is highly expressed in cardiac lymphatics of the epicardium and myocardium. Some blood vessels in the heart express low levels of RELN (**e**, arrows). $n = 3$ wild-type embryos. **f**, Immunostaining of E17.5 control and *Prox1*^{ΔLEC/ΔLEC} heart sections with antibodies against RELN and LYVE1 shows that cardiac lymphatics and RELN are absent in *Prox1*^{ΔLEC/ΔLEC} hearts (TAM injected at E13.5 and E14.5). $n = 3$ embryos per genotype from the same litter. Control embryos are TAM-treated littermate *cre*⁻ and *cre*⁺; *Prox1*^{+/+} embryos. **g**, Representative bright-field images show smaller hearts in E17.5 *Reln*^{-/-} embryos. **h**, Quantifications of organ weight (heart, liver and kidney) relative to body length indicate that hearts are smaller in E17.5 *Reln*^{-/-} embryos compared to controls. $n = 7$ (WT) and $n = 6$ (*Reln*^{-/-}) embryos from three separate litters. * $P = 0.03$. **i**, Whole-mount immunostaining shows that cardiac lymphatic development is normal in *Reln*^{-/-} embryos. $n = 3$ embryos per genotype from two separate litters.

Data are mean \pm s.e.m. P values were determined by unpaired two-tailed Student's t -test. Scale bars, 25 μm (d–f), 1 mm (g), 500 μm (i). [Source Data](#)

Extended Data Fig. 7 RELN is efficiently deleted in *Reln*^{ΔLEC/ΔLEC} cardiac-associated lymphatics.

a, Immunostaining of E17.5 control and *Reln*^{ΔLEC/ΔLEC} heart sections with antibodies against RELN and LYVE1 confirms that RELN is deleted from cardiac lymphatics in *Reln*^{ΔLEC/ΔLEC} hearts (TAM injected at E13.5 and E14.5). $n = 3$ embryos per genotype from two separate litters. Control embryos are TAM-treated *cre*[−] embryos and *cre*⁺; *Reln*^{+/+} embryos. **b**, Co-immunostaining with antibodies against vimentin, PECAM1, CD68, SIX2 and HNF4A, together with EdU labelling shows comparable proliferation of cardiac fibroblasts, blood endothelial cells and macrophages, and of nephron progenitors and hepatocytes between controls and E17.5 *Reln*^{ΔLEC/ΔLEC} hearts (TAM injected at E13.5 and E14.5). White arrows indicate EdU⁺ proliferating cells. Right, quantification of the proliferation for each cell type. $n = 3$ embryos per genotype from two separate litters. Control embryos are TAM-treated *cre*[−] and *cre*⁺; *Reln*^{+/+} littermates. Data are mean \pm s.e.m. P values determined by unpaired two-tailed Student's t -test. Scale bar, 25 μm . [Source Data](#)

Extended Data Fig. 8 Cardiac size is reduced in E17.5 *β1ACM/+; Reln+/-* embryos.

a, qPCR analysis shows efficient *Reln* knockdown in LECs after siRNA treatment. $n = 3$. Data are mean \pm s.e.m. * $P < 0.05$, unpaired two-tailed Student's t -test. **b**, Representative western blot of primary CMs cultured with DMEM, conditioned medium from CMs treated with short interfering RNA (siRNA) against *Reln* (siReln) or control siRNA (siCtrl), or with conditioned medium plus integrin- β 1 blocking antibody overnight. The addition of the LEC-conditioned medium (siCtrl group) to primary CMs increased DAB1, FAK, AKT and ERK activities. These activities are reduced when cultured CMs are treated with RELN-deficient LEC-conditioned medium or with LEC-conditioned medium with integrin- β 1

blocking antibody. Experiments were repeated three times. Data are mean \pm s.e.m. * $P < 0.05$, ** $P < 0.01$, *** $P < 0.001$, two-way ANOVA followed by Bonferroni test. **c**, Ki67 quantification of immunostained cultured cells (similar to Extended Data Fig. 5c) shows that addition of the LEC-conditioned medium (siCtrl group) to cultured primary CMs improves CM proliferation and this effect is partially abolished in CMs treated with *Reln*-deficient (si*Reln*) LEC-conditioned medium or with LEC-conditioned medium containing integrin- β 1 blocking antibody. Percentage of CM proliferation was quantified by the number of Ki67 $^+$ PROX1 $^+$ CMs relative to total numbers of PROX1 $^+$ CMs. $n = 3$. Data are mean \pm s.e.m. ** $P < 0.01$, two-way ANOVA followed by Bonferroni test.

d, Quantification of cultured CMs immunostained with active CASP3 $^+$ shows that the addition of the LEC-conditioned medium (siCtrl group) to primary CMs protects them from apoptosis and this effect is partially abolished in CMs treated with *Reln*-deficient LEC-conditioned medium or with LEC-conditioned medium with integrin- β 1 blocking antibodies. Percentage of apoptotic CMs was quantified by the number of active CASP3 $^+$ CMs relative to PROX1 $^+$ CMs. $n = 3$. Data are mean \pm s.e.m. * $P < 0.05$, ** $P < 0.01$, two-way ANOVA followed by Bonferroni test.

e, Representative western blot of primary CMs after treatment with RELN-conditioned medium from RELN-transfected cells, or conditioned medium from mock-transfected cells (control) or RELN-conditioned medium with integrin- β 1 blocking antibody (ab) shows that RELN treatment increases DAB1, FAK, AKT and ERK activities in primary CMs, and these activities are reduced by adding the integrin- β 1 blocking antibody. $n = 3$. Data are mean \pm s.e.m. * $P < 0.05$; ** $P < 0.01$ by one-way ANOVA followed by Tukey's test.

f, Bright-field images show no difference in embryo size at E17.5 among control, *Reln* $^{+/-}$, β 1 $^{\Delta CM/+}$ and β 1 $^{\Delta CM/+}, Reln$ $^{+/-}$ embryos.

Quantification of organ weight (heart, liver and kidney) relative to body length indicates that hearts are smaller in E17.5 β 1 $^{\Delta CM/+}, Reln$ $^{+/-}$ embryos. $n = 9$ (control), $n = 7$ (*Reln* $^{+/-}$), $n = 6$ (β 1 $^{\Delta CM/+}$) and $n = 6$ (β 1 $^{\Delta CM/+}, Reln$ $^{+/-}$) embryos from three separate litters. Data are mean \pm s.e.m. * $P = 0.015$, one-way ANOVA followed by Tukey's test.

g, Whole-mount immunostaining using LYVE1 antibodies shows normal cardiac lymphatic development in control, β 1 $^{\Delta CM/+}$, β 1 $^{\Delta CM/+}, Reln$ $^{+/-}$ and *Reln* $^{+/-}$ embryos.

$n = 3$ embryos per genotype from three separate litters. Scale bars, 1 mm

(f), 500 µm (g). For western blot source data, see Supplementary Figs. 8 and 9. Exact *P* values included in Source Data. [Source Data](#)

Extended Data Fig. 9 RELN promotes CM proliferation and survival through *Itgb1* signalling.

a, Co-immunostaining using cell proliferation markers (EdU, Ki67, pH3 and auroraB) together with CM markers (cTnC, PROX1, α-actinin and/or MEF2C) shows reduced CM proliferation in $\beta 1^{\Delta CM/+}, Reln^{+/-}$ hearts at E17.5. Arrows indicate proliferating CMs. Quantification in the bottom panel shows reduced proliferation in E17.5 $\beta 1^{\Delta CM/+}, Reln^{+/-}$ hearts, as indicated by the percentage of EdU⁺ and Ki67⁺ CMs and the number of pH3⁺ and auroraB⁺ CMs. $n = 4$ embryos per genotype from three separate litters. **P* = 0.022 (EdU), 0.029 (Ki67), ****P* = 0.0001 (pH3) and **P* = 0.033 (auroraB). **b**, Active CASP3⁺ immunostaining shows increased CM apoptosis in $\beta 1^{\Delta CM/+}, Reln^{+/-}$ hearts at E17.5, as quantified by the percentage of active CASP3⁺ CMs relative to PROX1⁺ CMs. Arrows indicate apoptotic CMs. $n = 4$ embryos per genotype from three separate litters. Control embryos are *cre*⁻ embryos and *cre*⁺; $\beta 1^{+/+}$ littermates. **P* = 0.01. **c**, Co-immunostaining with antibodies against vimentin, PECAM1, CD68, SIX2 and HNF4A, together with EdU labelling shows comparable proliferation of cardiac fibroblasts, blood endothelial cells and macrophages, and of nephron progenitors and hepatocytes between controls and E17.5 $\beta 1^{\Delta CM/+}, Reln^{+/-}$ embryos. White arrows indicate EdU⁺ proliferating cells. Right, quantification of the proliferation analysis for each of cell type. $n = 3$ embryos per genotype from three separate litters. Control are *cre*⁻ embryos and *cre*⁺; $\beta 1^{+/+}$ littermates. Data are mean ± s.e.m. *P* values determined by unpaired two-tailed Student's *t*-test. Scale bars, 25 µm. Lower magnification images for **a** and **b** are included in Supplementary Fig. 5. [Source Data](#)

Extended Data Fig. 10 RELN expression is developmentally downregulated, but is upregulated in newly formed cardiac lymphatics after myocardial infarction.

a, Immunostaining with RELN, PROX1 and PECAM shows RELN is highly expressed in cardiac lymphatics in the epicardium and myocardium nearby the base of the heart at E17.5. RELN expression level is gradually downregulated during development from P2 to P14. $n = 3$ hearts per stage. Arrows indicate PROX1⁺ cardiac lymphatics. **b**, qPCR analysis using sorted cardiac lymphatics shows *Reln* levels are drastically downregulated in cardiac LECs during development. $n = 3$. *Reln* relative level from each experiment is presented as fold changes relative to E17.5. Data are mean \pm s.e.m. ** $P = 0.009$ (P2 versus E17.5), 0.004 (P7 versus E17.5), 0.001 (P14 versus E17.5) by one-way ANOVA followed by Tukey's test. **c**, Immunostaining shows RELN expression is highly upregulated in the newly formed cardiac lymphatics in wild-type P7 pups (myocardial infarction was performed at P2). Notably, the pre-existing cardiac lymphatics in the non-infarcted area express low levels of RELN. *Reln*^{-/-} hearts completely lack RELN expression in both, newly formed cardiac lymphatics and pre-existing lymphatics. Arrows indicate cardiac lymphatics. $n = 3$ hearts per group. **d**, Immunostaining against the pan-endothelial marker PECAM1 and the lymphatic marker LYVE1 shows normal lymphangiogenesis in wild-type and *Reln*^{-/-} hearts 21 days after myocardial infarction (myocardial infarction performed at P2). $n = 3$ hearts per group. Data are mean \pm s.e.m. P values determined by unpaired two-tailed Student's *t*-test. **e**, EdU labelling shows no differences in LECs proliferation in wild-type and *Reln*^{-/-} hearts 21 days after myocardial infarction (myocardial infarction performed at P2). $n = 3$ hearts per group. Data are mean \pm s.e.m. P values determined by unpaired two-tailed Student's *t*-test. Arrow indicates EdU⁺ LECs. Scale bars, 100 μ m (**d**), 25 μ m (**a, c, e**). [Source Data](#)

Extended Data Fig. 11 RELN improves cardioprotection in neonates and adult mice after myocardial infarction.

a-d, Co-immunostaining using cell proliferation markers (EdU, Ki67, pH3 and auroraB) together with the CM markers PROX1, α -actinin or MEF2C shows decreased CM proliferation in the border of the infarcted area of *Reln*^{-/-} hearts at P7. Arrows indicate proliferating CMs. $n = 4$ mice per group. **e**, Immunostaining using active CASP3⁺ shows increased CM

apoptosis in the infarcted area of *Reln*^{-/-} hearts at P7. Arrows indicate apoptotic CMs in the section. $n = 4$ mice per group. **f**, Immunostaining against the cell proliferation markers EdU, Ki67 and pH3 together with the CM markers MEF2C or cTnC shows no differences in CM proliferation in the infarcted areas between control patch or RELN patch treated hearts 7 days after myocardial infarction. Arrows indicate proliferating CMs. $n = 4$ hearts per group. **g**, Immunostaining using active caspase-3 shows reduced CM apoptosis in the infarcted area of RELN patch-treated hearts. Arrows indicate apoptotic CMs. $n = 4$ mice per group. Arrows indicate apoptotic CMs. Scale bars, 25 μ m. Lower magnification for **a–c, e** and **g** are included in Supplementary Fig. [3](#).

Supplementary information

[Supplementary Figures 1-10](#)

This file contains Supplementary Figures 1-5 showing lower magnification images for CM proliferation and apoptosis; Supplementary Figures 6-9 showing source data for Western blots; and Supplementary Figure 10 showing gating strategy for flow cytometry.

[Reporting Summary](#)

Source data

[Source Data Fig. 1](#)

[Source Data Fig. 2](#)

[Source Data Fig. 3](#)

[Source Data Fig. 4](#)

[Source Data Extended Data Fig. 1](#)

[Source Data Extended Data Fig. 2](#)

[Source Data Extended Data Fig. 3](#)

[Source Data Extended Data Fig. 4](#)

[Source Data Extended Data Fig. 5](#)

[Source Data Extended Data Fig. 6](#)

[Source Data Extended Data Fig. 7](#)

[Source Data Extended Data Fig. 8](#)

[Source Data Extended Data Fig. 9](#)

[Source Data Extended Data Fig. 10](#)

Rights and permissions

[Reprints and Permissions](#)

About this article



Check for
updates

Cite this article

Liu, X., De la Cruz, E., Gu, X. *et al.* Lymphoangiocrine signals promote cardiac growth and repair. *Nature* **588**, 705–711 (2020).
<https://doi.org/10.1038/s41586-020-2998-x>

Download citation

- Received: 13 June 2019
- Accepted: 07 October 2020
- Published: 09 December 2020
- Issue Date: 24 December 2020
- DOI: <https://doi.org/10.1038/s41586-020-2998-x>

Comments

By submitting a comment you agree to abide by our [Terms](#) and [Community Guidelines](#). If you find something abusive or that does not comply with our terms or guidelines please flag it as inappropriate.

[Access through your institution](#)

[Change institution](#)

[Buy or subscribe](#)

This article was downloaded by **calibre** from <https://www.nature.com/articles/s41586-020-2998-x>

- Article
- [Published: 16 December 2020](#)

Small-molecule inhibitors of human mitochondrial DNA transcription

- [Nina A. Bonekamp](#) ORCID: orcid.org/0000-0001-9748-8089^{1,na1},
- [Bradley Peter](#) ORCID: orcid.org/0000-0003-0885-3131^{2,na1},
- [Hauke S. Hillen](#) ORCID: orcid.org/0000-0002-1206-0129³,
- [Andrea Felser](#) ORCID: orcid.org/0000-0003-4806-2940⁴,
- [Tim Bergbrede](#) ORCID: orcid.org/0000-0002-0930-1884⁵,
- [Axel Choidas](#) ORCID: orcid.org/0000-0003-2132-4939⁵,
- [Moritz Horn](#) ORCID: orcid.org/0000-0002-5324-7256^{6,7,8},
- [Anke Unger](#) ORCID: orcid.org/0000-0003-1288-3763⁵,
- [Raffaella Di Lucrezia](#) ORCID: orcid.org/0000-0001-6510-9945⁵,
- [Ilian Atanassov](#) ORCID: orcid.org/0000-0001-8259-2545²,
- [Xinping Li](#) ORCID: orcid.org/0000-0002-7427-0017⁹,
- [Uwe Koch](#) ORCID: orcid.org/0000-0002-5413-283X⁵,
- [Sascha Menninger](#) ORCID: orcid.org/0000-0002-3665-3973⁵,
- [Joanna Boros](#) ORCID: orcid.org/0000-0001-7336-6474⁵,
- [Peter Habenberger](#) ORCID: orcid.org/0000-0002-1251-264X⁵,
- [Patrick Giavalisco](#)¹⁰,
- [Patrick Cramer](#) ORCID: orcid.org/0000-0001-5454-7755³,
- [Martin S. Denzel](#)⁶,
- [Peter Nussbaumer](#) ORCID: orcid.org/0000-0002-2761-629X⁵,
- [Bert Klebl](#)⁵,
- [Maria Falkenberg](#) ORCID: orcid.org/0000-0001-8713-173X²,
- [Claes M. Gustafsson](#) ORCID: orcid.org/0000-0003-3531-8468² &
- [Nils-Göran Larsson](#) ORCID: orcid.org/0000-0001-5100-996X^{1,4,11}

[Nature](#) volume 588, pages712–716(2020)Cite this article

- 12k Accesses
- 298 Altmetric
- [Metrics details](#)

Subjects

- [Cancer therapy](#)
- [Mitochondria](#)
- [Transcription](#)

Abstract

Altered expression of mitochondrial DNA (mtDNA) occurs in ageing and a range of human pathologies (for example, inborn errors of metabolism, neurodegeneration and cancer). Here we describe first-in-class specific inhibitors of mitochondrial transcription (IMTs) that target the human mitochondrial RNA polymerase (POLRMT), which is essential for biogenesis of the oxidative phosphorylation (OXPHOS) system^{1,2,3,4,5,6}. The IMTs efficiently impair mtDNA transcription in a reconstituted recombinant system and cause a dose-dependent inhibition of mtDNA expression and OXPHOS in cell lines. To verify the cellular target, we performed exome sequencing of mutagenized cells and identified a cluster of amino acid substitutions in POLRMT that cause resistance to IMTs. We obtained a cryo-electron microscopy (cryo-EM) structure of POLRMT bound to an IMT, which further defined the allosteric binding site near the active centre cleft of POLRMT. The growth of cancer cells and the persistence of therapy-resistant cancer stem cells has previously been reported to depend on OXPHOS^{7,8,9,10,11,12,13,14,15,16,17}, and we therefore investigated whether IMTs have anti-tumour effects. Four weeks of oral treatment with an IMT is well-tolerated in mice and does not cause OXPHOS dysfunction or toxicity in normal tissues, despite inducing a strong anti-tumour response in xenografts of human cancer cells. In

summary, IMTs provide a potent and specific chemical biology tool to study the role of mtDNA expression in physiology and disease.

[Access through your institution](#)

[Change institution](#)

[Buy or subscribe](#)

Access options

Subscribe to Journal

Get full journal access for 1 year

\$199.00

only \$3.83 per issue

[Subscribe](#)

All prices are NET prices.

VAT will be added later in the checkout.

Rent or Buy article

Get time limited or full article access on ReadCube.

from \$8.99

[Rent or Buy](#)

All prices are NET prices.

Additional access options:

- [Log in](#)
- [Access through your institution](#)
- [Learn about institutional subscriptions](#)

Fig. 1: IMTs affect stability, substrate binding and enzyme activity of POLRMT and inhibit mitochondrial gene expression.

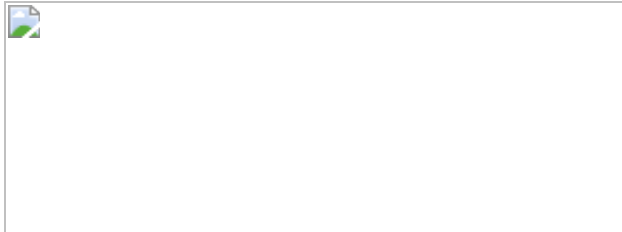


Fig. 2: POLRMT is the in vivo target of IMTs.

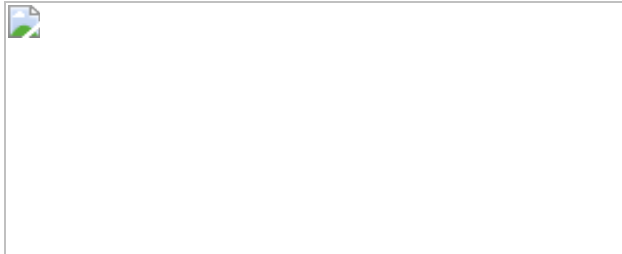


Fig. 3: IMTs specifically inhibit proliferation of cancer cells.

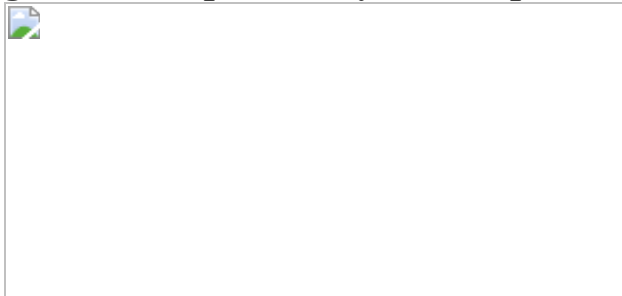


Fig. 4: IMT treatment inhibits tumour growth in vivo and mitochondrial gene expression in a dose-dependent manner.



Data availability

All relevant data generated and analysed in this study are included in the Article. Uncropped gels are provided in Supplementary Fig. 1. Publicly available datasets used in this study are the human proteome database (UP000005640, UniProt) and POLRMT structures (PBD codes 5OLA and 4BOC). Further information and requests for unique reagents should be directed to the corresponding authors. Proteomics data and R scripts for analysis have been deposited in PRIDE with the dataset identifier

PXD018426. The electron microscopy maps have been deposited with the Electron Microscopy Data Bank (accession code [EMD-11679](#)) and the structural model of POLRMT bound to IMT1B has been deposited in the PDB (accession code [7A8P](#)). [Source data](#) are provided with this paper.

References

1. 1.

Kühl, I. et al. POLRMT does not transcribe nuclear genes. *Nature* **514**, E7–E11 (2014).

[PubMed](#) [Google Scholar](#)

2. 2.

Kühl, I. et al. Transcriptomic and proteomic landscape of mitochondrial dysfunction reveals secondary coenzyme Q deficiency in mammals. *eLife* **6**, e30952 (2017).

[PubMed](#) [PubMed Central](#) [Google Scholar](#)

3. 3.

Kühl, I. et al. POLRMT regulates the switch between replication primer formation and gene expression of mammalian mtDNA. *Sci. Adv.* **2**, e1600963 (2016).

[ADS](#) [PubMed](#) [PubMed Central](#) [Google Scholar](#)

4. 4.

Posse, V. et al. The amino terminal extension of mammalian mitochondrial RNA polymerase ensures promoter specific transcription initiation. *Nucleic Acids Res.* **42**, 3638–3647 (2014).

[CAS](#) [PubMed](#) [PubMed Central](#) [Google Scholar](#)

5. 5.

Ringel, R. et al. Structure of human mitochondrial RNA polymerase. *Nature* **478**, 269–273 (2011).

[ADS](#) [CAS](#) [PubMed](#) [Google Scholar](#)

6. 6.

Schwinghammer, K. et al. Structure of human mitochondrial RNA polymerase elongation complex. *Nat. Struct. Mol. Biol.* **20**, 1298–1303 (2013).

[CAS](#) [PubMed](#) [PubMed Central](#) [Google Scholar](#)

7. 7.

Birsoy, K. et al. Metabolic determinants of cancer cell sensitivity to glucose limitation and biguanides. *Nature* **508**, 108–112 (2014).

[ADS](#) [CAS](#) [PubMed](#) [PubMed Central](#) [Google Scholar](#)

8. 8.

Bosc, C., Selak, M. A. & Sarry, J. E. Resistance is futile: targeting mitochondrial energetics and metabolism to overcome drug resistance in cancer treatment. *Cell Metab.* **26**, 705–707 (2017).

[CAS](#) [PubMed](#) [Google Scholar](#)

9. 9.

Funes, J. M. et al. Transformation of human mesenchymal stem cells increases their dependency on oxidative phosphorylation for energy production. *Proc. Natl Acad. Sci. USA* **104**, 6223–6228 (2007).

[ADS](#) [CAS](#) [PubMed](#) [Google Scholar](#)

10. 10.

Kuntz, E. M. et al. Targeting mitochondrial oxidative phosphorylation eradicates therapy-resistant chronic myeloid leukemia stem cells. *Nat. Med.* **23**, 1234–1240 (2017).

[CAS](#) [PubMed](#) [PubMed Central](#) [Google Scholar](#)

11. 11.

Lee, J. et al. Effective breast cancer combination therapy targeting BACH1 and mitochondrial metabolism. *Nature* **568**, 254–258 (2019).

[ADS](#) [CAS](#) [PubMed](#) [PubMed Central](#) [Google Scholar](#)

12. 12.

Shi, Y. et al. Gboxin is an oxidative phosphorylation inhibitor that targets glioblastoma. *Nature* **567**, 341–346 (2019).

[ADS](#) [CAS](#) [PubMed](#) [PubMed Central](#) [Google Scholar](#)

13. 13.

Škrtić, M. et al. Inhibition of mitochondrial translation as a therapeutic strategy for human acute myeloid leukemia. *Cancer Cell* **20**, 674–688 (2011).

[PubMed](#) [PubMed Central](#) [Google Scholar](#)

14. 14.

Vander Heiden, M. G. & DeBerardinis, R. J. Understanding the intersections between metabolism and cancer biology. *Cell* **168**, 657–669 (2017).

[PubMed Central](#) [Google Scholar](#)

15. 15.

Viale, A. et al. Oncogene ablation-resistant pancreatic cancer cells depend on mitochondrial function. *Nature* **514**, 628–632 (2014).

[ADS](#) [CAS](#) [PubMed](#) [PubMed Central](#) [Google Scholar](#)

16. 16.

Martínez-Reyes, I. et al. Mitochondrial ubiquinol oxidation is necessary for tumour growth. *Nature* **585**, 288–292 (2020).

[PubMed](#) [Google Scholar](#)

17. 17.

Vasan, K., Werner, M. & Chandel, N. S. Mitochondrial metabolism as a target for cancer therapy. *Cell Metab.* **32**, 341–352 (2020).

[CAS](#) [PubMed](#) [Google Scholar](#)

18. 18.

Bergbrede, T., Hoberg, E., Larsson, N. G., Falkenberg, M. & Gustafsson, C. M. An adaptable high-throughput technology enabling the identification of specific transcription modulators. *SLAS Discov.* **22**, 378–386 (2017).

[CAS](#) [PubMed](#) [Google Scholar](#)

19. 19.

Horn, M. et al. Unbiased compound-protein interface mapping and prediction of chemoresistance loci through forward genetics in haploid stem cells. *Oncotarget* **9**, 9838–9851 (2018).

[PubMed](#) [PubMed Central](#) [Google Scholar](#)

20. 20.

Hillen, H. S. et al. Mechanism of transcription anti-termination in human mitochondria. *Cell* **171**, 1082–1093 (2017).

[CAS](#) [PubMed](#) [PubMed Central](#) [Google Scholar](#)

21. 21.

Hillen, H. S., Morozov, Y. I., Sarfallah, A., Temiakov, D. & Cramer, P. Structural basis of mitochondrial transcription initiation. *Cell* **171**, 1072–1081 (2017).

[CAS](#) [PubMed](#) [PubMed Central](#) [Google Scholar](#)

22. 22.

Sriskanthadevan, S. et al. AML cells have low spare reserve capacity in their respiratory chain that renders them susceptible to oxidative metabolic stress. *Blood* **125**, 2120–2130 (2015).

[CAS](#) [PubMed](#) [PubMed Central](#) [Google Scholar](#)

23. 23.

Weinberg, F. et al. Mitochondrial metabolism and ROS generation are essential for Kras-mediated tumorigenicity. *Proc. Natl Acad. Sci. USA* **107**, 8788–8793 (2010).

[ADS](#) [CAS](#) [PubMed](#) [Google Scholar](#)

24. 24.

Bralha, F. N. et al. Targeting mitochondrial RNA polymerase in acute myeloid leukemia. *Oncotarget* **6**, 37216–37228 (2015).

[PubMed](#) [PubMed Central](#) [Google Scholar](#)

25. 25.

Wang, J. et al. Dilated cardiomyopathy and atrioventricular conduction blocks induced by heart-specific inactivation of mitochondrial DNA gene expression. *Nat. Genet.* **21**, 133–137 (1999).

[PubMed](#) [Google Scholar](#)

26. 26.

Sørensen, L. et al. Late-onset corticohippocampal neurodepletion attributable to catastrophic failure of oxidative phosphorylation in MILON mice. *J. Neurosci.* **21**, 8082–8090 (2001).

[PubMed](#) [PubMed Central](#) [Google Scholar](#)

27. 27.

Viader, A. et al. Schwann cell mitochondrial metabolism supports long-term axonal survival and peripheral nerve function. *J. Neurosci.* **31**, 10128–10140 (2011).

[CAS](#) [PubMed](#) [PubMed Central](#) [Google Scholar](#)

28. 28.

Wredenberg, A. et al. Increased mitochondrial mass in mitochondrial myopathy mice. *Proc. Natl Acad. Sci. USA* **99**, 15066–15071 (2002).

[ADS](#) [CAS](#) [PubMed](#) [Google Scholar](#)

29. 29.

Larsson, N. G. et al. Mitochondrial transcription factor A is necessary for mtDNA maintenance and embryogenesis in mice. *Nat. Genet.* **18**, 231–236 (1998).

[CAS](#) [PubMed](#) [Google Scholar](#)

30. 30.

Hillen, H. S., Temiakov, D. & Cramer, P. Structural basis of mitochondrial transcription. *Nat. Struct. Mol. Biol.* **25**, 754–765 (2018).

[CAS](#) [PubMed](#) [PubMed Central](#) [Google Scholar](#)

31. 31.

Peter, B. et al. Defective mitochondrial protease LonP1 can cause classical mitochondrial disease. *Hum. Mol. Genet.* **27**, 1743–1753 (2018).

[CAS](#) [PubMed](#) [PubMed Central](#) [Google Scholar](#)

32. 32.

Falkenberg, M. et al. Mitochondrial transcription factors B1 and B2 activate transcription of human mtDNA. *Nat. Genet.* **31**, 289–294 (2002).

[CAS](#) [PubMed](#) [Google Scholar](#)

33. 33.

Morozov, Y. I. et al. A novel intermediate in transcription initiation by human mitochondrial RNA polymerase. *Nucleic Acids Res.* **42**, 3884–3893 (2014).

[CAS](#) [PubMed](#) [PubMed Central](#) [Google Scholar](#)

34. 34.

Vos, S. M., Farnung, L., Urlaub, H. & Cramer, P. Structure of paused transcription complex Pol II–DSIF–NELF. *Nature* **560**, 601–606 (2018).

[ADS](#) [CAS](#) [PubMed](#) [PubMed Central](#) [Google Scholar](#)

35. 35.

Vos, S. M., Farnung, L., Linden, A., Urlaub, H. & Cramer, P. Structure of complete Pol II–DSIF–PAF–SPT6 transcription complex reveals RTF1 allosteric activation. *Nat. Struct. Mol. Biol.* **27**, 668–677 (2020).

[CAS](#) [PubMed](#) [Google Scholar](#)

36. 36.

Macao, B. et al. The exonuclease activity of DNA polymerase γ is required for ligation during mitochondrial DNA replication. *Nat. Commun.* **6**, 7303 (2015).

[ADS](#) [CAS](#) [PubMed](#) [PubMed Central](#) [Google Scholar](#)

37. 37.

Tegunov, D. & Cramer, P. Real-time cryo-electron microscopy data preprocessing with Warp. *Nat. Methods* **16**, 1146–1152 (2019).

[CAS](#) [PubMed](#) [PubMed Central](#) [Google Scholar](#)

38. 38.

Punjani, A., Rubinstein, J. L., Fleet, D. J. & Brubaker, M. A. cryoSPARC: algorithms for rapid unsupervised cryo-EM structure determination. *Nat. Methods* **14**, 290–296 (2017).

[CAS](#) [Google Scholar](#)

39. 39.

Scheres, S. H. RELION: implementation of a Bayesian approach to cryo-EM structure determination. *J. Struct. Biol.* **180**, 519–530 (2012).

[CAS](#) [PubMed](#) [PubMed Central](#) [Google Scholar](#)

40. 40.

Tan, Y. Z. et al. Addressing preferred specimen orientation in single-particle cryo-EM through tilting. *Nat. Methods* **14**, 793–796 (2017).

[CAS](#) [PubMed](#) [PubMed Central](#) [Google Scholar](#)

41. 41.

Emsley, P., Lohkamp, B., Scott, W. G. & Cowtan, K. Features and development of Coot. *Acta Crystallogr. D* **66**, 486–501 (2010).

[CAS](#) [PubMed](#) [Google Scholar](#)

42. 42.

Adams, P. D. et al. PHENIX: a comprehensive Python-based system for macromolecular structure solution. *Acta Crystallogr. D* **66**, 213–221 (2010).

[CAS](#) [PubMed](#) [Google Scholar](#)

43. 43.

Ruzzenente, B. et al. LRPPRC is necessary for polyadenylation and coordination of translation of mitochondrial mRNAs. *EMBO J.* **31**, 443–456 (2012).

[CAS](#) [PubMed](#) [Google Scholar](#)

44. 44.

Kauppila, J. H. K. et al. Base-excision repair deficiency alone or combined with increased oxidative stress does not increase mtDNA point mutations in mice. *Nucleic Acids Res.* **46**, 6642–6669 (2018).

[CAS](#) [PubMed](#) [PubMed Central](#) [Google Scholar](#)

45. 45.

Busch, J. D. et al. MitoRibo-tag mice provide a tool for in vivo studies of mitoribosome composition. *Cell Rep.* **29**, 1728–1738 (2019).

[CAS](#) [PubMed](#) [PubMed Central](#) [Google Scholar](#)

46. 46.

Rappsilber, J., Ishihama, Y. & Mann, M. Stop and go extraction tips for matrix-assisted laser desorption/ionization, nanoelectrospray, and LC/MS sample pretreatment in proteomics. *Anal. Chem.* **75**, 663–670 (2003).

[CAS](#) [PubMed](#) [Google Scholar](#)

47. 47.

Cox, J. & Mann, M. MaxQuant enables high peptide identification rates, individualized p.p.b.-range mass accuracies and proteome-wide protein quantification. *Nat. Biotechnol.* **26**, 1367–1372 (2008).

[CAS](#) [PubMed](#) [Google Scholar](#)

48. 48.

Ritchie, M. E. et al. limma powers differential expression analyses for RNA-sequencing and microarray studies. *Nucleic Acids Res.* **43**, e47 (2015).

[PubMed](#) [PubMed Central](#) [Google Scholar](#)

49. 49.

R Development Core Team. R: A Language and Environment for Statistical Computing (R Foundation for Statistical Computing, 2010).

50. 50.

Perez-Riverol, Y. et al. The PRIDE database and related tools and resources in 2019: improving support for quantification data. *Nucleic*

Acids Res. **47**, D442–D450 (2019).

[CAS](#) [PubMed](#) [PubMed Central](#) [Google Scholar](#)

51. 51.

Wong, J. M. et al. Benzoyl chloride derivatization with liquid chromatography-mass spectrometry for targeted metabolomics of neurochemicals in biological samples. *J. Chromatogr. A* **1446**, 78–90 (2016).

[CAS](#) [PubMed](#) [PubMed Central](#) [Google Scholar](#)

52. 52.

Schwaiger, M. et al. Anion-exchange chromatography coupled to high-resolution mass spectrometry: a powerful tool for merging targeted and non-targeted metabolomics. *Anal. Chem.* **89**, 7667–7674 (2017).

[CAS](#) [PubMed](#) [Google Scholar](#)

[Download references](#)

Acknowledgements

This work was supported by the Max Planck Society, the Swedish Research Council (2015-00418 to N.-G.L., 2013-3621 to M.F., 2012-2583 to C.M.G.), Swedish Cancer Foundation (to M.F., C.M.G. and N.-G.L.), the Knut and Alice Wallenberg foundation (to M.F., C.M.G. and N.-G.L.), the Deutsche Forschungsgemeinschaft (SFB1218/A06 to N.-G.L.), European Research Council (Advanced Grant 2016-741366 to N.-G.L.) and grants from the Swedish state under the agreement between the Swedish government and the county councils, the ALF agreement to M.F. (ALFGBG-727491), C.M.G. (ALFGBG-728151) and N.-G.L. (SLL2018.0471). P.C. was supported by the Deutsche Forschungsgemeinschaft (SFB860, SPP1935), the European Research Council (advanced investigator grant TRANSREGULON, grant agreement no. 693023), the Volkswagen Foundation and Germany's Excellence

Strategy (EXC 2067/1- 390729940). H.S.H. was supported by the Deutsche Forschungsgemeinschaft (FOR2848). We thank N. Hochhard and S. Miethe for technical assistance; M. del Pilar Miranda for assistance; T. Colby, A. Taha, Y. Hinze, S. Perin and C. Edlich-Muth for support; I. Ivanov at Oncolead for providing cell panel data; C. Dienemann for assistance with cryo-EM data collection and processing; and Y. Chen for providing purified RNA polymerase II.

Author information

Author notes

1. These authors contributed equally: Nina A. Bonekamp, Bradley Peter

Affiliations

1. Department of Mitochondrial Biology, Max Planck Institute for Biology of Ageing, Cologne, Germany

Nina A. Bonekamp & Nils-Göran Larsson

2. Department of Medical Biochemistry and Cell Biology, University of Gothenburg, Gothenburg, Sweden

Bradley Peter, Maria Falkenberg & Claes M. Gustafsson

3. Department of Molecular Biology, Max Planck Institute for Biophysical Chemistry, Göttingen, Germany

Hauke S. Hillen & Patrick Cramer

4. Department of Medical Biochemistry and Biophysics, Karolinska Institutet, Stockholm, Sweden

Andrea Felser & Nils-Göran Larsson

5. Lead Discovery Center, Dortmund, Germany

Tim Bergbrede, Axel Choidas, Anke Unger, Raffaella Di Lucrezia, Uwe Koch, Sascha Menninger, Joanna Boros, Peter Habenberger, Peter Nussbaumer & Bert Klebl

6. Metabolic and Genetic Regulation of Ageing, Max Planck Institute for Biology of Ageing, Cologne, Germany

Moritz Horn & Martin S. Denzel

7. Acus Laboratories, Cologne, Germany

Moritz Horn

8. JLP Health, Vienna, Austria

Moritz Horn

9. Proteomics Core Facility, Max Planck Institute for Biology of Ageing, Cologne, Germany

Ilian Atanassov & Xinping Li

10. Metabolomics Core Facility, Max Planck Institute for Biology of Ageing, Cologne, Germany

Patrick Giavalisco

11. Max Planck Institute for Biology of Ageing–Karolinska Institutet Laboratory, Karolinska Institutet, Stockholm, Sweden

Nils-Göran Larsson

Authors

1. Nina A. Bonekamp
[View author publications](#)

You can also search for this author in [PubMed](#) [Google Scholar](#)

2. Bradley Peter

[View author publications](#)

You can also search for this author in [PubMed](#) [Google Scholar](#)

3. Hauke S. Hillen

[View author publications](#)

You can also search for this author in [PubMed](#) [Google Scholar](#)

4. Andrea Felser

[View author publications](#)

You can also search for this author in [PubMed](#) [Google Scholar](#)

5. Tim Bergbrede

[View author publications](#)

You can also search for this author in [PubMed](#) [Google Scholar](#)

6. Axel Choidas

[View author publications](#)

You can also search for this author in [PubMed](#) [Google Scholar](#)

7. Moritz Horn

[View author publications](#)

You can also search for this author in [PubMed](#) [Google Scholar](#)

8. Anke Unger

[View author publications](#)

You can also search for this author in [PubMed](#) [Google Scholar](#)

9. Raffaella Di Lucrezia

[View author publications](#)

You can also search for this author in [PubMed](#) [Google Scholar](#)

10. Ilian Atanassov

[View author publications](#)

You can also search for this author in [PubMed](#) [Google Scholar](#)

11. Xinpingle Li

[View author publications](#)

You can also search for this author in [PubMed](#) [Google Scholar](#)

12. Uwe Koch

[View author publications](#)

You can also search for this author in [PubMed](#) [Google Scholar](#)

13. Sascha Menninger

[View author publications](#)

You can also search for this author in [PubMed](#) [Google Scholar](#)

14. Joanna Boros

[View author publications](#)

You can also search for this author in [PubMed](#) [Google Scholar](#)

15. Peter Habenberger

[View author publications](#)

You can also search for this author in [PubMed](#) [Google Scholar](#)

16. Patrick Giavalisco

[View author publications](#)

You can also search for this author in [PubMed](#) [Google Scholar](#)

17. Patrick Cramer

[View author publications](#)

You can also search for this author in [PubMed](#) [Google Scholar](#)

18. Martin S. Denzel

[View author publications](#)

You can also search for this author in [PubMed](#) [Google Scholar](#)

19. Peter Nussbaumer

[View author publications](#)

You can also search for this author in [PubMed](#) [Google Scholar](#)

20. Bert Klebl

[View author publications](#)

You can also search for this author in [PubMed](#) [Google Scholar](#)

21. Maria Falkenberg

[View author publications](#)

You can also search for this author in [PubMed](#) [Google Scholar](#)

22. Claes M. Gustafsson

[View author publications](#)

You can also search for this author in [PubMed](#) [Google Scholar](#)

23. Nils-Göran Larsson

[View author publications](#)

You can also search for this author in [PubMed](#) [Google Scholar](#)

Contributions

M.F., C.M.G. and N.-G.L. conceptualized the original IMT idea. M.F., C.M.G., N.-G.L., B.K., N.A.B. and B.P. conceptualized research goals and experiments. N.A.B. and B.P. planned, performed and analysed the majority of the experiments. N.A.B. conducted and analysed qPCR and western blotting experiments in tissue culture (IMT1, IMT1B and con IMT) and xenografts, performed and analysed siRNA transfection experiments, cell

proliferation assays, ROS measurement, metabolomics, quantitative proteomics and in organello translation assays. B.P. performed and analysed differential scanning fluorimetry, microscale thermophoresis analysis and in vitro transcription assays (IMT1, IMT1B and con IMT) and expressed mutant POLRMT constructs. H.S.H. designed and carried out cryo-EM experiments and RNA Pol II primer extension assays. A.F. planned, performed and analysed qPCR, western blotting and respiration measurements using IMT1. T.B. designed the HTRF-based POLRMT detection method and analysed experiments in the course of IMT development. A.C. and P.H. planned, performed and analysed cell proliferation assays. M.H. planned, performed and analysed the forward genetic screens and generated A2780 mutant cell lines. A.U. designed and analysed toxicology, pharmacology and efficacy data. R.L. designed IMT compounds and synthesis routes, analysed data and devised strategies to elaborate the structure–activity relationship of inhibitors. I.A. and X.L. performed, analysed and interpreted quantitative proteomics data. P.G. performed, analysed and interpreted metabolomics data. U.K. carried out structural modelling of human POLRMT, docking of compounds and aided in cluster analysis of inhibitors. S.M. and J.B. designed and carried out qPCR and western blot experiments in the course of IMT development. M.S.D. planned and interpreted the forward genetic screens. P.N. aided in compound and synthesis design. P.C. designed and supervised cryo-EM experiments and RNA Pol II primer extension assays. M.F. planned, performed and analysed in vitro assays on RPO41, T7 RNA Pol, *E. coli* RNA Pol, RevertAid reverse transcriptase and POLG. N.A.B., B.P., C.M.G. and N.-G.L. wrote the manuscript, with input from all authors.

Corresponding authors

Correspondence to [Claes M. Gustafsson](#) or [Nils-Göran Larsson](#).

Ethics declarations

Competing interests

The IMT compound intellectual property is published as WO 2019/057821 and has been licensed by the Max Planck Society and the Lead Discovery Center GmbH.

Additional information

Peer review information *Nature* thanks Navdeep Chandel, Angela Koehler and the other, anonymous, reviewer(s) for their contribution to the peer review of this work. Peer reviewer reports are available.

Publisher's note Springer Nature remains neutral with regard to jurisdictional claims in published maps and institutional affiliations.

Extended data figures and tables

[Extended Data Fig. 1 IMT1 affects POLRMT stability and DNA binding.](#)

a, Overview of the high-throughput screening procedure for IMTs. **b**, Chemical structure of IMT1 (LDC195943). **c**, Differential scanning fluorimetry performed in the presence IMT1. The shift in melting temperature (ΔT_m) is plotted against the IMT1 concentration ($n = 2$ independent experiments). **d**, Template used in the single ribonucleotide incorporation and MST assays. NT2, non-template strand; TS2, template strand; R14, 14-mer RNA. **e**, Representative gels used for the determination of Michaelis–Menten kinetics in Fig. [1c](#). The P32-labelled 14-mer scaffold and the extended 15-mer product are indicated. A representative image of $n = 3$ independent experiments is shown. **f**, Residuals of the fits to the steady-state POLRMT kinetics data. **g**, Single nucleotide incorporation at varying substrate concentrations in the presence of 0–10 μM IMT1 (mean values of $n = 2$ independent experiments). **h**, In vitro promoter-dependent transcription on linear LSP and supercoiled circular LSP templates in the presence of 0–10 μM IMT1B. A representative image of $n = 2$ independent experiments is shown. Quantification is shown in Fig. [1d](#). **i**, A concentration-dependent decrease in binding affinity (K_d) was observed between POLRMT and a RNA–DNA scaffold at increasing levels of

IMT1B (mean \pm s.d., $n = 3$ independent experiments). **j**, Raw MST traces. [Source data](#)

[Extended Data Fig. 2 IMT1 affects mitochondrial gene expression.](#)

a, Mitochondrial transcript levels of ND1 after 6 h and 4 d of IMT1 treatment (mean \pm s.e.m., $n = 3$ –4 biological replicates, two-way ANOVA, Sidak's multiple comparisons test, DMSO–IMT1). **b**, mtDNA levels after IMT1 treatment (mean \pm s.e.m., $n = 3$ (144 h, 192 h), 4 (4 h, 6 h, 96 h), 6 (24 h, 48 h, 72 h) or 8 (DMSO) biological replicates). **c**, Immunoblot analysis of OXPHOS protein levels after IMT1 treatment (30 μ g per lane). A representative image of $n = 3$ independent experiments is shown. **d**, Quantitative proteomics of IMT1 treatment over time ($n = 5$ biological replicates). Within each time point, IMT-treated samples were compared to control samples (DMSO). Changes in the protein levels of OXPHOS complexes, mitoribosomal subunits and cytosolic ribosomes are plotted as log₂-transformed change in abundance relative to control over time. The exact values for median, upper and lower box hinge and upper and lower whiskers are shown in Supplementary Table 6 (compound IMT1). **e**, Intact cell respiration in HeLa cells after IMT1 exposure. Basal respiration, leak respiration and maximum respiration was determined (mean \pm s.e.m.; $n = 4$ independent measurements, two-way ANOVA, Sidak's multiple comparisons test, respective DMSO control–IMT1). **f**, Comparison of ND1 transcript levels after IMT1 (Extended Data Fig. 2a) and IMT1B (Fig. 1f) treatment in HeLa and A2780 cells. Dashed lines indicate ND1 transcript levels in DMSO-treated controls. [Source data](#)

[Extended Data Fig. 3 IMTs are highly specific.](#)

a–c, Single ribonucleotide incorporation assay using the template displayed in Extended Data Fig. 1d. IMT1B inhibits POLRMT, but does not affect RPO41 (**a**), T7 RNA polymerase (**b**) or *E. coli* RNA polymerase (**c**). The first lane in each panel is template only, without added enzyme. Representative images from $n = 3$ independent experiments are shown. **d**, IMT1B does not inhibit cDNA synthesis by RevertAid reverse

transcriptase. Reverse transcriptase was omitted in the second lane. A representative image from $n = 3$ independent experiments is shown. **e**, Primer extension assay of POLRMT and RNA polymerase II performed in the presence of increasing concentrations of IMT1B. A representative image from $n = 3$ independent experiments is shown. **f**, IMT treatment does not affect the expression of nuclear RNA polymerase targets. HeLa and A2780 cells were treated with either DMSO or IMT1, IMT1B and a commercially available IMT (con IMT) used as a control. mRNA levels of polymerase targets (RNA Pol I: 18S, 28S; RNA Pol II: POLRMT, β -actin; RNA Pol III: 5S; POLRMT: ND1, CYTB, COX1) are given as mean \pm s.e.m. ($n = 4$ (con IMT) or 5 (IMT1, IMT1B) biological replicates, two-way ANOVA, Sidak's multiple comparisons test, DMSO–respective IMT treatment). **g**, IMT1B does not inhibit POL γ primer elongation. The input template for POL γ is 3,800-nt single-stranded DNA that becomes a 3,800-bp nicked circular template product when synthesized. A representative image from $n = 3$ independent experiments is shown. First lane, ddCTP control. **h**, In organello translation of freshly isolated mitochondria in the presence or absence of IMT1B. A representative image from $n = 2$ biological replicates is shown. **i**, Chemical structure of con IMT (SC-6238532), a structurally related analogue of IMTs. **j**, Differential scanning fluorimetry performed in the presence or absence of con IMT ($n = 2$ independent experiments). **k**, In vitro promoter-dependent transcription on linear LSP and supercoiled circular LSP templates was performed in the presence of 0–10 μ M con IMT. A representative image from $n = 2$ independent experiments is shown. R/O, run-off transcript. **l**, Quantification of **k**. Mean values of $n = 2$ independent experiments are shown. **m**, Mitochondrial transcript levels of ND1 and CYTB determined after treatment of HeLa cells with different concentrations of con IMT for 6 h (mean \pm s.e.m., $n = 3, 4$ (0.1 μ M) or 5 (DMSO, 10 μ M, 5 μ M) biological replicates). **n**, mtDNA levels in HeLa cells treated with con IMT (mean \pm s.e.m., $n = 3, 4$ (72 h) or 5 (DMSO) biological replicates). **o**, Immunoblot analysis of OXPHOS protein levels in HeLa cells treated with Con IMT for 4 d (20 μ g per lane). A representative image from $n = 2$ independent experiments is shown. **p**, Quantitative proteomics of con IMT treatment over time ($n = 5$ biological replicates). Within each time point, treated samples were compared to control samples (DMSO). Changes in the protein levels of OXPHOS complexes, mitoribosomal subunits and

cytosolic ribosomes are plotted as \log_2 -transformed change in abundance relative to control over time. The exact values for median, upper and lower box hinge and upper and lower whiskers are shown in Supplementary Table 6 (compound con IMT). [Source data](#)

Extended Data Fig. 4 Identification of the IMT-binding pocket.

a, Schematic of the experimental workflow of the IMT-resistance screen using chemical mutagenesis. **b**, In vitro promoter-dependent transcription using the IMT-resistant L816Q and A821V POLRMT mutants in the presence of 0–10 μ M IMT1B. A representative image from $n = 2$ independent experiments is shown. **c**, Quantification of **b**. Mean values of $n = 2$ independent experiments are shown. **d**, Inhibition of transcription initiation on IMT-resistant POLRMT mutants. In vitro transcription initiation was performed on linear LSP templates using wild-type and IMT-resistant POLRMT protein in the presence or absence of IMT1. A representative image from $n = 2$ independent experiments is shown. **e**, Increasing amounts of POLRMT do not rescue wild-type activity in the presence of IMT1B. In vitro promoter-dependent transcription on supercoiled circular LSP templates was performed in the presence of 10 μ M IMT1B using increasing concentrations of wild-type or mutant POLRMT (L816Q or A821V). A representative image from $n = 2$ independent experiments is shown. **f**, Quantification of **e**. Mean values of $n = 2$ independent experiments are shown. **g**, Sanger sequencing of CRISPR–Cas9-engineered POLRMT mutations introduced into A2780 cells. **h**, Mitochondrial gene expression in POLRMT mutant cell lines (L796Q and L816Q, # denotes two independent clones). Data are expressed as fold of untreated wild-type control (DMSO) and given as mean \pm s.e.m. ($n = 7$ –9 biological replicates; two-way ANOVA, Sidak’s multiple comparisons test, DMSO–IMT1). [Source data](#)

Extended Data Fig. 5 Structure determination of POLRMT with IMT1B by cryo-EM.

a, Representative micrograph from 40° tilted data collection ($n = 2,077$ micrographs). **b**, Most populated classes from 2D classification using

cryoSPARC 6. **c**, Cryo-EM processing workflow. **d**, Binding pocket of IMT1B between the POLRMT thumb and palm domains. POLRMT is shown as a translucent cartoon, and residues within 4 Å of IMT1B are shown as sticks. IMT1B was modelled on the basis of the cryo-EM density and chemical considerations (Methods). **e**, Fourier shell correlation plot. **f**, Angular distribution of particle views. **g**, Local resolution estimation calculated using RELION 3. The position of IMT1B is indicated with a red dashed box. **h**, Cryo-EM density around IMT1B. IMT1B is shown as sticks, and the cryo-EM density is shown as blue mesh with a carve of 2 Å.

Extended Data Fig. 6 Loss of POLRMT leads to a decrease in cell viability.

a, POLRMT silencing in HeLa cells affects cell viability. Cell viability was assessed using a ViCell Cell counter. Mean of $n = 2$ independent experiments is shown. NT, non-transfected. **b**, Immunoblot analysis of POLRMT levels 4 d after transfection (20 µg per lane). A representative image of $n = 2$ independent experiments is shown. **c**, Analysis of cancer cell proliferation using an SRB proliferation assay indicates that IMT1 treatment specifically inhibits cancer cell proliferation in a variety of cancer cell lines, but not in control cells. IC₅₀ values of IMT1 on a panel of 89 cancer cell lines (grey) and primary cells (black, IMR90 lung fibroblasts and human PBMCs) are plotted. **d**, Cell growth in HeLa cells (IC₅₀ = 0.838 µM), lung carcinoma cells (A594) (IC₅₀ = 0.643 µM) and IMR90 lung fibroblast cells (IC₅₀ > 30 µM) after IMT1 treatment was assessed using an SRB assay. **e**, Cytotoxicity against human (h)PBMCs (two different donors, left) or primary human hepatocytes (right) was assessed using the CellTiter-Glo assay at the indicated inhibitor concentrations ($n = 2$ independent experiments). [Source data](#)

Extended Data Fig. 7 Basis of IMT-induced cellular toxicity.

a, ROS levels after IMT1 treatment in A2780 cells were determined using the Cellular ROS assay kit Orange (mean ± s.e.m., $n = 5$ biological replicates). **b**, Immunoblot analysis of the apoptosis marker cleaved PARP. A2780 cells were treated with IMT1 for the indicated time points and

collected by trypsin treatment (attached). For later time points, cell culture supernatants were collected and detached or dead cells were isolated by centrifugation (supernatant) (20 µg per lane). A representative image of $n = 3$ independent experiments is shown. **c**, Heat maps illustrating the fold-change in protein levels in apoptosis (top, left), one-carbon pathway (bottom, left), degradation and stress response (right). **d**, Overview of changes in central carbon metabolism after IMT1 treatment. Changes in metabolite levels are given as fold of control at the indicated time points. Dark blue, minimum (0); dark red, maximum (2). **e**, Immunoblot analysis of the proliferation marker PCNA. A2780 cells were treated with IMT1B (+) or DMSO (−) for the indicated time points (20 µg per lane). A representative image of $n = 2$ independent experiments is shown. [Source data](#)

Extended Data Fig. 8 IMT treatment in vivo.

a, b, Pharmacokinetic (PK) parameters of IMT1B used in the in vivo studies: intravenous dosing (**a**) or oral dosing (**b**) ($n = 3$ biological replicates). $t_{1/2}$, elimination half-life; T_{\max} , time to reach peak plasma concentration following drug administration (that is, C_{\max}); C_0 , concentration extrapolated to the origin; C_{\max} , peak plasma drug concentration; $AUC_{0-\infty}$, area under the plasma concentration time curve from time zero to infinity; V_z , volume of distribution; CL, total plasma clearance; F , bioavailability. **c**, Mouse POLRMT is stabilized by IMT1B. Differential scanning fluorimetry performed in the presence or absence of IMT1B using human (left) or mouse (right) POLRMT ($n = 2$ independent experiments). The determined melting temperatures are given. **d**, IMT1B inhibits promotor-dependent transcription using mouse POLRMT in a concentration-dependent manner in vitro. In vitro promoter-dependent transcription on linear LSP and supercoiled circular LSP templates was performed in the presence of 0–10 µM IMT1B. A representative image of $n = 2$ independent experiments is shown. **e**, A2780 xenograft tumour growth in vivo (study 2). Mice were treated once per day with either vehicle (veh) or IMT1B (100 mg kg^{−1}). Mean ± s.e.m.; $n = 8$ biological replicates, Mann–Whitney *U* test, exact significance, one-tailed, vehicle–IMT1B). **f**, IMT1B treatment inhibits DLD-1 xenograft tumour growth in vivo. Mice

were treated once per day with either vehicle or IMT1B (100 mg kg^{-1}). Mean \pm s.e.m., $n = 8$ biological replicates, Mann–Whitney U test, exact significance, one-tailed, vehicle–IMT1B. **g**, Mean body weight of IMT1B-treated mice in comparison to vehicle-treated controls in the A2780 xenografts. Mean \pm s.e.m., $n = 8$ biological replicates. **h**, IMT1B treatment induces no acute liver or kidney toxicity after four weeks of treatment. NMRI mice were treated with either vehicle or IMT1B for four weeks orally once per day. Blood was taken after fasting at the first day (baseline) and last day (4 weeks IMT) of treatment from the tail vein. Blood parameters analysed include alanine transaminase levels (ALT, in U l^{-1}) and aspartate aminotransferase (AST, in U l^{-1}) to determine liver toxicity as well as creatinine (CREA, in mg dl^{-1}) to determine kidney toxicity. Data are presented as mean \pm s.e.m., $n = 4$ biological replicates. **i**, IMT1B treatment does not affect blood count after IMT treatment. Female NMRI mice were treated with either vehicle or IMT1B for four weeks orally once per day. Blood was taken on the last day of the experiments and analysed for the abovementioned parameters. Data are presented as mean \pm s.e.m., $n = 4$ biological replicates. MCHC, mean corpuscular haemoglobin concentration; MCH, mean corpuscular haemoglobin; MCV, mean corpuscular volume. **j**, Mitochondrial DNA levels in tumour, liver and heart (mean \pm s.e.m., $n = 8$ biological replicates). **k**, Immunoblot analysis of phosphorylated AMPK and ribosomal S6 protein levels in tumour tissue lysates. For determination of total AMPK levels, samples were run on a separate gel and processed in parallel (20 μg per lane). A representative image of $n = 3$ independent experiments is shown. [Source data](#)

Supplementary information

[Supplementary Information](#)

This file contains Supplementary Figure 1: Uncropped gels of Figures 1, 3–4 and Extended Data Figures 1–4, 6–8, Supplementary Methods: Detail description of the synthesis procedure and quality control for IMTs and Supplementary Tables 1–6.

[Reporting Summary](#)

Source data

[Source Data Fig. 1](#)

[Source Data Fig. 2](#)

[Source Data Fig. 3](#)

[Source Data Fig. 4](#)

[Source Data Extended Data Fig. 1](#)

[Source Data Extended Data Fig. 2](#)

[Source Data Extended Data Fig. 3](#)

[Source Data Extended Data Fig. 4](#)

[Source Data Extended Data Fig. 6](#)

[Source Data Extended Data Fig. 7](#)

[Source Data Extended Data Fig. 8](#)

Rights and permissions

[Reprints and Permissions](#)

About this article



Check for
updates

Cite this article

Bonekamp, N.A., Peter, B., Hillen, H.S. *et al.* Small-molecule inhibitors of human mitochondrial DNA transcription. *Nature* **588**, 712–716 (2020). <https://doi.org/10.1038/s41586-020-03048-z>

[Download citation](#)

- Received: 30 May 2019
- Accepted: 22 October 2020
- Published: 16 December 2020
- Issue Date: 24 December 2020
- DOI: <https://doi.org/10.1038/s41586-020-03048-z>

Comments

By submitting a comment you agree to abide by our [Terms](#) and [Community Guidelines](#). If you find something abusive or that does not comply with our terms or guidelines please flag it as inappropriate.

[Access through your institution](#)

[Change institution](#)

[Buy or subscribe](#)

Associated Content

Collection

[Cancer at Nature Research](#)

| [Section menu](#) | [Main menu](#) |

The effect of interventions on COVID-19

[Download PDF](#)

- [Matters Arising](#)
- [Published: 23 December 2020](#)

The effect of interventions on COVID-19

- [Kristian Soltesz](#) [ORCID: orcid.org/0000-0001-6378-7646¹](#),
- [Fredrik Gustafsson²](#),
- [Toomas Timpka^{3,4}](#),
- [Joakim Jaldén⁵](#),
- [Carl Jidling⁶](#),
- [Albin Heimerson¹](#),
- [Thomas B. Schön](#) [ORCID: orcid.org/0000-0001-5183-234X⁶](#),
- [Armin Spreco](#) [ORCID: orcid.org/0000-0003-0985-8209^{3,4}](#),
- [Joakim Ekberg^{3,4}](#),
- [Örjan Dahlström⁷](#),
- [Fredrik Bagge Carlson⁸](#),
- [Anna Jöud^{9,10}](#) &
- [Bo Bernhardsson¹](#)

[Nature](#) volume 588, pages E26–E28(2020) [Cite this article](#)

- 2002 Accesses
- 16 Altmetric
- [Metrics details](#)

Subjects

- [Computational science](#)
- [Epidemiology](#)
- [SARS-CoV-2](#)

[Matters Arising](#) to this article was published on 23 December 2020

The [Original Article](#) was published on 08 June 2020

[Download PDF](#)

arising from S. Flaxman et al. *Nature* <https://doi.org/10.1038/s41586-020-2405-7> (2020)

Flaxman et al.¹ took on the challenge of estimating the effectiveness of five categories of non-pharmaceutical intervention (NPI)—social distancing encouraged, self isolation, school closures, public events banned, and complete lockdown—on the spread of severe acute respiratory syndrome coronavirus 2 (SARS-CoV-2). On the basis of mortality data collected between January and early May 2020, they concluded that only one of these, the lockdown, had been effective in 10 out of the 11 European countries that were studied. However, here we use simulations with the original model code to suggest that the conclusions of Flaxman et al. with regard to the effectiveness of individual NPIs are not justified. Although the NPIs that were considered have indisputably contributed to reducing the spread of the virus, our analysis indicates that the individual effectiveness of these NPIs cannot be reliably quantified.

Flaxman et al.¹ presented a method to estimate the effects of NPIs on the time-varying reproduction number (R_t) of SARS-CoV-2 infection. Data from 11 European countries were pooled on the basis of the assumption that the effects of NPIs on R_t are not country-specific: the factor of relative change in R_t resulting from a particular NPI was assumed to be independent of the country in which the NPI was implemented.

Some country-specific flexibility was, however, provided through the basic reproduction number (R_0) being country-specific. More notably, additional flexibility was introduced by ascribing a country-specific effect to the NPI that was introduced last in each country. This replaced the parameterization in a preprint version (Imperial College Report 13)², in which a country-specific effect was instead assigned to the lockdown NPI.

Our criticism concerns the final published version of the model^{1,3}. Previous iterations of the model are not explicitly considered, but we reference them for two purposes: (1) to demonstrate the sensitivity of the final published model to subtle and realistic alterations in parameter values; (2) to illustrate how the modelling choices appear to lack motivation other than to introduce flexibility, which masks sensitivity issues pertaining to the fundamental structure of the model. As made evident below, we believe the core problem is that the death data are not descriptive enough to support

the conclusions of Flaxman et al., which were based on simulation results obtained using an over-flexible model.

Of the 11 modelled countries, Sweden is worthy of particular attention, given that it was the only country in which no lockdown took place. As we have previously shown⁴, the estimated effects of NPIs change markedly when the model is not allowed to give the Swedish data the special treatment that the country-specific last NPI parameter enables. The country-specific last NPI parameter is needed to explain the decrease of R_t supported by the Swedish death data, and to provide a good model fit despite the absence of a lockdown in Sweden.

Figure 1 shows the outcome for Sweden when executing the model^{3,5} either with (Fig. 1a) or without (Fig. 1b) the last NPI adjustment in place. With the last NPI adjustment in place, the public events ban results in a mean reduction of R_t of 71% (95% credible interval: 59–81%) in Sweden, which contrasts with the negligible effect of the public events ban in the other 10 countries (less than 2% mean reduction of R_t and less than 15% with 95% credibility). Notably, the estimated effectiveness of the public events ban in Sweden is comparable to that of lockdown in the 10 countries in which one was implemented. As lockdown was the last intervention in most countries, its estimated effect comprises a pooled effect (82% mean reduction of R_t) and a separate country-specific ‘last NPI’ effect (mean change in R_t of between –24% and 18% for the countries considered).

Fig. 1: Estimated effectiveness of the public events ban in Sweden.



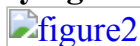
Top, posterior credible intervals for the reproduction number R_t in Sweden. Bottom, effectiveness of the pooled interventions in the 11 modelled European countries. **a**, Reproduced results from Flaxman et al.¹, using the original model code^{3,5}, including a country-specific effectiveness parameter for the last NPI to be implemented in each country. This corresponds to a country-specific effectiveness for the public events ban in Sweden and for lockdown in the other 10 countries. **b**, Results using the same code, but with the ‘last NPI’ parameters replaced with country-specific parameters for the lockdown NPI, as in the preceding report². This change does not affect the 10 countries for which lockdown was the last NPI, but for Sweden it removes the flexibility of a last NPI parameter, which is needed to explain the R_t value supported by the Swedish death data.

[Full size image](#)

The result above—that is, the public events ban and the lockdown being mutually effective in Sweden and 10 other European countries—was not addressed by Flaxman et al, which is noteworthy as this result undermines the conclusion of lockdown being especially effective. Furthermore, without the introduction of the last intervention parameter after the publication of the preprint², the inconsistency would have been readily visible in reported plots (Fig. 1b).

It seems unlikely to be a result of circumstance that lockdown was implemented in the 10 countries in which it had a large effect on R_t , and omitted in the single country in which the public events ban instead had a similar effect (sufficient to drive R_t below 1). An alternative hypothesis is that the infection-to-death distribution used by the model, combined with the death data that were available by early May, makes the model ascribe almost all of the reduction in R_t to the last intervention that was implemented in each country. This hypothesis is supported by executing the model code^{3,5} with different interventions being defined as having occurred last in the country in which no lockdown occurred (Sweden), as shown in Fig. 2.

Fig. 2: The effects of interventions on virus spread in Sweden, with slightly varying definitions of the interventions.



a, School closure defined to have taken place on 18 March 2020; public events ban defined to have taken place on 29 March 2020. **b**, Same as **a**, but with the public events ban moved back to 12 March 2020. **c**, Same as **b**, but with school closure defined not to have taken place. As expected, the visual appearance of the plots is similar, with the last intervention contributing most to the reduction of virus spread. This is problematic, as the last intervention differs between **a**, **b** and **c**, with each relying on equally motivated NPI implementation dates that were introduced by Flaxman et al.^{1,2} in different versions of the model code³. The conclusion is that subtle changes in the definitions of NPIs result in a great deal of variation in the estimated effectiveness of the NPI categories considered.

[Full size image](#)

Exchanging the last intervention for a different one is not merely interesting from a theoretical perspective. For example, it is hard to judge whether transitioning to online teaching at high school and university levels, while keeping elementary schools and preschools open, constitutes a school closure or not. Similarly, the crowd-size limit associated with the public events ban NPI remains a parameter to be decided by the modeller. Early versions of the model defined the public events ban to have taken place in Sweden on 12 March 2020, when gatherings exceeding 500 persons were prohibited. This was later changed to 29 March 2020, when gatherings exceeding 50 persons were prohibited. These subtle alterations of the definitions alter which NPI, of school closure, public events ban, or social distancing encouraged, was the last to be implemented in Sweden. In each case, the model uses the last intervention to explain the majority of the drop of R_t to below 1, which is needed to stay consistent with the decrease in reported deaths.

As mentioned above, our analyses were conducted using the original model implementation^{3,5} referenced from the final published paper¹, and we have considered the definitions of NPIs reported in the preceding versions of the model^{1,2,3} solely to highlight how small and plausible perturbations of these definitions can result in a lack of practical identifiability, in the statistical sense. Identifiability issues have to some extent been acknowledged by the authors; Flaxman et al. state that “The close spacing of interventions in time [...] means that the individual effects of the other interventions are not identifiable”¹. However, this is overshadowed by the subsequent presentation of credible intervals for the effects of the different NPIs, and the claim that “Lockdown has an identifiable large effect on transmission (81% (75–87%) reduction)”¹. We believe that the basis of this claim is unclear. As seen in the supplementary videos of the *Nature* article¹, the credible intervals narrow as more data become available, further hiding the identifiability problems of the underlying model and potentially giving the results a false sense of reliability.

Our point here is not to argue whether or not a school closure took place in Sweden, or what the most appropriate crowd-size limit is. Instead, our findings highlight that the model presented by Flaxman et al. is very sensitive to reasonable, minor changes in the input data. As indicated by our simulation examples, and further supported by our previous analyses⁴, there is a fundamental problem with the identifiability of the effectiveness of individual NPIs, including the lockdown. This problem is caused by the close temporal spacing between the implementation of these NPIs throughout Europe. In particular, we note in relation to the lockdown NPI that an estimated value that is considerably larger than zero should not be confused with statistical identifiability of the corresponding parameter.

Although we fully support the ambition of Flaxman et al.¹—to estimate the effectiveness of different NPIs from the available data—we find the underlying modelling approach problematic. Flexible parameterization leads to issues with identifiability, which are masked by model assumptions. In particular, we find it questionable to designate a country-specific effectiveness parameter to the last NPI that was introduced in each country. Besides the problems illustrated in Fig. 2, with large variations in the estimated effectiveness of NPIs, this prohibits prospective use of the model, as it is unknown at any given time whether the latest NPI will also be the last to be implemented in a particular country.

We conclude that the model^{1,3} is in effect too flexible, and therefore allows the data to be explained in various ways. This has led the authors to go beyond the data in reporting that particular interventions are especially effective. This kind of error—mistaking assumptions for conclusions—is easy to make, and not especially easy to catch, in Bayesian analysis. As NPIs are revoked, and possibly reintroduced over an extended period of time, more data will become available and practical identifiability of the separate effects of NPIs may be obtained. Until then, we suggest that the model^{1,3}, and its conclusion that all NPIs apart from lockdown have been of low effectiveness, should be treated with caution with regard to policy-making decisions.

Reporting summary

Further information on research design is available in the [Nature Research Reporting Summary](#) linked to this paper.

Data availability

A fork of the original code and associated data, which was used to generate the figures presented here, is provided in a separate GitHub repository⁵. This fork is based on the GitHub repository commit 885466d of the original code³, in which the README file

states that it was “the exact code that was used [in the *Nature* article¹]”. We have, however, noticed discrepancies between the original code³ and the figures in the article¹. For example, the code that was used to generate figure 1 in Flaxman et al.¹ defines the self-isolation NPI as having been implemented as the last NPI in Spain on 17 March 2020, whereas the code in the commit defines this date as 14 March 2020.

References

1. 1.

Flaxman, S. et al. Estimating the effects of non-pharmaceutical interventions on COVID-19 in Europe. *Nature* **584**, 257–261 (2020).

[CAS Article](#) [Google Scholar](#)

2. 2.

Flaxman, S. et al. Report 13: Estimating the number of infections and the impact of non-pharmaceutical interventions on COVID-19 in 11 European countries. <https://doi.org/10.25561/77731> (Imperial College London, 2020).

3. 3.

Imperial College London. covid19model. Available at <https://github.com/ImperialCollegeLondon/covid19model> (2020).

4. 4.

Soltesz, K. et al. On the sensitivity of non-pharmaceutical intervention models for SARS-CoV-2 spread estimation. Preprint at <https://doi.org/10.1101/2020.06.10.20127324> (2020).

5. 5.

Heimerson, A. covid19model fork. Available at <https://github.com/albheim/covid19model> (2020).

[Download references](#)

Acknowledgements

We acknowledge Ericsson Research for hosting our model runs in their data centre. This work has been partially supported by the Wallenberg AI, Autonomous Systems and Software Program (WASP) funded by the Knut and Alice Wallenberg Foundation; the ELLIIT strategic research area on IT and mobile communications; the Swedish Research Council (grant reference number 2017-04989); the Swedish Foundation for Strategic Research (SSF) via the project ASSEMBLE (grant reference number RIT15-0012); and ALF Grants, Region Östergötland.

Author information

Affiliations

1. Department of Automatic Control, Lund University, Lund, Sweden

Kristian Soltesz, Albin Heimerson & Bo Bernhardsson

2. Department of Electrical Engineering, Linköping University, Linköping, Sweden

Fredrik Gustafsson

3. Department of Public Health, and Department of Health, Medicine and Caring Sciences, Linköping University, Linköping, Sweden

Toomas Timpka, Armin Spreco & Joakim Ekberg

4. Unit for Public Health and Statistics, Region Östergötland, Linköping, Sweden

Toomas Timpka, Armin Spreco & Joakim Ekberg

5. Division of Information Science and Engineering, KTH Royal Institute of Technology, Stockholm, Sweden

Joakim Jaldén

6. Department of Information Technology, Uppsala University, Uppsala, Sweden

Carl Jidling & Thomas B. Schön

7. Department of Behavioural Sciences and Learning, Linköping University, Linköping, Sweden

Örjan Dahlström

8. Acoustic Research Laboratory, National University of Singapore, Singapore, Singapore

Fredrik Bagge Carlson

9. Department of Laboratory Medicine, Lund University, Lund, Sweden

Anna Jöud

10. Department of Research and Development, Skåne University Hospital, Lund, Sweden

Anna Jöud

Authors

1. Kristian Soltesz

[View author publications](#)

You can also search for this author in [PubMed](#) [Google Scholar](#)

2. Fredrik Gustafsson

[View author publications](#)

You can also search for this author in [PubMed](#) [Google Scholar](#)

3. Toomas Timpka

[View author publications](#)

You can also search for this author in [PubMed](#) [Google Scholar](#)

4. Joakim Jaldén

[View author publications](#)

You can also search for this author in [PubMed](#) [Google Scholar](#)

5. Carl Jidling

[View author publications](#)

You can also search for this author in [PubMed](#) [Google Scholar](#)

6. Albin Heimerson

[View author publications](#)

You can also search for this author in [PubMed](#) [Google Scholar](#)

7. Thomas B. Schön

[View author publications](#)

You can also search for this author in [PubMed](#) [Google Scholar](#)

8. Armin Spreco

[View author publications](#)

You can also search for this author in [PubMed](#) [Google Scholar](#)

9. Joakim Ekberg

[View author publications](#)

You can also search for this author in [PubMed](#) [Google Scholar](#)

10. Örjan Dahlström

[View author publications](#)

You can also search for this author in [PubMed](#) [Google Scholar](#)

11. Fredrik Bagge Carlson

[View author publications](#)

You can also search for this author in [PubMed](#) [Google Scholar](#)

12. Anna Jöud

[View author publications](#)

You can also search for this author in [PubMed](#) [Google Scholar](#)

13. Bo Bernhardsson

[View author publications](#)

You can also search for this author in [PubMed](#) [Google Scholar](#)

Contributions

Study conceptualization: B.B., F.G., J.J. and K.S. Analysis and interpretation of model weaknesses: B.B., F.B.C., J.J. and K.S. Code preparation and execution: A.H. and C.J. Background literature review: B.B., A.J., A.S. and T.T. Manuscript writing and reviewing: B.B., O.D., J.E., J.J., A.J., T.B.S., K.S., A.S. and T.T.

Corresponding author

Correspondence to [Kristian Soltesz](#).

Ethics declarations

Competing interests

The authors declare no competing interests.

Additional information

Publisher's note Springer Nature remains neutral with regard to jurisdictional claims in published maps and institutional affiliations.

Supplementary information

[Reporting Summary](#)

Rights and permissions

[Reprints and Permissions](#)

About this article



Check for
updates

Cite this article

Soltesz, K., Gustafsson, F., Timpka, T. *et al.* The effect of interventions on COVID-19. *Nature* **588**, E26–E28 (2020). <https://doi.org/10.1038/s41586-020-3025-y>

[Download citation](#)

- Received: 15 June 2020
- Accepted: 13 November 2020
- Published: 23 December 2020

- Issue Date: 24 December 2020
- DOI: <https://doi.org/10.1038/s41586-020-3025-y>

Comments

By submitting a comment you agree to abide by our [Terms](#) and [Community Guidelines](#). If you find something abusive or that does not comply with our terms or guidelines please flag it as inappropriate.

[Download PDF](#)

This article was downloaded by **calibre** from <https://www.nature.com/articles/s41586-020-3025-y>

| [Section menu](#) | [Main menu](#) |

Reply to: The effect of interventions on COVID-19

[Download PDF](#)

- Matters Arising
- [Published: 23 December 2020](#)

Reply to: The effect of interventions on COVID-19

- [Seth Flaxman](#)¹ na1,
- [Swapnil Mishra](#)² na1,
- [James Scott](#)¹ na1,
- [Neil Ferguson](#)² na1,
- [Axel Gandy](#)¹ na1 &
- [Samir Bhatt](#) ORCID: orcid.org/0000-0002-0891-4611² na1

[Nature](#) volume 588, pagesE29–E32(2020) [Cite this article](#)

- 753 Accesses
- 10 Altmetric
- [Metrics details](#)

Subjects

- [SARS-CoV-2](#)
- [Statistical methods](#)
- [Viral infection](#)

The [Original Article](#) was published on 23 December 2020

[Download PDF](#)

replying to K. Soltesz et al. *Nature*<https://doi.org/10.1038/s41586-020-3025-y> (2020)

The accompanying Comment¹ concerns our original paper, Flaxman et al.², in which we introduced a Bayesian hierarchical model to estimate the transmission intensity (in terms of the time-varying reproduction number, R_t) of severe acute respiratory syndrome coronavirus 2 (SARS-CoV-2) from observed counts of coronavirus disease 2019 (COVID-19)-related deaths. We parameterized R_t in terms of a binary set of government-mandated non-pharmaceutical interventions (NPIs), with the motivation of examining how effective NPIs were at controlling the transmission of SARS-CoV-2. We concluded that the NPIs that were widely used across Europe successfully drove R_t below 1, thus controlling the epidemic. However, we were unable to disentangle the effect sizes of the NPIs we considered, except for concluding that lockdown had a stronger effect than the other NPIs.

We start by giving some background on the evolution of the paper. Our first preprint, released as Imperial College Report 13³, was based on data up to 28 March 2020 and used a simpler model in which the effect size of each intervention on transmission is the same across countries (here referred to as a full pool model; in our published paper² we use this model for the single-country analyses reported in supplementary discussion 8 of the paper). As more data became available (Flaxman et al.² uses data up to 4 May 2020), more heterogeneity between countries became evident and we therefore extended the full pool model.

This extended model, which is the one used in Flaxman et al.², includes a random effect, with the aim of capturing country-specific variation in the effectiveness of the last government-mandated intervention or interventions; for example, lockdown in Italy, lockdown and a ban on public events in the UK, and a ban on public events in Sweden (see Extended Data Fig. 1). Random effects are common components of statistical models to account for heterogeneity not explained by covariates^{4,5,6}.

The focus of Soltesz et al.¹ is the size of the random effect assigned by our model to the last intervention in Sweden. Specifically, a large random effect is needed to explain the Swedish data, and this could have been more explicitly stated in our original paper. Soltesz et al.¹ claim that the difference between effect sizes in a full pool model and in Flaxman et al.² points to our model having little practical statistical identifiability. On this basis, Soltesz et al.¹ question whether the effectiveness of lockdown can be resolved to the degree our paper stated.

The main goal of our paper was to examine multiple countries to see what worked in most places, not to explain the trajectory of the epidemic in each individual country. Although we feel that Soltesz et al.¹ raise an interesting point, we stand by our assessment that the effectiveness of NPIs can in principle be identified when looking at what worked in most countries, subject of course to the available data.

Here we present further analyses that support our finding reported in Flaxman et al.² that lockdown was an identifiable intervention with a major effect. We accept that additional covariates beyond the timing of mandatory measures are likely to be needed to provide a fully satisfactory explanation of the trajectory of the epidemic in Sweden, as that country relied on voluntary social distancing measures rather than government-mandated interventions.

Because our goal was to estimate which NPIs worked consistently in most countries, we argue that an analysis of the effectiveness of NPIs should be robust to leaving any one country out. In Extended Data Fig. 1 of this Reply we compare results from the full pool model (used by Soltesz et al.¹), the model used in Flaxman et al.², and a partial pool model, removing one country at a time from the input data. In the partial pool model^{4,6,7}, all NPIs have both a random effect component shared between all countries and a country-specific random effect (via a Gaussian shrinkage prior).

In the full pool model, results for effect sizes are dependent on whether Sweden is included, hence Sweden has a very high statistical influence⁸. As seen in Extended Data Fig. 1, when Sweden is left out of the full pool model, we recover the results from Flaxman et al.², but when Sweden is included the estimates change markedly. This happens because the full pool model attributes a large effect size to the ban on public events to explain the Swedish death data.

However, both the model we considered in Flaxman et al.² and the partial pool model discussed here show consistent effect sizes across all ‘held-out’ (that is, excluding a given country from fitting) countries. (For space, only the UK, Italy and Sweden are shown in Extended Data Fig. 1.) This explains our choice to move from a full pool model, which is the one used by Soltesz et al.¹, to the model used in Flaxman et al.².

The partial pool model is what we recommend (and are currently adopting) for such analyses in future. Partial pooling allows all interventions to have a shared effect and an effect specific to each country for each intervention. Thus, it stands somewhere between a full pool model and 11 separate models, with the data informing this location. These choices mean the partial pool model has no specific affinity towards a country or a specific intervention.

To further explore issues around identifiability at an individual country level versus across countries, in Fig. 1 we present the effects of NPIs for each country from separate country-specific models, a meta-analysis of these effects, and the estimates from our various joint models. In summary, we see that although the overall mean effect for lockdown is lower in the meta-analysis, it is still the only NPI with an identifiable effect size. The individual country fits provide insight into why this occurs; the only intervention that is consistently significant is lockdown (and the

banning of public events in Sweden, as discussed in the legend of Extended Data Fig. 1).

Fig. 1: Inferred intervention effect sizes.

 figure1



The x axis shows the relative reduction in transmission. Rows show model predictions for our published model (Flaxman et al.²), the model from Soltesz et al.¹ (full pool), a generalized version of our published model (partial pool) and fits to individual countries (reported in supplementary discussion 8 of our original paper²; the model is the same one considered by Soltesz et al.¹). We also include the mean effect size derived from a meta-analysis (mean across countries for each individual sample) of the individual country effects.

[Full size image](#)

Considering the single-country models, we see that the effectiveness of lockdown is not merely the result of a modelling choice on our part. In countries such as Italy, no

intervention is estimated to be significantly more effective than any other. The lack of identifiability is not a feature inherent to our model, but a limitation of the data available at the time, as we noted in our paper². In particular, although we noted the close spacing of interventions in time, in a few countries lockdowns and the banning of public events coincided exactly (for example, in the UK). The result is that in the separate country analyses and full pooling (Soltesz et al.¹), there is a strong posterior correlation between the effects of these two NPIs (Pearson correlation of -0.59 in separate country analyses; -0.67 in full pooling analysis): when one has a large effect, the other by necessity has a small effect.

It is crucial to note here that Soltesz et al.¹ are correct that the relative effect of different interventions cannot be disentangled for a single country treated in isolation. This probably reflects the limitation of using time series of deaths to infer transmission changes, given the high mean and variance of the distribution of the delay from infections to deaths. However, when looking across multiple countries, all aggregate models suggest that the lockdown intervention has an identifiable effect. This is true for all models considered, including the full pool model of Soltesz et al.¹, in which the posterior probability that lockdown is the most effective intervention is 76%, as compared with 96% in the meta-analysis and 100% in both partial pooling models. Therefore, by simultaneously analysing trends in multiple countries, our model has the ability to resolve an identifiable signal of the effect of lockdown.

To further reinforce this point, we also undertook a simulation study examining the extent to which the timing and ordering of the interventions used fundamentally limit the ability to infer effect sizes reliably.

We used our model to simulate synthetic epidemics for all 11 countries, keeping the original timing and ordering of interventions and the same initialization priors, but assigning hypothetical effect sizes to each intervention. We assigned small effect sizes (5% with a tight prior) to all but one NPI, giving the remaining one an effect size with a mean of 59%, also with a tight prior, across countries. In addition, to better reflect reality, we simulate another, country-varying NPI, at a random time, which we treat as unobserved in our model. This unknown and unobserved NPI has a diffuse prior bounded between 0% and 100%, with a mean of 27%, and it is included to assess whether an omitted variable (for example, representing spontaneous behaviour change in response to government messaging) could bias the effect-size estimates of our modelled NPIs. We keep the dates for NPIs the same as the ones in the real data to account for concerns raised about the possible effects of coincident timing on the identifiability of effect sizes.

Next, we fitted the Flaxman et al. model² to these simulated datasets (20 different simulations for each setting). As shown in Fig. 2, the estimates from the Flaxman et al.

fitted model² (without any information about the unobserved NPI) are in agreement with the NPI effect sizes that were used to generate the data. This analysis provides further evidence that the results we found were not merely artefacts of the modelling approach; if there is a strong signal in the data for a specific NPI, our model can recover it.

Fig. 2: Estimated effect sizes from simulated data.

 figure2

Top to bottom, three separate simulations for lockdown, school closure and self isolation, with a mean of 59% effect size (grey lines), were repeated 20 times each. In each panel, effect sizes from the Flaxman et al. model² fitted to the 20 simulations are plotted as the mean point estimate with 95% intervals from the 20 runs.

[Full size image](#)

However, this does not on its own show that the converse is necessarily true. To evaluate competing explanations for the observed dynamics of transmission, additional empirical evidence—such as NPI efficacy or alternative epidemiological explanations—is needed.

In summary, we believe that the additional evidence we present here confirms that the key conclusion from our paper is robust: within our model we can conclude that all NPIs together brought the epidemic under control; lockdown had the strongest effect and was identifiable; and the precise effect of the other NPIs was not identifiable.

Although our work shows that lockdowns had the largest effect size, we did not and do not claim that they were the only path to controlling the virus; merely that among the NPIs we considered, lockdown was the most effective single measure. We of course acknowledge that improvements could be made to our model, such as including random processes, partial pooling (see above) or more prior analysis. Improved models and more granular information on NPIs and population behaviour will in future hopefully give a more nuanced understanding of which measures—whether mandatory or voluntary—contributed most to reductions in transmission.

Data availability

No new data are used in this response; all data are available in the original publication.

References

1. 1.

Soltesz, K. et al. The effect of interventions on COVID-19. *Nature* <https://doi.org/10.1038/s41586-020-3025-y> (2020).

2. 2.

Flaxman, S. et al. Estimating the effects of non-pharmaceutical interventions on COVID-19 in Europe. *Nature* **584**, 257–261 (2020).

[CAS Article](#) [Google Scholar](#)

3. 3.

Flaxman, S. et al. Report 13: Estimating the number of infections and the impact of non-pharmaceutical interventions on COVID-19 in 11 European countries.

<https://doi.org/10.25561/77731> (Imperial College London, 2020).

4. 4.

Gelman, A. & Hill, J. *Data Analysis Using Applied Regression and Multilevel/Hierarchical Models* (Cambridge University Press, 2006).

5. 5.

Gelman, A., Carlin, J. B., Stern, H. S. & Rubin, D. B. *Bayesian Data Analysis* 2nd edn (Chapman & Hall/CRC, 2003).

6. 6.

Laird, N. M. & Ware, J. H. Random-effects models for longitudinal data. *Biometrics* **38**, 963–974 (1982).

[CAS](#) [Article](#) [Google Scholar](#)

7. 7.

Efron, B. & Morris, C. Data analysis using Stein's estimator and its generalizations. *J. Am. Stat. Assoc.* **70**, 311–319 (1975).

[Article](#) [Google Scholar](#)

8. 8.

Belsley, D. A., Kuh, E. & Welsch, R. E. *Regression Diagnostics: Identifying Influential Data and Sources of Collinearity* (John Wiley & Sons, 2005).

[Download references](#)

Acknowledgements

We would like to acknowledge Microsoft AI for Health for their grant of Azure Cloud Computing.

Author information

Author notes

1. These authors contributed equally: Seth Flaxman, Swapnil Mishra, James Scott, Neil Ferguson, Axel Gandy, Samir Bhatt

Affiliations

1. Department of Mathematics, Imperial College London, London, UK
Seth Flaxman, James Scott & Axel Gandy
2. MRC Centre for Global Infectious Disease Analysis, Abdul Latif Jameel Institute for Disease and Emergency Analytics (J-IDEA), Imperial College London, London, UK
Swapnil Mishra, Neil Ferguson & Samir Bhatt

Authors

1. Seth Flaxman
[View author publications](#)

You can also search for this author in [PubMed](#) [Google Scholar](#)

2. Swapnil Mishra
[View author publications](#)

You can also search for this author in [PubMed](#) [Google Scholar](#)

3. James Scott
[View author publications](#)

You can also search for this author in [PubMed](#) [Google Scholar](#)

4. Neil Ferguson
[View author publications](#)

You can also search for this author in [PubMed](#) [Google Scholar](#)

5. Axel Gandy
[View author publications](#)

You can also search for this author in [PubMed](#) [Google Scholar](#)

6. Samir Bhatt
[View author publications](#)

You can also search for this author in [PubMed](#) [Google Scholar](#)

Contributions

All authors analysed, wrote and drafted this response. The work done in this response was performed by a subset of the original authorship, and therefore many of the original authors have been excluded. A new author who contributed to the R package used in this work has been added (J.S.).

Corresponding author

Correspondence to [Samir Bhatt](#).

Ethics declarations

Competing interests

The authors declare no competing interests.

Additional information

Publisher's note Springer Nature remains neutral with regard to jurisdictional claims in published maps and institutional affiliations.

Extended data figures and tables

[Extended Data Fig. 1 Effect-size plot for each intervention for a partial pool model, the Flaxman et al. model and the Soltesz et al. full pool model.](#)

Data are mean and 95% credible intervals. The blue lines show the fits with all 11 countries; additional lines are from holding countries out and refitting. For example, the red line for shows a fit in which the UK data are not used, and the model is fitted to the 10 remaining countries. These results show that the full pool model is not robust to outliers.

Rights and permissions

[Reprints and Permissions](#)

About this article



Check for
updates

Cite this article

Flaxman, S., Mishra, S., Scott, J. *et al.* Reply to: The effect of interventions on COVID-19. *Nature* **588**, E29–E32 (2020). <https://doi.org/10.1038/s41586-020-3026-x>

[Download citation](#)

- Published: 23 December 2020
- Issue Date: 24 December 2020
- DOI: <https://doi.org/10.1038/s41586-020-3026-x>

Comments

By submitting a comment you agree to abide by our [Terms](#) and [Community Guidelines](#). If you find something abusive or that does not comply with our terms or guidelines please flag it as inappropriate.

[Download PDF](#)

Associated Content

Nature | Article

[Estimating the effects of non-pharmaceutical interventions on COVID-19 in Europe](#)

- Seth Flaxman
- , Swapnil Mishra
- , Axel Gandy
- , H. Juliette T. Unwin
- , Thomas A. Mellan
- , Helen Coupland

- , Charles Whittaker
- , Harrison Zhu
- , Tresnia Berah
- , Jeffrey W. Eaton
- , Mélodie Monod
- , Pablo N. Perez-Guzman
- , Nora Schmit
- , Lucia Cilloni
- , Kylie E. C. Ainslie
- , Marc Baguelin
- , Adhiratha Boonyasiri
- , Olivia Boyd
- , Lorenzo Cattarino
- , Laura V. Cooper
- , Zulma Cucunubá
- , Gina Cuomo-Dannenburg
- , Amy Dighe
- , Bimandra Djaafara
- , Ilaria Dorigatti
- , Sabine L. van Elsland
- , Richard G. FitzJohn
- , Katy A. M. Gaythorpe
- , Lily Geidelberg
- , Nicholas C. Grassly
- , William D. Green
- , Timothy Hallett
- , Arran Hamlet
- , Wes Hinsley
- , Ben Jeffrey
- , Edward Knock
- , Daniel J. Laydon
- , Gemma Nedjati-Gilani
- , Pierre Nouvellet
- , Kris V. Parag
- , Igor Siveroni
- , Hayley A. Thompson
- , Robert Verity
- , Erik Volz
- , Caroline E. Walters
- , Haowei Wang
- , Yuanrong Wang
- , Oliver J. Watson

- , Peter Winskill
 - , Xiaoyue Xi
 - , Patrick G. T. Walker
 - , Azra C. Ghani
 - , Christl A. Donnelly
 - , Steven Riley
 - , Michaela A. C. Vollmer
 - , Neil M. Ferguson
 - , Lucy C. Okell
 - & Samir Bhatt
-

This article was downloaded by **calibre** from <https://www.nature.com/articles/s41586-020-3026-x>

| [Section menu](#) | [Main menu](#) |

Amendments & Corrections

- [**Author Correction: Fasting-mimicking diet and hormone therapy induce breast cancer regression**](#) [04 December 2020]
Author Correction •
- [**Author Correction: Coupling of hippocampal theta and ripples with pontogeniculoccipital waves**](#) [09 December 2020]
Author Correction •
- [**Author Correction: Virological assessment of hospitalized patients with COVID-2019**](#) [11 December 2020]
Author Correction •
- [**Author Correction: Enteric neurons increase maternal food intake during reproduction**](#) [11 December 2020]
Author Correction •
- [**Publisher Correction: Self-assembled poly-catenanes from supramolecular toroidal building blocks**](#) [09 December 2020]
Publisher Correction •

Author Correction: Fasting-mimicking diet and hormone therapy induce breast cancer regression

[Download PDF](#)

- Author Correction
- [Published: 04 December 2020](#)

Author Correction: Fasting-mimicking diet and hormone therapy induce breast cancer regression

- [Irene Caffa](#)^{1 na1},
- [Vanessa Spagnolo](#)^{2,3 na1},
- [Claudio Vernieri](#)^{3,4},
- [Francesca Valdemarin](#)^{1,5},
- [Pamela Becherini](#)^{1,5},
- [Min Wei](#)⁶,
- [Sebastian Brandhorst](#)⁶,
- [Chiara Zucal](#)⁷,
- [Else Driehuis](#)^{8,9},
- [Lorenzo Ferrando](#) [ORCID: orcid.org/0000-0002-4025-7930](#)⁵,
- [Francesco Piacente](#)^{1,5},
- [Alberto Tagliafico](#)¹⁰,
- [Michele Cilli](#)¹,
- [Luca Mastracci](#)^{1,11},
- [Valerio G. Vellone](#)^{1,11},
- [Silvano Piazza](#) [ORCID: orcid.org/0000-0002-7156-5434](#)⁷,
- [Anna Laura Cremonini](#)^{1,5},
- [Raffaella Gradaschi](#)¹,

- [Carolina Mantero¹](#),
- [Mario Passalacqua](#) [ORCID: orcid.org/0000-0003-2779-6259¹²](#),
- [Alberto Ballestrero^{1,5}](#),
- [Gabriele Zoppoli^{1,5}](#),
- [Michele Cea](#) [ORCID: orcid.org/0000-0003-3345-0799^{1,5}](#),
- [Annalisa Arrighi⁵](#),
- [Patrizio Odetti^{1,5}](#),
- [Fiammetta Monacelli^{1,5}](#),
- [Giulia Salvadori](#) [ORCID: orcid.org/0000-0001-5175-2868^{2,3}](#),
- [Salvatore Cortellino³](#),
- [Hans Clevers](#) [ORCID: orcid.org/0000-0002-3077-5582^{8,9,13}](#),
- [Filippo De Braud^{2,4}](#),
- [Samir G. Sukkar¹](#),
- [Alessandro Provenzani⁷](#),
- [Valter D. Longo](#) [ORCID: orcid.org/0000-0002-0946-7534^{3,6 na2}](#) &
- [Alessio Nencioni](#) [ORCID: orcid.org/0000-0001-5068-8884^{1,5 na2}](#)

[Nature volume 588](#), page E33(2020) [Cite this article](#)

- 1550 Accesses
- 3 Altmetric
- [Metrics details](#)

Subjects

- [Breast cancer](#)
- [Cancer metabolism](#)

The [Original Article](#) was published on 15 July 2020

[Download PDF](#)

Correction to: *Nature* <https://doi.org/10.1038/s41586-020-2502-7> Published online 15 July 2020

In this Article, there are several errors in the attribution of affiliations to authors. Francesca Valdemanin and Francesco Piacente should have affiliations 1 (IRCCS Ospedale Policlinico San Martino, Genoa, Italy) and 5 (Department of Internal Medicine and Medical Specialties, University of Genoa, Genoa, Italy) rather than 1 and 2 (Department of Oncology and Hemato-Oncology, University of Milan, Milan, Italy); Lorenzo Ferrando should have affiliation 5 rather than 1; and Valerio G. Vellone should have affiliations 1 and 11 (Department of Integrated Surgical and Diagnostic Sciences, University of Genoa, Genoa, Italy) rather than 2 and 11. In Fig. 2e, the *P* values for the comparison of ‘TMX’ and ‘Fasting + TMX’ and for the comparison of ‘TMX’ and ‘FMD + TMX’ should both be 0.0001 instead of 0.6873. In the Methods section ‘Cell lines and reagents’, ‘tamoxifen and V’ should read ‘tamoxifen and **fulvestrant**’. In the Methods section ‘Animal models’, the text ‘(experiments shown in Fig. 2c, d...)’ should read ‘(experiments shown in Fig. 2a, b...)’, and in the equation for tumour volume, the 2 should be superscript such that the equation becomes ‘tumour volume = ($w^2 \times W$) $\times \pi/6$ '. In the first sentence of the Methods section ‘Tissue preparation, histology and immunohistochemistry’, the text ‘and breast gland’ should be removed to read ‘Tissue samples of uterus were formalin fixed...’. In the Methods section ‘Clinical studies of FMDs in patients undergoing ET for HR⁺ BC’, ‘effects of the FMD on blood growth’ should read ‘effects of the FMD on blood growth **factors**’. In the caption of Extended Data Fig. 1e, ‘with or without STS, TMX or FULV, or their combinations...’ should be changed to ‘with or without STS, FULV, or their combinations...’. In the legend of Extended Data Fig. 3, panel e should not be cited in the legends for Extended Data Fig. 3d and f. In addition, owing to an error during the production process, ‘EGR1’ was incorrectly defined as ‘epidermal growth factor 1’ instead of ‘early growth response protein 1’. The original Article has been corrected online.

Author information

Author notes

1. These authors contributed equally: Irene Caffa, Vanessa Spagnolo
2. These authors jointly supervised this work: Valter D. Longo, Alessio Nencioni

Affiliations

1. IRCCS Ospedale Policlinico San Martino, Genoa, Italy

Irene Caffa, Francesca Valdemanin, Pamela Becherini, Francesco Piacente, Michele Cilli, Luca Mastracci, Valerio G. Vellone, Anna Laura Cremonini, Raffaella Gradaschi, Carolina Mantero, Alberto Ballestrero, Gabriele Zoppoli, Michele Cea, Patrizio Odetti, Fiammetta Monacelli, Samir G. Sukkar & Alessio Nencioni

2. Department of Oncology and Hemato-Oncology, University of Milan, Milan, Italy

Vanessa Spagnolo, Giulia Salvadori & Filippo De Braud

3. IFOM, FIRC Institute of Molecular Oncology, Milan, Italy

Vanessa Spagnolo, Claudio Vernieri, Giulia Salvadori, Salvatore Cortellino & Valter D. Longo

4. Medical Oncology and Hematology Department, Fondazione IRCCS Istituto Nazionale dei Tumori, Milan, Italy

Claudio Vernieri & Filippo De Braud

5. Department of Internal Medicine and Medical Specialties, University of Genoa, Genoa, Italy

Francesca Valdemanin, Pamela Becherini, Lorenzo Ferrando, Francesco Piacente, Anna Laura Cremonini, Alberto Ballestrero, Gabriele Zoppoli, Michele Cea, Annalisa Arrighi, Patrizio Odetti, Fiammetta Monacelli & Alessio Nencioni

6. Longevity Institute, Leonard Davis School of Gerontology and Department of Biological Sciences, University of Southern California, Los Angeles, CA, USA

Min Wei, Sebastian Brandhorst & Valter D. Longo

7. Department of Cellular, Computational, and Integrative Biology (CIBIO), University of Trento, Trento, Italy

Chiara Zucal, Silvano Piazza & Alessandro Provenzani

8. Oncode Institute and Hubrecht Institute, Royal Netherlands Academy of Arts and Sciences, Utrecht, The Netherlands

Else Driehuis & Hans Clevers

9. University Medical Center Utrecht, Utrecht, The Netherlands

Else Driehuis & Hans Clevers

10. Department of Health Sciences, University of Genoa, Genoa, Italy

Alberto Tagliafico

11. Department of Integrated Surgical and Diagnostic Sciences, University of Genoa, Genoa, Italy

Luca Mastracci & Valerio G. Vellone

12. Department of Experimental Medicine, University of Genoa, Genoa, Italy

Mario Passalacqua

13. Princess Maxima Center for Pediatric Oncology, Utrecht, The Netherlands

Hans Clevers

Authors

1. Irene Caffa

[View author publications](#)

You can also search for this author in [PubMed](#) [Google Scholar](#)

2. Vanessa Spagnolo

[View author publications](#)

You can also search for this author in [PubMed](#) [Google Scholar](#)

3. Claudio Vernieri

[View author publications](#)

You can also search for this author in [PubMed](#) [Google Scholar](#)

4. Francesca Valdemarin

[View author publications](#)

You can also search for this author in [PubMed](#) [Google Scholar](#)

5. Pamela Becherini

[View author publications](#)

You can also search for this author in [PubMed](#) [Google Scholar](#)

6. Min Wei

[View author publications](#)

You can also search for this author in [PubMed](#) [Google Scholar](#)

7. Sebastian Brandhorst

[View author publications](#)

You can also search for this author in [PubMed](#) [Google Scholar](#)

8. Chiara Zucal

[View author publications](#)

You can also search for this author in [PubMed](#) [Google Scholar](#)

9. Else Driehuis

[View author publications](#)

You can also search for this author in [PubMed](#) [Google Scholar](#)

10. Lorenzo Ferrando

[View author publications](#)

You can also search for this author in [PubMed](#) [Google Scholar](#)

11. Francesco Piacente

[View author publications](#)

You can also search for this author in [PubMed](#) [Google Scholar](#)

12. Alberto Tagliafico

[View author publications](#)

You can also search for this author in [PubMed](#) [Google Scholar](#)

13. Michele Cilli

[View author publications](#)

You can also search for this author in [PubMed](#) [Google Scholar](#)

14. Luca Mastracci

[View author publications](#)

You can also search for this author in [PubMed](#) [Google Scholar](#)

15. Valerio G. Vellone

[View author publications](#)

You can also search for this author in [PubMed](#) [Google Scholar](#)

16. Silvano Piazza

[View author publications](#)

You can also search for this author in [PubMed](#) [Google Scholar](#)

17. Anna Laura Cremonini
[View author publications](#)

You can also search for this author in [PubMed](#) [Google Scholar](#)

18. Raffaella Gradaschi
[View author publications](#)

You can also search for this author in [PubMed](#) [Google Scholar](#)

19. Carolina Mantero
[View author publications](#)

You can also search for this author in [PubMed](#) [Google Scholar](#)

20. Mario Passalacqua
[View author publications](#)

You can also search for this author in [PubMed](#) [Google Scholar](#)

21. Alberto Ballestrero
[View author publications](#)

You can also search for this author in [PubMed](#) [Google Scholar](#)

22. Gabriele Zoppoli
[View author publications](#)

You can also search for this author in [PubMed](#) [Google Scholar](#)

23. Michele Cea
[View author publications](#)

You can also search for this author in [PubMed](#) [Google Scholar](#)

24. Annalisa Arrighi
[View author publications](#)

You can also search for this author in [PubMed](#) [Google Scholar](#)

25. Patrizio Odetti

[View author publications](#)

You can also search for this author in [PubMed](#) [Google Scholar](#)

26. Fiammetta Monacelli

[View author publications](#)

You can also search for this author in [PubMed](#) [Google Scholar](#)

27. Giulia Salvadori

[View author publications](#)

You can also search for this author in [PubMed](#) [Google Scholar](#)

28. Salvatore Cortellino

[View author publications](#)

You can also search for this author in [PubMed](#) [Google Scholar](#)

29. Hans Clevers

[View author publications](#)

You can also search for this author in [PubMed](#) [Google Scholar](#)

30. Filippo De Braud

[View author publications](#)

You can also search for this author in [PubMed](#) [Google Scholar](#)

31. Samir G. Sukkar

[View author publications](#)

You can also search for this author in [PubMed](#) [Google Scholar](#)

32. Alessandro Provenzani

[View author publications](#)

You can also search for this author in [PubMed](#) [Google Scholar](#)

33. Valter D. Longo

[View author publications](#)

You can also search for this author in [PubMed](#) [Google Scholar](#)

34. Alessio Nencioni

[View author publications](#)

You can also search for this author in [PubMed](#) [Google Scholar](#)

Corresponding authors

Correspondence to [Valter D. Longo](#) or [Alessio Nencioni](#).

Rights and permissions

[Reprints and Permissions](#)

About this article



Check for
updates

Cite this article

Caffa, I., Spagnolo, V., Vernieri, C. *et al.* Author Correction: Fasting-mimicking diet and hormone therapy induce breast cancer regression. *Nature* **588**, E33 (2020). <https://doi.org/10.1038/s41586-020-2957-6>

[Download citation](#)

- Published: 04 December 2020

- Issue Date: 24 December 2020
- DOI: <https://doi.org/10.1038/s41586-020-2957-6>

Comments

By submitting a comment you agree to abide by our [Terms](#) and [Community Guidelines](#). If you find something abusive or that does not comply with our terms or guidelines please flag it as inappropriate.

[Download PDF](#)

This article was downloaded by **calibre** from <https://www.nature.com/articles/s41586-020-2957-6>

| [Section menu](#) | [Main menu](#) |

Author Correction: Coupling of hippocampal theta and ripples with pontogeniculooccipital waves

[Download PDF](#)

- Author Correction
- [Published: 09 December 2020](#)

Author Correction: Coupling of hippocampal theta and ripples with pontogeniculooccipital waves

- [Juan F. Ramirez-Villegas](#)^{1,2} nAff8,
- [Michel Besserve](#) [ORCID: orcid.org/0000-0003-0025-2323](#)^{1,3},
- [Yusuke Murayama](#)^{1,4},
- [Henry C. Evrard](#)^{1,4,5,6},
- [Axel Oeltermann](#)¹ &
- [Nikos K. Logothetis](#) [ORCID: orcid.org/0000-0001-7728-4118](#)^{1,4,7}

[Nature](#) volume 588, page E34 (2020) [Cite this article](#)

- 600 Accesses
- 2 Altmetric
- [Metrics details](#)

Subjects

- [Anatomy](#)
- [Cognitive neuroscience](#)
- [Neuroscience](#)

The [Original Article](#) was published on 18 November 2020

[Download PDF](#)

Correction to: *Nature* <https://doi.org/10.1038/s41586-020-2914-4> Published online 18 November 2020

In this Article, author Henry C. Evrard should have been associated with the affiliations ‘Nathan Kline Institute for Psychiatric Research, Orangeburg, NY, USA’ and ‘International Center for Primate Brain Research, Songjiang, Shanghai, China’, in addition to their other affiliations (‘Department of Physiology of Cognitive Processes, Max Planck Institute...’ and ‘Werner-Reichardt Centre for Integrative Neuroscience...’). The original Article has been corrected online.

Author information

Author notes

1. Juan F. Ramirez-Villegas

Present address: IST Austria (Institute of Science and Technology Austria), Klosterneuburg, Austria

Affiliations

1. Department of Physiology of Cognitive Processes, Max Planck Institute for Biological Cybernetics, Tübingen, Germany
Juan F. Ramirez-Villegas, Michel Besserve, Yusuke Murayama, Henry C. Evrard, Axel Oeltermann & Nikos K. Logothetis
2. Graduate School of Neural and Behavioral Sciences, International Max Planck Research School, Eberhard-Karls University of Tübingen, Tübingen, Germany
Juan F. Ramirez-Villegas

3. Department of Empirical Inference, Max Planck Institute for Intelligent Systems, Tübingen, Germany

Michel Besserve

4. International Center for Primate Brain Research, Songjiang, Shanghai, China

Yusuke Murayama, Henry C. Evrard & Nikos K. Logothetis

5. Werner-Reichardt Centre for Integrative Neuroscience, Tübingen, Germany

Henry C. Evrard

6. Nathan Kline Institute for Psychiatric Research, Orangeburg, NY, USA

Henry C. Evrard

7. Centre for Imaging Sciences, Biomedical Imaging Institute, The University of Manchester, Manchester, UK

Nikos K. Logothetis

Authors

1. Juan F. Ramirez-Villegas

[View author publications](#)

You can also search for this author in [PubMed](#) [Google Scholar](#)

2. Michel Besserve

[View author publications](#)

You can also search for this author in [PubMed](#) [Google Scholar](#)

3. Yusuke Murayama

[View author publications](#)

You can also search for this author in [PubMed](#) [Google Scholar](#)

4. Henry C. Evrard

[View author publications](#)

You can also search for this author in [PubMed](#) [Google Scholar](#)

5. Axel Oeltermann

[View author publications](#)

You can also search for this author in [PubMed](#) [Google Scholar](#)

6. Nikos K. Logothetis

[View author publications](#)

You can also search for this author in [PubMed](#) [Google Scholar](#)

Corresponding author

Correspondence to [Nikos K. Logothetis](#).

Rights and permissions

[Reprints and Permissions](#)

About this article



Check for
updates

Cite this article

Ramirez-Villegas, J.F., Besserve, M., Murayama, Y. *et al.* Author Correction: Coupling of hippocampal theta and ripples with

pontogeniculooccipital waves. *Nature* **588**, E34 (2020).
<https://doi.org/10.1038/s41586-020-03068-9>

[Download citation](#)

- Published: 09 December 2020
- Issue Date: 24 December 2020
- DOI: <https://doi.org/10.1038/s41586-020-03068-9>

Comments

By submitting a comment you agree to abide by our [Terms](#) and [Community Guidelines](#). If you find something abusive or that does not comply with our terms or guidelines please flag it as inappropriate.

[Download PDF](#)

This article was downloaded by **calibre** from <https://www.nature.com/articles/s41586-020-03068-9>

Author Correction: Virological assessment of hospitalized patients with COVID-2019

[Download PDF](#)

- Author Correction
- [Published: 11 December 2020](#)

Author Correction: Virological assessment of hospitalized patients with COVID-2019

- [Roman Wölfel](#)^{1 na1},
- [Victor M. Corman](#)^{2 na1},
- [Wolfgang Guggemos](#)^{3 na1},
- [Michael Seilmaier](#)³,
- [Sabine Zange](#)¹,
- [Marcel A. Müller](#)²,
- [Daniela Niemeyer](#) [ORCID: orcid.org/0000-0002-1897-6365](#)²,
- [Terry C. Jones](#) [ORCID: orcid.org/0000-0003-1120-9531](#)^{2,4},
- [Patrick Vollmar](#)¹,
- [Camilla Rothe](#)⁵,
- [Michael Hoelscher](#)⁵,
- [Tobias Bleicker](#)²,
- [Sebastian Brünink](#)²,
- [Julia Schneider](#) [ORCID: orcid.org/0000-0002-0494-1022](#)²,
- [Rosina Ehmann](#)¹,
- [Katrin Zwirglmaier](#)¹,
- [Christian Drosten](#) [ORCID: orcid.org/0000-0001-7923-0519](#)^{2 na2} &
- [Clemens Wendtner](#) [ORCID: orcid.org/0000-0003-2866-2260](#)^{3 na2}

[Nature](#) volume 588, page E35(2020) [Cite this article](#)

- 991 Accesses
- 2 Citations
- 2 Altmetric
- [Metrics details](#)

Subjects

- [Epidemiology](#)
- [SARS-CoV-2](#)
- [Viral infection](#)

The [Original Article](#) was published on 01 April 2020

[Download PDF](#)

Correction to: *Nature* <https://doi.org/10.1038/s41586-020-2196-x> Published online 01 April 2020

In this Article, the text “For swab and sputum samples, interpolation based on a probit model was done to obtain laboratory-based infectivity criteria for the discharge of patients (Fig. 1e, f).” should have been updated when another panel was added to Fig. 1. The new Fig. 1f and g only contain data from sputum samples because their viral loads are relevant for the discharge decision. The sentence should read: “For sputum samples, interpolation based on a probit model was done to obtain laboratory-based infectivity criteria for the discharge of patients (Fig. 1f, g).” This error has been corrected online.

Author information

Author notes

1. These authors contributed equally: Roman Wölfel, Victor M. Corman, Wolfgang Guggemos
2. These authors jointly supervised this work: Christian Drosten, Clemens Wendtner

Affiliations

1. Bundeswehr Institute of Microbiology, Munich, Germany
Roman Wölfel, Sabine Zange, Patrick Vollmar, Rosina Ehmann & Katrin Zwirglmaier
2. Charité Universitätsmedizin Berlin, Berlin, Germany
Victor M. Corman, Marcel A. Müller, Daniela Niemeyer, Terry C. Jones, Tobias Bleicker, Sebastian Brünink, Julia Schneider & Christian Drosten
3. Klinikum München-Schwabing, Munich, Germany
Wolfgang Guggemos, Michael Seilmaier & Clemens Wendtner
4. Center for Pathogen Evolution, Department of Zoology, University of Cambridge, Cambridge, UK
Terry C. Jones
5. University Hospital LMU Munich, Munich, Germany
Camilla Rothe & Michael Hoelscher

Authors

1. Roman Wölfel
[View author publications](#)

You can also search for this author in [PubMed](#) [Google Scholar](#)

2. Victor M. Corman

[View author publications](#)

You can also search for this author in [PubMed](#) [Google Scholar](#)

3. Wolfgang Guggemos

[View author publications](#)

You can also search for this author in [PubMed](#) [Google Scholar](#)

4. Michael Seilmaier

[View author publications](#)

You can also search for this author in [PubMed](#) [Google Scholar](#)

5. Sabine Zange

[View author publications](#)

You can also search for this author in [PubMed](#) [Google Scholar](#)

6. Marcel A. Müller

[View author publications](#)

You can also search for this author in [PubMed](#) [Google Scholar](#)

7. Daniela Niemeyer

[View author publications](#)

You can also search for this author in [PubMed](#) [Google Scholar](#)

8. Terry C. Jones

[View author publications](#)

You can also search for this author in [PubMed](#) [Google Scholar](#)

9. Patrick Vollmar

[View author publications](#)

You can also search for this author in [PubMed](#) [Google Scholar](#)

10. Camilla Rothe

[View author publications](#)

You can also search for this author in [PubMed](#) [Google Scholar](#)

11. Michael Hoelscher

[View author publications](#)

You can also search for this author in [PubMed](#) [Google Scholar](#)

12. Tobias Bleicker

[View author publications](#)

You can also search for this author in [PubMed](#) [Google Scholar](#)

13. Sebastian Brünink

[View author publications](#)

You can also search for this author in [PubMed](#) [Google Scholar](#)

14. Julia Schneider

[View author publications](#)

You can also search for this author in [PubMed](#) [Google Scholar](#)

15. Rosina Ehmann

[View author publications](#)

You can also search for this author in [PubMed](#) [Google Scholar](#)

16. Katrin Zwirglmaier

[View author publications](#)

You can also search for this author in [PubMed](#) [Google Scholar](#)

17. Christian Drosten

[View author publications](#)

You can also search for this author in [PubMed](#) [Google Scholar](#)

18. Clemens Wendtner

[View author publications](#)

You can also search for this author in [PubMed](#) [Google Scholar](#)

Corresponding authors

Correspondence to [Christian Drosten](#) or [Clemens Wendtner](#).

Rights and permissions

[Reprints and Permissions](#)

About this article



Check for
updates

Cite this article

Wölfel, R., Corman, V.M., Guggemos, W. *et al.* Author Correction: Virological assessment of hospitalized patients with COVID-2019. *Nature* **588**, E35 (2020). <https://doi.org/10.1038/s41586-020-2984-3>

[Download citation](#)

- Published: 11 December 2020
- Issue Date: 24 December 2020
- DOI: <https://doi.org/10.1038/s41586-020-2984-3>

Comments

By submitting a comment you agree to abide by our [Terms](#) and [Community Guidelines](#). If you find something abusive or that does not comply with our terms or guidelines please flag it as inappropriate.

[Download PDF](#)

This article was downloaded by **calibre** from <https://www.nature.com/articles/s41586-020-2984-3>

| [Section menu](#) | [Main menu](#) |

Author Correction: Enteric neurons increase maternal food intake during reproduction

[Download PDF](#)

- Author Correction
- [Published: 11 December 2020](#)

Author Correction: Enteric neurons increase maternal food intake during reproduction

- [Dafni Hadjieconomou](#)^{1,2},
- [George King](#)^{1,2},
- [Pedro Gaspar](#)^{1,2},
- [Alessandro Mineo](#)^{1,2},
- [Laura Blackie](#)^{1,2},
- [Tomotsune Ameku](#)^{1,2},
- [Chris Studd](#)^{1,2},
- [Alex de Mendoza](#) [ORCID: orcid.org/0000-0002-6441-6529](#)^{3,4,5},
- [Fengqiu Diao](#)⁶,
- [Benjamin H. White](#)⁶,
- [André E. X. Brown](#)^{1,2},
- [Pierre-Yves Plaçais](#)⁷,
- [Thomas Préat](#) [ORCID: orcid.org/0000-0001-9976-1763](#)⁷ &
- [Irene Miguel-Aliaga](#) [ORCID: orcid.org/0000-0002-1082-5108](#)^{1,2}

[Nature](#) volume 588, page E36(2020) [Cite this article](#)

- 746 Accesses
- 4 Altmetric

- [Metrics details](#)

Subjects

- [Drosophila](#)
- [Feeding behaviour](#)
- [Reproductive biology](#)

The [Original Article](#) was published on 28 October 2020

[Download PDF](#)

Correction to: *Nature* <https://doi.org/10.1038/s41586-020-2866-8> Published online 28 October 2020

In this Article, there were three issues with the references. First, citations to Ahmed et al. (2020)¹ and Zipper et al. (2020)², published while our manuscript was in revision, were missing, and have now been added as refs. 95 and 96 after the modified sentence: “Levels of the steroid hormone ecdysone, which promotes egg production **and intestinal stem-cell proliferation**, increase after mating”. Second, a citation to Kohl and Dulac (2018)³ was inadvertently deleted during the re-formatting of the Article and has now been added as ref. 94 after the sentence: “Internal state has profound effects on brain function”. Third, a typo in ref. 38 of the original Article (Davey and Treherne, 1964) has also been rectified. Finally, ‘reduce’ should have been ‘increase’ in the text: “Expression of a dominant-negative EcR—which targets all EcR isoforms—confined to the Ms neurons of adult flies was found to **increase** intracellular Ms levels...”. The original Article has been corrected online.

References

1. 1.

Ahmed, S. M. H. et al. Fitness trade-offs incurred by ovary-to-gut steroid signalling in *Drosophila*. *Nature* **584**, 415–419 (2020).

[CAS](#) [PubMed](#) [Google Scholar](#)

2. 2.

Zipper, L., Jassmann, D., Burgmer, S., Görlich, B. & Reiff, T. Ecdysone steroid hormone remote controls intestinal stem cell fate decisions via the PPAR γ - homolog Eip75B in *Drosophila*. *eLife* **9**, e55795 (2020).

[CAS](#) [PubMed](#) [Google Scholar](#)

3. 3.

Kohl, J. & Dulac, C. Neural control of parental behaviors. *Curr. Opin. Neurobiol.* **49**, 116–122 (2018).

[CAS](#) [Article](#) [Google Scholar](#)

[Download references](#)

Author information

Affiliations

1. MRC London Institute of Medical Sciences, London, UK

Dafni Hadjieconomou, George King, Pedro Gaspar, Alessandro Mineo, Laura Blackie, Tomotsune Ameku, Chris Studd, André E. X. Brown & Irene Miguel-Aliaga

2. Faculty of Medicine, Imperial College London, London, UK

Dafni Hadjieconomou, George King, Pedro Gaspar, Alessandro Mineo, Laura Blackie, Tomotsune Ameku, Chris Studd, André E. X. Brown & Irene Miguel-Aliaga

3. Australian Research Council Centre of Excellence in Plant Energy Biology, School of Molecular Sciences, The University of Western Australia, Perth, Western Australia, Australia

Alex de Mendoza

4. Harry Perkins Institute of Medical Research, Perth, Western Australia, Australia

Alex de Mendoza

5. School of Biological and Chemical Sciences, Queen Mary University of London, London, UK

Alex de Mendoza

6. Laboratory of Molecular Biology, National Institute of Mental Health, National Institutes of Health, Bethesda, MD, USA

Fengqiu Diao & Benjamin H. White

7. Genes and Dynamics of Memory Systems, Brain Plasticity Unit, CNRS, ESPCI Paris, PSL Research University, Paris, France

Pierre-Yves Plaçais & Thomas Préat

Authors

1. Dafni Hadjieconomou

[View author publications](#)

You can also search for this author in [PubMed](#) [Google Scholar](#)

2. George King

[View author publications](#)

You can also search for this author in [PubMed](#) [Google Scholar](#)

3. Pedro Gaspar

[View author publications](#)

You can also search for this author in [PubMed](#) [Google Scholar](#)

4. Alessandro Mineo

[View author publications](#)

You can also search for this author in [PubMed](#) [Google Scholar](#)

5. Laura Blackie

[View author publications](#)

You can also search for this author in [PubMed](#) [Google Scholar](#)

6. Tomotsune Ameku

[View author publications](#)

You can also search for this author in [PubMed](#) [Google Scholar](#)

7. Chris Studd

[View author publications](#)

You can also search for this author in [PubMed](#) [Google Scholar](#)

8. Alex de Mendoza

[View author publications](#)

You can also search for this author in [PubMed](#) [Google Scholar](#)

9. Fengqiu Diao

[View author publications](#)

You can also search for this author in [PubMed](#) [Google Scholar](#)

10. Benjamin H. White

[View author publications](#)

You can also search for this author in [PubMed](#) [Google Scholar](#)

11. André E. X. Brown

[View author publications](#)

You can also search for this author in [PubMed](#) [Google Scholar](#)

12. Pierre-Yves Plaçais

[View author publications](#)

You can also search for this author in [PubMed](#) [Google Scholar](#)

13. Thomas Préat

[View author publications](#)

You can also search for this author in [PubMed](#) [Google Scholar](#)

14. Irene Miguel-Aliaga

[View author publications](#)

You can also search for this author in [PubMed](#) [Google Scholar](#)

Corresponding author

Correspondence to [Irene Miguel-Aliaga](#).

Rights and permissions

[Reprints and Permissions](#)

About this article



Check for
updates

Cite this article

Hadjieconomou, D., King, G., Gaspar, P. *et al.* Author Correction: Enteric neurons increase maternal food intake during reproduction. *Nature* **588**, E36 (2020). <https://doi.org/10.1038/s41586-020-3013-2>

[Download citation](#)

- Published: 11 December 2020
- Issue Date: 24 December 2020
- DOI: <https://doi.org/10.1038/s41586-020-3013-2>

Comments

By submitting a comment you agree to abide by our [Terms](#) and [Community Guidelines](#). If you find something abusive or that does not comply with our terms or guidelines please flag it as inappropriate.

[Download PDF](#)

This article was downloaded by **calibre** from <https://www.nature.com/articles/s41586-020-3013-2>

Publisher Correction: Self-assembled poly-catenanes from supramolecular toroidal building blocks

[Download PDF](#)

- Publisher Correction
- [Published: 09 December 2020](#)

Publisher Correction: Self-assembled poly-catenanes from supramolecular toroidal building blocks

- [Sougata Datta](#) ORCID: [orcid.org/0000-0003-2237-0857¹](https://orcid.org/0000-0003-2237-0857),
- [Yasuki Kato](#) ORCID: [orcid.org/0000-0001-5242-0777²](https://orcid.org/0000-0001-5242-0777),
- [Seiya Higashiharaguchi](#)²,
- [Keisuke Aratsu](#) ORCID: [orcid.org/0000-0001-9744-2558²](https://orcid.org/0000-0001-9744-2558),
- [Atsushi Isobe](#) ORCID: [orcid.org/0000-0001-7567-1480²](https://orcid.org/0000-0001-7567-1480),
- [Takuho Saito](#) ORCID: [orcid.org/0000-0002-5941-6006²](https://orcid.org/0000-0002-5941-6006),
- [Deepak D. Prabhu](#) ORCID: [orcid.org/0000-0003-2177-3339¹](https://orcid.org/0000-0003-2177-3339),
- [Yuichi Kitamoto](#) ORCID: [orcid.org/0000-0003-4827-6375³](https://orcid.org/0000-0003-4827-6375),
- [Martin J. Hollamby](#)⁴,
- [Andrew J. Smith](#) ORCID: [orcid.org/0000-0003-3745-7082⁵](https://orcid.org/0000-0003-3745-7082),
- [Robert Dalgliesh](#) ORCID: [orcid.org/0000-0002-6814-679X⁶](https://orcid.org/0000-0002-6814-679X),
- [Najet Mahmoudi](#)⁶,
- [Luca Pesce](#) ORCID: [orcid.org/0000-0001-6364-9577⁷](https://orcid.org/0000-0001-6364-9577),
- [Claudio Perego](#) ORCID: [orcid.org/0000-0001-8885-3080⁷](https://orcid.org/0000-0001-8885-3080),
- [Giovanni M. Pavan](#) ORCID: [orcid.org/0000-0002-3473-8471^{7,8}](https://orcid.org/0000-0002-3473-8471) &
- [Shiki Yagai](#) ORCID: [orcid.org/0000-0002-4786-8603^{1,2,3}](https://orcid.org/0000-0002-4786-8603)

- 842 Accesses
- 3 Altmetric
- [Metrics details](#)

Subjects

- [Interlocked molecules](#)
- [Supramolecular polymers](#)

The [Original Article](#) was published on 15 July 2020

[Download PDF](#)

Correction to: *Nature* <https://doi.org/10.1038/s41586-020-2445-z> Published online 15 July 2020

In this Article, owing to an error during the production process, the citation to Fig. 4d in the sentence beginning ‘In these samples, the number of toroids...’ erroneously read ‘Fig A Star of David catenane. 4d’. The original Article has been corrected online.

Author information

Affiliations

1. Department of Applied Chemistry and Biotechnology, Graduate School of Engineering, Chiba University, Chiba, Japan
Sougata Datta, Deepak D. Prabhu & Shiki Yagai
2. Division of Advanced Science and Engineering, Graduate School of Science and Engineering, Chiba University, Chiba, Japan

Yasuki Kato, Seiya Higashiharaguchi, Keisuke Aratsu, Atsushi Isobe, Takuho Saito & Shiki Yagai

3. Institute for Global Prominent Research (IGPR), Chiba University, Chiba, Japan

Yuichi Kitamoto & Shiki Yagai

4. School of Chemical and Physical Sciences, Keele University, Keele, UK

Martin J. Hollamby

5. Diamond Light Source Ltd, Diamond House, Didcot, UK

Andrew J. Smith

6. ISIS Pulsed Neutron and Muon Source, Rutherford Appleton Laboratory, Chilton, UK

Robert Dalgliesh & Najet Mahmoudi

7. Department of Innovative Technologies, University of Applied Sciences and Arts of Southern Switzerland, Manno, Switzerland

Luca Pesce, Claudio Perego & Giovanni M. Pavan

8. Department Applied Science and Techology, Politecnico di Torino, Turin, Italy

Giovanni M. Pavan

Authors

1. Sougata Datta

[View author publications](#)

You can also search for this author in [PubMed](#) [Google Scholar](#)

2. Yasuki Kato

[View author publications](#)

You can also search for this author in [PubMed](#) [Google Scholar](#)

3. Seiya Higashiharaguchi

[View author publications](#)

You can also search for this author in [PubMed](#) [Google Scholar](#)

4. Keisuke Aratsu

[View author publications](#)

You can also search for this author in [PubMed](#) [Google Scholar](#)

5. Atsushi Isobe

[View author publications](#)

You can also search for this author in [PubMed](#) [Google Scholar](#)

6. Takuho Saito

[View author publications](#)

You can also search for this author in [PubMed](#) [Google Scholar](#)

7. Deepak D. Prabhu

[View author publications](#)

You can also search for this author in [PubMed](#) [Google Scholar](#)

8. Yuichi Kitamoto

[View author publications](#)

You can also search for this author in [PubMed](#) [Google Scholar](#)

9. Martin J. Hollamby

[View author publications](#)

You can also search for this author in [PubMed](#) [Google Scholar](#)

10. Andrew J. Smith

[View author publications](#)

You can also search for this author in [PubMed](#) [Google Scholar](#)

11. Robert Dalgliesh

[View author publications](#)

You can also search for this author in [PubMed](#) [Google Scholar](#)

12. Najet Mahmoudi

[View author publications](#)

You can also search for this author in [PubMed](#) [Google Scholar](#)

13. Luca Pesce

[View author publications](#)

You can also search for this author in [PubMed](#) [Google Scholar](#)

14. Claudio Perego

[View author publications](#)

You can also search for this author in [PubMed](#) [Google Scholar](#)

15. Giovanni M. Pavan

[View author publications](#)

You can also search for this author in [PubMed](#) [Google Scholar](#)

16. Shiki Yagai

[View author publications](#)

You can also search for this author in [PubMed](#) [Google Scholar](#)

Corresponding author

Correspondence to [Shiki Yagai](#).

Rights and permissions

[Reprints and Permissions](#)

About this article



Cite this article

Datta, S., Kato, Y., Higashiharaguchi, S. *et al.* Publisher Correction: Self-assembled poly-catenanes from supramolecular toroidal building blocks. *Nature* **588**, E37 (2020). <https://doi.org/10.1038/s41586-020-3012-3>

[Download citation](#)

- Published: 09 December 2020
- Issue Date: 24 December 2020
- DOI: <https://doi.org/10.1038/s41586-020-3012-3>

Comments

By submitting a comment you agree to abide by our [Terms](#) and [Community Guidelines](#). If you find something abusive or that does not comply with our terms or guidelines please flag it as inappropriate.

[Download PDF](#)

This article was downloaded by **calibre** from <https://www.nature.com/articles/s41586-020-3012-3>